Copyright 2019. De Gruyter. All rights reserved. May not be reproduced in any form without permission from the publisher, except fair uses permitted under U.S. or applicable copyright law.

DE GRUYTER

Blahoslav Sedláček (Ed.)

MORPHOLOGY OF POLYMERS

EBSCO Publishing : eBook Collection (EBSCOhost) - printed on 2/13/2023 3:45 AM via
AN: [illegible]573 ; Blahoslav Sedlek.; Morphology of Polymers : Proceedings, 17th
Euro[illegible]ics Conference on Macromolecular Physics, Prague, Czechoslovakia, July
1518[illegible]35
Acco[illegible] ns335141

Morphology of Polymers

EBSCOhost - printed on 2/13/2023 3:45 AM via . All use subject to https://www.ebsco.com/terms-of-use

EBSCOhost - printed on 2/13/2023 3:45 AM via . All use subject to https://www.ebsco.com/terms-of-use

Morphology of Polymers

Proceedings
17th Europhysics Conference on
Macromolecular Physics
Prague, Czechoslovakia, July 15 – 18, 1985

Editor
Blahoslav Sedláček

Walter de Gruyter · Berlin · New York 1986

EBSCOhost - printed on 2/13/2023 3:45 AM via . All use subject to https://www.ebsco.com/terms-of-use

Editor

Blahoslav Sedláček, PhD., DSc.
Institute of Macromolecular Chemistry
Czechoslovak Academy of Sciences
Heyrovský sq. 2
CS-162 06 Prague 616
Czechoslovakia

Library of Congress Cataloging in Publication Data

Europhysics Conference on Macromolecular Physics (17th : 1985 : Prague, Czechoslovakia)
Morphology of polymers.
Includes bibliographies and indexes.
1. Polymers and polymerization--Congresses.
2. Crystals--Congresses. I. Sedláček, B. (Blahoslav) II. Title.
QD380.E9 1985 620.1'92 86-13546
ISBN 0-89925-183-8 (U.S.)

CIP-Kurztitelaufnahme der Deutschen Bibliothek

Morphology of polymers : proceedings / 17th Europhysics Conference on Macromolecular Physics, Prague, Czechoslovakia, July 15-18, 1985.
Ed. Blahoslav Sedláček. - Berlin ; New York : de Gruyter, 1986.
ISBN 3-11-010519-5 (Berlin)
ISBN 0-89925-183-8 (New York)
NE: Sedláček, Blahoslav [Hrsg.]; Europhysics Conference on Macromolecular Physics <17, 1985, Praha>

Copyright © 1986 by Walter de Gruyter & Co., Berlin 30.
All rights reserved, including those of translation into foreign languages. No part of this book may be reproduced in any form - by photoprint, microfilm or any other means nor transmitted nor translated into a machine language without written permission from the publisher. Printing: Gerike GmbH, Berlin. Binding: Lüderitz & Bauer Buchgewerbe GmbH, Berlin. - Printed in Germany.

EBSCOhost - printed on 2/13/2023 3:45 AM via . All use subject to https://www.ebsco.com/terms-of-use

PREFACE

The proceedings of the 17th Europhysics Conference on Macromolecular Physics, devoted to the morphology of polymers, is a collection of the majority of the main lectures, short special lectures and papers based on poster contributions given at the conference. It was held, under the sponsorship of the European Physical Society, at the Institute of Macromolecular Chemistry (Czechoslovak Academy of Sciences), Prague, on July 15-18, 1985; EPS was represented by the International Advisory Committee: F.J. Baltá Calleja (Madrid), G. Bodór (Budapest), H.H. Kausch (Lausanne), E.W. Fisher (Mainz), A. Keller (Bristol), A. Kovacs (Strasbourg), A.A. Marikhin (Leningrad), E. Martuscelli (Naples), Z. Pelzbauer (Prague), I.M. Ward (Leeds). Cosponsors were the Czechoslovak Academy of Sciences and the Union of Czechoslovak Mathematicians and Physicists.

The Conference was organized by the Local Organizing Committee consisting of: V. Kubánek (IMC Director), P. Čefelín (IMC Scientific Secretary and PMM Chairman), B. Sedláček (PMM Editor), J. Chudáček (Representative of UCSMP); Z. Pelzbauer (Chairman of the Conference); J. Baldrian, J. Biroš, F. Lednický and J. Spěváček (members of the Programme Committee); and the secretariat and technical staff of Prague Meetings on Macromolecules (PMM).

The volume deals with a broad problem spectrum of the morphology of polymers and their systems on all levels of organization, with regard to their physical and chemical properties, either static or dynamic. This multiformity of approaches to the problem studied makes it rather difficult to arrange the individual articles adequately. The system accepted (see "Contents") is therefore a compromise, intended to serve as no more than a first guideline.

In the first section, papers relating to the main lectures are collected, reviewing selected branches of polymer morphology. Section two concerns molecular and macroscopic crystallization processes. A large part of the book (third section) is devoted to the characterization of the morphology of polymers (both synthetic and natural), either homopolymers or copolymers and blends.

EBSCOhost - printed on 2/13/2023 3:45 AM via . All use subject to https://www.ebsco.com/terms-of-use

There are also some papers on failure behaviour collected in a separate subsection, irrespective of the fact that such behaviour is examined ad hoc in other contributions. Textures are the topic of the fourth section, viz. fibers and films, but excluding spherulites which are discussed or mentioned nearly in all the papers. The remaining three papers, due to their specific character, are published separately in the last section.

We tried to do our best to improve the texts so that they were really camera-ready and, which is more important, clear and understandable. Unfortunately, in view of the nature of a camera-ready publication, such an ideal can be achieved only to a limited extent. It was very gratifying, however, that many of the authors submitted excellent or nearly perfect papers; a large part of the authors had to work hard to keep the deadline and/or to improve the text within the time available. I would like to express my warm thanks to all the authors who contributed to this volume.

Also, my thanks are due to the de Gruyter Publishers and their internal and external coworkers; I greatly appreciate their careful preparation of the manuscripts, precise printing (especially with regard to the electron micrographs) and the excellent layout of the volume.

Prague, April 1986

Blahoslav Sedláček
PMM Editor

EBSCOhost - printed on 2/13/2023 3:45 AM via . All use subject to https://www.ebsco.com/terms-of-use

Contents

Morphology: A Survey

Recent Developments in Morphology of Crystalline Polymers
A. Keller 3

Influence of Chain Defects on the Perfection of Lamellar Polymer Crystals
F.J. Baltá Calleja 27

Organization in Melt-Crystallized Polymers
D.C. Bassett 47

Morphological Aspects of Fracture Phenomena
H.H. Kausch 69

Thermal History Effects in Polybutylene
P.H. Geil, K.W. Chau, A. Agarwal, and C.C. Hsu 87

Rheology-Processing-Property-Morphology Relationship in Heterogeneous Polymer Blends
Chang Dae Han and Hsiao-Ken Chuang 103

Advances in Indirect Methods of Polymer Morphology Characterization
H.G. Zachmann and R. Gehrke 119

Crystallization Processes

Relations between the Conformation of Macromolecules and their Structural Characteristics
E. Turska 141

Crystal of Polymers and of Intercalates with Polymeric Host. Relation between Morphology and Chain Conformation
J.J. Point, M.C. Colet, and M. Dosière 153

EBSCOhost - printed on 2/13/2023 3:45 AM via . All use subject to https://www.ebsco.com/terms-of-use

The Concentration Dependence of the Linear Growth Rate G_{110} in a Polyethylene Single Crystal Grown from Dilute Solution
M. Dosière, M.-Ch. Colet, and J.J. Point 171

Melting and Recrystallization of Surface Grown Poly(Ethylene) Crystals
R. Hirte and D. Zenke 179

Effect of the Addition of Polyglycol on the Melt Crystallization of Polypropylene
Ch. Bechev and J. Mishinev 189

The Study of Crystallization by TSD Method
R. Bakule, J. Nedbal, and P. Štrof 197

Quantum Interpretation of the Primary and Secondary Nucleation Rate of Polymers
A.M. Atanassov 205

Quantum Interpretation of the Secondary Nucleation Rate and the Reptation Rate Theory - A Comparative Study
A.M. Atanassov 225

Equilibrium Crystallinity and Phase Transition Mechanism of Bulk Polymers of Linear Flexible Chain Molecules
A.M. Atanassov 235

Light Emission from a Crystallizing Polymer
A.M. Atanassov 249

Morphology of Polymers and Blends

1. Polyolefins

Crystal Morphology and Molecular Interactions in Isotactic Polypropylene and its Blends
B. Lotz and J.C. Wittmann 259

Orientation in Injection Moulded Polypropylene Copolymer
A. Brenna and D. Slotfeldt-Ellingsen 271

EBSCOhost - printed on 2/13/2023 3:45 AM via . All use subject to https://www.ebsco.com/terms-of-use

Morphology of Deformed Polypropylene
M. Kojima, H. Satake, M.J. Shankernarayanan, and J.H. Magill 279

The Role of the Skin-Core Structure in the Ageing of Semi Crystalline Polymers
J.P. Trotignon, J. Verdu, and R. Roques 297

Crystal Structure of γ-Irradiated and Thermal Treated Polypropylene
V.P. Krestev, B. Dobreva, A.M. Atanassov, and E.T. Nedkov 303

Selective Etching of Polyolefines. II. Isotactic Polypropylene Linear and Branched Polyethylene
F. Rybnikář 309

Structure and Deformation of Polyethylene Spherulites
Kaoru Shimamura 319

Influence of Molecular Structure on the Morphology of Semi-Crystalline Polymers
G.H. Michler and I. Naumann 329

Morphology in Crosslinked Polyethylene
U.W. Gedde 337

Polypropylene Morphology in Blends with Polyethylene
M. Plešek and Z. Maláč 347

Spin Diffusion Studies on Morphology of Linear Polyethylene
L. Deutschbein, B. Walter, and T. Willing 355

Heterogeneity of Linear Low Density Polyethylene as Studied by Fractionation and DSC
V.B.F. Mathot, H.M. Schoffeleers, A.M.G. Brands, and M.F.J. Pijpers 363

2. Other Polymers

The Formation of PVC Morphology and its Importance during Subsequent Processing
M. Clark 371

EBSCOhost - printed on 2/13/2023 3:45 AM via . All use subject to https://www.ebsco.com/terms-of-use

The Effect of Processing on Morphology of Heterogeneous Polymer Systems
M. Kozłowski and J. Pigłowski 381

Lamellar Textures in Melt-Crystallized Polystyrene
A.S. Vaughan, D.C. Bassett, and R.H. Olley 387

The Different TSL Behaviour of Statistical and Block Butadiene-Styrene Copolymers
J. Pospíšil and A. Havránek 399

Morphologic Characteristics of Products of Styrene-Butadiene 1,3'-Polybutadiene Copolymerization in the Presence of $ZnCl_2$ and a Network Reagent
D. Kechajov 405

The Effects of Molecular Weight on the Morphology and Crystallization of Cis-1,4-Polybutadiene
Enle Zhou, Guiping Jing, Huizhen Hu, Xuemei Xu, and Hong Li 411

Morphological Study of the Melting of Polycaprolactone/Poly(Styrene-Co-Acrylonitrile) Blends Using Synchrotron Radiation
M. Vandermarliere, G. Groeninckx, H. Reynaers, C. Riekel, and M.H.J. Koch 421

Synthesis, Morphology and Properties of Rubber Modified Poly(ε-Caprolactam) by Fast in Situ-Polymerization
G.C. Alfonso, G. Dondero, S. Russo, and A. Turturro 427

Morphology and Phase Transitions of Crystalline Polyphosphazenes
M. Kojima and J.H. Magill 435

Morphology of Polycarbonate Crystallized under the Influence of Solvent Vapours
I. Daniewska, E. Kocinska, and Z. Dobkowski 449

Crystallization Behaviour of Poly(Ethylene Terephthalate) Glasses with Different Orientation
Ch. Bechev, L.L. Chapoy, and J. Mishinev 457

Ring Spherulite Structure in Polyethylene Adipate
J. Foks, H. Janik, J. Osipiuk, and Z. Głowacki 463

EBSCOhost - printed on 2/13/2023 3:45 AM via . All use subject to https://www.ebsco.com/terms-of-use

Fully Oriented Crystalline Polyacetylene of Non-Fibrous Morphology
G. Leissing, O. Leitner, and H. Kahlert 469

Morphological Changes in the Copolymer of Trioxan with Phenylglycidyl Ether
R. Mateva, G. Sirashki, and M. Krasteva 477

Recent WAXS- and TEM-Results on Phase Transition of Cellulose
H.-P. Fink, H.J. Purz, and B. Philipp 487

Ageing of Oriented and Non-Oriented Cellulose Triacetate under Heat Treatment
M.K. Kurbanaliev, Kh.M. Abdullaev, and
V.A. Mirzoeva 501

A Study on Crystalline Structure of Polyglycine I and II at Low Temperature
J. Garbarczyk 509

Thermotropic Main-Chain Polyesters
L. Makaruk, H. Polańska, and B. Wazyńska 515

The Role of Mesomorphic State in the Formation of Structure and Properties of Poly(Urethane Methacrylates)
L.A. Sukhareva and Z. Pelzbauer 521

3. Failure Behaviour

A One Polymer Composite Polyethylene Film: Failure Morphology
R. Hirte, V. Hnát, J.P. Melior, Z. Pelzbauer,
M. Raab, E. Schulz, and D. Zenke 527

Possibilities of the Estimation of Polymer Morphology from Fracture Surfaces
F. Lednický 541

The Analysis of Polyurethane Fracture Surface below its Glass Transition
H. Janik and J. Foks 549

EBSCOhost - printed on 2/13/2023 3:45 AM via . All use subject to https://www.ebsco.com/terms-of-use

Fracture Surface Morphology of Carbon/Epoxy Composites
A. Krsová, M. Jirouš, and Z. Sucharda 555

Effect of Morphology on Thermooxidation Process of Semicrystalline Polymers
M. Mucha 563

TEXTURES

1. Fibres

Morphology of Porous Polypropylene Fibres
V. Marcian 573

Envelopment of High Strength Poly(Ethylene) Fibres
E. Schulz and R. Hirte 585

The Heat Capacity and Thermal Expansivity of Annealed Poly(Ethylene Terephthalate) Fibers
G.W. Urbanczyk and G. Michalak 591

Structural Changes of PETP Fibre during the Heat Treatment in Different Media
B. Lipp-Symonowicz 601

Radial Structure Differentiation of PET Filaments and its Influence on the Dyestuff Diffusion
B. Lipp-Symonowicz 607

Morphology of PET Fibres in a Range of Spinning Speeds
O. Ďurčová, M. Mitterpachová, and M. Jambrich 615

Morphology and Viscoelastic Properties of Highly Drawn Polyethylene Terephthalate Textile Fibres
B. Košková 625

Morphology of Methylamine-Treated Poly(Ethylene Terephthalate) Fibers
L. Kudláček, M. Hepner, and Z. Kašparová 631

Influence of Structure on the Changes during Heat Treatment and Properties of Acrylic Fibers
A.I. Stoyanov and V.P. Krustev 639

EBSCOhost - printed on 2/13/2023 3:45 AM via . All use subject to https://www.ebsco.com/terms-of-use

Influence of Radiation Grafting of Acrylic Acid
on Some Thermoanalytical Characteristics of
Polyamide Fibres
P. Veselý and D. Provazníková 645

2. Films

The Influence of the Morphology of Block Copolymers
on their Gas Permeability
A. Ferdinand and J. Springer 651

X-Ray Study of Fibrillation of Polypropylene Films
J. Baldrian 661

Surface Microstructure of Polybutadiene Films
during Dissolution
S. Tkaczyk, A. Kwiatkowska, and J. Swiatek 669

Electric Field-Dependence of Crystallinity and
Dipole Orientation in Poly(Vinylidene Fluoride)
A. Janke, W. Künstler, D. Geiss, R. Danz,
and W. Stark 673

Influence of the Crystallinity on the Charge Carrier
Photogeneration in Poly(N-Vinylcarbazole)
S. Nešpůrek, V. Cimrová, and B. Klein-Szymanska 681

Charge Transport in Thin Films of Polyvinylcarbazole
N-Vinylcarbazole
I. Chudáček, G. Naumenko, and J. Urban 689

The Influence of Physical Structure on the Polarization
Currents in Poly(Ethylene Terephthalate)
K.-L. Voß, W. Neumann, and H. Hänsel 699

3. Other Textures

Problems in Quantitative Texture Investigations of
Polymers and Averaged Physical Properties
J. Ganster and D. Geiss 707

The Viscoelasticity of Temporary Polymer Networks
E. Kröner 717

EBSCOhost - printed on 2/13/2023 3:45 AM via . All use subject to https://www.ebsco.com/terms-of-use

Zone Drawing of Poly(Vinyl Alcohol) Gels
D.T. Grubb and P.D. Garrett 731

A Mechanism of Supermolecular Structure Formation Suggested for Polyassociated Complexes of Group I, III Metal Alkoxides
G.F. Bolshakov and Z.T Dmitrieva 739

OTHER CONTRIBUTIONS

Progress in Polymer Investigations by High Voltage Electron Microscopy
G.H. Michler 749

The Morphology of Ion Exchange Resins and Other Functional Polymers. Comment on the Systematization and the Terminology
G. Schwachula and K. Häupke 757

A Model of Free Volume Distribution of Amorphous Polymers at Glass Transition
V. Bouda 765

ABBREVIATIONS 777

AUTHOR INDEX 779

SUBJECT INDEX 781

EBSCOhost - printed on 2/13/2023 3:45 AM via . All use subject to https://www.ebsco.com/terms-of-use

Morphology: A Survey

EBSCOhost - printed on 2/13/2023 3:45 AM via . All use subject to https://www.ebsco.com/terms-of-use

EBSCOhost - printed on 2/13/2023 3:45 AM via . All use subject to https://www.ebsco.com/terms-of-use

RECENT DEVELOPMENTS IN MORPHOLOGY OF CRYSTALLINE POLYMERS

A. Keller

H.H. Wills Physics Laboratory, University of Bristol, Tyndall Avenue, Bristol BS8 1TL, Great Britain

Introduction: Scope

In this presentation, I shall focus on one of the first recognized manifestations of polymer morphology, i.e. on the texture of crystalline polymers. This is a subject with which I have been associated over more than three decades. Specifically, I shall be concerned with lamellar crystals and the underlying chain folded crystallization. It is to be noted that this is a remarkable phenomenon, and possibly the first of its kind where external shape and size on the one hand and molecular organization on the other are intrinsically linked.

Crystallization by chain folding is a uniquely polymeric phenomenon, totally general within the polymer field. I shall review some aspects of it here on the example of polyethylene which can be regarded as the best approximation to the totally unspecific, flexible chain. Chemically more specific groups in appropriate polymers will influence chain folding either by affecting chain flexibility, hence the position where the chain may fold, and/or by producing specific sites where adjacent chain stems will interact preferentially, thus in turn affecting the folding behaviour. By considering the influence of specificity on chain folding one may instructively erect a bridge between crystalline synthetic and biopolymers(1). However, in the present article I shall confine myself to the idealized unspecific chain as best represented by polyethylene.

In what follows, my emphasis will be on the generality and overall simplicity of the pattern of chain folding. One would expect general and simple effects to have explanations which are both

Morphology of Polymers
© 1986 Walter de Gruyter & Co., Berlin · New York - Printed in Germany.

EBSCOhost - printed on 2/13/2023 3:45 AM via . All use subject to https://www.ebsco.com/terms-of-use

simple and compelling. I feel that this assertion should serve as a guideline in the elucidation of problems which are still outstanding, to be touched upon by the present article.

The article will deal with the following topics:
1) The primary fold length. 2) Crystal growth rates. 3) The fold surface problem. 4) The effect of chain length for short chains at the interface of paraffins and polyethylene. In addition, brief reference will be made to theories. Further, while drawing attention to some open ended problems it is hoped that the article will bring out the point that the folding behaviour of long chains can display a variety of features such as previously were held to be mutually incompatible leading to conflicting views. As will emerge, this need not be so: some of the different features merely correspond to different conditions of crystallization or chain lengths and are part of the same overall picture.

Finally, an important point of definition. I shall be referring to the fold length 'ℓ' throughout. 'ℓ' in this instance will refer to the overall lamellar thickness, the quantity directly determined by electron microscopy (EM), or by small angle X-ray (SAX) or low frequency Raman (LAM) measurements. No attempt is being made to subdivide this quantity into crystal core and amorphous layer interface; while recognizing the importance of this subdivision, it was simply not required for the material to be presented. Also for the present purposes the 'ℓ' values obtained by SAX and LAM (after appropriate obliquity corrections) are taken as equal. The justification for the latter could be explicitly verified in the special case of long paraffins, (see below), while in others the differences, such as there might be, are of no consequence for the present argument.

The Primary Fold Length; Isothermal Thickening

The background of the enquiry

The fold length ℓ is the most important molecular parameter characterising chain folded crystallization, and the corresponding

EBSCOhost - printed on 2/13/2023 3:45 AM via . All use subject to https://www.ebsco.com/terms-of-use

lamellar thickness is the most important structural parameter defining the resulting texture. For describing chain folded crystallization and for understanding its origin we need to know this fold length. As recognised early (2) this ℓ value is not constant but depends in a remarkably well defined way on the supercooling ΔT corresponding to the crystallization (where $\Delta T = T_m^o - T_c$, with T_c being the chosen crystallization temperature and T_m^o the melting point, or dissolution point in case of crystallization from dilute solution of the infinitely extended crystal,) broadly according to the relation

$$\ell \propto 1/\Delta T \qquad (1)$$

Equation (1) was observed to be uniquely obeyed for crystallization from solutions, not only regarding functional relation, but also absolute values. However, in crystallizations from the melt, ℓ was not as uniquely defined (while broadly obeying eq. (1) there were variations between different experiments), and the values of ℓ were significantly higher (Fig. 1). This variability of ℓ has in the course of time found explanation through the recognition of isothermal thickening, namely that the lamellae can thicken, which means that the chains refold in the course of the crystallization itself resulting in ℓ values which are higher than the ones by which the crystal formed initially. If isothermal thickening only applied to melt crystallization then the observed higher ℓ values would follow, and so would the variability of the final ℓ if this isothermal thickening were not strictly identical in different experiments, assuming of course that the same relation based on eq. (1) applies throughout initially. In widest generality all this amounts to the fact that by merely recording ℓ we have no assurance of obtaining the actual fold length by which the chains have deposited initially.

We considered the knowledge of the primary ℓ important for the following reasons:

i) First, it affects the issue whether chain folded crystallization proceeds according to the relation expressed by eq. (1). If isothermal thickening can change the primary ℓ (to be denoted ℓ_g^*)

EBSCOhost - printed on 2/13/2023 3:45 AM via . All use subject to https://www.ebsco.com/terms-of-use

we have no assurance as to the limits of this effect, in fact as to the applicability of eq.(1), and ultimately as to whether ℓ_g^* is variable at all, not to speak of the actual magnitude of the ℓ_g^* values. Irrespective of any theory the assessment of this point is a primary necessity.

ii) A considerable amount of past work due mainly to Hoffman and colleagues (e.g. refs. 3,4) has gone into the establishment of a theoretical framework along the well known kinetic lines. As familiar, the theories have led to a relation

$$\ell_g^* = \frac{2\sigma_e T_m^o}{\Delta H \Delta T} + \delta\ell \qquad (2)$$

where σ_e is the free energy of the fold surface, ΔH the heat of fusion of the crystal and $\delta\ell$ an additional term defined explicitly by the theories, which while small (hence can often be ignored in comparison with experiments) is nevertheless an indispensible ingredient, because without it the crystals would not be able to grow at all, at least by the kinetic arguments. These theories were originally set up to account for chain folding itself, for the magnitude of the initially depositing fold length, together with the observed supercooling dependence of the latter. When the influence of isothermal thickening on the final ℓ-s became recognized, work that followed has changed emphasis shifting from the fold length to the lateral growth rates which remain directly assessable. While according to the kinetic theories initial fold length (ℓ_g^*) and lateral growth rate (G) should be intimately linked, G nevertheless remains second in importance to ℓ_g^* (where the folds of this length terminate growth along the chain direction). Clearly, knowledge of ℓ_g^* should therefore be important for the assessment of theories.

iii) Chain refolding is one of the most salient and intriguing features of polymer crystals. The phenomenon of isothermal thickening is particularly poorly explored. Further knowledge on it, which would arise from following ℓ back to the initial ℓ_g^*, would therefore be particularly welcome.

When undertaking the programme of work aimed at ascertaining ℓ_g^* we were guided by the following working hypothesis: ℓ_g^* is determined

EBSCOhost - printed on 2/13/2023 3:45 AM via . All use subject to https://www.ebsco.com/terms-of-use

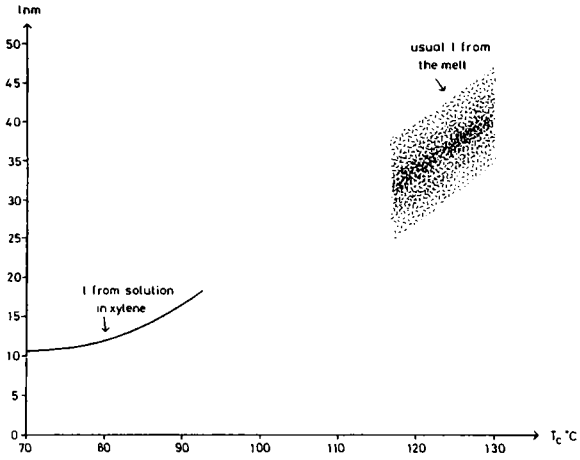

Fig. 1a

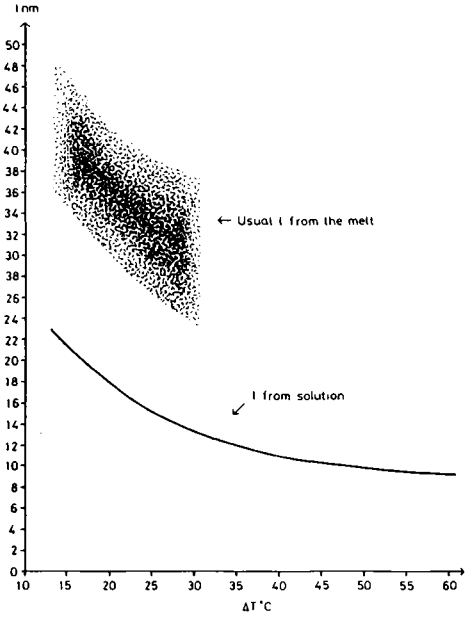

Fig. 1b

Figure 1. Illustration of differences between solution and melt crystallization regarding the value of ℓ (lamellar thickness - fold length): a) Supercooling (ΔT) dependance. b) Crystallization temperature (T_c) dependance.

EBSCOhost - printed on 2/13/2023 3:45 AM via . All use subject to https://www.ebsco.com/terms-of-use

by ΔT while the rate of isothermal thickening by T_c (i.e. absolute temperature). This would mean that the final value of ℓ for crystallization at higher temperatures (such as in the usual melt, compared with solutions) should be increasingly in excess of ℓ_g^*, which thus should account for the gap between solution and melt crystallization regarding the observed ℓ (Fig. 1). As will be seen this expectation (except for the unexpectedly high stability of the solution grown crystals against refolding) was in fact confirmed. The full programme of work (5-12) proceeded in two stages. In the first stage (5-7) we only went part of the way (as recognized subsequently) in tracking down crystallization to its initial stages. Identification of the inception of the crystals, hence the true ℓ_g^* value (in cases where isothermal thickening was in fact found to intervene), became possible only through the synchrotron X-ray source with its inherently high intensity, which became available during the second stage of the programme (8-12).

The new results

As the subject itself cannot be developed analytically in brief, at this place only the end results will be quoted. These are as follows:

1) There is no sizeable isothermal thickening in crystallization from solutions. Thus the ℓ_g^* values as obtained from such preparations are safeguarded, reaffirming the existing theoretical framework against suggestions to the contrary.

2) There is substantial isothermal thickening in melt crystalization, attributable to the higher absolute temperature pertaining to crystallization from the melt as compared with that from solution even for equivalent supercooling, presumably due to the higher chain mobility within the crystal. Once the effect of this thickening has been assessed the $\ell v. \Delta T$ curves became all coincident (Fig. 2), thus achieving at last the long outstanding unification of crystalizations from melts and solutions (11, 12).

3) Isothermal thickening itself turned out to be a two stage phenomenon. The first stage consists of a stepwise increase in

EBSCOhost - printed on 2/13/2023 3:45 AM via . All use subject to https://www.ebsco.com/terms-of-use

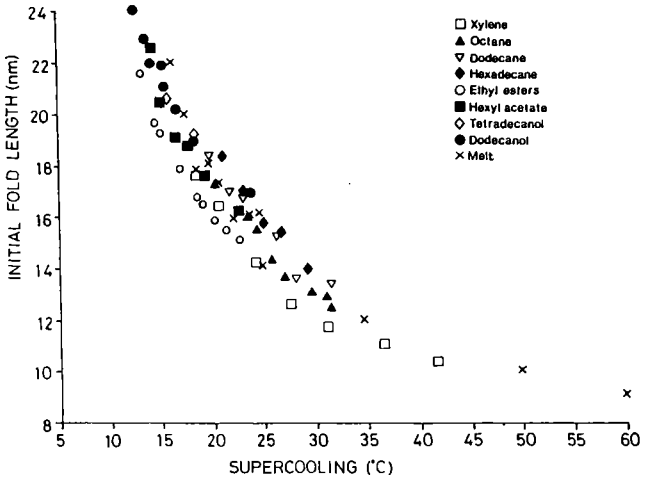

Figure 2. Initial fold length (ℓ_g^*) as a function of supercooling (ΔT) for both melt (X) and solution crystallization from a variety of solvents as designated by the symbols in Fig. 3 (12).

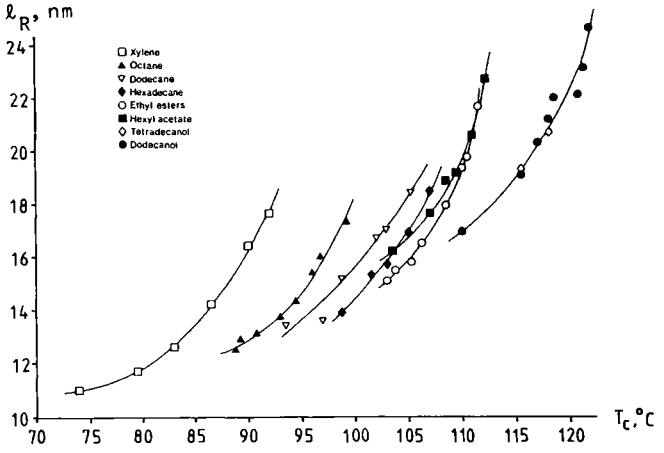

Figure 3. Fold length as a function of crystallization temperature (T_c) for a variety of solvents (10).

EBSCOhost - printed on 2/13/2023 3:45 AM via . All use subject to https://www.ebsco.com/terms-of-use

the thickness of the primary lamella by about a factor of 2 [13] (Fig. 4). This is then followed by a gradual, in fact logarithmic, increase with time. This two stage sequence is particularly noteworthy as lamella thickening has been traditionally considered as a continuous process proceeding logarithmically with time. Nevertheless, occasionally discontinuous increases, often by a factor of 2, have been reported (see in ref. 2). Both these effects, the stepwise and the slow gradual increase, have important implications for the mechanism of chain refolding within the crystal. We now see that reports on the two types of thickening processes do not represent conflicting claims but that both can exist, and in fact are two consecutive stages of the same overall phenomenon.

A comment on crystal habits

As will be apparent, Fig. 2 was obtained by growing crystals both from the melt and from solution. In the solution case the plot contains data referring to crystals grown from a variety of solvents of different solvent power. This is best displayed by plotting ℓ as a function of the crystallization temperature T_c shown by Fig. 3. The concomittant microscopic examination of the crystals provided an opportunity to document the dependence of the lateral habit features of the crystals on T_c and ΔT, the subject of the present section. It emerged that the crystal habit was determined by T_c (and not ΔT), and further, that there is a systematic trend with T_c as represented by Fig. 5. While features contained by Fig. 5 have been often seen before (14), here we are placing emphasis on the gradual development of curvature with T_c (with an actual example in Fig. 6) which, as will be pointed out below, has special forward looking consequences. Even at this stage it will be apparent that ℓ, by being uniquely determined by ΔT, is unaffected by the lateral morphology: the same ℓ value can be realized by widely differing morphologies within the sequence in Fig. 5 as long as ΔT is identical.

On Crystal Growth Rates

The significance of growth rates in crystallization studies in general needs no special emphasis. Even so in the case of polymers

EBSCOhost - printed on 2/13/2023 3:45 AM via . All use subject to https://www.ebsco.com/terms-of-use

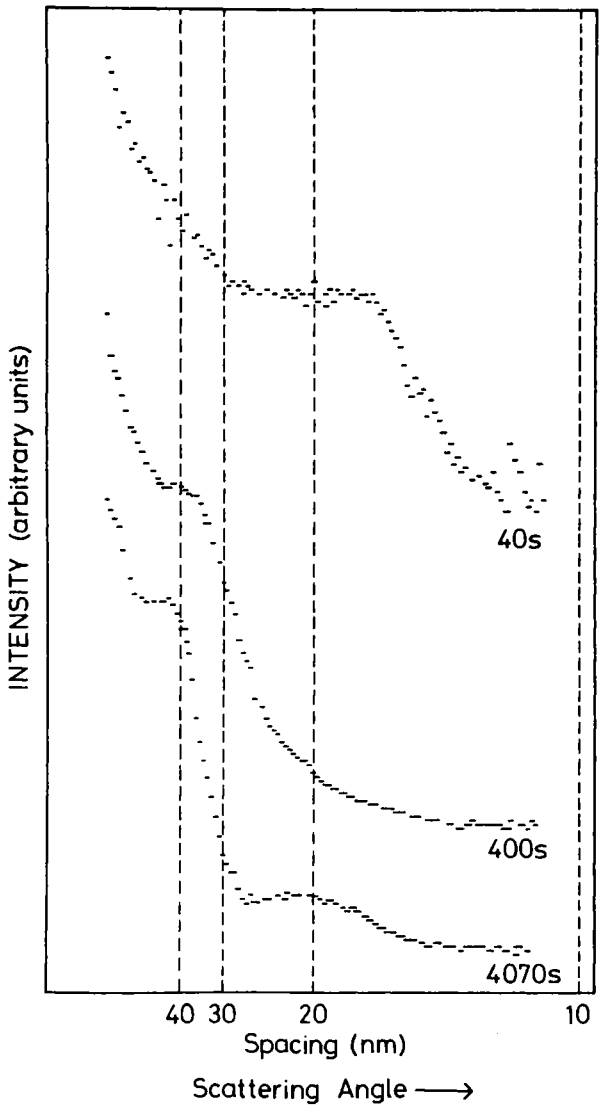

Figure 4. Low angle x-ray scattering traces (with intensities corrected) at three consecutive times during isothermal crystallization and thickening of a sharp fraction of polyethylene. T_c = 127.6°C. Primary crystallization is complete after 300 s. The traces show that the first stage of thickening corresponds to doubling of long period (the ~20 nm peak for the 4070 s trace is a second order (13)).

EBSCOhost - printed on 2/13/2023 3:45 AM via . All use subject to https://www.ebsco.com/terms-of-use

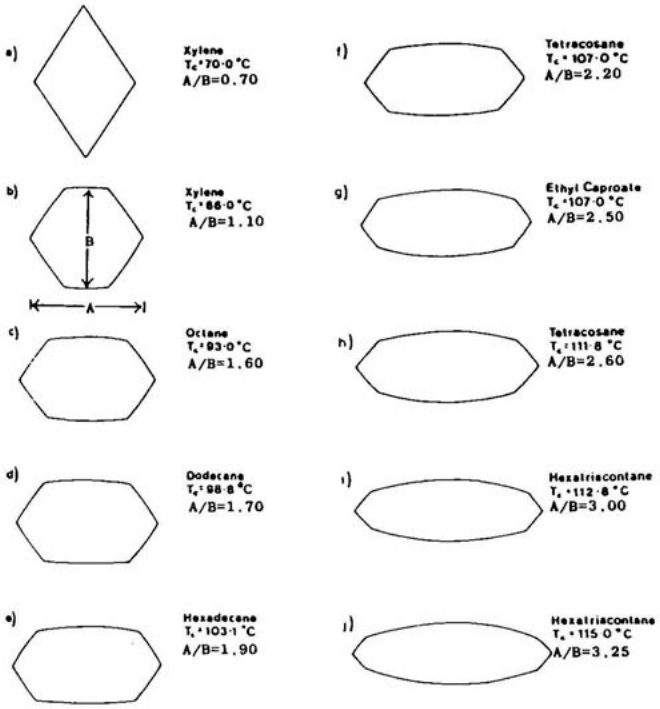

Figure 5. Illustration of systematic lateral habit changes of polyethylene crystals with increasing crystallization temperature (T_C). To cover the wide T_C range involved a range of solvents needs to be used (8).

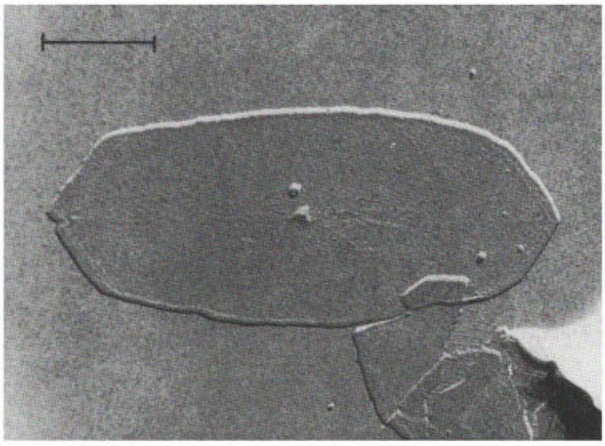

Figure 6. An actual electron micrograph of a crystal with curving edges corresponding to g) in Fig. 5 (8).

EBSCOhost - printed on 2/13/2023 3:45 AM via . All use subject to https://www.ebsco.com/terms-of-use

it is second to that of the fold length: crystals of any kind grow, but only polymer chains fold. Yet whatever the ultimate reason for chain folding, the fold length and growth rates must be closely linked. As to be recalled below, through the kinetic theories, this link is explicit and can be expressed quantitatively.

The unique phenomenological simplicity of crystal growth in the case of polymers is not always fully appreciated. By this I refer to the fact that, except for quite close to its termination, the lateral growth rate of the lamellae is constant throughout the growth of the crystal, and so is the radial growth of spherulites constituted by these lamellae. This means that both crystal and spherulite growth can be defined by a single growth rate parameter (G) which is readily measurable by familiar microscopic methods and by turbidity (15), the latter particularly as calibrated by microscopy. Two features merit particular attention: the absolute value of G and its temperature dependence.

Taking the temperature dependence first, it has been long established, in the first instance on spherulites (16), then on single crystals, that a relation such as

$$G \propto e^{-\frac{Q}{T_c \Delta T}} \qquad (3)$$

is being obeyed throughout. Having examined crystallization of PE over a wider temperature range and more systematically than has been done before in service of the fold length ℓ (the issue presented above), the extension of that investigation to lateral growth rates seemed appropriate. Some of the results are shown by Fig. 7. As seen, the relation in eq. (3) is being closely obeyed with a change of slope (i.e. of constant Q) by a factor of 2.0 from solvents where a sufficiently large ΔT range was covered. Note further the large T_c range covered by the totality of the curves, the extreme lower and upper value being marked on the bottom and top curves respectively. This T_c range embraces the full morphological sequence displayed in Fig. 5. It follows, that the two main features of crystal growth, i.e. constancy of the rate during most of the growth and its temperature dependence, are unaffected by the lateral habit. Accordingly, we have the surprisingly simple finding that neither the fold length nor the

EBSCOhost - printed on 2/13/2023 3:45 AM via . All use subject to https://www.ebsco.com/terms-of-use

above mentioned characteristics of the growth rates are influenced by the shape of the crystal, a point to which I shall return below.

In contrast to the above, the absolute value of G increases dramatically with T_c which forms a link-up between solution and melt growth.

Some Comments on Theories

The origin of chain folding and the consequent growth of the crystals has of course been the subject of intensive enquiry. As familiar, the generally accepted theoretical approach has been kinetics based (3,4) and has had notable success to which our latest experimental work has made further contributions. Nevertheless I have one important reservation which should serve as a pointer for future enquiries.

As recognized early by myself (17), eq. (2) has the same form as the temperature dependence of the size of a critical nucleus in phase transitions. Further, even before any knowledge about the existence of single crystals, eq. (3), as observed in connection with spherulites, was identified with the temperature dependence of secondary crystal nucleation rate. Putting the two issues together, as a broad retrospective assessment, it would follow that ℓ itself reflects the size of a critical nucleus and G is an expression of the rate by which such a nucleus (secondary in this case) grows, or rather spreads out laterally while retaining its dimensions ℓ along one direction, corresponding to that of the chain. This is essentially the original core of the kinetic approach. Theories themselves, as developed by Hoffman and associates over the years, require the working out of the actual fluxes as a function of ℓ. It follows, amongst others, that crystals of thickness ℓ by eq. (1) will not grow because of absence of any flux for such an ℓ corresponding to the minimum stable size. It follows in turn that the fold length pertaining to the actual growth (ℓ_g^*) must be larger. This is the conceptual origin of $\delta\ell$ in eq. (2), more explicitly emerging from the actual theories. As indicated earlier by the kinetic approach, ℓ_g^* and G are closely linked, ℓ_g^* being the ℓ value by which the crystal face advances most rapidly, i.e. when G is largest.

EBSCOhost - printed on 2/13/2023 3:45 AM via . All use subject to https://www.ebsco.com/terms-of-use

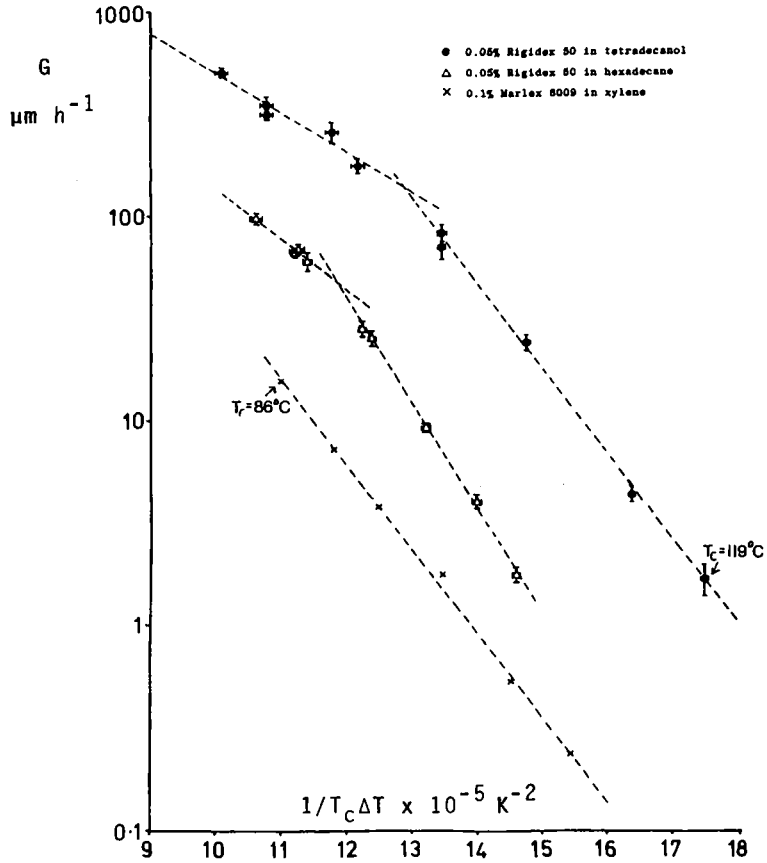

Figure 7. Supercooling (ΔT) dependance of lateral crystal growth rates (G) of polyethylene crystals from three different solvents plotted as a log G v. $1/T_c\Delta T$ (T_c=crystallization temperature, the highest and the lowest T_c values being marked). Note the slope change in the two upper curves, slope ratios≈2.0 (15).

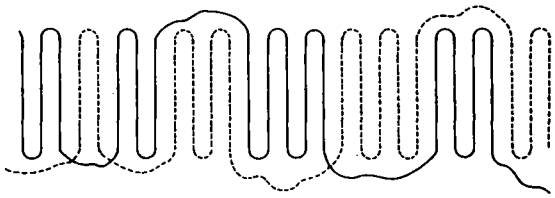

Figure 8. A two-dimensional sketch of the chain trajectory in a solution grown polyethylene crystal as derived from combined neutron scattering and infra-red spectroscopic studies. A given chain is drawn by solid, while another by interrupted line. The emphasis is on the local clustering of stems from the same chain. In the real crystal the chain will 'superfold' so as to be part of multiply stacked layers.

EBSCOhost - printed on 2/13/2023 3:45 AM via . All use subject to https://www.ebsco.com/terms-of-use

As well known, G is expressed explicitly as

$$G = G_o \exp \frac{-\Delta E}{(kT)} \quad \exp \left(\frac{-\alpha \sigma_e \sigma T_m^o}{KT\Delta T}\right) \qquad (4)$$

with the familiar meaning of the symbols (see refs. 2,3), α being a constant.

It follows from the above that the formation of the secondary nucleus should be the rate determining step in G. This is defined as Regime I in the theories with α in eq. (4) turning out to be 4. With increasing ΔT the rate of nucleus formation increases; when it becomes comparable with the rate of spreading along the substrate we enter another regime of crystal growth, Regime II, where α becomes equal to 2 producing a reduction in slope by 2 of the lines in plots as Fig. 7.

The following recent findings of ours are in qualitative and quantitative agreement with the above approach: The uniqueness of ℓ_g^* and its identical dependence on ΔT in the case of melts and solutions, the validity of relation in eq. (3) overthe full ΔT range including the first ever demonstration of a Regime I→II transition in case of solutions. ΔT corresponding to this transition is in quantitative agreement with predictions and further, the substrate length of growth (L in the theories, see ref. 4) is also comparable with anticipation from the theory, at least within the limits of uncertainties involved (15).

However, the drastic increase in G with T_c does not follow obviously. It certainly cannot be associated with the transport term (first exponential in eq. (4)) because it pertains also for very dilute solutions with solvents which are more viscous than those giving rise to slower rates. More serious, however, is the problem of the existence of curved edges, particularly in Regime I. Namely, curved edges require necessarily steps along the growth face: for some of the observed curved shapes as many as one every 3-4 fold stems. It is difficult to envisage how growth through such faces can be nucleation controlled, as each step should act as a potential growth initiator without requiring the formation of a new secondary nucleus.

EBSCOhost - printed on 2/13/2023 3:45 AM via . All use subject to https://www.ebsco.com/terms-of-use

The applicability of the kinetic theory in case of curved edges is currently receiving attention (18). Yet when the problem with all its implications was recognized, it has formed the starting point of a new theoretical departure. In order to account for the existence of curved edges Sadler (19,20) has invoked a concept of crystal growth based on equilibrium surface roughness, familiar from crystals of simple substances going back to Burton, Cabrera and and Frank (21). Accordingly, any crystal face will have a certain equilibrium roughness, which beyond a certain temperature (the roughening temperature) can lead to the advancing of the face, hence growth of the crystal, without the need of a stable secondary nucleus forming first. This kind of nucleation - free growth usually leads to curving facets (e.g. spherical crystals of helium), hence its invoking for the case of polymers where, as we have seen, curved edges occur systematically at high T_c-s. Sadler has applied this surface roughening concept to chain folded crystallization of polymers and has shown that such a growth mechanism can at least be compatible with the observed supercooling dependences of ℓ and G according to eq. (1) and (3). As just stated, in this approach there is no conflict with the existence of curved edges, even if at the present stage explicit curvatures themselves have not yet been predicted. It is too early to assess the implications of the equilibrium surface roughening approach for the existing picture on polymer crystallization: it may well turn out to represent one further regime of growth, in addition to those invoked by the long established (and otherwise well supported) kinetic theories. Without prejudging the issue, it may be said that the new approach was generated by the recognition of a conflict (whether true or apparent yet needs to be seen), and that it originates, as in fact does the traditional kinetic approach, from the general body of knowledge on crystal growth. Whatever the outcome, this recent emphasis on an explicitly morphological feature (curved edges), has thus focussed attention on the underlying fundamentals of crystal growth.

The Fold Surface Structure

Here it will be taken for granted that the issues of adjacent v. non-adjacent fold stem reentry and that of sharp v. loose folds are familiar, and that so are some of the methods being used in

EBSCOhost - printed on 2/13/2023 3:45 AM via . All use subject to https://www.ebsco.com/terms-of-use

the study of these problems (e.g. ref. 22). At this point one particular trend in present results will be lifted out for the purposes of this article. This is the model of subgroups or clusters of adjacently reentrant stems, all from the same molecule, with the clusters being separated by intervening other molecules, the clusters from the same molecule being necessarily linked by long, possibly loose fold loops somehow as sketched in Fig. 8. By this scheme, further issues reduce to the identification of size, shape and distribution of clusters. Thus in melt crystallization the clusters are smaller and more widely distributed. This is in contrast to some earlier formulations of the problem, according to which the issue centered more on a mean representative structure, a random distribution of its constituents (i.e. pairs, triplets, etc. of reentry) being implicitly assumed.

As well known, in more recent times the method for studying this issue has involved the use of isotopically tagged probe molecules, the conformation of which within the environment of isotopically different, but otherwise identical host molecules can be explored by neutron scattering. Similarly, in such an isotopically distinct guest-host assembly the isotopic environment of fold stems, which provides leads to the molecular trajectory, can be characterized by infra-red spectroscopy. Over the recent years the two approaches involving isotopic probes, namely neutron scattering and infra-red spectroscopy, have been applied in combination in our laboratory leading to largely identical results (23-25). In what follows one example will be given of effects, such as lead to the cluster model and to its detailed characterization.

Fig. 9a) represents the stem distribution in a solution grown single crystal as obtained both by neutron scattering and infra-red spectroscopy. Fig. 9b) is the infra-red spectrum as recorded and as after deconvolution, together with the calculated spectrum as expected from a stem distribution such as in Fig. 9a). The distribution in Fig. 9a) was in fact obtained by optimising the fit between experiment and calculation. 'Mutato mutatis' the same procedure was adopted in the neutron scattering experiments. The finding that closely identical conclusions were arrived at by experiments along different lines and based on different

EBSCOhost - printed on 2/13/2023 3:45 AM via . All use subject to https://www.ebsco.com/terms-of-use

Fig. 9a

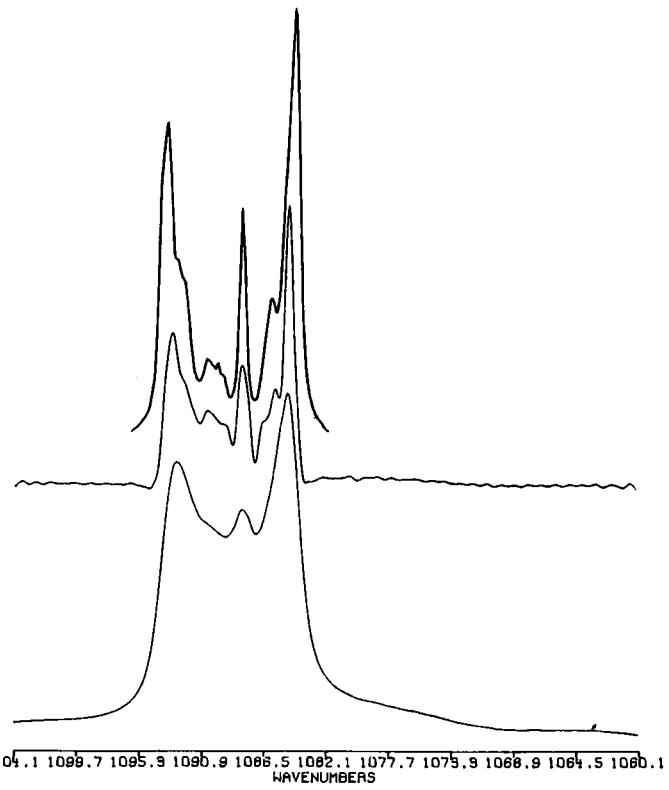

Fig. 9b

Figure 9. a) The stem arrangement as in Fig. 8, but comprising several 110 growth planes (horizontal) as seen along the c axis projection. Stems due to one given isotopically distinct probe molecule are seen as heavy dots.
b) An example of infra-red evidence for structure of the type as in a).
Bottom: Experimental IR spectrum of polyethylene doped with 3% deuterated polyethylene.
Middle: Above spectrum after deconvolution.
Top: Calculated spectrum based on a model as in a) but with 11 sheets.

EBSCOhost - printed on 2/13/2023 3:45 AM via . All use subject to https://www.ebsco.com/terms-of-use

physical properties and principles, but carried out on the same sample, is therefore very encouraging.

The result embodied by Figs. 8 and 9 is significant in its own right in the light of the existing disputes in this field. It will be invoked again in the last section as part of a wider scheme emerging from recent works on paraffins to be sketched below.

From Paraffins to Polyethylene

The crystal structure of paraffins is well known in atomic detail. Here the chains are extended, forming layers with the methyl end groups at the layer surface, the methylene groups along the chains being all in the same crystallographic register as those in polyethylene.

The layers of extended chains are then stacked on top of each other but in this case in exact crystallographic register. There are several different stacking modes corresponding to slight differences in methyl group packing which give rise to different polymorphs in paraffin crystals. The question which clearly arises is what happens as the chain length is being increased and that of polymeric polyethylene is approached? More explicitly, will the chains stay straight or will they fold? If the latter, at what stage and how? This subject has a long history by which the onset of chain folding beyond some chain length is definitely indicated. Nevertheless, the unavailability of paraffins of strictly uniform length prevented these earlier studies to be as definitive as could be desired. There was more and highly interesting progress with the analogue system of polyethylene oxide (26), not to be enlarged on in detail at this place, where nevertheless the chains, while forming sharp fractions, were still not strictly uniform and contained rather specific end groups.

The present section will refer to quite recent progress along the above route of enquiry. It was made possible through the availability of paraffins of strictly uniform length (by the stringent criteria of traditional organic chemistry), up to much greater lengths than available so far, thanks to a new method of synthesis

EBSCOhost - printed on 2/13/2023 3:45 AM via . All use subject to https://www.ebsco.com/terms-of-use

by Whiting et al. (27,28). At the time of writing the longest is $C_{390}H_{782}$, which is well in the range we may call low molecular weight polyethylene. These paraffins were crystallised both from the melt and from solution, and the 'layer' thickness determined by X-ray diffraction and low frequency Raman spectroscopy (29,30). In this case we know the chain length exactly to the precision of a single carbon atom, hence we should be able to tell when a chain folds and how.

The results which have emerged are definitive and clear cut even at this preliminary stage and deserve quoting (29). By the criterion of measuring the straight chain portion by the same methods as in polyethylene, the paraffin of $C_{150}H_{302}$ is already capable of folding, and such folding occurs with increasing propensity with longer paraffins for crystallisations both from melts and solution. The fold length which has emerged is always such as to correspond close to an integer fraction of the total chain length. Thus, if we define the ratio n_c/n_{LAM} as that formed by the number of carbon atoms in the chain (n_c) to that contained by the straight chain portion (n_{LAM} as assessed by the Raman LAM method) we obtain values such as:
for $C_{150}H_{302}$ (solution) n_c/n_{LAM} can be 0.99 or 1.93; for $C_{198}H_{398}$ (solution) it can be 2.0 or 3.01; for $C_{246}H_{494}$ (slow cooled melt) it can be 0.99 or 1.98, for $C_{390}H_{782}$ 5.09 or 1.93 for solution and slow cooled melts respectively, to quote only a few figures from the much larger number available (29).

Of the many consequences embodied by results such as just quoted one is the fact that even quite short chains will fold. Further, that folding will be such as to complete a full fold, which implies that the end groups will 'want' to be at the fold surface, even when it is only a methyl group, which hardly differs from the methylene chain member itself. Further results, not to be itemised here, show that higher crystallization temperatures lead to longer fold lengths, and further, that crystals with a given fold length can increase their fold length through annealing, in both instances the closely integral relation between fold length and total chain length being retained.

EBSCOhost - printed on 2/13/2023 3:45 AM via . All use subject to https://www.ebsco.com/terms-of-use

A quite recently observed effect deserves separate mention as, amongst much else, it provides an unexpected link between the quantized and uniformly varying fold lengths in paraffins and polyethylene respectively. When the fold length was followed during crystallization in situ at the elevated temperatures by the SAX technique with the aid of a synchrotron X-ray source (30) it was found that the fold length, as first registered, was in general not an integer fraction of the chain length, but could have any value determined by the supercooling, varying in a continuous manner with supercooling just as in polyethylene (as for as can be generalized from the few experiments carried out so far). However, such non-integer fractional fold lengths were transient and changed into the nearest integer fractional value still during crystallization and/or subsequent slow cooling. This change could correspond either to isothermal thickening or, rather surprisingly, to isothermal thinning as schematically illustrated for a once folded - extended chain situation by Fig. 10. A further feature of these experiments deserves mention. The intensity of the low angle reflexion corresponding to the non-integer fold length was unusually high, but decreased substantially on attainment of an integer fractional value on subsequent rearrangement. This we associate with substantial initial disorder along the fold surface (high electron density difference) healing out on subsequent regularization, Fig. 10 having been drawn accordingly.

Some Unifying Features

We may now attempt to form a unified picture from the structural evidence presented. The work on paraffins has shown that the chain molecules of 150 carbon atoms and longer indeed crystallize predominantly by chain folding and, further, that the folds must be adjacently reentrant and, if given any chance to perfect themselves (which seems to be usually the case for the paraffins we examined), the folds will be sharp. The above holds for chain folded structures comprising at least five stems. What the upper limit of such adjacently reentrant stem sequences may be we were unable to assess with the materials available so far, but it is almost certainly higher than five.

EBSCOhost - printed on 2/13/2023 3:45 AM via . All use subject to https://www.ebsco.com/terms-of-use

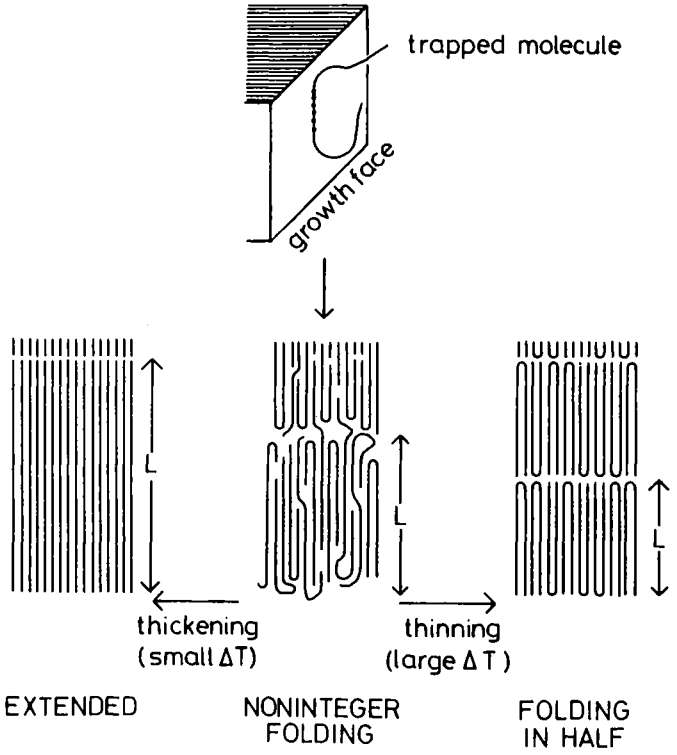

Figure 10. Crystallization of an ultra-long chain paraffin in the extended chain - once folded chain length and ΔT regime by latest evidence through in situ SAX studies using a synchrotron x-ray source.

Top: Envisaged initial attachment of chain.

Bottom middle: Initial lamellae formed by non-integer fractional stem lengths with a corresponding irregular fold surface and defect containing crystal core.

Bottom left: After rearrangement through thickening to extended chains.

Bottom right: After rearrangement through thinning leading to once folded chains with stem length closely one half the chain length.

Note: Rearrangements by thickening and thinning can both occur simultaneously in the same specimen.

EBSCOhost - printed on 2/13/2023 3:45 AM via . All use subject to https://www.ebsco.com/terms-of-use

At the other end of the spectrum, in the case of "real life" polyethylene, our structure studies established the existence of groups of adjacent stems, themselves more or less widely separated, arising from portions of the same molecule (Figs. 8,9). We tend to reconcile this structure feature with the findings on the paraffins as follows: We consider the structure observed with paraffins as the basic trend which the polyethylene chain will try to realize. However, in case they are beyond a certain length they will be hindered or prevented from doing so due to the self evident possibility that the deposition of a given chain will be interrupted by that of other chains, and/or that different remote parts of a given chain will start to deposit in a chain folded manner independently. It is easy to see that this will lead to structures such as Figs. 8 and 9. It is important to note that the existence of long loose loops and substantial stem separations in such a structure does not invalidate the existence of what we believe to be the basic trend, as realized by the paraffins, nor does the latter diminish the significance of the various manifestations of departure from the idealized structure in "real life" polyethylene. Each feature is important in its own right.

To the above two qualifying remarks need adding. First, that we have only discussed the structure within a single layer, the relation between consecutive layers, together with whatever material may lie between them or may connect them, was left out of consideration. Secondly, there is no direct information on the structure of the fold itself; references to it are only by implication from other evidence.

As will be apparent, the above structure features combine what previously have been considered mutually irreconcilable trends. We may add to these the supercooling dependence of the fold length which, as we have noted for the case of long paraffins, can be both continuous and discontinuous (the latter on the scale of maintaining integral relation between chain length and stem length), in the former case the fold being sharp and in the latter disordered. It will be apparent further that the most significant issue is not whether one or the other structure feature pertains, but under what conditions the different features arise, and consequently how to

EBSCOhost - printed on 2/13/2023 3:45 AM via . All use subject to https://www.ebsco.com/terms-of-use

control their formation. I believe that having recognized the effects and issues described in this article we are well on the way to providing an answer.

There remains the issue of "why?". In future search for the basic underlying cause for the structures observed in general, and chain folding in particular, the material in the present article has highlighted the following salient facts: i) Flexible chains have an astonishingly persistent tendency to fold; they will fold even when the chain length is only marginally (less than 2x - see Fig. 10) longer than the primary fold length. ii) The primary fold length is uniquely determined by the supercooling. iii) The chains may tend to rearrange immediately after the primary chain folded deposition, with a tendency to bring the chain ends to the surface in the case of uniform paraffins (leading to quantized fold length - Fig. 10) and to increase the overall fold length in the usual longer chain polyethylene. iv) The rate of lateral growth is uniquely determined by the supercooling. The uniqueness expressed under ii) and iv) is to be noted, and further that this is unaffected by the crystal habit pertaining to the particular conditions (absolute temperature) of crystallization. Finally, the remarkable mobility of the chain within the crystal already formed, as manifested by iii) above, commands attention. It is hoped that the above firmly established experimental facts will serve as guidance for future endeavours towards an understanding of the unique phenomenon of folded crystallization of polymer chains.

References

1. Atkins, E.D.T., Keller, A., to be published.
2. Keller, A. 1984. In: Polymers, Liquid Crystals and Low-Dimensional Solids, (M. March and M. Tosi eds.). Plenum Press, p. 3-142.
3. Hoffman, J.D., Davis, G.T., Lauritzen, J.I. 1976. In: Treatise on Solid State Chemistry, (N.B. Hanney edt.) Plenum Press, v. 3, p. 335.
4. Hoffman, J.D. 1985, Polymer, 26, 803.
5. Barham, P.J., Chivers, R.A., Jarvis, D., Martinez-Salazar, J., Keller, A. 1981. J. Polymer Sci. Letters, 19, 539.

EBSCOhost - printed on 2/13/2023 3:45 AM via . All use subject to https://www.ebsco.com/terms-of-use

6. Chivers, R.A., Barham, P.J., Martinez-Salazar, J., Keller, A. 1982. J. Polymer Sci. Phys. Ed. 20, 1717.

7. Barham, P.J., Chivers, R.A., Keller, A. 1982. J. Polymer Sci. Phys. Ed., 20, 1743.

8. Organ, S.J., Keller, A. 1985. J. Material Sci. 20, 1571.

9. Organ, S.J., Keller, A. 1985. J. Material Sci. 20, 1586.

10. Organ, S.J., Keller, A. 1985. J. Material Sci. 20, 1602.

11. Martinez-Salazar, J., Barham, P.J., Keller, A. 1985. J. Material Sci. 20, 1616.

12. Barham, P.J., Chivers, R.A., Keller, A., Martinez-Salazar, J., Organ, S.J. 1985. J. Material Sci. 20, 1625.

13. Barham, P.J., Keller, A., Spells, S.J. to be published.

14. Khoury, F., Bolz, L.H. 1980. In: 38th Ann. Proc. Electron Micr. Soc. America (G.W. Bailey ed.)

15. Organ, S., Keller. A. 1985. J. Polymer Sci., Phys. Ed. Submitted.

16. Flory, P.J., McIntyre, A.D. 1955. J. Polymer Sci., 18, 592.

17. Keller, A. 1958. In: Discussions of the Faraday Soc. No. 25, p. 114.

18. Hoffman, J.D. 1985. Private Communication.

19. Sadler, D.M. 1983. Polymer, 24, 1401.

20. Sadler, D.M., Gilmer, G.H. 1984. Polymer, 25, 1446.

21. Burton, W.K., Cabrera. N., Frank, F.C. Phil. 1951. Trans Roy. Soc. A, 243, 299.

22. Faraday Discussions, No. 68. 1979.

23. Spells, S.J., Sadler, D.M. 1984. Polymer, 25, 739.

24. Spells, S.J., Keller, A., Sadler, D.M. 1984. Polymer, 25, 749.

25. Spells, S.J. 1984. Polymer Commun. 25, 162.

26. Buckley, C.P., Kovacs, A.J. 1984. In: Structure of Crystalline Polymers, (I.H. Hall, ed.). Elsevier Appl. Sci. Publ. p.261.

27. Paynter, O.J., Simmonds, D.J., Whiting, M.C. 1982. Chem. Commun. 1166.

28. Bidd, I., Whiting, M.C. 1985. Chem. Commun., 543.

29. Ungar, G., Stejny , J., Keller, A., Bidd, I., Whiting, M.C. 1985. Science, 229, 444.

30. Ungar, G., Keller, A., Whiting, M.C., to be published.

EBSCOhost - printed on 2/13/2023 3:45 AM via . All use subject to https://www.ebsco.com/terms-of-use

INFLUENCE OF CHAIN DEFECTS ON THE PERFECTION OF LAMELLAR POLYMER CRYSTALS

F.J. Baltá Calleja

Instituto de Estructura de la Materia CSIC
Serrano 119. 28006 Madrid. Spain.

Abstract

This paper discusses four topics relating to the microstructure of polymers with a low content of chain defects: The assessment of defect inclusion within the crystals, the dependence of internal crystal perfection on the level of chain defects, the influence of crystallization conditions and size of the defects on the amount of defect incorporation and the plastic deformation, and annealing behaviour regarding the defect inclusion level.

Introduction

It has been often assumed that when crystallization of chain molecules with lateral chain defects (branches) statistically distributed is carried out very slowly, all the noncrystallizable comonomer units are fully rejected from the crystal lattice. There are various kinds of experimental evidence that suggest that the rejection of defects is not complete. One is that the unit cell dimensions of the crystalline lattice of polymers with lateral chain defects are much larger that those of the linear homopolymer. The effect has been amply reported for copolymers of polyethylene (PE) (1-11). A second line of evidence stems from the study of melting temperatures. As a general trend a decrease in the values of T_m^o with the amount of defects is observed. The experimental T_m^o values are, however, lower than the theoretical values predicted from copolymer theories (12-14). The amount of deviation from the theory has been shown to depend on the size of the comonomer unit (15-16). The third type of evidence is that electron microscopic observations of solution grown crystals indicate that the regularity of

Morphology of Polymers
© 1986 Walter de Gruyter & Co., Berlin · New York - Printed in Germany.

EBSCOhost - printed on 2/13/2023 3:45 AM via . All use subject to https://www.ebsco.com/terms-of-use

the crystals deteriorates with increasing number of chain defects (7,12,14). When the number of defects is sufficiently large it is impossible to find crystallization conditions leading to monolayer single crystals with a simple morphology. Instead, complex multilayer crystals and no effect of the seeding temperature on the crystal size are observed (14).

One of the points of interest in characterizing the structure of polymers with a low content ε of chain defects (comonomer units, branches) is the distribution of the non-crystallizable units between the crystalline and amorphous phases of the material. Four general aspects will be discussed in this paper: 1) The assesment of defect inclusion within the crystals, 2) the crystal perfection dependence on the level of chain defects, 3) influence of crystallization conditions and size of the defects on the amount of defect incorporation, and 4) plastic deformation and annealing behaviour regarding the defect inclusion level. These topics were chosen not only because there are points of interest in our laboratory but also because the defect distribution between crystalline and amorphous phases determines the physical properties of the material (17-18). In addition, a knowledge of the degree of partitioning is necessary for the advancement of theories of crystallization and melting of polymers (19-20).

Assessment of Defect Inclusion within the Crystals

The dilation of crystalline lattices by random point defects has been proved theoretically (21) and observed frequently with crystals of simple inorganic materials. A calculation of the concentration of defects within the expanded lattice of polyethylene has been developed using the concept of defect accommodation through generation of kinks (22). Vonk postulated for the first time the formation of kinked chains to allow the incorporation of side groups by substitutional solution (23). The 2g1 kink ($gt\bar{g}$) represents the most abundant equilibrium conformation in PE crystals (24) and has been used in the present calculation. The formation of each 2g1 kink reduces the length of the chain by a c/2 unit and enlarges the interchain separation in such a way that a CH_2 group

EBSCOhost - printed on 2/13/2023 3:45 AM via . All use subject to https://www.ebsco.com/terms-of-use

is replaced by a conformation detail with a $\Delta V \tilde{=} 60$ Å^3 larger volume (24). Since each lattice cell contains four monomers concentration ε_c of chain defects incorporated in the lattice produces an increase in the average volume $\bar{V}$ of all lattice cells by:

$$\varepsilon_c \tilde{=} \frac{V-V_0}{4\Delta V} \qquad |1|$$

where V_0 is the volume of the undisturbed lattice cell and ε_c is given as number of defects per 10^2 CH_2 groups. If the defect concentration ε_c is larger than 10^{-3} then the unit cell suffers a measurable expansion. For PE with butyl or larger alkyl groups slowly cooled from the melt, ε_c rises from 0.04% for $\varepsilon \sim 0.2$ to about 1% for $\varepsilon \sim 7\%$ (22)(see Fig. 7). The low concentration of defects incorporated into the crystals demands a much larger branching concentration in the amorphous layer:

$$\varepsilon_a = (\varepsilon - \alpha\varepsilon_c)/(1-\alpha) \qquad |2|$$

where α is the crystalline volume content. For these PE samples $\varepsilon_a \tilde{=} 10\ \varepsilon_c$. The fraction of defects incorporated in the lattice is simply defined by:

$$\chi_c = \varepsilon_c \alpha/\varepsilon \qquad |3a|$$

Similarly, the fraction of defects excluded from the lattice is:

$$\chi_a = 1-\chi_c = \frac{\varepsilon_a}{\varepsilon}\ (1-\alpha) \qquad |3b|$$

For melt crystallized PE the degree of partitioning $\Gamma = \chi_c/\chi_a$ |4|, i.e. the ratio of concentration of defects in the crystalline phase to that in the amorphous phase, decreases from 0.25 for $\varepsilon \sim 0.2\%$ down to 0.05 for $\varepsilon \sim 7\%$. This means that the large alkyl groups show a tendency towards a total exclusion ($\Gamma = 0$) from the crystal with increasing branching ratio.

A second calculation on the inclusion of chain defects in the PE lattice has been developed on a simple statistical calculation (25). This approach leads to a relation between crystallinity, α, and defect content times crystal thickness, yielding the average number of defects incorporated per crystalline chain segment. If we denote $(1-\varepsilon)$ the concentration of crystallizable units (CH_2) and ε the

EBSCOhost - printed on 2/13/2023 3:45 AM via . All use subject to https://www.ebsco.com/terms-of-use

concentration of noncrystallizable units (defects), then the case of a fully exclusion of defects from the crystals can be shown to be equal to:

$$\alpha^{o} = (1-\varepsilon)^{\nu} = \ell^{\nu\, \ell n(1-\varepsilon)} \simeq e^{-\nu\varepsilon} \qquad |5|$$

where ν is the number of backbone units within a crystalline stem of length ℓ. If also chain sequences containing one defect are allowed to crystallize, then:

$$\alpha^{1} = (1-\varepsilon)^{\nu} + \nu\varepsilon(1-\varepsilon)^{\nu-1} \simeq e^{-\nu\varepsilon}(1+\nu\varepsilon) \qquad |6|$$

This model demands 0.5 defects per crystalline stem. If additionally, chain sequences having 2 defects can crystallize, then:

$$\alpha^{2} = e^{-\nu\varepsilon}\left(1+\nu\varepsilon + \frac{(\nu e)^{2}}{2}\right) \qquad |7|$$

This model yields on average the incorporation of one defect per crystalline stem. One generates in this way all possible models with different inclusion values. Comparison of experiment with the plot of α vs $\nu\varepsilon$ allows a straightforward distinction between models with different amounts of defect incorporation. Fig. 1 illustrates the excellent linear correlation obtained between ε_c values according to equation |1|, and crystalline defect content derived using the statistical approach for melt crystallized PE.

Another route used to determine the level of defect incorporation within the crystals is through analysis of the paracrystalline lattice distortions (27). If kinks are simultaneously the cause of lattice distortions and the accommodation sites for the chain defects one may attempt to calculate the level of defects within the crystals from the distortion parameter $g_{hk\ell}=\Delta d/\bar{d}_{hk\ell}$, where d is the lattice plane separation and Δd represents the mean statistical fluctuation. The 2g1 kink isomers do not fit efficiently into the lattice thus producing a cell expansion preferentially along the (110) direction. This dilatation is approximately of 50% with respect to the undisturbed zig-zag interchain separation. If dR/R is the relative thickening of the chain (R being the radius of the molecular cross section normal to c) due to the formation of a 2g1 kink in the (110) direction and γ is the concentration of kinks within the lattice, the value of the distortion parameter will be:

EBSCOhost - printed on 2/13/2023 3:45 AM via . All use subject to https://www.ebsco.com/terms-of-use

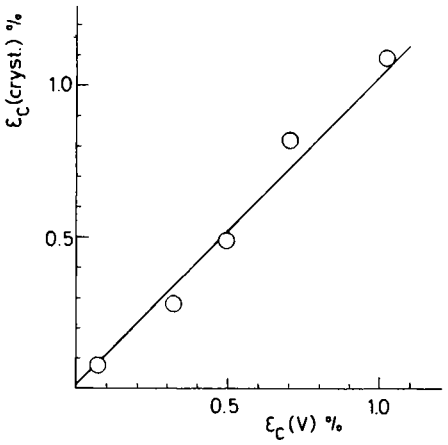

Fig. 1. Correlation between the level of defects incorporated within PE crystals using the statistical approach (Ref. 25) and ε_c (from eq. 1).

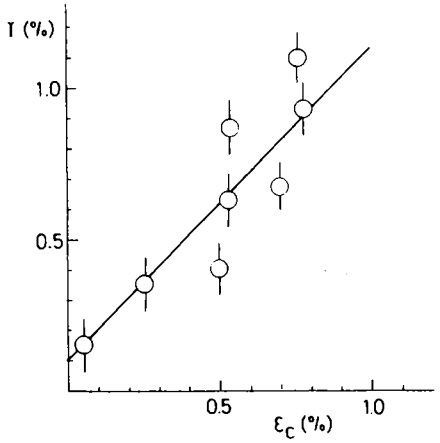

Fig. 2. Correlation between γ (from eq. 8) and ε_c (from eq. 1) for PE containing large alkyl defects.

EBSCOhost - printed on 2/13/2023 3:45 AM via . All use subject to https://www.ebsco.com/terms-of-use

$$g = \left[(\gamma(1-\gamma)\right]^{1/2} dR/R \qquad |8|$$

The correlation found between γ and ε_c for isothermally crystallized PE (Fig. 2) supports the concept of generation of 2g1 kinks around chain defects. The data of Fig. 2 show that $\gamma > \varepsilon_c$ suggesting that γ offers the sum of a background level of kinks, ε_o, plus a number of conformers generated by inclusion of chain defects in the crystals. From Fig. 2 one would derive an approximate value $\varepsilon_o \sim 1x10^{-3}$. A further method used for the evaluation of the number of defects occluded in the crystals is the removal of the noncrystalline regions through chemical degradation of the polymer (28-29). The level of chain defects in the remnant crystalline regions is then evaluated by a suitable technique. For low defect concentrations, quantitative results are, sometimes, difficult to obtain. For melt crystallized PE the use of the methyl band at 1376 cm^{-1} has confirmed the levels of defect inclusion derived from unit cell dilatation data (29). In case of solution-grown crystals of copolymers L and D lactides, the degree of partitioning of the optically active units has been, likewise, measured succesfully by photometric methods after selective hydrolysis on the disordered regions (30).

Finally, in certain cases the distribution of defects can be investigated by scattering techniques. Specifically from the scattering power, studied by low-angle X-ray scattering and the density, the partition coefficient has been evaluated for chlorinated polyethylene (9). The partition coefficient of chlorine decreases gradually with increasing concentration of chlorine in the polymer, similarly as in the case of alkyl branches. Comparison of the intensities of small-angle neutron and X-ray scattering also permits a direct estimation of the degree of partitioning of the noncrystallizable side units of semicrystalline polymers. It is found that SANS is very sensitive to the presence of small amounts of defects if their scattering length is sufficiently different from that of the crystallizable units. The capability of the method has been also tested on chlorinated PE (11). However, the results reported in this case show, contrary to the above data, that the fraction of incorporated defects (chlorine) rises, instead to sink, if ε is increased. No explanation about this discrepancy is available. Comparison of the level of defect incorporation using low angle scattering techniques

EBSCOhost - printed on 2/13/2023 3:45 AM via . All use subject to https://www.ebsco.com/terms-of-use

and unit cell dilatation could illuminate this problem.

The above calculations are based on the concept of a two phase model. According to Kilian (31) the morphology should be rather described by a three-phase model which is derived by inserting a transition region between the two phases with an enhanced concentration of chain defects. Most significant in this model is the fact that the properties of the nonhomogeneous microphase (crystal core plus defective surface boundary) can be regarded as a thermodynamically autonomous region.

Crystal Perfection: Dependence on the Level of Defects

We wish to discuss the influence of the level of defects on certain parameters which characterize the internal crystal perfection of the polymer. As a model system we employ a series of samples of PE containing butyl or longer branches isothermally crystallized ($\Delta T \sim 10°C$) from the melt (27). The lamellar thickness, ℓ, decreases with increasing defect concentration while the thickness of the noncrystallized layer, $L-\ell$, sandwiched between adjacent crystals rapidly increases with ε (Fig. 3). Such an increase in the defective layer suggests a gradual exclusion from the crystals of chain sequences containing an increasing number of chain defects. The average thickness of the lamellae, ℓ, is larger than the predictions of ℓ made from the nonhomogeneous microphase concept (31). This result together with the unit-cell volume increase obtained, favours the view that a fraction ε_c of defects is contained within the lattice.

In addition, the increasing level of defects within the chains drastically reduces the lateral crystal block dimensions, enlarges the anisotropy of the crystals (Table 1) and provokes a clear increase in the paracrystalline lattice distortions. The simultaneous average crystal size ($\bar{D}=(X+Y)/2$) decrease and lattice distortions increase obtained for slowly crystallized PE is illustrated in Fig. 4, and follows the relation:

$$\bar{D}/\bar{d} = (\alpha^*/g)^2 \qquad |9|$$

where $\alpha^* \sim 1/6$ and $d \sim 4.15$ Å.

EBSCOhost - printed on 2/13/2023 3:45 AM via . All use subject to https://www.ebsco.com/terms-of-use

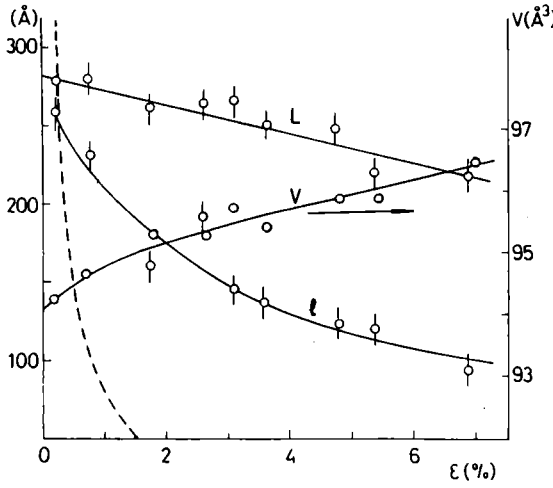

Fig. 3. Changes in lamellar dimensions (L, ℓ), average distance between defects (dotted line) and unit cell volume of PE with defect content.

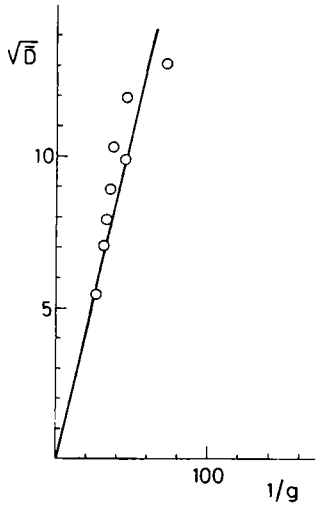

Fig. 4. Plot of $\bar{D}^{1/2}$ against 1/g according to eq. 9. Data from Fig. 3.

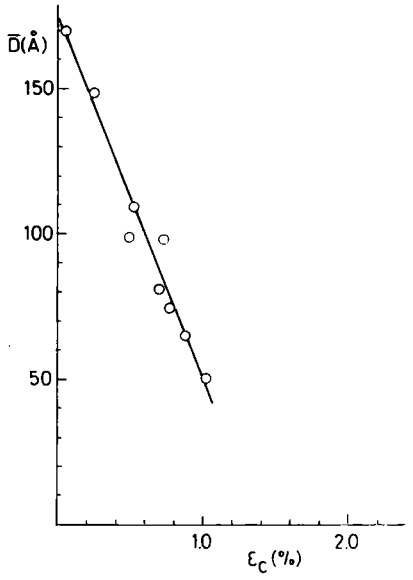

Fig. 5. Influence of ε_c on $\bar{D}$ (see text)

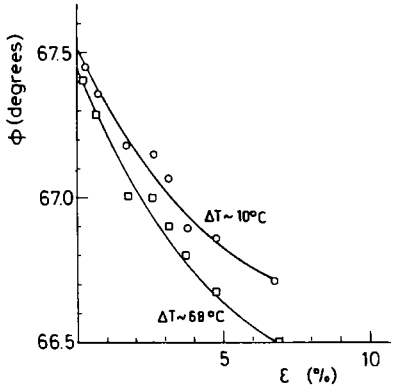

Fig. 6. The angle ϕ between unit cell diagonals vs. ε_c: influence of supercooling.

EBSCOhost - printed on 2/13/2023 3:45 AM via . All use subject to https://www.ebsco.com/terms-of-use

Table 1. Shape Ellipsoid Axes, X and Y, Eccentricity X/Y and Radius $\bar{D}_{100}$ in the (hkO) Plane of PE as a Function of ε (Ref. 27)

ε(%)	$\bar{D}_{100}$(Å)	X(Å)	Y(Å)	Y/X
0.17	151	206	137	.67
0.70	130	179	118	.66
1.76	83	145	73	.50
2.63	70	136	61	.45
3.04	53	116	45	.40
3.61	43	92	37	.40
4.77	47	111	40	.37
5.34	68	137	59	.43
6.90	36	71	32	.44

Thus, it is clear that the increasing amount of defect incorporation, $\varepsilon_c \sim \gamma$, not only induces, according to equation |9|, the observed lattice distortion increase but also causes a concurrent depression in $\bar{D}$ shown in Fig. 5. The mechanism of local plastic deformation of a semicrystalline polymer under compression has been shown, in fact, to be primarily governed by the initial mosaic block structure ($\bar{D}$), controlling the generation of a final system of shear planes (32). Hence, crystal perfection depends on the level of defects and controls the final mechanical behaviour of the polymer. The increasing defect penetration within the crystals causes additionally a change of the crystal structure from orthorhombic (ϕ=67.45°) towards hexagonal (ϕ=66.7°) symmetry. The reduction in size of $\bar{D}$ and concurrent anisotropy increase of the shape ellipsoid with increasing ε is consistent, on the other hand, with the increased rejection of a fraction of defects into the grain boundaries parallel to (110) growth surface. The probability for molecules with increasing defect content to contribute to the lateral crystal growth diminishes and growth soon stops with exclusion of defective molecules into the lateral grain boundary.

From the above considerations the incorporation of chain sequences containing alkyl branches in the lattice is visualized as a kind of chain disorder, which makes nearly perfect space-filling point

EBSCOhost - printed on 2/13/2023 3:45 AM via . All use subject to https://www.ebsco.com/terms-of-use

defects. Exposure of melt crystallized PE to fuming nitric acid has been shown to offer a possible way to distinguish between removal of these defects expanding the lattice and those from more defective regions in lamellar PE. In this sense comparison of the total concentration of branches - as derived from the methyl band analysis at 1376 cm^{-1} with the level of defect inclusion calculated from unit cell data sheds light on the nature of the defects throughout the stages of the degradation process (33). During the first stage (t~50h), about 2/3 of point defects, presumably located within thinner and more defective crystallites, are removed. The remaining branches persist within the crystals for more advanced stages of degradation (t~180h). However, a number of branches which do not expand the lattice, but yet, still detectable after the removal of the "amorphous" phase, are occluded probably as "amorphous"defects in the crystal cores. These "amorphous" defects are gradually digested from the crystal core and in long exposures are eventually removed. One possibility for the defects persisting after longer treatment times (~170h) is their incorporation in a cooperative manner efficiently filling intermolecular crystalline voids (33).

Influence of Crystallization Conditions and Size of Defects

According to kinetic theories of copolymer crystallization (19),the faster the crystal growth rate (low crystallization temperatures), the larger is the inclusion of non crystallizable units in the crystals. In case of melt crystallized PE containing large alkyl branches the level of defect inclusion ε_c has been studied for two different supercoolings (34). Table 2 indicates that, on the average, the amount of incorporation ε_c is about 20-30% larger for the PE samples crystallized at lower temperatures, in accordance with kinetic theories. Larger supercoolings, thus, lead to an increase in the rate of crystal growth and to a decrease in the time available for attachment of a chain sequence at the growing crystal face. The larger amount of defects incorporation for the samples crystallized at lower temperatures provokes, in addition, an enhanced modification of the crystal structure showing a faster shift from the orthorombic (ϕ=67.5°) towards hexagonal (ϕ=60°) symmetry than for samples melt crystallized at higher temperature (Fig. 6).

EBSCOhost - printed on 2/13/2023 3:45 AM via . All use subject to https://www.ebsco.com/terms-of-use

Table 2. Influence of Supercooling on the Level of Defect Incorporation within PE crystals (Ref. 34)

ε (%)	ε_c ($\Delta T \sim 10°C$)	ε_c ($\Delta T \sim 68°C$)
0.19	0.07	0.10
0.70	0.25	0.28
2.63	0.52	0.60
3.04	0.73	0.81
3.61	0.56	0.81
4.80	0.77	0.65
5.34	0.77	0.98
6.90	1.02	1.20

The amount of defect incorporation in the crystals is known to depend markedly on the size of the groups attached to the main chain (6,10,16). However, quantitative assessment about the degree of partitioning was missing. In Fig. 7 we give illustrative examples on the amount of defect incorporation, using equation |1|, for ethylene/α-olefin, ethylene - vinyl acetate and ethylene-acrylic acid copolymers, chlorinated PE, and PE containing known amount of short chain branching. The branching levels, ε, and unit-cell volumes were taken from references (8,10,12,22). The samples were cooled from melt. The data of Fig. 7 show that the smallest defects (methyl and ethyl) are more easily accommodated within the lattice offering the largest levels of defect inclusion (~0.7 crystalline defects per chain defect). The degree of incorporation is substantially much lower (~0.2 crystalline defects per chain defect) for chain sequences with butyl and longer alkyl branches and for chlorine side groups. Finally carboxylic-acid and ester side groups show the lowest values (0.15 and 0.1 respectively). It is shown that, according to kinetic predictions, the faster the crystallization the greater the level of inclusion. The increasing defect penetration in the crystals modifies, additionally, the chain packing within the cell depending on the defect size. Thus the angle between diagonals, ϕ, within the unit cell is shown to decrease at different rates in Fig. 8, as a function of ε. Smaller defects (methyl, ethyl) penetrate in the crystals very efficiently ($\varepsilon_c \sim 1\%$), showing a shift

EBSCOhost - printed on 2/13/2023 3:45 AM via . All use subject to https://www.ebsco.com/terms-of-use

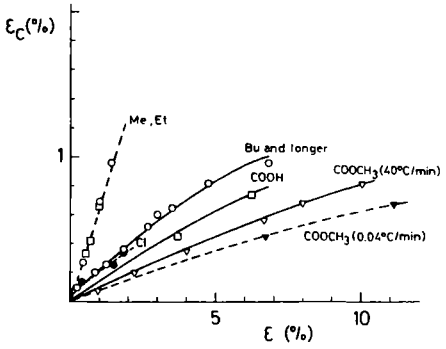

Fig. 7. Level of defect incorporation within crystals vs. ε for different defect types.

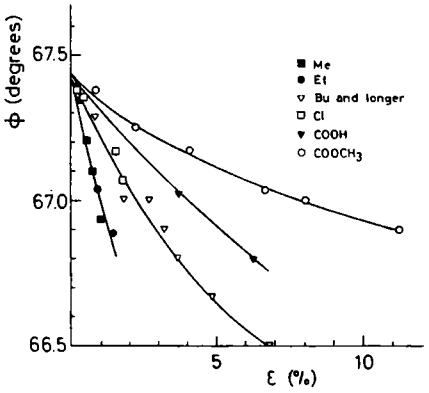

Fig. 8. Unit cell symmetry as a function of ε. Same defect types as in Fig. 7.

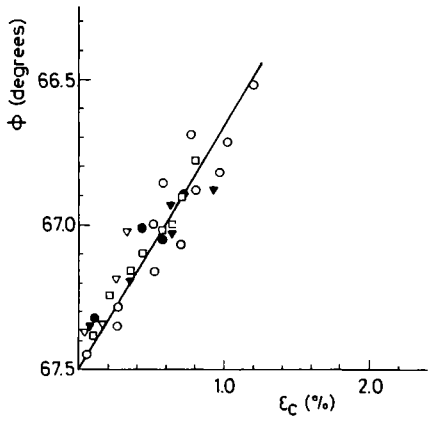

Fig. 9. Plot of ϕ against ε_c for PE with different defects.

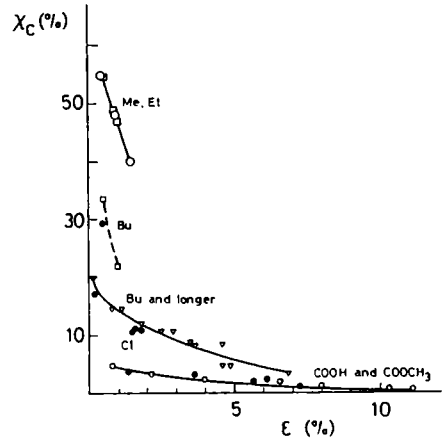

Fig. 10. Fraction of defects incorporated within the PE crystalline phase as a function of ε. Same data as in Fig. 7.

EBSCOhost - printed on 2/13/2023 3:45 AM via . All use subject to https://www.ebsco.com/terms-of-use

from orthorhombic symmetry (67.4°) to 66.9°at ε~1%. On the contrary, bulkier defects, penetrating much less, like ester side groups (ε_c~0.1%), require a much higher defect content (ε~11%) to reach the symmetry of ϕ~66.9. Thus, the measure of ϕ provides an indirect mode to estimate the defect inclusion within the crystals. The linear correlation found between ϕ and ε_c is depicted in Fig. 9.

The overall fraction of defects, χ_c, incorporated within the crystals for the different defect types is shown in Fig. 10. For polymer chains with methyl and ethyl branches the partition of defects between crystalline and amorphous regions is nearly at random (Γ=0.7-1.0). For PE containing longer alkyl branches and chlorine side groups, Γ=0.05-0.25, i.e. a large content of defects is excluded from the lattice. For chains with carboxylic acid and ester side groups, Γ=0.01-0.09, indicating that only a very small amount of defects are incorporated into the lattice. In all cases χ_c or $\Gamma=\chi_c/\chi_a$ is a decreasing function of the overall concentration of defects within the polymer. In addition, the fraction of defects rejected into the noncrystalline regions, $\chi_a=1-\chi_c$ increases more rapidly with ε for the small groups than for the bulkier defects.

Plastic Deformation and Annealing Behaviour

Further studies concerning the degree of partitioning of PE have been provided by measurement of the unit cell dilatation in drawn PE with known levels of large chain defects, varying from ε=0.05 to ε=3% (35). The samples were cold drawn to their natural draw ratio (36). The values for the level of defect incorporation in the crystals, ε_c, and the degree of partitioning are collected in Table 3 as a function of ε. For defect levels, $\varepsilon \leq 1\%$, the amount of incorporation, ε_c=0. For ε>1%, ε_c increases linearly with ε though at a much higher rate (40%) than for melt crystallized case (~20%). Thus during plastic deformation of samples with low levels of defects ($\varepsilon \leq 1\%$ and ε_c~0.2) a total rejection of defects from the crystals takes place (Γ=0). Such a defect exclusion of chain defects from the crystal lattice during drawing sheds light on the mechanism of deformation. Indeed, during transformation of the lamellar structure, through neck formation, into the fiber structure not only the initial crystals are severely modified into

EBSCOhost - printed on 2/13/2023 3:45 AM via . All use subject to https://www.ebsco.com/terms-of-use

Table 3. Chain Defect Inclusion Data within Crystals in Cold Drawn PE

ε (%)	ε_a (%)	ε_c (%)	α	$\Gamma=\chi_c/\chi_a$
0.05	0.1	0	0.95	0
0.6	1.7	0	0.65	0
0.9	2.0	0	0.60	0
1.74	3.44	0.35	0.55	0.11
2.5	4.77	0.64	0.55	0.14
3.0	5.6	0.83	0.55	0.15

smaller blocks but also the chain sequences containing branches are segregated into the noncrystalline regions through a diffusion mechanism involving a liquid-like (37) state. For defect concentrations larger than $\varepsilon \sim 1\%$ the equilibrium state of segregation is not any longer maintained and the fraction of defects incorporated in the lattice suddenly increases up to $\chi_c \tilde{=} 11\text{-}12\%$. The degree of partitioning here ($\Gamma \sim 11\text{-}0.15$) is similar to that for melt crystallized PE having a similar number of defects.

A salient property of polymer lamellae is their ability to thicken in the axis direction when annealed isothermally above the crystallization temperature. How does annealing affects the level of defects accommodated within the crystals? The level ε_c of the remnant defects after annealing, has been examined for melt crystallized and drawn PE with a defect content of $\varepsilon=3\%$, using unit cell data (38-40). In case of drawn polyethylene substantial superstructure changes occur on annealing (41). At high enough temperatures strong retractive forces reverse the sliding motion of microfibrils. In addition, molecular mobility allows lateral alignment of crystals in adjacent fibrils, as well as concurrent growth of lamellar thickness by means of solid state refolding. The linear decrease in the number of incorporated defects that expanded the lattice and, concurrent increase in L as a function of annealing temperature T_A is shown in Fig. 11. The gradual rejection of chain defects to the lateral and axial surfaces of the crystal blocks is probably related to the enhanced longitudinal chain mobility in the crystal lattice and lateral boundaries. Thus, the degree of partitioning for the drawn

EBSCOhost - printed on 2/13/2023 3:45 AM via . All use subject to https://www.ebsco.com/terms-of-use

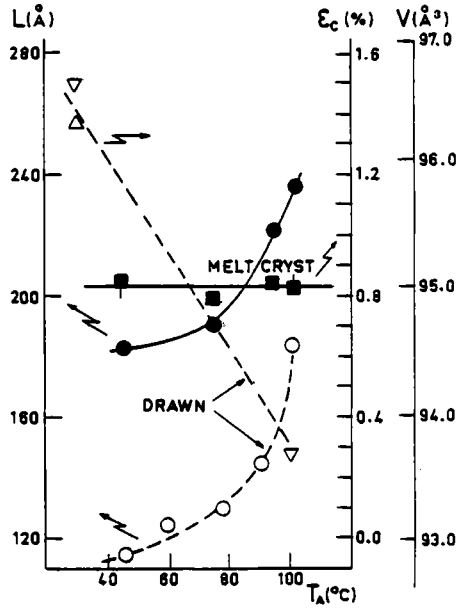

Fig. 11. Long period (L), unit cell volume (V) and amount of defect incorporation (ε_c) for PE with ε=3%, melt crystallized and drawn (room temperature) as a function of annealing temperature (T_A).

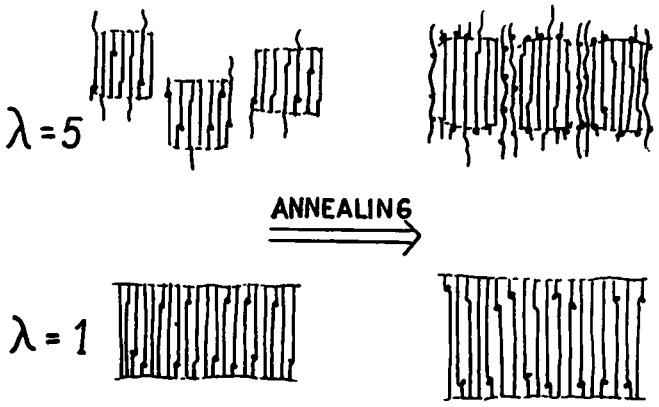

Fig. 12. Schematics of changes in defect inclusion within crystals of melt crystallized (bottom) and drawn PE (ε=3%) (top), after annealing at T_m-T_A~10°C.

EBSCOhost - printed on 2/13/2023 3:45 AM via . All use subject to https://www.ebsco.com/terms-of-use

sample (Table 3) decreases from $\Gamma \sim 0.15$ to $\Gamma \sim 0$, after annealing at $T_A \sim 100°C$. In case of melt crystallized PE with $\varepsilon = 3\%$, the major effect on annealing is the increase in lamellar thickness from 185 Å up to 240 Å (Fig. 11). However, no significant change in the lattice spacing is observed, showing that the concentration of defects does not change appreciably with the heat treatment. This observation is in accordance with the findings of Holdsworth and Keller (7) on ethyl and methyl branched copolymers of PE from dilute solution. Fig. 12 summarizes schematically the changes in defect incorporation and lamellar thickness within melt crystallized (bottom) and drawn PE with $\varepsilon \sim 3\%$ after annealing at $T_m - T_a \sim 10\ °C$. In summary: The removal of chain defect sequences from the crystal, strongly depends on whether the polymer exhibits a fibrilar or a lamellar morphology. The main difference between both morphologies, relating to the defect rejection behaviour, lies in the different surface to volume ratio for the crystals of each type. Thus the microfibril structure of the drawn polymer offers a multitude of longitudinal grain boundaries with small crystallites, favouring a defect exclusion on annealing. The structure for the melt crystallized polymer is characterized by stacks of wider lamellae with fewer grain boundaries. Hence, on annealing, despite the increase in lamellar thickness, the chain defects cannot diffuse out of the crystals.

Conclusions

a) It is shown that the use of unit cell dilatation data, assuming the concept of defect accommodation through generation of kinks within the crystals is a satisfactory method for an evaluation of the amount of defect incorporation, ε_c, in a semicrystalline polymer. The values obtained yield an excellent agreement with those derived from a simple statistical approach based on crystallinity and crystal thickness data.

b) The level of defect incorporation derived from the analysis of paracrystalline distortions yields slightly larger values than, ε_c due, probably, to the presence of additional conformational defects.

EBSCOhost - printed on 2/13/2023 3:45 AM via . All use subject to https://www.ebsco.com/terms-of-use

c) The incorporation of chain defects causes a deterioration of the internal crystal structure: a significant crystallite volume decrease and crystal anisotropy increase, a modification of the crystal structure towards an hexagonal symmetry, development of paracrystalline lattice distortions, and formation of "amorphous" defects and other imperfections.

d) The "inclusion" model (Γ=1, random distribution) describes adequately the structure of polyethylene containing a low content of methyl and ethyl groups. For the rest of the systems investigated a predominant degree of defect exclusion, with a tendency towards a full "exclusion", for high defect concentrations, was found. The partition coefficient Γ was observed to decrease in all cases with increasing ε. Crystallization conditions also influence the level of defect inclusion in line with kinetic predictions.

e) The "exclusion" model ($\Gamma \sim 0$) describes properly the structure of cold drawn PE containing large alkyl branches and low defect content. For $\varepsilon > 1\%$ the partition coefficient reaches a value $\Gamma \sim 0.11\text{-}0.14$, increasing with ε.

f) Annealing of drawn PE with ε=3% results in a healing of crystal defects due to the enhancement of chain mobility leading to rejection of many branches into the available grain boundaries of the fiber structure. For $T_A = T_m - 10°C$ a total defect exclusion is proposed (Γ=0). On the contrary, annealing of melt crystallized PE with ε=3% does not influence significantly the average concentration of incorporated defects within crystals despite the observed increase in lamellar thickness.

References

1. Eichhorn, R.M. 1956. J. Polymer Sci. 31, 197.

2. Cole, E.A., Holms, D.R. 1960. J. Polymer Sci. 46, 245.

3. Swan, P.R. 1962. J. Polymer Sci. 56, 409.

4. Wunderlich, B., Poland, D. 1963. J. Polymer Sci. A1, 357.

5. Kilian, H.G., Müller, F.H. 1963. Kolloid Z.Z. Polymere, 192, 34.

EBSCOhost - printed on 2/13/2023 3:45 AM via . All use subject to https://www.ebsco.com/terms-of-use

6. Baker, C.H., Maldelkern, L. 1966. Polymer, 7, 71.

7. Holdsworth, P.J., Keller, A. 1967. J. Polym. Sci. Polym. Lett. 5, 605.

8. Kortleve, G. Tuijnman, C.A.F., Vonk, C.G. 1972. J. Polymer Sci. A2-10, 123.

9. Roe, R.J. Gieniewski, C. 1973. Macromolecules. 6, 212.

10. Preedy, J.E. 1973. Br. Polym. J. 5, 13.

11. Kalepky, U., Fischer, E.W., Herchenröder, P., Schelten, J., Lieser, G. Wegner, G. 1979. J. Polym. Sci. Polym. Phys. Ed. 17, 2117.

12. Roe, R.J., Cole, H.F., Morrow, D.R. "Advances of Polymer Science and Engineering". Pae, K.D., Morrow, D.R. and Chen, Y. Ed. Plenun Press. N.Y. 1972. p. 27.

13. Martuscelli, E., Pracella, M. 1974. Polymer. 15, 306.

14. Martuscelli, E. 1975. J. Macromol. Sci. Phys. B11(1), 1.

15. Griskey, R.G., Foster, G.N. 1966. J. Polym. Sci. A1-8, 1623.

16. Richardson, M.R., Flory, P.J., Jackson, J.B. 1963. Polymer. 4,221.

17. Peterlin, A., Baltá Calleja, F.J. 1970. Kolloid Z.Z. Polymere, 242, 1093.

18. Martinez Salazar, J., Baltá Calleja, F.J. 1983. J. Materials Sci. 18, 1077.

19. Helfand, E., Lauritzen, J.I.Jr. 1973. Macromolecules. 6, 631.

20. Sanchez, I.C. 1977. J. Polym. Sci. Polym. Symp. 59, 109.

21. Keating, D.T. 1968. J. Phys. Chem. Solids. 29, 771.

22. Baltá Calleja, F.J., Gonzalez Ortega, J.C., Martinez Salazar, J. 1978. Polymer. 19, 1094.

23. Vonk, C.G. 1972. J. Polymer Sci. C38, 429.

24. Pechhold, W., Blasenbrey, S. 1967. Kolloid Z.Z. Polymere. 235, 216.

25. Martinez Salazar, J., Baltá Calleja, F.J. 1980. Polymer Bulletin 2, 163.

26. Hosemann, R., Baltá Calleja, F.J. 1979. Polymer. 20, 1091.

27. Martinez Salazar, J., Baltá Calleja, F.J. 1979. J. Crystal Growth. 48, 283.

28. Holdsworth, P.J., Keller, A. 1964. Makromol. Chem. 125, 94.

EBSCOhost - printed on 2/13/2023 3:45 AM via . All use subject to https://www.ebsco.com/terms-of-use

29. Cagiao, M.E., Rueda, D.R., Baltá Calleja, F.J. 1980. Polymer Bulletin. 3, 305.

30. Fischer, E.W., Sterzel, J., Wegner, G. 1973. Kolloid Z.Z. Polymere. 251, 980.

31. Kilian, H.G. 1984. Colloid and Polymer Sci. 262, 374.

32. Baltá Calleja, F.J., Kilian, H.G. (in press) Colloid and Polymer Sci.

33. Cagiao, M.E., Baltá Calleja, F.J. 1982. J. Macromol. Sci. Phys. B21, 519.

34. Baltá Calleja, F.J., Martinez Salazar, J., Cackovic, H., Loboda-Cackovic, J. 1981. J. Materials Sci. 16, 739.

35. Baltá Calleja, F.J., Hosemann, R. 1980. J. Polym. Sci. Polym. Phys. Ed. 18, 1159.

36. Cackovic, H. Loboda-Cackovic, J. Hosemann, R. 1977. J. Polym. Sci. Polym. Symp. 58, 59.

37. Peterlin, A. 1971. J. Materials Sci. 6, 490.

38. Miyaji, H., Asai, K. 1978. J. Polym. Sci. Polym. Phys. Ed. 16, 1325.

39. Baltá Calleja, F.J., López Cabarcos, E. 1982. Colloid and Polymer Sci., 260, 694.

40. Baltá Calleja, F.J., Rueda, D.R., López Cabarcos, E. (in press) Colloid and Polymer Sci.

41. Yeh, G.S.Y., Hosemann, R., Loboda-Cacakovic, J., Cackovic, H. 1976. Polymer. 17, 309.

EBSCOhost - printed on 2/13/2023 3:45 AM via . All use subject to https://www.ebsco.com/terms-of-use

EBSCOhost - printed on 2/13/2023 3:45 AM via . All use subject to https://www.ebsco.com/terms-of-use

ORGANIZATION IN MELT-CRYSTALLIZED POLYMERS

D C Bassett

J J Thompson Laboratory
University of Reading UK

Introduction

Organization within polymers is of great practical importance because different processing treatments produce different properties. In the case of amorphous polymers these reflect primarily differences in molecular orientation and conformation. For crystalline polymers such factors are also present but now of crucial importance is the presence of crystallites, producing rigidity with enhanced strength and moduli. For many years it was thought, from X-ray evidence, that crystallites were small (of order 10nm) in all directions and were embedded like currants in a plum pudding. In these circumstances, with crystallites in essentially equivalent, disordered environments, many properties would depend primarily on the fraction of crystallites usually called the degree of crystallinity. Over limited changes in processing conditions this can be the case but during the last decade we have become accustomed to dramatic improvements in strength and stiffness of high performance fibres. These depend ultimately on achieving continuity of crystalline regions through a sample. The degree of crystallinity has little relevance in these circumstances. It is the placement of adjacent crystallites rather than their quantity which controls properties.

There is only one way directly to reveal the details and relative placing of crystallites of 10nm scale: transmission electron microscopy. (The resolution of scanning instruments is not usually adequate). In other branches of materials science the advent of double condenser transmission instruments thirty years ago brought great gains in the knowledge of

Morphology of Polymers
© 1986 Walter de Gruyter & Co., Berlin · New York - Printed in Germany.

EBSCOhost - printed on 2/13/2023 3:45 AM via . All use subject to https://www.ebsco.com/terms-of-use

microstructure not least in the observation of dislocations, and their distribution. The coincidental synthesis of linear and stereoregular macromolecules enabled better-defined polymeric systems to be studied with the new instruments. Polymer single crystals were discovered and shown to contain chain-folded molecules. In succeeding years there was much detailed investigation of solution-grown lamellae and their properties. Radiation damage, however, limited what could be achieved to comparatively low magnifications usually no more than a few thousand times, although for example with diffraction imaging and moire methods it was still possible to derive information on an interatomic scale ie of dislocation Burgers vectors. Even now with particularly resistant polymers and minimal exposures, to image a polymeric crystal lattice is difficult and systematic study of textural differences scarcely possible.

These important successes have, however, essentially been limited to solution-crystallized or solid-state polymerized systems. The direct extension to melt-crystallized polymers, necessary to understand commercial properties, is particularly difficult. A section of melt-crystallized polymer sufficiently thin (say 50nm) to transmit electrons is particularly vulnerable to radiation damage. In contrast to individual solution-grown lamellae supported on a rigid carbon substrate, thin sections suffer internal mass transport during examination in transmission. One then observes specimens change from an initially featureless appearance by developing internal features but the detail produced tends not to be sharp and it is, at best, only indirectly related to the unaltered original morphology. These difficulties of radiation damage are fundamental. No way is known of circumventing them and they seem certain to continue severely to limit direct high resolution studies of polymers by transmission electron microscopy. There are, however, alternative indirect ways of studying the interior morphology of melt-crystallized polymers, notably

EBSCOhost - printed on 2/13/2023 3:45 AM via . All use subject to https://www.ebsco.com/terms-of-use

the replication of surfaces.

Replication of external and especially of fracture surfaces has historically been the principal method of observing melt-crystallized polymers at high resolution with the electron microscope. Lamellae were so observed on banded spherulites of polyethylene as early as 1957[1] while Geil's book of 1963[2] provides copious illustrations of lamellar arrangements in many polymers. The use of replication avoids radiation damage by substituting a metal-shadowed carbon impression of a surface for the sample. High resolutions can be achieved provided there is sufficient detail in the surface. In addition, there can be some possibility of diffraction microscopy when lamellae are pulled off a sample during replication, thereby allowing the determination of orientation and differentiation between alternative crystal structures.

Whether surface replication is useful depends primarily on there being sufficient detail in the specimen. External surfaces often have little to show and may well also be damaged. Fracture surfaces do show fine detail but if this is to relate readily to the original morphology, it is essential that there be no ductility both in the formation of the surface (which at liquid nitrogen temperatures is usually the case) and also in the replication. In materials of low crystallinity and others such as ultra-high mass polyethylene ductility is difficult to avoid and fracture surfaces of such materials are liable to suffer from substantial obscuration (Figure 1). Moreover, in samples which undergo brittle fracture, structure can be created by the propagating crack. In materials such as PTFE and pressure-crystallized polyethylene there is a prominent striation parallel to the chain produced in this way. While this has its utility as an indicator of local molecular orientation, it also tends to mask other detail and eg to hinder microscopic studies of deformation.

Until recently microscopic evidence for the existence of lamellae in

EBSCOhost - printed on 2/13/2023 3:45 AM via . All use subject to https://www.ebsco.com/terms-of-use

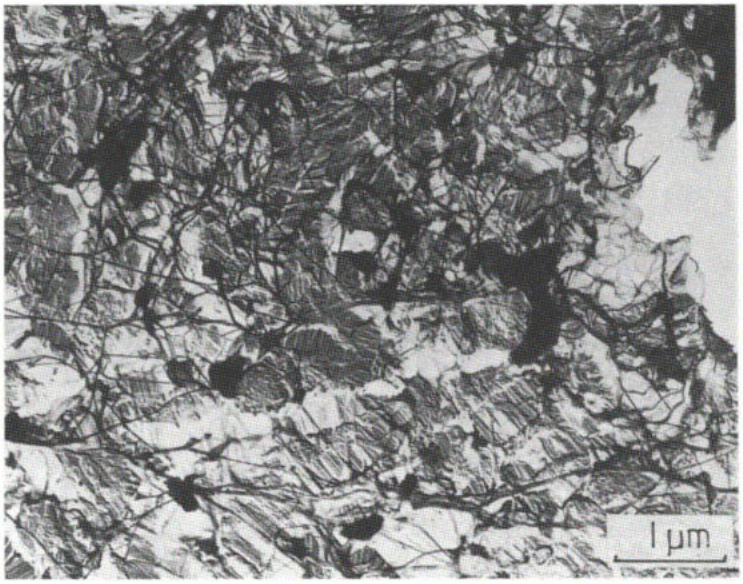

Figure 1. a. Fracture surface replica of Hifax ultra-high mass polyethylene crystallized at 5 kbar.
b. Replica of another portion of the same sample after permanganic etching.

EBSCOhost - printed on 2/13/2023 3:45 AM via . All use subject to https://www.ebsco.com/terms-of-use

crystalline polymers has had to come from examination of surfaces. Despite copious illustration, doubt always remained as to the reliability of such data and whether they were a sound guide to representative organization within the solid. Thus in some systems, for instance isotactic polypropylene, it can be observed optically during crystallization that the more soluble constituents of a specimen, ie the more stereoirregular, are comparatively mobile and can migrate to the exterior. One has then to decide whether lamellae observed on a surface relate to such special conditions or truly represent a typical situation. In a similar way, one must needs consider whether the crack which created a fracture surface propagated at random or not. We now know, for example, that fracture surfaces in polyethylene expose {200} surfaces with a high degree of preference, so much so that fracture fails to reveal important textural features lying normal to this plane. Nevertheless, we do now know that the presence of lamellae is reliably indicated and that their thickness can be adequately measured by sampling procedures. The undoubted bias occurs partly as selection of orientation and partly as the underrecording or even apparent absence of the more ductile populations in fracture surfaces.

Despite the considerable utility of fracture surface replication there are many specimens, such as textile fibres, for which it is not readily applicable. Alternative approaches have been sought notably via etching to expose or enhance detail in surfaces. Chemical etching, usually with a solvent, has been extensively attempted. It may be a fair generalization to say that, on the whole, such an approach is more suited to diferentiate between phases in blends rather than to reveal detail on a lamellar scale. Other approaches, using gases ionised in either AC or DC discharges, or activated at radio frequencies, have long been used to thin specimens but they have had little impact as aids to high resolution electron microscopy.

EBSCOhost - printed on 2/13/2023 3:45 AM via . All use subject to https://www.ebsco.com/terms-of-use

What has proved particularly useful is oxidative etching using strong acids. Following the initial discovery of Palmer and Cobbold[3], fuming nitric acid has been widely used for its effect on polyethylene. In samples crystallized from unperturbed melts, the acid penetrates between lamellae, cutting chains as it travels, eventually making samples friable and separable into individual lamellae but now consisting of paraffinoid chains with carboxyl and nitro end groups. To a first approximation, the length of these chains is that of the original lamellae measured along $\underline{c}$. Better approximations must recognize the presence of double and higher traverses, probably associated with folds buried deeply in the surface, and the diminution of thickness as attack proceeds. The predominant reaction is, however, the removal of side surfaces. This is sensitive to precise morphology and leads to differential removal among multiple lamellar populations.

The widest use of nitric acid treatment for microscopy has been in drawn polyethylene whose fibrous structure restricts penetration. This leaves a better surface for replication and has allowed Peterlin and coworkers among others to reveal lamellar outlines and normals within drawn samples and so to follow stages in tensile drawing. Unfortunately the method has been rather ineffective with other polymers while the acid's extensive penetration between lamellae tends to embrittle a sample and not to leave satisfactory surfaces for replication. Partly for these reasons, a search was initiated in this laboratory for alternative oxidising agents. This has led to the introduction of permanganic etching, a technique of wide applicability to many polymers. This approach and the advances which it has allowed will be discussed presently. Historically, however, it was preceded by the technique of chlorosulphonation of polyethylene. This is a quite different, and a complementary, method of revealing representative lamellar organization in a melt-crystallized polymer.

EBSCOhost - printed on 2/13/2023 3:45 AM via . All use subject to https://www.ebsco.com/terms-of-use

2. Chlorosulphonation of Polyethylene

The technique of chlorosulphonation has been developed principally by Kanig. It has been used by several groups to study internal lamellar morphologies in polyethylene, both linear and branched, but has remained confined in its application to this polymer. Treatment of polyethylene with chlorosulphonic acid causes chemical reaction. For linear polymers, immersion in the acid for 3 days at 60°C is typical but for highly branched or deformed samples much gentler treatment for short times at room temperature is appropriate. The result is to create internal contrast in samples by adding Cl and S atoms to lamellar surfaces. This level of contrast turns out to be essentially invariant and a property of the sample not subject to change by variation in the chemistry*. Thermal analysis of polyethylenes as a function of time of chlorosulphonation reinforces this point by producing endotherms with two peaks: one for the original state, one for the chlorosulphonated. The melting point is raised and the level of crystallinity drops (to zero in certain drawn samples). The change is accompanied by a very pronounced blackening, which moves into a sample as reaction proceeds. A specimen suitable for study is a thin section of the blackened polymer, which would be viewed in transmission.

The value of chlorosulphonation is not merely in the enhanced contrast produced, nor in the associated advantage of increased ease of sectioning. It is primarily because the contrast is stable in the electron

*Footnote

Although uranyl acetate is added after chlorosulphonation, it is not uranium which gives the contrast because essentially the same level is achieved if ammonium acetate is substituted instead. Moreover Cl and S atoms can be directly monitored in specimens by EDAX techniques.

EBSCOhost - printed on 2/13/2023 3:45 AM via . All use subject to https://www.ebsco.com/terms-of-use

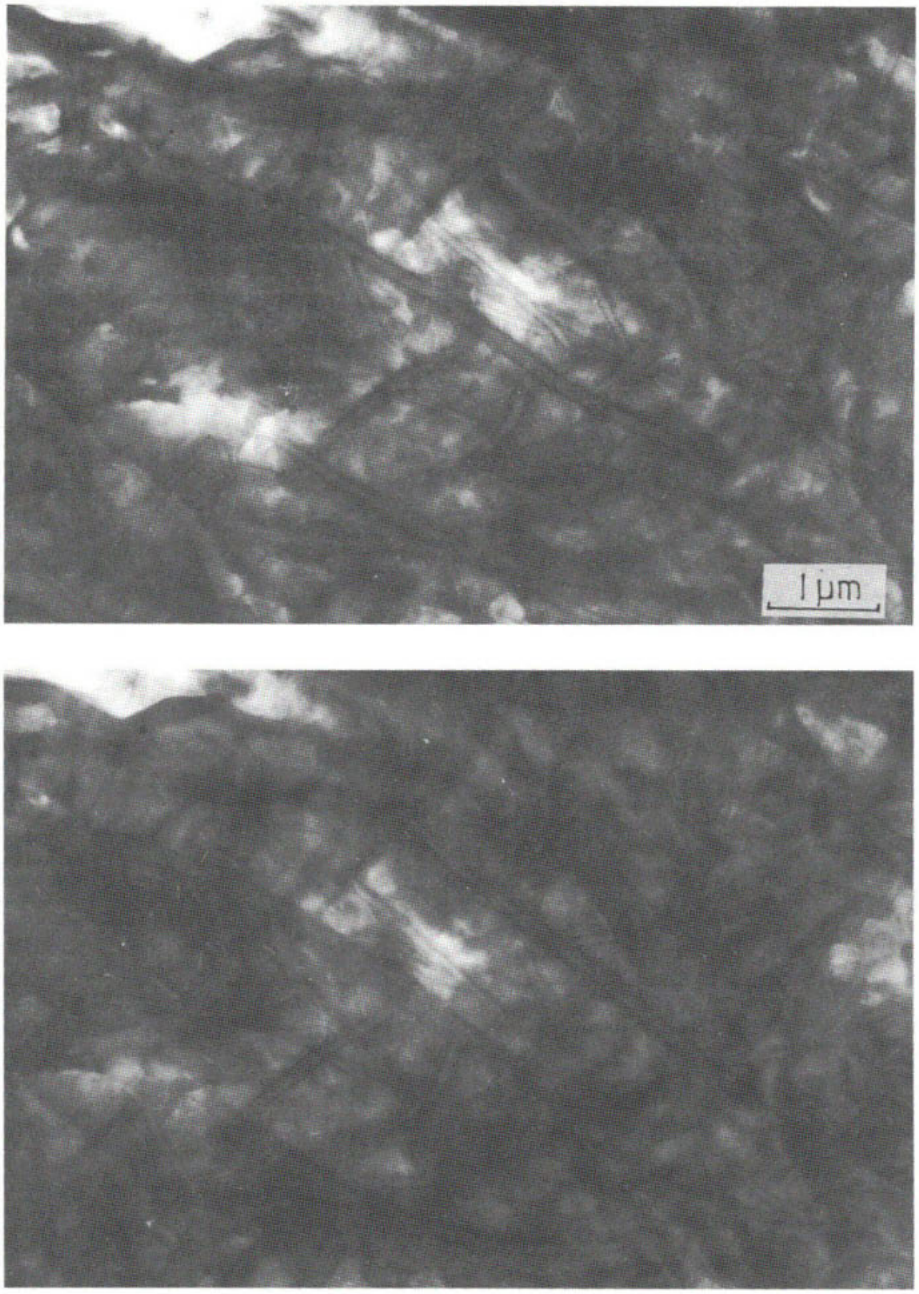

Figure 2. Two views of a chlorosulphonated section of the sample of figure 1. The sample has been rotated 18° about an axis at 4'oclock on the page between the two photographs.

EBSCOhost - printed on 2/13/2023 3:45 AM via . All use subject to https://www.ebsco.com/terms-of-use

beam. Chlorosulphonation achieved for the first time the opportunity of prolonged study of internal lamellar microstructure within the transmission microscope. Most of the studies performed have been concerned with morphology, using the enhanced contrast although diffraction imaging is possible in certain samples. The type of image which is usually reported is of arrays of parallel bands, white for lamellar interiors, black for surfaces. This represents a particular orientation when lamellae lie parallel to the electron beam. Other orientations are present but they present less contrast. In suitable circumstances, namely when section and lamellar thicknesses are comparable, it is possible to assess the orientation of lamellae directly from the separation and widths of the planes of contrast at fold surfaces (figure 2). Moreover, internal structure can be diagnosed when e.g. boundaries or line defects have afforded a path for reagents to penetrate and produce intralamellar contrast (figure 3).

The application of chlorosulphonation has demonstrated that melt-crystallized polyethylene is indeed a lamellar solid. This is true not only of the linear polymer but also of the less crystalline and highly branched materials. In particular it has validated in special cases[4] the structural models on which small angle X-ray scattering has been interpreted. In so doing it has brought us, together with the complementary technique of permanganic etching, the opportunity of developing a more fundamental knowledge and understanding of polymeric properties based on known rather than inferred or modelled structures. This is a position we might have hoped to have been in twenty five years ago but which radiation damage then denied us. Now that we do have the opportunity it is important to use it and develop understanding of polymers within the wider context of materials science.

EBSCOhost - printed on 2/13/2023 3:45 AM via . All use subject to https://www.ebsco.com/terms-of-use

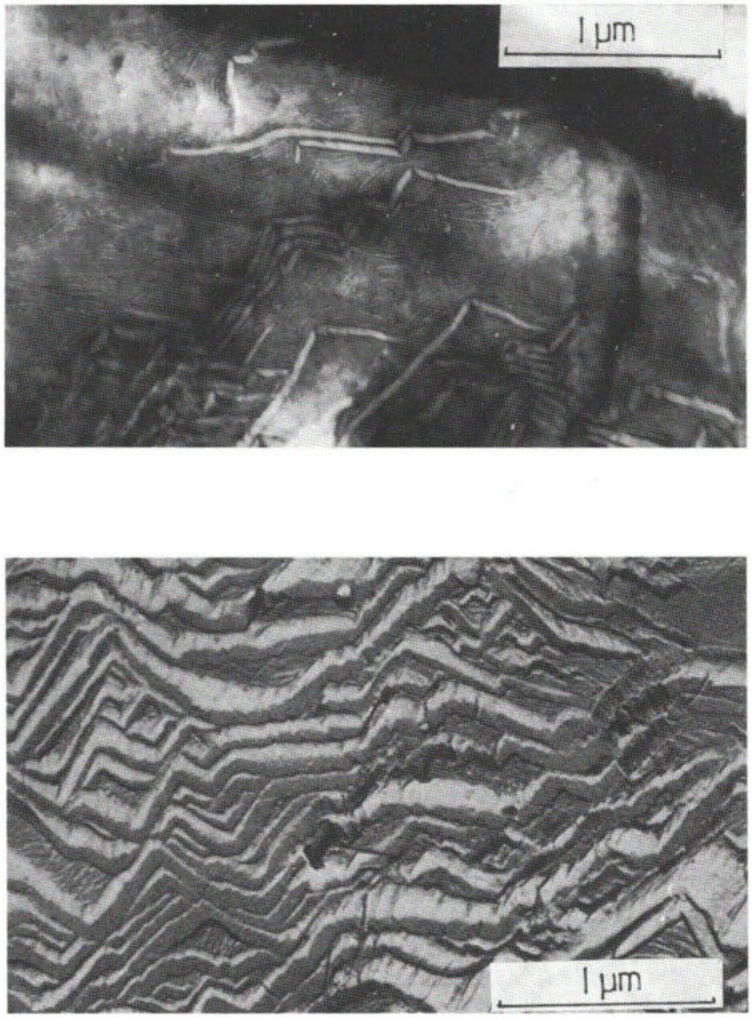

Figure 3. The same sample of linear polyethylene 85% of which crystallized at 130°C. Chlorosulphonated section (above). Replica of permanganically etched surface below.

EBSCOhost - printed on 2/13/2023 3:45 AM via . All use subject to https://www.ebsco.com/terms-of-use

3. Permanganic Etching

The technique of permanganic etching began to be developed in the University of Reading about ten years ago. It was found that solutions of potassium permanganate in sulphuric acid were capable of etching polyethylene surfaces and revealing copious lamellar detail. Early application was to the then current interest in pressure-crystallized polyethylene. This showed three important advantages over the previously used fracture surface methods namely (1) the striation created on fracture disappeared; (2) all orientations of lamellae were present instead of just projections down a and (3) multiple populations were seen as such whereas thinner lamellae were often not clearly present in fracture surfaces. For pressure-crystalized polyethylene such information confirmed what had been concluded by often laborious application of other techniques although particular details were new and interesting[5,6]. There was, however, an obvious and pressing need to apply the technique to the study of melt-crystallized polymers formed under more usual conditions.

This was undertaken using a standard etching condition and applied to linear polyethylenes (both fractionated and whole polymers) in the molecular weight range 25,000 to in excess of 10^6 and for crystallization temperatures from 130°C downwards[7-10]. What was discovered was in many ways unexpected. Lamellar profiles viewed down b the radial growth axis, were mostly non-planar. In the most regular ordering (where molecular lengths are about three crystal thicknesses) one finds repetitively-ridged sheets of facets close to {201}, with six or seven facets of order 0.5μm wide per sheet. (The alternation from (201) to ($20\bar{1}$) is invisible in the a projection presented in most fracture surfaces). These ridged sheets grow out individually into the melt enclosing columns of melt enriched in shorter molecular species. They have been termed dominant while later crystallizing lamellae into which the enclosed columns of melt eventually convert are

EBSCOhost - printed on 2/13/2023 3:45 AM via . All use subject to https://www.ebsco.com/terms-of-use

termed subsidiary. This dominant/subsidiary pattern is widespread, not only in polyethylene, but in all systems since investigated. In polyethylene itself, slight changes in growth conditions cause clear shifts in morphology. Thus whereas at 130°C, 30,000 mass polymer forms wholly ridged lamellae, in 40,000 mass material the dominant layers are now planar, or nearly so, sheets, but still {201}, and only the subsidiary lamellae are ridged. This is evidence of internal fractionation during isothermal crystallization which has been substantiated in related circumstances by selective extraction and molecular weight measurement. The continuing trend with either or both increasing molecular mass and decreasing crystallization temperature is from ridged, through planar or slightly curved lamellae to the totally unexpected S(or C-)-shaped profiles. In the great majority of conditions, certainly those of typical industrial use, the internal structure of melt-crystallized polyethylene is based on individual dominant layers with S(or C-)-shaped profiles down b and a few μm wide enclosing narrower, approximately planar subsidiary lamellae. Adjacent S's are in phase, thereby conforming to deductions of molecular conformation from polarizing microscopy, and their sense is uniquely related to the radial twist in banded spherulites: with increasing radial distance the rotation of an S is in the direction of the outward normals of its concave surfaces. All these morphological features have been confirmed independently both by permanganic etching and chlorosulphonation so that notwithstanding their novelty they are quite clearly genuine.

Traditional interpretation of spherulites has been in terms of radial fibres which branch and splay apart. There is not, however, any clear identification of a structural unit in homopolymers which might be identified with a fibre, certainly if one is looking for a fibre associated with a cellulation process and a width of order δ = Diffusion Coefficient/Growth Rate. The radial streaking seen in immature spherulites grown at high temperatures is,

EBSCOhost - printed on 2/13/2023 3:45 AM via . All use subject to https://www.ebsco.com/terms-of-use

for example, a consequence of the overlay of ridged sheets rather than a fibrous structure on the limit of resolution. Also one notes that dominant lamellae are individuals. Association of layers into what optically appear as discrete fibres (but are actually layers seen edge on) only occurs in heavily doped melts (figure 4) of say 1:1 linear: branched polyethylene or 1:1 isotactic: atactic polystyrene. In banded spherulites of polyethylene there is also only limited continuity of individual dominant lamellae along a given radius, of perhaps one third of a band period. The actual structure is more complex than arrays of radial fibres. Instead the twist giving the optical banding appears to propagate by rapid changes of lamellar normal direction around ordered arrays of screw dislocations separated by effectively untwisted lengths of S-shaped layer. This long-standing problem of crystal growth is linked to a more complex microstructure than had been realized but a solution may not be far off.

The importance for understanding properties of this new knowledge is based on internal fractionation which imposes periodic spatial variation of texture, molecular parameters and hence properties on samples. The basis of fractionation within spherulites is different from what had been supposed in that the individual dominant lamellae tend, in the systems studied, to be different from the more extensive cross-sections filled with subsidiary lamellae. Segregation between, or in internal pockets of, spherulites is of uncrystallizable or least crystallizable polymer with a further change in local properties. The significance of this microsegregation is well illustrated by the differences between linear and linear low-density polyethylenes. In the former, dominant lamellae consist of the longer molecules, subsidiary lamellae of the shorter. This results from the relative times of crystallization. Correspondingly the later-crystallizing species in the subsidiary lamellae of linear low density polymers is of the more branched species and these are

EBSCOhost - printed on 2/13/2023 3:45 AM via . All use subject to https://www.ebsco.com/terms-of-use

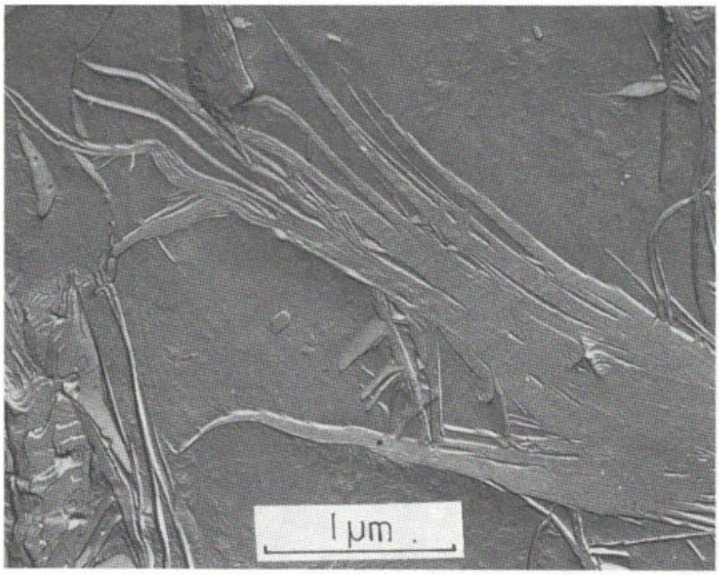

Figure 4. Linear polyethylene crystallized from a 1:1 blend with branched polymer at 130°C. Note the aggregation of lamellae into 'fibrous' units. Replica of etched surface.

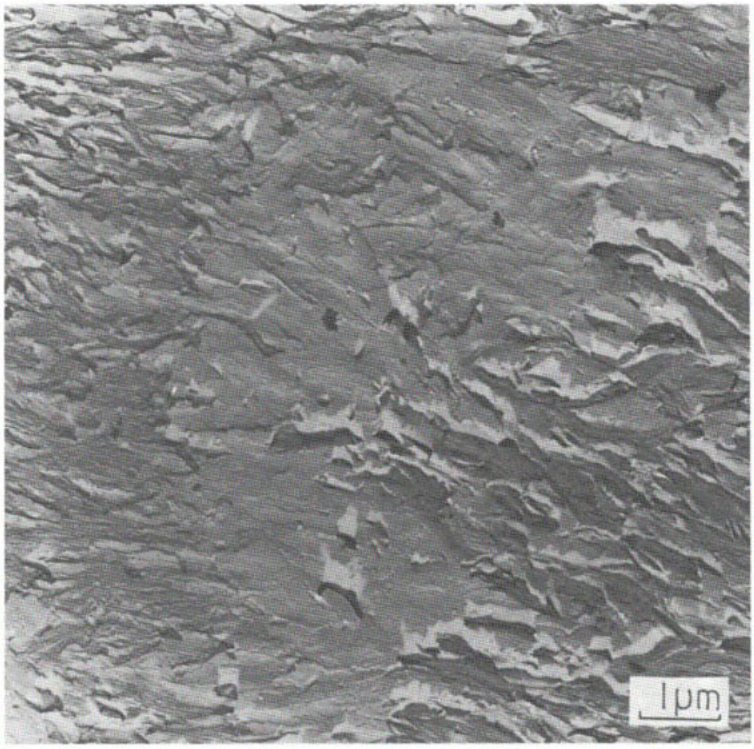

Figure 5. Replica of etched surface of a banded spherulite of α polyvinylidene fluoride crystallized at 160°C .

EBSCOhost - printed on 2/13/2023 3:45 AM via . All use subject to https://www.ebsco.com/terms-of-use

not necessarily short, despite a positive correlation of short length with increased branching ratios. In consequence the ability of material to blunt cracks should be better because the potentially brittle shortest molecules are no longer concentrated together. We may look to this for a partial explanation of the improved stress-cracking resistance of branched polyethylenes.

4. Recent Developments

The more recent developments in permanganic etching and its applications have proceeded along two interlinked lines. One has been the formulation of what is now a spectrum of permanganic reagents, the other their application to a range of polymers and particular treatment. On the first point, modification of concentration, reduction of temperature (to laboratory values) and the incorporation of phosphoric acid and water have allowed substantial increases in delicacy of etching and the avoidance of demonstrably false detail. Concerning the latter point, the original formulation[11] had a tendency, especially if continued too long, to lead to pseudo-structures termed artefacts. These had led certain low resolution studies[12] into misinterpretation but they do not form from the newer reagent[13]. What had been happening was that during oxidation, recrystallization was occurring on the polyethylene surface thereby inhibiting etching. The extraneous crystals disappeared on washing but left their profile behind. The revised etchant [13] not only solved this problem but had immediate application to a polypropylene whose previously inaccessible cross-hatched structure has since been investigated in detail. Further development has produced reagents which are suitable for isotactic polystyrene[14,15] and most recently for PEEK and for polyvinylidene fluoride (Figure 5). Extension to these last two polymers is particularly noteworthy as they are the first non-hydrocarbon polymers to respond to permanganic etching. It also takes the number of structures

EBSCOhost - printed on 2/13/2023 3:45 AM via . All use subject to https://www.ebsco.com/terms-of-use

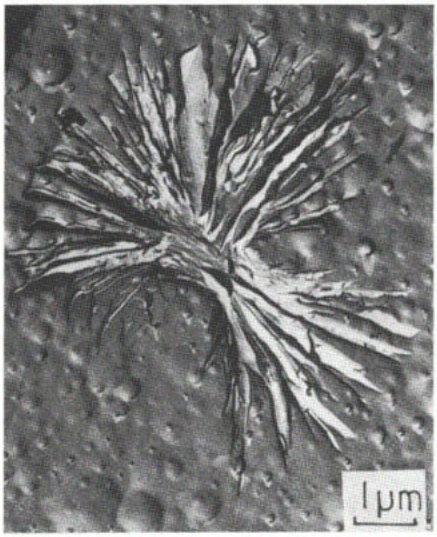

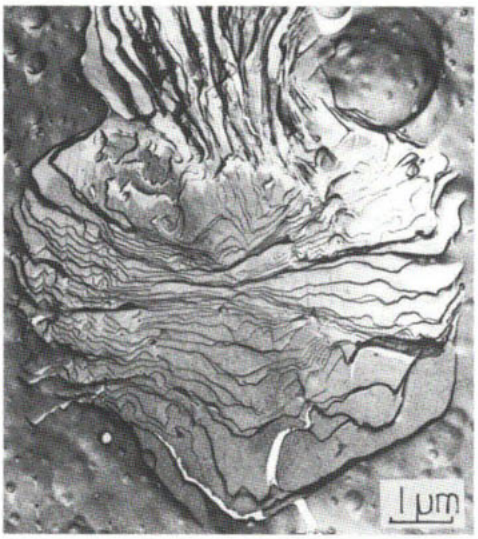

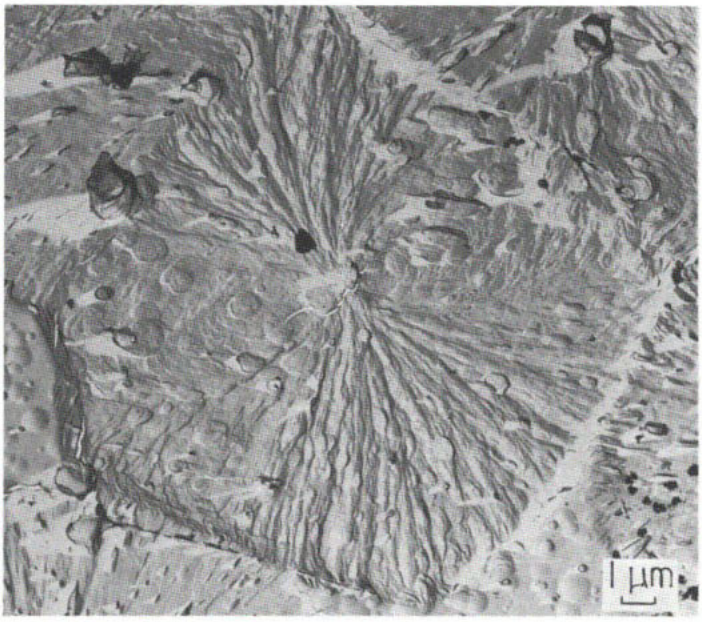

Figure 6. Different views of I-polystyrene
a, b crystallized at 210°C
c. crystallized at 190°C. Replicas of etched surfaces.

EBSCOhost - printed on 2/13/2023 3:45 AM via . All use subject to https://www.ebsco.com/terms-of-use

which have been successfully etched into double figures. Evidently the potential applications for permanganic etching are still growing. We do not yet know the limits of this increasingly versatile technique.

Here in Reading we have concentrated on investigating the fundamental lamellar organization within melt-crystallized polymers.[16] The work cited[7-10] on polyethylene had shown that spherulites developed by individual dominant lamellae forming a framework subsequently filled in by subsidiary lamellae. The characteristic textural dimension was found to be the separation between adjacent dominant lamellae rather than lamellar widths. Indeed neither lamellar widths nor any other dimension was observed to scale as the characteristic length δ = Diffusion Coefficient/Growth Rate. In further investigations both isotactic polystyrene[14,15] and isotactic polypropylene[17] have been investigated. In general terms they support the above generalizations although each system has its own characteristics.

Isotactic polystyrene is a system based on hexagonal lamellae. At high growth temperatures such as 220°C these branch and splay apart in what are usually termed axialites ie objects which have not developed sufficiently to produce a quasispherical envelope. It is particularly noteworthy that a similar construction continues at least down to 180°C, the temperature of maximum growth rate and especially that there is no evident narrowing of lamellae (Figure 6). The characteristic textural dimension is still the separation of adjacent dominant. This has been measured as a function of growth temperature for the homopolymer and at 190°C in melts doped with atactic polystyrene as functions of molecular weight of both host and dopant and of isotactic concentration. The measured relationships are rather complicated but they do seem to show, once again, that there is no obvious scaling with δ. The current position, therefore, is that we need to explain why dominant lamellae spread apart – repulsion from uncrystallized molecular cilia has been

EBSCOhost - printed on 2/13/2023 3:45 AM via . All use subject to https://www.ebsco.com/terms-of-use

suggested - and to understand how they branch. Screw dislocations occur in all systems and play a particulary prominent role in polyethylene.

By contrast, isotactic polypropylene is based on narrow lathlike lamellae. Usually these occur in the twinned arrangement known as cross-hatching, but at 160°C the twinning is absent[17,18]. Detailed investigation[17] of objects grown at 160°C has shown them to be arrangements of laths growing out along a^* and splaying around $\underline{b}$. Viewed down $\underline{b}$ they appear as sheaves but not when viewed along orthogonal directions. Our own investigations of objects grown at 150 and 155°C have led us to reproduce the optical results of Binsbergen[18] but now with the addition of details of the internal structure. In essentials what then happens is that there is an initial cross-hatched twin which develops along each of its four diagonals in a similar branching, splaying and curving manner as found in other systems (figure 7). Cross-hatching (figure 8) occurs non-randomly partly between radial laths but with especially high

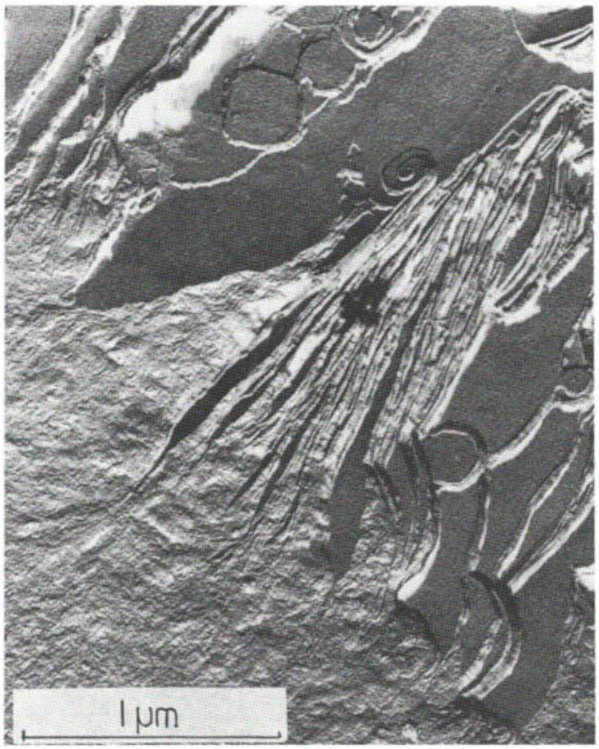

Figure 7. Dominant lamellae at the edge of a spherulite of β polypropylene. Replica of etched surface.

EBSCOhost - printed on 2/13/2023 3:45 AM via . All use subject to https://www.ebsco.com/terms-of-use

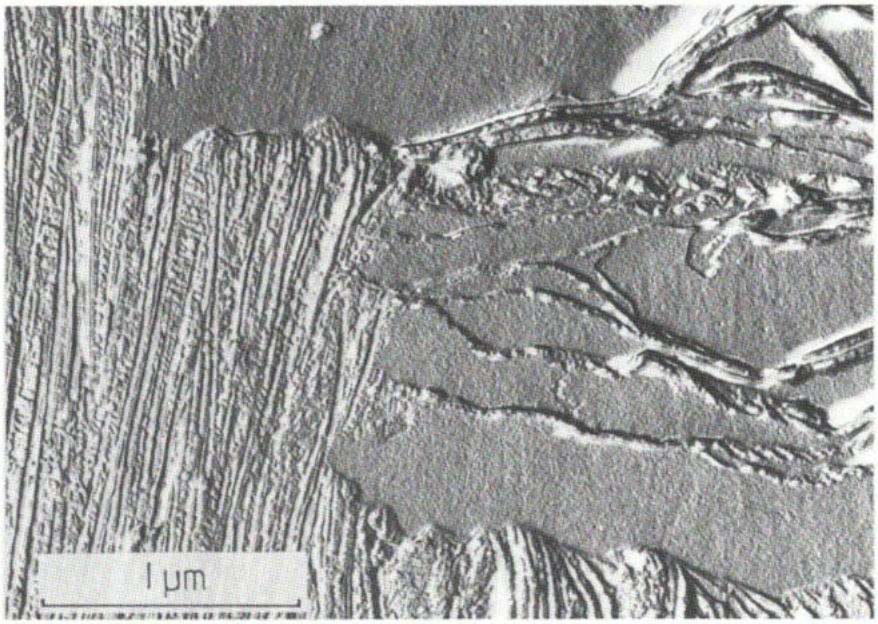

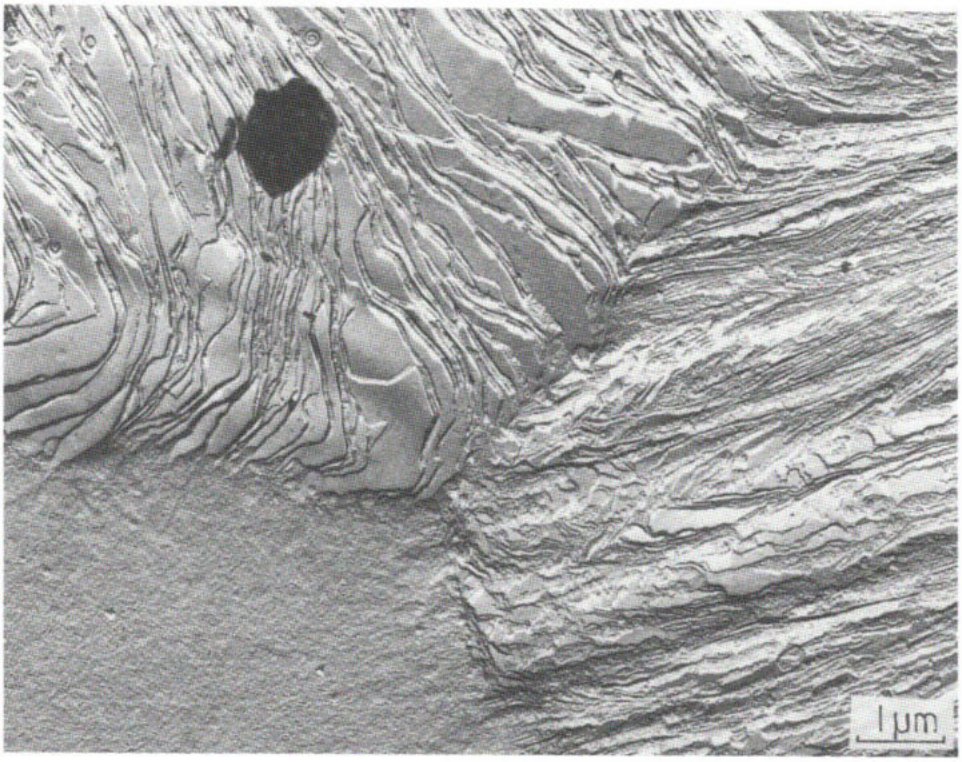

Figure 8. Junctions between α and β isotactic polypropylene. Replica of etched surfaces.

EBSCOhost - printed on 2/13/2023 3:45 AM via . All use subject to https://www.ebsco.com/terms-of-use

concentrations in internal 'eyes' where growth fronts from the four initial directions have enclosed residual melt. Such non-randomness needs to be borne in mind in relation to specific mechanisms of nucleating the cross-hatched twins. It also affects local birefringence which varies according to growth conditions. The two have recently been shown to have a detailed correspondence[19] in our own work[15] we have drawn attention to an extra textural feature occurring at growth temperatures of 130°C and below, which superficially resembles the structures formed by cellulation in organic alloys. Preliminary measurements of its lateral scale are in progress but the first indications are that it varies much less than growth rate.

The uses which have so far been made of permanganic etching have concentrated upon the nature of the textures revealed by its differential action. A next logical step is to enquire why certain regions etch more than others. In some instances this is evidently related to differences of lamella

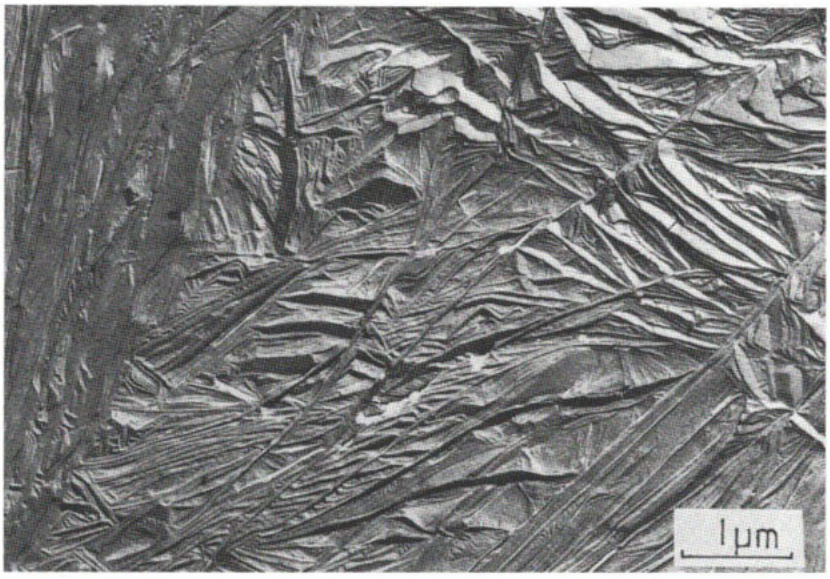

Figure 9. Linear polyethylene crystallized partly at 128°C and partly on quenching, used for the measurement of differential etching rates. Replicas of etched surface.

EBSCOhost - printed on 2/13/2023 3:45 AM via . All use subject to https://www.ebsco.com/terms-of-use

orientation, to different phases or to less ordered regions. It has, however, been noted that thinner lamellae are generally etched more than thicker ones and that, in linear polyethylene, they are also composed of shorter molecules. To interpret differential etching one needs to know, for example, whether molecular weight plays a significant role in addition to lamellar thickness which might be expected to control the number of diffusion channels for the reagent.

Preliminary measurements[20] have now been made of the etching rates for two populations in a linear polyethylene crystallized at two temperatures (figure 9). This has been done by measuring the (linear) change in the proportion of the two peaks in the melting endotherm for 5μm sections as a function of etching time. The etching rates are of order 5Å s^{-1} with a differential of only about 25% despite a threefold difference in lamellar thickness.

There are, of course, many other problems to which permanganic etching (and chlorosulphonation for polyethylene) can usefully be brought to bear. The two methods are complementary being analogous to light and dark field techniques respectively in that permanganic etching reveals all lamellar orientations present whereas chlorosulphonation is selective. Work on banded polyethylene spherulites has benefitted especially from this complementarity. It is a curious historical accident that the capability of studying representative internal microstructure in polymers with the transmission electron microscope has lagged behind that for other materials. Nevertheless the important fact is that they are now available and that we can confidently anticipate their contributing to a deepening of fundamental structure-property relationships across the spectrum of our subject.

EBSCOhost - printed on 2/13/2023 3:45 AM via . All use subject to https://www.ebsco.com/terms-of-use

Acknowledgments

I am indebted to Alison Hodge, Robert Olley, Alun Vaughan, Margaret Bradley and Tony Freedman for provision of photographs.

References

1. Fischer, E. W. Z. Naturforsch, 12a, 753 (1957).
2. Geil, P. H. Polymer Single Crystals, Wiley Interscience (1963).
3. Palmer, R. P. and Cobbold, A. J., Makromol. Chem. 76, 174 (1964).
4. Grubb, D. T., Dlugosz, J. and Keller, A. J. Mat. Sci. 10, 1826 (1975).
5. Hodge, A. M., Ph. D. Thesis, University of Reading (1978).
6. Bassett, D. C. Principles of Polymer Morphology, Cambridge (1981).
7. Bassett, D. C. and Hodge, A. M. Pruc. Roy. Soc. A. 359, 121 (1978).
8. Ibid, idem 377, 25 (1981).
9. Bassett, D. C., Hodge, A. M. and Olley, R. H. idem 377, 39 (1981).
10. Bassett, D. C. and Hodge A. M. idem 377, 61 (1981).
11. Olley, R. H., Hodge, A. M. and Bassett, D. C. J. Polymer Sci. (Phys Edn) 17, 627. (1979).
12. Workshop Proceedings, Morphology of Polyethylene and Cross-linked Polyethylene, EPRI (1981).
13. Olley, R. H. and Bassett, D. C. Polymer 23, 1707 (1982).
14. Vaughan, A. S. Ph. D. Thesis, University of Reading (1984).
15. Bassett, D. C. and Vaughan, A. S. Polymer 26, 717 (1985).
16. Bassett, D. C. CRC Critical Reviews 12, 97 (1984).
17. Bassett, D. C. and Olley, R. H. 25, 935 (1984).
18. Binsbergen, F. L. and de Lange, B. G. M. Polymer 9 23 (1968).
19. Norton, D. R. and Keller, A. Polymer 26, 704 (1985).
20. Freedman, A. M., Vaughan, A. S., Olley, R. H. and Bassett, D. C. Paper presented at Conference on Physical Aspects of Polymer Science, Reading. September 1985.

EBSCOhost - printed on 2/13/2023 3:45 AM via . All use subject to https://www.ebsco.com/terms-of-use

MORPHOLOGICAL ASPECTS OF FRACTURE PHENOMENA

H.H. Kausch
Laboratoire de Polymères, Ecole Polytechnique Fédérale de Lausanne, CH-1007 Lausanne

Introduction

The strong influence of molecular structure and sample morphology on fracture behaviour and strength of polymers is well known, the most important parameters being chain length, linearity, and stiffness on the one hand and intermolecular attraction, molecular orientation and nature and extent of the crystalline superstructure on the other [1-3]. Evidently, the strength of a sample will be the higher the more homogeneously in space and time stresses can be transferred onto the molecular chains. In this paper the principal aspects of the distribution of molecular stresses and of chain scission will be discussed in relation with morphological characteristics.

Stress Transfer in Non-Oriented Polymers

The essential mechanisms provoking, influencing and/or limiting the transfer of (axial) stresses onto a chain segment are evidently the shear loading of straight sections, conformational transitions contributing to stress release, bending of the skeleton, slip of chain ends or whole segments, and chain scission. In an apparently homogeneous matrix (solution, melt, amorphous polymer) the axial stresses ϕ experienced by an extended chain segment of length L can be described by the monomeric friction coefficient ζ_0 and the strain rate $\dot{\varepsilon}$:

$$\phi = \frac{\zeta_0 \dot{\varepsilon} \rho N_A}{M_0} \left(\frac{L^2}{8} - \frac{z^2}{2}\right). \qquad (1)$$

Morphology of Polymers
© 1986 Walter de Gruyter & Co., Berlin · New York - Printed in Germany.

EBSCOhost - printed on 2/13/2023 3:45 AM via . All use subject to https://www.ebsco.com/terms-of-use

The largest stresses are encountered in the middle (z=0) and amount to

$$\psi_{max} = \zeta_0 \dot{\varepsilon} M^2 \, L_{mon}/8 \, M_0^2. \qquad (2)$$

Equation (1) predicts that for a given system (ζ_0, L_{mon}, M_0) axial stresses are proportional to strain rate and square of molecular weight. Chain rupture occurs if ψ_{max} reaches or exceeds the chain strength ψ_b resulting in chain halving [4-6]. This defines a critical stress transfer length for dynamic chain scission :

$$L_{cr} = (8 \, M_0 \psi_b / \zeta_0 \dot{\varepsilon} \rho N_A)^{1/2} \qquad (3)$$

In a series of intriguing experiments Keller et al. [4,5] have recently studied the conformation of flexible molecular coils in solution subjected to elongational flow. Observing the birefringence of the volume element in the centre of a cross-slot device they showed for the first time that as a function of the rate $\dot{\varepsilon}$ of elongational strain there is a rapid transition from a coiled conformation to a fully extended one at a critical strain strain rate $\dot{\varepsilon}_c$ (coil-stretch transition). For an atactic polystyrene of $M_w = 4 \times 10^6$ in decalin the $\dot{\varepsilon}_c$ is of the order of 10^4 s^{-1}. If the strain rate of the solution is increased beyond $\dot{\varepsilon}_c$ the fully extended chains become energy-elastically loaded and they break at a second critical value, $\dot{\varepsilon}_f$, of strain rate (for the above PS at about 1.8×10^4 s^{-1}). From Eq. 1 it can be anticipated that

$$\dot{\varepsilon}_f \sim M^{-2}$$

and precisely this result was obtained by Keller et al. [4,5] for PS in decalin. By molecular weight analysis after chain scission the authors were also able to state that under these circumstances chain scission occurs in the centre: chains are being halved. They estimate [5] that this occurs at axial forces of

EBSCOhost - printed on 2/13/2023 3:45 AM via . All use subject to https://www.ebsco.com/terms-of-use

$F_f = 6 \times 10^{-9}$ N/chain.

In stressed semicrystalline polymers which are heterogeneous on a microscopic scale three different situations of molecular stress transfer arise : the strong and cooperative coupling of segments within crystalline regions, a weaker and irregular interaction in amorphous regions and the possibility of large stress concentration within molecules emanating from a crystallite. Evidently the failure mechanisms intimately depend on sample microstructure. Schultz [2] has given a detailed account of this dependency for spherulitic polymers. He draws a failure map relating temperature and strain rate with the failure pattern (ductile or semibrittle failure, spherulite boundary and intercrystallite cracking).

It follows from these and the previously discussed investigations that in all non-oriented polymers where the length L of an extended section will rarely exceed a few monomer units, the product $\zeta \bar{x} \dot{\varepsilon}$ must reach very high values before $\psi > \psi_{max}$. Such a condition is generally not fulfilled in creep (with $\dot{\varepsilon} \ll 10^{-2}$ s^{-1}) and not before large-scale deformation has taken place. However, in necking samples much larger strain rates and degrees of molecular orientation are observed, conditions for which chain scission has been reported [7,8].

Chain Scission in Conventional Fibres

The stressing of conventional fibres having draw ratios of between 3 and 6 leads to the loading and breakage of considerable amounts of chains (see e.g. [1,9-11]). The breakage of a highly stressed chain can potentially be traced in several ways:

- through the formed free radicals (by ESR)
- after radical reaction through new end-groups (by IR)
- through the ensuing molecular weight reduction (viscosimetry, GPC)
- through the energy irreversibly dispersed in (repeated) mechanical loading.

All these methods have been employed; their results, however, have

EBSCOhost - printed on 2/13/2023 3:45 AM via . All use subject to https://www.ebsco.com/terms-of-use

been interpreted quite differently.

Zhurkov and Zakrevski [9] observed (in PE, PP, PA6) the appearance of up to 5×10^{19} cm^{-3} microcracks per cm^3, up to 3×10^{19} "new IR end groups" and up to 5×10^{17} cm^{-3} spins. They concluded that through a radical chain reaction several hundred secondary chain breakages and thus new end groups are created per primary free radical; these secondary defects are arranged in the form of microcracks. Their critical concentration leads to macroscopic failure.

DeVries et al. [10] found that the apparent length distribution of taut tie-molecules obtained in quasi-static loading also explained quite well the kinetics of free radical formation in fatigue, at constant strain or in step-strain loading. They concluded that the destruction of the tie-chain population is instrumental in final failure.

Klinkenberg [11] very carefully analyzed the kinetics of radical formation in step-strain and step-temperature tests. He shows that the differential modulus $d\sigma/d\varepsilon$ decreases with the onset of chain scission; he points out, however that despite the similarity in shape of the $d\sigma/d\varepsilon$ and $d[\mathring{R}]/d\varepsilon$ curves the load carrying capability of the broken chains is by a factor of about 30 too small to explain the absolute value of sample softening.

Kausch [12] gave a fracture mechanics analysis stating that in short-time loading of semicrystalline fibres and bulk amorphous polymers chain molecule do not significantly contribute to the fracture surface energy through the energies of bond breakage and elastic retraction. Large values of chain length and chain strength contribute, however, to reduce the effect of material inhomogeneities as stress concentrators through the plastic deformation necessary before material separation occurs. In ultra-high modulus fibres chain backbone properties are directly utilized to an extent strongly determined by intermolecular interaction.

In recent years the question of the role of chain scission has been further discussed on the basis of more extended comparative studies also including molecular weight measurements [1,13-22]. Thus, Gaur [17] and Frank and Wendorff [18] analyzed the stress-

EBSCOhost - printed on 2/13/2023 3:45 AM via . All use subject to https://www.ebsco.com/terms-of-use

strain behaviour of PA 6 filaments. They determined the amount of energy W_{irr} irreversibly dissipated by defect formation in a first load cycle, the viscous energy dissipation and the elastically stored energy. They observed that almost up to fracture there was a linear correlation between W_{irr} and free radical concentration [R•] with a ratio of 1.5×10^{-17} J $spin^{-1}$. They also noted that the inflection point of the stress-strain curve coincided with the beginning of the free radical production. For this material and some other PA fibres Frank [16] also gave the decrease in molecular weight provoked by chain scission during straining as up to ~ 20 % (Table I).

In this paper it will be attempted to reconcile some of the apparently contradictory observations. To do so a conventional model of fibre structure will be used (Figure 1). Thus, it will be assumed that the chain scission points are essentially located within the microfibrils. The microfibrils can be modelled as a series arrangement of crystalline and amorphous regions, where the latter are traversed by highly extended tie molecules of various degrees

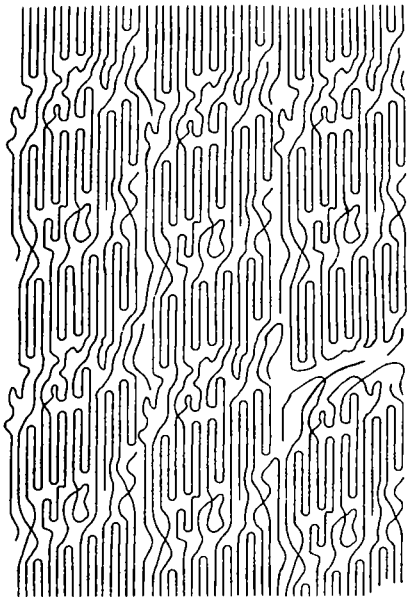

Figure 1. Model of a semi-crystalline fibre composed of microfibrils which are typically 50 to more than 100 nm in length and 7 to 25 nm in width [23].

EBSCOhost - printed on 2/13/2023 3:45 AM via . All use subject to https://www.ebsco.com/terms-of-use

of tautness. The fraction of taut tie molecules in PA 6 has been estimated by Friedland et al. [19] from analysis of the stress effect on IR absorption bands to vary between 0.03 and 0.05; more recently Zhizhenkov and Egorov [20] proposed, on the basis of NMR results, values between 0.04 and 0.10 depending on sample preparation.

The careful X-ray studies of Frank [14] have again confirmed that (at room temperature) the macroscopic strains ε_f also apply to the change of the long period L of the microfibrils. In view of the large longitudinal stiffness of the crystalline layers (E_c = 183 GN m^{-2}) and at a degree of crystallinity of 50% one easily calculates the strain ε_a of the amorphous regions to be :

$$\varepsilon_a = \frac{\Delta L_a}{L_a} = \frac{\Delta L - \Delta L_c}{L_a} = \frac{\varepsilon_f L - 0.5\varepsilon_c L}{0.5L} \qquad (4)$$

It should be kept in mind that the assumption of a homogeneous strain within the molecularly quite heterogeneous amorphous regions is restricted to distances of the order of 5 nm and is essentially based on the large lateral stiffness of the crystalline regions. For these microfibrils two regions of mechanical response were observed: the small strain region with $\varepsilon_a < 0.08$ and the large-strain region with $\varepsilon_a > 0.15$. Frank carefully investigated this response. For fibres held at 50 % relative humidity, he measured in a first load cycle an initial modulus E_1 of 4.6 GN m^{-2}; taking into consideration the existence of an intermicrofibrillar amorphous fraction of 0.4 he deduced in his PhD thesis for the microfibrils a modulus of the amorphous regions of E_{1a} = 2.88 GN m^{-2}. In a second load cycle he obtained E_2 = 1.80 GN m^{-2} and E_{2a} = 1.13 GN m^{-2}. The decrease in the elastic modulus after a first load cycle is a common observation and has correctly been explained by the "destruction of some structure" [see e.g. 16,21].

The following molecular interpretation can be given to the observed small-strain behaviour. In this region stresses are essentially transmitted in a continuous manner through the hydrogen-bond coupled segments; the elastic modulus decreases with strain due to the gradual destruction of hydrogen bonds with segment deformation

EBSCOhost - printed on 2/13/2023 3:45 AM via . All use subject to https://www.ebsco.com/terms-of-use

and orientation. If some completely extended segments should be present within the amorphous regions at zero strain, their number must be extremely small so as not to change the strain softening behaviour.

In a second region ($0.08 < \varepsilon_a < 0.20$), E_a increases and this behaviour is determined by the combined entropy- and energy-elastic loading of fairly extended tie chains [12,16,19-22]. The stressing of a partly extended chain of contour length L_i provokes to some extent conformational transitions towards an all-trans conformation; evidently, it depends on the nature and intensity of the intermolecular interactions whether entropy- or energy-elastic behaviour prevails in this region.

If it is assumed that within a strained amorphous region a chain is at first fully extended and only thereafter strained elastically then energy elastic chain stresses ϕ_i will only be built up in "taut" chains whose contour length L_i is smaller than $L_a(1+\varepsilon_a)$:

$$\phi_i = E_k \left[\frac{L_a}{L_i} (1+\varepsilon_a) - 1\right]. \qquad (5)$$

Given an amorphous strain ε_a of 20 % and a chain stiffness E_k of 200 GN m^{-2}, one arrives at the result that ϕ_i of chains with $L_i < 1.086\ L_a$ exceeds the chain strength of 21 GN m^{-2}, they must break. As has been shown in detail before [1] the condition $L_i < 1.086\ L_a$ is equivalent to demanding that there are 5 or less gtgt kinks in an otherwise all-trans planar segment. Such highly extended chain segments do exist in PA fibres and they start breaking at about these strains (ε_a>20 %). In their publications Frank and Wendorff give values of 1.5×10^{-17} [18] and 4.4×10^{-17} J/spin [16] for the ratio of irreversibly dissipated energy and free radical concentration which corresponds to an energy dissipation of 18 and 60 MJ per mol of chain scission events. These values are 20 to 69 times larger than the value of 870 kJ mol^{-1} calculated by Kausch [1] for the scission of highly stressed amorphous chains of 5 nm length solidly anchored in two opposite crystal lamellae. A small portion of this difference can

EBSCOhost - printed on 2/13/2023 3:45 AM via . All use subject to https://www.ebsco.com/terms-of-use

be ascribed to the fact that the chain segments breaking towards the end of the loading are longer than 5 nm; they will, therefore, contain (up to 15 %) more elastic energy. The major portion of the energy difference, however, will have to be sought elsewhere. Frank et al. propose that the free radical concentration determined by ESR is not a correct measure of the number of chain scission events since rapid radical recombination or chain scission without radical formation may occur. In that case, one chain scission event would not give rise to two free radicals seen by ESR but to a smaller number. Their hypothesis is based on the evaluation of the (slight) decrease in molecular weight M_n of their samples after rupture (Table I). This view is shared by Zakrevskii [24] who concludes from his studies of the mechano-emission of electrons (from PE and PA 6 films) that part of the scission products should appear in the form of ions and not of radicals.

This may be perfectly true. But even then it is claimed that the principal source of energy dissipation is the stress-induced conformational transition of partly extended chains containing a few double kinks. The annihilation of a double kink would increase the end-to-end distance of a chain segment by $\Delta L = 0.26$ nm. If the segment had been subjected to 5 GN m^{-2}then an energy dissipation of $0.25 \bar{\times} 10^{-18}$ J/segment would be observed (Friedland et al. even estimate that the average stress on the highly stressed bonds in PA 6 is 10 GN/m^2 which would correspond to an energy dissipation of $1 \bar{\times} 10^{-18}$ J per relaxing segment).

The above data may now be correlated with each other. In the amorphous regions at 32 % strain one determines by ESR that $4 \bar{\times} 10^{17}$ (out of 10^{21}) chains/cm^3 are broken. If each detected chain scission event would trigger between 120 and ~ 400 conformational transitions then the overall dissipated energy would exactly correspond to that measured by Frank. It seems to be quite realistic to expect such a number of rearrangements. From 10 000 amorphous chain segments of 5 nm length 300 to about 1 000 would classify as taut chains (IR [19], NMR [20] data); only four of these taut chains would be "seen" by ESR as being broken up to sample fracture; but even if Frank's hypothesis is correct that 10 times more chains are broken than are registered by ESR, the dominant role of

EBSCOhost - printed on 2/13/2023 3:45 AM via . All use subject to https://www.ebsco.com/terms-of-use

viscoelastic processes in the deformation of highly extended chains is still maintained [6,12].

On the basis of the above model some comments may be made with respect to the other defect concentrations indicated in Table I. In some cases the concentrations of new, oxygen-containing (IR-) end groups are unusually high. It is conceivable that a stress effect on the rate of oxidation such as oberved by Popov and Zaikov in elastomers [25] or by Rapoport in PP at 130 ^{0}C [26] plays a role. In vacuum, however, oxygen-free end-groups (vinyl) have also been observed in large numbers, especially in the surface layers of stressed PE and PP [27]. The comparative IR measurements by DeVries et al. [14] confirm that ESR radical concentrations are systematically lower than IR group concentrations. For PE those authors determined that [R•] was by a factor of 2 to 5 smaller. Molecular weight analysis shows that macroscopic fracture leads to roughly a 10 % decrease in molecular weight M_{η}. In random scission this corresponds to the breakage of every tenth molecule or of 0.3 % of all segments of 5 nm length. These values are compatible with the mechanical model given above. Undoubtedly further progress is to be expected in the domain of molecular weight determinations so that more precise data will become available.

At this time the best interpretation of the sometimes contradictory data on defect concentration is offered by an analysis of the experiments of DeVries et al. [14]. It is noted that the discrepancies between ESR, IR, and M_{η} data are small, if the defects are produced rapidly (grinding) and at low temperatures. Under those conditions a modest loss of ESR traced free radicals occurs (perhaps of the order of one half) and only a modest multiplication of IR groups takes place (by a factor of about 1.3). However, if more time is allowed for defect production and, consequently, for radical reactions the discrepancies between different data increase considerably (Table I).

Coming back now to the fracture criteria presented at the beginning of this section it must be mentioned that the absolute number of chain breakages at fracture is small. It is also observed that the slope of the stress-strain curve remains always positive and

EBSCOhost - printed on 2/13/2023 3:45 AM via . All use subject to https://www.ebsco.com/terms-of-use

Table 1. Defect Concentrations as Determined by Different Methods

Material:	Method: / Treatment:	ESR [R•] 10^{17} spins cm^{-3}	IR new groups 10^{17} cm^{-3}	molec. weight analysis [kg/mol] N_{rupt} 10^{17} cm^{-3}	visc. $\Delta M_\eta/M_\eta$	GPC M_n	GPC M_w	ref.
HDPE	fracture	0.05	100					Zhurkov [9]
	stressing at 500 MPa	0.035	3.2					DeVries [12]
	fracture	0.045		3.9	- 4/58			DeVries [12]
	grinding at 77K	0.10-0.12	4.9					DeVries [12]
	irrad. 3 Mrad	3.9	21					DeVries [12]
	" 50 "	48	110					DeVries [12]
UHMW	grinding at 77K	~1	11					DeVries [12]
PS	grinding at 77K	0.45-0.63	1.5-2.5	1.1-1.7	-10/200 to -166/916			DeVries [12]
PETP	11 % strain			19	- 0.8/28			Stoeckl [13]
PA 6	reference					34.2	74.7	Frank [16]
	18 % strain	5	not traceable, < 100			31.2	70.6	Frank [16]
	17 % strain	5.4		33	- 3.1/36.4			Stoeckl [13]
	reference					30.5	69.2	Roylance [15]
	fracture			31		26.7	60.6	Roylance [15]
	fracture	1.1		11	- 3.5/38.8			DeVries [12]

EBSCOhost - printed on 2/13/2023 3:45 AM via . All use subject to https://www.ebsco.com/terms-of-use

that the load bearing capability of the fibre material outside of the immediate fracture zone does not necessarily suffer. This excludes a decisive and permanent damaging of the total fibre through the chain scission events and invaldiates the use of critical defect concentrations or of the breakage of a given fraction of the chain length distribution as fracture criteria. The fracture of a fibre in short time loading must be seen as a dynamic event. Rupture of a fibre will occur if the failure of a microfibril places so important stresses on the surrounding microfibrils that they will fail instantaneously - be it in shear by pull-out or by rupture at a "weak" cross-section.

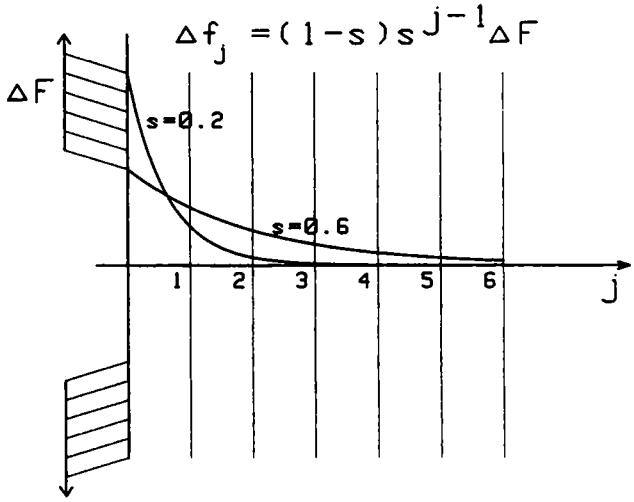

Figure 2. Distribution of excess axial forces Δf_j caused by differential straining of a strongly anisotropic coupled microfibrillar system.

An estimate of the macroscopic strength can be given by considering the simple model shown in Figure 2. There it is assumed that a shearing force ΔF applied to the strongly anisotropic coupled microfibrillar system will lead to excess axial force components Δf_i within the adjacent microfibrils :

$$\Delta f_i = (1-s)\, s^{j-1}\, \Delta F. \qquad (6)$$

EBSCOhost - printed on 2/13/2023 3:45 AM via . All use subject to https://www.ebsco.com/terms-of-use

Final fibre breakdown will occur if the accidental rupture of an arbitrary microfibril and its rapid retraction lead, by way of friction, to the transfer of additional loads ΔF which cannot be accommodated by the adjacent microfibril(s). From the above model one derives the following fracture criterion :

$$\sigma_{fib} = \sigma_0 + \Delta\sigma_{excess} > \sigma_{fb} \tag{7}$$

where σ_{fib} is the total axial stress acting on a microfibril, σ_0 the average applied stress, $\Delta\sigma_{excess}$ the excess stress provoked by the ruptured microfibril and σ_{fb} the microfibril strength . The first unbroken microfibril (j = 1) will rupture if :

$$\sigma_1 = \sigma_0 + (1-s)\frac{\Delta F}{q} > \sigma_{fb} \tag{8}$$

where q is the cross section of a microfibril. In terms of macroscopic stress one has breakdown if

$$\sigma_0 > \sigma_{fb} - (1-s)\Delta F/q \tag{9}$$

It is readily seen that for strongly coupled systems (s ~ 1) σ_0 can be very close to the microfibrillar strength. It has also to be expected that ΔF will depend on the fibril retraction distance which should correspond to the stress transfer length.

Ultra-high Strength Fibres

In the previous section the rupture mechanisms of conventional fibres have been discussed. At draw ratios λ of between 3 and 6 the amorphous regions within the microfibrils still contained more than 90 % of non-extended chain segments which support most of the load. This is different in ultra-highly oriented fibres with draw ratios λ of between 10 and more than 50. In linear PE for instance the number of non-extended, randomly oriented segments, of loops and chain folds decreases with increasing λ [3,28-30]. The microfibrillar structure with alternating amorphous and crystalline regions is initially still observed (depending on molecular weight

EBSCOhost - printed on 2/13/2023 3:45 AM via . All use subject to https://www.ebsco.com/terms-of-use

and sample preparation technique up to draw ratios of about 20 to 30. Samples of a higher draw ratio, however, contain broader crystallite size distributions with a small component of long crystals (100 to 800 nm). Moreover the strong coherence between crystallites seems to indicate the existence of intercrystalline bridges [30].

Very high draw ratios (λ>200) are be obtainable from the semi-crystalline state by pure tearing away or unraveling of the crystal lamellae. In fact, single crystal mats of ultra-high molecular weight polyethylene (UHMWPE of $M_w = 2\times10^6$) have been drawn to a λ of 247 [31]. At this extreme draw ratio the fibre elastic modulus approached a value of 220 GPa [31] which is close to the theoretical modulus of a perfect PE crystal (240 - 290 GPa).

According to all observations it has to be expected that the ultimate properties of ultra-high oriented fibres depend on the properties of the crystal blocks and on the way these blocks are linked together. Starting from this idea a simple shear lag theory of fibre composites has been proposed [32,33] to calculate the elastic moduli and the yield behaviour of ultra-oriented fibres. A definite and positive correlation between the total draw ratio, the elastic modulus and the fracture strength is observed (see [3,29,30] for an extended discussion). The creep sensitivity of PE gives rise to a pronounced rate dependency of strength; thus, at a temperature of -10 ^{0}C the stress at yield or break of ultra-oriented PE of comparatively low molecular weight (M_w ~ $60\text{-}100\times10^3$) varies from ~ 0.6 GPa at 10^{-5} s^{-1} to 1.4 GPa at 0.1 s^{-1}; at 20 ^{0}C the stress values are by about 0.2 GPa lower [34]. With the above samples final fracture is initiated by slippage of chains. As proposed by Woods et al. [35] this tendency for creep can be greatly reduced by controlled crosslinking by electron irradiation.

Very high draw ratios could also be obtained with ultra-high molecular weight samples (UHMWPE, M_w = 1.5 - 2×10^6) prepared by spinning from dilute solution (e.g.[36-38]). In a dilute solution the number of entanglements between chain molecules evidently decreases with decreasing volume fraction ϕ of the polymer. By

EBSCOhost - printed on 2/13/2023 3:45 AM via . All use subject to https://www.ebsco.com/terms-of-use

quenching and solvent evaporation thin films can be prepared from the solution which maintain the small entanglement concentration [36,37]. If these films are uniaxially drawn the molecular segments between "entanglement points" are gradually straightened. The maximum draw ratio λ_{max} corresponds to the complete extension of such a segment (of average length). According to the classical theories of rubber elasticity the maximum draw ratio varies with the number N_c of statistical chain segments between entanglement points as:

$$\lambda_{max} = (N_c)^{1/2}. \qquad (10)$$

In dilute solution this number increases with $1/\phi$. The experiments of Smith, Lemstra and Booij gave an excellent verification of this relation and of the entanglement concept [36]. Together with the draw ratio the strength of ultra-oriented fibres increases. So far the highest values, tensile strengths of up to 10 GPa, have been obtained in the Ioffe Institute in Leningrad [37,38]. This is still less than the (theoretical) tensile strength of an individual PE chain which has a value of between 20 and 40 GPa [1]. It is more, however, than the pull-out strength of a PE molecule from a crystal, calculated by Kausch and Becht [39] to be 1.37 nN per chain cross section of 0.19 nm^2. This means that chain scission processes must play a role in the rupture of ultraoriented PE fibres.

Strength of macromolecular single crystals

In oriented and ultra-oriented fibres stress-transfer between microfibrils had been an important strength limiting parameter. Under these circumstances single crystals of macroscopic dimensions should offer an additional advantage. Detailed investigations on high-modulus polydiacetylene crystals (DCHD) have been carried out by Galiotis et al. [40]. Contrary to ultra highly oriented PE fibres polydiacetylene single crystal fibres show practically no creep (up to 2 % strain and 100 ^{0}C). Their strength does depend, however, on fibre diameter (Figure 3).

EBSCOhost - printed on 2/13/2023 3:45 AM via . All use subject to https://www.ebsco.com/terms-of-use

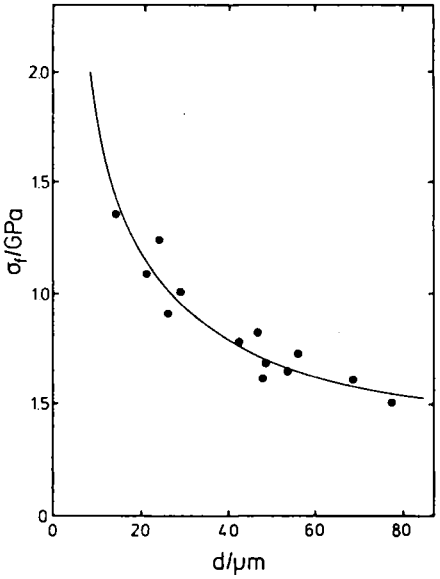

Figure 3. Dependence of the fracture stress upon effective fibre diameter for polyDCHD fibres (taken from Galiotis et al. [37]).

This is due to the stress concentration caused by steps in the fibre surface from which fracture initiates. Analyzing the geometry of such defects and applying fracture mechanics concepts the authors determine that the theoretical strength of the polydiacetylene is 3 ± 1 GPa which corresponds to about 3 nN per chain molecule. This is in fair agreement with the calculations of Keller et al. [5] cited earlier.

Conclusions

In this paper four different situations have been studied : coiled chains in solution and in amorphous polymers, highly and ultra-highly oriented fibres and single-crystal fibres. In all cases chain scission can be obtained if the chain length (ML_{mon}/M_0) is larger than the critical stress transfer length. Although the beginning of an irreversible deformation (yield, creep) is not related to chain length and strength - and thus to the critical stress transfer length - the onset of unstable deformation certainly is.

EBSCOhost - printed on 2/13/2023 3:45 AM via . All use subject to https://www.ebsco.com/terms-of-use

Acknowledgements

The author gratefully acknowledges valuable discussions with Prof. V.A. Marichin and Dr. L.P. Mjasnikova, Ioffe-Institute, Leningrad, and Dr. O. Frank, Röhm GmbH., Darmstadt.

References

1. Kausch H.H.. 1985. Polymer Fracture, 2nd Ed. Springer-Verlag, Berlin-Heidelberg.

2. Schultz, J.M.. 1984. Polym. Eng. Sci. 24, 770.

3. Marichin, V.A., Mjasnikova, L.P.. 1977. The supermolecular structure of polymers, Chimia: Leningrad (in Russian).

4. Odell, J.A., Keller, A., Miles, M.J.. 1984. Polymer Comm. 24, 1.

5. Keller, A., Odell, J.A.. 1985. Colloid & Polym. Sci. 263, 181.

6a. Kausch, H.H.. 1985. Colloid & Polym. Sci. 263, 312.

6b. Nguyen, T.Q., Kausch, H.H.. 1985. 30th IUPAC International Symposium on Macromolecules, The Hague, NL, 18-23.8.

7. Zaks, B.Yu., Lebedinskaya, M.L., Chalide, V.N.. 1970. Vysokomol.soedin.A12, 2669; 1971 Polymer Sci. USSR 12, 3025.

8. Lishnevskii, V.A.. 1968. Dokl. Akad. Nauk SSR 182/3, 596; 1969. Vysokomol. soedin., Ser. B11/1, 44.

9. Zhurkov, S.N., Zakrevskii, V.A., Korsukov, V.E., Kuksenko, V.S.. 1971. Fizika Tverdogo Tela 13/7, 2004; 1972. Soviet Phys. Solid State 13/7, 1680; 1972. J. Polym. Sci. A-2 10, 1509.

10. DeVries, K.L., Roylance, D.K., 1973. Progress in Solid State Chemistry 8, (J.O. McCaldin, G. Somorjai, eds.), Pergamon Press.

11. Klinkenberg, D., 1979. Progr. Coll. & Polym. Sci. 66, 341; 1979. Colloid & Polym. Sci. 257, 351.

12. Kausch, H.H.. 1977. Fracture 1977, Vol. 1, ICF4, Waterloo, Canada, June 18-24.

13. Stoeckel, T.M., Blasius, J., Crist, B., 1978. J. Polymer Sci., Polym. Phys. Ed. 16, 485.

EBSCOhost - printed on 2/13/2023 3:45 AM via . All use subject to https://www.ebsco.com/terms-of-use

14. DeVries, K.L., Smith, R.H., Fanconi, B.M.. 1980. Polymer 21, 949;
Fanconi, B.M., deVries, K.L., Smith, R.H.. 1982. Polymer 23, 1027;
Igarashi, M., DeVries, K.L.. 1983. Polymer 24, 1035.
Fanconi, B.M., 1983. J. Appl. Phys. 54, 5577.

15. Popli, R.K., Roylance, D.K.. 1982. Polym. Eng. Sci. 22, 1046.

16. Frank, O.. PhD Thesis, 1984. Technische Hochschule Darmstadt.

17. Gaur, H.A.. 1978. Colloid & Polym. Sci. 256, 64.

18. Frank, O., Wendorff, J.H.. 1981. Colloid & Polym. Sci. 259, 70.

19. Friedland, K.J., Marichin, V.A., Mjasnikova, L.P., Vettegren, V.I.. 1977. J. Polym. Sci., Polym. Symp., 58, 185.

20. Zhizhenkov, V.V., Egorov, E.A.. 1984. J. Polym. Sci., Polym. Phys. Ed. 22, 117.

21. Bonart, R., Schultze-Gebhardt, F.. 1972. Angew. Makromol. Chem. 22, 41.

22. Marichin, V.A.. 1979. Acta Polym. 30, 507.

23. Tucker, P., Waller, G.. 1972. Polym. Eng. Sci. 12/5, 364.

24. Zakrevskii, V.A., Pakhotin, V.A.. 1978. Sov. Phys. Solid State 20(2), 214.

25. Popov, A.A., Zaikov G.E.. 1983. JMS-Rev. Macromol. Chem. Phys. C23(1), 1.

26. Rapoport, N.. Institute of Chemical Physics, Moscow, personal communication.

27. Tshmel, A.E., Vettegren, V.I., Zolotarev, V.M.. 1982. J. Macromol. Sci.-Phys. B21(2), 243.

28. Ciferri, A., Ward, I.M.. 1979. Ultra-High Modulus Polymers-1, Applied Science Publishers London-New Jersey.

29. Marichin, V.A.. 1984. Makromol. Chem., Suppl. 7, 147.

30. Ward, I.M.. 1985. Adv.in Polym. Sci. 70, (to be published).

31. Kanamoto, T., Tsuruta, A., Tanaka, K. Takeda, M., Porter, R.S.. 1983. Polymer J. 15, 327.

32. Rider, J.G., Watkinson, K.M.. 1978. Polymer 19, 683.

33. Arridge, R.G.C., Barham, P.J.. ibid., 654.

34. Cansfield, D.L.M., Ward, I.M., Woods, D.W., Buckley, A., Pierce, J.M., Wesley, J.L.. 1983. Polym. Comm. 24, 130.

EBSCOhost - printed on 2/13/2023 3:45 AM via . All use subject to https://www.ebsco.com/terms-of-use

35. Woods, D.W., Busfield, W.K., Ward, I.M.. 1984. Polym. Comm. 25, 298.

36. Smith, P., Lemstra, P.J., Booij, H.C.. 1981. J. Polym. Sci.. Polym. Phys. Ed. 19, 877.

37. Savitsky, A.V., Gorshkova, I.A., Frolova, I.L., Shmikk, G.N.. 1984. Polym. Bulletin 12, 195.

38. Marichin, V.A., Mjasnikova, L.P., Zenke, D., Hirte, R., Weigel, P.. 1984. Polymer Bulletin 12, 287.

39. Kausch, H.H., Becht, J.. 1974. Deformation and Fracture of High Polymers, (J.A. Hassell, R.I. Jaffee, eds.), Plenum Press, 317.

40. Galiotis, C., Read, R.T., Yeung, P.H.J., Young, R.J., Chalmers, I.F., Bloor, D.. 1984. J. Polym. Sci., Polym. Phys. Ed. 22, 1589.

EBSCOhost - printed on 2/13/2023 3:45 AM via . All use subject to https://www.ebsco.com/terms-of-use

THERMAL HISTORY EFFECTS IN POLYBUTYLENE

P.H. Geil, K.W. Chau, A. Agarwal and C.C. Hsu
Polymer Group, University of Illinois, Urbana, Illinois 61801

Introduction

Polybutylene (PB) is an interesting polymer for morphology studies since it can be crystallized in at least four different crystal structures, involving three helical conformations. From the melt it crystallizes in a tetragonal unit cell (Form II) with an 11/3 helical conformation that melts between 100°C and 120°C (1). Form II is thermodynamically unstable, slowly transforming into the stable, hexagonal unit cell (Form I). Form I has a 3/1 helical conformation and melts between 105°C and 130°C (1). By precipitating polybutylene from various solvents, an orthorhombic structure (Form III) can readily be obtained (2). Form III has a 4/1 helical conformation and melts between 95°C and 100°C. Holland and Miller (2) also obtained hexagonal single crystals from solutions, differing from Form I in that their melting point ranges between 95°C and 100°C. Form I' yields simple, hexagonal single crystal diffraction patterns, whereas Form I obtained by the transformation of tetragonal single crystals is twinned (2). Form I' can also be obtained by crystallization from the glass (3). Although the relative hko reflection intensities from Forms I and I' are essentially the same, the difference of ca. 30°C in melting point suggests a larger difference in molecular packing than simply twinning.

It is generally assumed that a polymer in the melt and in solution has a random coil conformation and that the effect of melt or solution temperature on morphology and properties is determined primarily by nucleation effects, i.e., the higher the liquid state temperature and/or the longer the time, the fewer the nuclei. Rault and co-workers (4), however, have suggested that the lamellar thickness of a number of polymers quenched from the melt is a function of the coil diameter in the melt, as affected by the temperature of the melt and time at that particular temperature. For polybutylene, they have shown that the lamellar thickness increases with increasing melt temperature and increasing melt time. Thus the properties of a melt crystallized polymer would be expected to be related to both the melt temperature and, for insufficient

Morphology of Polymers
© 1986 Walter de Gruyter & Co., Berlin · New York - Printed in Germany.

EBSCOhost - printed on 2/13/2023 3:45 AM via . All use subject to https://www.ebsco.com/terms-of-use

melt time, the lamellar thickness before melting.

For solutions no such effect would be expected, the prevailing concept being the macromolecules in solution consist of random coils with an enormous number of conformers in rapid equilibrium: for PB, in particular, the helical structure in the solid would be expected to be destroyed upon dissolution. Mark and Flory (5) indicate that the characteristic ratio $\langle r^2 \rangle_0 / nl^2$ of polybutene-1 and, in fact, other isotactic vinyl polymers is similar to that of polyethylene, and thus a helical conformation in solution is not to be expected. Their experimental finding of a positive, but small, temperature coefficient, $d \ln \langle r^2 \rangle_0 / dT$, they indicate, also argues against helix retention in solution. One characteristic of paraffins in the liquid state and in solution is the high velocity of rotation around carbon-carbon single bonds from one energy minimum to another. The energy barriers among the staggered conformations of bonds are of the order of 3-6 kcal/mol. Rapid rotation occurs at room temperature such that, for most practical purposes, the carbon-carbon single bond may be considered to permit free rotation (6). Hence, for a great number of synthetic polymers which possess carbon-carbon single bonds in their backbones, the retention of helical order in the solution seems improbable.

On the other hand, there exists experimental evidence which supports the contrary view. By means of infrared spectroscopy, Kobayashi et al. (7) were able to show that isotactic polystyrene, polypropylene, and poly-p-chlorostyrene molecules assume regular helical conformations in the solution or gel state over a wide range of temperatures. In addition Holland and Miller (2), during their study of PB-1 single crystals, reported that the species of crystals precipitated from solution was dependent on the maximum temperature attained by the solution before cooling as well as the temperature of crystallization. In particular, they showed that if the aged, Form I, twinned hexagonal, 3/1 helix, solid material is dissolved in amyl acetate and the temperature of the solution is never raised above 90°C, crystallization at room temperature results in the formation of untwinned hexagonal, 3/1 helix, lamellar single crystals; whereas for the same conditions, except a maximum solution temperature (T_{ms}) of 120°C, most of the polymer crystallized as orthorhombic, 4/1 helix, lamellar single crystals. In both cases the samples were held at T_{ms} for 10 min before cooling.

In this paper we summarize our studies extending Holland and Miller's work on solution history effects, the majority of which have been published (8). In

EBSCOhost - printed on 2/13/2023 3:45 AM via . All use subject to https://www.ebsco.com/terms-of-use

addition we describe some studies of the effect of thermal history in the melt on the physical properties of PB (9). The melt history effects, which seem to be related to a nucleating effect of an added antioxidant, are both unexplainable in terms of usual heterogeneous nucleation effects and of significant practical concern; differences in modulus and yield stress of a factor of 2 were obtained for samples crystallized under identical conditions except for a 30° difference in melt temperature.

Experimental

Two samples of PB were used PB-1, of high molecular weight (M_n = 74,000, M_w = 740,000) and PB-4, of low molecular weight (M_n = 35,000, M_w = 350,000), both supplied by Shell Chemical Co. For a portion of the work an unstabilized sample, similar to PB-1, was used. The stabilizer in the commercial resins is believed to be butylated hydroxy toluene (BHT).

For the melt history effects the samples were compression molded at 160°C for 3 minutes and quenched into room temperature water; the samples were then remelted on semi-cylindrical brass blocks in drying pistols at melt temperatures (T_{mm}) of 138, 151, 172 and, occasionally, 195°C for times (t_{mm}) from 5 to 30 minutes and then quenched into room temperature air or 0°C water baths held at the mouth of the pistol. Differential scanning calorimetry (DSC) measurements were made on molded samples sealed in hermetic pans before the above thermal history. DSC measurements of melting point and crystallization temperature, tensile measurements on dumbbell shaped samples (gage length 4.75 cm, width 1.37 cm, thickness 0.025 to 0.04 cm), small angle laser light scattering measurement of spherulite size, x-ray diffractometer studies of crystallinity and phase (I and/or II) and mechanical relaxation spectra studies using a torsion pendulum were conducted.

For the solution studies amyl acetate, as used by Holland and Miller (2), and xylene were used. Weighed amounts of PB, cut from the molding cubes as supplied, were dissolved at the solution temperature (T_{ms}), to form solutions of 0.01, 0.03 and 0.06 % concentration by weight. After appropriate solution time (t_{ms}), measured following clearing, the samples were transferred to another isothermal bath at T_x and allowed to crystallize. For a 0.01% amyl acetate solution the crystals began to precipitate, as indicated by the development of turbidity, after about 1 h at room temperature: approximately

EBSCOhost - printed on 2/13/2023 3:45 AM via . All use subject to https://www.ebsco.com/terms-of-use

40 hours were required at 50°C. The suspensions were held at T_x for 48 hours after the development of turbidity, with crystals then being removed for examination by electron microscopy and electron diffraction.

Results and Discussion

Solution history effects

Representative micrographs and diffraction patterns of crystals obtained for various T_{ms}, with T_x = 24 and 50°C, are shown in Figs. 1-5, ref. 7. Even at 24°C, at which multilayer crystals grow, one can readily distinguish between the various crystal forms by the shape of the crystals. Relative amounts of the various forms were, in general, determined by observation. Figs. 1 and 2 show the results obtained using amyl acetate and starting with the two aged (hexagonal, Form I) PB samples. As reported by Holland and Miller (2), for T_{ms} at 90°C, hexagonal (Form I') crystals are obtained whereas for T_{ms} = 120°C orthorhombic (Form III) crystals develop. There is also, however, a clear effect of t_s. As shown in Fig. 2, experiment 9 and Fig. 3, the effect is reversible, the orthorhombic form upon dissolution at 90°C recrystallizes upon cooling as Form I'. Tetragonal crystals were obtained, in fluctuating relative amount, only if the tetragonal form was present before dissolution and then only for short time of solution t_s (Fig. 4). Not understood is experiment 14, in which short times of solution at 90°C lead to Form III rather than Form I'; longer solution times lead to Form I' with no residual Form II (experiment 15). Similar results were obtained using xylene as a solvent (Figs. 10 and 11, ref. 7).

Figure 1. PB-4, Twinned Hexagonal, 3/1 Helix

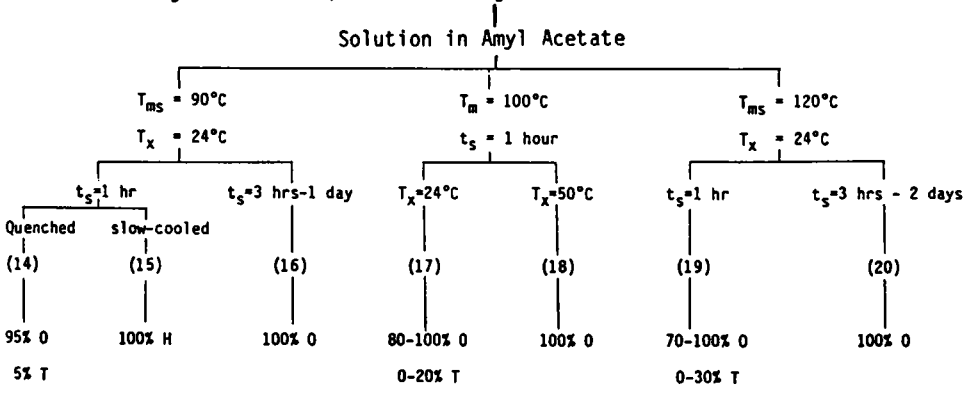

EBSCOhost - printed on 2/13/2023 3:45 AM via . All use subject to https://www.ebsco.com/terms-of-use

Figure 2. PB-1, Twinned Hexagonal, 3/1 Helix

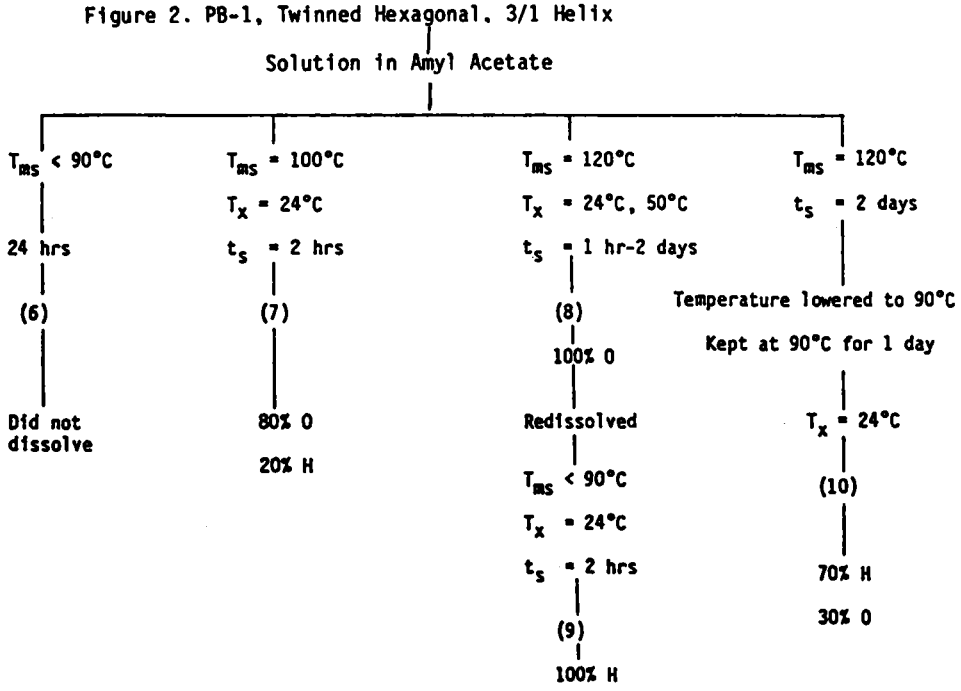

Figure 3. PB-4, Orthorhombic, 4/1 Helix

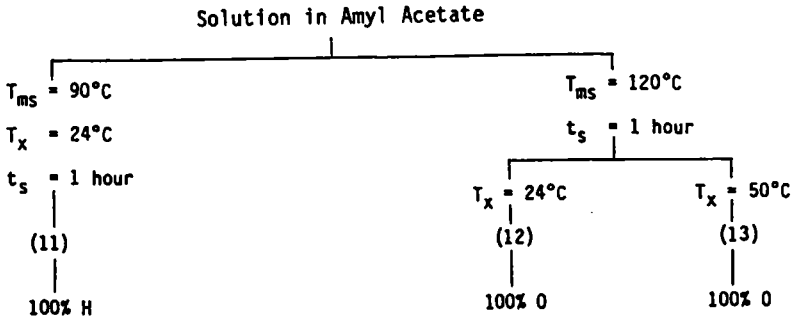

The results clearly show that the crystal structure formed during precipitation from solution depends on the crystal structure before dissolution, the temperature of the solution and the time at that temperature. The results suggest, we propose, a temperature dependent, helical structure in solution, one which determines the crystal structure formed during precipitation, and with only a slow conversion from the helix in the original solid to that form

EBSCOhost - printed on 2/13/2023 3:45 AM via . All use subject to https://www.ebsco.com/terms-of-use

Figure 4. PB-4, Tetragonal, 11/3 Helix

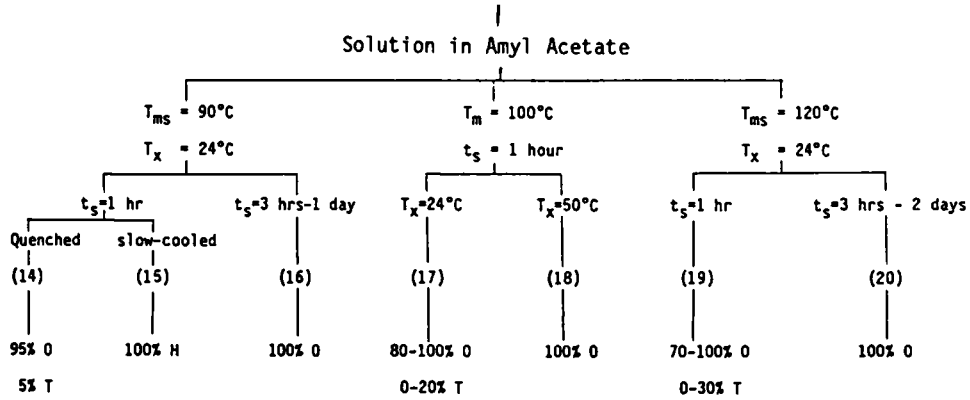

stable at T_{ms}. The 3_1 helix appears stable at low T_{ms} whereas the 4_1 helix is stable at higher temperatures. In reaching this hypothesis two factors need consideration: the possibility of nuclei retention (self-seeding) in solution and experimental evidence for the various helices in solutions at T_{ms}.

We consider first the possibility of self-seeding. Such an effect is certainly possible since PB-1 did not dissolve at 90°C in amyl acetate. If the crystals are self-seeded by retained nuclei the helix form in the nuclei must change with temperature, i.e. the 3/1 helix must transform to a 4/1 helix at temperatures above 90°C (experiments 2-5, 7 and 8), this despite the fact the melting point of the orthorhombic form in the solid is ca. 90°C. In addition, as shown by experiments 9 and 11, the effect must be reversible, the 4/1 helix transforming to 3/1 when heated to 90°C. While the latter effect might be possible, the orthorhombic form melting and recrystallizing in the hexagonal form, the conversion from hexagonal to orthorhombic is not expected. In addition, at 120°C both PB-1 and PB-4 would be expected to be completely dissolved and yet experiment 10 indicates the crystals grown after reducing the temperature to 90°C before crystallizing at 24°C, both remember the previous storage at 120°C and the storage at 90°C. Thus, we conclude, self seeding is not likely.

The other possibility is that a helical conformation is stable in solution, in segments of the molecule, is retained in the form present in the solid before dissolution for times of the order of an hour and that the stable form is temperature dependent and is retained and determines the crystal structure when cooled to the crystallization temperature. In view of the normally expected

EBSCOhost - printed on 2/13/2023 3:45 AM via . All use subject to https://www.ebsco.com/terms-of-use

rapidity of molecular conformational changes in both solution and the melt, the above explanation is also unexpected, in terms of the presence of any helical conformation in solution, the slowness of change to the "stable" form and its effect on nucleation. Thus attempts have been made to directly observe the presence of the helices, and changes therein, in solution. In ref. 7 intrinsic viscosity measurements at 62°C for PB-L are reported suggesting samples previously heated to 90 or 120°C differ by about 20%, the 90°C sample having the larger value of $[\eta]$. These measurements were made using polymer cut from individual pellets as supplied by Shell. Subsequent experiments suggest the variation may have been due to chance selections of pellets of additive containing concentrate and additive free, as polymerized polymer or of pellets from different original lots of resin blended as supplied. Similar variations from pellet to pellet were obtained for identical solution histories, samples from a given pellet having identical values of $[\eta]$. Attempts to use helix dependent IR bands have been unsuccessful. No appropriate PB IR bands were observed for xylene solutions even at concentrations up to ca. 40%. Currently attempts are being made to use C_{13} NMR, with initial experiments directed at determining if similar thermal history effects are observed for concentrated (ca. 5%) solutions. Thus, to date, no final conclusion can be made.

An obvious question is whether the above results are unique to PB. Charlet et al., however, have recently shown (9-11) that the crystal structure of poly-4-methyl pentene-1 (P4MP1) crystallized from cyclopentane solution can be affected by T_{ms}. The helix structure in the 2 forms obtained following cooling to room temperature depends on the maximum temperature attained before cooling.

Melt history effects

As indicated previously, Rault et al (4) have shown that the thickness of PB lamellae increases by about 10% for an increase in melt temperature of 100°C. This suggests the melting point would correspondingly increase. Potential changes in physical properties would be more difficult to predict, depending on details of the morphological structure and the crystallinity, neither of which were measured, but would not be expected to be large. The effects observed here, however, are large and, for the melting point, opposite those predicted on the basis of Rault's results. As will be shown, they apparently depend on a nucleating effect of the antioxidant BHT, an effect not yet fully understood. In the following we consider DSC, mechanical property and small angle light scattering studies of the properties and spherulite size of PB as a function of

EBSCOhost - printed on 2/13/2023 3:45 AM via . All use subject to https://www.ebsco.com/terms-of-use

T_{mm} and t_{mm}. The mechanical relaxation, transformation rate and crystallinity studies are described elsewhere (12).

Fig. 5 shows DSC measurements of T_m for samples of PB-4 (a,b) and PB-1 (c,d) held at T_{mm} = 172° for t_{mm} = 5 to 30 minutes and then quenched into ice water. The DSC measurements were made either 30 minutes (a,c) or 2 days (b,d) after quenching. Two days is sufficient to permit significant conversion to the stable hexagonal crystal form of the PB-1 sample whereas for PB-4 substantial conversion occurred in 30 minutes, the conversion being complete in 2 days. For both samples the total crystallinity increased by about 20% with aging, i.e. from ca. 35% to 43% for PB-1 and 38 to 46% for PB-4, as quenched to room temperature. In all but Fig. 5a T_m decreases with increasing t_{mm}, an effect opposite that predicted on the basis of Rault's results, assuming all prior appropriate thermal history was at temperatures below 172°C. The observed decrease in T_m could be due to degradation. However, in Fig. 5a T_m for both Forms II and I are seen to increase with t_{mm}, despite the decrease in T_m after the conversion is complete. The difference in conversion rate between PB-1 and PB-4 and the increase in T_m of the hexagonal form in PB-4 as conversion progresses is also seen. In both PBs the conversion rate is considerably faster for the ice water quenched than for the air quenched sample.

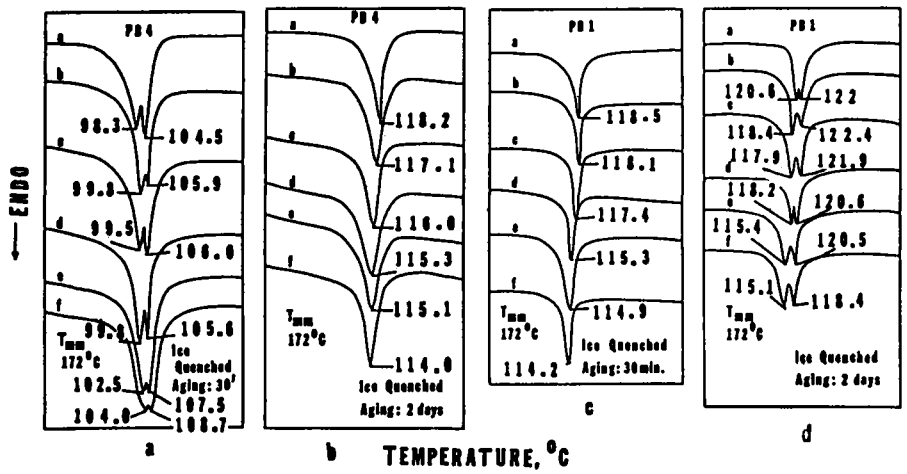

Figure 5. DSC scans of PB-4 (a,b) and PB-1 (c,d) heated to T_{mm} = 172°C for t_{mm} varying from 5 min (top) to 30 min (bottom) and quenched with 0°C H_2O. The samples were held at room temperature for 30 min (a,c) or 2 days (b,d) before measuring at 20°C/min.

EBSCOhost - printed on 2/13/2023 3:45 AM via . All use subject to https://www.ebsco.com/terms-of-use

The DSC data are listed in Tables 1 and 2. The results can be summarized as follows:

For PB-4

1. In ice water quenched 30 minute aged samples, $T_m(H)$ and $T_m(T)$ increases with decreasing T_{mm} for a given t_{mm} and for increasing t_{mm} for a given T_{mm}, where $T_m(H)$ refers to the T_m of the hexagonal form.
2. When aged 2 days, conversion is complete, there is a substantial increase in $T_m(H)$ for all T_{mm} and t_{mm} as compared to $T_m(H)$ after 30 minutes, but T_m now decreases with t_{mm} for a given T_{mm}. The variation in $T_m(H)$ with T_{mm} for a given t_{mm} is considerably smaller, there being a slight increase with decreasing T_{mm}.
3. For the air quenched sample the effect of t_{mm} is considerably less. $T_m(T)$ increases, however, with decreasing T_{mm}: $T_m(T)$ is also considerably higher for the air quenched samples than for the ice water quenched samples for short t_{mm}, being about the same for long t_{mm}.
4. Upon conversion, which is not complete after 2 days, $T_m(H)$ shows a slight increase with increasing t_{mm} for all T_{mm} but is essentially independent of T_{mm}. The residual $T_m(T)$ is slightly higher for T_{mm} = 172 and 151°C, and lower for T_{mm} = 138°C than after 30 minutes.

Table 1. Melting Points of PB-4 Samples

T_{mm}, °C, t_{mm}, min	Ice Quenched				Air Quenched			
	30 min		2 days		30 min		2 days	
	H	T	H	T	H	T	H	T
172, 5	104.4	98.3	118.2		109.6		117.8	110.3
10	105.9	98.8	117.1		109.6		118.9	110.2
15	106.0	99.5	116.0		109.6		120.2	110.8
20	105.6	99.8	115.3		109.8		120.8	110.7
25	107.5	102.5	115.1		109.1		120.0	110.8
30	108.5	104.0	114.0		108.7		116.6	110.1
151, 5	106.1	1002.	118.0		110.2		118.2	110.6
10	108.7	102.0	118.2		110.9		118.1	110.0
15	108.3	103.1	117.1		111.1		119.2	111.3
20	110.4	105.8	117.5		110.2		121.6	110.8
25	112.4	106.4	116.2		110.6		120.3	111.4
30	110.1	108.0	115.9		109.0		119.2	110.0
138,5	109.8	105.0	119.2		114.2		118.9	112.0
10	109.9	105.9	119.4		114.8		118.1	112.3
15	110.4	107.1	118.9		115.1		119.3	111.9
20	113.1	108.4	118.1		114.3		119.1	112.6
25	114.8	110.2	117.6		114.0		120.9	112.6
30	116.0	110.0	116.0		113.9		121.0	112.0

EBSCOhost - printed on 2/13/2023 3:45 AM via . All use subject to https://www.ebsco.com/terms-of-use

For PB-1

1. For the ice water quenched, 30 minute aged samples, $T_m(T)$ decreases with increasing t_{mm}, i.e. opposite the effect in PB-4, and is nearly independent of T_{mm}.
2. After 2 days' aging $T_m(T)$ and $T_m(H)$ decrease with t_{mm}, as for PB-L, but again are nearly independent of T_{mm}.
3. In the air quenched samples, after 30 minutes' aging, there is a clear decrease in $T_m(T)$ with t_{mm} and a slight increase with decreasing T_{mm}.
4. After aging $T_m(H)$ decreases with t_{mm} but $T_m(T)$ is nearly independent of both t_{mm} and T_{mm}.
5. $T_m(T)$, in the 30 minute samples, is considerably higher in PB-1 than in PB-4. After aging the $T_m(H)$ are only slightly higher.

Table 2. Melting Points of PB-1 Samples

	Ice Quenched				Air Quenched			
	30 min		2 days		30 min		2 days	
T_{mm}, °C, t_{mm}, min	H	T	H	T	H	T	H	T
172, 5		118.5	122.0	120.6		119.6	122.7	115.8
10		118.1	122.4	118.4		119.3	122.5	115.3
15		117.4	121.9	117.9		118.1	120.6	116.0
20		115.3	120.6	118.2		117.9	119.3	115.4
25		114.9	120.5	115.4		115.4	120.0	114.8
30		114.2	118.4	115.1		115.2	118.2	115.6
151, 5		119.9	124.4	120.0		120.1	120.4	116.4
10		117.4	122.1	119.6		119.6	121.1	116.0
15		116.2	122.3	119.1		119.4	119.8	115.7
20		116.6	120.2	118.5		117.2	120.6	116.0
25		114.3	120.0	115.2		116.5	120.3	115.8
30		111.1	118.4	115.0		115.9	119.4	115.4

The decrease in T_m with increasing T_{mm} and/or t_{mm}, that occurs in some but not all of the samples, suggests molecular degradation as a possible cause. However, not only do the PB-4, 30 minute results go in the opposite direction with t_{mm}, but, as shown later, apparently related mechanical property results are reversible. It is also noted the changes in T_m, for 20°C changes in T_{mm}, are considerably larger than would be expected if due solely to changes in lamellar thickness of the magnitude observed by Rault et al (2a) and, for PB-4, are in the opposite direction expected for changes in T_{mm}.

The changes in mechanical properties with T_{mm} and t_{mm} are, perhaps, even more dramatic. PB, in a tensile test, does not show a yield point. The yield

EBSCOhost - printed on 2/13/2023 3:45 AM via . All use subject to https://www.ebsco.com/terms-of-use

point, as discussed here, was determined by drawing a line intersecting the deformation axis at 2% deformation and parallel to the initial slope (modulus) of the load-deformation curve; the intersection of this line and the load-deformation curve is defined as the yield point.

The mechanical property data for PB-1, the only sample measured, are tabulated in Table 3 as measured 30 minutes after room temperature quenching. For the samples melted in air (T_{mm} = 138 to 172°C) there is a substantial decrease in mechanical properties with increasing t_{mm} and T_{mm}. Here again molecular degradation could result in the observed changes. When melted at 195°C, in vacuum, the small strain properties approach those of the 138°C melt, whereas the ultimate properties are low. The former might be due to high crystallinity and the latter again to degradation.

Table 3. Mechanical Properties of PB-1: Room Temperature Quenched, Aged for 30 minutes

T_{mm}, t_{mm} °C,min	Young's Modulus $x10^{-4}N/m^2$	Yield Stress $x10^{-4}N/m^2$	Engineering Stress $x10^{-4}N/m^2$	Elongation %
138, 10 (3)[a]	10961 (26%)[b]	374 (14%)	3984 (21%)	306 (7%)
20 (4)	9862 (21%)	339 (20%)	3254 (19%)	296 (11%)
30 (4)	9438 (17%)	298 (16%)	3435 (22%)	283 (6%)
151, 5 (6)	10284 (14%)	398 (12%)	3676 (20%)	274 (4%)
10 (6)	10341 (16%)	351 (22%)	3233 (24%)	294 (7%)
15 (5)	7371 (16%)	351 (16%)	3125 (18%)	256 (6%)
20 (5)	7094 (21%)	271 (17%)	2887 (19%)	243 (7%)
25 (5)	6845 (16%)	325 (15%)	2837 (19%)	283 (6%)
30 (5)	6963 (16%)	277 (18%)	2860 (22%)	240 (5%)
172, 5 (6)	5461 (14%)	222 (16%)	2417 (19%)	266 (6%)
10 (6)	6052 (18%)	244 (15%)	2245 (19%)	241 (12%)
15 (6)	9490 (17%)	302 (15%)	1861 (17%)	206 (6%)
20 (4)	4803 (15%)	169 (11%)	1261 (18%)	220 (4%)
25 (4)	6176 (15%)	208 (11%)	1504 (18%)	208 (4%)
30 (4)	5919 (14%)	239 (12%)	1612 (22%)	218 (4%)
195,10 (3)[c]	8362 (20%)	286 (16%)	1814 (14%)	194 (6%)
20 (3)	8029 (9%)	204 (24%)	1863 (21%)	189 (9%)
30 (3)	10734 (12%)	339 (16%)	2105 (19%)	190 (6%)

a) Number of samples
b) Maximum variation from average, standard deviations would be less
c) Samples prepared under vacuum

Before further considering the possibility of degradation, we first note that the small strain results, in particular, for T_{mm} = 172°C, t_{mm} = 15 and 20

EBSCOhost - printed on 2/13/2023 3:45 AM via . All use subject to https://www.ebsco.com/terms-of-use

minutes appear out of line with the other samples, those for 15 minutes being significantly larger than expected whereas those for 20 minutes are smaller. The differences appear to be beyond the experimental error but no reason for the effect is known.

As shown by the DSC results, PB-1, 30 minutes after quenching, is still essentially completely Form II. After 10 days of aging it will have approached an equilibrium conversion to Form I. The effect of T_{mm} and t_{mm} on the mechanical properties of the samples after aging is considerably smaller, Table 4, than as quenched. The small strain properties are essentially the same, while the ultimate properties appear to decrease with increasing T_{mm} and are independent of t_{mm}. One notes, again, that the effects could be related to molecular degradation, and that the samples annealed for the longest time at 195°C (in vacuum) have the best properties.

Table 4. Mechanical Properties of PB-1: Room Temperature Quenched, Aged for 10 days

T_{mm}, t_{mm} °C,min	Young's Modulus x10^{-4}N/m^2	Yield Stress x10^{-4}N/m^2	Engineering Stress x10^{-4}N/m^2	Elongation %
151,10 (3)[a]	27074 (24%)[b]	1258 (9%)	2315 (18%)	234 (4%)
20 (3)	22554 (18%)	1372 (14%)	2918 (22%)	300 (6%)
30 (4)	23216 (24%)	1331 (15%)	2738 (26%)	253 (6%)
172,10 (3)	24960 (21%)	1245 (18%)	2052 (18%)	198 (3%)
20 (3)	21050 (29%)	1361 (12%)	2019 (19%)	174 (5%)
30 (3)	22848 (18%)	1321 (11%)	2139 (21%)	192 (6%)
195,10 (3)[c]	26110 (17%)	1442 (13%)	2013 (12%)	174 (7%)
20 (3)	25901 (19%)	1640 (16%)	2518 (20%)	184 (6%)
30 (3)	28740 (16%)	1690 (20%)	2862 (16%)	167 (6%)

a) Number of samples
b) Maximum variation from average, standard deviation would be less
c) Samples prepared under vacuum

In addition to molecular degradation, another possible cause for at least some of the mechanical property and DSC results is removal of nuclei by sublimation of an additive and/or thermal destruction of heterogeneous nuclei. Either effect would result in crystallization at a lower temperature (T_c), the larger T_{mm} and/or t_{mm}, and an increase in spherulitic size, resulting in poorer mechanical properties for equivalent crystallization conditions. The possible contribution of molecular degradation and/or nuclei destruction was examined by heating samples to a T_{mm} of 172°C for 15 minutes, which should result in low

EBSCOhost - printed on 2/13/2023 3:45 AM via . All use subject to https://www.ebsco.com/terms-of-use

physical properties, followed by further heating at 151°C for an additional 15 minutes, the additional heating being both while the sample was still in the melt or after an intervening crystallization. As shown in Table 5, the effects described above cannot be due to molecular degradation or any normal nuclei destruction. Crystallization could reactivate hetero-geneous nuclei, resulting in effective nucleation at 151° on a second heating (experiment D) but should only result in further molecular degradation. When held in the melt for a further period, as in experiment C, both further degradation and nuclei destruction would be expected. However, the ultimate physical properties are considerably improved over those of the high temperature melt alone (experiment A) and, in fact, approach those of the 15 minute melt at the lower temperature alone (experiment B).

Table 5. Melt Hysteresis Effects for PB-1

	Samples			
	A	B	C	D
Engineering Stress (N/m^2) x 10^{-4}	1,861	3,125	2,922	2,971
Elongation (%)	206	256	224	248

A: 15 minutes at 172°C, R_TQ, age 30 minutes
B: 15 minutes at 151°C, R_TQ, age 30 minutes
C: 15 minutes at 172°C, 15 minutes at 151°C, R_TQ, age 30 minutes
D: 15 minutes at 172°C, R_TQ, 15 minutes at 151°C, R_TQ, age 30 minutes

The specific viscosities of dilute solution (and the extrapolated [η]) were identical for samples previously heated at 151°C for 5 minutes and 172°C for 30 minutes, again suggesting molecular weight degradation is not of significant concern.

Nucleation effects, although not expected as a result of the above experiments, may still be possible. In an attempt to study the effect of thermal history on the nuclei density, the spherulite sizes were measured in appropriate samples using small angle light scattering. The system was such that areas of ca. 1 mm diameter in the compression molded, remelted films were used. For the as-molded (160°C T_{mm}, 3 minute t_{mm}) samples the spherulite size was observed to vary as expected with cooling rate, the largest being in a slow cooled sample and the smallest in a 0°C quenched sample. The spherulite diameters differed by a factor of 2 for this difference in crystallization conditions. In most regions of the PB-H and PB-L samples used for the DSC and mechanical property studies the observations were opposite those expected, smaller spherulites

EBSCOhost - printed on 2/13/2023 3:45 AM via . All use subject to https://www.ebsco.com/terms-of-use

indicating a higher concentration of nuclei being present for larger T_{mm} and t_{mm}. However, in isolated regions of a given sample, regions on the order of at least 1/2 to 1 cm in diameter, significantly different, usually larger, spherulites could be found. These areas of essentially common spherulite size, differing from those in the major portions of the sample, appeared to be about that expected to be produced from the volume of one resin pellet.

To our knowledge only the antioxidant BHT is added to the PB we used, presumably as a concentrate. If so, pellets containing substantial amounts of BHT would be physically mixed with additive free pellets, homogenization occurring in subsequent processing. However, in our compression molding, this homogenization would not occur. This effect could also explain the variation in intrinsic viscosity from pellet to pellet, the concentrate likely having a different molecular weight than the bulk resins.

In order to examine the possible effects of the BHT, a BHT free sample of PB similar to PB-1 was obtained. The spherulites in this sample, of similar size throughout a film, increased slightly in size with increasing T_{mm} and t_{mm} suggesting a normal heterogeneous nucleation effect. In all samples they were larger than in any regions of the commercial samples, suggesting the presence of nucleating agent in the regions of the films formed even from the bulk resin pellets despite the lack of homogenization during film fabrication. The mechanical properties of the additive free polymer are shown in Table 6. Although the modulus shows a variation with T_{mm} similar to the commercial resin, the other parameters are the same within experimental error, the ultimate properties being even lower than those of the commercial polymer with T_{mm} = 172°C. Again, this is likely not due to molecular degradation since 138°C for 10 minutes is relatively mild.

That some form of nucleation effect is involved can be shown by DSC studies of the crystallization temperature during cooling (13). As shown in Fig. 6, the crystallization temperature, particularly of PB-1, is affected by the melt temperature. These data were obtained by successively heating the samples to lower T_{mm} after each crystallization and melting run; i.e. a sample was heated to 200°C, allowed to crystallize during cooling 20°C/minute (T_c = 43°C), remelted at 160°C, cooled (T_c = 43°C), etc. For T_{mm} below 160°C, T_c increases by almost 20°C, a difference which would be expected to yield difference in morphology and properties. That the effect, again, is not due to molecular degradation is shown both by the increase in T_c with increasing total time in

EBSCOhost - printed on 2/13/2023 3:45 AM via . All use subject to https://www.ebsco.com/terms-of-use

the melt and the reversibility of the effect; reheating the 120°C T_{mm} sample to 160°C results in T_c = 43°C.

Table 6. Mechanical Properties of unstabilized PB-1: Room Temperature Quenched, Aged 30 Minutes

T_{mm}, t_{mm} °C,min	Young's Modulus $x10^{-4}N/m^2$	Yield Stress $x10^{-4}N/m^2$	Engineering Stress $x10^{-4}N/m^2$	Elongation %
138ϕ, 10 (3)[a]	9860 (15%)[b]	316 (6%)	1924 (11%)	195 (8%)
151ϕ, 10 (4)	8954 (17%)	266 (8%)	1764 (14%)	190 (10%)
172ϕ, 10 (3)	5023 (14%)	310 (14%)	2186 (12%)	220 (9%)
30 (3)	4986 (12%)	296 (14%)	2090 (9%)	180 (9%)

[a]Number of samples [b]Maximum variation from average

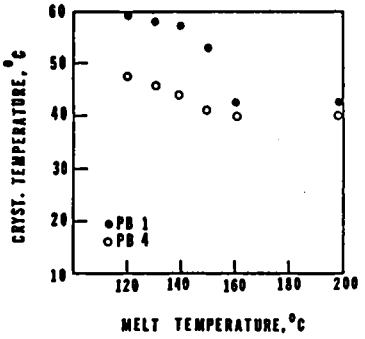

Figure 6. Crystallization temperature as a function of melt temperature for PB-1 and PB-4.

Summary

As of this time we know of no potential explanation for the solution history effects other than thermally stable helical conformations, conformations which only slowly change and which determine the crystal structure of the single crystals formed upon cooling. The fact that similar effects have been observed in P4MP1 (9-11) suggest the effect is not unique to PB or any additive therein. The results are of obvious concern in a number of areas including molecular weight characterization, solution conformation theory and the solid state properties of polymers precipitated following polymerization in solution.

The melt history effects are even less explainable at present. Although apparently related in some fashion to nucleation effects, the results of a number of the experiments are contrary to expectations for either thermal

EBSCOhost - printed on 2/13/2023 3:45 AM via . All use subject to https://www.ebsco.com/terms-of-use

destruction of heterogeneous nuclei or sublimation of the nucleating agent. Regardless of its origin, however, the effect is of obvious practical importance in the processing of PB. Although the physical properties following transformation to the stable hexagonal form are relatively unaffected by T_{mm} and t_{mm}, the properties immediately after solidification are strongly dependent on the thermal history. The effect of the history on crystallization temperature suggests a related effect on lamellar thickness, one which needs consideration in experimental studies concerned with crystallization theories. With a number of questions remaining, further study is obviously warranted.

Acknowledgements

This research was supported by Shell Chemical Co. and the National Science Foundation through the Polymer Program and the University of Illinois Materials Research Laboratory.

References

1. Natta, G., P. Pino, P. Corradini, F. Danusso, E. Mantica, G. Mazzanti, G. Moraglio . 1955. J. Am. Chem. Soc. 77, 1708.

2. Holland, V.F., R.L. Miller. 1964. J. Appl. Phys. 35, 3241.

3. Hsu, C.C., P.H. Geil. J. Macromol. Sci. (Phys.) (submitted).

4. Rault, J., M. Sotton, C. Rabourdin, E. Robelin. 1980. J. Physique 41, 1459.

5. Mark, J.E., P.J. Flory. 1965. J. Am. Chem. Soc. 87 1423.

6. Morrison, R.T., R.N. Boyd. 1966. Organic Chemistry, 2nd ed., Allyn and Bacon, Boston, 92-97.

7. Kobayashi, M., K. Tsumura, H. Tadokoro. 1968. J. Polym. Sci. A-2 5, 1493.

8. Chau, K.W., P.H. Geil. 1984. J. Macromol. Sci. (Phys.), B23, 115.

9. Charlet, G., G. Delmas. 1982. Polym.Bull. 6, 367.

10. Charlet, G., G. Delmas, J.F. Rievol, R.St.J. Manley. 1984. Polymer 25, 1613.

11. Charlet, G., G. Delmas. 1984. Polymer 25, 1619.

12. Agarwal, A. 1984. M.S. thesis, University of Illinois.

EBSCOhost - printed on 2/13/2023 3:45 AM via . All use subject to https://www.ebsco.com/terms-of-use

RHEOLOGY-PROCESSING-PROPERTY-MORPHOLOGY RELATIONSHIP IN HETEROGENEOUS POLYMER BLENDS

Chang Dae Han and Hsiao-Ken Chuang

Department of Chemical Engineering
Polytechnic Institute of New York
Brooklyn, New York 11201

Introduction

The polymer industry has been challenged to produce new polymeric materials by blending two or more homopolymers or copolymers, which are chemically incompatible. To meet the challenge, several attempts have been made by: (1) synthesizing new monomers, polymerizing them, and then blending them with existing polymers: (2) copolymerizing existing monomers and blending them with existing homopolymers; (3) modifying existing polymers by chemical and/or physical methods and blending them with existing homopolymers or copolymers; (4) synthesizing new compatibilizers that, when added to two incompatible polymers, can decrease the size of the dispersed domains and improve the interfacial properties or reactions, and thus the mechanical and/or physical properties desired.

There are some heterogeneous polymer blend systems that have met commercial success; for example, rubber-modified thermoplastics and thermoplastic elastomers. In such polymer systems, the matrix phase of rigid polymer contains the discrete phase of flexible polymers, consisting of globules with a certain size range. In the absence of any chemical reaction between the constituent components in a polymer blend system, it is generally understood today that success in improving physical/mechanical properties in

Morphology of Polymers
© 1986 Walter de Gruyter & Co., Berlin · New York - Printed in Germany.

EBSCOhost - printed on 2/13/2023 3:45 AM via . All use subject to https://www.ebsco.com/terms-of-use

heterogeneous polymer blend system depends on the control of the domain size of the dispersed phase and on the ability to increase interfacial interactions.

Indeed, during the past decades, an approach has been taken to graft reactive molecules having functional groups onto one polymer (say, Polymer A), which will then be melt-blended with another polymer (say, Polymer B) that, also, contains functional groups. The rationale behind this approach lies in that, when polymers A and B are melt-blended, the functional groups present in the individual polymers may react chemically to form a graft copolymer. This newly formed graft copolymer would then play the role of an "interfacial agent" promoting adhesion between the matrix and the dispersed phase. A number of patents and scientific literature (1-11) have reported such an approach. More specifically, maleic anhydride was grafted onto polypropylene (1,2), polystyrene (3), polyethylene (4-8), or onto ethylene-propylene-diene terpolymer (EPDM rubber) (9-11). The grafted polymer was then blended with various polymers to improve the mechanical properties of the blends.

In this paper, we shall present the results of our recent investigation into the rheology-processing-property-morphology relationships in blends of nylon 6 and an ethylene-based polymer with functional groups.

Experimental

Blends were prepared, having the following five blend ratios (by weight) of nylon 6/CXA 3101: 80/20, 60/40, 50/50, 40/60, and 20/80. The CXA 3101 resin (DuPont Company) used is known as ethylene-based polymer. Infrared spectroscopic analysis indicates that the CXA resin contains 18.1 wt.% of vinyl acetate and 2.1 wt.% of

EBSCOhost - printed on 2/13/2023 3:45 AM via . All use subject to https://www.ebsco.com/terms-of-use

-COOH groups. For comparison purposes, nylon 6/EVA blend system was also prepared, having the same blend ratios as those for the nylon 6/CXA 3101 system. In all cases, a twin-screw compounding machine (Werner & Pfleiderer ZKS-30) was used to prepare the blends. EVA refers to poly(ethylene-co-vinyl acetate).

In order to determine the melting behavior of the materials we used a DuPont 910 Differential Scanning Calorimeter (DSC), and for measuring the thermomechanical behavior of the materials we used a DuPont 981 Dynamic Mechanical Analyzer (DMA) in conjunction with a 1090 Thermal Analyzer. Before measurements were taken, the samples were dried in a vacuum oven at 65°C for 48 hours, and measurements were carried out in a nitrogen atmosphere, and at a heating rate of 10°C/min for DSC measurement and 5°C/min for DMA.

A cone-and-plate rheometer (a Weissenberg Model R-16 Rheogoniometer) was used to measure (1) steady shear flow properties, namely viscosity (η), shear stress (σ_{12}) and first normal stress difference (N_1), (2) oscillatory shear flow properties, namely dynamic viscosity (η'), storage modulus (G') and loss modulus (G"). These quantities were determined using the expressions described in the literature (12).

For the purpose of the present investigation, the melt-blended pellets were injection-molded to obtain test specimens for the measurement of tensile properties and Izod impact strength. Before their use, the test specimens were vacuum dried at 70°C for 30 hours to remove moisture and to relieve the frozen-in stress. The dried test specimens were stored in a dessicator until use. Tensile property measurements were done on an Instron machine at room temperature following the procedure described in ASTM D638. A cross-head speed of 0.508 cm/min was used in all measurements. All the specimens for the Izod impact strength measurements had the dimensions 6.35 cm x 1.27 cm x 0.317 cm, with a notch 0.0254

EBSCOhost - printed on 2/13/2023 3:45 AM via . All use subject to https://www.ebsco.com/terms-of-use

cm in radius. The notched Izod impact strength was measured, using a Baldwin impact testing machine at room temperature.

The Izod impact fracture surface and the tensile fracture surface of the test specimens were studied, using a scanning electron microscope (SEM) (AMR 1200) operated at 15 to 25 kV. The surfaces of the tensile and impact fracture specimens were coated with gold to avoid charging under an electron beam.

Results and Discussion

Figure 1 gives plots of first normal stress difference (N_1) versus shear stress (σ_{12}), and Figure 2 plots of storage modulus (G') versus loss modulus (G") at two different temperatures, for the nylon 6/CXA 3101 blend system. It is seen that the dependence of N_1 and G' on temperature is suppressed, showing little temperature dependency. Similar observations have been reported earlier by Han and co-workers (12-21). Note in Figure 3, however, that plots of viscosity (η) versus shear stress (σ_{12}) exhibit temperature dependency. As pointed out by Han (12,13), the use of σ_{12} is appropriate for correlating the rheological properties of multiphase polymer systems.

Figure 4 displays DSC thermograms of the nylon 6/CXA 3101 blend system. It is seen that nylon 6 has a melting point of 221°C and CXA 3101 has a melting peak at about 88°C. Note that there is no noticeable depression of the melting point in this blend system.

Figure 5 shows the results of DMA runs, plots of loss modulus versus temperature, for the nylon 6/CXA 3101 blend system. We observe three relaxation peaks in nylon 6: an α peak at 71°C, a β peak at -45°C, and a γ peak at -120°C, although the γ peak is not shown in Figure 5. The α peak is believed to be associated with

EBSCOhost - printed on 2/13/2023 3:45 AM via . All use subject to https://www.ebsco.com/terms-of-use

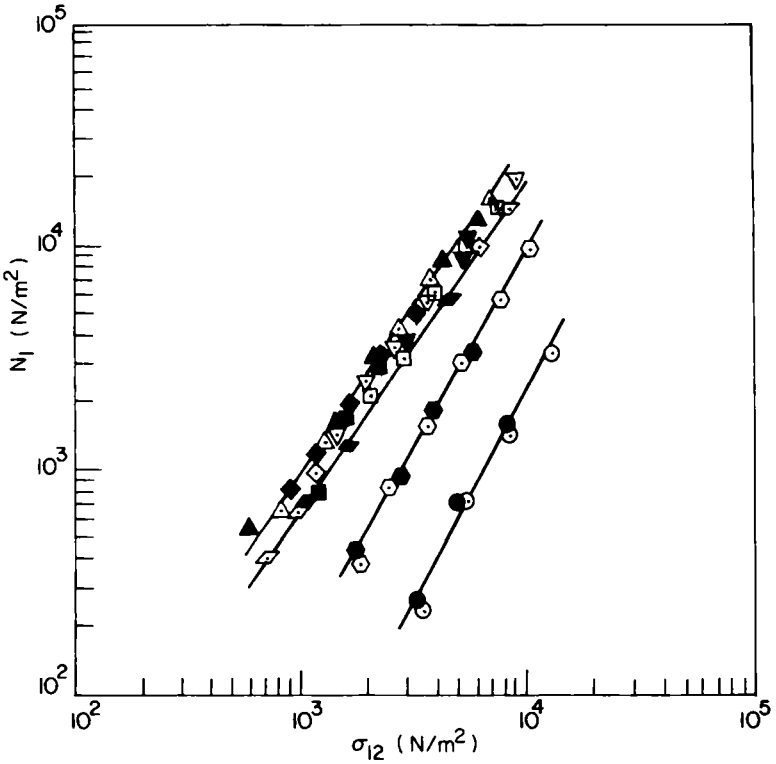

Figure 1. N_1 vs. σ_{12} for the nylon 6/CXA 3101 blend system: (⊙,●) nylon 6; (△,▲) CXA 3101; (⊡,■) nylon/CXA=20/80; (▽,▼) nylon/CXA=40/60; (◇,◆) nylon/CXA=50/50; (▱,▰) nylon CXA=60/40; (⊙,⬣) nylon/CXA=80/20. Open symbols are for 230°C and closed symbols for 240°C.

the glass transition, the β peak is due to the segmental motion of the amide groups which are not bonded to other amide groups, and the γ peak is thought to be associated with the crankshaft rotation of the $-(CH_2)_n$ groups in the main chain of the polyamide (22). In the nylon-rich blends, the glass transition temperature (T_g) of nylon 6 is little affected, whereas its β-transition (T_β) seems to have disappeared. Note in Figure 5 that strong shoulders are seen on the low temperature side of the peak and that the T_g of CXA 3101 is shifted toward lower temperatures (-32°C and -28°C

EBSCOhost - printed on 2/13/2023 3:45 AM via . All use subject to https://www.ebsco.com/terms-of-use

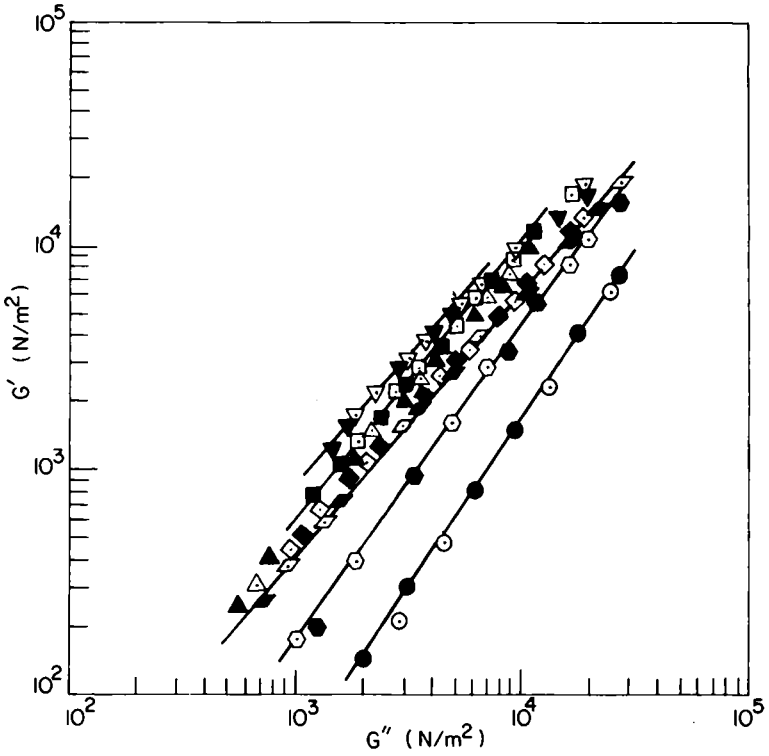

Figure 2. G' vs. G" for the nylon 6/CXA 3101 blend system. Symbols are the same as in Figure 1.

in the nylon 6/CXA 3101=80/20 and 60/40 blends, respectively) and no peak representing the T_β of nylon 6 is seen. In the CXA 3101-rich blends, no peak representing nylon 6 is seen, and the T_g of CXA 3101 (~23°C) is little affected by the presence of nylon 6.

We believe that, during the melt blending of nylon 6 and CXA 3101, chemical reactions have taken place between carboxyl or anhydride groups present in the CXA 3101 and amino end groups of nylon 6. We speculate that the chemical reactions made the β-transition of nylon 6 disappear in the nylon-rich blends. Note that the β-transition of nylon 6 is associated with the existence of polar groups forming hydrogen bonds. We confirmed that different heating rates

EBSCOhost - printed on 2/13/2023 3:45 AM via . All use subject to https://www.ebsco.com/terms-of-use

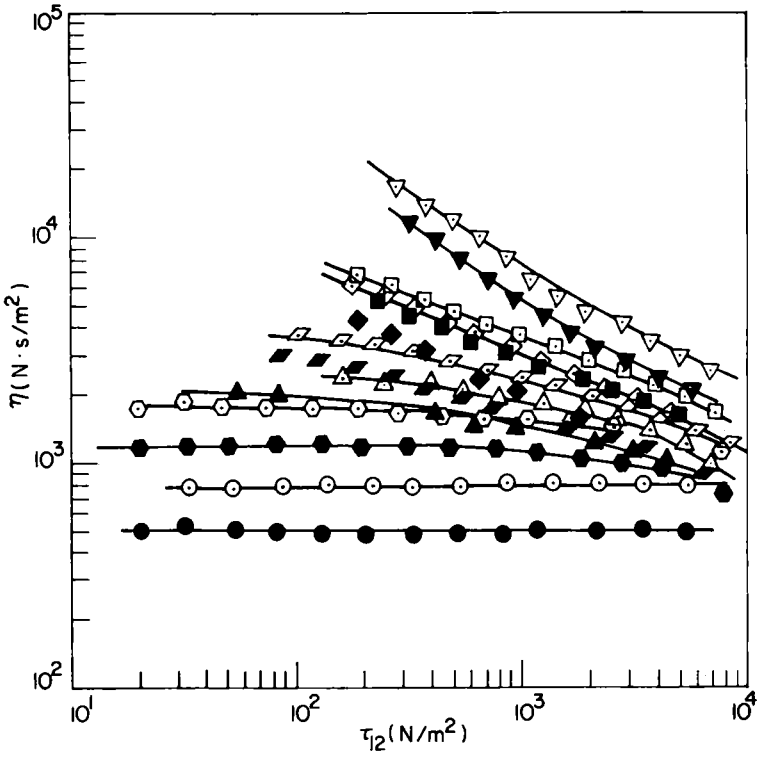

Figure 3. η vs. σ_{12} for the nylon 6/CXA 3101 blend system. Symbols are the same as in Figure 1.

(2°C/min and 10°C/min) in the DMA runs gave rise to the same results. Therefore, it is fair to conclude that possible overlaps between the T_β of nylon 6 and the T_g of CXA 3101 could not have caused the disappearance of the T_β of nylon 6.

In order to investigate the state of dispersion of the three blend systems employed, we have used both optical and scanning electron microscopies. Figure 6 shows representative SEM micrographs of the cryogenically fractured surfaces of compression-molded specimens of nylon 6/CXA 3101 blends. Phase-contrast optical microscopy enabled us to distinguish which of the two constituent components forms the discrete, and which the continuous phase, because

EBSCOhost - printed on 2/13/2023 3:45 AM via . All use subject to https://www.ebsco.com/terms-of-use

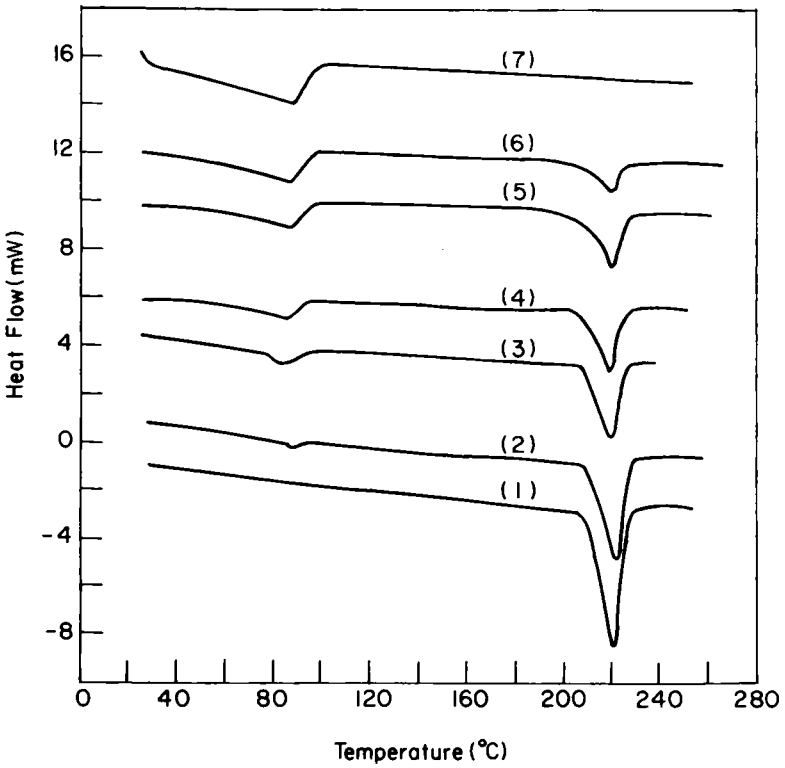

Figure 4. DSC thermograms of the nylon 6/CXA 3101 blend system: (1) nylon 6; (2) nylon/CXA=80/20; (3) nylon/CXA= 60/40; (4) nylon/CXA=50/50; (5) nylon/CXA=40/60; (6) nylon/CXA=20/80; (7) CXA 3101.

SEM was not effective for this purpose. The results of phase-contrast optical microscopy have given us the indication that, in the CXA-rich blends, nylon 6 forms the discrete phase dispersed in the continuous CXA 3101 phase, and that, in the nylon-rich blends, CXA 3101 forms the discrete phase dispersed in the continuous nylon phase. In other words, the blend ratio appears to have played a predominant role in determining which of the two components forms the discrete and which the continuous phase.

It is seen in Figure 6 that the domain size of the discrete phase is rather small (less than 1 μm on the average) and is uniformly

EBSCOhost - printed on 2/13/2023 3:45 AM via . All use subject to https://www.ebsco.com/terms-of-use

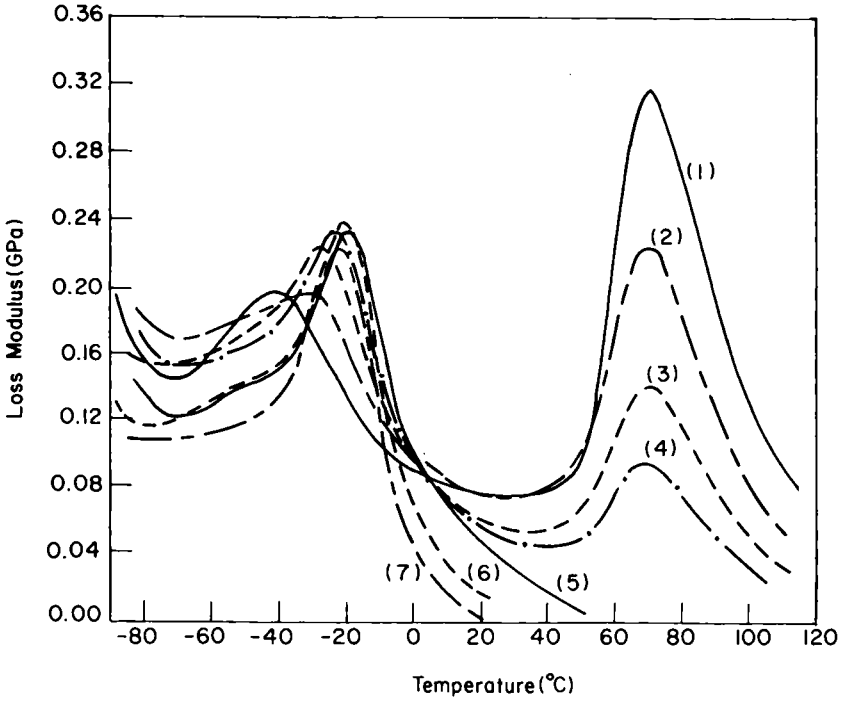

Figure 5. Loss modulus vs. temperature for the nylon 6/CXA 3101 blend system: (1) nylon 6; (2) nylon/CXA =80/20; (3) nylon/CXA=60/40; (4) nylon/CXA=50/50; (5) nylon/CXA=40/60; (6) nylon/CXA=20/80; (7) CXA 3101.

dispersed in the continuous matrix. Moreover, the discrete phase appears to have been anchored onto the continuous matrix. The fracture surface does not show sharp edges, indicating clearly that, during melt blending, chemical reactions have taken place between carboxyl or anhydride groups present in the CXA 3101 and amino end groups of nylon 6.

Figure 7 shows representative SEM micrographs of the cryogenically fractured surfaces of compression-molded specimens of nylon 6/EVA blends. It is seen that the sizes of the dispersed parti-

EBSCOhost - printed on 2/13/2023 3:45 AM via . All use subject to https://www.ebsco.com/terms-of-use

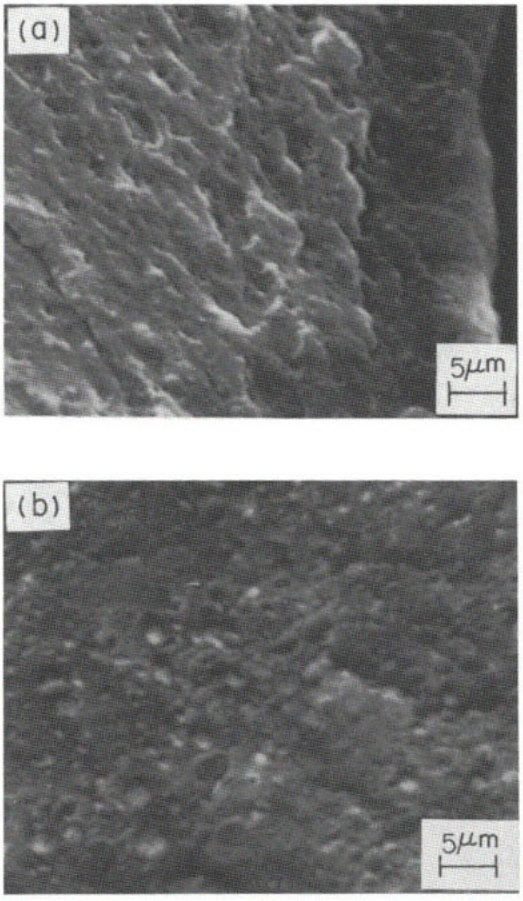

Figure 6. SEM micrographs of the cryogenically fractured surface of the nylon 6/CXA 3101 blend system: (a) nylon/CXA=20/80; (b) nylon/CXA=60/40.

cles (i.e., EVA particles in the nylon-rich blends, and nylon particles in the EVA-rich blends) are fairly large compared to those in the nylon 6/CXA 3101 blends (see Figure 6). It is also seen that, upon fracture, the particles were pulled off clean from the continuous phase, showing no evidence that any chemical reaction took place between nylon 6 and EVA.

EBSCOhost - printed on 2/13/2023 3:45 AM via . All use subject to https://www.ebsco.com/terms-of-use

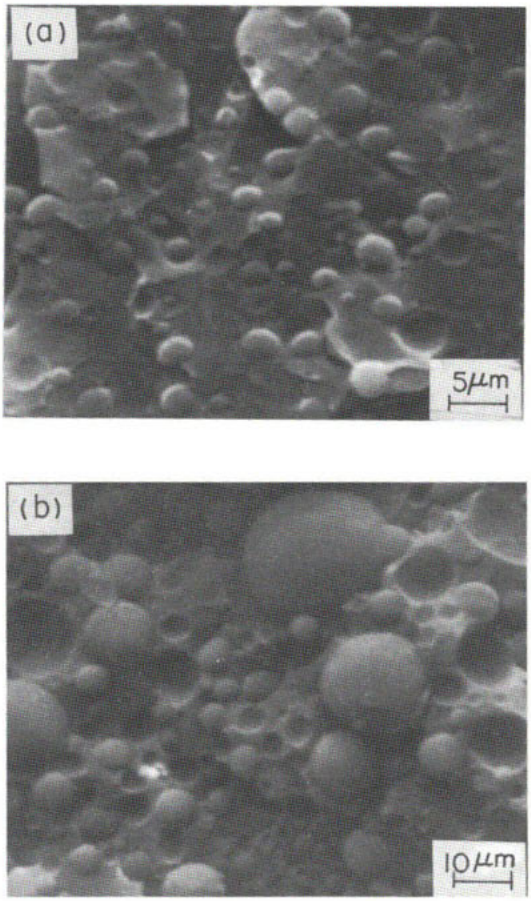

Figure 7. SEM micrographs of the cryogenically fractured surface of the nylon 6/EVA blend system: (a) nylon/EVA=20/80; (b) nylon/EVA=60/40.

The elongation at break for the nylon 6/CXA 3101 blends is given in Figure 8 as a function of blend composition. It is seen that in the nylon-rich blends containing 50 wt% and 60 wt% of nylon 6, respectively, the elongation at break of the nylon 6/CXA 3101

EBSCOhost - printed on 2/13/2023 3:45 AM via . All use subject to https://www.ebsco.com/terms-of-use

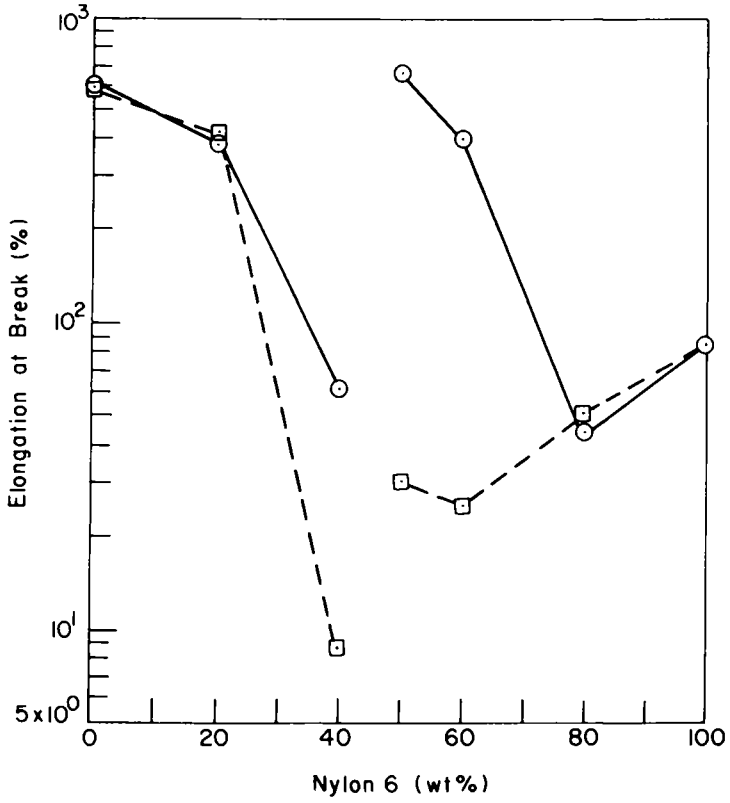

Figure 8. Percent elongation vs. blend composition for: (⊙) nylon 6/CXA 3101 blend system; (⊡) nylon 6/EVA blend system.

blend system is much greater than the elongation at break of the nylon 6 homopolymer, which forms the continuous phase. This phenomenon may be attributable to the existence of an interacting (i.e., overlapping) stress field between the neighboring particles, which can promote yielding and subsequently give rise to necking and cold drawing of the matrix phase. This synergism in ductility, which is uncommon in heterogeneous polymer blends, was also

EBSCOhost - printed on 2/13/2023 3:45 AM via . All use subject to https://www.ebsco.com/terms-of-use

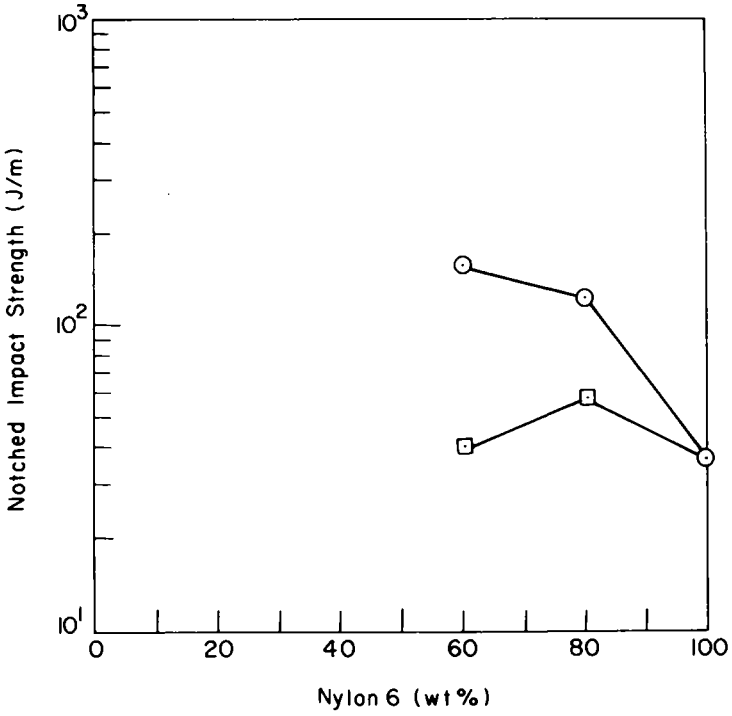

Figure 9. Izod impact strength vs. blend composition for: (⊙) nylon 6/CXA 3101 blend system; (⊡) nylon 6/EVA blend system.

observed in nylon/ionomer blends (23). The reason for this synergism is not well understood yet. However, it might have originated from the following factors: (1) interfacial adhesion between the discrete and continuous phases; (2) the matrix yielding induced by the inclusion; (3) the necking and cold-drawing mechanism of the nylon matrix. Note that when little adhesion

EBSCOhost - printed on 2/13/2023 3:45 AM via . All use subject to https://www.ebsco.com/terms-of-use

exists between the constituent components, the interfacial adhesion fails before the matrix phase yields.

The notched Izod impact strength of the blend systems investigated are plotted against the blend composition in Figure 9. It is seen that the impact strength of the nylon 6/CXA 3101 blends increases as the amount of CXA 3101 increases from 20 wt% to 40 wt%, whereas the opposite trend is observed with the nylon 6/EVA blends.

SEM micrographs of the Izod impact fracture surface of the blend systems investigated were obtained. We have found that, similarly to the SEM micrographs of the tensile fracture surface shown in Figures 6 and 7, the domain size of the EVA particles in the nylon 6/EVA blends is very large, compared to that in the nylon 6/CXA 3101 blends, and that the CXA 3101 particles in the nylon 6/CXA 3101 blends appear to have been covered by a layer of the graft copolymer formed by chemical reactions between the carboxyl or anhydride groups present in the CXA 3101 and the amino end groups of the nylon 6.

In the past, various theories have been proposed to explain the toughening of brittle polymer with rubber inclusions (24-26). They are: (1) rubber energy absorption; (2) crack branching induced by rubber particles; (3) energy absorption by yielding of the matrix and the ductility induced by strain dilation near the rubber inclusions; (4) matrix yielding. Depending on the material dealt with, each of the above toughening mechanisms may make a different contribution to the rubber-toughening effect.

Concluding Remarks

It has been demonstrated above that blends of nylon 6 and CXA 3101 containing functional groups give rise to unique rheological beha-

EBSCOhost - printed on 2/13/2023 3:45 AM via . All use subject to https://www.ebsco.com/terms-of-use

vior. The SEM micrographs of the cryogenically fractured surfaces of compression-molded specimens indicate that compatibilizing effects exist at the interface between the discrete and continuous phases in nylon 6/CXA 3101 blends. The domain size of the discrete phase in the nylon 6/CXA 3101 blends was found to be much smaller than that in the nylon 6/EVA blends. Phase-contrast optical microscopy has shown that blend ratio played a predominant role in determining which of the two constituent components forms the dispersed and which the continuous phase.

The unique rheological behavior and morphogical state observed in the nylon 6/CXA 3101 blends are attributable to the chemical reactions that have taken place, during melt blending, between carboxylic or anhydride groups in CXA 3101 and amino end groups of nylon 6.

The chemical reactions that have taken place between carboxyl or anhydride groups present in CXA 3101 and amino end groups of nylon 6 have enabled us to explain the complex thermal and thermomechanical behavior observed in DSC and DMA runs, namely (1) the shifting of T_g of CXA 3101 toward a lower value and (2) the disappearance of T_β of nylon 6 in nylon 6/CXA 3101 blends.

References

1. Minoura, Y., M. Ueda, S. Mizunuma, M. Oba. 1969. J. Appl. Polym. Sci., 13, 1625.

2. Ide, F., A. Hasegawa. 1974. J. Appl. Polym. Sci., 18, 963.

3. Narita, M., M. Akiyama, M. Okawara. 1967. Kogyo Kagaku Zashi, 70, 1432

4. Braun, D., U. Eisenlohr. 1975. Kunststoffe, 65, 139.

5. Shida, M., J. Machonis, S. Schmukler, R.J. Zeitlin. 1978. U.S. Patent 4,087,588.

EBSCOhost - printed on 2/13/2023 3:45 AM via . All use subject to https://www.ebsco.com/terms-of-use

6. Tanny, S.R., P.S. Blatz. 1980. U.S. Patent 4,230,830.

7. Illing, G. 1980. In: Polymer Blends: Processing, Morphology and Properties (E. Martuscelli, R. Palumbo and M. Kryszewski, eds.). Plenum press, New York. p. 167.

8. Gaylord, N.G., M. Mehta.1982. J. Polym. Sci., Polym. Lett. Ed. 20, 481.

9. Bruin, P., T.R. Rix. 1965. U.S. Patent 3,179,716.

10. Cimmino, S., L. D'Orazio, R. Greco, G. Maglio, M. Malinconico, C. Mancarella, E. Martuscelli, R. Palumbo, G. Ragosta. 1984. Polym. Eng. Sci., 24, 48.

11. DeVito, G., N. Lanzetta, M. Maglio, M. Malinconico, P. Musto, R. Palumbo. 1984. J. Polym. Sci., Polym. Chem. Ed., 22, 1335.

12. Han, C.D. 1976. Rheology in Polymer Processing. Academic Press, New York.

13. Han, C.D. 1981. Multiphase Flow in Polymer Processing, Academic Press, New York.

14. Han, C.D. 1975. J. Appl. Polym. Sci., 19, 1875.

15. Han, C.D., Y. J. Kim. 1975. Trans. Soc. Rheol., 19, 245.

16. Han, C.D., C.A. Villamizar. 1978. J. Appl. Polym. Sci., 24, 1677.

17. Han, C.D., D.A. Rao. 1979. J. Appl. Polym. Sci., 24, 225.

18. Han, C.D., K.W. Lem. 1982. Polym. Eng. Rev., 2, 135.

19. Han, C.D., Y.J. Kim, H.K. Chuang. 1983. Polym. Eng. Rev.,3, 1.

20. Han, C.D., Y.J. Kim, H.K. Chuang, T.H. Kwack. 1983. J. Appl. Polym. Sci., 28, 3435.

21. Chuang, H.K., C.D. Han. 1984. J. Appl. Polym. Sci., 29, 2205

22. Kawagushi, T. 1959. J. Appl. Polym. Sci., 2, 56.

23. Lindsey, C.R., J.W. Barlow, D.R. Paul. 1981. J. Appl. Polym. Sci., 26, 9.

24. Newman, S., S. Strella. 1965. J. Appl. Polym. Sci., 9, 2297

25. Bucknall, C.B. 1977. Toughened Plastics. Applied Science, London.

26. Wu, S. 1983. J. Polym. Sci., Polym. Phys. Ed., 21, 699.

EBSCOhost - printed on 2/13/2023 3:45 AM via . All use subject to https://www.ebsco.com/terms-of-use

ADVANCES IN INDIRECT METHODS OF POLYMER MORPHOLOGY CHARACTERIZATION

H.G. Zachmann and R. Gehrke
Institut für Technische und Makromolekulare Chemie, Universität Hamburg, Bundesstr. 45, D-2000 Hamburg 13

Introduction

Polymer morphology can be investigated directly by means of electron microscopy and polarized light microscopy (1). In addition, much information has been obtained by indirect methods like light scattering, X-ray diffraction, and birefringence. Measurements performed simultaneously employing different techniques prove very useful (2-4).

In the following, the application of small angle and wide angle X-ray scattering will be discussed. Most of the measurements were performed by using synchrotron radiation and position sensitive detectors. These techniques open up new possibilities (5) not only because one can obtain a scattering diagram within a few seconds and is thus able to follow rapid changes in morphology, but also because they make it feasible to measure, simultaneously the time dependence of the wide angle and small angle scattering.

The results which will be discussed here were obtained on polyethylene terephthalate. Keller (6) has presented a very impressive theory to explain the crystal thickening in polyethylene and paraffins. One is tempted to think that this theory leads to a uniform view of the crystallization process of polymers in general. However, the results on polyethylene terephthalate seem to indicate the existence of some additional effects, not present in polyethylene, which, in some other polymers, may determine predominantly the crystal growth.

It must be admitted that, with polyethylene terephthalate in contrast to polyethylene (6), there exist no measurements on well defined oligomers, none after selfseeding and none on single cry-

Morphology of Polymers
© 1986 Walter de Gruyter & Co., Berlin · New York - Printed in Germany.

EBSCOhost - printed on 2/13/2023 3:45 AM via . All use subject to https://www.ebsco.com/terms-of-use

stals grown from solution. Therefore, it is not so easy to find effects like doubling of the crystal thickness as discussed for polyethylene (6). However, in the experiments on polyethylene terephthalate performed up to now no indication of such an effect even exists. On the contrary, as we have shown many years ago (7) and as has been confirmed since (8), a decrease in the long period takes place with crystallization time. Some other effects can also be observed which reveal interesting insights into morphology changes during heat treatment.

Isothermal Crystallization

Unoriented material. Fig. 1 shows the small angle scattering of polyethylene terephthalate after different times of crystallization at 125°C. After 1.40 and 1.77 min a decrease in the scattering intensity with increasing angle without any peak is observed. After longer times, a peak appears which shifts with increasing time to larger angles.

For the further evaluation we have to consider the crystallization process more closely. During crystallization, spherulites are growing from some centers until they fill the total volume of the sample. Each spherulite consists of crystalline and noncrystalline regions. Therefore, during the period of spherulitic growth, as shown on the left side of Fig. 2, there exist three different kinds of regions (9). The crystals, the noncrystalline regions within the spherulites consisting of loops, tie-molecules and chain ends, and the amorphous regions between the spherulites

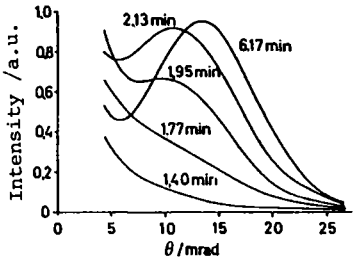

Fig. 1. Small angle X-ray scattering curves of polyethylene terephthalate after different times of isothermal crystallization from the melt at 125°C (8).

EBSCOhost - printed on 2/13/2023 3:45 AM via . All use subject to https://www.ebsco.com/terms-of-use

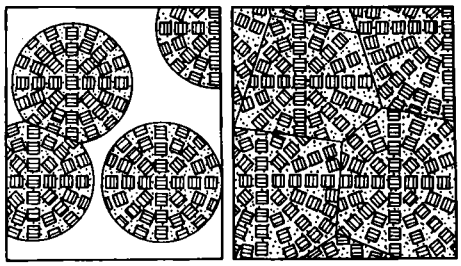

Fig. 2. Schematic representation of the morphology in spherulitic crystallized materials during crystallization (left side) and at the end (right side) ▤ crystals, ▨ noncrystalline regions within spherulites, □ completely amorphous regions.

containing complete molecules. At the end of the crystallization process (right side of Fig. 2) the amorphous regions between the spherulites have disappeared and therefore only two different kinds of regions remain. We designate the weight fraction of crystals within the spherulites by w_{cs}.

This quantity is identical with the degree of crystallinity obtained after the sample is completely filled with spherulites. The volume fraction of spherulites shall be designated by x_s. This quantity increases from 0 to 1 during the crystallization process considered in Fig. 2.

An important quantity that can be evaluated from small angle X-ray scattering is the scattering power Q which is given by the intensity of the small angle scattering integrated over all angles. For this quantity the following relation is valid:

$$Q = CV\, x_s\, w_{cs}\, (1-w_{cs})(\rho_c - \rho_a)^2 \qquad (1)$$

ρ_c is the density of the crystals, ρ_a that of the noncrystalline regions and V the scattering volume of the sample. C is a constant which depends on the intensity of the primary beam, and geometrical factors. If one assumes that w_{cs} and $\rho_c-\rho_a$ are constant during the main crystallization process, Q is proportional to the fraction of the spherulitic crystallized volume x_s and a change in Q reflects a change in crystallinity. Fig. 3 shows the dependence of the long period L on the crystallization time for three samples of different molecular weights. One can see that L decreases continuously with

EBSCOhost - printed on 2/13/2023 3:45 AM via . All use subject to https://www.ebsco.com/terms-of-use

time. There is no indication of an increase in the crystal thickness by a factor of 2 as observed with polyethylene (6). This decrease will be discussed in the following section on the oriented material.

In addition, the scattering power Q is plotted which, according to Eq. (1), during main crystallization, is proportional to the amount of material transformed into spherulites. One can see that the long period appears after about 25 % of the material has been transformed into spherulites. The main decrease in long period occurs during the time in which spherulitic growth takes place.

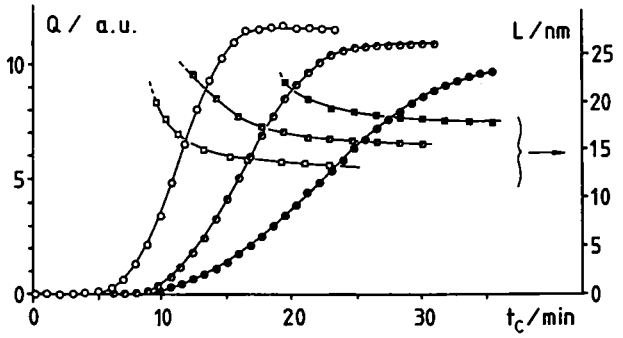

Fig. 3. Scattering power Q and long period L as a function of time t_c during crystallization from the melt at 235°C (○ □: M = 21000, ◐ ◪: M=33000, ● ■: M = 48000).

Fig. 4 shows the long period L obtained at the end of isothermal crystallization from the melt at different crystallization temperatures T_c. At each temperature the "end" of crystallization is assumed to be reached after 30 min. During this time the volume is completely filled with spherulites. One can see that the long period increases continuously with increasing crystallization temperature which is in agreement with results obtained on other polymers. In addition, the degree of crystallinity w_{cs} is plotted versus crystallization temperature. This value has been obtained from the scattering power Q by using Eq. (1). The constant C in this equation was determined by comparing the value of Q obtained for one crystallization temperature with the degree of crystallinity obtained on the same sample by wide angle X-ray scattering

EBSCOhost - printed on 2/13/2023 3:45 AM via . All use subject to https://www.ebsco.com/terms-of-use

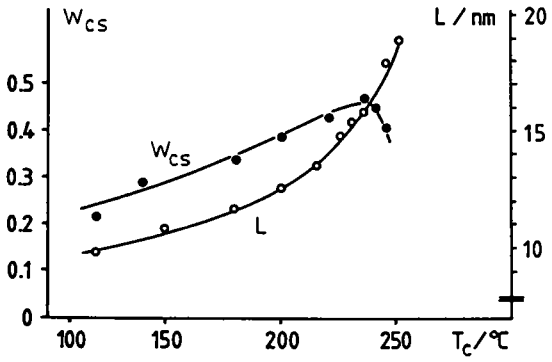

Fig. 4. Long period L and degree of crystallinity w_{cs} (from WAXS) as a function of crystallization temperature T_c after crystallization from the melt (M = 33000).

using Ruland's method (10). The change in $(\rho_c - \rho_a)$ with temperature has been taken into account with aid of measurements on samples with a constant degree of crystallinity at different temperatures (11). Up to 235°C, w_{cs} increases with increasing crystallization temperature T_c. Obviously, with higher temperature, a larger amount of material is able to crystallize due to an enhanced molecular mobility. Above 235°C a decrease in w_{cs} is observed. This is due to the well-known effect that, in a broad temperature range below the melting point, polymers are in a partially molten state (12).

From the long period L and the degree of crystallinity w_{cs} the thickness of the crystals, l_c, and that of the noncrystalline regions, l_a, were calculated using the equations

$$l_c = w_{cs} L \qquad (2)$$

and

$$l_a = (1-w_{cs}) L \qquad (3)$$

The limitations of these relations were discussed critically by Vonk and Pijpers (13). The results obtained are shown in Fig. 5. Up to 235°C, l_a is almost constant and l_c increases continuously with temperature. The increase in l_c can be explained if one assumes that l_c is determined by the thickness of the critical

EBSCOhost - printed on 2/13/2023 3:45 AM via . All use subject to https://www.ebsco.com/terms-of-use

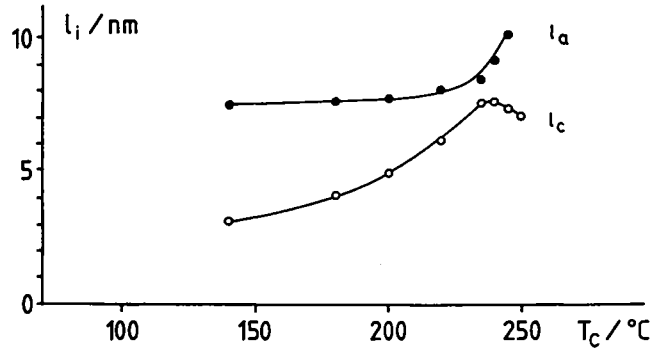

Fig. 5. Thickness of the amorphous regions (l_a) and crystalline regions (l_c) as a function of crystallization temperature T_c at the end of crystallization from the melt (M = 33000)

crystal nucleus according to the theory of Lauritzen and Hoffmann (14). l_a is obviously determined by other parameters than the temperature of crystallization (see last section).

Above 235°C, l_c decreases and l_a increases. This effect is a consequence of partial melting and can be explained in two ways:
(1) One can assume that, due to entropy effects, each crystal lamella melts gradually with increasing temperature starting from the surfaces (15,16). In this case the lengths of the chain loops hanging out of the crystals increase while the crystals become thinner.
However, it is difficult to understand why the entropy effects do not only increase l_a but do also decrease l_c whose value should only be determined by the critical nucleus.

(2) One can assume that in the partially molten state "amorphous islands" exist (17) which do not contribute to the measured small angle scattering. In this case, the application of these equation is incorrect leading to l_c values that are to small.

In order to decide which explanation is the correct one further evaluations have to be performed by which the degree of crystallinity related only to the lamellar crystallized material is determined from the shape of the small angle correlation function (13, 18).

EBSCOhost - printed on 2/13/2023 3:45 AM via . All use subject to https://www.ebsco.com/terms-of-use

Oriented material. We have also used synchrotron radiation to study the change of X-ray scattering during isothermal crystallization of polyethylene terephthalate which has been previously oriented in the amorphous state. In order to obtain two-dimensional patterns, the scattering was recorded by means of a vidicon system (19).

Fig. 6 shows the long period as a function of crystallization time for different crystallization temperatures (20). As with the unoriented sample, the long period decreases with time. In Fig. 7 the corresponding change in the azimuthal half-width of the small angle peaks is shown. A remarkable decrease in this half-width with crystallization time can be observed indicating that the orientation of the surfaces of the crystal lamellae improves considerably with crystallization time. On the other hand, the azimuthal half-width of the wide angle reflections are small from the very beginning of the crystallization process and do not change with time. From this one has to conclude that, in contrast to the orientation of the lamellae surfaces, the orientation of the molecules is constant.

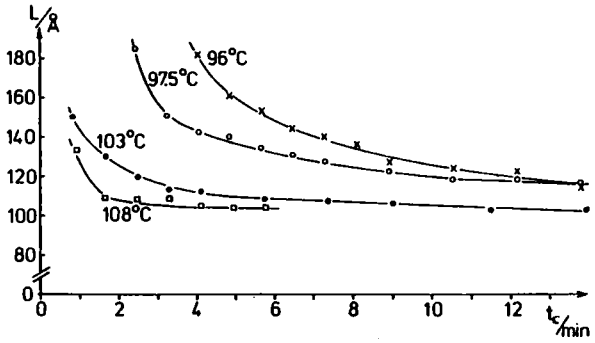

Fig. 6. Long period L as a function of crystallization time t_c of samples previously oriented in the amorphous state ($\Delta n_o = 19 \times 10^{-3}$). Parameter: Crystallization temperature T_c (20).

These results, including the decrease in the long period can be explained in the following way: Immediately after they are formed, the crystal lamellae are bent as indicated in Fig. 8 above.

Later on, by shifting of the chains parallel to each other, the lamellae become flat as indicated in Fig. 8 below. By this process

EBSCOhost - printed on 2/13/2023 3:45 AM via . All use subject to https://www.ebsco.com/terms-of-use

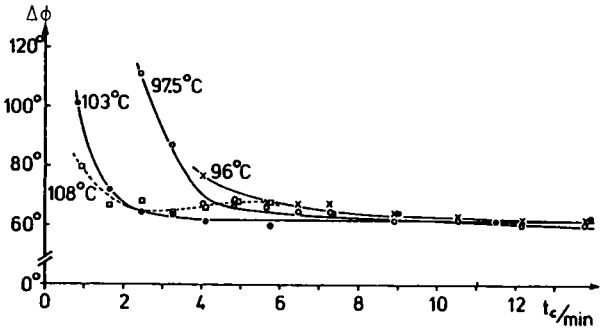

Fig. 7. Azimuthal half-width $\Delta\phi$ of the small angle maximum as a function of crystallization time t_c of the samples described in Fig. 6 (20).

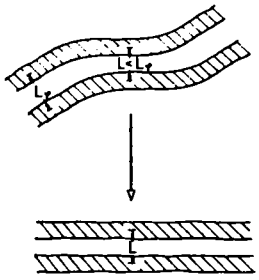

Fig. 8. Change of the shape of crystal lamellae during crystallization (20).

the orientation of the surfaces of the lamella is improved considerably while that of the chains remains unchanged. As an additional consequence, the long period decreases provided that the angle between crystal surface and chains is decreased by the shifting. This process is also connected with a decrease in the roughness of the surface.

Electron microscopy investigations indicate (21,22) that, during crystallization of polyethylene, new thinner crystal lamellae may grow in the noncrystalline regions between lamellae which already exist. How would such a process, if it occurred, change the small angle X-ray scattering? If the new lamellae grow at places distributed statistically, the diffuse scattering would increase and the position of the peak would remain unchanged. If one new lamella growth in-between every two neighbouring lamellae in a regular

EBSCOhost - printed on 2/13/2023 3:45 AM via . All use subject to https://www.ebsco.com/terms-of-use

manner, then a new peak corresponding to a long period exactly half as large as the old one should appear. A gradual shift of the long period as observed in Figs. 3 and 6 would result only in the case of a very broad distribution of long periods under special kinetic conditions which seem to be quite improbable.

Change in the Densities of Crystals and the Non-crystalline Regions

An important question is the following: Is the change in Q during isothermal crystallization only caused by the increase in the volume fraction filled with spherulites, X_s, or is it also affected by a change of the density difference $\rho_c - \rho_a$ in Eq. (1)? According to some authors (23, 24), with highly oriented polypropylene and polyethylene terephthalate, crystallization manifests itself mainly by an increase in $\rho_c - \rho_a$, caused by a process which could be called "spinodal decomposition of crystal defects". Though it cannot be assumed that this is also true for unoriented material, a small change in $\rho_c - \rho_a$ may occur in addition to spherulitic growth.

In order to determine any changes in $\rho_c - \rho_a$ during isothermal crystallization simultaneous measurements of wide angle and small angle X-ray scattering were performed by means of synchrotron radiation. The wide angle scattering was detected by photographic film, the small angle scattering passed through a hole in the center of the film and was registered by a position sensitive detector (25). The film was changed every 2 min. From the wide angle scattering the degree of crystallinity w_c was evaluated by using Ruland's method (10). By dividing w_c by w_{cs}, the degree of crystallinity obtained at the end of crystallization, the volume fraction of spherulites, x_s, was calculated. From the small angle scattering the scattering power Q was determined and divided by the value of this quantity at the end of crystallization, Q_e. Then Q/Q_e was plotted in the same diagram as w_c/w_{cs}. If $\rho_c - \rho_a$ is constant during the crystallization process, according to Eq. (1) the two plots should result in the same curve.

Fig. 9 shows the results. One can see that the increase in the two quantities with crystallization time is identical within the error of the experiment. Therefore, one has to conclude that $\rho_c - \rho_a$ is

EBSCOhost - printed on 2/13/2023 3:45 AM via . All use subject to https://www.ebsco.com/terms-of-use

constant during the crystallization.

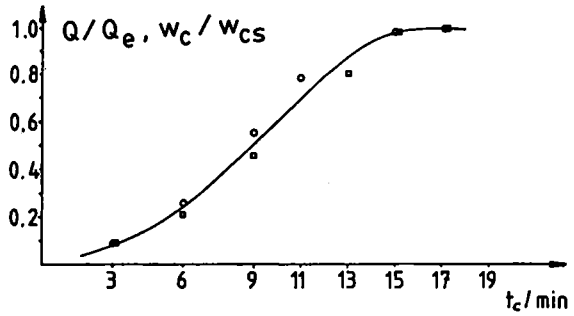

Fig. 9 . Relative scattering power Q/Q_e (o) and fraction of spherulitic crystallized material w_c/w_{cs} (□) as a function of crystallization time t_c during isothermal crystallization from the glass at 117°C.

In a previous investigation (11) it has been found that the constant k which, in applying Ruland's method, is a measure of the amount of crystal lattice distortions decreases during isothermal crystallization with crystallization time (see Fig. 10). This re-

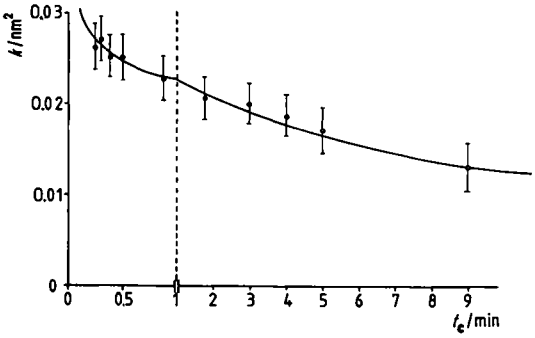

Fig. 10. Ruland's lattice distortion parameter k as a function of crystallization time t_c during isothermal crystallization from the glass at 206°C (10).

sult was obtained at a considerable larger crystallization temperature, namely 206°C than that in the present study. If one assumed that a corresponding decrease in the value of k takes place at lower crystallization temperatures, one would have to conclude that the decrease of lattice distortions does not affect the density of the crystals to an extent large enough to change the scattering power Q considerably.

EBSCOhost - printed on 2/13/2023 3:45 AM via . All use subject to https://www.ebsco.com/terms-of-use

Hashimoto et al. (26) have performed measurements of wide angle and small angle X-ray scattering during isothermal crystallization of crosslinked polybutadiene. In this case, the scattering power Q increased faster than the degree of crystallinity w_c measured by wide angle X-ray scattering. Though the measurements with the two methods were not performed simultaneously the effect seems to be real as, according to the authors, it was reproducible and the difference in the rates was quite large. Obviously, in the case of crosslinked polybutadiene, first regions of different densities are formed before any considerable crystal ordering takes place.

Melting and Recrystallization after Stepwise Heating

It is well known that the long period of polymers increases if the polymer is annealed at a temperature T_a that is higher than that at which it was crystallized, T_c. This effect is usually explained by an increase in crystal thickness which, in principle, can take place in two different way:

1. The crystal lamellae may melt completely and then crystallize again with larger thicknesses.
2. The thickness of the lamellae may increase by longitudinal diffusion of the chains without melting (27).

More detailed information on the crystal thickening process is obtained by measuring the change in the small angle X-ray scattering during annealing.

Polyethylene terephthalate, previously crystallized at 120°C from the amorphous state, was shot into an oven that was placed directly in the synchrotron radiation beam line and was already heated up to 250°C. During annealing at this temperature small angle scattering curves were registered within successive time intervalls of 20 s. The results are shown in Fig. 11, the parameter being the annealing time t_a corresponding to each curve. The scattering maximum, present at the beginning (t_a = 0 s) shifts rapidly to lower angles while the sample reaches its equilibrium temperature. After this temperature is reached, the maximum disappears completely (t_a = 120 s) and then a new peak is formed at smaller angles. From this it is evident, that the previously formed crystals melt completely before thicker crystals grow. Similar re-

EBSCOhost - printed on 2/13/2023 3:45 AM via . All use subject to https://www.ebsco.com/terms-of-use

sults were obtained by Grubb et al. (28) on polyethylene.

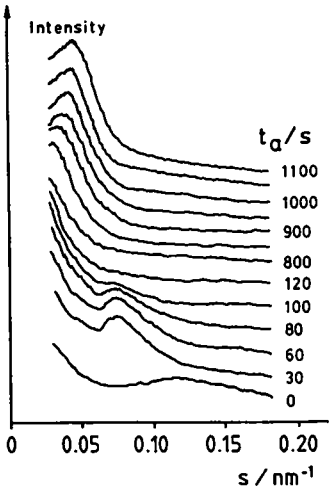

Fig. 11. Small angle X-ray scattering patterns of a sample (M = 33000) previously crystallized at 120°C during annealing at 250°C. Parameter: Annealing time t_a.

A different behaviour is observed if the annealing takes place at 240°C. This is illustrated in Fig. 12 for T_a = 235°C. Here the maximum does not disappear. It gradually moves to smaller angles.

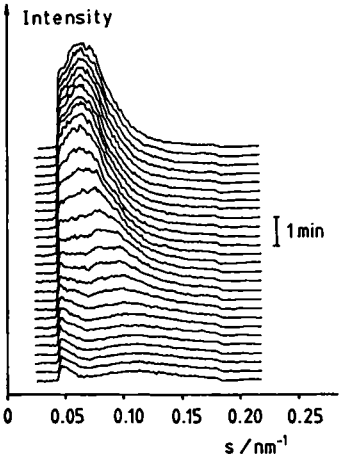

Fig. 12. Small angle X-ray scattering patterns of a sample (M = 33000) previously crystallized at 120°C during annealing at 235°C. Parameter: Annealing time t_a.

EBSCOhost - printed on 2/13/2023 3:45 AM via . All use subject to https://www.ebsco.com/terms-of-use

It is possible to explain this result by a gradual thickening of the crystals caused by longitudinal chain diffusion without melting. On the other hand, the result also agrees with the assumption of complete melting and recrystallization: Generally a broad peak may be a superposition of two peaks at different angles. A shift of the resulting peak to smaller angles can then be explained by an increase of the peak at the smaller angle accompanied by a decrease of that at the larger angle. Therefore, the question of the mechanism of recrystallization at lower temperatures is still open. More information on this mechanism is obtained from the kinetic measurements described in the following.

In a further evaluation of our results, we have determined the scattering power Q and, from this quantity, by means of Eq. (1), the degree of crystallinity w_{cs}.

Fig. 13 shows w_{cs} as a function of annealing time t_a for two different annealing temperatures T_a and for samples of different molecular weights. At 250°C, a large decrease in w_{cs} is observed before recrystallization occurs. This is not the case at 235°C.

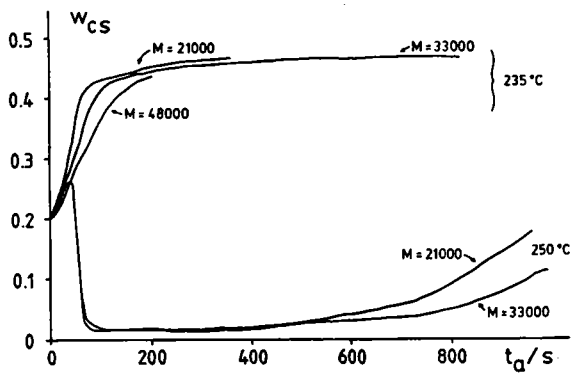

Fig. 13. Degree of crystallinity w_{cs} as a function of annealing time t_a of a sample previously crystallized at 120°C. Parameters: Molecular weight M and annealing temperature T_a.

At both temperatures however the rate of recrystallization depends considerably on the molecular weight as was observed with crystallization from the completely molten state (29). This seems to

EBSCOhost - printed on 2/13/2023 3:45 AM via . All use subject to https://www.ebsco.com/terms-of-use

favour the conclusion that, at 235°C, complete melting occurs as at 250°C.

From the degree of crystallization and the long period, both determined at the end of the recrystallization process, the thickness of the crystals, l_c, and that of the noncrystalline regions, l_a, was calculated. The results are shown in Fig. 14. At intermediate

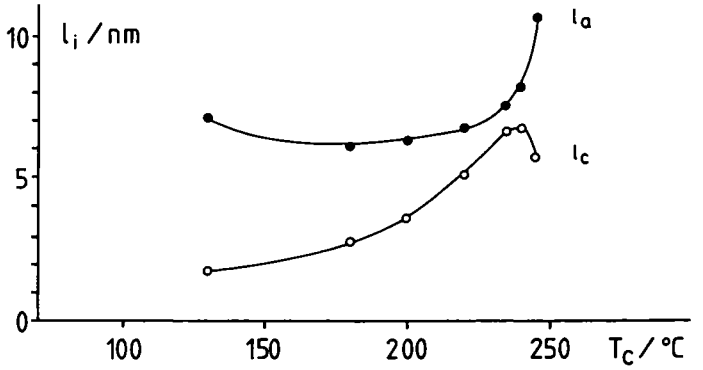

Fig. 14. Thickness of the amorphous regions (l_a) and crystalline regions (l_c) as a function of annealing temperature T_a. Annealing time: 30 min. Samples were crystallized previously at T_c = 120°C.

temperatures, l_a is smaller than in the case of isothermal crystallization from the melt (see Fig. 5). Generally, by recrystallization of samples previously crystallized at a lower temperature, smaller values for the long period and larger values for the degree of crystallinity are obtained than after isothermal crystallization from the melt at the same temperature as that of recrystallization. A better understanding of this phenomena is obtained by studying the change in the small angle scattering during continuous heating using different heating rates.

Melting and Recrystallization During Continuous Heating

Amorphous samples were inserted into the oven mounted in the synchrotron beam line. While the temperature was raised with constant rate, the small angle scattering was determined as a function of temperature. From the scattering patterns obtained, the long period, the scattering power, the degree of crystallinity, and the thickness of the crystalline and noncrystalline regions

EBSCOhost - printed on 2/13/2023 3:45 AM via . All use subject to https://www.ebsco.com/terms-of-use

were determined in the same way as above.

Fig. 15 shows the long period as a function of the temperature for different heating rates. If the sample is heated slowly (3°C/min) the long period remains constant up to 240°C and then a steep increase is observed. With larger heating rates (9°C/min and 100°C/min) an increase in the long period is already observed at lower temperatures. These results show that the "plateau" in the long period observed before by Rault and coworkers (30) occurs only if small heating rates are applied.

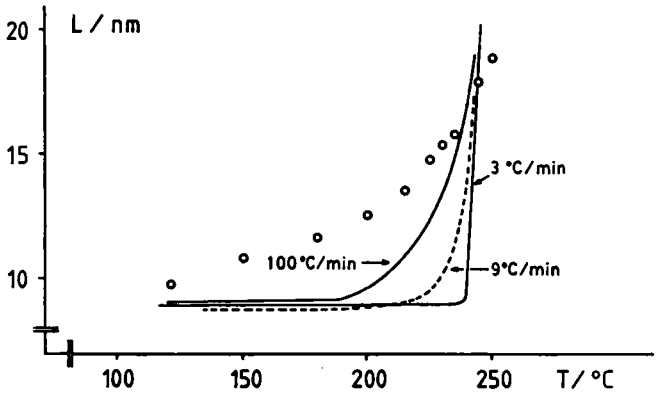

Fig. 15. Long period L as a function of temperature during heating from the amorphous state with constant rate (—, ---) and after isothermal crystallization from the melt (o). Parameter: Heating rate.

Fig. 16 shows the tickness of the crystals, l_c, and that of the noncrystalline regions, l_a. We see that for slow heating, with increasing temperature, the thickness of the crystals is increased while that of the noncrystalline regions is decreased. The long period remains the same. Therefore, we conclude that, during slow heating, the crystals grow by consuming the material in the noncrystalline regions. The necessary rearrangement of the molecules may take place simply by chain diffusion. In addition, one can think of transesterification reactions within the amorphous regions. Such chemical reactions are possible in a polymer obtained by polycondensation and have been proved to take place above the melting point within very short times (31). Besides chain diffusion and transesterification, the processes which lead to a de-

EBSCOhost - printed on 2/13/2023 3:45 AM via . All use subject to https://www.ebsco.com/terms-of-use

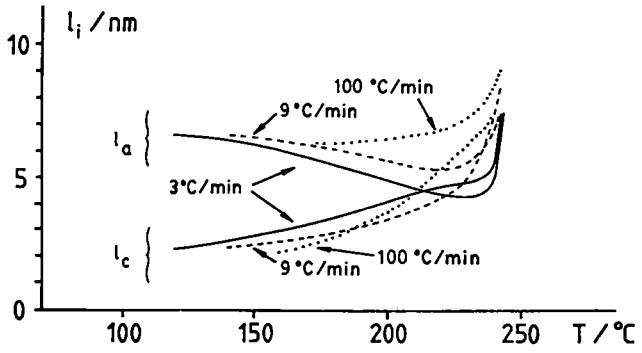

Fig. 16. Thickness of the amorphous regions (l_a) and crystalline regions (l_c) as a function of temperatures T during heating of initially amorphous samples with constant heating rates.

crease in the long period L during isothermal crystallization from the melt (see last section) may also occur during slow heating; this decrease in L may compensate for the increase due to the thickening of the crystals.

Rault et al.(30) assume that the constant long period during slow heating below 245°C reflects a constant lamellar thickness. From this they conclude, that l_c remains constant until the α-transition temperature is reached, where crystal thickening due to chain diffusion can occur. This interpretation is in contradiction to our findings that l_c actually increases with temperature though L remains constant.

In contrast to the results for low heating rates, for high heating rates, we observe an increase in l_c while l_a remains almost constant or increases also. As the increase in long period corresponds to the temperature dependence of the long period obtained after isothermal crystallization from the melt, we assume that, with rapid heating, a continuous process of complete melting of lamellae followed by recrystallization takes place.

In conclusion we see the following: If polyethylene terephthalate is heated above the temperature at which it was originally crystallized, the crystal lamellae become thermally more stable by thickening. Besides melting and recrystallization, other processes

EBSCOhost - printed on 2/13/2023 3:45 AM via . All use subject to https://www.ebsco.com/terms-of-use

like chain diffusion and transesterification seem to be involved in crystal thickening. Melting and recrystallization occurs only if heating proceeds so quickly that there is not enough time for these processes to make the crystals thicker.

Influence of Molecular Weight on the Long Period and the Crystal Thickness

Rault et al. (30) have shown that, after crystallization from the melt at a constant temperature, the long period obtained is proportional to the square root of the molecular weight M, while the crystal thickness l_c does not depend on M. We have performed further studies of these phenomena by applying different crystallization temperatures T_c. Fig. 17 shows the long period L obtained at the end of the isothermal crystallization as a function of the square root of the molecular weight M. The crystallization temperature T_c is written at each curve. One can see that a linear relation bet-

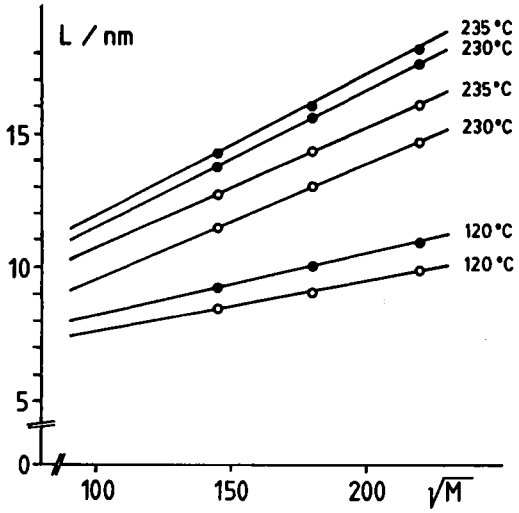

Fig. 17. Long period L of Polyethylene terephthalate as a function of the square root of molecular weight M. o: after crystallization from the melt, o: after recrystallization (T_c = 120°C).

ween L and $\sqrt{M}$ is confirmed for all crystallization temperatures. Fig. 18 shows the thickness of the crystals, l_c, and that of the non-crystalline regions, l_a, as a function of $\sqrt{M}$. Obviously, the crystal

EBSCOhost - printed on 2/13/2023 3:45 AM via . All use subject to https://www.ebsco.com/terms-of-use

thickness is constant and the increase in the long period with $\sqrt{M}$ is caused completely by an increase in the thickness of the non-crystalline regions. In addition, within the temperature range in which no partial melting takes place, l_a does not depend on the crystallization temperature (see Figs. 5,14).

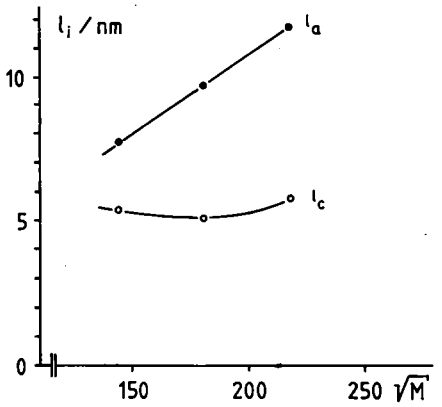

Fig. 18. Thickness of the amorphous regions (l_a) and crystalline regions (l_c) of samples crystallized from the melt at T_c = 235°C as a function of the square root of the molecular weight M.

It can be explained easily that the crystal thickness does not depend on the molecular weight. According to the theory of Lauritzen and Hoffmann (14), the crystal thickness is determined by the dimensions of the critical crystal nucleus. These dimensions can be calculated from surface free energies end melting enthalpies which, in the temperature region considered here, are expected not to depend on M.

It is more difficult to find an explanation for the increase in l_a with M. Rault et al. (30) assumed that the long period is related to the radius of gyration of the molecules in the melt, because the crystallization of two adjacent nuclei or lamellae separated by a distance less than the unperturbed dimensions of the coil would lead to a highly stressed amorphous phase. According to this, a molecule which is incorporated partly into a crystal is not allowed to enter another crystal. Such an explanation would be in agreement with calculations of entropy changes during crystallization (32).

EBSCOhost - printed on 2/13/2023 3:45 AM via . All use subject to https://www.ebsco.com/terms-of-use

However this would imply changes in the conformations of the chains in contradiction to neutron scattering experiments which have shown that the radius of gyration does not change during crystallization. In addition, the long period would be expected not to depend on the temperature; if the crystals become thicker, the thickness of the noncrystalline regions should become smaller. Therefore, though there is no doubt that there exists a relationship between the long period and the molecular weight, the explanation of this relation is still an open question.

References

1. Thomas, E.L., this book p.

2. Hoshino, S., E. Meinecke, J. Powers, R.S. Stein, S. Newman, 1965. J. Polym.Sci. A3, 3041.

3. Biangardi, H.J., H.G. Zachmann. 1977. Progr.Colloid a. Polymer Sci. 62, 71 and 1977. J. Polymer Sci.Polym.Symp. 58, 169.

4. Koberstein, J.T., T.P. Russell.1985. In: Polymer Research at Synchrotron Radiation Sources (T.P. Russell, A.N. Goland, eds.) Brookhaven National Laboratory. pp. 21-26.

5. Elsner, G., C. Riekel and H.G. Zachmann. 1985. Adv.Polymer Sci. 67, 1.

6. Keller, A., this book p. 1.

7. Zachmann, H.G., G.F. Schmidt. 1962. Makromol.Chem. 52, 23.

8. Elsner, G., M.H.J. Koch, J. Bordas, H.G. Zachmann. 1981. Makromol.Chem. 182, 1263.

9. Zachmann, H.G. 1967. Faserforschung und Textiltechnik, 18, 427.

10. Gehrke, R., H.G. Zachmann. 1981. Makromol.Chem. 182, 627.

11. Gehrke, R., Dissertation 1985, University of Hamburg.

12. Zachmann, H.G., H.A. Stuart. 1961. Makromol.Chem. 44-46, 622.

13. Vonk, C.G. and A.P. Pijpers. J.Polymer Sci. (Polymer Phys.Ed.) (in press).

14. Lauritzen, J.I., J.D. Hoffmann. 1969. J.Res.Natl.Bur.Standards 64 A, 79.

15. Zachmann, H.G., 1967. Kolloid-Z. u. Z.f. Polymere 216-217, 180.

16. Zachmann, H.G., A. Peterlin. 1969. J.Macromol.Sci. B3, 495.

EBSCOhost - printed on 2/13/2023 3:45 AM via . All use subject to https://www.ebsco.com/terms-of-use

17. Strobl, G.R. and E.W. Fischer, private communication.

18. Strobl, G.R. and M. Schneider. 1980. J.Polymer Sci. (Polym.Phys. Ed.) 18, 1343.

19. Prieske, W., C. Riekel, M.H.J. Koch, H.G. Zachmann. 1983. Nucl. Instr. & Methods, 208, 435.

20. Elsner, G., H.G. Zachmann. J.R. Milch, 1981. Makromol.Chem. 182, 657.

21. Kanig, G. 1982. Colloid and Polymer Sci. 260, 356.

22. Voigt-Martin, I.G. 1985. Advances in Polymer Sci. 67, 195.

23. Fischer, E.W. Report SFB 41, Mainz-Darmstadt.

24. Schultz, J.M., J.S. Lin, R.W. Hendricks, J. Petermann, R.M. Gohil, 1981. J.Polym.Sci.(Polym.Phys.Ed.) 19, 609.

25. Prieske, W., Dissertation 1984, University of Hamburg.

26. Saijo, K., A. Wasiak, S. Suehiro, H. Kawai and T. Hashimoto, Japan 1984. Preprints of the 1st SPSJ International Polymer Conference, Kyoto, p. 275.

27. Chivers, R.A., P.J. Barham, J. Martinez-Salazar, A. Keller, 1982. J.of Polym.Sci., Polym.Phys.Ed., 20, 1717.

28. Grubb, D.T., J.J.H. Lui, M. Caffrey, D.H. Bilderback. 1984. J.of Polym.Sci., Polym.Phys.Ed., 22, 367.

29. Günther, B., H.G. Zachmann. 1983. Polymer 24, 1008.

30. Rault,J.,E. Robelin and G. Perez. 1983. J.Macromol.Sci.-Phys. B22 (4), 577.

31. Gilmer, J.W., D. Wiswe, H.G. Zachmann, J. Kugler, E.W. Fischer. Proceedings of Rolduc Polymer Meeting,to be published.

32. Zachmann, H.G., New York - Copenhagen 1967. Proceedings of the IUPAC Meeting, Benjamin.

EBSCOhost - printed on 2/13/2023 3:45 AM via . All use subject to https://www.ebsco.com/terms-of-use

Crystallization Processes

EBSCOhost - printed on 2/13/2023 3:45 AM via . All use subject to https://www.ebsco.com/terms-of-use

EBSCOhost - printed on 2/13/2023 3:45 AM via . All use subject to https://www.ebsco.com/terms-of-use

RELATIONS BETWEEN THE CONFORMATION OF MACROMOLECULES AND THEIR STRUCTURAL CHARACTERISTICS

E. Turska

Institute of Polymer Chemistry, Polish Academy of Sciences
41-800 Zabrze, ul. Curie-Skłodowskiej 34, Poland

The conformation of macromolecules is a well-known and well defined physicochemical quantity. The already voluminous literature on this subject deals with problems of the methods of analyzing, determining and calculating macromolecular conformation parameters, and also with the influence of conformation exerted on the physical properties of polymers.

Nevertheless, numerous original papers and a number of pertinent review articles have preferably been concerned with parameters characterizing the conformation in terms related to the whole polymer chain. Much less attention has been paid, however, to macromolecular chain fragments corresponding to individual mers.

It is quite obvious that the two concepts should be interrelated in a certain manner, but can also be considered separately by virtue of their constituting different physicochemical quantities.

In order to avoid any ambiguity when considering these two types of conformation, the conformation of chain fragments will be termed "microconformation" in the present paper.

Since a comprehensive discussion of the available literature on conformations and microconformations would be certainly beyond the scope of this paper, only a brief outline of the main ideas and recent results on this topic (including those conducted by my research group) will be presented.

Conformation of macromolecules in dilute solution was thoroughly investigated by Flory (1) and other authors a long time ago, and may be treated today as standard textbook material. The situation is more complex when dealing with the conformation of macromolecules in a condensed state. There are distinct differences in opinion on that subject among many authors.

In earlier papers by Kargin (2), Yeh (3) and other authors a complex structure of amorphous polymers is postulated. These are as-

Morphology of Polymers
© 1986 Walter de Gruyter & Co., Berlin · New York - Printed in Germany.

EBSCOhost - printed on 2/13/2023 3:45 AM via . All use subject to https://www.ebsco.com/terms-of-use

sumed to possess groups of macromolecules with a certain degree of preliminary structural ordering and different conformation.
The more recent works, both of theoretical and experimental nature, published by Flory (4), Fisher (5), Dettenmayer (6) and others, put forward an opinion that in an amorphous polymer all macromolecules exist as random coils, characterized by a given value of the radius of gyration corresponding to specific theta point conditions.
Experimental data both supporting and, to a certain extent, contradicting the above assumption are to be found in the literature. However, in my opinion, supported also by results of experimental work, polymers capable of crystallization exist in a form that cannot be considered either partly crystalline or partly amorphous, according to the definition quoted earlier. The commonly used physical methods do not show any, even small, crystalline areas while indicating, within limits of experimental error, the presence of areas exhibiting different packing densities and certain conformational characteristics. Occurrence of those areas is generally determined by the thermal or chemical history of the given polymer.
I am of the opinion that the occurrence of the above indicated phenomena can be explained in terms of microconformation transitions.
In the case of dilute polymer solutions, Flory (7) and other authors postulated for many polymers a possibility to exist in different microconformations.
It is also a well-known fact that partly crystalline polymers have a strictly defined microconformation in the crystalline areas. Note that the microconformation of macromolecules is a quantity which, depending on conditions to which a given polymer molecule has been subjected, may exhibit changes sufficiently rapid to be regarded as transitions. It seems logical to expect those conformational transitions to influence very strongly the structural changes taking place in polymers, and therefore also their ability to crystallize.
Chala (8) in his work on the crystallization of isotactic polystyrene regards the presence of a given conformation to be an essential condition for the crystallization process to take place. Rather extensive investigations of the microconformations of poly-

EBSCOhost - printed on 2/13/2023 3:45 AM via . All use subject to https://www.ebsco.com/terms-of-use

ethylene terephthalate performed by Manley and Williams (9) indicate the existence of a relationship between the content of defined microconformations and that of the crystalline form. Mikhailov (10) also stresses the importance of conformational transition, though admittedly, from a different point of view. The works of Schneider (11), Spěváček (12) and others indicate the importance of conformational transitions in the processes of association.

There exists undoubtedly a large number of other works which are concerned to some extent with the above problem. Unfortunately, I cannot offer their systematic survey to the reader. Nevertheless, working on that problem for several years, we have accumulated some amount of experimental facts, which I shall present shortly. Taking into account all accessible data, we have arrived at certain conclusions which constitute an attempt to generalize the outcome of our experimental data.

Our ideas on the structure of non-crystalline polymers, which are however capable of crystallization, can be summarized as follows.

1. We assume Flory's concept that an amorphous polymer is composed of random macromolecular coils with dimensions corresponding to those existing in theta conditions.
2. As a result of the action of such factors as annealing, swelling, etc. on the polymer, the above state of the polymer can be disturbed, and areas with a different arrangement of macromolecules formed.
3. The effect of the above factors may be generally regarded as inducing conformational changes.
4. Polymer crystallization can occur only when the given polymer contains a sufficient number of conformations and microconformations corresponding to a crystalline structure.

We were able to confirm the above outlined concepts for some of the polymers studied by us. The first polymer studied in this connection was a polycarbonate derived from bisphenol A. Preceding our work on the same subject Dettenmayer's results, obtained by neutron diffraction measurements, which indicate the full homogeneity of the polymer sample in agreement with the views of Flory and Fischer. The non-crystalline polymer samples investigated by us showed the presence of certain inhomogeneities, i.e. areas with a different structural arrangement of macromolecules.

EBSCOhost - printed on 2/13/2023 3:45 AM via . All use subject to https://www.ebsco.com/terms-of-use

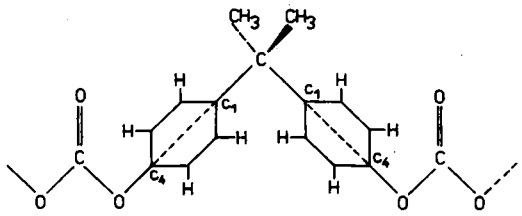

Fig. 1. Schematic representation of the polycarbonate chain.

These areas were found very small in size and rather small in number, viz., in the initial samples. However, the relative amount of such areas increased significantly on swelling, and less so on annealing.

The work with Dr Tekely (13) on the polycarbonates was based on broad line NMR investigations. The analysis of the BL-NMR spectra recorded at different temperature showed, among other things, that in the case of unswollen polymer samples there occurred a narrowing of line width at about 150°C, accompanied by a reduction in the second moment value of the line.

This fact is undoubtedly attributable to general motions characteristic of glass transition temperature. As seen from Fig.2, this phenomenon is of clearly two-stage nature. We interpreted that

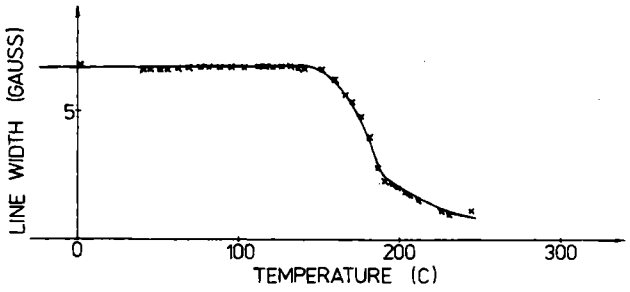

Fig. 2. Line width as a function of temperature for polycarbonate.

EBSCOhost - printed on 2/13/2023 3:45 AM via . All use subject to https://www.ebsco.com/terms-of-use

fact as being due to the inhomogeneity of amorphous polycarbonate. The first stage of line narrowing and reduction in second moment value corresponds to the temperature range of from +150°C to +180°C, and is to be attributed, in our opinion, to motions in areas with a nearly random conformation. In this case the slope is less steep than that found for the second stage determined by the temperature range between 180 and 190°C. The second stage corresponds most probably to the motions of macromolecules belonging to areas with a higher degree of structural ordering. These two stages were analyzed separately by us.

Calculating the values of the activation energy we found for the first and second stages, respectively, $E_1 = 15.3$ kcal/mol and $E_2 = 32.2$ kcal/mol; the picture of the second stage is characteristic of motions in areas with a preliminary ordering.

One cannot obviously treat such calculations as quantitatively exact, owing to large experimental errors committed due to the closeness of the two line narrowing stages. They do however furnish a qualitative picture of the observed phenomena, and indicate the heterogeneous nature of the amorphous polycarbonate studied.

As expected, in the case of swollen samples the glass transition temperature T_g decreases, and the NMR spectrum has a distinctly two-stage character as to the line width and the second moment value of the line.

It may be supposed on the basis of the data obtained, that the content of areas with a certain degree of structural ordering increases on swelling, the said increase referring rather to the number than to the size of those areas.

Further investigations, based among other things on studies of the fine structure of the NMR spectrum lines, showed that small mesophase areas were formed under certain conditions.

The relation between the motions of macromolecules and their conformation was suggested first by Hermans, and later by other authors.

Taking into account those and our data, we thought that this could explain the observed phenomena in terms of conformational changes related to the microconformations. Conformational changes leading to the formation of more ordered areas were expected to occur not only under the influence of low molecular mass liquids, but also as a result of prolonged annealing of the polycarbonate samples.

EBSCOhost - printed on 2/13/2023 3:45 AM via . All use subject to https://www.ebsco.com/terms-of-use

This duality seems to be supported by the fact that different observations and explanations were offered by various authors, and namely, that the annealing of polycarbonate even above T_g led to distinct changes in its physical properties.

In order to check the validity of our suggestion that the above phenomenon is accompanied by microconformational changes identical with those taking place on swelling, we investigated with Dr.Żmudziński the structure of the annealed polymer samples (4).

The process of thermal crystallization of polycarbonate was studied by many authors (15) who found the induction periods to be extremely long (well over a hundred hours). On the other hand, induction periods characteristic of liquid induced crystallization were observed to last, depending on conditions applied, from a few minutes to several hours, at most.

Certain changes were found to occur in the polymer on annealing, before the onset of crystallization, while using the method of X-ray diffraction patterns.

Suitably corrected X-ray patterns indicated the absence of peaks typical of the crystalline form, distinct changes in the amorphous halo being observed to occur on annealing. It may be shown readily

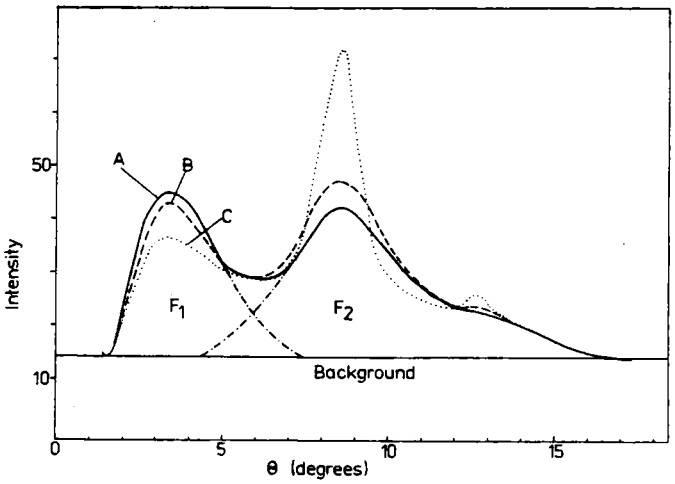

Fig. 3. X-ray diffraction patterns $I = f(\theta)$ of polycarbonate (Bistan AW). A–fused and non annealed sample; B–sample fused and annealed for 15 days; C–sample of partly crystalline polymer

EBSCOhost - printed on 2/13/2023 3:45 AM via . All use subject to https://www.ebsco.com/terms-of-use

that these changes could not be connected in any way with the possible formation of crystalline areas, but could be explained by the formation of areas with a certain non-crystalline degree of ordering.

A diffraction pattern of this type can be therefore regarded as a result of amorphous scattering due to two morphological forms, that is to a totally amorphous form and to a form close to a mesomorphic one.

Without going here into details of the analysis of the diffraction patterns obtained, the following interpretation can be given. The polymer sample contains initially areas that are completely amorphous with a portion of cis-trans microconformations, and also areas in which there is a sufficiently large number of trans-trans sequences.

The areas of the latter type are not of crystalline nature, but nevertheless exhibit a certain degree of ordering.

Flory and Williams (16) conducted a conformational analysis of polycarbonate macromolecules in solution, from which it followed that cis-cis sequences are impossible, cis-trans ones possible, but the most probable microconformation sequence in solution is the trans-trans sequence.

These data, coupled with our experimental results, enabled us to suggest that the initial polycarbonate samples may contain in condensed phase various amounts of those conformations, depending on the thermal and chemical history of the samples, and also on the method of their synthesis. The relative amount of the trans-trans

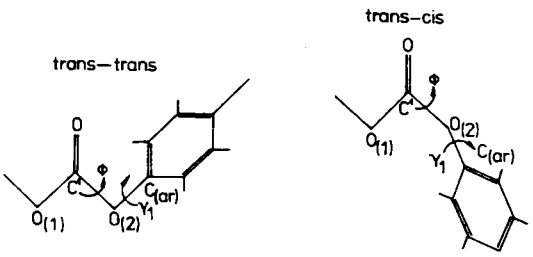

Fig. 4. Schematic representation of a portion of the polycarbonate chain with two conformations of the carbonate group

EBSCOhost - printed on 2/13/2023 3:45 AM via . All use subject to https://www.ebsco.com/terms-of-use

sequences increases under the influence of solvents in the similar way as on annealing. This process leads to the formation of areas with a more dense and more ordered packing. Crystallization can take place only when the content of the trans-trans microconformations has become sufficiently large. In order to confirm the validity of our ideas, it is obviously necessary to be able to determine quantitatively the content of different conformations. We are at the moment working (in cooperation with Dr.Schmidt, Institute of Macromolecular Chemistry, Prague) on the development of such a method based on the analysis of infrared spectra.

Poly(acrylonitrile) was the second polymer studied by us with a view to determining a relationship between conformational and structural changes. This polymer was investigated very often by various authors. There is however so far a lack of agreement as to the structural characterization of poly(acrylonitrile).

It is certain, however, that poly(acrylonitrile) is not present in a form that might be called amorphous according to Flory. In certain strictly determined conditions poly(acrylonitrile) may contain some amorphous areas. Studies conducted by members of our group, Dr. Grobelny and Mrs Sokół, indicated that conformational changes play a very significant role in the structural changes occurring in that polymer.

These investigations were done using the broad-line NMR technique for non-swollen poly(acrylonitrile) samples and also for poly(acrylonitrile) swollen in deuterated aqueous I_2/KI solution and in nitromethane (17). The X-ray studies included also those of poly (acrylonitrile) swollen in organic solvents.

The first conclusion drawn from our studies suggested the conformation of the poly(acrylonitrile) chain to be determined by the close contact of the protons of the H - C - CN groups. The proposed conformation is illustrated in Fig.5. Without going into details of the performed analytical determinations and calculations it can be said that the above conclusion is well supported by the analysis of the rather complex shape of the spectral lines recorded.

The quite good agreement between the found and calculated values of the second moment, and the results of the analysis of the BL-NMR spectrum of deuterated poly(acrylonitrile) would seem to suggest that the proposed model is correct.

EBSCOhost - printed on 2/13/2023 3:45 AM via . All use subject to https://www.ebsco.com/terms-of-use

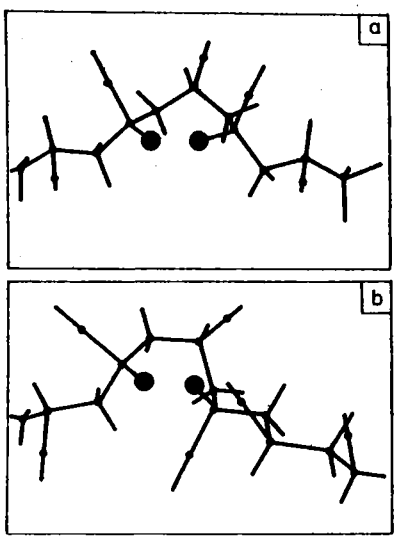

Fig. 5. Proposed conformation of (a) iso- and (b) heterotactic sequences of polyacrylonitrile

As the degree of swelling of the polymer increased, distinct changes of the BL-NMR spectrum were to be observed. These may be explained by conformational changes of the PAN that take place in the first stage of the swelling process proceeding at lower concentrations.

At the end of the first stage of swelling, the conformation of the polymer undergoes a distinct change.

The abrupt increase in the degree of swelling with the increase in iodine concentration may be regarded as a confirmation of that suggestion, which was also confirmed by results of additional IR analysis.

We therefore assumed that significant conformational changes could take place, under strictly defined swelling conditions, both in microconformations and in the conformation of the whole polymer chain, which indicates a decrease in the number of the neighbouring protons and is, hence, accompanied by a conformational transition from the rigid helix conformation to that more resembling the flexible coil.

EBSCOhost - printed on 2/13/2023 3:45 AM via . All use subject to https://www.ebsco.com/terms-of-use

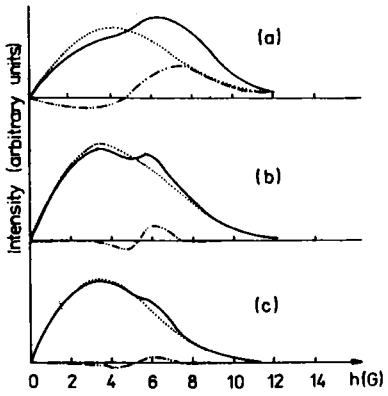

Fig. 6. Shapes of ^1H BL-NMR lines (one half shown) of PAN films of different equilibrium swelling degrees S, taken at room temperature (— · · —) Component of two-proton system with Gausian broadening; (·····) normalized Gausian component;
(a) S = 30 wt %; (b) S=300 wt %; (c) S = 400 wt %

A conformational transition of that kind should produce observable structural changes. X-ray investigations conducted by us using the WAXS technique confirmed that assumption (18). The X-ray patterns of unswollen poly(acrylonitrile) and those of poly(acrylonitrile) swollen in different swelling agents showed that, under certain specific conditions, a splitting of the recorded peaks was to be observed, which is in turn indicative of the formation of areas with a fairly high degree of structural ordering.
Depending on temperature and the swelling medium used, the structural ordering attained can either persist or disappear after drying the poly(acrylonitrile) sample. Poly(acrylonitrile) is known to be difficult to investigate and whose structure is rather complex and different from that of other polymers.
Consequently, our results are to be viewed at this stage as a contribution shedding some light on the problem of the existence of a relationship between conformational transitions and the supermolecular structure of poly(acrylonitrile). A complete elucidation of that complex question clearly necessitates further studies.

EBSCOhost - printed on 2/13/2023 3:45 AM via . All use subject to https://www.ebsco.com/terms-of-use

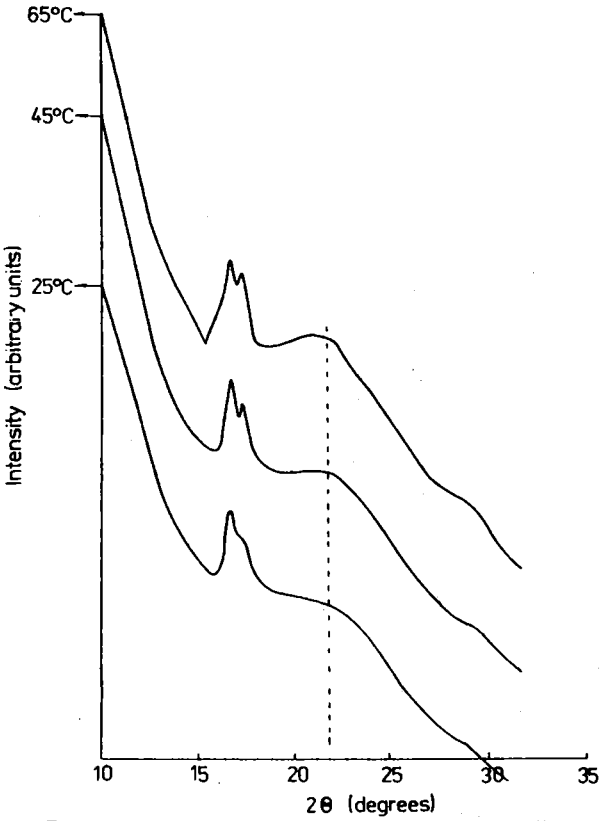

Fig. 7. Wide-angle X-ray diffraction traces of the PAN samples swollen in nitromethane at different temperatures (moist samples)

However, on the basis of results obtained by us so far, and on those reported by other authors, it is quite reasonable to suppose that conformational transitions in macromolecules play a most significant role in the crystallization of polymers. It may be therefore supposed that, at least for certain types of polymers, the occurrence of a strictly defined conformational transition to a sufficiently high extent, constitutes the indispensable condition for the polymer crystallization process to take place.

EBSCOhost - printed on 2/13/2023 3:45 AM via . All use subject to https://www.ebsco.com/terms-of-use

References

1. Flory, P.J. 1953. Principles of Polymer Chemistry, Cornell Univ. Press, Ithaca, N.Y.
2. Kargin, V.A. 1960. 2, 931.
3. Yeh, G.S.Y., P.H. Geil. 1967. J.Macromol.Sci. B1(2), 251.
   Yeh, G.S.Y., P.H. Geil. 1967. J.Macromol.Sci. B1(2), 235.
4. Flory, P.J. 1983. Conformation of Macromolecules in Condensed Phases. IUPAC MACRO 83.
5. Fischer, E.W. 1976. Structure of Amorphous Organic Polymers in Bulk. Fourth Inter.Conf., Clausthal-Zellerfeld.
6. Dettenmayer, M., S. Fischer, E.W. Fischer, Colloid.Polym.Sci. Fischer, E.W., J.M. Mendolff, M. Dettenmayer, S. Wieser and Wright-Martin. 1974. J.Macromol.Sci., ACS Polymer Preprints 15(2), 8
7. Williams, A.D., P.I. Flory. 1945. J.Polym.Sci. A2,1968, 6.
8. Lemstra, P.J., G. Chala. Ph.D.Theses, Univ. of Groningen.
9. Manley, T.R., D.A. Williams. 1969. Polymer 139.
10. Michailov, M., L. Terlemeryan, Pokl.Bulg.Akad.Nauk.
11. Terlemezyan, L., M. Michailov, P. Schmidt, B. Schneider. 1978. Makromol. Chem. 179, 867; 179, 2315.
12. Spěváček, J., B. Schneider. 1974. Makromol.Chem. 175, 2939.
    Spěváček, J., B. Schneider. 1975. Makromol.Chem. 176, 729.
    Spěváček, J., B. Schneider. 1975. Makromol.Chem. 176, 3409.
    Spěváček, J. 1978. J.Polym.Sci., Polym.Phys.Ed. 16, 523.
    Spěváček, J., B. Schneider. 1980. Polym.Bull. 2, 227.
    Spěváček, J., B. Schneider, M. Bohdanecký, A. Sikora. 1982. J.Polym.Sci., Polym.Phys.Ed. 20, No 9.
13. Tekely, P., E. Turska. 1978. J.Macromol.Sci., Phys. B15(3), 433.
    Tekely, P., E. Turska. 1978. Makromol.Chem. 180, 211.
    Tekely, P., E. Turska. 1975. Makromol.Chem. 180, 1835.
    Tekely, P., E. Turska. 1983. Acta Polym. 34, 660.
    Tekely, P., E. Turska. 1983. Polymer 24, 667.
14. Turska, E., I. Hurek, L. Zmudziński. 1980. Acta Polym. 31, 519.
15. Siegmann, A., P.H. Geil. 1970. J.Macromol.Sci., Phys. B4(2), 239.
    Galden, I.H., B.L. Hammot, E.A. Hazell. 1967. J.Appl.Polym.Sci. 11, 157.
    Hara, T., S. Okamoto. 1964. J.Appl.Phys.(Japan) 3, 499.
16. Williams, A.D., P.J. Flory. 1968. J.Polym.Sci. A2, 6, 1945.
17. Grobelny, J., P. Tekely, E. Turska. 1981. Polymer 22, 1649.
    Turska, E., J. Grobelny. 1983. Eur.Polym.J. 19, 985.
    Turska, E., J. Grobelny, A. Dworak. 1981. 32, 114.
    Grobelny, J., M. Sokoł, E. Turska. 1984. Polymer 25, 1515.
18. Sokoł, M., E. Turska. 1984. Acta Polym. 35, 135.

EBSCOhost - printed on 2/13/2023 3:45 AM via . All use subject to https://www.ebsco.com/terms-of-use

CRYSTAL OF POLYMERS AND OF INTERCALATES WITH POLYMERIC HOST. RELATION BETWEEN MORPHOLOGY AND CHAIN CONFORMATION

J.J. Point, M.C. Colet, M. Dosière
Faculté des Sciences, Université de l'Etat à Mons
Avenue Maistriau, 21, 7000 - MONS, Belgique.

1. Introduction

There exist several models to describe the conformation of crystalline polymers which differ mainly in the way on which the folding of the chain in the amorphous layer of the crystal is described. The most conceptually captivating model is the "adjacent reentry type model" of Keller (1) in which a regular folding of the molecules on the neighbouring lattice site in a particular direction is considered. In many instances (2) the validity of this model was clearly demonstrated from samples obtained in various conditions of crystallization. However the model was reasoned to be impossible by Yoon, et al.(3) who state notably that the mobility of the chains is a priori inadequate for adjacently reentrant folding. Conclusions quite different are obtained by others (4) who infer that such folding is at least permissible on mobility grounds. The present contribution to this debate is based on morphological observations and is divided into two parts.
In the first part, we discuss the use of kinetic data in conjunction with a study of the habit of the various sectors of polyethylene (PE) crystals with a view to measure or at least to bound the rate of lateral spreading of a surface nucleus and the kinetic length L_k. Clearly the rate of migration of the kink along the growth front is the most important input parameter in discussing the mobility issue. If the kinetic length L_k (which is the average distance between nucleation sites at least in the polynucleation regime) is compared to that of a molecular ribbon made of an adjacently folded single molecule, one can draw important conclusions about the ciliation and the conformation of loops in the amorphous

Morphology of Polymers
© 1986 Walter de Gruyter & Co., Berlin · New York - Printed in Germany.

EBSCOhost - printed on 2/13/2023 3:45 AM via . All use subject to https://www.ebsco.com/terms-of-use

part of the lamellae. Both these quantities g and L_k were considered inaccessible by direct probing so far and are thus estimated from theoretical considerations. But these a priori estimations depend on various assumptions and may vary by several orders of magnitude. Thus measurements of these quantities are clearly needed and, as shown here, are feasible.

In the second part of this paper we discuss the concept according to which a single molecule folded with adjacent reentry is an entity distinct from its surroundings. If this view is accepted, pulling such molecular layers apart allows arrays of small molecules to be sandwiched between them. Recently (5) we succeeded in preparing various intercalates of the general formula $[(pC_6H_4XY)_3 \supset (CH_2\text{-}CH_2\text{-}O)_{10}]_n$ (where X and Y are either halogen atom or methyl group) and which have a layered structure. New data on these compounds show that the conformation and the mutual disposition of the stems in the high polymers sheets are very similar to those found in pure poly(ethylene oxide). This supports the view that polymer crystals are made of molecular layers and is a way to isolate such layers in view to study them either by spectroscopy or neutron scattering.

2. A Method of Measurement of g. Theoretical Approach

The aim of this section is to show that the kinetic length can in principle be measured or at least bounded by a determination of the dependance of the growth rate as a function of the size of small crystals. Provided L_k is known, g can be calculated : i) If crystallization occurs in the mononucleation regime the initiation rate i is calculated from the values of the growth rate G and of the persistence length L_p and of the thickness of a molecular layer. Then the value of g is deduced from those of i and L_k.
ii) If crystallization occurs in the polynucleation regime the value of G allows the calculation of the product gi though the ratio g/i is obtained from the value of L_k and both the values of g and/or i can be calculated. The crux of the matter is thus the determination of L_k.

In a simplified version of the theory fully developed elsewhere

EBSCOhost - printed on 2/13/2023 3:45 AM via . All use subject to https://www.ebsco.com/terms-of-use

(6) we consider first the case where the measured crystals are smaller than the hypothetical persistence length L_p and we assume that the nucleus prepared by the selfseeding method is much smaller than L_p. We study, then, the shape of the growth curve as a function of the kinetic length. Let us show briefly that these assumptions are realistic. The size L_o of the nuclei obtained by the selfseeding is very small (7). A currently accepted value for L_p is 1 μm. Estimations of L_k come from the Hoffman-Lauritzen (H.L.) theory. They depend tremendously on the temperature of crystallization but range from 1 to more than 10^3 nm. Clearly a part of this range belongs to that of possible experimental determinations. Thus it appears that provided that the kinetic length is in the range of electron microscopy this length may be calculated from the shape of the growth curve. We indicate now an exact procedure to determine L_k, g and i. As shown by Frank (8) the length and the growth rate of a facet can be expressed as a function of an auxiliary dimensionless quantity (denoted by Q in reference 8)

$$G = b\sqrt{2gi}\,\sin Q \qquad L = \sqrt{2g/i}\;Q/\cos Q$$

Thus $\ln [G/(b\sqrt{2gi})]$ is a well defined function of $\ln (L/L_k)$ represented in Fig. 1. The point corresponding to $L = L_k$ is denoted P. Use of the isochronous decoration technique (6) allows a measurement of growth rate as a function of the length of the involved facet. By a suitable translation the graph ln G versus ln L is to be superimposed on the theoretical curve of Fig. 1. The abscissa of the point corresponding to P is $\ln L_k$ and its ordinate gives $b\sqrt{2gi}\,\sin Q_k$ (where the angle Q_k obeys $Q_k \sec Q_k = 1$). From these values both g and i are deduced.

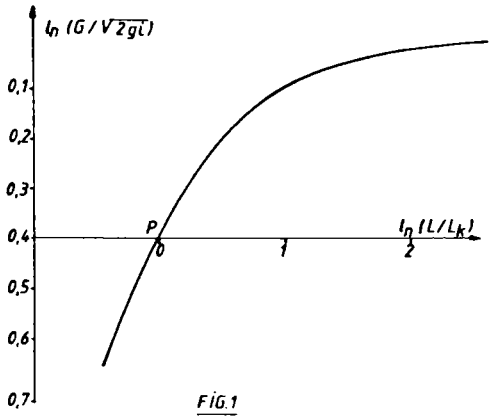

FIG.1

EBSCOhost - printed on 2/13/2023 3:45 AM via . All use subject to https://www.ebsco.com/terms-of-use

Throughout our discussion we have assumed surface nucleation controlled growth in the polynucleation regime. That assumption is clearly often valid and is discussed further in section 5. In the case of very small crystals considered here the possible occurrence of the mononucleation regime is easily ruled out. For regime I the growth rate must be proportional to the length of the facet (by contradistinction with the situation pictured in Fig. 1) and this was (with a possible exception (9)) never observed.

3. Study of the {110} Facet of Lozenge Shaped PE Crystals. Experimental Upper Bounds for L_k and g.

By a new method of decorating the fold surface (isochronous decoration) (10) we have recently measured the growth rate of {110} facet of lozenge shaped crystals as a function of their size. The measurements were performed on a sharp (M_w/M_n = 1.15) PE fraction of moderate molecular weight (M_w = 17000) dissolved in paraxylene at different temperatures of crystallization and concentrations. These measurements were repeated by Colet (11) on a fraction of higher molecular weight (M_w = 115000 ; M_w/M_n = 1.15). Both fractions were prepared and characterized at the Centre de Recherches Société Nationale des Pétroles d'Aquitaine. Although the theory predicts that the growth rate must increase with the crystal size, such an increase was not experimentally observed. (Note incidentally that in all previous studies (12) the initial part of the L versus time curve is claimed to be linear, and the existence of a time lag is denied though in most papers the paucity of experimental details does not allow us to know what was the minimum dimension of the measured crystals and how far the linearity was obeyed). The possibility that the initial linearity of the growth rate curve may result from a balance of opposite effects (an increase with increasing size of the crystals one the one hand, and a decrease with decreasing concentration and fractionation, on the other hand) was thouroughly examined and ruled out (6). We are not in the mononucleation regime because the length of the facet is smaller than any reasonable value of the hypothetical persistence length. Moreover, the fact that the growth rate does not increase with the crystal size shows that the inequality L_k < 50 nm probably

EBSCOhost - printed on 2/13/2023 3:45 AM via . All use subject to https://www.ebsco.com/terms-of-use

holds. (This conclusion is obtained because our isochronous decoration technique allows the measurement of very small crystals with a precedently unattained precision). Let us now take a typical value of G (for instance) 1 nm/s and calculate g and i. We have $L_k = \sqrt{2g/i} \leq 50$ nm ; $G = b\sqrt{2gi} = 1$ nm/s and with b = 0.415 nm we obtain $L_k < 50$ nm ; $g < 60$ nm s^{-1}; $i > 5 \times 10^7$ $(ms)^{-1}$. If the thickness of the lamella is 10 nm the length of a molecular ribbon made of a single molecule adjacently folded is more or less 70 nm for $M_w = 15000$ and 500 nm for $M_w = 115000$. Ciliation is expected. But perhaps the most important conclusion is that g is much lower and i much larger than theoretical estimates from the H.L. theory. This implies that there is no theoretical objection to the apposition of fresh molecules in a regularly folded conformation along the lateral growth face of the crystals.

To illustrate the extent of the discrepancy between experimental and theoretical estimates of L_k and g, let us apply the H.L. theory (13) to the closely related problem of growth of extended chain crystals. Application (13,14) of the H.L. theory to the data of Leung (15) on a polyethylene fraction of molecular weight 3100 leads to a kinetic length higher than 5 mm and to a meaningless value (> 30 m/s) for the rate of lateral spreading of a secondary nucleus. In the context of the present communication notice that the relations $L_p = 1$ µm and $L_k > 5$ mm deduced from H.L. theory cannot hold because Leung (15) claims that the growth curve is linear for crystals smaller than 1 µm.

What are the origin and the significance of these deceptive conclusions about the applicability of the H.L. theory ? From the first principles of this theory L_k is expressed by

$$L_k^2 = C\, a^2 (A - B + B_1)/A_o$$

in which A_o (or B_1) and A (or B) are the rate constants for the attachment (or removal) of the first and subsequent full stems of a secondary nucleus, where a is the width of a stem and C a numerical constant. The overestimation of L_k is a direct consequence of the occurrence in the expression of A_o of the factor $\exp(-2b\sigma\ell/kT)$ which represents the effect of the large free energy barrier associated with the formation of the lateral surfaces of a full first stem. For any reasonable value of σ this free energy barrier is more than 1 order of magnitude higher than kT.

EBSCOhost - printed on 2/13/2023 3:45 AM via . All use subject to https://www.ebsco.com/terms-of-use

The way to escape this difficulty is, as shown in detail in previous paper (16), to assume that the first and subsequent stems are built up piecemeal by successive additions of short segments of the macromolecule. In this way we get a free energy barrier expressed by $2b\sigma\Delta\ell$ in which $\Delta\ell$ is much smaller than ℓ. (This description implies that the mechanism of limitation of fold length differs from that assumed by Hoffman and Lauritzen ; this point, outside of the scope of the present paper, has been examined in detail (16,17)).

4. Shape of Six Sectored PE Crystals. A Theoretical Approach

The aim of the present section is to show how morphological observations on diamond shaped polyethylene crystals may be used in principle to estimate the value of L_k on the {200} facet. For the sake of simplicity, in introducing the discussion of transient effects, a drawing of the crystal in Fig. 2 depicts the lamella as being flat. The crystal is bounded laterally by {110} and {200} growth faces. Taking 2x and 2X to be respectively the lengths of the 200 facets and the short diagonal of the crystal the lateral habit of the crystal, in terms of the truncation ratio, is x/X. As discussed in the previous section for constant temperature and constant polymer concentration in the mother liquid, the growth rate of {110} faces is a constant. But for sufficiently small length of the {200} facets (i.e. smaller than both the persistence and the kinetic lengths) the growth normal to the face would be nonlinear with time and the truncation ratio would change with the size of the crystal as often observed. There are two possible complications : in fact concentration changes during the growth of the crystal and it would be expected that fractionation on the basis of molecular weight would occur. Nevertheless, we intend first to make a theoretical approach of the effect of the relative values of x, L_p and L_k in steady state external conditions. A general model is studied elsewhere, but for the sake of brevity we make here various simplifying assumptions. We assume thus i) that crystallization occurs in the polynucleation regime and that the product gi varies as a function of the temperature on a similar fashion for both {200} and {110} facets. In other words we assume

EBSCOhost - printed on 2/13/2023 3:45 AM via . All use subject to https://www.ebsco.com/terms-of-use

that for sufficiently large facets the values of K_g for {110} and {200} facets are almost equal. This was observed in fact by Colet (11) in a sharp PE fraction (M_w = 17000 ; M_w/M_n = 1.15). ii) Clearly dangling chain ends are generated during the course of crystal growth ; a fraction of these cilia participate (18) in nucleating new growth strips on the crystal faces and the crystal is quite capable of propagating itself without the benefit of external nucleating species. We assume that this selfnucleating mechanism predominates (on both {110} and {200} facets), and more precisely that the initiation rate exhibits no concentration dependance. According to the analysis of Sanchez et al. this may be the case at least above molecular weight of 10^5. On this basis the concentration dependance of growth rate of the {110} facet may be described by the relation $G \propto c^{\alpha}$ with $\alpha = 0.5$ (if g is proportional to c) or $\alpha \approx 0.5$ but lower if (as discussed extensively in the literature) g is not really proportional to the concentration. This conclusion is quite realistic in view of the α values obtained by study of sharp PE fractions (12). We study now in the framework of this model the trajectory of the ends of a 200 facet. We choose (Fig. 2) a clockwise system of coordinates OXY with OY parallel to G_{200} and we denote by φ the angle between G_{110} and OX. The components v_{xA} and v_{yA} of the end A of the {200} facet obeys the relations

$$v_{xA} = G_{100} \qquad v_{xA} \cos \varphi + v_{yA} \sin \varphi = G_{110} \tag{1}$$

From Frank's equations

$$2x = L_{k200}\, Q/\cos Q \quad (2); \qquad v_{xA} = b\sqrt{2g_{200}i_{200}} \sin Q \tag{3}$$

we get the differential equation of the trajectory of A

$$\frac{dx_A}{dy_A} = \frac{1}{\cos \varphi}\left[\frac{G_{110}}{b\sqrt{2g_{200}i_{200}}}\,\frac{1}{\sin Q} - \sin \varphi\right] \tag{4}$$

Equations (2) and (4) show that the shape of the limits of the 200 sectors depends on 2 parameters

$$L_{k200} = \sqrt{2g_{200}/i_{200}} \qquad \text{and} \qquad \rho = \frac{G_{100}}{b\sqrt{2g_{200}i_{200}}} \tag{5}$$

Note in addition that in our simplified model ρ depends neither on the temperature of crystallization nor on the concentration, and that L_k is proportional to $\sqrt{c}$ and increases as a function of the

EBSCOhost - printed on 2/13/2023 3:45 AM via . All use subject to https://www.ebsco.com/terms-of-use

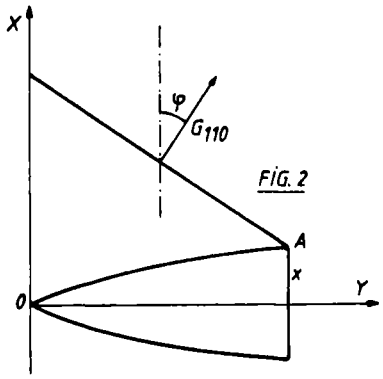

FIG. 2

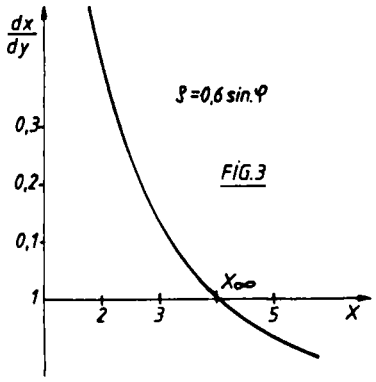

FIG. 3

temperature. For values of $\rho > \sin\varphi = 0.553$ the limits of the 200 sectors have oblique asymptotes : dx_A/dy_A tends to

$$\frac{1}{\cos\varphi}\left[\frac{G_{110}}{b\sqrt{2g_{200}i_{200}}} - \sin\varphi\right] \quad \text{as Q tends to } \pi/2$$

The graph of Fig. 3 shows the variation of dx_A/dy_A as a function of x_A provided that $\rho < \sin\varphi$. There is a value x_∞ of x_A for which $(dx_A/dy_A) = 0$; x_∞ (half the width of the 200 sector) is a stable value because if $x_A > x_\infty$ $(dx_A/dy_A) < 0$; and if $x_A < x_\infty$ $(dx_A/dy_A) > 0$. In any case the truncation ratio depends on the size of the crystal. Fig. 4 shows the shape of 200 sectors for various values of the parameters L/L_k and ρ. Fig. 5 shows how the

FIG. 4

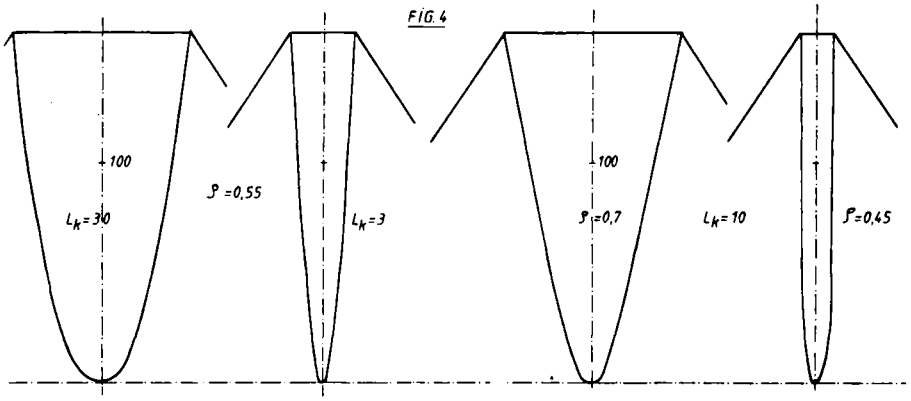

EBSCOhost - printed on 2/13/2023 3:45 AM via . All use subject to https://www.ebsco.com/terms-of-use

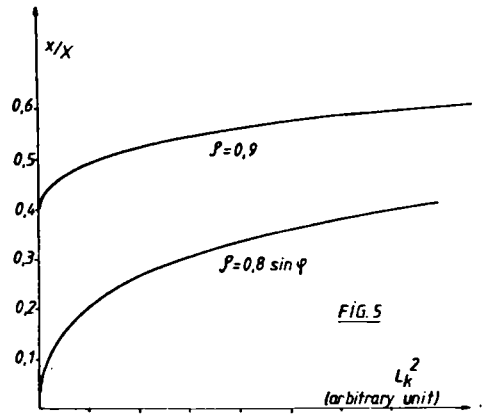

FIG. 5

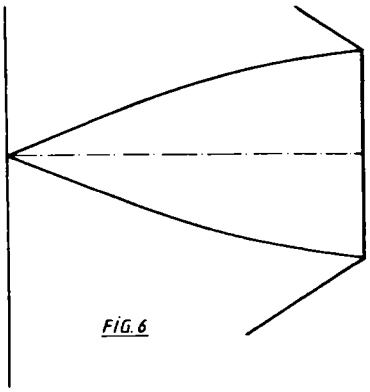

FIG. 6

truncation ratio depends on L_k for a constant value of X and for two different value of ρ. In that figure, for a reason which will appear soon, the value of the truncation ratio is given as a function of L_k^2 which in turn is proportional to c (if g is increased linearly with c). As shown later this new and very simple model has a good predictive ability.

Until now we have assumed steady state external conditions. Actually during the course of the crystallization, the progressive exhaustion of the solution affects the shape of the {200} sectors. For an illustration of this effect, we assume now that the kinetic lengths are very small and we use experimental data of Valenti et al. (19) (in a particular experiment on PE crystals grown from solutions of Marlex 6009 in xylene) to calculate the shape of {200} sectors when the initial concentration is 0.5 wt %. As shown in Fig. 6, near the centre of the crystal, the {200} sector remains triangle shaped but the slope of its limits tends to zero when the concentration drops to zero.

5. Shape of the {200} Sectors. Comparison with Experiments

In conclusion, morphology of {200} sectors is very significant. Three parameters affect their shape:

EBSCOhost - printed on 2/13/2023 3:45 AM via . All use subject to https://www.ebsco.com/terms-of-use

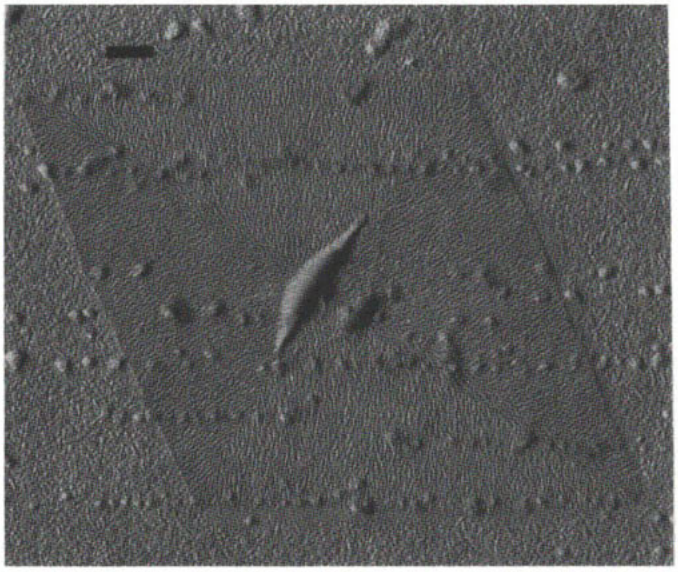

Scale bar: 1 µm

Fig. 7 . PE in xylene (M_w = 115000 ; M_w/M_n = 1.15 ; t_c = 86.15 °C)

a) The first one is $\rho = G_{110}/b\ \sqrt{2g_{200}i_{200}}$. Despite the fact that actually the large departure to the steady state situations is incontrovertible (see later), this is the sole parameter taken into account in the sophisticated theory of Passaglia e.al. (20) who consider hypothetical variations as a function of temperature and concentration of the surface free energies σ and σ_e and of ϕ, the parameter which in the H.L. theory apportions the bulk free energy. The discussion of this theory is outside the scope of the present paper but from a physical point of view it must be, at least, modified to take into account the transient effects which we analyze now.

b) Usually, near the centre of the crystal, the {200} sectors are not perfectly triangle shaped, we conclude thus, from direct morphological observation that in this area, the length of the {200} facet is of the same order of magnitude or smaller than L_k and that L_{200}/L_k is another parameter which controls the shape of {200} sectors. We show now that the simple model described in section 4 works qualitatively. i) {200} sectors similar to some represented in Fig. 4 have been often observed. ii) This model leads to the very new prediction of rectangle shaped {200} sectors which will

EBSCOhost - printed on 2/13/2023 3:45 AM via . All use subject to https://www.ebsco.com/terms-of-use

be observed provided than $\rho < \sin \varphi$. Fig. 7 shows such a sector revealed by the decoration technique of Wittman et al. (21). An interesting question is why, when the condition $\sin \varphi < \rho$ is satisfied, one can observe lozenge shaped crystals. In our opinion, this results from the fact that the length of a {200} facet cannot be considered as an arbitrary small quantity but is an integer multiple of the width of a stem. In contradistinction, until now this length was considered as a real number and the reasoning of the previous section cannot apply when L_k is too small. iii) A feature of the results of Valenti and Pedemonte is illustrated in Fig. 8 drawn from the data of ref. (19): for the same temperature of crystallization the truncation ratio increases with increasing concentration. These curves display close similarity with those given in Fig. 5. (As anticipated the abscissa of these theoretical curves may be arbitrarily taken as L_k^2 or c). It is also well established (20) that for the same molecular weight and concentration and solvent, the truncation ratio becomes larger the higher the crystallization temperature T_c. This fact is qualitatively accounted for by our model because L_k increases also with T_c.

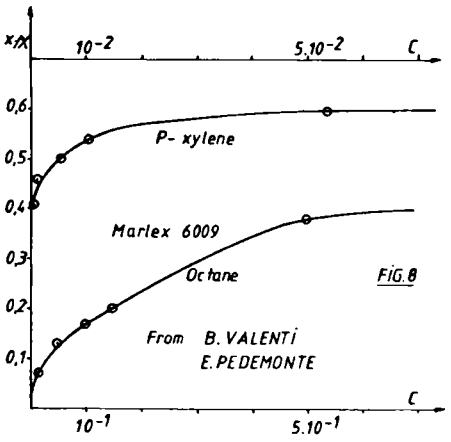

FIG. 8

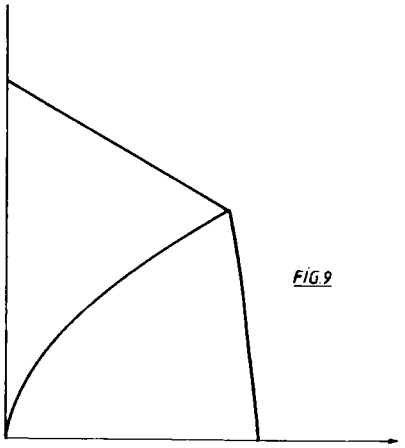

FIG. 9

However the fact that the variation of the truncation ratio may be explained by the sole variation of L_k does not preclude that variation of ρ is not a part of the explanation.

c) The third parameter which affects the shape of the external parts of the {200} sectors is the progressive exhaustion of the

EBSCOhost - printed on 2/13/2023 3:45 AM via . All use subject to https://www.ebsco.com/terms-of-use

solution, an effect which hitherto was not fully recognized but which is significant.

6. Final Remarks

We have shown in the previous section what are the parameters which control the shape of {200} sectors. In principle these effects would be studied in a complete set of experiments in which concentration of the solution and the seeding temperature were systematically changed, the final objective being the determination of the functions G(c,M,L). An additional complication is the possible segregation of the molecules according their molecular weights. For a sharp fraction (M_w/M_n = 1.1) of moderate molecular weight (M_w = 17000) we have shown by kinetic and GPC experiments (6) that fractionation occurs to a previously unexpected extent. The effect of segregation on the 115 K fraction used here is much less pronounced (11). Another remark is that throughout our discussion, we have used the approach of Frank (8) to the theory of surface nucleation controlled growth. This is certainly justified when {110} faces are considered because these faces are fairly straight and because the growth rate exhibits a temperature dependance of the type expected for secondary nucleation. However at the highest temperature of crystallization, slight curvature of the {200} faces is observed in truncated crystals. In this context, Sadler (22) has shown that models incorporating a rough surface growth may be capable of treating many observations on poly(ethylene oxide) crystals grown from the melt and on PE crystals grown from the melt or grown at high T_c from paraffinic or polar solvents, all these crystals having rounded habits. From our point of view, the curvature of the {200} faces, which we observe here at our highest temperature of crystallization is not necessarily present when the crystals actually grow. As they grow these crystals are in fact tentshaped. They readily collapse under the influence of forces of surface tension when they are deposited and allowed to dry on a flat substrate. The effect was calculated (Fig. 9) by assuming that the surfaces of the {110} sectors were {312} surfaces and that the collapsing occurs without change of dimensions along the

EBSCOhost - printed on 2/13/2023 3:45 AM via . All use subject to https://www.ebsco.com/terms-of-use

[010] direction. This is a rough model because there is no proof that the surface obliquities of the crystal follow low index plane and the collapsing of a crystal is clearly a complex process. Thus no quantitative agreement is expected between the calculated and actual shapes of collapsed crystals. But this interpretation reproduces qualitatively the experimental fact that the larger the truncation ratio, the higher the curvature of the {200} faces (presumed linear in the as grown crystal). (This does not preclude the possibility that rough surfaces are present in other circumstances).

7. Possible Design of Intercalates in which the Host is a High Molecular Weight Linear Polymer

We consider here morphological features at a different scale. In most linear crystalline polymer the molecule appears as an entity, the conformation of which being primarily determined by intrachain potential energies. Frequently arrangements of molecules each with respect to the others is close to hexagonal compact. There are however other classes of linear polymer where the formation of strong bonds between adjacent molecules or stems are significant. For instance in many polyamides a sheetlike arrangement of the stems results from this particularity. Our new suggestion is that even in the absence of specific bonding a sheet made of a single molecule adjacently folded on itself may be considered as a structural entity distinct from its surroundings. If such view is accepted polymer crystals have a layered structure and increasing interlayer separation allows the creation between these layers of planar voids the Van der Waals surface of which is determined by the shape of the individual stems and their mutual disposition. Possibly these voids may be filled by arrays of small molecules provided that the size and shape of these small guest molecules are appropriate. In this view we have recently (5) designed and observed an intercalate $[(pC_6H_4Br_2)_3 \supset (CH_2\text{-}CH\text{-}O)_{10}]_n$ presumably made of $pC_6H_4Br_2$ layers sandwiched between poly(ethylene oxide) (PEO) sheets. The aim of the present section is to show that new experimental data first indicate that the structure of these PEO sheets are closely similar to these observed in pure PEO and second that

EBSCOhost - printed on 2/13/2023 3:45 AM via . All use subject to https://www.ebsco.com/terms-of-use

many paradisubstituted benzene derivatives may be used instead of $pC_6H_4Br_2$ in the preparation of the intercalate.
Kovacs et al. (23) have shown that the usual habit of solution grown PEO platelets is a square with {120} faces. As shown by Takahashi et al. (24), the unit cell of PEO is monoclinic (a sin β =0.656 ; b = 1.304 ; c = 1.98 nm and β = 126.1°). Moreover, a regular 7/2 helix is a good approximation of the conformation of the molecule. From the fractional coordinates of the axis of the four chains contained in a unit cell it appears that the crystal may be thought as made of molecular ribbons in which stems alternatively right and left handed are regularly disposed in a plane parallel to either 120 or $1\bar{2}0$ planes i.e. parallel to a fast growth face of the PEO platelets. Otherwise we have prepared intercalates in which PEO is the host. All the observed reflections given by these crystalline compounds are explained on the basis of monoclinic unit cells. The parameters of these unit cells depend slightly on the guest compound but are very close together as exemplified in the Table 1. Planes parallel to 010

Table 1 . Unit Cell for $[(pC_6H_4XY)_3 \supset (CH_2\text{-}CH_2\text{-}O)_{10}]_n$ Intercalates

X	Y	a (nm)	b (nm)	c (nm)	γ (°)	r (*)
Cl	Cl	0.951	0.951	2.786	120.0	0.702
Br	Br	0.967	0.968	2.798	120.0	0.706
Cl	Br	0.957	0.958	2.810	120.0	0.710
Br	F	0.946	0.946	2.856	120.0	0.683
Cl	I	0.970	0.973	2.824	120.1	0.709

(*) packing coefficient.

contain similarly handed helices the axes of which being 0.968 nm apart. The intense layer line are the 3^d, the 6^{th}, the 9^{th} and this suggest a $10/\bar{3}$ helical structure with a pitch of 0.94 nm. IR spectra of the pure PEO and of the intercalate confirm the close analogy between these helices and the 7/2 helices of pure PEO. The unit cell contains 2 polymer molecules, and if the axes of these two molecules are assumed to be in the same {010} plane we may

EBSCOhost - printed on 2/13/2023 3:45 AM via . All use subject to https://www.ebsco.com/terms-of-use

conclude the complete similarity of the polymer sheets in the intercalates and in the pure PEO. We have drawn the shape of the voids obtained by disposing two such sheets 0.836 nm apart. Their size and shape are such that they can accomodate $pC_6H_4Br_2$ molecules with a high packing density. No specific interactions are expected between PEO and the many paradihalogenobenzenes or parahalogenotoluenes from which the intercalates were prepared. The heat of formation from the solid components is very low (few kcal per mole of pC_6H_4XY). Finally, neither ortho nor meta derivatives are complexed by the PEO. From all these arguments it is concluded that complexation is due to the adequation of the shapes of the Van der Waals surfaces of the PEO layers and of the pC_6H_4XY guest molecules. This example shows the usefulness of the concept according to which a molecular ribbon made of adjacently folded linear macromolecule is a real entity.

Conclusion

Morphological studies are a powerful and somewhat neglected method of investigation. This is illustrated in two ways. First we show that a careful study of the habits of the various sectors in a crystal leads, when used in conjunction with kinetic studies, to the measurement of the rate of lateral spreading of surface nuclei and of the kinetic length which is the average distance between two nucleation sites. So far both these quantities were considered as inaccessible to direct experimental probing.
Secondly we suggest that a molecular ribbon made of single molecule adjacently folded may be considered as an entity distinct from its surrounding. In this respect we show the close analogy between the poly(ethylene oxide) sheets in PEO and in intercalates in which PEO is the host compound.

Aknowledgement

The authors gratefully acknoledge C. Coutelier for collaboration in the work on the PEO intercalates. They are indebted to R. Andrew for assistance in revision of the manuscript and to

EBSCOhost - printed on 2/13/2023 3:45 AM via . All use subject to https://www.ebsco.com/terms-of-use

M. Lefebvre and F. Grossmann for technical assistance. This work has been partly supported by the F.N.R.S. (Fonds National de la Recherche Scientifique).

References

1. Keller, A. 1957. Phil. Mag. 2, 1171.

2. Keller, A. 1979, Disc. Far. Soc. 69, 145.

3. Yoon, D.Y., Flory, P.J. 1979. Ibid., 288.

4. Klein, J., Ball, R. 1979. Ibid. 198 ; DiMarzio, E.A., Guttman, C.M., Hoffman, J.D. 1979. Ibid., 210.

5. Point, J.J., Coutelier, C. 1985. J. Polym. Sci., Polym. Phys. Ed. 23, 231.

6. Point, J.J., Colet, M.C., DOSIERE, M. submitted to J. Polym. Sci., Polym. Phys. Ed.

7. Blundell, D.J., Keller, A. 1968. J. Macromol. Sci. B2, 301.

8. Frank, F.C. 1974. J. Cryst. Growth 22, 233.

9. Lanceley, H.A., Sharples, A. 1966. Makromol. Chem. 94, 30.

10. Dosière, M., Colet, M.C., Point, J.J. submitted to J. Polym. Sci., Polym. Phys. Ed.

11. Colet, M.C. (to be published).

12. Cooper, M., Manley, R.St.J. 1975. Macromolecules 8, 219.

13. Hoffman, J.D. 1985. Macromolecules 13, 399.

14. Point, J.J. submitted to Macromolecules.

15. Leung, W.M., Manley, R.St.J. 1985. Macromolecules 13, 399.

16. Point, J.J. 1979. Macromolecules 12, 770.

17. DiMarzio, E.A., Guttman, C.M. 1982. J. Appl. Phys. 53, 6581.

18. Sanchez, J.C., DiMarzio, E.A. 1971. Macromolecules 4, 677.

19. Valenti, B., Pedemonte, E. 1972. La Chimica e l'Industria 54, 112.

20. Passaglia, E., Khoury, F. 1984. Polymer 25, 631.

21. Wittman, J.C., Lotz, B. 1984. J. Polym. Sci., Polym. Phys. Ed. 22

EBSCOhost - printed on 2/13/2023 3:45 AM via . All use subject to https://www.ebsco.com/terms-of-use

22. Sadler, D.M. 1983. Polymer 24, 1401.

23. Kovacs, A.J., Lotz, B., Keller, A. 1969. J. Macromol. Sci. Phys. B3, 385.

24. Takahashi, Y., Tadokoro, H. 1973. Macromolecules 6, 672.

EBSCOhost - printed on 2/13/2023 3:45 AM via . All use subject to https://www.ebsco.com/terms-of-use

EBSCOhost - printed on 2/13/2023 3:45 AM via . All use subject to https://www.ebsco.com/terms-of-use

THE CONCENTRATION DEPENDENCE OF THE LINEAR GROWTH RATE G_{110} IN A POLYETHYLENE SINGLE CRYSTAL GROWN FROM DILUTE SOLUTION

M. Dosière, M.-Ch. Colet, J.J. Point
Université de l'Etat à Mons, Faculté des Sciences
Avenue Maistriau, 21, 7000 - MONS (BELGIUM).

Introduction

The crystallization of polyethylene (PE) single crystals from dilute solution has been much investigated since their discovery by Keller (1). At the same time, Mandelkern (2) showed that the growth kinetics implied repeated surface nucleation. The initial version of the kinetic theory proposed by Hoffman and Lauritzen (3) and Frank and Tosi (4) has been revised many times and in various ways to take into account new experimental data. However, we still do not understand either why the rate of crystal growth G is proportional to a fractional exponent of the concentration C ($G \propto C^{\alpha}$) (5), or the physical origin of the persistence length L_p. The main aim of this paper is to show that a new experimental technique, "the isochronous decoration method", allows us to follow the growth of a single crystal throughout the course of its formation (6). Examination of the experimental results obtained with this isochronous decoration method raises interesting questions about the dependence of the growth rate G on the size of the crystal, on the solution concentration and on a possible fractionation even for polyethylene samples having a very low polydispersity ($1 < M_w/M_n < 1.15$). Until now, the growth of polymer crystals is followed by sampling at various stages of crystallization (7). Such a procedure is only successful when all crystals have an uniform size at a given time so that the whole crystal population can be characterized by any one crystal. Such a requirement is satisfied by using the self-seeding method (8). The number of seeds and hence the ultimate crystal size can be controlled by an appropriate choice of the seeding temperature T_s (9).
In order to avoid sampling in the crystallization device and to

Morphology of Polymers
© 1986 Walter de Gruyter & Co., Berlin · New York - Printed in Germany.

EBSCOhost - printed on 2/13/2023 3:45 AM via . All use subject to https://www.ebsco.com/terms-of-use

perform diameter measurements on various crystals, we have proposed an isochronous decoration method to measure linear growth rate of polymer crystals (6). The basic features of this technique are the following : a) the long spacing ℓ of PE single crystals increases with the crystallization temperature T_c : for low degrees of supercooling ΔT ($\Delta T = T_d^\circ - T_c$ where T_d° is the equilibrium dissolution temperature), $\Delta\ell/\Delta T$ is around 0.5 nm K^{-1} for PE single crystals grown from p-xylene (10) ; b) a heat transfer analysis showed that a time delay of 10 seconds is needed to change by 5 K the temperature of a dilute solution of PE in p-xylene contained in a glass tube having a sufficient small diameter. Such rapid change in the crystallization temperature from $T_{c,1}$ to $T_{c,2}$ results in a sharp increase or decrease in the thickness ℓ of the single crystal depending on whether $T_{c,1}$ is larger or smaller than $T_{c,2}$. The steps can be observed in the electron microscope after the isochronous decorated crystals have been metal shadowed.

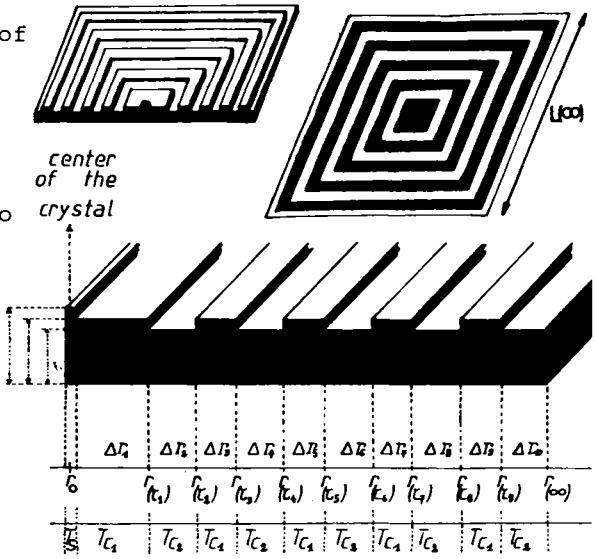

Fig. 1. Schematic drawing of an "isochronous decorated" PE single crystal. $L(\tau)$ is the length of the face (110) ; $r(\tau)$ is the distance from the center to the (110) face ; $\ell_1(T_{c,1})$ and $\ell_2(T_{c,2})$ are the thicknesses of the single crystal at $T_{c,1}$ and $T_{c,2}$; ℓ^* is the thickness of the nucleus.

As during the course of the experiment the solution is progressively exhausted one obtains in fact in a single experiment the values of the growth rate at two crystallization temperatures $T_{c,1}$ and $T_{c,2}$ but for values of polyethylene concentration ranging from the initial concentration C_o to zero. The concentration after a given crystallization time delay τ is obtained by a simple

EBSCOhost - printed on 2/13/2023 3:45 AM via . All use subject to https://www.ebsco.com/terms-of-use

calculation. A schematic drawing of an isochronous decorated PE single crystal is given in Fig. 1. The total areas $A_1(\tau)$ and $A_2(\tau)$ of the portions of the single crystal grown respectively at $T_{c,1}$ and $T_{c,2}$ depend on the time τ. Denoting by $A_1(\infty)$ and $A_2(\infty)$ these areas when the solution is fully exhausted, the actual concentration at time τ is :

$$C(\tau) = C_o \frac{[A_1(\infty) - A_1(\tau)]\ \ell_1 + [A_2(\infty) - A_2(\tau)]\ \ell_2}{A_1(\infty).\ell_1 + A_2(\infty).\ell_2} \qquad (1)$$

where ℓ_1 and ℓ_2 are respectively the thickness of the crystal when crystallization occurs either at temperature $T_{c,1}$ or $T_{c,2}$; C_o is the initial concentration.

If we call respectively $r(\tau)$ [and $r(\infty)$] the size of the crystal at time τ [and at the end of the crystallization] and $x = r(\tau)/r(\infty)$ its actual reduced size, the relation

$$C(\tau) = C_o\ (1 - x^2) \qquad (2)$$

can be used in place of eq. (1) as a first approximation at least if the crystal has many ridges and if $A_1(\tau)$ and $A_2(\tau)$ are of the same order of magnitude. Therefore it may be that the isochronous decoration method allows us to obtain on each single crystal the values of the concentration exponent α of the relation $G_{110} \propto G^{\alpha}$ at both crystallization temperatures $T_{c,1}$ and $T_{c,2}$ in only one experiment.

Experimental

Two sharp fractions of linear polyethylene called LPE 17 K and LPE 115 K prepared and characterized at the Centre de Recherches, Société Nationale des Pétroles d'Aquitaine (France) were used. Their characteristics are given in Table 1.

Table 1. Characteristics of the Polyethylene Fractions (SNPA)

	$\bar{M}_w$	M_w/M_n
LPE 17	17000	1.11
LPE 115	115000	1.15

EBSCOhost - printed on 2/13/2023 3:45 AM via . All use subject to https://www.ebsco.com/terms-of-use

The crystallization device and the experimental procedure have been fully described elsewhere (6).

Results

Fig. 2 shows a typical micrograph of an isochronous decorated single crystal grown at $T_{c,1}$ = 88.0 °C and $T_{c,2}$ = 81.0 °C from a dilute solution of LPE 115 K in p-xylene having an initial concentration C_o = 0.00218 wt %. Table 2 contains the experimental results obtained from the electron micrograph shown in Fig. 2.

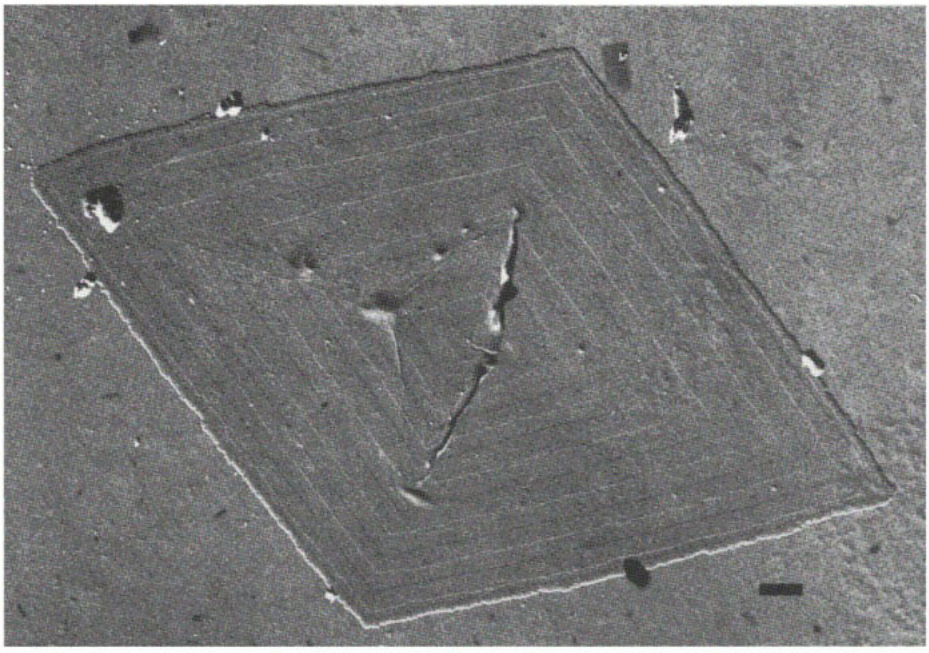

Fig. 2. Isochronous decorated LPE 115 K single crystal shadowed with Palladium-Gold (40/60); scale bar = 1 µm ; p-xylene ; $C_o = 2.18\ 10^{-3}$ wt % ; $T_{c,1}$ = 88 °C ; $T_{c,2}$ = 81 °C.

EBSCOhost - printed on 2/13/2023 3:45 AM via . All use subject to https://www.ebsco.com/terms-of-use

Table 2. Typical Data Obtained from the "Isochronous Decorated" LPE Single Crystal Given in Fig. 2.

T_c/°C	Δτ/min	L/μ	r/μ	G_{110}(μ/hr)	x
87.9	20	0.509	0.2376	0.713	
81.0	1	1.159	0.5204	16.97	0.2359
88.0	20	1.442	0.7805	0.780	0.3385
81.0	1	2.036	1.0464	15.950	0.4623
88.0	20	2.489	1.2443	0.594	0.4480
81.25	1	2.941	1.4367	11.538	0.5221
88.0	30	3.535	1.7647	0.656	0.9342
81.15	1.5	4.185	2.0532	11.538	1.1137
88.0	31	4.666	2.3303	0.536	1.2264
81.15	2	5.420	2.5905	7.805	1.3135
88.0	41	5.939	2.7998	0.306	1.1897
81.20	2.5	6.448	3.0430	5.837	1.5063
88.2	92	6.957	3.2636	0.144	1.4786
81.2	-	7.183	3.3654	1.222	0.7197
-		7.466	3.4785	-	0.8284

ℓ_1 (88 °C) = 15 nm ; ℓ_2 (81 °C) = 12.2 nm.

Graphs of ln G versus ln $C(\tau)/C_o$ are drawn for each isochronous decorated single crystal having grown at $T_{c,1}$ and $T_{c,2}$. Data plotted in Fig. 3 are mean values obtained at least on 10 single crystals. The slope of these plots gives the concentration exponent α. It clearly appears from Fig. 3, that all our values thus determined are rather larger than values obtained by Cooper and Manley (11) (dashed lines). The decrease of the growth rate with the concentration is much sharper for the LPE 17 K fraction than for the LPE 115 K.

Discussion

The following objections to the validity of the isochronous decoration method can be formulated : a) partial dissolution or reorganization of thin crystal portions grown at $T_{c,2}$ when the growing

EBSCOhost - printed on 2/13/2023 3:45 AM via . All use subject to https://www.ebsco.com/terms-of-use

crystal in the dilute solution comes back to $T_{c,1}$ with $T_{c,1} > T_{c,2}$; b) when the temperature of the dilute solution containing the growing PE crystals is increasing from $T_{c,2}$ to $T_{c,1}$, the finite height of the substrate is smaller than the lamellar thickness at $T_{c,1}$. These objections have been discussed elsewhere (6) and ruled out. Three hypotheses are examined hereafter as possible explanations to our larger values of the concentration exponent α.

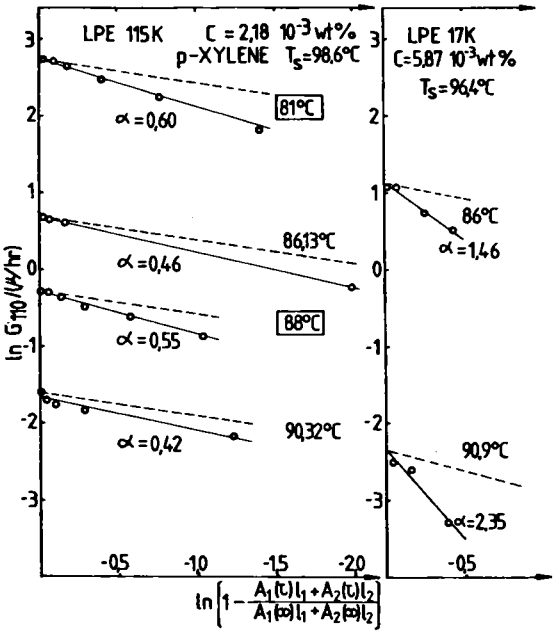

Fig. 3. ln G versus ln C. Dashed lines are calculated from exponent concentration α given by Manley (α ≃ 0.3). Our results (o) are mean values obtained on 10 single crystals. Values of α are given for each T_c.

As qualitatively shown in Fig. 2, growth rates G_{110} (88 °C) in a single crystal as a function of the reduced size x, are obtained for larger and larger growing faces (110). The lengths of the growing (110) faces are respectively 0.509 μm, 1.442 μm, 2.489 μm, 3.535 μm and 4.66 μm for the five following values of G_{110} : 0.713, 0.780, 0.695, 0.621 and 0.538 μm h^{-1} (Table 2).

Even taking into account the small dimension of the growing crystal, theoretical development of the Frank's argumentation (12) presented elsewhere shows that in the first stage of crystallization the growth rate can only increase with the size of the crystal, whether crystallization occurs following regime I or II (13). A decrease in the growth rate of paraffins is generally observed when the solution contains impurities at a low concentration (14). Qualitatively, the number of available sites for the deposit of the

EBSCOhost - printed on 2/13/2023 3:45 AM via . All use subject to https://www.ebsco.com/terms-of-use

macromolecule is decreasing when impurities are adsorbed on the crystal face (110). Now, we have no argument to confirm or to discard the hypothesis of the contamination of the PE faces when the dimension of the growing face (110) is increasing. There is a third and more likely explanation which demonstrated to be valid in the case of growth rate measurement on LPE 17 K (13). Although LPE samples have a sharp molecular weight distribution (Table 1), a segregation of macromolecules according to their molecular weight during crystallization has been reported for LPE 17 K single crystals grown at high crystallization temperature (13) : molecular weight distribution measurements carried out by gel permeation chromatography show that the highest molecular weight components of the distribution have disappeared from the filtrate when crystallization is stopped after a reduced size $x = 0.1$. Until now, GPC analysis of these small crystals has been unsuccessfully carried out. As the crystallization is stopped when the reduced size of the crystal is around 0.1, only a small quantity of crystallized material is obtained. As molecular weight distribution measurements by gel permeation chromatography require at least a sample of around 5 to 10 mg, large volumes of solution or more concentrated solutions are needed. Molecular weight distribution measurements of on LPE 115 K crystals are actually in progress.

Conclusions

The isochronous decoration method allows the measurement of the growth rate as a function of the size of a single crystal. There is agreement between our initial value of growth rate and values reported by Cooper and Manley on similar samples. When the solution is progressively exhausted the growth rate decreases more sharply than can be predicted from the value of the concentration exponent α obtained by the conventional method of growth rate measurement. Referring to a previous work on LPE 17 K (13), we conclude that the fall in the growth rate for LPE 115 K must certainly result from molecular weight segregation even though PE samples with a low polydispersity index are used.

EBSCOhost - printed on 2/13/2023 3:45 AM via . All use subject to https://www.ebsco.com/terms-of-use

References

1. Keller, A. 1957. Phil. Mag. 2, 1171.

2. Mandelkern, L. 1958. Proc. Int. Conf. Crystal Growth, Cooperstown, 457.

3. Lauritzen, J.I. Jr., Hoffman, J.D. 1960. J. Res. Nat. Bur. Std. 64A, 73.

4. Frank, T.C., Tosi, M. 1961. Proc. Roy. Soc. 263, 323.

5. Blundell, D.J., Keller, A. 1968. J. Polym. Sci., Polym. Lett. 6, 433.

6. Dosière, M., Colet, M.-Ch., Point, J.J. : J. Polym. Sci., Polym. Phys. Ed. (accepted for publication).

7. Lindenmeyer, P.H. 1963. J. Polym. Sci. C1, 5.

8. Blundell, D.J., Keller, A., Kovacs, A.J. 1966. J. Polym. Sci., Polym. Phys. Ed. 4 481.

9. Blundell, D.J., Keller, A. 1968. J. Macromol. Sci. B2, 301.

10. Huseby, T.W., Bair, H.E. 1968. J. Appl. Phys. 39, 4949.

11. Cooper, M., Manley, R.St.J. 1975. Macromolecules 8, 219.

12. Franck, F.C. 1974. J. Cryst. Growth 22, 233.

13. Point, J.J., Colet, M.-Ch., Dosière, M., submitted to J. Polym. Sci., Polym. Phys. Ed.

14. Simon, B., Grasse, A., Boistelle, R. 1974. J. Cryst. Growth 26, 90.

15. Colet, M.-Ch. (to be published).

EBSCOhost - printed on 2/13/2023 3:45 AM via . All use subject to https://www.ebsco.com/terms-of-use

MELTING AND RECRYSTALLIZATION OF SURFACE GROWN POLY(ETHYLENE) CRYSTALS

R. Hirte, D. Zenke

Akademie der Wissenschaften der DDR, Institut für Polymerenchemie "Erich Correns", 1530 Teltow-Seehof, German Democratic Republic

Introduction

Surface grown poly(ethylene) crystals which contain remarkable amounts of extended chains besides low ordered "kebab"-material, that means very long stretched and fixed non-shrinkable molecules besides weakly fixed and folded molecules, show very complicated melting behaviour, as Pennings et al. (1) demonstrated by means of DSC, EM and X-ray-analysis.
Concerning the surface of such highly ordered materials Hill, Barham and Keller (2) studied the so called "hair-dressing"-effects, that means the morphological transformations in the surface in consequence of the actual thermal history.
We are interested in the morphological transformations in the volume of surface grown crystals and one way of solving such problems is to study the premelting and recrystallization behaviour. In performing such experiments we hope for a better explanation of the complex morphology of such fibers.

Experimental

As material we used a high-density-poly(ethylene) of VEB Chemische Werke Buna with $\overline{M}_w \simeq 2 \times 10^5$ and broad distribution of the molecular weight. Surface grown fibers were produced from 0.5 % solution in p-xylene at 373 K with a velocity of about 0.35 m/min. The dried fiber had a profile of 0.8 x 0.07 mm^2.
In comparison with surface grown fibers from long chain material, e.g. Hostalen GUR, our fibers show qualitatively the same melting

Morphology of Polymers
© 1986 Walter de Gruyter & Co., Berlin · New York - Printed in Germany.

EBSCOhost - printed on 2/13/2023 3:45 AM via . All use subject to https://www.ebsco.com/terms-of-use

behaviour but all transition temperatures were about 3 - 4 K lower. The mechanical values are not as high as with GUR. The advantage of the short-chain material is in higher splitting and bending resistance.
DSC measurements were performed with Perkin-Elmer DSC-1B. All values obtained were determined at 8 K/min. Given temperatures are not corrected for thermal lag etc. Shrinkable samples were prepared as long interlaced fibers, not shrinking fibers as usual on Al-strips with fixed ends.
Figure 1 shows the regime of measurements. The "1st melting" was

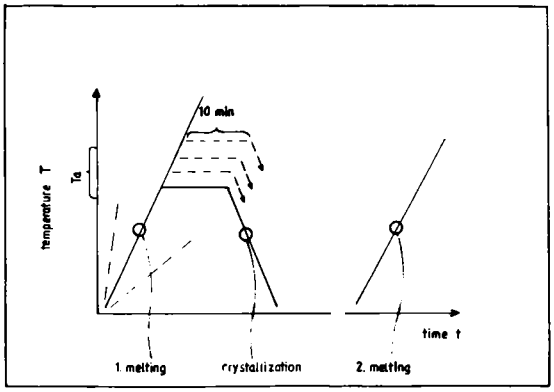

Fig. 1. Regime of the DSC-measurements.

preliminary investigated under usual conditions to gain an oversight, then with always new samples the measurements were interrupted at temperatures T_a by an annealing time of 10 minutes and finally the samples were cooled down with the result of nonisothermal crystallization. Later each sample was measured under usual conditions ("2nd melting"). All results will be presented and discussed on the basis of the different T_a-values.
With T_a-values ranging from 405 to 425 K most of the complex melting process can be scanned. As to the dynamical aspect of the melting a peak-maximum deflection between 8 K/min and the extrapolated zero velocity value of about 2 - 4 K with the fixed and about 3 - 5 K with the shrinkable sample were detected. The higher the peak the larger the deflection. The mean temperature differences of about 6 - 7 K between the various melting peaks allows us - as the isothermal DSC-curve within the annealing time

EBSCOhost - printed on 2/13/2023 3:45 AM via . All use subject to https://www.ebsco.com/terms-of-use

reveals - to separate the melting process in its steps. All temperatures were determined at peak maximum. This includes a systematic error depending on peak width. Transition heats were determined peak by peak. In the case of very small peaks being expressed only by a shoulder on larger neighbouring peaks the estimation is uncertain.

Results

Fig. 2 shows the absolute values of transition heats obtained over the T_a-values with the shrinking (a) and fixed (b) materials.

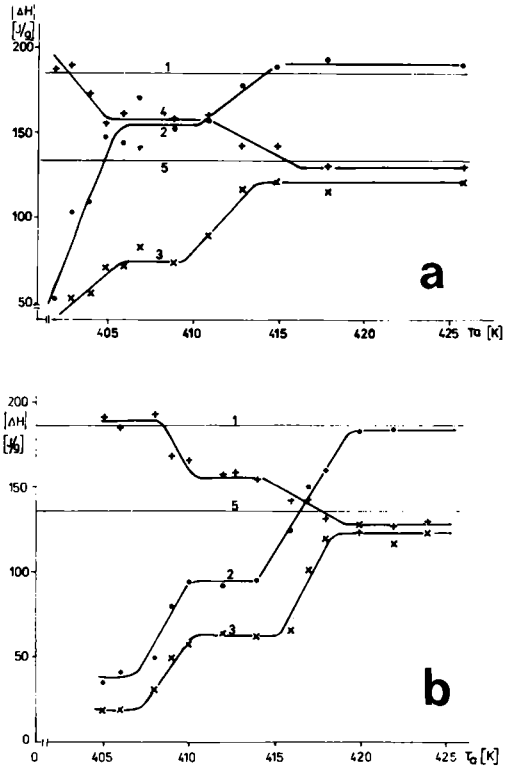

Fig. 2. Absolute values of transition heats $|\Delta H|$:
a) shrinking material,
b) fixed material.

EBSCOhost - printed on 2/13/2023 3:45 AM via . All use subject to https://www.ebsco.com/terms-of-use

Curve 1 and 5 depict the melting enthalpies of the wholly molten highly ordered fiber (1) and the free crystallized material (5) which are independent of T_a.
Curve 2 shows the melting heat of samples heated up to T_a, including heats of isothermal melting at T_a in the 10 min annealing time.
Curve 3 illustrates the crystallization heats of those samples.
Curve 4 provides values of the final 2nd melting process.
At the first glance two transformation regions are seen, the temperatures depending on the state of the fibre. Fixing of fibre ends shifts the transformations to higher temperatures. The second transformation region finishes - within the limits of measuring accuracy - at temperatures considerably far of the last peak of a real melting process (at about 423 - 425 K). This is due to the very high deflection of the highest melting peak and the pecularities of the measuring procedure.
Curve 2 represents the melting heat up to temperatures T_a and in the annealing time. It reflects the step by step loss of order. By comparing the curves of shrinking and fixed samples a retarded loss with the fixed sample is visible in the medium range.
Curve 3 shows the crystallization heats, which arise in cooling the samples from the T_a-level. This dependence has to equal curve 2 as far as reversible processes are involved. Differences are besides experimental errors, due to lasting loss of order. Thus the case of shrinking is seen to be characterized by a strongly increasing difference in the first transition region (that means, as Fig. 3 shows, in the shrinking process), whereas the fixed fiber exhibits a continuously increasing difference without any particular points.
Curve 4 indicates the melting heats in a real melting process of the samples, which were annealed before at T_a. Here again the step by step transformation of highly ordered material to normal fold crystallized material occurs. It is interesting, that bebesides temperature shift, no differences between the two kinds of samples are observed.
Fig. 3 shows the shrinking-curve in a regime that equals the first melting regime: Heating up to temperature T_a, 10 minutes annealing time, and then cooling down. The first range of transformation in the discussed figures involves the shrinking range

EBSCOhost - printed on 2/13/2023 3:45 AM via . All use subject to https://www.ebsco.com/terms-of-use

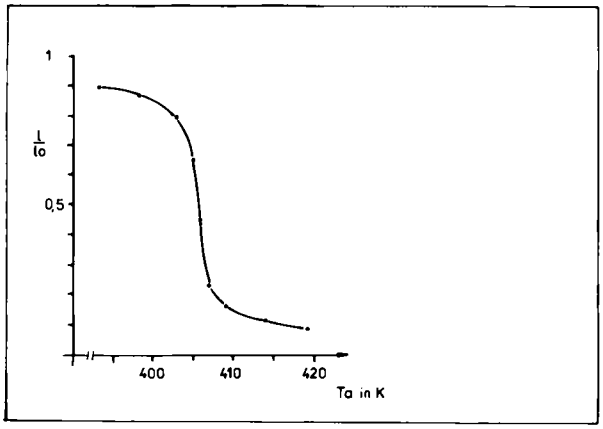

Fig. 3. Shrinking curve in a regime equal to the DSC-measurements (shrinking time 10 min at each temperature step).

as this figure confirms.
Before discussing the peak by peak alterations let us consider the whole picture of peak transformations.
Fig. 4 gives a scheme of peaks in melting and recrystallization. The upper line indicates the peak temperatures of the uninterrupted melting process with shrinking, the lower line refers to the fixed sample. Fixing the sample shifts the whole melting process to higher temperatures as seen before.
In both cases we find in principle four melting peaks and three crystallization peaks. In the diagram the percentage of melting heats in uninterrupted melting process are indicated. Attention should be paid to the characteristic difference of heat consumption in the 2nd or 3rd peak, depending of the possibility to shrink. It is possible to explain the little third peak in the upper row and the little second peak in the lower scheme as connected with incomplete shrinking or fixing. In both cases we find the last peak having a share of less than 10 percent.
The small first melting peak, almost lacking in the first melting curve will increasingly dominate with increasing T_a in the second melting process. The lasting difference of first peak temperatures in both schemes is to be contributed to the fact, that the fixed fiber despite a real melting treatment up to

EBSCOhost - printed on 2/13/2023 3:45 AM via . All use subject to https://www.ebsco.com/terms-of-use

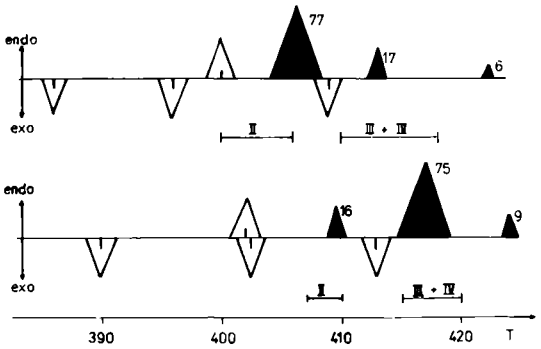

Fig. 4. Scheme of peak temperature and area in melting and recrystallization (upper part: shrinking samples; lower part: fixed samples):
▲ peaks, appearing in both the complete melting process and the second melting process after T_a-treatment (with percentage of the peak areas in fully melting),
△ peaks, appearing in recrystallization and in second melting,
⊢⊣ transition ranges and number of peaks which belong to these transitions.

about 450 K preserves the fiber form. Thus we have a partly oriented material. The influence of this lasting orientation may cause the always higher crystallization temperatures of the fixed fiber too.
The transition ranges, shown in Fig. 2, are given with the numbers of peaks which belong to these transitions.
Before the discussion of peak behaviour in crystallization and second melting let us give a short description of physical meaning of peaks. We believe that No. 1 is connected to free crystallized, folded material; second peak means shrink-process with the connected transformations of fine structure, third peak transformation to the hexagonal phase and the last destruction of the actual "shish".

EBSCOhost - printed on 2/13/2023 3:45 AM via . All use subject to https://www.ebsco.com/terms-of-use

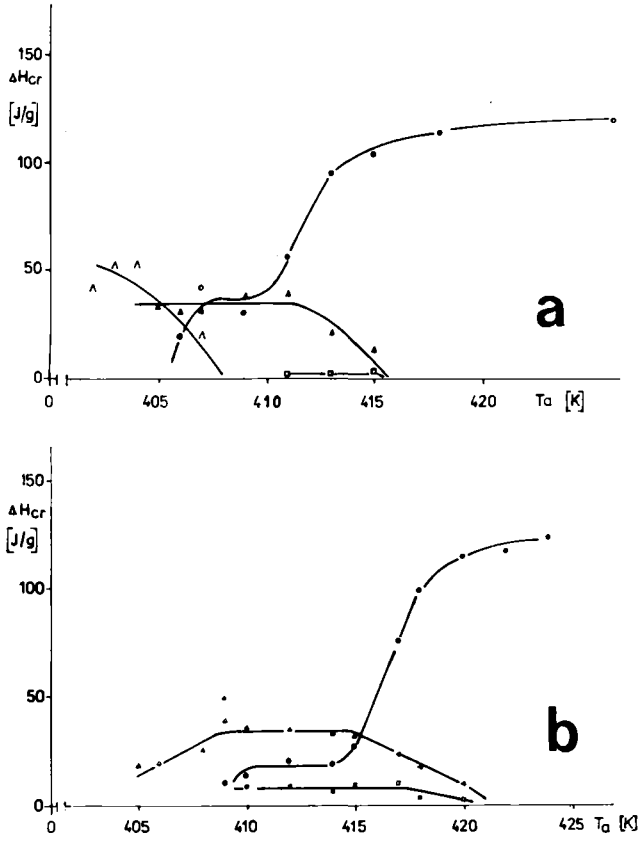

Fig. 5. Peak shares of crystallization heats:
a) shrinking material,
b) fixed material;
o - low temperature crystallization peak (see Fig. 4),
Δ Δ - medium temperature crystallization peak,
□ - high temperature crystallization peak.

Fig. 5 compares the peak by peak shares of crystallization heats. The lowest peak starts somewhat surprisingly late, after completion of the shrink-process. The connection to the shrinking process causes the lower values of this peak in the case of the fixed fiber in the medium temperature range. This peak col-

EBSCOhost - printed on 2/13/2023 3:45 AM via . All use subject to https://www.ebsco.com/terms-of-use

lects all the intensity at higher temperatures. So we are able to conclude that it represents the crystallization of free folding material.
The next peak has a very high intensity from the very beginning of melting range. One finds the same values in both cases of measuring conditions. That means the peak represents the crystallization of material independent of shrinking-state of the fiber.
Because of the higher crystallization temperature we are inclined to declare it as connected with recrystallization of preordered material (better to say: incomplete molten material). In the range of low temperatures, but only in the case of free shrinking material exists a decreasing neighbour peak which we think is connected with a direct "hair-dressing"-process - that means reorganization of e.g. folded material on high ordered surfaces.
The upper peak start to appear in the range of shrinking peak. It has constant value and disappears in the range of last peak, that means disappearing of high ordered "shish". Its value depends on the fiber state. We propose an interpretation as quick reorganization of material at or in the "shish".
Fig. 6 shows the results of 2nd melting. That means in this case real melting of samples which had a rest at the temperature T_a before. Here we find all the before mentioned four melting peaks together.
The lowest peak corresponds to the lowest crystallization peak and increased step by step proportional to the share of melting peak 2 or 3 in the case of shrinking or fixed fiber corresponding.
Second peak represents the lowest melting parts of the surface grown fiber in the virginal state. It disappears with passing over shrinking temperature. In the case of fixed end its share is minimal.
The third peak decreases step-like in the case of fixed ends whereas it has a low constant value in the case of shrinking sample. The different course does not collide with the interpretation, which found Pennings for this peak: as connected with a phase transformation. This transformation includes in the case of fixed ends a larger share than in the case of shrink.

EBSCOhost - printed on 2/13/2023 3:45 AM via . All use subject to https://www.ebsco.com/terms-of-use

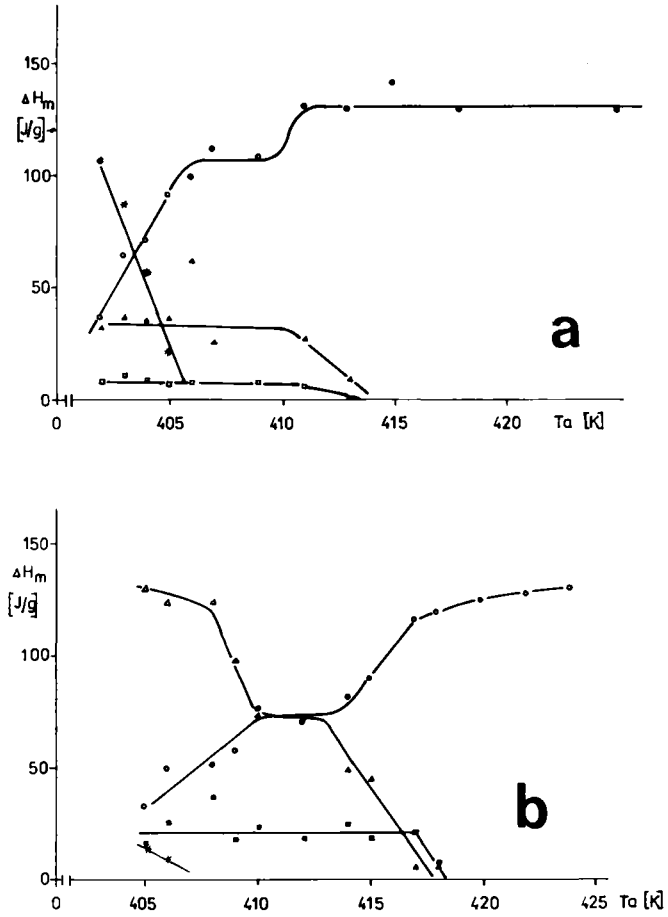

Fig. 6. Peak shares in the second melting process:
a) shrinking material
b) fixed material;
o - low temperature melting peak (first peak, Fig. 4),
* - second melting peak,
Δ - third melting peak,
□ - high temperature melting peak.

The last peak is constant most of the melting interval and vanishes at temperatures which are about 6 K lower than maximum temperature of the last peak in first melting.

EBSCOhost - printed on 2/13/2023 3:45 AM via . All use subject to https://www.ebsco.com/terms-of-use

Conclusion

The step-like investigation of melting and recrystallization process has confirmed the dependence of various structural transformations from each other in surface grown fibers caused by high ordered material.
The differentiation of melting steps by means of DSC has to be completed by morphological investigations. Transformations of properties are interesting to record.
The results, we hope, can be used not only to dress the hair on surface grown fibers but to create them another hair-style.

References

1. Pennings, A.J., A. Zwijnenburg. 1979. J. Polymer Sci.: Polymer Phys. Ed. 17, 1011.

2. Hill, M.J., P.J. Barham, A. Keller. 1980. Colloid & Polymer Sci. 258, 1023-1037; 1981. Colloid & Polymer Sci. 259, 335 to 341; 1983. Colloid & Polymer Sci. 261, 721-735.

EBSCOhost - printed on 2/13/2023 3:45 AM via . All use subject to https://www.ebsco.com/terms-of-use

EFFECT OF THE ADDITION OF POLYGLYCOL ON THE MELT CRYSTALLIZATION OF POLYPROPYLENE

Ch. Bechev
Higher Institute of Chemical Technology, 8 Kl. Ohridski Str., Sofia 1156, Bulgaria

J. Mishinev
Dimitar Dimov Chemical Works, Jambol 8600, Bulgaria

Introduction

In a previous paper (1) the authors demonstrated the effect of ε-caprolactam on the melt crystallization of polypropylene. It is known that lactones and lactams of fatty amino acids are widely used as dispersing agents in the production of spin dyed polypropylene fibres (2). It is interesting to study the crystallization behaviour of polypropylene-polyglycol blends (3). Information about the mechanism of crystallization of polypropylene containing additives is very important from the technological point of view.
The aim of this work is to study in detail the crystallization kinetics of polypropylene-polyglycol blends.

Experimental

Our studies were conducted on commercial isotactic polypropylene (Hercules) with melt index 14 g/min. Polyglycol-2000 was used as an additive. The concentration of polyglycol was varied in the range of 0 up to 2%. The blend samples were of very high homogeneity. Each sample was heated from ambient temperature up to 488 ± 5K in the molten state for 10 minutes. The operations were carried out under nitrogen. Then the sample was subsequently transferred to the calorimetric cell. It was necessary to check whether any degradation of polyglycol took place at this temperature. Differential thermal analysis and thermogravimetry of the

Morphology of Polymers
© 1986 Walter de Gruyter & Co., Berlin · New York - Printed in Germany.

EBSCOhost - printed on 2/13/2023 3:45 AM via . All use subject to https://www.ebsco.com/terms-of-use

blends were performed for this purpose, showing that the additive was stable at the experimental temperatures.
Isothermal crystallization studies were carried out using a calorimeter of own design based on a variation of Calvet (4). The response time of the calorimeter, t_c, was 50 s. The melting point, T_m, of the blends studied after crystallization at isothermal conditions was determined by differential scanning calorimetry (DSC) using an apparatus DSM-2M (USSR). Thermomechanical measurements of glass temperature, T_g, of the samples studied were performed on apparatus UIP (USSR) at a heating rate of 1 deg/min.

Results and Discussion

Experimental data for isothermal crystallization of blends studied were analysed in terms of Avrami´s equation (5):

$$\ln\left(1 - \frac{x}{x_\infty}\right) = Kt^n \qquad (1)$$

where x is the degree of crystallinity after time t; x is the equilibrium degree of crystallinity; K is the crystallization rate constant and n is a dimensionless exponent depending on the type of nucleation and the geometry of the crystalline growth. The relative degree of crystallinity x/x_∞ = a referred to the state of equilibrium and was calculated from the ratio S_t/S_∞, where S_t is the area under the corrected exotherm according to the theory of Calvet´s calorimeter (4) up to time t and S_∞ is the total area under the experimental exotherm.
Plots of $\ln[-\ln(1-a)]$ against $\ln(t)$ for pure polypropylene at several temperatures are presented in Fig. 1 and those for the samples containing 1.0 and 2.0% polyglycol in Figs 2 and 3, respectively.
Half-time of crystallization, $t_{0.5}$, and kinetic parameters n and k, calculated by the least squares method are summarized in Table 1.
As can be seen from data obtained the Avrami exponent n was close to 3 at high temperature and decreased with decreasing the temperature of crystallization. According to Godovsky (6) it can be

EBSCOhost - printed on 2/13/2023 3:45 AM via . All use subject to https://www.ebsco.com/terms-of-use

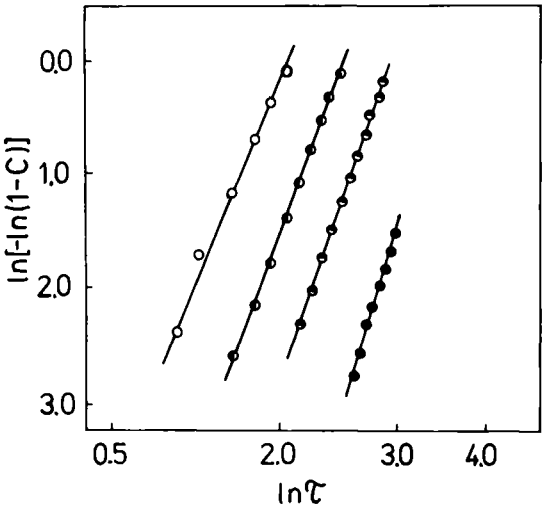

Fig. 1. Crystallization isotherm of polypropylene in Avrami coordinates: o 411 K; ◐ 413 K; ◒ 415 K; ● 417 K.

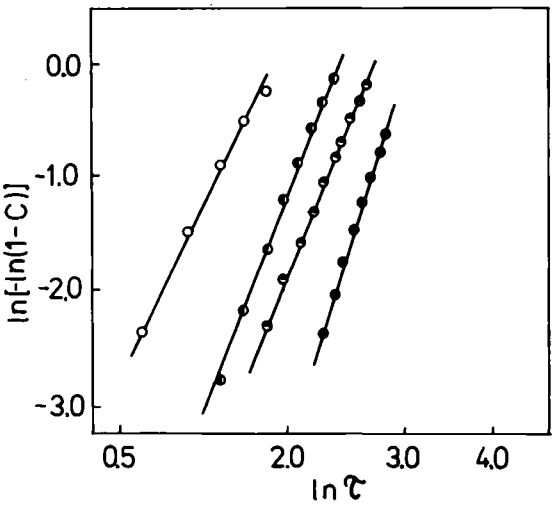

Fig. 2. Crystallization isotherms of polypropylene containing 1.0% polyglycol: o 411 K; ◐ 413 K; ◒ 415 K; ● 417 K.

EBSCOhost - printed on 2/13/2023 3:45 AM via . All use subject to https://www.ebsco.com/terms-of-use

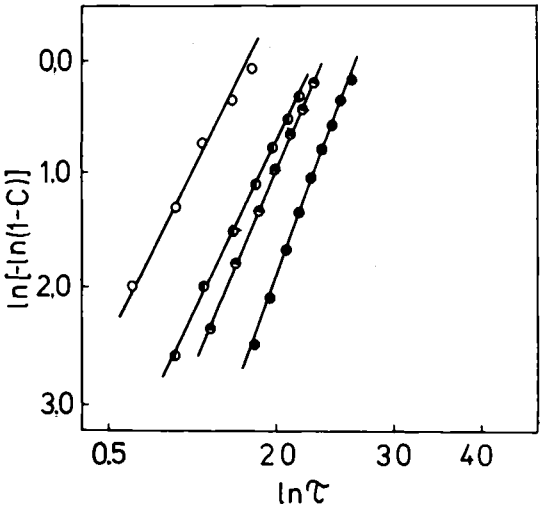

Fig. 3. Crystallization isotherms of polypropylene containing 2.0% polyglycol; o 411 K; ◐ 413 K; ◓ 415 K; ● 417 K.

Table 1. Half-time of Crystallization ($t_{0.5}$, min), Avrami Exponent (n) and Crystallization Rate Constant (K) as a Function of Temperature and Polyglycol Content

T	0.0% PG			1.0% PG			2.0% PG		
K	$t_{0.5}$	n	lnK	$t_{0.5}$	n	lnK	$t_{0.5}$	n	lnK
411	7	2.4	5.0	6	2.0	3.7	5	1.8	3.2
413	12	2.7	6.9	10	2.7	6.4	8	2.1	4.9
415	18	2.9	8.6	14	2.9	6.4	10	2.3	5.6
417	32	3.2	11.3	19	3.1	9.6	13	2.6	7.4

concluded that there is a homogeneous nucleation in general. On the other hand, there is still the possibility for heterogeneous nucleation to occur at lower crystallization temperature. Moreover, the crystallization rate definitely increases in the presence of polyglycol. Therefore we conclude that the interpretation of crys-

EBSCOhost - printed on 2/13/2023 3:45 AM via . All use subject to https://www.ebsco.com/terms-of-use

tallization kinetics of the polypropylene-polyglycol blends using only Avrami´s equation (1) does not give a clear picture. The surface free energies could be calculated from the chemical nucleation theory (7) and assuming that the crystallization in the samples investigated in general occurs on homogeneous crystal nuclei and is controlled by the secondary surfacial nucleation. The required modification (8) of the nucleation and growth theory has been employed. According to Hoffman and Lauritzen the following equation relating bulk crystallization rate can be presented:

$$(1/n)\ln(K) = \text{constant} + [\ln \theta_o \exp(-\Delta G^*/RT) - (4b_o/k\Delta h_m)(\sigma.\sigma_e)(T_m^o/T\Delta T)] \quad (2)$$

where b_o is the monomolecular thickness, $\theta_o \exp(-\Delta G^*/RT)$ is the jump rate at the interface region, Δh_m is the heat of crystallization per unit volume of crystal, k is the Boltzman constant, σ and σ_e are the lateral and end (chain-folded) surface free energies, respectively, T_m^o is the equilibrium melting point, and $\Delta T = T - T_m^o$ is the supercooling. Using the approach suggested by Wunderlich (7) in conjunction with the expression of Williams, Landel and Ferry it can be shown that $\Delta G^* = \Delta G_\eta = 4.12\times10^3 T/(51.6+T-T_g)$, where ΔG_η is the free energy of activation at supercooled liquid-growth nucleation interface. Hence plotting the relationship $1/n.\ln K + \Delta G_\eta/kT$ versus $T_m^o/T.\Delta T$; the free energy of the formation of secondary nuclei, ΔG^{**}, which is proportional to the product $4b_o/k\Delta h_m)\times(\sigma.\sigma_e)$, which is given by the slope of the straight line. The results of this work have revealed that T_g is constant for all samples studied, the T_g determined by thermomechanical measurement being 260 ± 0.5 K. Similar values has been reported by Grebowicz et al.(9). Therefore it can be concluded that according to the W-L-F equation the effect of the polyglycol on the viscosity of polypropylene melt is probably not large.

DSC measurements were used to determine the latent heat of crystallization, ΔH_c of the samples studied giving a value of (92 ± 2) J/g. T_m^o was determined by the relationship between observed melting point and crystallization temperature (6). The value of T_m^o was

EBSCOhost - printed on 2/13/2023 3:45 AM via . All use subject to https://www.ebsco.com/terms-of-use

found 460.5 K, which was in agreement with results obtained by other authors (10).
For the calculation of Δh_m and σ we accepted the following expressions (6):

$$\Delta h_m = \rho . \Delta H_c \qquad \sigma = \beta . b_o . \Delta h_m \tag{3}$$

and values $b_o = 6.56 \times 10^{-10}$ m. $\rho_c = 950$ kg/m^3 (11), $\beta = 0.1$ (6). The resulting values of ΔG^{**} and σ_e for the blends containing 0.0, 1.0 and 2.0 polyglycol are summarized in Table 2.

Table 2. Free Energy of the Formation of Secondary Nuclei (ΔG^{**}), Chain-folded Surface Free Energy (σ_e), Work of Chain Folding (q) and Critical Secondary Nuclei Size (ℓ^*) as a Function of Polyglycol Content

PG content %	$\Delta G^{**} \times 10^{-3}$ J/mol	$\sigma_e \times 10^3$ J/m^2	$q \times 10^{-3}$ J/mol	$\ell^* \times 10^{10}$ m
0.0	22.3	49.8	21.5	123.2
1.0	18.9	42.1	18.2	104.2
2.0	16.0	35.6	15.3	88.1

The following expressions were used to calculate work of chain folding q and critical secondary nuclei size ℓ^*, using the data obtained for σ_e, at crystallization temperature of 417 K (7):

$$q = 2A_o\sigma_e \qquad \ell^* = 2\sigma_e T_m^o / \Delta h_m \rho_c . \Delta T \tag{4}$$

It can be seen that the presence of polyglycol in polypropylene leads to a decrease in the surface free energy σ_e resulting a decrease in work of chain folding q. The decrease in σ_e causes a decrease in the energy barrier for secondary nucleation, ΔG^{**}, therefore, leads to a decrease in critical secondary nuclei size ℓ^*. Similar results were obtained previously (1) for investigations on the crystallization of polypropylene-ε-caprolactam system. Therefore it can be concluded that polyglycol can be used as a dispersing agent in the production of spin-dyed polypropylene

EBSCOhost - printed on 2/13/2023 3:45 AM via . All use subject to https://www.ebsco.com/terms-of-use

fibres. The acceleration of crystallization of polypropylene containing small amounts of polyglycol can be explained by the decrease in the energy barrier for secondary nucleation. There are still possibilities though previously discounted that there is an increase in the number of heterogeneous nuclei with decreasing temperature of crystallization.

References

1. Bechev, Ch., J.Mishinev. 1985. Polymer Communication. 26, 118.
2. Zverev, M.P. 1976. In: Karbotsepnye Volokna (K.E.Perepelkin, ed.), Khimiya, Moscow, p. 567-569.
3. Bechev, Ch., J.Michinev, K.Dimov. 1981. In: Preprints of 3rd International Symposium on Man-Made Fibres (E.P.Krasnov and J.V.Glaskovski, eds), Vol. 1, Kalinin, USSR, p. 54.
4. Calvet, E., H.Prat. 1956. Microcalorimetrie. Librairies de l´Academie de Médecine, Paris.
5. Avrami, M. 1939. J.Chem.Phys. 7, 1103.
6. Godovski, Yu.K. 1976. Teplofizicheskie Metody Issledovaniya Polymerov, Khimiya, Moscow.
7. Wunderlich, B. 1976. Macromolecular Physics, Part 2: Crystal Nucleation, Growth, Annealing. New York.
8. Hofman, D., J.Laurietzen. 1961. J.Res.NBS: Phys.Chem. 66A, 297.
9. Grebowicz, J., S.F.Lau, B.Wunderlich. 1984. J.Polym.Sci., Polym.Symp. 71, 19.
10. Wunderlich, B. 1980. Macromolecular Physics, Vol. 3, Crystal melting. Academic, New York.
11. Van Krevelen, D.W. 1972. Properties of Polymer Correlation with Chemical Structure. Elsevier Publ., New York.

EBSCOhost - printed on 2/13/2023 3:45 AM via . All use subject to https://www.ebsco.com/terms-of-use

EBSCOhost - printed on 2/13/2023 3:45 AM via . All use subject to https://www.ebsco.com/terms-of-use

THE STUDY OF CRYSTALLISATION BY TSD METHOD

R. Bakule, J. Nedbal, P. Štrof
Department of Polymer Physics, Faculty of Mathematics and Physics, Charles University
V Holešovičkách 2, 180 00 Praha 8, Czechoslovakia

Introduction

In this article are shown experimental results of thermally stimulated depolarization (TSD) currents on samples of natural and synthetic rubbers. The measurement was done at a temperature from 150 K to 300 K at a constant cool down and warmed up rate corresponding to 0.067 K/s. On the whole there has been observed 5 TSD peaks. These peaks are resulting from various molecular mechanisms. Our efforts were directed to possibilities in the use of TSD method to study crystallization of polymers.

Experimental

TSD method was used for crystallization of rubbers. The measurements were carried out on natural and natural deproteinised cis 1,4-polyisoprene, synthetic Ziegler-type polyisoprene SKI - 3 with content of cis-conformation 96 % and on synthetic polyisoprene prepared through lithium catalysis (IR-305) with content of cis-conformation 92 %. The samples has been hot-pressed at 400 K for an hour and their parts (1 mm thick and 30 mm in diameter) were placed in a three-electrode condenser with a smaller measuring electrode of 20 mm in diameter. The measuring condenser enabled definable temperature changes, e.g. to warm up and cool down the samples at a constant rate and to stabilize any selected temperature.
Measured samples were cooled down to the chosen temperature from the interval of 240 K to 260 K and an electric field with intensity of 2 MV/m was applied. The samples were let at this temperature for a certain time selected ahead as to increase their crystallinity.

Morphology of Polymers
© 1986 Walter de Gruyter & Co., Berlin · New York - Printed in Germany.

EBSCOhost - printed on 2/13/2023 3:45 AM via . All use subject to https://www.ebsco.com/terms-of-use

Then the samples were cooled down to 150 K with a constant rate. At this temperature the electrodes were short-circuited over the picoammeter. The depolarization current with several peaks was measured while the samples were warmed up with a constant rate.

Results

Five relaxation peaks α, λ_1, λ_2, λ_3, ρ were detected in the TSD spectrum of natural rubber. The peak marked ρ is caused by

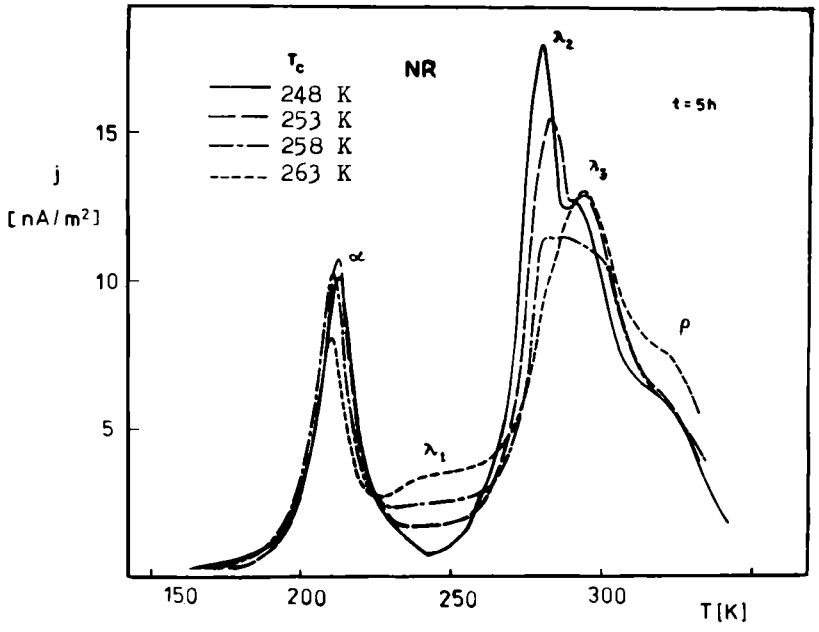

Fig.1. TSD of natural rubber at tempering time of 5 hours.

a space charge polarisation and it is outside our interest. We tried to reduce its influence upon the current peaks localised at lower temperatures. The α-peak at the lowest temperatures corresponds to the main transition region. We focus our attention to the two intermediate peaks denoted λ_1 and λ_2. The current λ_1 and λ_2 peaks are localised at 250 K and 280 K respectively and in both cases their magnitude is influenced by the temperature

EBSCOhost - printed on 2/13/2023 3:45 AM via . All use subject to https://www.ebsco.com/terms-of-use

history of the sample. Considerable changes in the height of

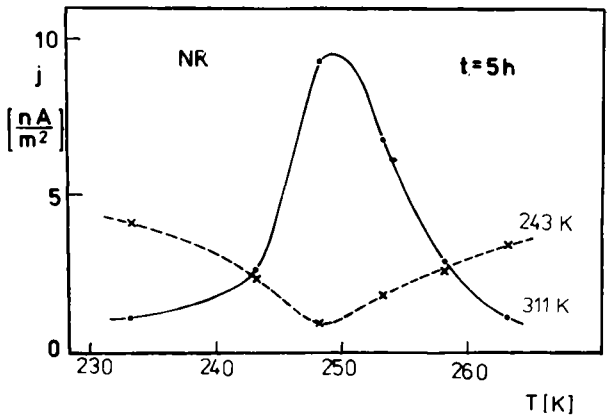

Fig.2. The temperature dependence of the height of λ_1 and λ_2 peaks. Tempering time 5 hours.

both peaks are shown in Fig.2 in the temperature dependence at constant tempering time (5 hours). The largest changes were observed at the temperature 248 K. At this temperature the rate of crystallization of natural rubber reaches the highest value (1).

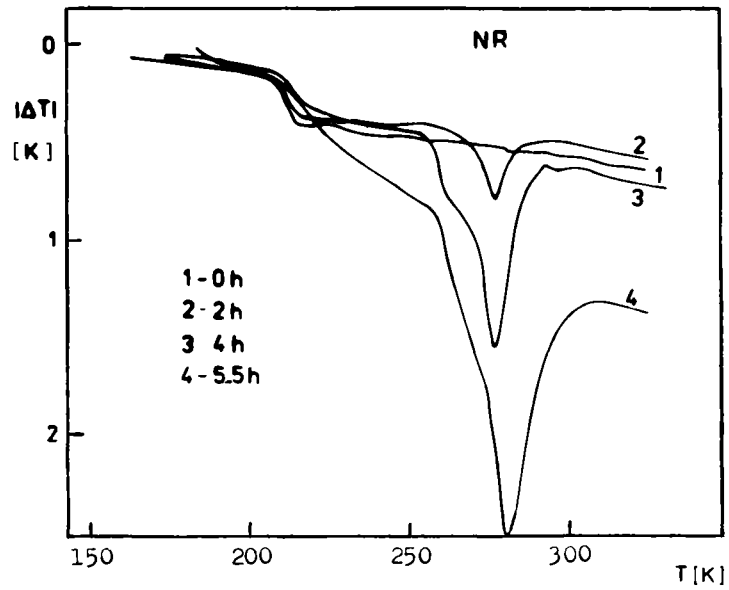

Fig.3. DTA of natural rubber. Tempering time up to 5.5 hours at 248 K.

EBSCOhost - printed on 2/13/2023 3:45 AM via . All use subject to https://www.ebsco.com/terms-of-use

The λ_1 peak diminishes with the time of stay at 248 K, the λ_2 peak increases. The height of α peak decreases only a little.

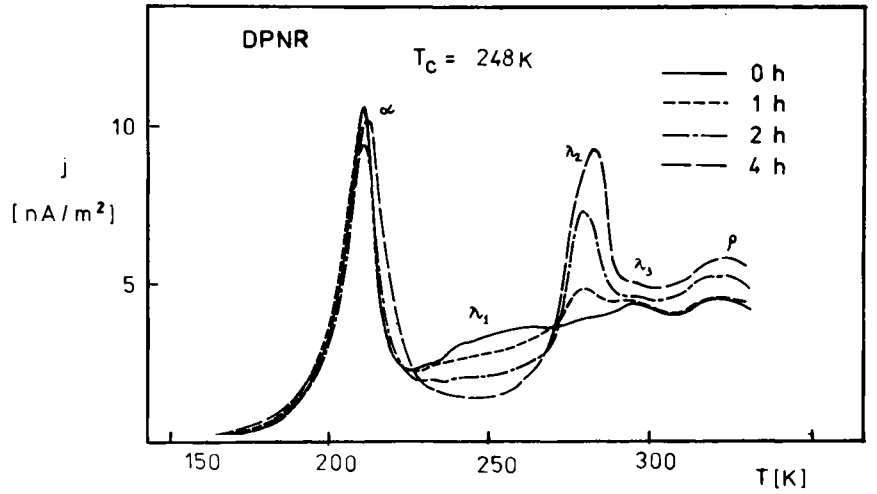

Fig.4. TSD of deproteinised natural rubber. Tempering time at 248 K up to 4 hours.

We assume that the experimental results can be explained by the crystallization of samples. This opinion is also supported by differential thermal analysis (DTA). The experimental results are shown in Fig.3. There one can observe an expressive characteristic endothermic peak at 281 K. The height of this peak rises in dependence on the tempering time in the same way as the height of the λ_2 peak observed by TSD method. The higher the crystallinity degree of rubber, the lower the number of monomer units in the amorphous part of the sample. This is the reason of a slight decrease in the height of α peak.

The λ_2 peak is therefore connected with the release of monomer units movement in crystalline regions. This peak is relatively high though the crystallinity degree is rather low, because the current is brought about by the depolarisation of oriented domains. The λ_1 peak is supposed to be caused by depolarisation of locally arranged regions, too. As the height of this peak decreases when the crystallinity degree rises, we suppose that this locally arranged regions act as crystallization nucleuses. Their number decreases with the rise in degree of crystallinity.

The height of the λ_3 peak is not depending on the thermal

EBSCOhost - printed on 2/13/2023 3:45 AM via . All use subject to https://www.ebsco.com/terms-of-use

history of the sample. The changes in the height of this peak are caused only by reciprocal ovelapping with the λ_2 peak. This relaxation region has also been examined by frequency measurements

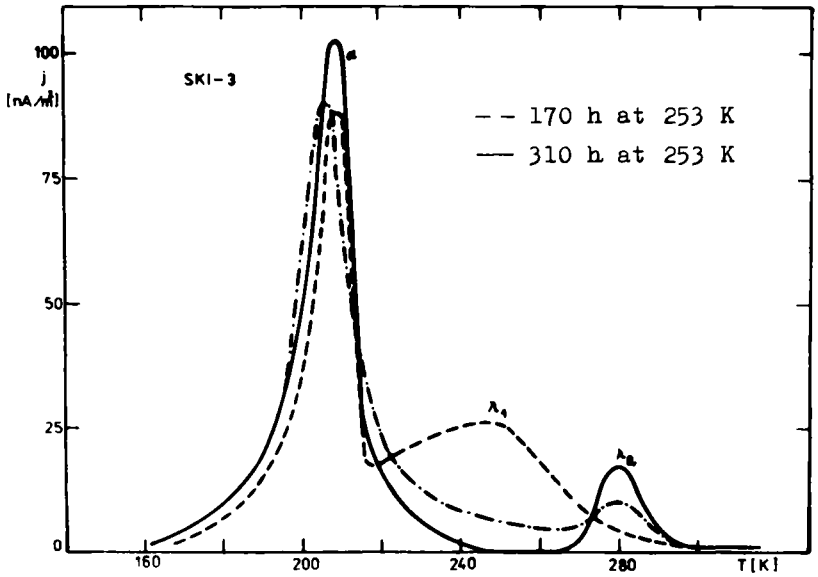

Fig.5. TSD of synthetic rubber SKI-3. Tempering time 0, 170 and 310 hours at 253 K.

of a complex permittivity (2). We assume that the said peak is caused by orientation of protein groups in bond with the ends of polyisoprene chains. This explanation is supported also by the fact that the peak λ_2 is much lower at experiments with deproteinised rubber (Fig.4) and at experiments with synthetic rubbers λ_2 peaks were not observed at all (Figs.5,6).
The shape of TSD spectrum of deproteinised rubber (Fig.4) is analogous to the spectrum of natural rubber (Fig.1). Only the height of the λ_2 peak is changing rather slowly with tempering time.
Crystalline λ_2 peaks of synthetic rubbers SKI-3 and IR-305 were not observed at tempering times up to 10 hours. For this reason the samples were tempered in an ice-box at a temperature of 253 K. The tempering time was substantially longer and the sample without applied electric field (field missing) can cause a certain error in the height of the λ_2 peak. After tempering, individual

EBSCOhost - printed on 2/13/2023 3:45 AM via . All use subject to https://www.ebsco.com/terms-of-use

samples were warmed up in a measuring condenser to the temperature of 283 K, then the electric field applied and the samples measured. The λ_2 peak was at first observed at sample SKI-3 after 170 hours tempering time. Sample IR-305 has shown λ_2 peak after 160 days of tempering time (Figs.5 and 6). The time dependence of the relative height of λ_2 peak is shown in Fig.7. Thus it is evident

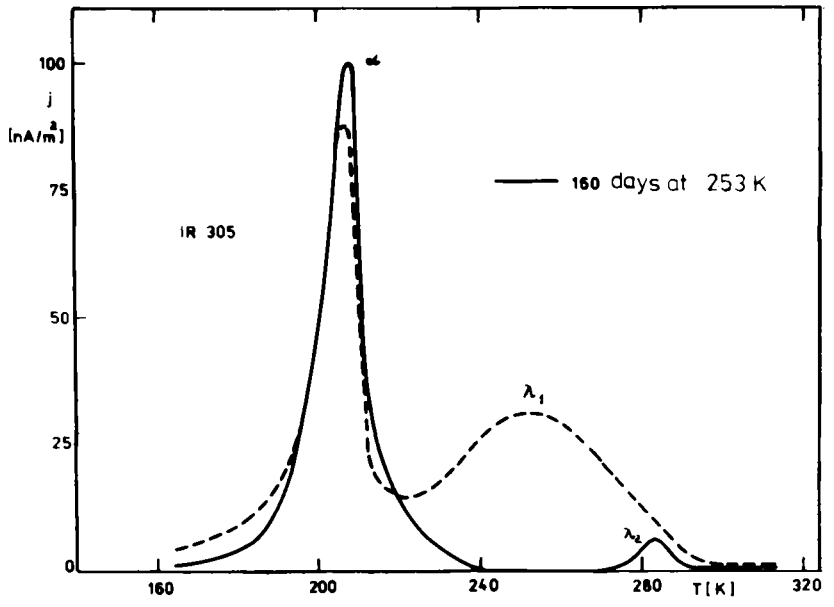

Fig.6. TSD of synthetic rubber IR-305. Tempering time 0 and 160 days at 253 K.

that the crystallization of synthetic rubbers is slower than that of natural rubber. The slowing down of the crystallization corresponds to the increase in the trans-conformation. This result is in a good agreement with the work (3). Our measurements show that the 1 % increase in the trans-conformation content causes the growth of the above mentioned temperation time by half an order of magnitude.

EBSCOhost - printed on 2/13/2023 3:45 AM via . All use subject to https://www.ebsco.com/terms-of-use

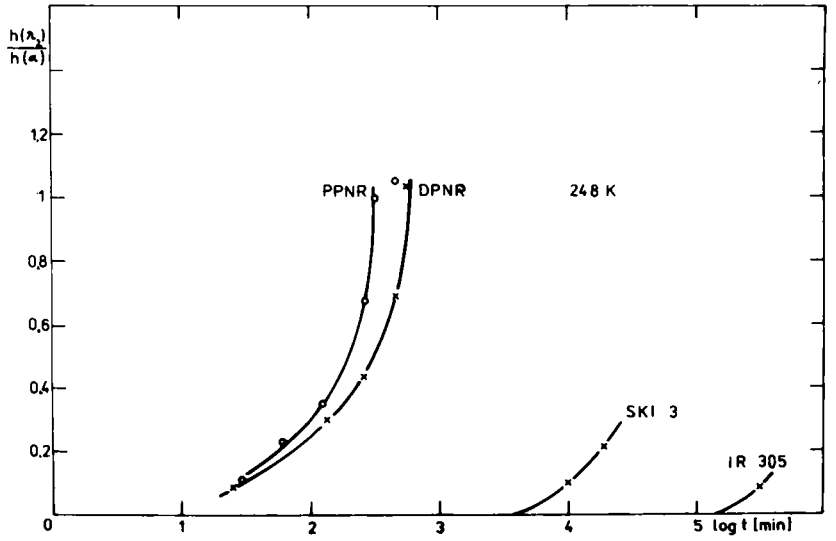

Fig.7. The time dependence of the relative height of λ_2 peak for all the measured samples.

References

1. Wunderlich, B. 1973. Macromolecular Physics I, II. Academic Press, New York and London.

2. Bakule, R., B. Stoll. 1977. Dielektrische Messungen an Naturkautschuk im Gebiet der Hochtemperaturrelaxation. Colloid Polymer Sci. 255, 1176-2414.

3. Andrews, E.H., P.J. Owen, A. Sinh. 1971. Microkinetics of lamellar crystallization in a Long chain polymer. Proc. Roy. Soc. Lond. A. 324, 79-97.

EBSCOhost - printed on 2/13/2023 3:45 AM via . All use subject to https://www.ebsco.com/terms-of-use

EBSCOhost - printed on 2/13/2023 3:45 AM via . All use subject to https://www.ebsco.com/terms-of-use

QUANTUM INTERPRETATION OF THE PRIMARY AND SECONDARY NUCLEATION RATE OF POLYMERS

A.M.ATANASSOV
Department of Chemistry, Higher School of Electrical and Mechanical Engineering, 1156 Sofia, Bulgaria

Introduction

In order to explain the temperature dependence of the lamella thickness of polymers some theories appeared: those of Fischer and Peterlin (1-4), Hoffman (5-8), Frank and Tosi (9), Price (10), and Lindenmeyer (11-13). However, only the kinetic theory of Hoffman has the indisputable advantage to be in position to describe mathematically the temperature dependence of the polymer crystal growth rate and the rate of primary nucleation.
According to Turnbull and Fisher the equilibriun rate of homogeneous (primary) nucleation in a supercooled bulk phase may be written as (14):

$$I = I_o \times exp(-E_d/kT) \times exp(-\Delta F^*/kT) \qquad (1)$$

where: $I_o = N_a \cdot kT/h \times M_o \bar{V}$ (N_a -Avagadro's number; k-Boltzmann's constant; h-Plank's constant; T-the absolute temperature; M_o-molecular weight of a monomer unit of length l_o; $\bar{V}$-the specific volume of the supercooled liquid at the crystalization temperature).
The kinetic theory of secondary (2-D) nucleation controlled polymer crystal growth with chain folds (15) gave the expression:

$$G = G_o \times exp(-E_d/kT) \times exp(-\Delta F^{**}/kT) \qquad (2)$$

where G is the preexponential constant in $cm.s^{-1}$.

Morphology of Polymers
© 1986 Walter de Gruyter & Co., Berlin · New York - Printed in Germany.

EBSCOhost - printed on 2/13/2023 3:45 AM via . All use subject to https://www.ebsco.com/terms-of-use

In Eqs.(1-2) E_d is the transport activation energy. The empirical equation of Williams-Landel-Ferry (16) is most frequently used for the value of E_d (5, 7, 8):

$$E_d = 4120T/(C_2+T-T_g) \qquad (3)$$

Generally, $C_2 = 51.6°C$. In order to match the experimental data some workers change the value of C_2. The main purpose of this work is to consider how the quantities I_o and G_o depend on polymer nature and thus,as a first approximation, the fixed value $C_2=51.6$ in Eq.(3) will be used. ΔF^* and ΔF^{**} in Eqs.(1-2) are free energies of formation of a primary (homogeneous) and secondary(2-D) chain-folded nucleus, respectively. Assuming square cross-section of the primary nucleus with a length of l^* and width a^*, it has been found (15) that:

$$\Delta F^* = 32\sigma^2 \times \sigma_e/(\Delta f_o)^2 \qquad (4)$$

where the quantities σ, σ_e are the works required to form a unit area of the latteral surface (σ) and the fold surface (σ_e).The free energy ΔF^{**} of formation of a secondary chain-folded nucleus (SCFN) is given by nucleation theory as (15, 17):

$$\Delta F^{**} = 4b_o \sigma \times \sigma_e/(\Delta f_o) \qquad (5)$$

(b_o-the thickness of the newly deposited layer).
In Eqs. (4-5) Δf_o is the free energy difference between the sub-cooled liquid and the crystal. For the value of Δf_o approximations could be used in the form (18):

$$\Delta f_o = \Delta H_f^\circ(T_m^\circ - T)/T_m^\circ = \Delta H_f^\circ \Delta T/T_m^\circ \qquad (6)$$

or

$$\Delta f_o = \Delta H_f^\circ \Delta T \times T/(T_m^\circ)^2 \qquad (7)$$

(ΔH_f°-melting enthalpy in ergs per cm^3; ΔT-under cooling T_m°-equilibrium melting temperature).
The isothermal primary nucleation and growth rate data enable us to calculate: 1) the values of σ and σ_e, thus describing the primary nucleation and crystallization energetics; 2) the values of I_o and G_o from the intercepts on the logI (logG) coordinate of the plots logI vs $1/T(\Delta T)^2$ and logG vs $1/T\Delta T$, respectively.

EBSCOhost - printed on 2/13/2023 3:45 AM via . All use subject to https://www.ebsco.com/terms-of-use

Analysis of the Available Data for G_o of the Linear Chain Molecules

Hoffman and Mandelkern (5, 19-21) assumed that G_o should be essentially constant for all the linear chain molecules crystallizing from a bulk, independently of their chemical nature, molecular weight, etc. It is established that this assumption is not supported by the crystallization data of some polymers (22-24). In the equation for the nucleation controlled crystal growth rate:

$$\log G = (\log G_o - E_d/2.3kT) - 4b_o \sigma \sigma_e T_m^\circ / 2.3 \times \Delta H_f^\circ kT\Delta T \quad (8)$$

the crystallization rate G is controlled much more strongly by the variation with temperature (in the temperature range $T_{max} < T < T_m^\circ$) of the term involving $(4b_o.\sigma.\sigma_e.T_m/2.3k\Delta H_f T.\Delta T)$ than that involving $(E_d/2.3kT)$. The variation with temperature of the last term (using WLF Eq.) is low and $(E_d/2.3kT)$=const. could be set. Then, if G_o is really a constant value a lower crystallization rate G should be expected for those polymers crystallizing with higher σ_e values. Fig. 1 and 2 summarize the data available for G_o and G_{max} respectively (G_{max} is the maximum value of G on the logG vs T plot). There is a great dispersion in the plots $\log G_o$ vs σ_e and $\log G_{max}$ vs σ_e, most probably due to the indirect influence of many other factors. Nevetheless, it is easy to notice that the values of G_o und G_{max} tend to increase with raising σ_e. Thus, the reason for the higher crystallization rates of some polymers could not be the lower values of σ_e but the higher values of G_o, i.e. G_o could not be regarded as a constant for all polymers. As a first attempt to explain the different value of G_o, Hoffman proposed (5, 7, 8):

$$G_o = b_o \, i_o = b_o \times kT_{max}/h \quad (9)$$

($i_o = kT_{max}/h$ is the "standard" secondary nucleation frequency). Following Eq. (9) G_o is expected to increase with increasing b_o. In fact, $\log\log G_o$ decreases strongly with increasing b_o value (Fig.3). Even double increase in T_{max} would not compensate for ten order reduction of $G_o \times \log G_{max}$ vs b_o plot (Fig.4) appears to be similar. $\log G_o$ and $\log G_{max}$ depend also on the chain unit length ℓ_o ($\ell_o = c_o/n$; c_o is the unit cell dimension in direction of the molecular axes;

EBSCOhost - printed on 2/13/2023 3:45 AM via . All use subject to https://www.ebsco.com/terms-of-use

n-number of the repeating chain units entering the cell; for PE $n=2$). For polymers with short chain units (PE, POM, PP, PS, Se) $\log G_o$ takes values from 0 (for s-PP) to 11 (for POM) or even 12 (for PE) at constant l_o value. The quantity $\log G_{max}$ takes values from - 6,4 (for PS) up to -2 (for PE). For polymers with longer chain units (PETF, PA-6, PA-66, PES etc.) the values of $\log G_o$ and

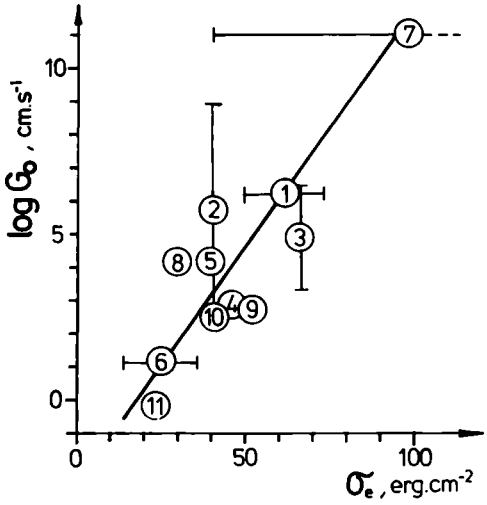

Fig.1. $\log G_o$ versus the fold surface free energy σ_e.

1) Polyethylene (PE); 2) i-Polypropylene (i-PP); 3) Nylon-6 (PA-6); 4) Nylon-66 (PA-66); 5) Polychlorotrifluoroethylene (PCTFE); 6) Polystyrene (PS); 7) Polyoxymethylene (POM); 8) Polyoxypropylene (POP); 9) Polyethylene succinate (PES); 10) Polyethylene oxide (PEO); 11) s-Polypropylene (s-PP).

$\log G_{max}$ increase with increasing l_o.
Having made a detailed analysis, Privalko (25) suggested the use of $G_o \exp(\Delta S/k)$ in Eq.(8) instead of G_o (ΔS is formally the activation entropy of the transition). He classified all linear polymers into two groups. The first group shows higher values of G_o (PE, PCTFE, PA-6, PA-66, POM, Se, PE succinate) and he established that for polymers just mentioned

$$\Delta S \approx 3\Delta S_m^\circ \qquad (10)$$

(ΔS_m° is the melting entropy for a mol of unit bonds in the main

EBSCOhost - printed on 2/13/2023 3:45 AM via . All use subject to https://www.ebsco.com/terms-of-use

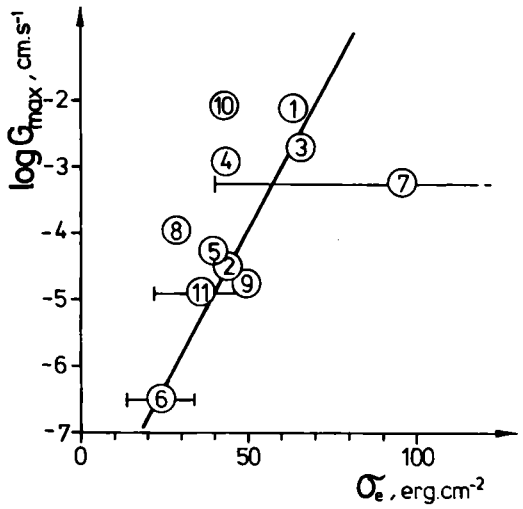

Fig.2. logG_{max} vs the fold surface free energy. Polymers:same as in Fig.1.

chain).

Eq.(10)predicts that the "growing segment" of the polymers in the first group should be essentially larger than 3 bonds of the main carbon chain.

For the second group (PP, PS, POP):

$$\Delta s \leq \Delta s_m^* \qquad (11)$$

i.e. segments, commensurable in length with a length of a unit bond will precipitate on the growing face.

These empirical conclusions of Privalko are in good agreement with the theoretical evaluations of Lauritzen and Hoffman (26) predicting existence of two different crystallization mechanisms, the first of them being realized by gradual precipitation of large chain segments (regime I kinetics, higher values of G_o); in the second one (regime II kinetics, lower value of G_o) multiple surface nuclei (with a smaller chain length) begin to occur on the substrate because of the rapid increase in the secondary nucleation rate i, associated with the larger undercooling ΔT.

Actually, PE (at lower ΔT), classified by Privalko in the first group, crystallizes following regime I crystallization kinetics while PS (polymer of the second group) crystallizes according to

EBSCOhost - printed on 2/13/2023 3:45 AM via . All use subject to https://www.ebsco.com/terms-of-use

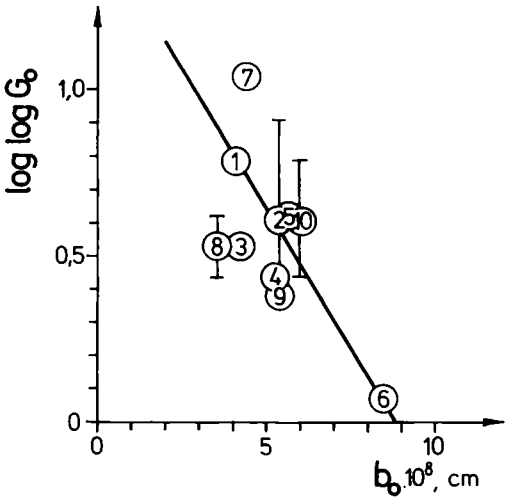

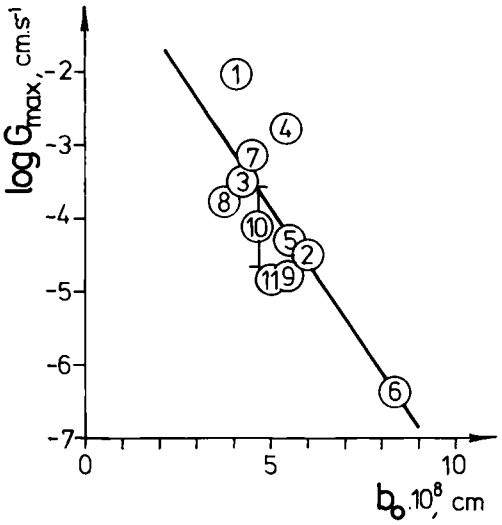

Figs.3 and 4. log logG_o(Fig.3) and logG_{max}(Fig.4) versus the monolayer thickness b_o. The figures are as per Figs. 1 and 2.

EBSCOhost - printed on 2/13/2023 3:45 AM via . All use subject to https://www.ebsco.com/terms-of-use

regime II kinetics. The explanation of Privalko is that the higher value of the free volume (and higher mobility, respectively) of the first group of polymers causes higher crystallization rate while for the second group the crystallization process should be hampered (25).

The overall conclusion of the crystallization rate data analysis given here, can be summarized as follows:

1) G_o depends strongly on the individual properties of a specific polymer.

2) Eq.(9)does not give a reasonable explanation of the differences in the G_o value.

3) It is to be anticipated that G_o is a function of the flexibility and mobility of the chain molecules.

Quantum Hypothesis and Secondary Nucleation Rate

During crystallization of a substance, the quantity ΔH_m° is liberated which is the enthalpy difference between the amorphous (H_{am}) and the crystalline (H_{cr}) state:

$$\Delta H_m^\circ = (H_{am} - H_{cr}) \qquad (12)$$

The amorphous state of a monomer unit at a given crystallization temperature below the melting point can be regarded as an excited state. The monomer unit transition energy

$$\Delta E_1 = \Delta H_m^\circ / N_a \qquad (13)$$

(as a first approximation the energy distribution of the units in melt state is neglected) could in principle be emitted as a quantum of energy:

$$\Delta E_1 = h\nu \qquad (14)$$

(ν is the frequency of radiation).

If ζ monomer units crystallize simultaneously:

$$\Delta E_\zeta = \zeta . \Delta H_m^\circ / N_a \qquad (15)$$

EBSCOhost - printed on 2/13/2023 3:45 AM via . All use subject to https://www.ebsco.com/terms-of-use

the radiation frequency will be:

$$\vartheta_\zeta = \frac{\zeta . \Delta H_m}{N_a \, h} \qquad (16)$$

Recalling that the quantity G_o is a frequency factor in Eq. (2), an attempt will be made to derive an equation for that value, using radiation frequency ϑ_ζ (Eq.(15)).

The preexponential factor is in fact the maximum possible value of growth rate G under hypothetical conditions in which no transport limitations do exist $(exp(-E_d/kT)=1)$ and because of the infinite undercooling $exp(-\Delta F^{**}/kT)=1$.

In practice this is a simple extrapolation of the secondary nucleation-controlled part of the log$G$ vs $(1/T\Delta T)$ plot for $(1/T.\Delta T) \to 0$.

Thus G_o represents the maximum rate of forming critical secondary (2D) chain-folded nucleus (CSCFN).

As noted in refs.(7, 8, 14) CSCFN dimensions are:

$$a^{**} = 2\sigma/\Delta f_o \qquad \ell^{**} = 2\sigma_e/\Delta f_o \qquad (17)$$

Then the volume of the SCFN V^{**} is:

$$V^{**} = b_o \, a^{**} \, \ell^{**} = 4b_o \, \sigma . \sigma_e/(\Delta f_o)^2 \qquad (18)$$

The length L^{**} of a molecular chain with a cross-section $(a_o . b_o)$ forming the SCFN:

$$L^{**} = b_o \, a^{**} \, \ell^{**}/(a_o . b_o) = 4\sigma . \sigma_e/a_o(\Delta f_o)^2 \qquad (19)$$

(a_o-the width of the molecular chain in the folding plane).

The number ζ^{**} of chain units of c_o length, forming SCFN:

$$\zeta^{**} = L^{**}/c_o = 4\sigma . \sigma_e/a_o \times c_o (\Delta f_o)^2 \qquad (20)$$

If ζ monomer units (making an effective segment length deposited for a unit of time) crystallize simultaneously, the number of the crystallization acts to form SCFN is:

$$\zeta^{**}/\zeta = 4\sigma . \sigma_e/\zeta \times a_o c_o (\Delta f_o)^2 \qquad (21)$$

Assuming that the time for crystallizing of ζ monomer units is determined by the radiation frequency

$$t^\circ_\zeta = 1/\vartheta_\zeta = N_a \, h/\zeta \times \Delta H^\circ_m \qquad (22)$$

EBSCOhost - printed on 2/13/2023 3:45 AM via . All use subject to https://www.ebsco.com/terms-of-use

the time for realizing (ζ^{**}/ζ) crystallization acts to form SCFN will be as follows:

$$t^{**}_{NUCL} = \zeta^{**}\ t^{\circ}_{\zeta}/\zeta = \frac{4\sigma\ \sigma_e\ N_a\ h}{\zeta^2\ a_o\ c_o.\Delta H^{\circ}_m\ (\Delta f_o)^2} \qquad (23)$$

The maximum secondary nucleation rate (i_o) could be written as:

$$i_o = 1/t^{**}_{NUCL} = \frac{\zeta^2\ a_o\ c_o.\Delta H^{\circ}_m\ (\Delta f_o)^2}{4\sigma\ \sigma_e\ N_a\ h} \qquad (24)$$

Taking into account Eqs.(7) and (9), the preexponential factor will be given by the following equation:

$$G_o = \frac{\zeta^2\ a_o\ b_o\ c_o.\Delta H^{\circ}_m\ (\Delta H^{\circ}_f\ T.\Delta T)^2}{4\sigma\ \sigma_e\ N_a\ h\ (T^{\circ}_m)^4} \qquad (25)$$

The quantity ζ as well as the unit cell dimensions, the quantities ΔH°_m, ΔH°_f, $(\sigma.\sigma_e)$, T°_m and ΔT in Eq. (25) are strongly individual characteristics of a particular polymer. Moreover, G_o appears to be dependent on the temperature and undercooling directly and indirectly by the temperature dependence of ζ.

In order to assess how much G_o is influenced by the temperature and undercooling we will turn now to some numerical values. We choose to measure ΔT from $T^{\circ}_m = 414K$ and utilize the following values of the parameters in Eq.(25): $a_o = 4.55\times10^{-8}$ cm; $b_o = 4.11\times10^{-8}$ cm; $c_o = 2.54\times10^{-8}$ cm; $\Delta H^{\bullet}_f = 2.87\times10^{9}$ erg.cm^{-3}; $\Delta H^{\bullet}_m = 7.54\times10^{10}$ erg.mol^{-1}; (parameters for PE), $(\sigma.\sigma_e) = 250$ erg.^{2}.cm^{-4} and two values of ζ ($\zeta = 1$ and $\zeta = 12$).

Fig. 5 shows that at higher temperatures of crystallization T_c (lower undercoolings, respectively) the quantity G_o depends strongly on ΔT. At lower T_c (higher ΔT) G_o is an approximately constant value. It is of great significance that G_o depends on ΔT in the nucleation-controlled temperature range. If this fact is not taken into account, higher values of $(\sigma.\sigma_e)$ product will be obtained from the crystallization experiments. On Fig. 5 the term $E_d/2.3kT$ according to WLF equation (at $T_g = 153K$) is also plotted, as well as the temperature dependence of log$G$ (at $\zeta = 1$ and $\zeta = 12$ and $\sigma.\sigma_e = 250$ erg.^{2}cm^{-4}) following the provisional estimate:

$$\log G = \log[\zeta^2 (T.\Delta T)^2 \times 0.254/\sigma\times\sigma_e] - 905/(T-101.4) - 31233.\sigma.\sigma_e/T^2\times\Delta T \qquad (26)$$

EBSCOhost - printed on 2/13/2023 3:45 AM via . All use subject to https://www.ebsco.com/terms-of-use

Fig. 6 and 7 illustrate the theoretical curves $\log G$ vs T at $\zeta = 1$ and $\zeta = 12$, respectively. For $(\sigma.\sigma_e)$ product some directly observed values (27, 28) were used:

1) $\sigma.\sigma_e = 250\ erg^2.cm^{-4}$ (27),

2) $\sigma.\sigma_e = 952.5\ erg^2.cm^{-4}$ (28),

as well as a higher value:

3) $\sigma.\sigma_e = 1905\ erg^2.cm^{-4}$,

Varying the values of the quantity ζ and the product of the surface free energies $(\sigma.\sigma_e)$, many theoretical curves $\log G$ vs T for PE were estimated and compared with the experimental ones of Hoffman (14). As an example, the experimental curve for the sample, designated as 30.6K (weight average molecular weight 30600) is plotted on Fig. 8. The calculated absolute growth rates fall close to the experimental values of Hoffman when ζ and $(\sigma.\sigma_e)$ take the following values:

1) For the higher temperature range $(T>400K)$ in which the equation of regime I crystallization kinetics is valid (14), at $\zeta = 12$ and $(\sigma.\sigma_e) = 550\ erg^2.cm^{-4}$

2) For the lower temperature range $(T<400K)$ - at $\zeta = 1$ and $(\sigma.\sigma_e) = 375\ erg^2.cm^{-4}$ (if one accepts that ΔF^{**} is determined by Eq.(5). If however, this portion of the curve is identified as regime II crystallization kinetics, the free energy of formation of SCFN is (14):

$$\Delta F^{**} = 2\sigma\ \sigma_e.b_o/(\Delta f_o) \qquad (27)$$

Then the theoretical curve is consistent with the experimental one at $\zeta = 1$ and $(\sigma.\sigma_e) = 750\ erg^2.cm^{-4}$.

Hoffman obtained $(\sigma.\sigma_e) = 1198\ erg^2.cm^{-4}$ for the crystallization plot at $T>400K$ and $(\sigma.\sigma_e) = 1272\ erg^2.cm^{-4}$ at $T<400K$.

It is easily understood that the discrepancies between the values of $(\sigma.\sigma_e)$ calculated in the present work and those of Hoffman are obviously due to the fact that the temperature dependence of G_o is taken into account here.

Recently, Hoffman extended the kinetic nucleation theory of chain folding including the effect of reptation (curvilinear diffusion) (29, 30). In the equations of the developed theory the retardation parameter β_g is involved. This quantity represents the resistance in the melt of the molecule being pulled onto the substrate:

EBSCOhost - printed on 2/13/2023 3:45 AM via . All use subject to https://www.ebsco.com/terms-of-use

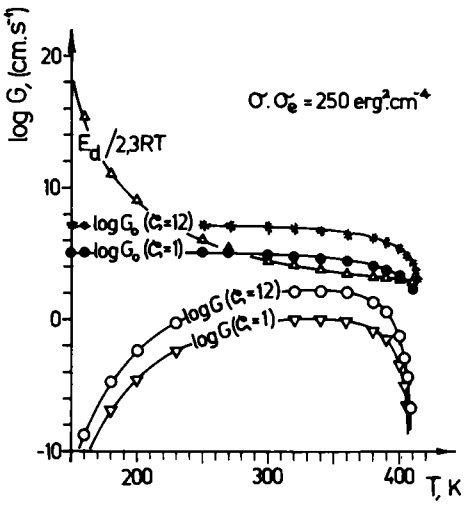

Fig.5. The terms $\log G_o$ *(at* ζ*=1 and* ζ*=12),* $E_d/2.3kT$ (acc. to WLF Eq.) and $\log G$ *(at* ζ *= 1* and ζ *= 12,* acc. to Eq.(26)).

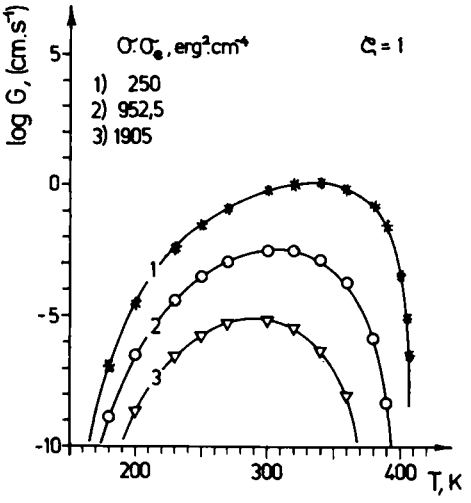

Fig. 6. Theoretical curves $\log G$ vs T at ζ *= 1* and different values of $(\sigma.\sigma_e)$ product given in the figure.

EBSCOhost - printed on 2/13/2023 3:45 AM via . All use subject to https://www.ebsco.com/terms-of-use

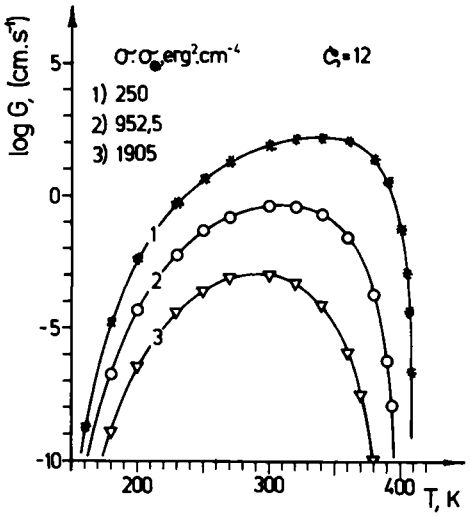

Fig. 7. Theoretical curves log$G$ vs T at $\zeta = 12$ and different values of $(\sigma.\sigma_e)$ given in the figure.

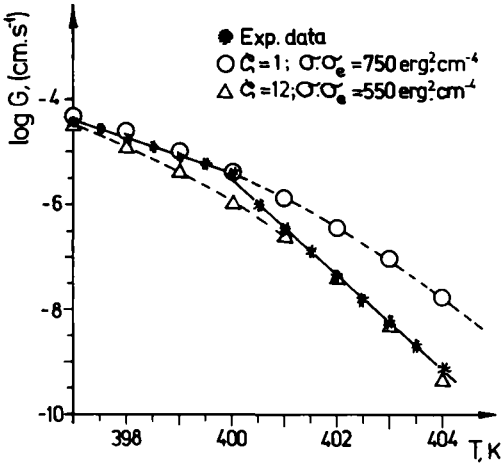

Fig. 8. Experimental data of Hoffman (14) (*) and theoretical curves at $\zeta = 12$ and $(\sigma.\sigma_e) = 550\ erg^2.cm^{-4}$ (higher temperature range, Δ) and $\zeta = 1$ and $(\sigma.\sigma_e) 750\ erg^2.cm^{-4}$ (lower temperature one, o).

EBSCOhost - printed on 2/13/2023 3:45 AM via . All use subject to https://www.ebsco.com/terms-of-use

$$\beta_g = \left(\frac{\delta}{n}\right)\left(\frac{kT}{h}\right) \exp\left(-Q_d^*/RT\right) \qquad (28)$$

where: Q_d^* - the activation energy for the reptation process; (1/n) is intended to represent the effect of chain length on the reptation rate in the melt. As a first approximation Hoffman accepted $\underline{n}$ to be the number of monomer units corresponding to the molecular weight of the fraction under consideration, followed by the assumption that $\underline{n}$ is mostly the "slack" portion of the chain, only; the quantity δ (originally designated as $\underline{k}$) is a numerical factor, constructed to represent the number of chain units act as an effective segment length in the liquid state.

In order to combine the basic idea of the present work with the brilliant theory of Hoffman an attempt is made to modify his equations as follows:

1) The quantity δ is set equal to the quantity ζ, because ζ was also designated to be the number of chain units, crystallizing simultaneously. 2) The quantity $\underline{n}$ should more realistically be considered as the number of monomer units ζ^{**} in a melt chain with a length enough to form SCFN (Eq.(20)). Thus, temperature dependence of this quantity is involved, reflecting the actual physical picture (the lower the temperature of crystallization, the shorter "slack" portion of the reptating chain). 3) Finally, the frequency factor, derived in the present work (Eq.(16)) can be used instead of the quantity (kT/h).

Then the retardation factor becomes:

$$\beta_g = \frac{\zeta^2 . \Delta H_m^\circ \; a_o \; c_o \; (\Delta f_o)}{4 N_a \; h \; \sigma \; \sigma_e} \times \exp\left(-Q_d^*/RT\right) \qquad (29)$$

Using Eq. (29) numerical calculations were made for the preexponential factors of the three regimes of crystallization kinetics, and compared with G_o values of Hoffman (30). Because of lack of space they will be considered separately in a further work. But it should be pointed-out here, that δ-value in Hoffman's theory (Eq.(28)) is determined by equalizing the theoretical value of G_o to the experimental one, i.e. δ can be regarded as an adjusting parameter, whilst the quantity ζ in Eq. (29) could be calculated by measuring the wavelength of the discrete radiation emitted by the crystallizing polymer.

EBSCOhost - printed on 2/13/2023 3:45 AM via . All use subject to https://www.ebsco.com/terms-of-use

Proceeding in the same way, a brief treatment of the preexponential factor I_o of the primary nucleation (PN) rate equation will be given in this section.
The critical primary *(3-D)* chain-folded nucleus (PCFN) dimensions are (7, 8, 14):

$$a^* = b^* = 4\sigma/\Delta f_o, \qquad \ell^* = 4\sigma_e/\Delta f_o \tag{30}$$

and it's volume V^* is:

$$V^* = a^* b^* \ell^* = 64\sigma^2 \sigma_e/(\Delta f_o)^3 \tag{31}$$

The volume of a monomer unit in crystalline state is approximately

$$V = a_o b_o c_o \tag{32}$$

and the number ζ^* of monomer units, forming the PCFN will be:

$$\zeta^* = 64\sigma^2 \sigma_e/(a_o b_o c_o)(\Delta f_o)^3 \tag{33}$$

If ζ monomer units is assumed to crystallize simultaneously, the number of crystallization acts to form PCFN is:

$$\zeta^*/\zeta = 64\sigma^2 \sigma_e/(\zeta a_o b_o c_o)\times(\Delta f_o)^3 \tag{34}$$

The time t°_ζ for crystallization of ζ monomer units simultaneously is given by Eq. (22). The time $(t^*_{NUCL} = \zeta^* t^\circ_\zeta/\zeta)$ to accomplish the whole PCFN becomes:

$$t^*_{NUCL} = \frac{64 N_a h \sigma^2 \sigma_e}{\zeta^2 . \Delta H^\circ_m (a_o b_o c_o)(\Delta f_o)^3} \tag{35}$$

Then PN frequency in the volume $V^* = a^* b^* I^*$

$$I^*_o = 1/t^*_{NUCL} = \frac{\zeta^2 . \Delta H^\circ_m (a_o b_o c_o)(\Delta f_o)^3}{64 N_a h \sigma^2 \sigma_e} \tag{36}$$

PN frequency I_o in the volume of one mol of monomer

EBSCOhost - printed on 2/13/2023 3:45 AM via . All use subject to https://www.ebsco.com/terms-of-use

units in melt state at the crystallization temperature ($V_{mol} = M_o \bar{V}$) will be expressed as follows:

$$I_o = I_o^* V_{mol}/V^* = \frac{\zeta^2 M_o \bar{V} \Delta H_m^\circ (a_o b_o c_o)(\Delta f_o)^6}{4096 N_a . h . \sigma^4 . \sigma_e^2} \qquad (37)$$

(I_o in nuclei.mol^{-1}.s^{-1})

The corresponding equation for PN rate in nuclei.cm^{-3}.s^{-1}:

$$I_o = \frac{\zeta^2 . \Delta H_m^\circ (a_o b_o c_o) (\Delta f_o)^6}{4096 N_a h \sigma^4 \sigma_e^2} \qquad (38)$$

and in nuclei.g^{-1}.s^{-1}, respectively:

$$I_o = \frac{\zeta^2 \bar{V} . \Delta H_m^\circ (a_o b_o c_o)(\Delta f_o)^6}{4096 N_a . h . \sigma^4 . \sigma_e^2} \qquad (39)$$

Having replaced I_o in Eq.(1) with that of Eq. (37) and utilizing WLF Eq. for E_d value and Eq.(7) for the crystallization driving force Δf_o, some theoretical curves log$I$ vs T have been plotted following the provisional equation:

$$\log I = \log \left[\frac{\zeta^2 (T.\Delta T)^6 \times 1.59 \times 10^{14}}{\sigma^4 \sigma_e^2} \right] - \left(\frac{905}{T-101.4} \right) - \frac{3.92 \times 10^8 \times \sigma^2 . \sigma_e}{T^3 (\Delta T^2)} \qquad (40)$$

Fig. 9 depicts log$I$ vs T (K) curves at $\zeta = 12$ and ($\sigma^2 \sigma_e$) values, written there.

For the purpose of comparison with the experimental data of Koutsky et al. (31) we will use now the numerical values of the PE constants, cited in that work: $b_o = 4.11 \times 10^{-8}$ cm; $\Delta H_f^\circ = 2.48 \times 10^9$ erg.cm^{-3}; $\Delta H_m^\circ = 6.515 \times 10^{10}$ erg.mol^{-1}; $T_m^\circ = 416K$; $T_g = 153K$ [$E_d/kT = 2081/(T-101.4)$] and for Δf_o the approximation in the form:

$$\Delta f_o = \frac{\Delta H_f \, T.\Delta T}{(T_m^\circ)^2} \times \frac{2T}{(T_m^\circ + T)} \qquad (41)$$

For an average temperature $T_{av} = 360K$ the factor $2T/(T_m^\circ + T) = 0.928$.

EBSCOhost - printed on 2/13/2023 3:45 AM via . All use subject to https://www.ebsco.com/terms-of-use

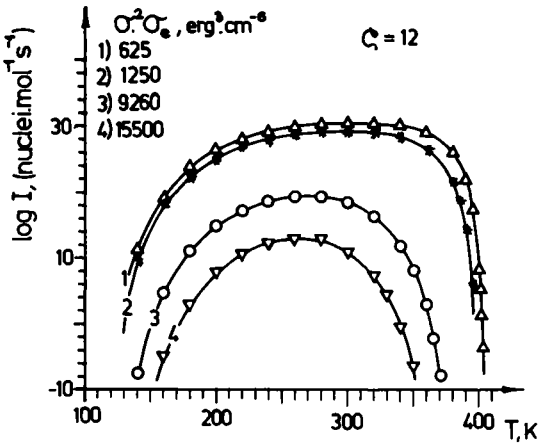

Fig.9. log$I$ vs T curves for PN in PE at $\zeta = 12$ and four values of $(\sigma^2.\sigma_e)$; the first being the smallest possible one, the other three being directly observed values (27, 31, 32).

I_o is replaced by Eq.(38). This yields:

$$\ln I = \ln \left[\frac{\zeta^2 (T\Delta T)^6 \times 1.03 \times 10^{12}}{\sigma^4 \sigma_e^2} \right] - \frac{2081}{(T-101.4)} - \frac{1.31 \times 10^9 \times \sigma^2 \sigma_e}{T^3 (\Delta T)^2} \qquad (42)$$

(I in nuclei, $cm^{-3}.s^{-1}$).
Because of the very narrow temperature range investigated by Koutsky et al. a set of $(\zeta; \sigma^2.\sigma_e)$ values fit their experimental data $\ln I$ vs $1/T^3(\Delta T)^2$: 1) $\zeta = 1$; $\sigma^2.\sigma_e = 4870$; 2) $\zeta = 2$; $\sigma^2.\sigma_e = 5020$; 3) $\zeta = 3$; $\sigma^2.\sigma_e = 5090$; 4) $\zeta = 4$; $\sigma^2.\sigma_e = 5160$; 5) $\zeta = 6$; $\sigma^2.\sigma_e = 5250$; 6) $\zeta = 8$; $\sigma^2.\sigma_e = 5310$; 7) $\zeta = 12$; $\sigma^2.\sigma_e = 5400\ erg^3.cm^{-6}$.

The slopes of the theoretical plots differ from pair to pair but within an error of 15%, the error of the slopes in ref.(31) remains constant. In a wide temperature range only one of these pairs would be recognized as the actual one, but in the present case this was impossible. An alternative way to identify the actual

EBSCOhost - printed on 2/13/2023 3:45 AM via . All use subject to https://www.ebsco.com/terms-of-use

pair (ζ, σ^2, σ_e) does exist: measuring of the wavelength emitted from the crystallizing polymer will fix ζ value and $\sigma^2.\sigma_e$ value, respectively.

Although the experimental measurements are not yet made, it is evident from the foregoing comparison that in all cases for $\sigma^2.\sigma_e$ product we obtain lower values than those calculated by Koutsky et al. ($\sigma^2.\sigma_e = 6800\ erg^3.cm^{-6}$).

The differences in ($\sigma^2.\sigma_e$) values for PN are too small compared with the differences in ($\sigma.\sigma_e$) values obtained for the secondary nucleation-controlled crystallization. The reason is that the latter process proceeds close to the equilibrium temperature while the former occurs at lower temperatures where the preexponential factor depends rather weekly on ($T.\Delta T$) value.

Conclusions

Quantum hypothesis has been applied to develop expressions for the preexponential factors I_o and i_o of the primary and secondary nucleation rate equations. The result is that I_o and i_o (respectively, G_o, the pre-exponential factor of the secondary nucleation-controlled crystallization rate) depend on ζ^2, the square number of chain units crystallizing simultaneously ($\zeta.c_o$ being the chain segment length). Both quantities (I_o, i_o) contain some material constants of the specified polymer as well, and what is very important, they depend strongly (i_o particularly) on the value of ($T.\Delta T$). The expression for G_o derived in the present work provides a basis for explanation of the different values of this quantity, available in literature for polymers crystallizing at low indercoolings, i.e. PE, POM, PA-6, etc. In terms of the present treatment, the very high values of G_o for PE (G_o ranging up to 10^{12} cm.s^{-1}) and POM ($G_o = 10^{11}\ cm.s^{-1}$) are considered to be a result of: 1) a higher value of ζ, and 2) the extrapolation of the log$G$ vs ($1/T.\Delta T$) plot being made in the temperature range close to the equilibrium temperature ($\Delta T \to 0$) where G_o depends strongly on ΔT (Fig. 5).

EBSCOhost - printed on 2/13/2023 3:45 AM via . All use subject to https://www.ebsco.com/terms-of-use

An example confirming the above said is that for regime I crystallization kinetics Hoffman's data for crystallization of PE (Fig. 8) are consistent with the theoretical curve log$G$ vs T according to Eq.(26) at $\zeta = 12$ and $\sigma.\sigma_e = 550\ erg^2.cm^{-4}$ which for $T = 300K$ and $\Delta T = 114K$ gives the value $G_o = 7.8\times10^7\ cm.s^{-1}$ instead of $G_o = (5\times10^{13}/n_z)\ cm.s^{-1}$ of Hoffman. Using a specialized very sensitive equipment the wavelength of radiation, emitted by the crystallizing polymer could be measured, thus obtaining an experimental ζ value for the temperature range under investigation. As a result the actual value of the surface free energy product $(\sigma.\sigma_e)$ could be calculated from the crystallization data which value is not influenced by the temperature dependence of G_o.

References

1. Fischer, E.W. 1958.Z.Naturforsch. A14, 548.
2. Peterlin,A. 1960. J.Appl. Phys. 31, 1934.
3. Peterlin, A.,E.W. Fischer. 1960. Z.Physic. 159, 272.
4. Peterlin,A.,E.W.Fischer, C.Reinhold. 1962.J.Chem.Phys.37,1403.
5. Hoffman,J.D. 1964. SPE Trans. 4,315.
6. Hoffman,J.D., J.I.Lauritzen, Jr., E. Passaglia, G.S.Ross, L.J. Frolen, J.J. Weeks. 1969. Kolloid Z.Z. Polymere 231, 564.
7. Hoffman,J.D., J.J.Weeks. 1962.J.Chem. Phys. 37, 1723.
8. Gornick,F., J.D.Hoffman. 1966. Ind. Eng. Chem. 58, 41.
9. Frank,F.C., M.Tosi. 1961. Proc.Roy.Soc.A, London 263, 323.
10. Price,F.P. 1961. J.Polym.Sci. 54, 540.
11. Lindenmeyer,P.H. 1967. J.Chem.Phys. 46, 1902.
12. Lindenmeyer,P.H. 1967.J.Polym.Sci.:Polym.Symp.20, 145.
13. Lindenmeyer,P.H., J.M.Peterson. 1968.J.Appl.Phys. 39, 4929.
14. Turnbull,D., J.C.Fisher. 1949. J.Chem.Phys.17, 71.

EBSCOhost - printed on 2/13/2023 3:45 AM via . All use subject to https://www.ebsco.com/terms-of-use

15. Hoffman,J.D., J.I.Lauritzen,Jr. 1961. J.Res.Natl.Bur.Stand. 65A, 297.

16. Williams,M.L., R.F.Landel, J.D.Ferry. 1955. J.Amer.Chem. Soc. 77, 3701.

17. Lauritzen,J.I. Jr., J.D.Hoffman. 1960. J.Res.Natl.Bur. Stand. 64A, 73.

18. Hoffman,J.D. 1958. J.Chem. Phys. 29, 1192.

19. Mandelkern,L., N.L. Jain, H.Kim. 1968. J.Polym.Sci.,p.A-2, 6, 165.

20. Kim, H., L.Mandelkern. 1968. J.Polym. Sci.p.A-2, 6, 695.

21. Devoy, C., L.Mandelkern. 1969. J.Polym. Sci.p.A-2, 7, 1883.

22. Boon,J., G.Challa, D.W.Van Krevellen. 1968. J.Polym.Sci. p.A-2, 6, 1791.

23. Berghmans,H., E.Lanza, G.Shets. 1973. J.Polym.Sci.:Polym. Phys. Ed. 11, 87.

24. Lemstra, P.J., J.Postma, G.Challa. 1974. Polymer 15, 757.

25. Privalko, V.P. 1978. In: Structural peculiarities of polymers. Naukova dumka Kiev, p. 32.

26. Lauritzen,J.I., Jr., J.D. Hoffman. 1973. J.Appl. Phys.44,4340.

27. Wunderlich,B. 1976. Macromolecular Physics: Crystal Nucleation, Growth, Annealing.Academic Press, New York-San Francisco-London.

28. Holland,V.F., P.H.Lindenmeyer. 1962. J.Polym.Sci.57, 589.

29. Hoffman,J.D. 1982. Polymer 23, 656.

30. Hoffman,J.D. 1983. Polymer 24, 3.

31. Koutsky,J.A., A.G.Walton, E.Baer. 1967. J.Appl.Phys. 38, 1832.

32. Cormia,R.L., F.P.Price, D.Turnbull.1962. J.Chem.Phys. 37, 1333, following B.Wunderlich (27).

EBSCOhost - printed on 2/13/2023 3:45 AM via . All use subject to https://www.ebsco.com/terms-of-use

EBSCOhost - printed on 2/13/2023 3:45 AM via . All use subject to https://www.ebsco.com/terms-of-use

QUANTUM INTERPRETATION OF THE SECONDARY NUCLEATION RATE AND THE REPTATION RATE THEORY - A COMPARATIVE STUDY

A.M. ATANASSOV

Department of Chemistry, Higher School of Electrical and Mechanical Engineering, 1156 Sofia, Bulgaria.

Introduction

Recently, on the basis of the assumption that quanta are emitted from a crystallizing polymer, an expression has been derived for the preexponential factor of the secondary nucleation rate equation (1). Several years ago Hoffman extended the kinetic nucleation theory of chain folding including the effect of reptation (2,3)which also gave an expression for the preexponential factor of the secondary nucleation rate equation.
The aim of the present study is to compare both approaches stated above, using numerical calculations.

Results

Regime-III kinetics

Applying the equation for the total flux s_T, Hoffman obtained the following equation for the nucleation rate i' in regime-III crystallization:

Morphology of Polymers
© 1986 Walter de Gruyter & Co., Berlin · New York - Printed in Germany.

EBSCOhost - printed on 2/13/2023 3:45 AM via . All use subject to https://www.ebsco.com/terms-of-use

$$i' = S_T/(n_s\, a_o) = (N_o\, \beta_g\, P_i/n_s \times a_o) \times exp(-\frac{K_g^{III}}{T.\Delta T}) \qquad (1)$$

where: a_o is the width of the molecular chain in the folding plane; N_o - effective number of reacting species or effective occupation number of the ground (subcooled liquid) state:

$$N_o = (\bar{z}\, n_s) \times (C_n\, P_o) \qquad (2)$$

($\bar{z}.n_s$ is the number of monomer units on the growth front; n_s -number of available stems where crystallization on the substrate may begin; C_n - coordination number, $C_n \approx 4$; P_o - configurational path degeneracy; P_o takes on values of unity to upwards of 25 (2), and

$$P_i = kT/c_o \times b_o\, \sigma$$

Further in ref.(3): $c_o = 2\ell_u$ (ℓ_u is the length of the chain unit), and

$$K_g^{III} = 4b_o\, \sigma.\sigma_e\, T_m^\circ/\Delta H_f^\circ \times k \qquad (3)$$

In Eq.(3) b_o is the thickness of a monolayer; σ and σ_e are the latteral surface free energy and the fold surface free energy respectively; ΔH_f° - melting enthalpy of an infinite crystal in ergs per cm^3; k - Boltzmann's constant; T_m° - equilibrium melting temperature; $\Delta T = (T_m^\circ - T)$ - undercooling; T - crystallization temperature.

The retardation factor β_g(events.s^{-1}) is (2):

$$\beta_g = (\frac{\delta}{n}) \times (\frac{kT}{h}) \times exp(-E_d/kT) \qquad (4)$$

where:

(kT/h) is the frequency factor of the reptation process; n - number of monomer units in the dangling chain in the melt that is being reptated onto the crystal surface. As a conservative approximation Hoffman has taken n to be the number of monomer units corresponding to the molecular weight of the fraction under consideration, followed by the assumption that n is mostly the "slack" portion of the chain; δ is a numerical constant in the range of about 1 to 10, determined experimentally (2); E_d is the activation energy of the reptation process.

In order to relate the basic idea of the present work with the

EBSCOhost - printed on 2/13/2023 3:45 AM via . All use subject to https://www.ebsco.com/terms-of-use

Hoffman's reptation rate theory (2,3) an attempt is made to modify his retardation factor equation by forwarding a conception called "hot channel conception".

Low viscosity hot channel conception. It has been assumed that the energy of crystallization of ζ monomer units (making an effective chain segment):

$$\Delta E_\zeta = \zeta . \Delta H_m^\circ / N_a \qquad (5)$$

(N_a - Avogadro's number; ΔH_m° - melting enthalpy in ergs per mol) is liberated as a quantum of energy (4):

$$\Delta E_\zeta = h \vartheta_\zeta \qquad (6)$$

where:

h is Plank's constant; ϑ_ζ is the radiation frequency of the emitted quantum:

$$\vartheta_\zeta = \frac{\zeta . \Delta H_m^\circ}{N_a \; h} \qquad (7)$$

The emission process could be regarded as a two-stage one:

1) When the effective chain segment gets closer to the crystal surface its energy is lowered and the respective energy increment ΔE_ζ increases the energy (the effective temperature respectively) of the part of the molecule remaining in the amorphous phase thus causing energy redistribution in the whole molecule.

2) Emission of a quantum of energy from the whole amorphous part of the chain molecule looks like emission of an antenna. The latter process most probably occurs at the end of the ordering process. Thus, the time for emitting of the quantum could not be longer than the time for the chain segment crystallization. It could not also be shorter than the time for the crystallization of the chain segment, because at shorter time the energy ΔE_ζ is not yet completely pushed in the amorphous part of the chain. Then the time for crystallization of the chain segment could be set equal to the time for a quantum emission:

$$t_{CRYST} = 1/\vartheta_\zeta = N_a \; h/\zeta \times \Delta H_m^\circ \qquad (8)$$

and consequently instead of (kT/h) in Hoffman's Eq.(4) the radiation frequency ϑ_ζ could be used.

EBSCOhost - printed on 2/13/2023 3:45 AM via . All use subject to https://www.ebsco.com/terms-of-use

The emitted quantum is immediately absorbed from one of the amorphous molecules in the most neighbouring vicinity, thus raising its energy and its effective temperature, respectively. The subsequent quanta will raise the effective temperature of the other molecules surrounding the reptation one, which is pulling onto the growing surface. In this way a "hot channel" is formed in the vicinity of the crystallizing molecule with a radius of several molecular width distances. In the hot channel low viscosity conditions similar to the low viscosity conditions in a solution do exist (5), and they are regarded as the major cause for formation of adjacent re-entries preferentially in the crystallites. Futhermore, recalling that G_o is a quantity proportional to the maximum value of the secondary nucleation rate i_o, the quantity n in Eq.(4) should more realistically be considered as the number of monomer units ζ^{**} in a melt chain with a length enough to form a secondary chain-folded nucleus (SCFN). In ref.(1) it was shown that:

$$\zeta^{**} = 4\sigma\ \sigma_e / a_o \times (\Delta f_o)^2 \qquad (9)$$

Thus, temperature dependence of this quantity is involved, reflecting the actual physical picture in crystallization: at $T = T_m^\circ$ (zero undercooling ΔT), $\Delta f_o = 0$ and $\zeta^{**} \to \infty$; the lower the temperature of crystallization, the shorter the "slack" portion of the chain. Finally, the quantity δ, ranging from 1 up to 10 was originally constructed to represent the number of chain units acting as an effective segment length in the liquid state. In the terms of the present work:

$$\delta = \zeta \qquad (10)$$

Replacing the respective quantities in Eq. (4), a new form of the retardation factor β_g is obtained:

$$\beta_g^* = \frac{\zeta^2 . \Delta H_m^\circ\ a_o\ c_o\ (\Delta f_o)^2}{4 N_a\ h\ \sigma\ \sigma_e} \times exp(-E_d / kT) \qquad (11)$$

The driving force for crystallization Δf_o is given by (6):

$$\Delta f_o = \Delta H_f^\circ . \Delta T / T_m^\circ \qquad (12)$$

or by:

$$\Delta f_o = \Delta H_f^\circ\ T . \Delta T / (T_m^\circ)^2 \qquad (13)$$

EBSCOhost - printed on 2/13/2023 3:45 AM via . All use subject to https://www.ebsco.com/terms-of-use

Then the nucleation rate i' for regime-III crystallization kinetics will be:

$$i' = \frac{\zeta^2 \bar{z} C_n P_o kT.\Delta H_m^\circ (\Delta f_o)^2}{4 b_o N_a h \sigma^2 \sigma_e} \times exp(-E_d/kT) \times exp(-K_g^{III}/T.\Delta T) \quad (14)$$

and the crystal growth rate G, respectively:

$$G^{III} = b_o i' L' = b_o i' n_s' a_o \quad (15)$$

(n_s' - mean number of stems that are laid down in the "niche" adjacent to the newly nucleated stem (3); $L' = n_s'.a_o$ is the "effective" substrate length), or

$$G^{III} = \frac{\zeta^2 n_s' \bar{z} C_n P_o kT a_o.\Delta H_m^\circ (\Delta f_o)^2}{4\sigma^2 \sigma_e N_a h} \times exp(-E_d/kT) \times$$

$$\times exp(-K_g^{III}/T.\Delta T) \quad (16)$$

where:

$\bar{z} = l_g^*/c_o$ ($\bar{z}$ - the number of monomer units with length c_o each that go to make up the lamellar thickness l_g^*).
In Hoffman's work (3) $\bar{z} = 150$ because he accepted that $c_o = 1.27x10^{-8}$ cm. In our equations $\bar{z} = 75 (c_o = 2.54x10^{-8}$ cm, i.e. two chain units $-CH_2-$make a monomer unit).
Following Hoffman (3) for PE we will use the values: $(C_n P_o) = 100$; $n_s = 242$; $n_s' = 3$; $\sigma = 11.2$ $erg.cm^{-2}$; $\sigma_e = 50$ $erg.cm^{-2}$; $T_m^\circ = 414K$(7); $T_{av} = 353$ K; $\Delta T_{av} = 61K$; $M_o = 28$; density of the crystal $\rho_c = 1 g.cm^{-3}$; $a_o = 4.55x10^{-8}$ cm; $\Delta H_m^\circ = 7.54x10^{10}$ $erg.mol^{-1}$ (7); $\Delta H_f^\circ = 2.87x10^9$ $erg.cm^{-3}$.
Then for the preexponential factor G_o^{III}:

$$G_o^{III} = \frac{\zeta^2 n_s' \bar{z} C_n P_o kT a_o.\Delta H_m^\circ (\Delta H_f^\circ T.\Delta T)^2}{4\sigma^2 \sigma_e h N_a (T_m^\circ)^4} \quad (17)$$

the following provisional estimate is obtained:

$$G_o^{III} = \zeta^2 x 4.44x10^9 \ cm.s^{-1} \quad (18)$$

Hoffman found:

$$G_o^{III} = (6.2x10^{11}/n_z) \ cm.s^{-1} \quad (19)$$

With n_z ranging from 1900 (molecular weight $M_z = 26500$) to

EBSCOhost - printed on 2/13/2023 3:45 AM via . All use subject to https://www.ebsco.com/terms-of-use

$n_z = 7040 (M_z = 98500)$, G_o^{III} takes on values of:

$$G_o^{III} = 3.3 \times 10^8 \, cm.s^{-1} \tag{20}$$

to downwards of:

$$G_o^{III} = 0.88 \times 10^8 \, cm.s^{-1} \tag{21}$$

If the value $n^* = n_z = 150$ (n^* being the number of monomer units associated with the slack length) is used in Eq.19, then the value:

$$G_o^{III} = 4.13 \times 10^9 \, cm.s^{-1} \tag{22}$$

is obtained, which is close to the value:

$$G_o^{III} = 4.44 \times 10^9 \, cm.s^{-1} \tag{23}$$

found in this work at $\zeta = 1$. It is quite expectable that at low temperatures, at which regime-III kinetics is realized, the number of monomer units ζ, crystallizing simultaneously, will be extremely small, because of the higher viscosity (lower values of the diffusion coefficient, respectively), hampering the chain movement and rotation (8).

Regime-I kinetics

The corresponding quantities for regime-I are:

$$G^I = b_o \, i \, (n_s \, a_o) = G_o^I \times exp(-E_d/kT) \times exp(-K_g^I/T.\Delta T) \tag{24}$$

In the same way it is found that:

$$G_o^I = \frac{\zeta^2 \, \bar{z} \, n_s \, C_n P_o \, kT.\Delta H_m^\circ \, a_o \, (\Delta H_f^\circ \, T \, \Delta T)^2}{4\sigma^2 \, \sigma_e \, h \, N_a \, (T_m^\circ)^4} \tag{25}$$

Utilizing the following values of the parameters for regime-I crystallization of PE inEq.(25):$\Delta T_{av} = 6K$; $T_{av} = 408K$; $\bar{z} = 75$, one obtains:

EBSCOhost - printed on 2/13/2023 3:45 AM via . All use subject to https://www.ebsco.com/terms-of-use

$$G_o^I = \zeta^2 \times 5.87x10^9 cm.s^{-1} \qquad (26)$$

The length of a statistical segment of *PE* in a solution is $20x10^{-8}$ cm (about 8 monomer units of length $c_o = 2.54x10^{-8}$ *cm* each. In a subcooled melt at low undercoolings, at which regime-I crystallization kinetics equation is valid, this number should be higher. If we suppose that $\zeta = 12$, then:

$$G_o^I = 8.45x10^{11} cm.s^{-1} \qquad (27)$$

For this regime Hoffman has found:

$$G_o^I = 5x10^{13}/n_z \qquad (28)$$

Utilizing for $n^* = n_z = 150$ (Hoffman used $n = 150$, because he accepted for c_o the value $c_o = 1.27x10^{-8} cm$), Eq. (28) gives:

$$G_o^I = 3.33x10^{11} cm.s^{-1} \qquad (29)$$

This value is a little lower than the value $G_o^I = 8.45x10^{11} cm.s^{-1}$, obtained in present work.

Regime-II kinetics

The growth rate G^{II} in regime-II kinetics is expresses as (2): (2):

$$G^{II} = b_o(2i.g)^{0,5} = G_o^{II} \times exp(-E_d/kT) \times exp(-K_g^{II}/T.\Delta T) \qquad (30)$$

where:

$$G_o^{II} = \left(\frac{2kT\, a_o\, \Delta f_o}{c_o\, b_o\, \sigma^2}\right)^{0.5} \times \frac{(C_n P_o)^{0.5} \times \delta}{n} (kT/h)\, b_o(\bar{z})^{0.5} \times exp(-q/2kT) \qquad (30')$$

In Eq. (30) the quantity $q = 4900\ cal.mol^{-1}$ is the work of chain folding and the term $exp(-q/2kT)$ represents the retardation of the substrate completion process because of chain folds forming. Replacing in the same way the terms (kT/h), δ and n in Eq.30' with the quantities ϑ_ζ, ζ and ζ^{**}, respectively, we find that:

EBSCOhost - printed on 2/13/2023 3:45 AM via . All use subject to https://www.ebsco.com/terms-of-use

$$G_o^{II} = \frac{\zeta^2 (2a_o^3\ b_o\ c_o\ kT\ C_n P_o\ \bar{z})^{0.5}\ \Delta H_m^\circ\ (\Delta f_o)^{2.5}}{4\sigma^2\ \sigma_e\ h\ N_a} \times exp(-q/2kT) \qquad (31)$$

The use of the above mentioned values for the quantities $(C_n P_o)$, σ, σ_e, T_m°, ΔH_m°, ΔH_f° as well as the values $T_{av} = 394K$, $T_{av} = 20K$, $n_s = 242$ yields:

$$G_o^{II} = \zeta^2 \times 6.43x10^4\ cm.s^{-1} \qquad (32)$$

Hoffman's experimental data for PE with an weight average molecular weight 30600 (9) are consistent with the theoretical curve for regime-II crystallization only if one assumes $\zeta = 1$.
Then the value of G_o^{II} is:

$$G_o^{II} = 6.43x10^4\ cm.s^{-1} \qquad (33)$$

For the same regime Hoffman has obtained:

$$G_o^{II} = (3.34x10^7/n_z)\ cm.s^{-1} \qquad (34)$$

and if gives $G_o^{II} = 2.23x10^5\ cm.s^{-1}$ at $n_z = n^* = 150$.
The difference is most probably due to the fact that Hoffman's value for G_o^{II} depends rather weakly on the product $(T.\Delta T)$ through $(\Delta f_o)^{0.5}$ while our value for G_o^{II} depends strongly on $(T.\Delta T)$ through $(\Delta f_o)^{2.5}$, i.e. in our case $G_o^{II} = 6.43x10^4\ cm.s^{-1}$ is an average value for the whole temperature range ($T_{av} = 394K$, $\Delta T_{av} = 20K$) of regime-II crystallization. The other reason could either be the dependence of G^{II} on the substrate completion rate g, i.e. the quantity n_z in this regime will represent a larger part of the molecule, not only the chain length sufficient to form SCFN. Most probably in regime-II crystallization the quantity n_z corresponds to the number of chain units of the whole molecule, i.e. $n_z = 1900$ for $M_z = 26500$ (at $M_o = 14$) and $n_z = 7040$ for $M_z = 98500$.
Then G_o^{II} will take on the values:

$$G_o^{II} = \begin{matrix} 1.76x10^4\ (n_z = 1900) \\ 0.47x10^4\ (n_z = 7040) \end{matrix} \qquad (35)$$

being very close to the value $G_o^{II} = 6.43x10^4\ cm.s^{-1}$, the result of our estimate.

EBSCOhost - printed on 2/13/2023 3:45 AM via . All use subject to https://www.ebsco.com/terms-of-use

Conclusions

Proceeding from comparative calculations for the crystallization rate using either Hoffman's retardation factor β_g or a modified retardation factor β_g^*, the following conclusions could be derived:
1) For the three crystallization regimes the modified factor β_g^* gives values for G_o close to Hoffman's values.
2) β_g^* (G_o, respectively) depends strongly on subcooling ΔT through the crystallization driving force Δf_o, and takes on the value $\beta_g^* = 0$ at $\Delta T = 0$, i.e. β_g^* reflects the net reptation rate resulting in crystallization onto the substrate, and the latter should also be zero at $T = T_m^o$ ($\Delta T = 0$).
3) β_g^* depends on i^2, the square number of chain units crystallizing simultaneously, i.e. on the flexibility, being inherent for the specific polymer molecule.

References

1. Atanassov,A.M. 1985. Quantum Interpretation of the Primary and Secondary Nucleation Rates. Paper P15 and P16 of the 17th Europhysics Conference "Morphology of Polymers", Prague, July, 15-18.

2. Hoffman, J.D.1982. Polymer, 23, 656.

3. Hoffman, J.D. 1983. Polymer, 24, 3.

4. Atanassov,A.M. 1985. Light Emission from a Crystallizing Polymer. Paper P14 of the 17th Europhysics Conference "Morphology of Polymers", Prague, July, 15-18.

5. Sanchez, I.C. 1974. J.Macromol. Sci.-Revs. Macromol. Chem. C10, 113.

6. Hoffman, J.D. 1958. J.Chem.Phys. 29, 1192.

7. Van Krevelen, D.W. 1972. Properties of Polymers. Correlation with Chemical Structure. Elsevier Publishing Company, Amsterdam-London-New York.

EBSCOhost - printed on 2/13/2023 3:45 AM via . All use subject to https://www.ebsco.com/terms-of-use

8. Jarecky, L. 1985. Effect of Rotational Diffusion on Oriented Nucleation. Paper P56 of the 17th Europhysics Conference "Morphology of Polymers", Prague, July, 15-18.

9. Hoffman, J.D., L.J. Frolen, G.S.Ross, J.I.Lauritzen, Jr. 1957. J.Res.Natl.Bur.Stand. 79A, 671.

EBSCOhost - printed on 2/13/2023 3:45 AM via . All use subject to https://www.ebsco.com/terms-of-use

EQULLIBRIUM CRYSTALLINITY AND PHASE TRANSITION MECHANISM OF BULK POLYMERS OF LINEAR FLEXIBLE CHAIN MOLECULES

A.M.ATANASSOV

Department of Chemistry, Higher School of Electrical and Mechanical Engineering, 1156 Sofia, Bulgaria.

Introduction

Some people suppose that equilibrium melting of a polymer because of its lamellar structure is not an infinitely sharp transition of first order. In this case the individual chain molecule traverses the crystalline phase as well as the amorphous one, and hence the conformation entropy of the chain segments remaining in the amorphous phase depends on the crystalline amount. The variation of entropy s with crystallinity x expressed by the function $(-\partial s/\partial x > 0)$ results in gradually free energy increase of the amorphous segments thus stabilizing the partially crystalline state (1-5).

On the basis of the idea that equilibrium crystallinity x^* lower than unity does exist in a system of small crystallites connected by tie molecules, the following has been done (6-8):

1) The quantity melting rate v_m was defined for a process running nonisothermally in a differential scanning calorimeter (DSC);

2) a statistical equation for the temperature dependence of v_m has been derived; 3) using an appropriate model of a crystallite, an experimentally determinable quantity (the initial value of the long period L_{001}) has been introduced into the kinetic equation.

However, some questions for the details of the phase transition in such a system are still open.

The aims of the present work are:

1) to propose an appropriate mechanism for melting and crystallization in a system the entropy of which is governed by the

Morphology of Polymers
© 1986 Walter de Gruyter & Co., Berlin · New York - Printed in Germany.

EBSCOhost - printed on 2/13/2023 3:45 AM via . All use subject to https://www.ebsco.com/terms-of-use

function $(-\partial S/\partial X>0)$;
2) to clarify the way of secondary nucleation prevention when equilibrium crystallinity X^* is reached, independent of the non-crystallized melt still available;
3) to explain the variations of the fold surface free energy σ_e of the crystallites in drawn polymers and in heterogeneous blends.

Experimental

The following homopolymers and blends have been used in experimental data collection: isotactic polypropylene *(i-PP)* of "Hercules" (USA) with a viscosity average molecular weight $\bar{M}_\eta = 500\ 000$; ultrahigh molecular weight polyethylene *(UHMWPE,* $\bar{M}_\eta = 1000\ 000$*)* (9); blends of *i-PP* and *UHMWPE*, prepared by mixing the powders and multiple processing in an injection moulding machine "Boy" (FRG). Specimen drawing was carried out by "Instron" testing machine at temperature $T = 383$ K. The small angle X-ray scattering (SAXS) investigations cited in the present work were made using KRM-1 equipment of the USSR with *Ni*-filtered *Cu*-K_α radiation. Differential scanning calorimeter DSM-2 (product of the Soviet Acad. Sci) was used for the melting studies.

Results

Melting of *i-PP* solution crystallized samples

The plots $\log V_m$ vs the temperature variable $(\Delta T/T)^{0.5}$ for bulk PP samples consist of a lower temperature and a higher temperature portion, both being strictly linear (10). The lower temperature melting plot was identified as the one where the melting process is controlled by the function $(-\partial S/\partial X>0)$, while the higher temperature

EBSCOhost - printed on 2/13/2023 3:45 AM via . All use subject to https://www.ebsco.com/terms-of-use

plot is believed to be a sharp transition of first order, broadened as the heating rate $v_h > 0$. It has been established that the first order transition starts only after 63% of the available crystalline phase has been melted, i.e. when the entropy S no more depends on the crystallinity $X (-\partial S/\partial X = 0)$.

Melting of hot drawn *i-PP* samples

The long period L_{001} of hot drawn *PP* samples, calculated using both methods (melting kinetics and *SAXS*), increases from $L_{001} = 174$Å at a draw ratio $\lambda = 0$ up to $L_{001} = 245$Å at $\lambda = 5.5$ (10). Using Mucha's data (11) for *i-PP* lamellar thickness l vs L_{001}, the lamellar thickness values have been calculated. The values of ℓ thus obtained and the melting temperatures T_m from DSC melting peaks were substituted in Thomson-Gibbs equation:

$$T_m = T_m^\circ \, (1 - 2\sigma_e / \Delta H_f^\circ . \ell) \qquad (1)$$

(ΔH_f° is the melting enthalpy of an infinite crystal in erg.cm^{-3}; T_m° is the equilibrium melting temperature).
From the slope of the plot T_m vs l^{-1} the value $\sigma_e = 67.4$ erg.cm^{-2} was obtained, which is rather low compared to those cited for *i-PP*: $\sigma_e = 157$ erg.cm^{-2} (12); $\sigma_e = 175$ erg.cm^{-2} (13).

Melting of *i-PP/UHMWPE* blends, crystallized nonisothermally in the mould

Both melting kinetics investigations and *SAXS* data have shown that the long period values L_{001} of *PP* in the blends have been increased from $L_{001} = 174$Å (pure *PP*) up to $L_{001} = 250$Å (for 40% *PP*/60% *UHMWPE* blend) (10). Following Thomson-Gibbs equation one expects that the melting temperature T_m of *i-PP* would also increase (Eq.(1)). In fact,

EBSCOhost - printed on 2/13/2023 3:45 AM via . All use subject to https://www.ebsco.com/terms-of-use

T_m of PP reduces from $T_m = 438.5K$ down to $T_m = 434\ K$, respectively (10). In the terms of Eq.(1) the melting temperature could be lower when $\ell(L_{001})$ is higher only if σ_e value is markedly increased.

It follows from the above mentioned results that the fold surface free energy σ_e is strongly affected by the crystallization conditions, and its value depends on the amount of the additional free energy stocked in the noncrystalline part of the bulk polymer.

Discussions

The quantitative histologic investigations made by Voigt-Martin (14) and Strobl et al. (17) on polymer object at different temperatures in the melting range have shown that the lamella thickness distribution is almost unchanged with the progress of melting. It is mainly the distance between them that varies such that at a specified temperature T_1 there exists some critical distance L_1, while at another $T_2>T_1$, another distance $L_2>L_1$ exists (Fig. 1).

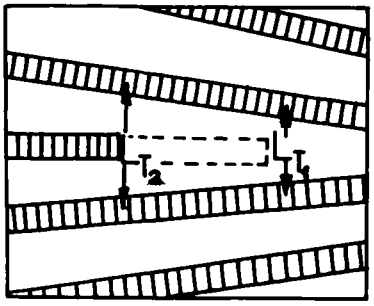

Fig. 1. Schematic representation of the histologic results of Strobl, Schneider and Voigt-Martin (15).

EBSCOhost - printed on 2/13/2023 3:45 AM via . All use subject to https://www.ebsco.com/terms-of-use

These are experimentally determined facts, which Voigt-Martin and Strobl et al. failed to bound with the hypothesis for nonlinear dependence of the conformation entropy on the crystallinity.
Taking into account the investigations made up to now we could picture the processes of crystallization and melting as follows: During crystallization from a "virgin" melt initially there are formed "ideal" crystal lamellae. When 18-20% of the polymer have experienced phase transition, all macromolecules occur to be with fixed ends from the crystals already existing, i.e. from the very moment on, the melt behaves as a cross-linked one and the subsequent to crystallize lamellae are crystallizing from a melt of reduced entropy (increased free energy). With the progress of the crystallization process, crystallization is running in sections of the melt, having higher and higher free energy.
For explaining the regular changes in the crystal and amorphous phases under conditions of crystallization from a melt of continuously rising free energy we could proceed from the equation of Thomson-Gibbs (Eq. 1) and transform it in its original form:

$$\Delta H.\Delta T/T_m^\circ = 2\sigma_e/\ell \qquad (2)$$

Since:

$$\Delta H.\Delta T/T_m^\circ = \Delta f$$

then

$$\Delta f = 2\sigma_e/\ell \qquad (3)$$

Eq.(3)has been obtained from the most common equation:

$$\Delta f = 2(\sigma_e/\ell + \sigma_a/a + \sigma_b/b) \qquad (4)$$

supposing that the dimensions a and b (crystal thicknesses in the respective directions) have taken infinite values, i.e. crystallization impeded in direction of ℓ is regarded.
The surface free energies σ_a and σ_b of the surfaces perpendicular to the other two unit cell directions (a_o and b_o, respectively) could be calculated according to the following equation, (16):

$$\sigma_a = \sigma_b = 0.11x\Delta H_m^\circ(a_o.b_o)^{0.5} \qquad (5)$$

EBSCOhost - printed on 2/13/2023 3:45 AM via . All use subject to https://www.ebsco.com/terms-of-use

For polyethylene: $a_o = 4.55 \times 10^{-8}$ cm; $b_o = 4.11 \times 10^{-8}$ cm; $\Delta H_f^\circ = 2.87 \times 10^9$ erg.cm^{-3} and

$$\sigma_a = \sigma_b = 16{,}2 \text{ erg.cm}^{-2} \qquad (6)$$

while σ_e value for PE is at average $\sigma_e = 100$ erg.cm^{-2}.
Assuming that: $\ell = 100 \times 10^{-8}$ cm; $a = 162 \times 10^{-8}$ cm; $b = 162 \times 10^{-8}$ cm
Eq.(4) yeilds:

$$\Delta f = 2 \times 10^8 \ (1+0.1+0.1) \text{ erg.cm}^{-3}$$

i.e. because of the small values of the quantities σ_a and σ_b even at very small thicknesses a and b the contribution of both last terms in the above equation is 20% only, being negligible at higher values for a and b. It has been mentioned that in a long chain system the dependence $(-\partial S/\partial X>0)$ is activated when 18-20% of the bulk polymer is yet in crystalline state. In this moment a and b dimensions of the originally formed lamellae exceed many times the value $a = b = 162 \times 10^{-8}$ cm. Consequently, in the subsequent crystallization only the term (σ_e/ℓ) will be influenced by the variation of S with X.
Then if we designate with Y the lamella growth direction (Fig. 1) and consider σ_e and 1 as variables:

$$\frac{\partial \Delta f}{\partial Y} = \frac{2}{l} \left(\frac{\partial \sigma_e}{\partial Y} - \frac{\sigma_e}{l} \frac{\partial l}{\partial Y} \right) \qquad (7)$$

Eq.(4) shows that crystallization from a melt with increased free energy (and hence increased Δf of the transition) is accompanied by increase in σ_e and reduction in lamella thickness ℓ in the direction of crystallization.
The rise in σ_e is readily explainable taking into account that this quantity is the isothermal work required to form ℓ cm^2 of surface from the crystal interior (6):

$$\sigma_e = \Delta h_e - T.\Delta S_e \qquad (8)$$

where:

Δh_e and ΔS_e are the heat and the entropy of transition from the interior crystal state (cr) to the rotator state on the surface (e), respectively.

EBSCOhost - printed on 2/13/2023 3:45 AM via . All use subject to https://www.ebsco.com/terms-of-use

Then:

$$\sigma_e = (h_e - h_{cr}) - T(S_e - S_{cr}) \qquad (9)$$

Reduction of the surface entropy S_e without being accompanied by rather higher reduction of surface enthalpy h_e (increased interaction forces) will result in an increase in σ_e value.
Reduction of lamella thickness in direction Y (this is a diversity from the model of Strobl et al.) is also explainable: the reduction in entropy of the macromolecules in contact with (001) crystal face and entering in the crystallite provokes the appearance of entropy stresses destroying the crystal order close to the crystallite surface. The higher the entropy stresses the larger the destroyed part of the lamella thickness (17). It is noted that with increase in the molecular weight of polymer, crystallinity reduces (18), and this is in support to the above explanation.
In deducing the melting equations the existence of lamellae of thickness less than the average one was neglected. From the above considerations it becomes clear that the theory of melting kinetics does not deny the existence of these lamellae, it rather considers them as being a result of the crystallization in melts, in which a gradient of the free energy is present. The much higher value of σ_e on the surface of these lamellae caused by the existing gradient of the free energy becomes the cause for their melting at much lower temperatures than the temperatures calculated from Thomson-Gibbs equation for the specified lamella thickness.
The crystallization at a specified temperature $T = T_2$ in direction Y continues until the equilibrium value of Gibbs free energy is reached (or equally until the equilibrium crystallinity at a specified temperature $X^*_{T_2}$ is reached). Further, crystallization at this temperature is not running, as on the contrary it could have resulted in total free energy increase, which is thermodynamically impossible.
With decrease in temperature down to $T = T_1$ the crystallization of the lamella in Y direction continues until the new equilibrium value of $X(X^*_{T_1})$ is reached, etc.
In the terms of Strobl-Voigt-Martin this means that at $T = T_2$ a specific critical value has been reached for the distance $L = L_2$,

EBSCOhost - printed on 2/13/2023 3:45 AM via . All use subject to https://www.ebsco.com/terms-of-use

while at $T = T_1$ - another critical value $L = L_1$ $(L_1<L_2)$ has been reached.

Why at a specified temperature (for example $T = T_2$) crystallization in Y direction ceases?

For the formation of a new layer on the front of the growing crystal a two-dimensional nucleus of 1 thickness should be formed. If ϑ is the number of chains in direction c_o of the nucleus and a is their cross-section, the variation in the free energy ΔF, accompanying the nucleus formation is (19):

$$\Delta F = 2\vartheta a\sigma_e + c\sqrt{\vartheta a}\,\ell.\sigma - \vartheta a\ell\Delta f \qquad (10)$$

(c is numerical constant, depending on the nucleus shape).
From the differentiation of Eq. (10) in respect to ϑ

$$\frac{\partial \Delta F}{\partial \vartheta} = \frac{c\sigma\sqrt{a\ell}}{2\sqrt{\vartheta}} + a(2\sigma_e - \ell\Delta f) \qquad (11)$$

it becomes quite clear that Eq.(10) has a maximum (the nucleus could attain stability, respectively) only when the lamella thickness becomes higher than a specified value:

$$\ell > \frac{2\sigma_e}{\Delta f} = \frac{2\sigma_e . T_m^\circ}{\Delta H . \Delta T} \qquad (12)$$

If for a temperature $T = T_2$, σ_e in a given part has risen as a result of the entropy reduction and the thickness ℓ has been reduced resulting from the destructions provoked by the entropy stresses, then the function expressed by Eq. (10) has no maximum at this temperature and hence addition of new segments ϑ would not contribute for the stabilization of the nucleus. Such a nucleus could not become a stable one at the specified temperature and crystallization in Y direction ceases. It is only when ΔT grows that the condition expressed by Eq.(18) is satisfied and crystallization at the new value of undercooling continues until new equilibrium value of crystallinity is reached at that temperature. The very moment this value is reached the formation of a stable nucleus on the growing face of the crystal becomes again impossible, etc.
The differentiation of Eq.(1) in respect to Y gives:

$$-\frac{\partial T_m}{\partial Y} = \frac{2T_m^\circ}{\ell\Delta H}\left(\frac{\partial \sigma_e}{\partial Y} - \frac{\sigma_e}{\ell}\frac{\partial \ell}{\partial Y}\right) \qquad (13)$$

EBSCOhost - printed on 2/13/2023 3:45 AM via . All use subject to https://www.ebsco.com/terms-of-use

It is evident from Eq.(13) that resulting from the crystal growth in r direction, whereas a gradient of surface free energy σ_e and gradient of the thickness appear on (001) crystal faces, the as-formed lamella in its different parts in the crystallization direction has different melting temperatures, i.e. the gradient of σ_e and 1 means the presence of gradient of T_m. Consequently, at a repeated heating of the sample, melting will begin from the ends of the lamella formed during the last stage of crystallization in a melt with a maximum free energy, i.e. melting begins from the most high energetic crystal face, but this is different from (001) face. From the above considerations it becomes obvious that the most energetic crystal face is the growing face being connected with (001) face with maximum σ_e. Most probably the contribution of the second term in the righthand side of Eq.(13) is much lower than that of the first one, and that is why the melting process manifests as a process where the lamella thickness remains almost unchanged, and the only variation is in the distance between the lamellae.

In a recent work (10) some investigation was made on the melting kinetics of polypropylene samples of differing lamella thickness obtained by uniaxial hot drawing up to a different draw ratio λ. It was established that the temperature of melting grows with increase in λ, and σ_e reduces. How is this to be explained?

In differentiating Eq.(1) in respect to λ it is found that:

$$\frac{\partial T_m}{\partial \lambda} = \frac{2T_m^\circ}{l \Delta H} \left(- \frac{\partial \sigma_e}{\partial \lambda} + \frac{\sigma_e}{l} \frac{\partial l}{\partial \lambda}\right) \qquad (14)$$

Taking into account Eq.(8) as well, we obtain:

$$\frac{\partial T_m}{\partial \lambda} = \frac{2T_m^\circ}{l \Delta H} \left(- \frac{\partial \Delta h_e}{\partial \lambda} + T \frac{\partial \Delta S_e}{\partial \lambda} + \frac{\sigma_e}{l} \frac{\partial l}{\partial \lambda}\right) \qquad (15)$$

With increase in λ the term $T \frac{\partial \Delta S_e}{\partial \lambda}$ reduces, i.e. $T \frac{\partial \Delta S_e}{\partial \lambda} < 0$ (16)

because of considerable reduction in entropy of the amorphous phase.

It was found experimentally that σ_e of drawn PP samples is reduced, i.e.

$$(\partial \sigma_e / \partial \lambda) < 0 \qquad (17)$$

Comparing Eqs.(8,16 and 17) it is readily seen that the following

EBSCOhost - printed on 2/13/2023 3:45 AM via . All use subject to https://www.ebsco.com/terms-of-use

conditions should be satisfied for drawn samples:

$$(\partial \Delta h_e / \partial \lambda) < 0 \qquad (18)$$

and

$$\left| \frac{\partial \Delta h_e}{\partial \lambda} \right| > \left| T \frac{\partial \Delta S_e}{\partial \lambda} \right| \qquad (19)$$

Eq.(18) expresses the reduction in surface enthalpy (h_e) with raising draw ratio λ, i.e. the interaction forces among the chains on(001) crystallite surfaces are increased for drawn samples.
Consequently, during deformation there has been obtained a system of crystals sunk in the amorphous phase with reduced enthalpy and entropy and for its melting additional amount of energy is required. Such a case has been described for stretched polyethylene by Meinel and Peterlin (20) and Sumita, Miyasaka, Ishikawa (21). These authors have recorded considerable increase in melting enthalpy (up to 16% from the initial value).
The prevalence of the enthalpy contribution over that of the entropy one, predetermines also the increased melting temperatures in accordance with the equation:

$$T_m = \frac{\partial H}{\partial S} \qquad (20)$$

A reverse case is that of melting of test samples made of *PP-UHMWPE* blends. It was established for them that irrespective of the increase in lamella thickness of *PP* with the increase in *UHMWPE* concentration the melting temperature of *PP* reduces. From *WAXS* data analysis the conclusion was made that the defectness of *PP* crystals grows with increase in *UHMWPE* concentration in the blend (22).
After differentiation of Eq.(1) in relation to *UHMWPE* concentration *(C)* one obtains:

$$\frac{\partial T_m}{\partial C} = \frac{2T_m^\circ}{\ell \Delta H} \left(- \frac{\partial \Delta h_e}{\partial C} + T \frac{\partial \Delta S_e}{\partial C} + \frac{\sigma_e}{\ell} \frac{\partial \ell}{\partial C} \right) \qquad (21)$$

The thickness of *PP* lamellae grows with the increase in *PE* concentration and hence $\partial \ell / \partial C > 0$; entropy reduces with increasing of *PE* concentration because the larger thickness of *PP* lamellae is due to crystallization in a field of internal stresses. Hence $\partial \Delta S_e / \partial C < 0$. The latter however is not accompanied by a reduction

EBSCOhost - printed on 2/13/2023 3:45 AM via . All use subject to https://www.ebsco.com/terms-of-use

in enthalpy because the defectness of *PP* crystals grows and consequently the term $\frac{\partial \Delta h_e}{\partial c} > 0$.

Then, most probably

$$\left| \frac{\partial \Delta h_e}{\partial c} + T \frac{\partial \Delta s_e}{\partial c} \right| > \left| \frac{\sigma_e}{\ell} \frac{\partial \ell}{\partial c} \right| \qquad (22)$$

which is the reason for the reduction of melting temperature with increase in *UHMWPE* concentration $(\partial T_m / \partial c < 0)$.

Conclusions

From the energetic analysis made so far a conclusion could be made that it is not realistic to neglect the nonlinear dependence of the entropy on the crystallinity in a bulk polymer made of linear flexible long chain molecules. The function $(-\partial s / \partial x > 0)$ in fact controls the melting and crystallization processes; it is the cause for the overheating as well as for the lower temperature portion of the DSC melting peaks.

Acknowledgements

The author is greatly indebted to:

Prof.Dr.V.Privalko (Inst.Macromol.Chem., Ukr. Acad. Sci., USSR)
Prof.Dr.E.W.Fischer (Univ. Mainz, FRG)
Prof.Dr.G.Wegner (Max-Planck Inst., FRG)
Prof.Dr.R.Bonart (Univ.Regensburg, FRG)
Prof.Dr.G.Strobl (Johannes-Gutenberg Univ., FRG)
Doz.Dr.H.Baur (BASF, FRG)
Prof.Dr.J.G.Fatou (Spain)
Prof.Dr.M.Sumita (Tokyo Univ.)
Prof.Dr.S.Miyata (Tokyo Univ.)
Prof.Dr.M.Iguchi (Res.Inst.Polym.Textiles,Japan)
Prof.Dr.G.Wilks (Polym.Materials & Interface Laboratory, Virginia Univ., USA)

EBSCOhost - printed on 2/13/2023 3:45 AM via . All use subject to https://www.ebsco.com/terms-of-use

Prof.Dr.J.M.Schultz (Univ.Delaware, USA)
for their fruitfull discussions and remarks.

References

1. Münster,A.1955.Ric.Sci.Suppl.25, 648.

2. Roe,R.J.,K.J.Smith,Jr.,W.R.Krigbaum.1961.J.Chem.Phys. 35, 1306.

3. Zachmann,H.G.1967.Kolloid-Z. & Z.Polymere 216/217, 180.

4. Fischer,E.W.1967.Kolloid-Z. & Z.Polymere 218, 97.

5. Baur,H.1980.Pure & Appl.Chem.52, 457.

6. Atanassov,A.M.,E.Nedkov.1983.Abstract No 46 of IUPAC's MACRO'83, Bucharest,Sept.,5-9.

7. Atanassov,A.M.,E.Nedkov.1983.Comm.Dept.Chem.Bulg.Acad.Sci. 16, 527(in English).

8. Atanassov,A.M.,E.Nedkov.1983.Comm.Dept.Chem.Bulg.Acad.Sci. 16, 541 (in English).

9. Damianov,D.,M.Velikova,L.Petkov.1979.European Polym.J.15, 233.

10. Atanassov,A.M.1984.Dissertation Thesis (36 pages short version in English available).

11. Mucha,M.1981.J.Polym.Sci.:Polym.Symp.69, 79.

12. Martuscelli,E.,C.Silvestre,G.Abate.1982.Polymer 23, 229.

13. Blais,J.J.,R.St.John Manley.1967.J.Macromol.Sci.B1, 525.

14. Voigt-Martin,I.G.1981.J.Polym.Sci.:Polym.Phys.Ed.19, 1769.

15. Strobl,G.R.,M.J.Schneider,I.G.Voigt-Martin.1980.J.Polym. Sci.:Polym.Phys.Ed.18, 1361.

16. Hoffman,J.D., J.I.Lauritzen,Jr.,E.Passaglia,G.S.Ross,L.J. Frolen,J.J.Weeks.1969.Kolloid-Z. & Z.Polymere 231, 564.

17. Schultz,J.M.,W.Robinson,G.Pound.1967.J.Polym.Sci.A-2,5, 511.

18. Smola,V.N.,V.P.Dushtchenko.1975.Polym.Sci.(USSR),B17,112.

19. Lauritzen,J.I.,Jr.,J.D.Hoffman.1960.J.Res.Natl.Bur.Stand. A64, 73.

EBSCOhost - printed on 2/13/2023 3:45 AM via . All use subject to https://www.ebsco.com/terms-of-use

20. Meinel,G.,A.Peterlin.1967.J.Polym.Sci.:Polym.Letters Ed.5, 613.

21. Sumita,M.,K.Miyasaka,K.Ishikawa.1977.J.Polym.Sci.:Polym. Phys.Ed.15,837.

22. Nedkov,E.,A.M.Atanassov.1983.Bulg.J.Phys.10,652 (in English).

EBSCOhost - printed on 2/13/2023 3:45 AM via . All use subject to https://www.ebsco.com/terms-of-use

EBSCOhost - printed on 2/13/2023 3:45 AM via . All use subject to https://www.ebsco.com/terms-of-use

LIGHT EMISSION FROM A CRYSTALLIZING POLYMER

A.M. Atanassov

Department of Chemistry, Higher School of Electrical and Mechanical Engineering, 1156 Sofia, Bulgaria.

Introduction

It is broadly accepted that during crystallization the energy difference between the amorphous and the crystalline state ΔE is transformed into heat, resulting in continuous spectrum emission. An assumption is made in this work that the energy of the crystallization process is initially liberated by quanta of relatively close wavelengths (in comparisson with the broad wave length range radiation of a heated body). In this case the intensity of the continuous spectrum of the heated body will change close to the wavelength, corresponding to the average energy of the crystallization process.

Results and Discussions

The amorphous state of a chain unit in a polymer molecule below the melting point could be regarded as an excited state. The enthalpy difference ΔH_m° (in ergs per mol of monomer units) between the amorphous (H_{am}) and the crystalline state (H_{cr}):

$$\Delta H_m^\circ = (H_{am} - H_{cr}) \qquad (1)$$

is liberated during the crystallization process. For a monomer

Morphology of Polymers
© 1986 Walter de Gruyter & Co., Berlin · New York - Printed in Germany.

EBSCOhost - printed on 2/13/2023 3:45 AM via . All use subject to https://www.ebsco.com/terms-of-use

unit the average energy difference:

$$\Delta E_1 = \Delta H^\circ_m / N_a \qquad (2)$$

(N_a - Avogadro's number) could in principle be emitted as a quantum of energy:

$$\Delta E = h\,\vartheta \qquad (3)$$

($h = 6.62 \times 10^{-27}$ $erg.s$ - Plank's constant, ϑ - frequency).
If ζ monomer units, making an effective chain segment, crystallize simultaneously, the emitted energy will be:

$$\Delta E_\zeta = \zeta . \Delta H^\circ_m / N_a \qquad (4)$$

and radiated frequency is expressed as:

$$\vartheta_\zeta = \frac{\zeta . \Delta H^\circ_m}{N_a\ h} \qquad (5)$$

As: $$n\,\lambda\,\vartheta = C \qquad (6)$$

(n - refractive index; λ - wavelength in cm; C - light velocity in vacuum; $C = 3 \times 10^{10}$ $cm.s^{-1}$)

$$\lambda = \frac{C\ h\ N_a}{\zeta . \Delta H^\circ_m . n} \qquad (7)$$

In spectroscopy the wave numbers $\tilde{\vartheta}$ are commonly used:

$$\tilde{\vartheta} = 1/\lambda = \frac{\zeta . \Delta H^\circ_m . n}{C\ h\ N_a} \qquad (8)$$

The IR absorption spectra of polymers could be used as an indirect support to the hypothesis for discrete light emission during crystallization (a main postulate in the atomic physics is that if a body absorbs some frequences it is able to emit them). Replacing C, h and N_a with their numerical values yields the provisional equation:

$$\tilde{\vartheta} = 8.35 \times 10^{-9} \times \zeta\ \Delta H^\circ_m\ n \qquad (9)$$

For polyethylene (PE) melting enthalpy is $\Delta H^\circ_m = 7.54 \times 10^{10}$ $erg.mol^{-1}$. The refractive index $\underline{n}$ of polymers ranges from $n = 1.35$ to 1.7 at a temperature $t = 20^\circ C$, becoming lower with temperature increase.

EBSCOhost - printed on 2/13/2023 3:45 AM via . All use subject to https://www.ebsco.com/terms-of-use

Taking into account that $\underline{n}$ consists of a real and an imaginery part, the latter predominating, at a resonance frequency (in the absorption bands) one could set as a first approximation $\underline{n} = i$. A set of wave numbers is obtained using different ζ values (Table 1, column 1-2).

Table 1. Theoretical, $(\tilde{\vartheta})_{CALC}$, and experimental, $(\tilde{\vartheta})_{EXP}$ wave numbers at different values of simultaneously crystallizing units (ζ).

ζ	$(\tilde{\vartheta})_{CALC}$	$(\tilde{\vartheta})_{EXP}$	$(\Delta H_m^\circ.n)_{IR}$ $x10^{-10}$ erg.mol^{-1}	$(\tilde{\vartheta})_R$
0.5	315	320	7.66	362
1	630	720	8.62	723
		731	8.75	
2	1259	1473	8.82	1447
4	2518	2848	8.52	2893
5	3150	3600	8.62	3617
6	3780	very strong		4340
8	5037	5780	8.65	5787
10	6300			7234
12	7560	average intensity		8681

As it was expected, the calculated values $\tilde{\vartheta}_{CALC}$ differ from $\tilde{\vartheta}_{EXP}$, shown in column 3 of Table 1. Replacing $(\tilde{\vartheta})_{EXP}$ in Eq.(9) one could calculate the product $(\Delta H_m^\circ.n)$, designated as $(\Delta H_m^\circ.n)_{IR}$ in column 4. The average value of this quantity is $(\Delta H_m^\circ.n)_{IR} = 8.66x10^{10}$ erg.mol^{-1}. Comparing with the real value of $\Delta H_m^\circ (7.54x10^{10})$ the refractive index value $n = 1.149$ in the regions close to the absorption bands is found. The real wave numbers, $(\tilde{\vartheta})_R$, illustrating the main idea of this work, are presented in column 5. In the same way using the value $\Delta H_m^\circ = 1.09x10^{11}$ erg.mol^{-1} (melting enthalpy of polypropylene) and $n = 1.093$, the following wave numbers were obtained: 998 ($\zeta = 1$); 2994 ($\zeta = 3$); 3992 ($\zeta = 4$);

EBSCOhost - printed on 2/13/2023 3:45 AM via . All use subject to https://www.ebsco.com/terms-of-use

5988 ($\zeta = 6$) etc., while the experimental $\tilde{\vartheta}$ values in the IR spectrum (1) are: $(\tilde{\vartheta})_{EXP}$=998; 2875; 4065; 5814 cm^{-1}.
For polyoxymethylene (POM) at $\Delta H^{\circ}_{m} = 7.123x10^{10}$ $erg.mol^{-1}$ the calculated wave numbers $(\tilde{\vartheta})_{CALC}$ are: 595($\zeta = 1$); 1190 ($\zeta = 2$); 1785($\zeta = 3$); 2380 ($\zeta = 4$); 2975($\zeta = 5$), etc. The experimental values for orthorombic POM (1) $(\tilde{\vartheta})_{EXP}$ are 600 ; 1200; 3000 respectively.No experimental data were found for POM in the range from 1600 cm^{-1} up to 2700 cm^{-1}(1).
Similar calculations are carried out for many other linear polymers which support the main idea of the work.
Then a question arises: If radiation is emitted during crystallization at such a relatively narrow wave length range then why this radiation is not yet experimentally established?
The most probable reason is the low energy liberated per unit of time, to be illustrated with the following:
The energy ΔE liberated from 1 cm^2 surface of the sample is:

$$\Delta E = \frac{\Delta H^{\circ}_{m} . N^{*}}{N_a} \qquad (10)$$

where: N^{*} is the number of chain units, spread on 1 cm^2 surface:

$$N^{*} = (a_o . c_o)^{-1} = 8.65x10^{14}$$

($a_o = 4.55x10^{-8}$ cm; $c_o = 2.54x10^{-8}$ cm width and length of a chain unit of PE in crystalline state).
Assuming that the crystallization process is over in 20 minutes (1200 seconds), the average power, liberated for 1s is:

$$\Delta E/\Delta t = \frac{7.54x10^{10}x8.65x10^{14}}{6.02x10^{23}x1200} = 9x10^{-2}\ erg.s^{-1} \qquad (11)$$

i.e. the power is approximately 10^{-8}W, which is rather low value even for the present day instrumentation for scientific work.

EBSCOhost - printed on 2/13/2023 3:45 AM via . All use subject to https://www.ebsco.com/terms-of-use

Some Possible Applications

Crystallization kinetics using emission spectra

By means of a monochromator or band-pass filters, and with very sensitive detectors the wavelength of the emitted quanta could be identified, thus justifying the foregoing hypothesis.
The measurements enable us to calculate ζ, the average number of simultaneously crystallizing polymer chain units, being present in the equations for the preexponential factors of primary and secondary nucleation rate derived in ref.(2). Having identified the average emitted wave length one could make isothermal crystallization kinetics experiments, recording the light intensity of the broad emitted line as a function of time. The electrical signal of the solid state detector is proportional to (dH/dt), the signal from the differential scanning calorimeter (DSC). However, the use of emission spectra for crystallization experiments should most probably result in higher sensitivity and accuracy as the inertia effects are avoided.
Some preliminary experiments of polymers melting by means of laser light heaters (or by a combination of a monochromator and a band-pass filter) with a wave length, calculated by Eq.(7) have shown that overheating is completely avoided if one uses: for PE $\tilde{\vartheta} = 1473\ cm^{-1}$ $(\zeta = 2)$; for PP $\tilde{\vartheta} = 998\ cm^{-1}$ $(\zeta = 1)$, etc. The latter means that the melting polymer absorbs one wavelength predominantly. The remaining wave lengths, available in the spectrum of the heater lead to sample temperature increase, i.e. this is the cause for overheating when using higher heating rates in DSC.

EBSCOhost - printed on 2/13/2023 3:45 AM via . All use subject to https://www.ebsco.com/terms-of-use

Cancer therapy by wave radiation

It has been established that some cancer formations contain tentimes more DNA molecules and show optical anisotropy. Observing similar anisotropy of a virus head, Astbury (3) suggested that DNA was crystalline and folded. If it is assumed that DNA of the cancer formations is also in a crystalline state, the hypothesis for the discrete light emission during the polymer crystallization process could be used for some practical purposes. By means of either very sensitive detectors and filters in the IR wave region, or multichannel analyzers (in the visible and UV ones) the wavelength of the emitted radiation could be determined. The cancer formations are expected to be destroyed (melted) applying a powerfull flux of approximately coherent light of the same frequency. Nowadays a higher energy ^{60}Co-radiation is used to delay the cancer progress. It is a misconception upon our opinion. The γ-quantum causes crosslinking of DNA-molecules without destroying the crystal (for doses used in γ-therapy). The "reparative" cancer enzymes find easily the additional links and cut them off. It looks quite reasonable to use a lower energetic coherent radiation (e.g. IR or visible) for melting the DNA crystals at first, followed by a small dose of ^{60}Co-radiation for crosslinking the molten molecules. Thus, the "reparative" enzymes will not be able to reconstruct a "building" which is completely destroyed.

More that 1200 publications could be cited in which heat, *He-Ne* laser light and UV light have been applied independently or in combination with ^{60}Co radiation. However, the cancer formations have been completely destroyed in some cases only. The most probable reason is that the attack has not been carried out by the appropriate wavelength radiation. By means of either detecting the characteristic wave emission of the cancer or calculating it, the latter being nowadays very difficult, we could establish the correct value of the appropriate wavelength. Application of broad spectrum radiation results in overheating, which probably causes cancer cell genesis intensification.

EBSCOhost - printed on 2/13/2023 3:45 AM via . All use subject to https://www.ebsco.com/terms-of-use

This work deals with many approximations, assumptions and guess-works and the author will greatly appreciate any comment and experimentally supported criticism.

References

1. Dechant, J., R.Danz, W.Kimmer, R.Schmolke. 1972. Ultrarotspectroscopische Untersuchnungen an Polymeren. Akademie-Verlag,Berlin.

2. Atanassov,A.M. 1985. Quantum Interpretation of the Primary and Secondary Nucleation Rates. Abstracts of the 17th Europhysics Conference "Morphology of Polymers", Prague, July 15-18.

3. Astbury, W.T. 1958. Discussions Faraday Soc. 25, 80.

EBSCOhost - printed on 2/13/2023 3:45 AM via . All use subject to https://www.ebsco.com/terms-of-use

EBSCOhost - printed on 2/13/2023 3:45 AM via . All use subject to https://www.ebsco.com/terms-of-use

Morphology of Polymers and Blends

1. Polyolefins	259-370
2. Other Polymers	371-526
3. Failure Behaviour	527-570

EBSCOhost - printed on 2/13/2023 3:45 AM via . All use subject to https://www.ebsco.com/terms-of-use

EBSCOhost - printed on 2/13/2023 3:45 AM via . All use subject to https://www.ebsco.com/terms-of-use

CRYSTAL MORPHOLOGY AND MOLECULAR INTERACTIONS IN ISOTACTIC POLYPROPYLENE AND ITS BLENDS

B. Lotz, J.C. Wittmann

INSTITUT Charles SADRON (CRM-EAHP), CNRS-ULP Strasbourg
6, rue Boussingault 67083 STRASBOURG CEDEX (France)

Introduction

The crystallite morphology of isotactic polypropylene (iPP) and its crystallization behaviour in polymer blends or in the presence of heterogeneous nucleating agents reveal some curious and hitherto unexplained features. It appears indeed that :

- the most common, monoclinic α form of iPP has a characteristic and unique crystallite morphology in which chain-folded lamellae branch repeatedly from parent ones. This behaviour is illustrated in Figure 1 for thin film growth. The branching occurs for nearly every crystallization condition ; in solution crystallization, it gives rise to "quadrites" (1) ; in bulk, it gives rise to spherulites with unexpected positive birefringence (2) ; in fibers, it gives rise to a bimodal orientation in which the chain axes of the branched constituent are nearly at right angle to the fiber axis (3).
- in blends of polyethylene (PE) and iPP, the linear PE may act as a nucleating agent for the helical iPP and reciprocally (4). Furthermore, in oriented blends of the two polymers, the PE adopts a "cross hatched" morphology with its chain axis inclined at some 50° to the iPP one (5).
- finally, a number of nucleating agents of PE are known to be also active towards iPP and induce the formation of its α - monoclinic modification (6). This behaviour is most surprising in view of the conformational and structural differences between the two polymers.

The above observations suggest crystallographic and structural interactions between (a) the lattices of parent and daughter lamellae in the branched structures observed in iPP and (b) the iPP and PE (or, as will be seen, polyamide) lattices. Interactions of a crystallographic nature are indeed suggested by the specificity of

Morphology of Polymers
© 1986 Walter de Gruyter & Co., Berlin · New York - Printed in Germany.

EBSCOhost - printed on 2/13/2023 3:45 AM via . All use subject to https://www.ebsco.com/terms-of-use

Figure 1. Thin film growth of iPP in the α form. The lamellae are seen edge-on. Note the extensive branching leading to a double population of tangential and radial lamellae. Scale bar : 5 μm.

the geometrical relationships which exist in the iPP branching mechanism and the blend structure. More specifically, recent work in our laboratory has established that in both cases, the interactions are of epitaxial character. The present article summarizes this work, reported extensively elsewhere (7-9). It analyzes the structural foundations of the epitaxies and therefore provides a single, structurally reasonable explanation for several puzzling aspects of the crystallization behaviour of isotactic polypropylene in its most common, monoclinic crystal form.

Crystal Morphology of iPP Blends

The structural analysis is most easily developed for blends of isotactic polypropylene with polyethylene and polymers that include aliphatic segments in their repeat unit, e.g. polyamides (PA). Previous observations dealing with fiber oriented blends have revealed in part the geometrical characteristics of the interactions. For example, melt spun blends of polyamide 11 and iPP have (for low iPP content)a fiber orientation of the PA 11 and three different chain orientations of the iPP constituent. One is parallel to the fiber axis, the second nearly normal to it ; these

EBSCOhost - printed on 2/13/2023 3:45 AM via . All use subject to https://www.ebsco.com/terms-of-use

orientations are also observed in pure iPP fibers. The third orientation is specific to the blend ; it is characterized by the orientation of the iPP chain axis at ∿ 50° to the fiber axis (10).
A related behaviour is observed when PE crystallizes on fiber-oriented iPP. This time, however, the chain axis of the linear polymer is at ∿ 50° to the fiber axis and iPP chain axis direction, since iPP crystallizes first (5).
The iPP-PA 11 and the iPP-PE interactions can both be analyzed in terms of epitaxy, although this phenomenon has sometimes been rejected in early as well as more recent works. Demonstration of epitaxy is very difficult in blend and even in fiber crystallization since the crystallographic planes that are in contact, and therefore are susceptible of interaction, cannot be determined with certainty, in the absence of sufficient or adequate orientation. The availability of well-oriented polymer substrates produced by epitaxial crystallization on appropriate solvent-substrates (11,12) and the use of electron microscopical observation and diffraction techniques have made it possible to determine the planes in contact for both iPP-PE and iPP-PA blends. The morphological evidences are shown in Figures 2a and 2b.
Figure 2a displays an iPP "quadrite" (the structure of which will be discussed in the next section of this article) grown from a blend of iPP and a paraffinic diluent. After removal of the latter, the quadrite has been "decorated" with polyethylene vapours (13) that have partly remelted and recrystallized. Analysis of the present morphology (and of the corresponding diffraction data) indicates that the three populations of iPP and PE lamellae are seen edge-on : the chain axes lie in the plane of the preparation. The viewing direction is parallel to the $\underline{b}_{iPP}$ and $\underline{a}_{PE}$ axes. The interacting planes are therefore the $\underline{ac}_{iPP}$ and $\underline{bc}_{PE}$ ones. Furthermore, the PE chain is exactly parallel to the [101] direction of iPP which, given the near identity of $\underline{a}$ and $\underline{c}$ parameters, corresponds to the bisectrix of the monoclinic β angle.
Figure 2b displays a very similar behaviour for an iPP-polyamide 11 system. In the present case, the linear PA serves as a substrate for the crystallization of an iPP film obtained by condensation of vapours. The PA 11 oriented substrate is itself obtained by epitaxial crystallization (12) and has the plane of the hydrogen-bonded sheet ($\underline{ac}$ plane) as exposed face. iPP has grown in the form

EBSCOhost - printed on 2/13/2023 3:45 AM via . All use subject to https://www.ebsco.com/terms-of-use

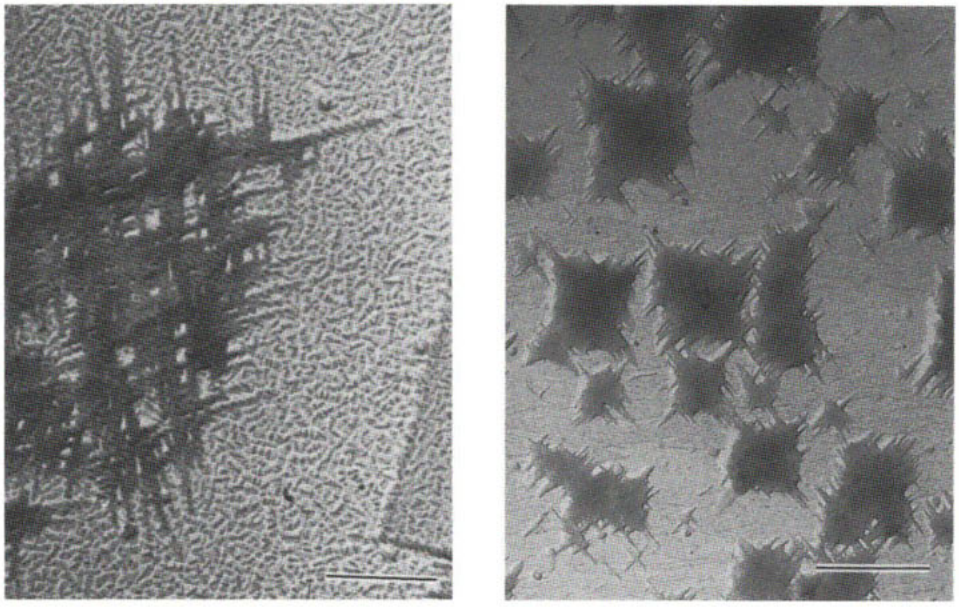

a b

Figure 2. a. Quadrite of iPP grown in thin film and decorated with PE vapors. The PE chain axis and lamellae are parallel to the bisectrix of the obtuse and acute angle of the quadrite, respectively. b. Epitaxial growth of iPP quadrites on a thin film of oriented epitaxially grown polyamide 11. Scale bars: 1 μm.

of quadrites which have ac contact planes and their [101] direction again parallel to the PA chain axis.

Both PE-iPP and PA-iPP interactions can be analyzed in similar terms at a molecular level. This analysis rests on the peculiar structure of the ac plane of the common, monoclinic form of iPP. The argument is summarized in Figure 3.

The crystal structure of iPP is made of ternary helices. The setting angle of these helices is such that successive (010) planes have a different lateral structure (cf. Figure 5a), since either two methyl groups (in planes of type A) or only one (in planes of type B) project out of the plane per unit-cell: the two planes have different methyl group densities. In the following, we consider planes of type A which appear preferable (although planes of type B cannot be excluded). They are characterized by nearly continuous rows of methyl groups parallel to [101], i.e. to the bisectrix of the monoclinic angle, which is therefore a strong structural

EBSCOhost - printed on 2/13/2023 3:45 AM via . All use subject to https://www.ebsco.com/terms-of-use

feature. Furthermore, these rows are at a distance of 5.05 Å (101 interplanar spacing). A quite reasonable epitaxy is therefore realized when PE chains are aligned parallel to $[101]_{iPP}$ and with the bc plane as contact plane (interchain distance of 4.94 Å, leading to a ∿ 2% mismatch (Figure 3).

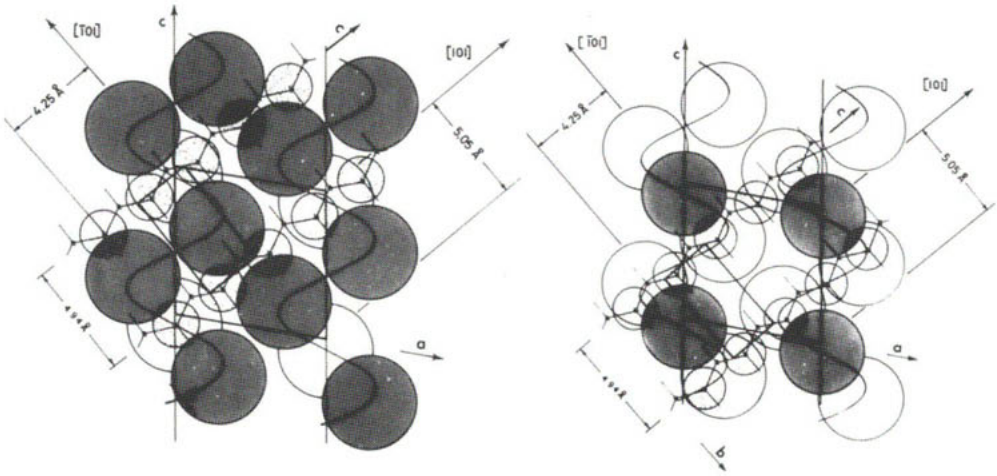

a b

Figure 3. Scheme of the interactions of the PE (100) face with the two types of (010) planes of iPP : a, face A, b, face B (cf. Figure 4a). The outer methyl groups of the iPP helices are shaded, as well as one hydrogen atom of the PE chains. Note the 50° tilt of the PE and iPP chain axes and the different density of methyl side groups in planes of types A and B.

A similar epitaxy is valid for iPP-PA systems : the PA has a planar zig-zag chain conformation dictated by the paraffinic segments ; differences of chemical nature and shortening of interchain distances introduced by the amide linkages are small enough so as to maintain the epitaxial relationship determined for PE.
The above analysis further serves as a basis for the elucidation of the molecular mechanism giving rise to lamellar branching in the crystallization of iPP, which rests on a more complicated pattern of interactions between two helical chains.

EBSCOhost - printed on 2/13/2023 3:45 AM via . All use subject to https://www.ebsco.com/terms-of-use

Lamellar Branching in Monoclinic iPP

The structure of quadrites as observed in Figure 1 but grown from dilute solutions has been investigated in great detail by Khoury (1). This structure is shown in Figure 4. Several models for the branching have been proposed which suppose epitaxial growth of the daughter branches on the fold surface of the parent lamella (1,14), or on its lateral growth faces (15,16). A recently proposed model (17) of bimodal mechanical orientation of molecules on spinning would only be valid for fibers, and is therefore inappropriate. The molecular origin of the branching can be traced back by analyzing the models proposed by Padden and Keith (15) and Binsbergen and de Lange (16), which rest on the initiation of the daughter branches on the lateral (010) faces of the parent lamellae (8). It can also be deduced from an analysis of the quadrite structure. This latter approach is presented here.

The α monoclinic form of iPP has a crystalline structure characterized by the presence of both right and left handed helices. Packing considerations lead to a structure in which each helix of a given hand is surrounded by helices of opposite hand. Interestingly, successive (010) planes are made of helices of different hand. Furthermore, these (010) planes are well developed crystal planes since they correspond to the lateral faces of the lath-like crystals. We now examine the hand of the helices in the lateral faces of the quadrite component, admitting that these faces are of type A (cf. Figures 5a and 3a).

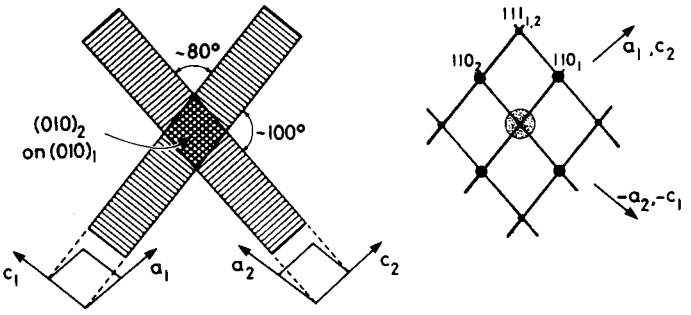

Figure 4. The lamellar organization, unit-cell orientation and diffraction pattern of iPP quadrites. The $-b_1$ and b_2 directions stick out of the plane of the paper, respectively.

EBSCOhost - printed on 2/13/2023 3:45 AM via . All use subject to https://www.ebsco.com/terms-of-use

Examination of Figures 3a and 5c indicates that the helical path on the exterior of a (010) plane of type A is parallel to the short diagonal of the ac face of the unit-cell, which is nearly a lozenge, ($a \sim c \sim 6.50$ Å, $\beta \sim 100°$). Knowing the unit-cell orientation in the quadrite (as determined by electron diffraction, cf. Figure 4) and the chain axis direction in each set of lamellae (normal to the lamellar fold surface), it is a simple matter to deduce that in the quadrite of Figure 5b the sets of shaded and unshaded lamellae have front, exposed (010) planes made of left and right handed helices, respectively (Figure 5c).

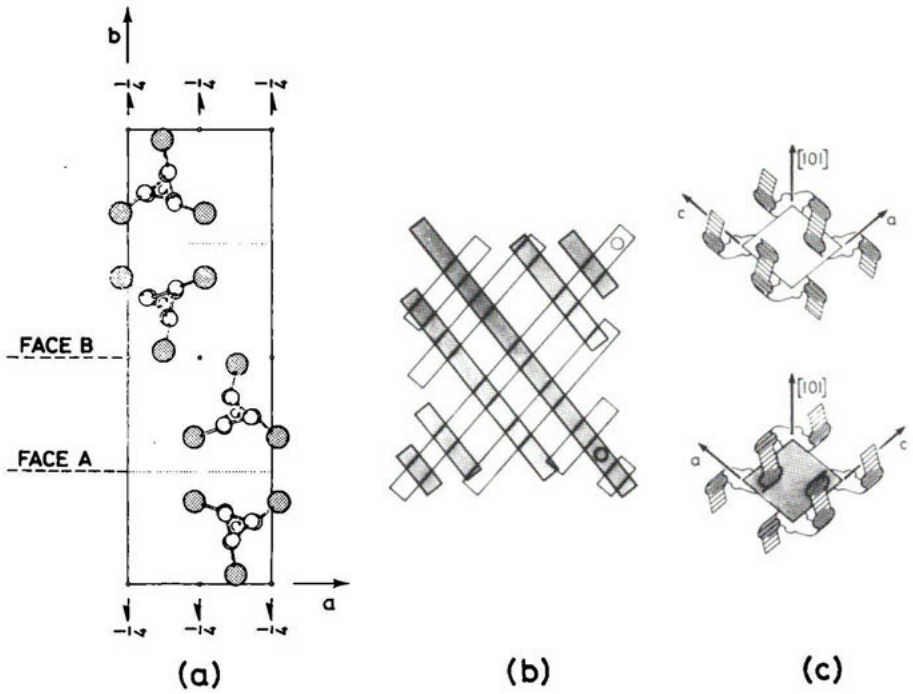

Figure 5. a. The iPP α form crystal lattice in c axis projection. Note the different azimuthal setting and helical hand of chains in the b axis direction, giving rise to two (010) faces : A and B (cf. Figure 3). b and c.Schematic representation of the iPP quadrite and of the helices in its exposed (010) faces. The helical sense is opposite in the shaded and unshaded growth faces (here supposed to be of type A).

EBSCOhost - printed on 2/13/2023 3:45 AM via . All use subject to https://www.ebsco.com/terms-of-use

Examination of Figure 5a on the other hand demonstrates that for (010) planes of a given type the helical sense is opposite in the two lateral (010) faces of any lamella (i.e. in the front and the back faces of the lamellae which build up the quadrite).
Combining these two pieces of information leads to the following conclusion : the (010) front faces of one set of lamellae in the quadrite, and the back faces of the other set are made of helices of the same hand. If a daughter lamella is generated on the lateral (010) face of a parent one, the "branched" orientation must result from specific interactions between helices of the same hand.
These interactions are schematized in Figure 6 which represents (a) interactions between a layer of right handed helices and a layer of left handed helices (i.e. the contact across plane A in Figure 5a); (b) interactions between two layers made of right handed helices, arranged so as to have their rows of methyl groups facing each other, but keeping their chain axes parallel; (c) the same situation as in (b) but after a 100° rotation of one layer which brings the a_1 and c_2 axes of the unit-cell in parallel. This rotation restores contacts between the two layers very similar to those in (a) i.e. to those existing in the actual crystal structure. It is in particular characterized by the alignment of the rows of methyl groups which are the prominent structural features of the faces in contact.
The above analysis therefore indicates that branching in iPP is linked with the deposition on the lateral faces of the lamellae of chains of the same hand as the substrate ones, while the crystallographic structure would require chains of opposite hand : the branching corresponds to a rupture of the alternation of right and left hand of helices in successive (010) planes. The branching is of course also favoured by the near identity of the a and c parameters of the unit-cell, and can therefore be analyzed in terms of epitaxy, as has been done by Padden and Keith and in particular by Binsbergen and de Lange. The molecular picture is consistent with and actually complements these early "crystallographic" analyses of the branching mechanism.

EBSCOhost - printed on 2/13/2023 3:45 AM via . All use subject to https://www.ebsco.com/terms-of-use

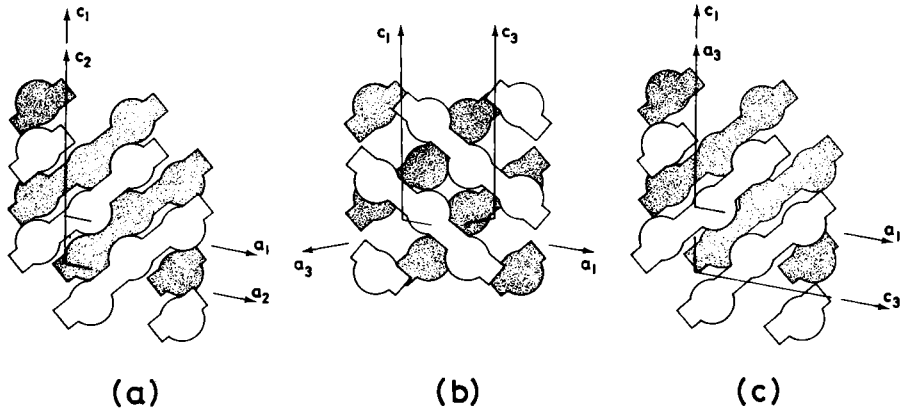

Figure 6. Helical and methyl side groups arrangement in contact planes of type A for (a) the normal crystal packing. The methyl rows have been underlined by bars ; the bottom layer is shaded. The top layer (unshaded) is its mirror image (chains of opposite hand). (b) Sheets made of helices of the same hand and with their faces of type A in contact. Note the steric conflicts arising from the different orientation of the methyl rows. (c) The situation in (b) after a 100° rotation of the top layer, which gives rise to the epitaxy and the lamellar branching.

Discussion

The elucidation of the molecular events giving rise to lamellar branching in α iPP, and the determination of the structural relationships in blends of iPP and aliphatic polymers (PE, polyamides and polyesters (9)) underline the importance of the structural characteristics of the lateral (010) faces of iPP. Specifically, the arrangement of methyl side chains in well aligned rows inclined at ∿ 50° to the chain axis and distant by ∿ 5 Å accounts for most of the reported structural puzzles : alignment of the aliphatic polymer parallel to the rows results in the 50° chain tilt relative to iPP ; parallel alignment of methyl rows for interacting helices of the same hand results in interhelical angles double this value, i.e. 100°, which characterize the lamellar branching of the quadrites. In both cases however the crystallographic analysis, in terms of epitaxy, applies : near identity of the methyl rows separation and aliphatic chain separation (∿ 5 Å) ; very similar a

EBSCOhost - printed on 2/13/2023 3:45 AM via . All use subject to https://www.ebsco.com/terms-of-use

and c parameters (∿ 6.5 Å) of α iPP in the homoepitaxy giving rise to the quadrites.

The structural models make it also possible to further analyze the structure of isotactic polypropylene, and to reinterpret some earlier works dealing with polymer-polymer or polymer-foreign substrate interactions.

(a) The model suggests that generation of lamellar branches involves the α form of iPP only and does not require intervening of γ phase material, as had been once suggested (15b).

As a matter of fact, γ phase crystals are nucleated on the lateral (010) faces of α phase crystals (15,18), but their apparent branching has a "morphological" origin since the chain axis is tilted at some 40° to the lamellar normal (19) in γ phase crystals. To the opposite, α phase branching clearly has a crystallographic, epitaxic origin.

(b) The unusual orientation of chain axes in iPP-PE blends and the resulting lamellar inclination of the constituents has been shown to improve the mechanical properties of PE-iPP laminates. Gross and Peterman (5) have established quite conclusively that generation of the cross-hatched morphology on annealing a PE-iPP oriented laminate increases the Young's modulus and fracture stress ; they relate the improvement with the bridging of the interlamellar, amorphous areas of iPP by the inclined crystalline, mechanically stronger, PE lamellae formed on annealing and recrystallization. It is not known whether similar reasons explain the improvement of mechanical properties observed for iPP-PE blends in certain composition ranges (20). Finally, a recent short report indicates that adhesion of iPP plies in a laminate is remarkably improved by treatment with thin coats of PE ; an epitaxial orientation of the PE on iPP has been established (21) although details are not available. It appears quite likely that the above mentioned epitaxies are of the type analyzed in the present Figure 3.

The epitaxic interactions between lattice planes of iPP and PE help understand the mutual nucleating activity of the linear and helical polymers. Such an interaction could not be foreseen from a direct comparison of the chain conformation and unit-cell geometries and parameters.

(c) iPP has often been used as a model for helical polyolefins when evaluating the nucleating efficiency of heterogeneous

EBSCOhost - printed on 2/13/2023 3:45 AM via . All use subject to https://www.ebsco.com/terms-of-use

additives. The ability of certain agents to nucleate both aliphatic polymers and helical iPP remained unexplained. The apparent "universality" of nucleating agents was actually considered as a strong argument against polymer-nucleating agent interactions of epitaxic character (6). The present results suggest, to the opposite, that the structural correspondence between $(100)_{PE}$ and $(010)_{iPP}$ also applies when dealing with foreign substrates. Indeed, nucleating agents that interact with the $(100)_{PE}$ contact plane create a "quadrite-like" morphology of iPP, which is expected if it assumed that the rows of methyl groups in iPP and the PE chains play comparable roles (9). Elucidation of the structural correspondence between PE and iPP therefore reverses the above argument and strongly reinforces the case of epitaxy as an important physical process in the heterogeneous nucleation of polymers.

Conclusion

The structural analysis and investigation of lamellar branching in iPP, and of blends of iPP and polyethylene or aliphatic polymers has revealed the key role played by the lateral (010) faces of iPP and their arrays of CH_3 side chains. The molecular picture which explains the lamellar branching rests on interactions between helices of the same hand ; these interactions of epitaxic character result in chain axes $\sim 100°$ apart. When interactions involve a polymer with aliphatic chain segments, the epitaxy results in a most curious 50° tilt. In addition to solving a number of morphological puzzles, the structural analysis also contributes to establish a useful conceptual framework for the understanding of molecular interactions in heterogeneous nucleation of polymers.

References

1. Khoury, F. 1966. J.Res.Natl.Bur.Stand. 70 A, 29.

2. Padden, F.J., H.D. Keith. 1959. J.Appl.Phys. 30, 1479.

3. Andersen, P.G., S.H. Carr. 1975. J.Mater.Sci. 10, 870.

4. Last, A.G.M. 1959. J.Polym.Sci. 39, 543.

EBSCOhost - printed on 2/13/2023 3:45 AM via . All use subject to https://www.ebsco.com/terms-of-use

5. Gross, B., J. Petermann. 1984. J.Mater.Sci. 19, 105.

6. Binsbergen, F.L. 1970. Polymer. 11, 253.

7. Lotz, B., J.C. Wittmann. 1984. Makromol.Chem. 185, 2043.

8. Lotz, B., J.C. Wittmann: J.Polym.Sci.Polym.Phys.Ed. (submitted).

9. Lotz, B., J.C. Wittmann: J.Polym.Sci.Polym.Phys.Ed. (submitted).

10. Seth, K.K., C.J.E. Kempster. 1977. J.Polym.Sci.Polym.Symp. 58, 297.

11. Wittmann, J.C., B. Lotz. 1981. J.Polym.Sci.Polym.Phys.Ed. 19, 1837; ibid., 1981. 19, 1853.

12. Wittmann, J.C., A.M. Hodge, B. Lotz. 1983. J.Polym.Sci.Polym. Phys.Ed. 21, 2495.

13. Wittmann, J.C., B. Lotz. 1985. J.Polym.Sci.Polym.Phys.Ed. 23, 205.

14. Clark, E.S., J.E. Spruiell. 1976. Pol.Eng.Sci. 16, 176.

15. Padden, F.J., H.D. Keith. 1966. J.Appl.Phys. 37, 4013; ibid., 1973. 44, 1217.

16. Binsbergen, F.L., B.G.M. de Lange. 1968. Polymer. 9, 23.

17. Sakthivel, A., A.S. Abhiraman. 1984. J.Appl.Polym.Sci. 29, 4257.

18. Morrow, D.R., B.A. Newman. 1968. J.Appl.Phys. 39, 4944.

19. Lotz, B., S. Graff, J.C. Wittmann: J.Polym.Sci.Polym.Phys.Ed. (submitted).

20. Lovinger, A.J., M.L. Williams. 1980. J.Appl.Polym.Sci. 25, 1703.

21. Lee, I-Hwa., J.M. Schultz. 1985. Bull.Am.Phys.Soc. 30(3), 444 (paper GUc 13).

EBSCOhost - printed on 2/13/2023 3:45 AM via . All use subject to https://www.ebsco.com/terms-of-use

ORIENTATION IN INJECTION MOULDED POLYPROPYLENE COPOLYMER

A. Brenna, D. Slotfeldt-Ellingsen
Senter for Industriforskning (SI)
P.O.Box 350, Blindern, 0134 Oslo 3, Norway

Introduction

Melt flow during injection moulding of plastic parts always causes an orientation of macromolecules. The subsequent frozen-in orientation of molecules and crystallites depends on the processing conditions and the relaxation time of the polymers.

As a result the structure and orientation will vary from part to part of the product and also through the thickness of the part, giving products with highly anisotropic and heterogeneous mechanical properties (1,2).

The morphology of injection moulded semi-crystalline polymers may be described as a skin-core structure (3,4,5) where the skin layer represents the portion of the part that crystallize during the filling period. Katti et al. give in ref. (6) a very useful review of the current state of knowledge regarding the interrelations between processing, microstructure and properties of semicrystalline injection moulded materials, using results reported for several different polymers.

The skin has generally been found to be highly oriented and many workers have tried to correlate the thickness of the skin layer with the anisotropic mechanical properties of moulded polypropylene parts (3,7). The core is usually described as being relatively randomly oriented.

The aim of this work has been to investigate more thoroughly the interrelation between the molecular and crystalline orientation of the different morphological zones, the anisotropical mechanical properties and processing conditions.

Morphology of Polymers
© 1986 Walter de Gruyter & Co., Berlin · New York - Printed in Germany.

EBSCOhost - printed on 2/13/2023 3:45 AM via . All use subject to https://www.ebsco.com/terms-of-use

Experimental

Series of boxes, 380x185x2mm, have been injection moulded under widely different conditions in an instrumented mould, using a 1200 ton clamping force Battenfield injection moulding machine. The material used was a PP block copolymer from Statoil. Normal moulding conditions were as follows: melt temperature: 260°C, mould temperature: 25^0C, injection time: 3s, injection pressure: 110MPa, holding pressure: 60MPa, holding time: 10s.

The morphology is characterized by optical polarization microscopy. 10 μm thick samples cut parallel to flow direction using a Jung microtom. Orientation of the different morphological zones are measured by wide angle x-ray diffraction, WAXD, using a Laue camera on a General Electric XRD-3 and CuKα radiation. Both morphology and crystalline orientation have been studied at different parts of the boxes, but the results reported here are from samples cut from the bottom of the boxes 120mm from the gate.

Mechanical properties have been studied at room temperature using samples taken 120mm from the gate. Impact properties have been tested by an instrumented pendulum using double notched samples with 3mm between the notches. Tensile properties have been tested using an Instron tensile testing machine and dumb-bell samples.

Removal of uniform layers of the cross section was carried out using a high speed, 1200 rpm, diamond tool. The method is similar to the layer removal method used for studying residual stresses (8). Some machined surfaces have been investigated in SEM and all surfaces are controlled by surface roughness analysis. Typical RA values were about 0.2-0.4.

Results and Discussion

Microstructure and orientation

Figure 1 shows the typical microstructure of cross section parallel to flow direction for injection moulded polypropylene. The different morphological zones are easily distinguishable.

EBSCOhost - printed on 2/13/2023 3:45 AM via . All use subject to https://www.ebsco.com/terms-of-use

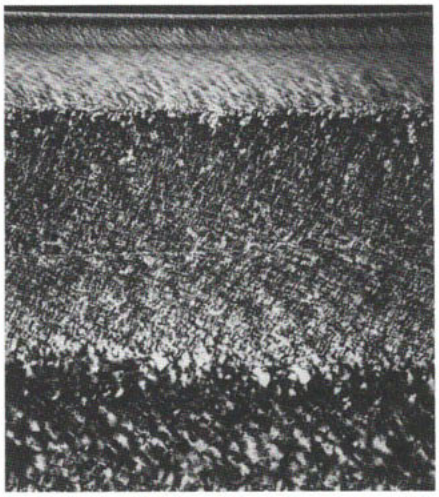

Fig. 1. Microstructure of cross section parallel to flow direction 120mm from the gate.

The skin layer, which is the portion of the part that crystallize during filling of the mould, has mainly a non spherulitic structure. Only a narrow zone near the outer surface has a very fine spherulitic structure showing that it has crystallized with a high undercooling. As this solid layer builds up, the melt lying deeper is forced into a larger degree of shearing flow over the solid to which it is molecularly connected. The deeper lying melt will therefore crystallize by fibrillar nucleation and growth, giving the non spherulitic structure (6).

The formation of molecular orientation is not only limited to the filling of the mould. There will always be a certain amount of melt motion during the compression and pressure holding period. The portion of the part that crystallize during this period is called the packing zone. Figure 1 shows that this zone has a spherulitic structure. The α-spherulites are slightly deformed and oblate, with their short axis almost parallel to flow direction. In the transition zone near the skin layer there are numerous β-spherulites which preferably develop from shear-stressed melts (9).

The core consists of 20-40μm rotational symmetrical spherulites.

EBSCOhost - printed on 2/13/2023 3:45 AM via . All use subject to https://www.ebsco.com/terms-of-use

Figure 2 shows WAXD-patterns from the different morphological zones of the cross section. The flow direction is vertical.

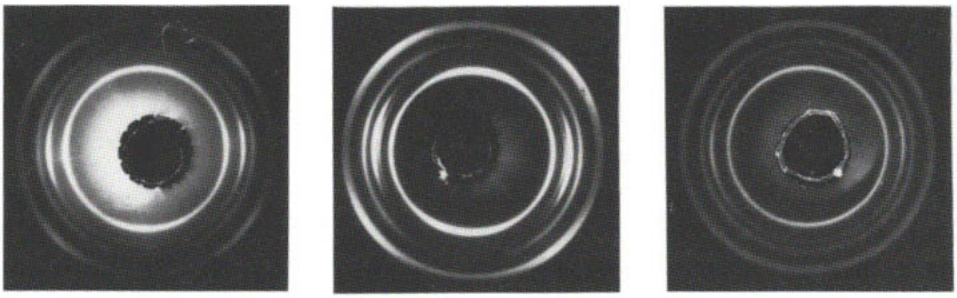

Fig. 2. WAXD-patterns from the different morphological zones. To the left the pattern from the skin layer, in the middle the pattern from the packing zone and to the right the pattern from the central part of the core.

Figure 2 shows that the skin layer and packing zone have about the same degree of crystalline orientation even though the structure are widely different. The central part of the core is almost randomly oriented.

The WAXD-patterns from the skin layer and the packing zone show the bimodal orientation typical of polypropylene (9,11). This indicates that most of the lamellae are oriented with the chain axis parallel to the flow direction, but there is a secondary population of lamellae which are oriented with the chain axis transverse to the flow direction.

Higher shear rates in the cavity during filling of the mould gives as a result a higher degree of orientation in the skin layer. This can be seen from WAXD-patterns which are similar to those from drawn films and fibres (10). Equivalently oriented injection moulded samples have been reported by Mencik et al. (5) at short injection times or low melt temperatures.

Anisotropical mechanical properties

Figure 3 shows the results of impact and tensile testing of samples cut parallel and transverse to the flow direction. The skin layer, about 0.1mm thick, has been removed from either side of some of the samples and the anisotropical mechanical properties of these samples are compared with those of untreated samples.

EBSCOhost - printed on 2/13/2023 3:45 AM via . All use subject to https://www.ebsco.com/terms-of-use

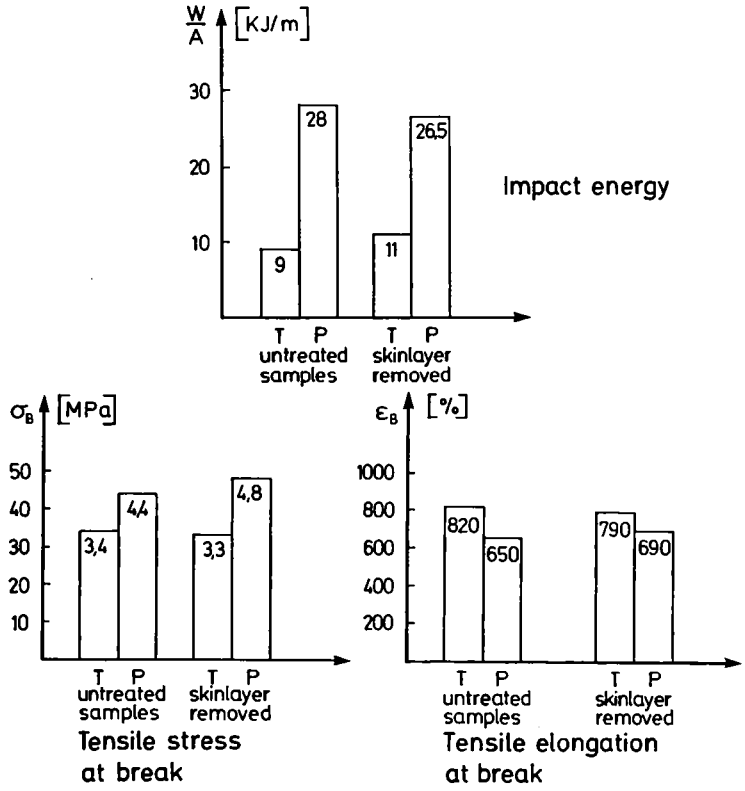

Fig. 3. Results of impact and tensile testing of samples taken parallel and transverse to the flow direction. The oriented skin layer, about 0.1mm thick, has been removed from either side of some of the samples.

The brittle failure of transverse samples and the more ductile failure of parallel samples are caused by the molecular and crystalline orientation in the flow direction.

The degree of anisotropy will be modified by moulding conditions and will also vary from part to part of the boxes. The impact properties have been studied as a function of processing conditions and at different parts of the boxes. These results will be published elsewhere. The general trend is that the failure mechanism, both parallel and transverse, is more brittle near the gate and more ductile further away. Another important point is that

EBSCOhost - printed on 2/13/2023 3:45 AM via . All use subject to https://www.ebsco.com/terms-of-use

there were no correlation between the thickness of the skin layer and the anisotropic impact properties.

Figure 3 shows that the mechanical properties are highly anisotropic even though the skin layer is removed. This is not unexpected since the WAXD-patterns show that the packing zone is as highly oriented as the skin layer.

Conclusion

Wide angle x-ray diffraction shows that the packing zone may have as high a degree of crystalline orientation as the skin layer, even though the microstructure is very different. The crystalline orientation of the packing zone highly influences the anisotropic mechanical properties which are retained when the skin layer is removed.

The mechanical properties varies with the moulding conditions and from part to part of the boxes. The general trend, regardless of this variation, is that the skin layer has little influence on the short term mechanical properties of injection moulded PP parts, as long as it constitutes a minor volume of the part.

Work has been started to characterize more thoroughly the molecular and crystalline orientation and the mechanical properties of the different morphological zones. This is necessary to understand how the processing conditions influence the microstructure and the mechanical properties of moulded parts.

References

1. Tadmor, Z. 1974. J.Appl.Polym.Sci. 18, 1753.

2. Clark, E.S. 1973. Appl.Polym.Symp. 20, 325.

3. Kantz, M.R. 1974. Int.J.Polym.Mater. 3, 246.

4. Menges, G., G. Wübken, B. Horn. 1976. Colloid Polym.Sci. 254, 267.

EBSCOhost - printed on 2/13/2023 3:45 AM via . All use subject to https://www.ebsco.com/terms-of-use

5. Mencik, Z., D.R. Fitchmun. 1973. J.Polym.Sci., Polym.Phys.Ed. 11, 973.

6. Katti, S.S., J.M. Schultz. 1982. Polymer.Engn.Sci. 22, 1001.

7. Fujiyama, M., K. Azuma. 1979. J.Appl.Polym.Sci. 23, 2897.

8. Coxon, L.D., J.D. White. 1980. Polym.Engn.Sci. 20, 230.

9. Samuels, R.J., R.Y. Yee. 1972. J.Polym.Sci. A-2, 10, 385.

10. Samuels, R.J. 1974. Structural Polymer Properties. John Wiley & Sons, New York.

11. Lovinger, A.J. 1983. J.Polym.Sci., Polym.Phys.Ed. 21, 97.

EBSCOhost - printed on 2/13/2023 3:45 AM via . All use subject to https://www.ebsco.com/terms-of-use

EBSCOhost - printed on 2/13/2023 3:45 AM via . All use subject to https://www.ebsco.com/terms-of-use

Morphology of Deformed Polypropylene

M. Kojima, H. Satake

Chisso Corporation, 2-7-3, Marunouchi,
Chiyoda-ku, Tokyo, Japan

M. J. Shankernarayanan, J. H. Magill

Metallurgical and Materials Engineering Department,
School of Engineering, University of Pittsburgh,
Pittsburgh, PA 15261, U.S.A.

Summary

The ion etching technique has been applied in this morphological and structural study of deformed polypropylene and propylene/ethylene block copolymer. The surface morphological features of bulk specimens are enhanced using this technique which allows ultra thin films to be removed for electron microscopical investigations. The morphology of ion-etched surfaces reflects the surface specimen features that are representative of sample history. Some specimens were made by isothermal crystallization at predetermined temperature after fusion. Spherulitic bulk specimens were slightly deformed by uniaxial drawing and by a process which caused doubly orientation. This rolltrusion technique produces flat oriented sample strips which were examined primarily with the electron microscope after ion-etching. Ion-etched surfaces essentially exhibits layered textures comprised of crystalline arrays extending perpendicular to the oriented (draw) direction. Doubly oriented bulk samples also contain stacked crystalline layers which become clearer with increasing a draw ratio. The complex morphology of propylene/ethylene block copolymers has also been studied using ion-etching and electron microscopy.

Introduction

Isotactic polypropylene crystallizes in a cross-hatched type of texture from the melt or from solution (1)-(3). Although the crystal structure of this type of spherulites is usually monoclinic modification (α-form), two other

Morphology of Polymers
© 1986 Walter de Gruyter & Co., Berlin · New York - Printed in Germany.

EBSCOhost - printed on 2/13/2023 3:45 AM via . All use subject to https://www.ebsco.com/terms-of-use

modifications (β- and γ-forms) are still formed depending upon molecular weight (4)-(7), crystallization conditions (8)-(11) or treatment of polymer for instance by irradiation with ^{60}Co (12).

Spherulites of the α-form of polypropylene are comprised of lath-shaped lamellar crystals growing radially so that the [a] axis of crystals are parallel to the radial direction with a textural habit forming twin crystals at 79°08' or 80°40' to their (001) planes (1). It has been considered that the broad surface of two dimensional melt-grown spherulites of the α-form polypropylene is perpendicular to the [c] axis of crystals (13). Occasionally, arrays of plate-like crystals stacked, edge-on have been observed with the scanning electron microscopy (13).

It has been shown that spherulites of polypropylene are deformed continuously through a process of slip and, rotation of lamellar crystals and material separation occurs by fibrillations (14), (15). Final deformation produces molecular axis alignment corresponding to the draw direction. On the other hand, when polymers are rolled and drawn in a single operation, a planar orientation obtains in addition to uniaxial orientation producing samples with enhanced transparency in the [010] direction for nylon 6, nylon 66 (16), (17), and polypropylene (18), (19).

Spherulitic birefringence depends on the crystallization temperature from the melt (20). The spherulitic textures of isotactic polypropylene is complicated and it is closely associated with its crystal structure (3). However the surface texture of bulk polymeric materials for electron microscopy can be enhanced by ion-etching (21)-(25). The technique has been used to enhance the morphology of polyolefins (26), (28)-(30). Ultra thin films may be detached from the ion-etched surface of the bulk polymer specimens (28), (29). These films have been examined successfully by electron transmission and diffraction microscopy. Detailed surface information of the bulk polyolefin specimens has been obtained (28), (29), so that ion etching is a useful technique for studying deformed bulk polymers. In this paper the morphological and structural features of deformed isotactic polypropylene and propylene/ethylene block copolymer were investigated.

Experimental

Polymers used in the present study are commercially available polypropylene and propylene-ethylene block copolymer with characteristics listed in Table 1.

EBSCOhost - printed on 2/13/2023 3:45 AM via . All use subject to https://www.ebsco.com/terms-of-use

Table 1. Characteristics of polypropylene and propylene/ethylene block copolymer used in the present study.

Polymer	Molecular weight($\times 10^{-4}$) M_n	M_w	M_z	Melting temperature(°C)	Ethylene content (wt-%)
Polypropylene - A	5.38	30.1	98.1	165	-
Polypropylene - B	8.57	41.3	144.0	-	-
Propylene/Ethylene block copolymer	4.04	43.8	293	122, 162	9.7

Preparation of spherulitic films

Spherulitic films about 100 μm thick were prepared mostly from the melt. Polymers were isothermally crystallized at 120°C or 140°C for 24 h after fusion at 220°C for 10 min in a nitrogen atmosphere.

Crystallization was conducted at 100°C for the block copolymer.

Spherulitic films were drawn slightly in boiling water using a hand-drawer. Afterwards specimens were fixed on a glass plate or on a specimen holder for scanning electron microscopy. Most of these specimens were ion bombarded.

Doubly oriented samples

Specimens were also produced via a doubly orientation process which consisted of drawing a necked unoriented bar under pressure (ie. rolltrusion) between thermostatted metal cylinders maintained at 137°C.

A schematic of the rolltrusion procedure already reported (31) is given in Fig.1 with a designation of the deformation directions of the polymer

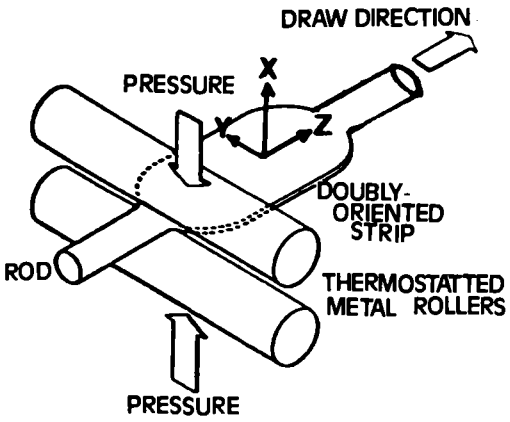

Fig.1. Schematic of the rolltrusion procedure (31).

EBSCOhost - printed on 2/13/2023 3:45 AM via . All use subject to https://www.ebsco.com/terms-of-use

specimens. The bulk specimens produced in this way were fractured in liquid nitrogen and the texture inside the samples could be investigated.

Microscopy and X-ray diffraction measurements

Ion etching was carried out in a JEOL JFC-1100 ion sputtering instrument at 500 V (ac) and 3 mA in air at a chamber pressure of 27 Pa for 60 min periods. Surface replication was carried out in the standard manner using gelatin or acetyl cellulose as an adhesive after backing with carbon film to prevent destruction of the replicated layer. After dissolving away the gelatin or the acetyl cellulose with aqueous potassium thiocyanate solution or methyl acetate, the specimen was washed well with distilled water. Thus ultra thin film of about 50 nm thick was obtained from the surface of these polymer specimens.

These specimens were examined with the JEOL JEM-100CX transmission electron microscope. The specimens used for scanning electron microscopy were always coated with a Au/Pd (60/40) alloy in a vacuum of 27 Pa and subsequently examined with the JEOL JSM-T200 scanning electron microscope. Electron diffraction was also used to study the detached thin films from the ion-etched surfaces. X-ray diffraction was also used for structure identification of the bulk specimens. Cu K_{α} radiation was employed.

Results and Discussion

Spherulitic morphology

Polypropylene forms four types of spherulites. Their birefringence and morphology depends upon crystallization temperature from the melt (20). Figure 2 typifies a scanning electron micrograph of ion-etched surface of polypropylene spherulites which was isothermally crystallized at 120°C for 24 h after fusion at 220°C for 10 min in nitrogen gas. Other crystallizations were also carried out at 140°C for 24 h from the melt.

Padden and Keith (20) showed that the predominant form of polypropylene spherulite is the type I which forms at temperatures below about 134°C, even though three other types of spherulites may grow with it (20).

It has been shown that the type II spherulites grow preferentially at temperature above 138°C (20). However, in the present study, the spherulites crystallized at 140°C were indistinguishable morphologically from those formed at 120°C. The specimens used in this study were basically of the type shown in Fig. 2.

EBSCOhost - printed on 2/13/2023 3:45 AM via . All use subject to https://www.ebsco.com/terms-of-use

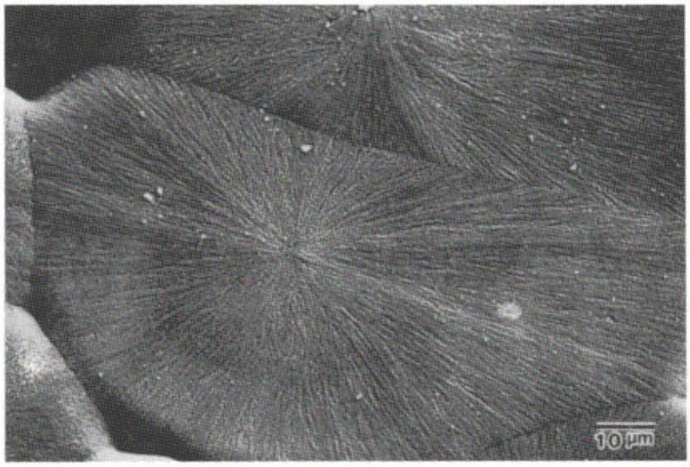

Fig.2. Scanning electron micrograph of polypropylene spherulites crystallized at 120°C for 24 h after fusion at 220°C for 10 min. Surface of the spherulites was ion-etched.

Uniaxially drawn polypropylene

When an ion-etched surface of highly drawn polyolefins is examined by electron microscopy, arrays of layered crystalline polymer (extending perpendicular to the draw direction) are observed (26)-(28). Figure 3 (a) is a transmission electron micrograph of a thin film detached from the ion-etched surface of highly drawn polypropylene film which exhibits a layered morphology. The arrow is the molecular [c] axis of the crystals, identified on the electron diffraction insert in the figure.

The ion etching emphasizes the underlying crystalline features of the

(a) (b) (c)

Fig.3. Electron micrograph of the thin film peeled from the ion-etched surface of highly oriented polypropylene specimen; (a) unrotated, (b), and (c) rotated through an angle of 40° clockwise and anti-clockwise respectively around the [c] axis with respect to position (a) in microscope.

EBSCOhost - printed on 2/13/2023 3:45 AM via . All use subject to https://www.ebsco.com/terms-of-use

specimen since less ordered regions are removed preferentially. Fine texture is clearly seen amongst the skeleton-like crystalline materials. When the thin specimens are examined after rotating 40° away from Fig.3 (a), around the axis parallel [see Fig. 3 (b) and (c)] and then perpendicular [see Fig. 4 (a) and (b)] to the draw direction, the fine texture amongst the crystalline arrays become emphasised.

The ion etching accentuates the terraced morphology seen in Fig.3 (a), and there is clear evidence for a plate-like lamellar crystals of approximately the same dimensions as the skeletal outline in Fig.3 (a).

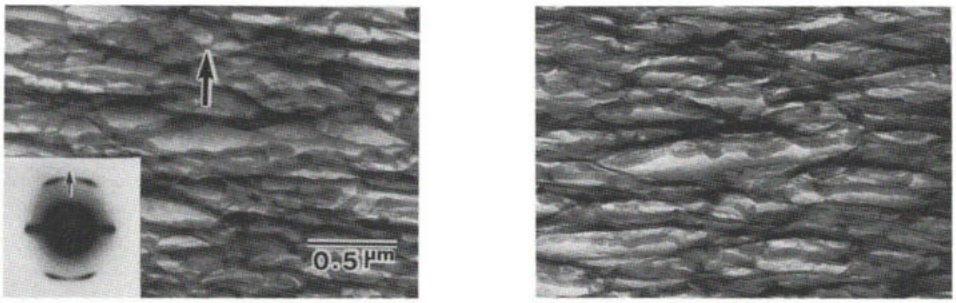

(a) (b)

Fig.4. Electron micrograph of the thin films in Fig.3; (a) rotated through an angle of 40° around the axis perpendicular to the draw direction, ie to (a) clockwise and (b) anti-clockwise from Fig.3 (a), respectively.

The width of these crystals lies between 100 nm and 250 nm, approximately. Striated layers are visible extending perpendicular to the orientation direction, where each crystal is comprised of three to five lamellae which are oriented with respect to the draw direction. Note that fibrillation among the crystalline arrays is not apparent, but this feature may be diminished or removed by over etching. Anyhow, the diffraction inserts indicate that there must be considerable coherence between these crystals. It is difficult to obtain both a well defined texture and to see fibrillation or tie molecules simultaneously after ion etching because of difficulties in controlling the etching conditions. Even so amorphous material must exist since the crystallinity of the highest drawn sample is well below 100 %.

Figure 5 (a) is a transmission electron micrograph of the thin film removed from the ion-etched surface of spherulitic polypropylene probably nucleated heterogeneously. Figures 5 (b) and (c) are electron diffraction patterns from areas A and B of this spherulite. Figure 5 (c) shows that the molecules are oriented perpendicular to the spherulite surface in this area as all of the reflections can be indexed as (hko). The morphology in the area B revealed

EBSCOhost - printed on 2/13/2023 3:45 AM via . All use subject to https://www.ebsco.com/terms-of-use

by ion etching corresponds to the (001) plane being perpendicular to the so-

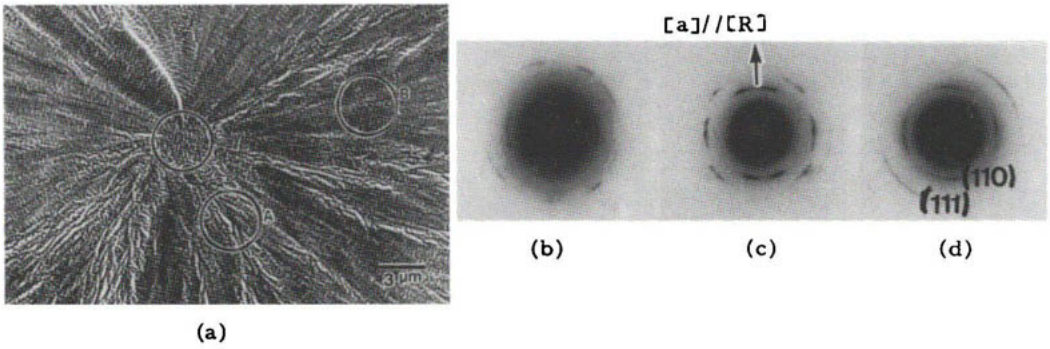

Fig.5. (a) Electron micrograph of the thin film peeled off from the ion-etched surface of underformed polypropylene spherulites; (b), (c), (d) are electron diffraction patterns from the circled area A, B, and C in the micrograph (a).

called chain folded (010) plane in polypropylene crystals. Besides Fig. 5 (c) indicates that the [a] axis lies along the radius of the spherulite.

In etched textures, the surface of the oriented polymers lies parallel to molecular chain axes and its morphology is enhanced considerably by ion-etching. The (001) plane etches smoothly for example, see area B depicted in Fig. 5 (a) along the radius of the spherulite. This morphology can be recognized easily even in scanning electron micrograph (Fig. 2).

On the contrary, the area A showing a more complex morphology is less well oriented as the diffraction pattern Fig. 5 (b) shows. Here the [a] axis lies partially along the radius of the spherulite, while it nucleated initially so that its [c] axis extended radially from the center. This orientation is confirmed in Fig. 5 (d) where the reflections are indexed as (110) and (111) from the innermost reflection outwards.

The same trend is still maintained in area A, which is closer to the center of the spherulite [Fig. 5 (b)] than area B.

Thus morphological and structural features of melt-grown spherulites and highly oriented films of isotactic polypropylene have been revealed using ion-etching technique which was successfully applied to the study of deformed bulk polymers too.

Oriented spherulites

Scanning electron micrograph of the drawn spherulite surface of polypropylene is illustrated in Fig. 6. For convenience the spherulites are divided into the four quadrants. Figure 6 (b) shows a higher magnification micrograph of the circled area in section I in Fig. 6 (a). Cracks and

EBSCOhost - printed on 2/13/2023 3:45 AM via . All use subject to https://www.ebsco.com/terms-of-use

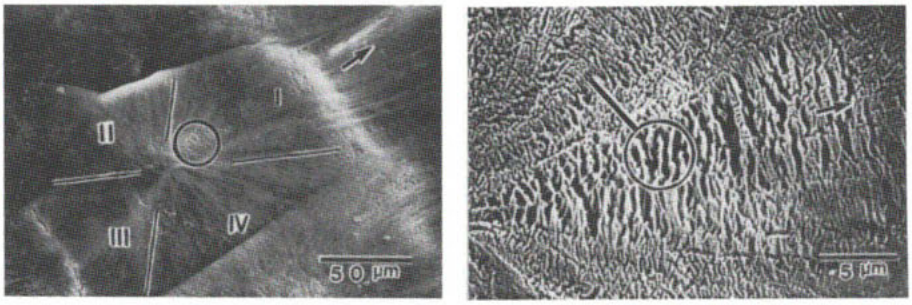

(a) (b)

Fig.6. Scanning electron micrograph of slightly deformed and then ion-etched surface of the spherulites of polypropylene: (a) low magnification; (b) higher magnification of the circled area in (a).

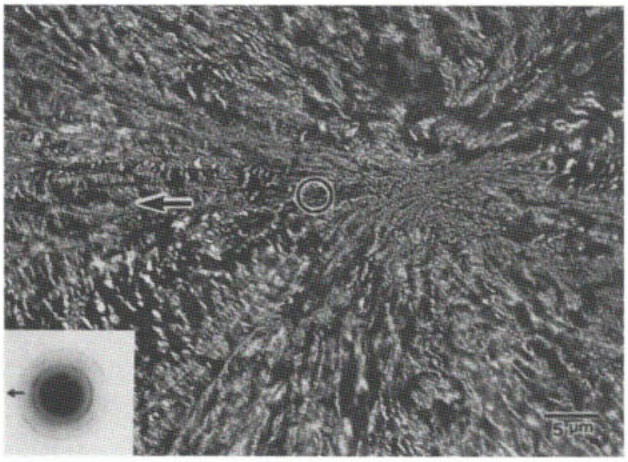

Fig.7. Transmission electron micrograph of the thin film peeled off from the ion-etched surface of the deformed polypropylene spherulite and electron diffraction pattern (insert) selected from the circled area.

plate-like crystals run transverse to the spherulite radius along with a somewhat irregular texture. Some fibrils are visible between the cracks. In the circled area of Fig. 6 (b) "tree-like" branches are visible (see insert). It can be deduced that the [c] axis is aligned along the draw direction (arrowed) in this area as revealed by ion-etching. Before deformation, the branches are believed to be caused by pulling molecular chains from the (100) plane of component lamellae along the radius in the twinned crystals (1). The fibrillation so created can be explained as above.

Figure 7 is a bright field micrograph from the thin film comprised of spherulites slightly drawn along the arrowed direction. The electron diffraction pattern (insert) is obtained from the circled area.

EBSCOhost - printed on 2/13/2023 3:45 AM via . All use subject to https://www.ebsco.com/terms-of-use

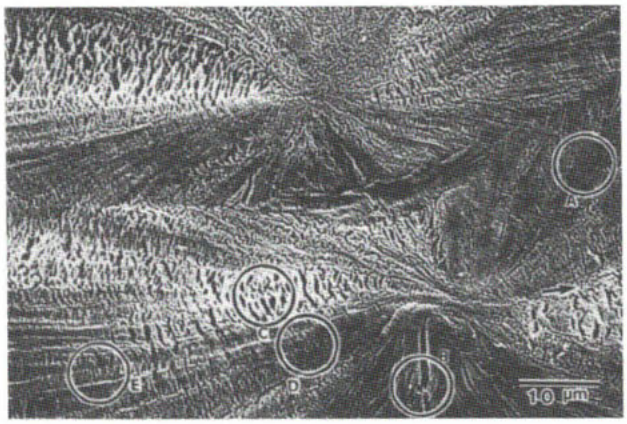

Fig.8. Scanning electron micrograph of drawn (X3) spherulites of polypropylene.

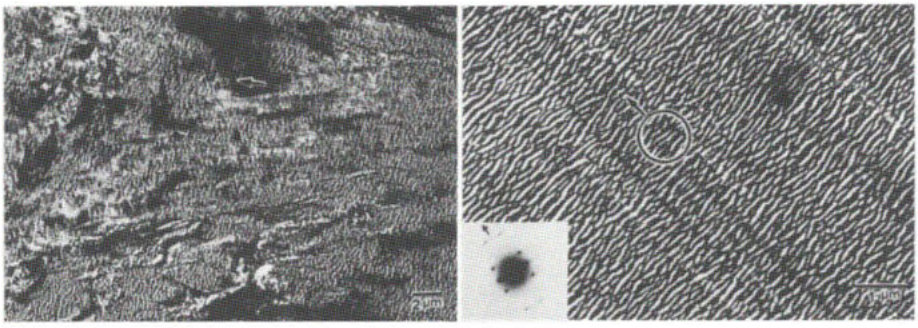

(a) (b)

Fig.9. Electron micrographs of the thin films obtained from more highly oriented regions such as the circled area D (a), and E (b) in Fig. 8. The electron diffraction pattern (insert) comes from the circled area in this micrograph.

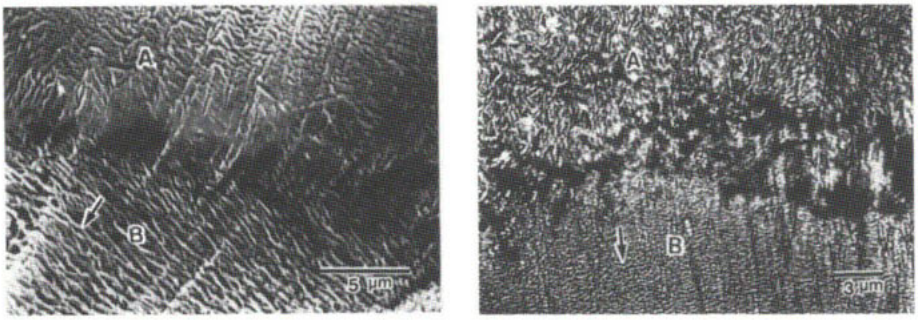

(a) (b)

Fig.10. Scanning (a) and transmission (b) electron micrographs of drawn spherulites of polypropylene.

EBSCOhost - printed on 2/13/2023 3:45 AM via . All use subject to https://www.ebsco.com/terms-of-use

The diffraction pattern shows that the orientation is poor in accord with the morphology which indicates poor alignment of crystals. The molecular chains propagate along the spherulite radius with poor [c] axis orientation. The striations observed (after ion-etching) cross the radial direction irregularly in areas where the nucleus started. When the spherulites are drawn to a higher degree (x3) localized cracks extending perpendicular and also nearly parallel to the draw direction (arrowed region) are formed as Fig. 8 illustrates. Cracks are probably created by slip (area A), or separation of the lamellar crystals in their chain folded plane (area B) when the [c] axis lies perpendicular to the surface of the spherulites in these regions.
Cracks in the area C were created by fibrillation during [c] axis orientation.
Figures 9 (a) and (b) are electron micrographs from more highly oriented areas, for example D and E in Fig. 8, respectively.
The striations (created by plate-like crystals) extending perpendicular to the draw direction (arrowed) are clearly visible in Fig. 9 (a). In Fig. 9 (b) there is much better alignment of the crystals as the diffraction pattern (insert) from the circled area shows. Fibrils bridging the crystals are observed. The crystals near the spherulite periphery are displaced prior to necking, as illustrated in the upper portion A in the scanning electron micrograph of Fig. 10 (a) and in the bottom B (necked area).
Corresponding morphologies (A and B) in the thin film are illustrated in an electron micrograph of Fig. 10 (b). Disordered arrays of the lamellae are first created in area A, and especially at the interfacial region between the areas A and B, and afterwards the lamellae aligns so that the [c] axis direction is along the draw direction.
Regions A and B exhibit electron diffraction patterns similar to those in Fig. 7 and Fig. 9 (b), respectively.

Doubly oriented polypropylene

When doubly orientation is carried out by rolling and drawing continuously, the planar orientation in the rolled plane increases with increasing draw ratio at fixed temperature. Figures 11 (a), (b), and (c) are X-ray diffraction patterns of doubly oriented polypropylene-B with a draw ratio of 37.
The incident X-ray beam is parallel to the direction X (a), Y (b), and Z (c), respectively. The formation of a planar orientation is shown by changes of (0k0) reflections. For example, it is observed that (040), and (060) reflections indicated in Fig. 11 (a), (b) are weakened when X-ray diffraction occurs with the incident beam along the X direction [Fig.11 (a)].
The ion-etched morphology in the rolled planes in the thin films is obtained

EBSCOhost - printed on 2/13/2023 3:45 AM via . All use subject to https://www.ebsco.com/terms-of-use

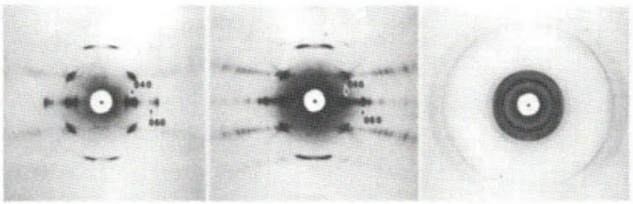

(a) (b) (c)

Fig.11. X-ray diffraction patterns of doubly oriented polypropylene B with the draw ratio of 37. The direction of incident X-ray beam is along (a); X, (b); Y and (c); Z, respectively.

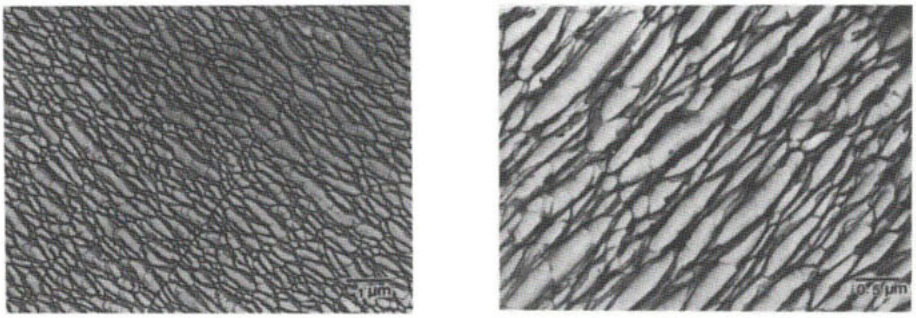

(a) (b)

Fig.12. Electron micrographs of thin films of doubly oriented polypropylene with DR=10 (a), DR=37 (b), respectively.

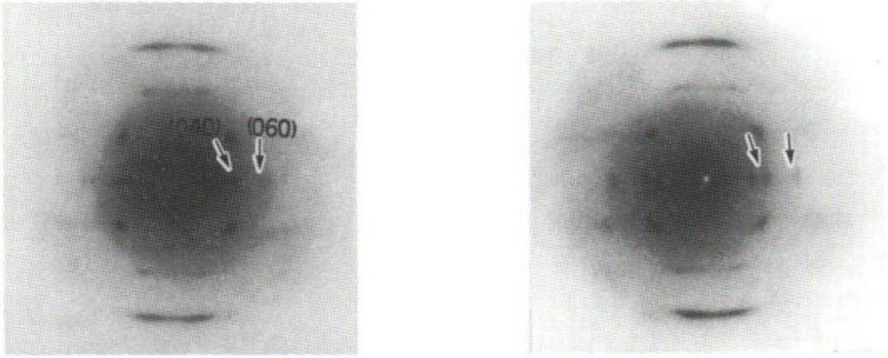

(a) (b)

Fig.13. Electron diffraction patterns of the thin films in Fig. 12. (a); DR=10, and (b); DR=37 (electron beam //[X])

from the inside of each specimen by fracturing specimens in liquid nitrogen are shown in Fig. 12 (a) DR=10 and (b) DR=37, respectively.

The specimen of low draw ratio shows fibrils bridging the crystals [Fig. 12

EBSCOhost - printed on 2/13/2023 3:45 AM via . All use subject to https://www.ebsco.com/terms-of-use

(a)], while the higher drawn specimen [Fig. 12 (b)] is nearly devoid of fibrils and the terraced morphology seen earlier, now appears between the crystals. The morphological features correspond closely to the texture noted in highly-uniaxially oriented polypropylene shown in Fig. 3. However, the crystals in the doubly oriented specimens are oriented preferentially with the [c] axis parallel to the draw direction and with (010) planar orientation. The intensity from (0k0) planes decreases with draw ratio as shown in the electron diffraction patterns of Figs. 13 (a) DR=10 and (b) DR=37. Figures 14 (a), (b), (c), and (d) are scanning electron micrographs of the ion-etched (XZ) plane located in the inside (mid-plane) of the doubly oriented polypropylene with the draw ratios of 8.2 (a), 10 (b), 30 (c), and 37 (d), respectively. The layered texture in the specimen of DR=8.2 approximately 10 μm thick is observed in Fig. 14 (a). The layered morphology gradually improves with increasing the draw ratio. Layer separation seems to originate from cracks within the layers propagating parallel to the draw direction as seen in Fig. 14 (b). Thus thinner layered films at higher draw ratios may be peeled away easily from the rolled surface in the case of highly drawn specimens.

Figure 15 illustrates simultaneously the morphology of both the (XZ) and the (YZ) plane, Fig.14, of the specimen with DR=37. The (YZ) plane shows striations extending perpendicular to the draw direction in the ion etched

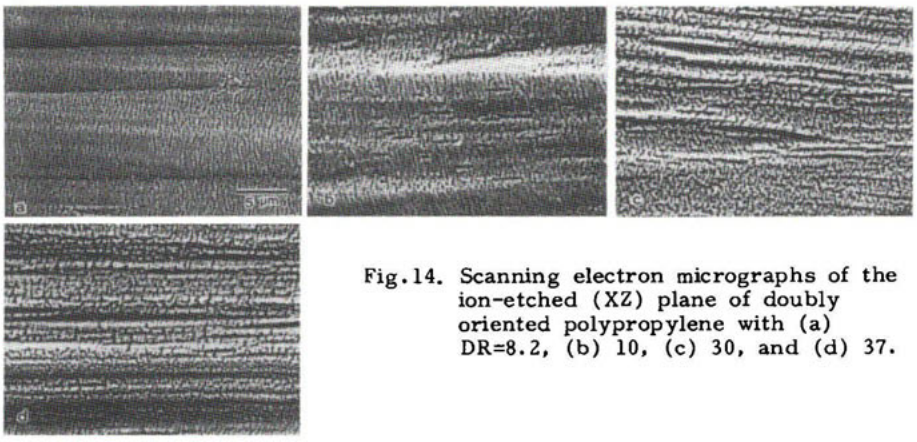

Fig.14. Scanning electron micrographs of the ion-etched (XZ) plane of doubly oriented polypropylene with (a) DR=8.2, (b) 10, (c) 30, and (d) 37.

sample (see region A in Fig. 15) because of the orderly alignment of the [c] axis in the (YZ) plane. On the other hand, the (XZ) plane (area B) shows an irregularly etched texture together with a layered morphology. Note that fibrils still connect the layers (arrowed) even after high deformation.

EBSCOhost - printed on 2/13/2023 3:45 AM via . All use subject to https://www.ebsco.com/terms-of-use

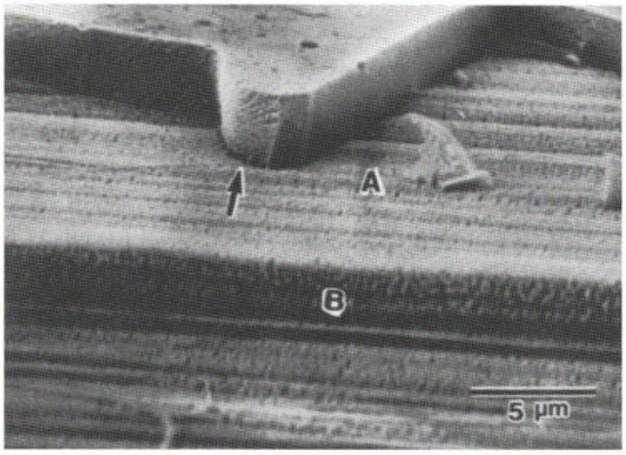

Fig.15. Scanning electron micrograph showing the (YZ) (area A) and (XZ) (area B) planes of the doubly oriented polypropylene with DR=37.

The morphology produced in the rolltrusion process indicates that the polypropylene samples can be very well oriented three dimensionally, at high draw ratio (DR=37). From the unoriented state up to this value, physical properties are enhanced monotonically with draw ratio. The ion-etching technique serves to highlight the polypropylene texture and enables one to make direct comparisons with highly uniaxially polymer.

Propylene/ethylene block copolymer

Commercial propylene/ethylene block copolymers are basically composed of two crystalline phases and a non-crystalline EPR phase (27) (28).

Two crystalline phases in the present specimen are characterised by two endothermic peaks in the differential scanning calorimetry curve at 122°C and 162°C for the polyethylene and polypropylene component respectively. The ethylene component exhibits a globular texture in the polypropylene matrix (27) (28).

Crystallization behavior of polypropylene crystals is influenced considerably by the presence of the ethylene component. Figure 16 is typical of the morphology of ion-etched spherulites of copolymer.

The morphology is very complex and it is difficult to recognize the polyethylene components within the copolymer spherulite in Fig. 16 (a).

However, an electron micrograph of the thin film detached from the ion-etched surface of the spherulites shows an aggregate of small particles, arrowed in Fig. 16 (b). These particles are the ethylene component. An electron diffraction pattern of the aggregate depicts polyethylene crystals

EBSCOhost - printed on 2/13/2023 3:45 AM via . All use subject to https://www.ebsco.com/terms-of-use

seen in Fig. 16 (c). At higher magnification, details of the dispersion of

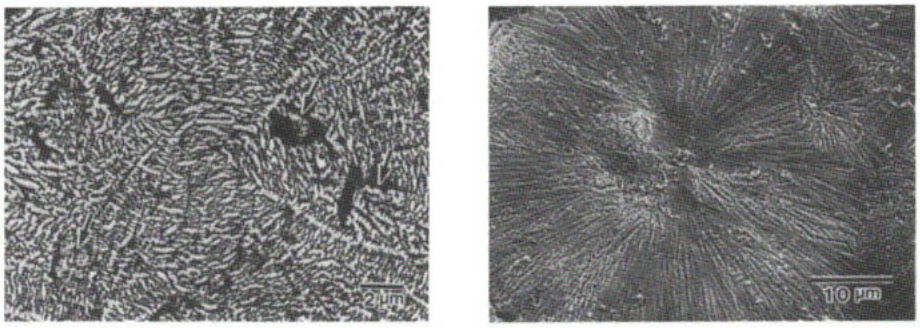

(a) (b)

Fig.16. Scanning electron micrograph of (a) the ion-etched spherulite and (b) transmission electron micrograph of the thin film obtained from the ion-etched spherulite of propylene/ethylene block copolymer. The specimen was isothermally crystallized at 100°C for 24 h in nitrogen gas.

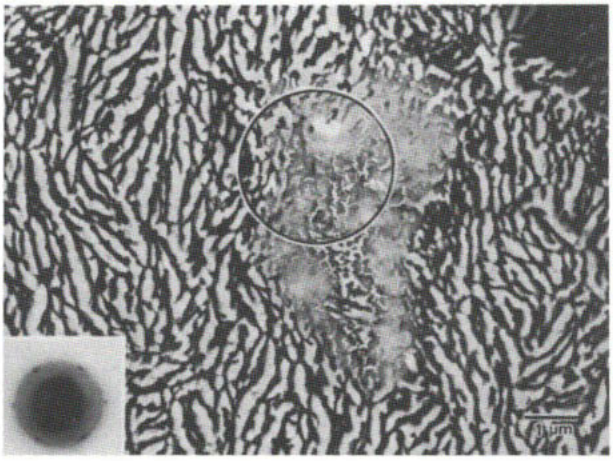

Fig.16. (c) Electron micrograph of the thin film peeled away from the ion-etched surface of P/E block copolymer.
The aggregate of small particles (central portion) and the electron diffraction pattern (insert) from the aggregate are shown.

the small particles within the polypropylene component may be seen.

Figure 17 (a) is an example of the morphology where polypropylene crystals form irregular texture as compared with a homo-polypropylene spherulite shown in Fig.17 (b). Small particles are approximately 20 nm in size are dispersed among the crystals which grown from the polypropylene component in the copolymer. The particles also adhered to the crystals. It is reasonable

EBSCOhost - printed on 2/13/2023 3:45 AM via . All use subject to https://www.ebsco.com/terms-of-use

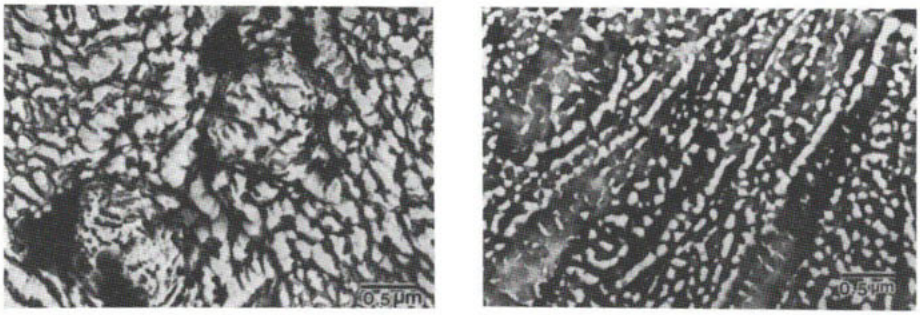

(a) (b)

Fig.17. Higher magnification electron micrographs of the thin films detached from the ion-etched spherulite surface of (a) propylene/ethylene block copolymer and of (b) polypropylene.

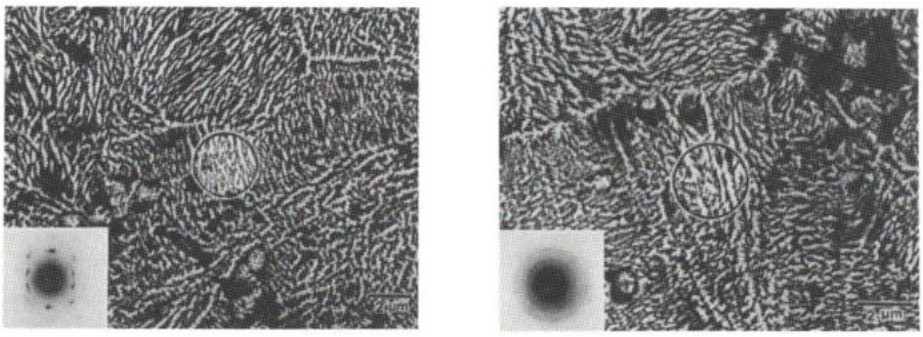

(a) (b)

Fig.18. Electron micrographs of the thin films detached from the ion-etched spherulite surfaces of block copolymer with their electron diffraction patterns (insert).

to assume that their dispersion in the polypropylene matrix influences physical properties of the block copolymers. Figures 18 (a) and (b) are electron micrographs of the thin film specimens detached from the surface of the block copolymer spherulites. Diffraction patterns from selected areas are indicated in Fig.18 (a) and (b), respectively. Branching similar to that shown in slightly deformed polypropylene, Fig.6 (b), is observed together with small particles adhering to the crystals as illustrated in Fig.18 (a). The diffraction pattern taken from this area does not reveal any crystalline ethylene component despite a concentration of something like 9.7 % w/w ethylene component present as small particles. This is probably due to either weak (scattering reflection) intensity from crystalline polyethylene unless the small particles are aggregated as illustrated in Fig.16 (c). An irregular alignment of polypropylene crystals in such areas is confirmed

EBSCOhost - printed on 2/13/2023 3:45 AM via . All use subject to https://www.ebsco.com/terms-of-use

by electron diffraction, see insert in (a) from this type of area.
We believe that this irregularity in alignment of polypropylene crystals is caused during crystallization of polypropylene. Electron diffraction pattern

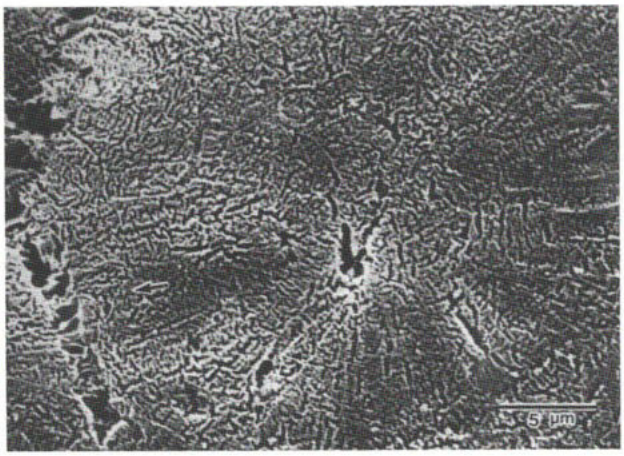

Fig.19. Scanning electron micrograph of the slightly deformed spherulite of propylene/ethylene block copolymer.

in Fig.18 (b) shows that the molecular chains are arrayed perpendicular to the spherulite surface in the circled area, but their alignment seems to be perturbed compared with pure polypropylene spherulites illustrated in Fig.5 (c). Figure 19 is a scanning electron micrograph of the slightly deformed spherulite of copolymer obtained by drawing in the arrowed direction.
There is little or no preferred orientation anywhere within the spherulites, but cracks are seen propagating along or across the radius, as well as irregularly at the central parts of the spherulite. The disruption of the polypropylene component occurs mostly around the aggregated ethylene component and it is associated with the pulling-out of the matrix into the fibrillar bundles. Craze whitening has been observed in the tensile testing of this copolymer (28).
It may be argued that the ion-etching process does not provide details of the lamellar texture in polymers. However, it is evident from the work presented here that it can be used to monitor changes in texture with processing conditions provided that artifacts, produced through overheating etc., are avoided in sample preparation. Certainly, the method highlights aspects of the underlying morphology in fractured surfaces. However, other morphological investigations using established chemical etchants, such as permanganate etching (32), are now being employed to study intricate

EBSCOhost - printed on 2/13/2023 3:45 AM via . All use subject to https://www.ebsco.com/terms-of-use

changes in morphology with processing and other physical parameters.

Conclusion

1. The thin films were easily detached from the spherulite surfaces of polypropylene and propylene/ethylene block copolymer after ion-etching.

2. The ion-etched surfaces of uniaxially oriented specimens exhibit arrays of the striations extending perpendicular to the oriented direction.

3. It was clearly shown in the ion-etched texture that the doubly oriented specimens are constructed of crystalline layers stacked perpendicular to the roll direction. The overall thickness of the layers decreases with increasing the draw ratio.
   An (010) planar orientation is found in these specimens.

4. Morphology of deformed propylene/ethylene block copolymer depends strongly on the size and distribution of the aggregates of the ethylene component distributed with in polypropylene matrix.

Acknowledgement

Partial report from the National Science Foundation (Polymer Division) is greatly acknowledged. JHM also wishes to thank the Alexander von Humboldt Foundation. The authors wish to express their hearty thanks to Miss K. Hirano of Chisso Corporation for her generous assistance in this work.

References

1. F. Khoury, J. Res. Natl. Bur. Std., 70A 29 (1966).
2. F. J. Padden, Jr., and H. D. Keith, J. Appl. Phys., 37, 4013 (1966).
3. M. Kojima, J. Polymer Sci., A-2 5, 597 (1967).
4. H. Awaya, J. Polymer Sci., B 4, 127 (1966).
5. M. Kojima, J. Polymer Sci., B 5, 245 (1967), A-2, 6, 1255 (1968).
6. F. J. Addink and J. Beintema, Polymer 2, 185 (1961).

EBSCOhost - printed on 2/13/2023 3:45 AM via . All use subject to https://www.ebsco.com/terms-of-use

7. A. Turner-Jones, J. M. Aizlewood, and D. R. Bekett, Makromol, Chem., 75, 134 (1964).
8. J. L. Kardos, A. W. Christiansen, and E. Bear, J. Polymer Sci., A-2 4, 777 (1966).
9. K. D. Pae, D. R. Morrow, and J. A. Sauer, Nature 211, 514 (1966).
10. J. A. Sauer and K. D. Pae, J. Appl. Phys., 39, 4959 (1968).
11. A. J. Lovinger, J. O. Chua, and C. C. Gryte, J. Polymer Sci., 15, 641 (1977).
12. M. Kojima and K. Mori., J. Polymer Sci., A-2, 10 1171 (1972).
13. M. Kojima, J. Polymer Sci., Polym. Lett. Ed., 17, 609 (1979).
14. R. J. Samuels, J. Polymer Sci., A-2, 6, 1101 (1968).
15. J. M. Schultz, "Polymer Materials Science" Prentice-Hall Inc. N. J. P.500 (1974).
16. I. Matsubara and J. H. Magill, Polymer 7, 199 (1966).
17. D. P. Pope and A. Keller, J. Macromol. Sci.-Phys., B 13, 1 (1977).
18. H. Sobue and Y. Tabata, J. Appl. Polymer Sci., 2, 62 (1959).
19. K. Nakayama, H. Tamamura, H. Asazawa, and H. Kanetsuna, "SOSEI TO KAKO" 21, 1096 (1980) (in Japanese).
20. F. J. Padden, Jr. and H. D. Keith, J. Appl. Phys., 30, 1479 (1959).
21. J. S. Mijovic and J. A. Koutsky, Polym. Plast. Technol. Eng., 9, 139 (1977).
22. R. H. Olley, A. M. Hodge, and D. C. Bassett, J. Polymer Sci., Polym. Phys. Ed., 17, 627 (1979).
23. A. Garton, D. J. Carlsson, and D. M. Wiles, Text. Res. J., 48, 115 (1978).
24. A. Garton, P. Z. Sturgeon, D. J. Carlsson, and D.M. Wiles, J. Materials Sci., 13, 2205 (1978).
25. D. R. Fitchmun and Z. Mencik, J. Polymer Sci., Polym. Phys. Ed., 11, 951 (1973).
26. T. Tagawa and J. Mori, J. Electron Microsc., 27, 267 (1978).
27. M. Kojima and J. H. Magill, J. Appl Phys., 45, 4159 (1974).
28. M. Kojima, J. Macromol. Sci.,-Phys. B 19, 523 (1981).
29. M. Kojima and H. Satake, J. Polymer Sci., Polym. Phys. Ed., 20, 2153 (1982), 22, 285 (1984).
30. J. E. Breedon, J. F. Jackson, M. J. Marcinkowski, and M. E. Taylor, J. Materials Sci., 8, 1071 (1973).
31. J. H. Magill, M. Kojima, S. S. Pollack, and M. N. Haller, "Advances in Chemistry Series", No.154, Am. Chem. Soc., P.17 (1976).
32. R. H. Olley and D. C. Bassett, 23 1707 (1982).

EBSCOhost - printed on 2/13/2023 3:45 AM via . All use subject to https://www.ebsco.com/terms-of-use

THE ROLE OF THE SKIN-CORE STRUCTURE IN THE AGEING OF SEMI-CRYSTALLINE POLYMERS

J.P. Trotignon, J. Verdu
ENSAM, 151 bd de l'Hôpital, 75640 Paris Cedex 13, France

R. Roques
CEA DESICP/SETI, 30205 Bagnols sur Cèze, France

Introduction

During processing, the dependence of crystallization kinetics, resulting crystallite morphology and relaxation of melt orientation on the local rate of cooling leads to a more or less contrasted, more or less complex skin-core structure. Detailed descriptions of this structure are now available, e.g. in the case of polypropylene (1,2).
Considering the great importance of the surface layers in the majority of ageing mechanisms (diffusion mechanisms, crack initiation, etc.), a surprisingly small amount of work has been devoted to the study of the influence of the skin-core structure on the long term behaviour. The aim of this work is to present some examples of this influence in the case of injection molded samples of polypropylene (PP). Three different aspects of the problem are studied: the distribution of photostabilizers (PP), the distribution of radiochemical oxidation products (Ld PE), and the crack-initiation in fatigue (PVDF).

Experimental

The materials under study and ageing conditions are described in the results section.The samples were tensile bars (NFT 51034), injection molded with a Creusot-Loire 250 T or a DK CODIM 140 T machine operating under usual conditions used in practice for

Morphology of Polymers
© 1986 Walter de Gruyter & Co., Berlin · New York - Printed in Germany.

EBSCOhost - printed on 2/13/2023 3:45 AM via . All use subject to https://www.ebsco.com/terms-of-use

these polymers. The mold temperatures were 30°C for PP and LdPE and 63°C for PVDF. The sample characterization was made on microtome sections (35-40 µm), taken with a Reichert-Jung microtome DSC (20 $K.min^{-1}$); X-ray diffraction and FTIR measurements were made for each layer, in order to determine the crystallinity ratio, beta phase content and stabilizer concentration.

Results and Discussion

1. Stabilizer distribution in PP samples

The depth distribution of crystallinity ratio and beta phase content (3) are presented in Fig. 1 for a PP sample of the melt flow index 5.0.

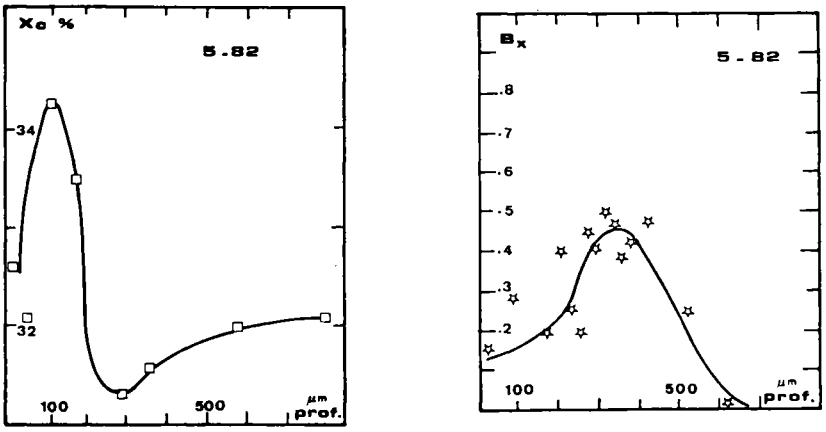

Fig.1. Depth distribution of crystallinity ratio (a) and beta phase content (b) for (MFI=5).

Three layers of different structure are clearly distinguished. Their mechanisms of formation have been (2) or will be discussed elsewhere. The polymer is stabilized by 1% of hindered amine light stabilizer (Tinuvin 722). This molecule contains ester groups which can be easily titrated by IR spectrophotometry at 1734 cm^{-1}. We used FTIR to measure for each microtome section the absorbances of this peak and of the 998 cm^{-1} peak which is usually taken for crystallinity measurements. The PP peak at 974 cm^{-1} was used as internal standard.

EBSCOhost - printed on 2/13/2023 3:45 AM via . All use subject to https://www.ebsco.com/terms-of-use

In Fig. 2, we plotted two normalized absorbancies (cm^{-1}) $S = A_{1738}/A_{974}$ against $C = A_{998}/A_{974}$ for the outer layers (depth $\sim$ 400 µm) of many injection molded samples. A negative correlation appears clearly: the lower the crystallinity ratio, the higher the stabilizer concentration. The fluctuations of the latter can reach almost 20%, which could have a not negligible influence on the polymer lifetime during weathering. This result is consistent with many data published previously, showing the low solubility of polar antioxidants in hydrocarbon polymers (4) and segregation of stabilizers at the spherulite boundaries during crystallization (5).

2. Radiochemical oxidation of LdPE

In the case of oxygen diffusion controlled photochemical or radiochemical ageing, a good kinetic model for prediction purposes must take into account the depth distribution, at each time, of photo or radio products. A simple model based on Fickian kinetics, in which diffusivity and solubility values measured in undegraded samples are considered constant, seems insufficient to explain, in the case of LdPE, some anomalies observed, for instance, in the overall photo-oxidation kinetics (6) or in the distribution of photo-products (CO groups) within the sample thickness (7). For an injection molded piece of LdPE exposed to 50 mrad pile radiation (3 $mrad.day^{-1}$), we determined the distribution of CO groups by FTIR and the crystallinity ratio x_c by DSC on microtome sections. The results are presented in Fig. 3.
In the CO distribution, we observed the same anomaly near the surface as in photodegraded samples (7). It is interesting to note that the depth of this "abnormal" layer closely corresponds to the "skin" depth. Although this phenomenon is not completely understood, it seems reasonable to suppose that the skin-core structure is involved.

EBSCOhost - printed on 2/13/2023 3:45 AM via . All use subject to https://www.ebsco.com/terms-of-use

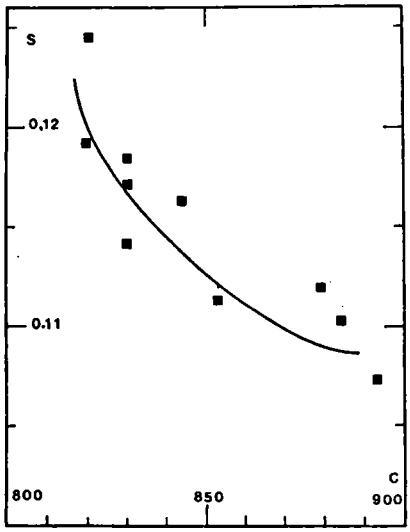

Fig.2. Normalized absorbancies S versus C for PP samples.

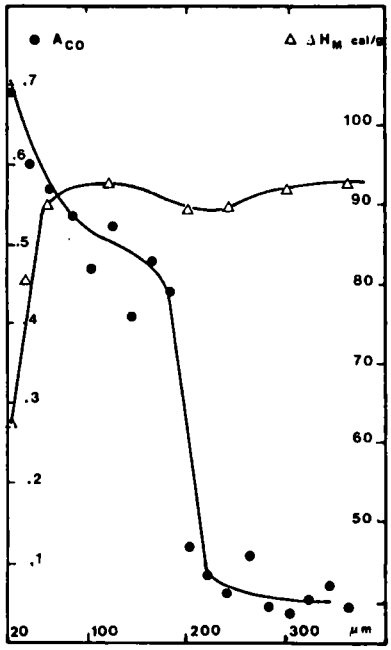

Fig.3. Absorbancy (A_{CO}) and DSC (ΔH_M) data distribution versus depth for LdPE.

3. Flexural fatigue of PVDF

Two samples P (M_n = 120 000) and S (M_n = 36 000) were molded in the same conditions and fatigue tested as molded (PN, SN), or after 14 hours annealing at 150°C (PA, SA). The machine described elsewhere (8) was operated at 22 Hz, 40°C and constant amplitude of deformation. The induced stresses continuously recorded remained constant over the whole lifetime except for the very short final period of rupture. No temperature increase was observed.
DSC was used to determine the crystallinity ratio x_c. Some initial characteristics of the samples under study are given in Table 1, including x_c, melting point, static flexural strength at break, and skin thickness determined by DSC on microtome sections (the x_c distribution has the same shape as for PP (Fig.1)).

EBSCOhost - printed on 2/13/2023 3:45 AM via . All use subject to https://www.ebsco.com/terms-of-use

In the range of induced stresses under study (between 40 and 20 MPa), the lifetime (time to break) can be expressed by a linear relationship:

$$\sigma = \sigma_0 - A \log N$$

where σ is the induced stress, σ_0 and A are constants, N is the number of cycles at rupture. The graphically determined σ_0 and A values are given in Table 1 in which we report also two series of lifetime values corresponding respectively to the induced stress of 30 MPa or a half value of the static flexural strength $\sigma_f/2$. Indeed the curves $\sigma = f(\log N)$ are not linear in the whole range of stresses: this explains why $\sigma_0 \geq \sigma_f$.

Table 1: Initial Characteristics and Fatigue Properties of Non Annealed and Annealed (14 hours at 150°C) PVDF Samples

Characteristics	P (molded)	P annealed	S (molded)	S annealed
Crystallinity ratio	0.67	0.74	0.74	0.79
Melting point (°C)	171 ± 1	171 ± 1	178	178
Skin thickness (μm)	400		300	
Flexural strength (MPa)	75	77.5	83	85
σ_0, MPa	175	152.5	98.5	84
A (constant)	20	17.3	9.7	7.8
Life time (cycles)				
at σ = 30 Mpa	17.8×10^6	12×10^6	11.5×10^6	8.4×10^6
at $\sigma = 0.5\,\sigma_f$	7.5×10^6	3.8×10^6	0.75×10^6	0.21×10^6

Whatever the chosen criterion, it is clear that the higher the molecular weight, the higher the stability. It seems however difficult to explain the observed differences only in term of chain length (entanglements in amorphous phase, tie molecules etc.), because these parameters would affect in the same way the static flexural strength, which is not the case. Considering the difference in crystallinity ratio of the samples before and after annealing and the disfavourable effect of the latter on durability, it seems more convenient to assume that the resistance to crack initiation is linked to the amorphous (ductile) phase content which allows large strains without any damage nucleation.

EBSCOhost - printed on 2/13/2023 3:45 AM via . All use subject to https://www.ebsco.com/terms-of-use

Indeed, the differences in the overall crystallinity ratio are relatively low; however, if we consider the stress gradients near the surface, the noticeable difference in skin thickness (Table 1) can account for the observed results as clearly shown in the case of fatigue of PP samples differing in their molecular weight and processing conditions (9).

References

1. Kantz M.R., H.D. Newman, F.H. Stigale. 1972. J. Appl. Polym. Sci. 16, 1249.
2. Trotignon J.P., J. Verdu. 1984. 1st SPSJ Inter. Polymer. Conf., Kyoto (Japan).
3. Turner Jones A., J.M. Aizlewood, D.R. Beckett. 1964. Makromol Chem. 75, 134.
4. See for instance Bair H.E. 1973. Polym. Eng. Sci. 13, 435.
5. Ryan T.G., P.D. Calvert, N.C. Billingham. 1978. Adr. Chem. Ser. 169, 261.
6. Huvet A., P. Philippe, J. Verdu. 1978. Europ. Polym. J. 14, 709.
7. Cunliffe A.V., A. Davis. 1982. Polym. Degr. Stab. 4, 17.
8. Gauvin R., J.P. Trotignon. 1978. J. Testing Eval. ASTM 6, 48.
9. Trotignon J.P.. 1985. Thèse d'Etat. Univ. P. et M. Curie, Paris.

Aknowledgment

This research (concerning PVDF) was supported by the Commissariat à l'Energie Atomique (CEA).

EBSCOhost - printed on 2/13/2023 3:45 AM via . All use subject to https://www.ebsco.com/terms-of-use

CRYSTAL STRUCTURE OF γ-IRRADIATED AND THERMAL TREATED POLYPROPYLENE

V.P. Krestev, B. Dobreva
Department of Physics, University of Sofia, 1126 Sofia, Bulgaria

A.M. Atanasov
Department of Chemistry, Higher School of Electrical and Mechanical Engineering (WMEI "Lenin"), 1156 Sofia, Bulgaria

E.T. Nedkov
Central Laboratory of Polymers, Bulgarian Academy of Science, 1040 Sofia, Bulgaria

Introduction

Isotactic polypropylene (PP) has three crystal modifications, α-monoclinic being the most common. β-hexagonal phase can be obtained from the α-monoclinic modification under specific conditions (1). The γ-modification is triclinic, and it has been suggested, its unit cell differs from that of the α-phase only by a simple shear parallel to the (010) planes (2,3).
It is known that γ-modification could be obtained from low molecular weight fractions by slow cooling (3) and from normal comercial PP by crystallization at high pressure (4). It has been observed that both β and γ-forms tend to convert into monoclinic α-form when the material is subjected to mechanical deformation (3) or to appropriate heat treatment (5,6).
There has been a number of investigations on the effect of gamma irradiation on PP with respect to various properties. Most of these investigations have considered the effect of gamma irradiation on the mechanical properties or on the crystalline structure (7,8).

Morphology of Polymers
© 1986 Walter de Gruyter & Co., Berlin · New York - Printed in Germany.

EBSCOhost - printed on 2/13/2023 3:45 AM via . All use subject to https://www.ebsco.com/terms-of-use

Experimental

In this work selected data on the crystal structure of γ-irradiated PP after thermal treatment are reported. The samples used as 4 mm thick plates were injection moulded from isotactic PP "Profax" (94% isotactic, $M_v = 5x10^5$ and 0.2% antioxidants) supplied by Hercules Inc (USA).
Irradiation was carried out at room temperature in air with ^{60}Co γ-source.
Having obtained the WAXS patterns, the irradiated samples were annealed in evacuated sealed tubes at 195°C for 15 min, crystallized subsequently at 120°C for 2 hours. Cooling continued in the oven that is already off.
Diffraction patterns were recorded with a TUR-M 62 diffractometer (DDR) using $Cu\text{-}K_\alpha$ radiation and a scintillation detector equipped with an analyzer.
Differential scanning calorimetric measurements were made with DSC instrument DSM-2 (USSR), using sample weights of 10 *mg* and a fixed scanning rate of $8°C.min^{-1}$.

Results and Discussion

Fig.1 shows a series of *X*-ray diffraction patterns obtained for specimens of different radiation doses, as denoted on the figures. Fig.1b presents the scans of the same samples after heat treatment. To facilitate comparison, a scan of the unirradiated samples is presented on both Fig.1a and 1b. Taking into account that strong reflections of α-form lie very close to those of β or γ-forms, the phase composition of the samples is determined using the following reflections of low and medium intensity: for α-phase the peak at $\Theta = 9.26°$ ($d = 4.77$ Å), for β-phase, the peak at $\Theta = 8.07°$ ($d = 5.49$ Å), and for γ-phase, the peak at $\Theta = 10.06°$ ($d = 4.415$ Å). The positions of those peaks are marked in the bottom of Fig.1. Careful study of Fig.1a shows some quantity of β-phase to be found along with the virgin α-phase. Its presence has been explained in the works of Muschik et al. (9) by the effect of cooling conditions and the shear stress in material processing.

EBSCOhost - printed on 2/13/2023 3:45 AM via . All use subject to https://www.ebsco.com/terms-of-use

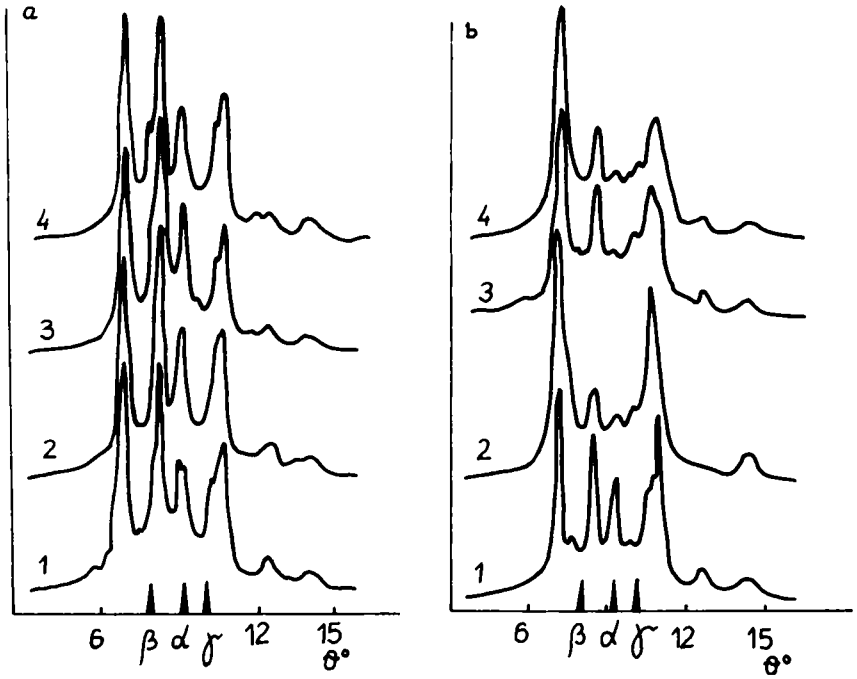

Fig.1. WAXS patterns obtained for iPP sample irradiated at different doses: 1) 0 Mrad; 2) 100 Mrad; 3) 150 Mrad; 4) 200 Mrad. a) without heat treatment; b) after heat treatment.

Fig.2a presents the melting thermograms as a function of the dose. Our results agree with some previous investigations (7). With increasing dose the melting points of the samples are strongly reduced.

DSC scans for thermally treated samples are shown in Fig.2b. The melting characteristics of these samples are much more affected by heat treatment then their *x*-ray scans (Fig.1b).

Although the unirradiated samples exhibit a single melting peak, the irradiated samples show broad doublets where the smaller peaks are at the lower temperature side. These peaks exist as shoulders for the samples irradiated at 150 and 200 Mrad.

Fig.1b shows *x*-ray diagrams obtained for the same specimens after heat treatment, as explained previously. It is readily seen that the phase composition of the samples has drastically changed. γ-form predominates and a small residue amount of α-form remains. Evidence for that is the presence of the peak at $\Theta = 10.06^{\circ}$ and

EBSCOhost - printed on 2/13/2023 3:45 AM via . All use subject to https://www.ebsco.com/terms-of-use

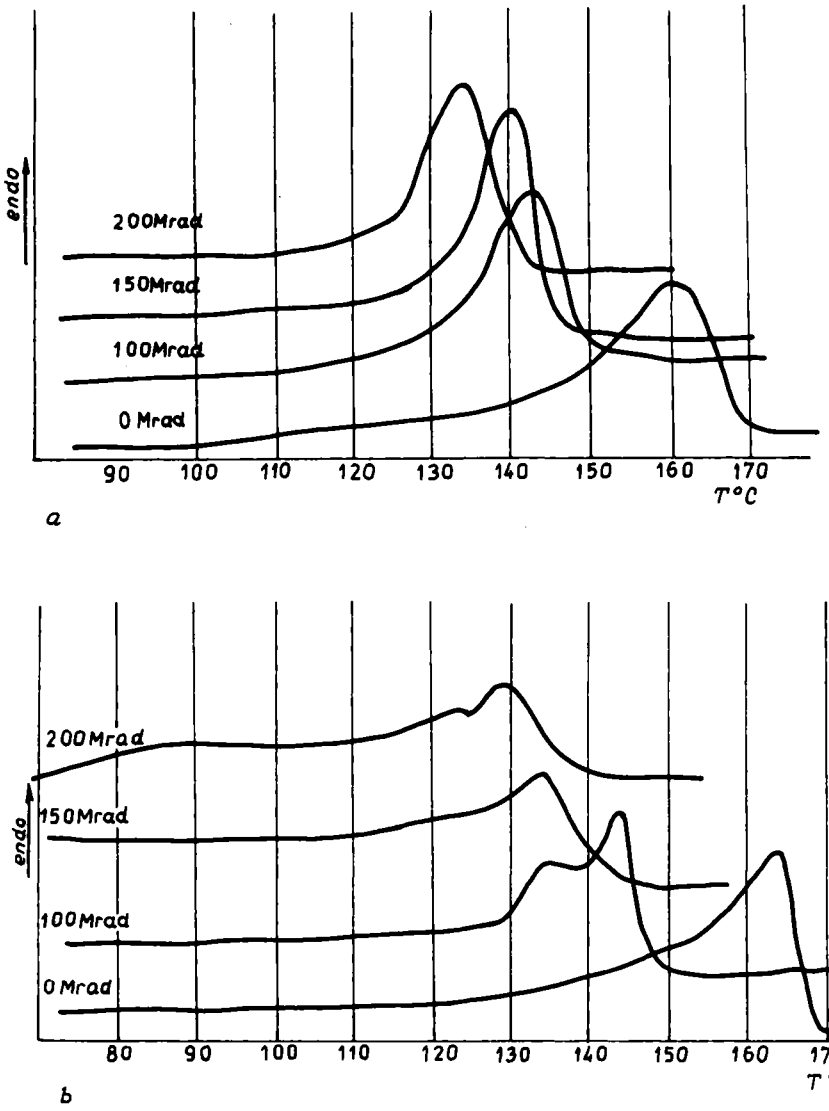

Fig.2. DSC melting thermograms of the irradiated PP samples at doses shown in the figure: a) without thermal treatment; b) after thermal threatment.

the changed intensity of the other stronger peaks.

The crystallization curves are not presented here, as for all the samples they are similar sharp single peaks, being also shifted

EBSCOhost - printed on 2/13/2023 3:45 AM via . All use subject to https://www.ebsco.com/terms-of-use

towards lower temperatures as a result of the irradiation. The data indicates that a two-phase system is present in all the irradiated samples. Obviously, the process of conversion of α to γ-form has occurred during heating.

All the results reported here undoubtly show that such heat treatment of γ-irradiated samples of isotactic PP causes major changes in their crystalline structure. These results allow us to suggest that crystallization process occurs in a field of stress created by crosslinking and at the presence of a large variety of molecular fractions. Further experiments involving WAXS and DSC are in progress now.

References

1. Leugering, H.J., G. Kirsch. 1973. Angew. Macromol. Chem. 33, 17.
2. Morrow, D.R., B.A. Newman. 1963. J.Appl. Phys. 39, 4944.
3. Turner-Jhones, A., J.M. Aizlewood, D.R. Beckett. 1964. Macromol. Chem. 75, 134.
4. Pae, K.D., D.R. Morrow, J.A. Sauer. 1966. Nature. 211, 514.
5. Pae, K.D. 1968. J. Polym. Sci. A-2, 6, 657.
6. Forgas, P., B.P. Tolochko, M.A. Sheromov. 1981. Polym. Bull,. 6, 127.
7. Busfield, W.K., J.H. O'Donnell. 1979. Europ. Polymer J. 15, 379.
8. Wang, C.S., G.S.J. Yeh. 1981. Polym. J. 13, 741.
9. Dragann, H., A. Hubeny, H. Muschik. 1977. J. Polymer Sci. Ed. 15, 1779.

EBSCOhost - printed on 2/13/2023 3:45 AM via . All use subject to https://www.ebsco.com/terms-of-use

EBSCOhost - printed on 2/13/2023 3:45 AM via . All use subject to https://www.ebsco.com/terms-of-use

SELECTIVE ETCHING OF POLYOLEFINES. II. ISOTACTIC POLYPROPYLENE, LINEAR AND BRANCHED POLYETHYLENE

František Rybnikář
Technical University Brno, Faculty of Technology
762 72 Gottwaldov, Czechoslovakia

Introduction

Selective etching of polyolefines by solutions of $KMnO_4$ in concentrated H_2SO_4 or o-H_3PO_4 represents an important preparation technique for electron microscopy. It has been successfully applied to morphological studies of many polymers (1-6). In our previous paper (4), we have studied selective etching of isotactic polypropylene (PP) by solutions of $KMnO_4$ in concentrated H_2SO_4 (Mn-S) or in 85% o-H_3PO_4 (Mn-P). The course of etching was investigated by measuring weight loss of quenched and annealed samples. The morphology of etched samples was studied by light and electron microscopy. On the macroscopical scale, amorphous and defective structures were removed together with crystalline regions, as the thickness of the removed layer largerly surpassed accepted dimensions of amorphous and defective domains. This macroscopical etching runs through a series of local selective etchings on a nm scale. Selective etching of polyolefines was achieved with all sample types and surfaces by a suitable selection of etching conditions. Here we report on further research aimed to elucidate differences in etching with Mn-S and Mn-P at higher $KMnO_4$ content and on etching with $MMnO_4$ solutions in acid mixtures. Finally, the course of PP etching was compared with that of linear and branched polyethylene.

Experimental

Materials. Commercial samples of PP Mosten 58412 (Chemopetrol, ČSSR), linear polyethylene (lPE) Marlex 6050 (Phillips, USA), and branched polyethylene (bPE) Bralen Na7-25 (Slovnaft, ČSSR) were used as melt pressed sheets. Two kinds of samples were examined:

Morphology of Polymers
© 1986 Walter de Gruyter & Co., Berlin · New York - Printed in Germany.

EBSCOhost - printed on 2/13/2023 3:45 AM via . All use subject to https://www.ebsco.com/terms-of-use

one was quenched from the melt (220°C) into ice water (-Q), the other was cooled 5 h from the melt to room temperature (-T).

Etchants. For etching the solutions of $KMnO_4$ in 96% H_2SO_4, 85% o-H_3PO_4 or in 1:1 mixture of these acids were used. Weighed amounts of fine powdered $KMnO_4$ were slowly added under agitation to known volumes of the acid. The Mn-S solution was dark green and that of Mn-P dark violet.

Etching procedure. Samples (27 × 19 × 0.5 mm) were etched with a fresh etchant. First, each sample was washed for 15 min in acetone, dried, weighed and submerged in 20 cm^3 of the etchant for the determined time without stirring. No important differences were found between stirred and unstirred experiments. After etching the liquid was sucked off the samples by filter paper; the samples were then washed 30 min in streaming water, rinsed 15 min in H_2O_2 to remove MnO_2, soaked in distilled water, washed 15 min in acetone dried over P_2O_5 in vacuo and weighed. Each point of the etching curve represents at least two independent measurements. The thickness of the layer removed, $\underline{l}$, was calculated from the weight loss assuming uniform surface etching. Taking into account errors in measuring the sample surface and weight, the experimental scatter of $\underline{l}$ values should approximately be, at $\underline{l}$ = 1, ± 0.1 μm and, at $\underline{l}$ = 10, ± 0.01 μm.

Electron microscopy. Sample morphology was studied via replication. Sample surface was shadowed by Pt at a 30° angle and backed with C-film. The replica was stripped off by poly(acrylic) acid.

Results and Discussion

Mechanism of etching. Etching isotherms of PP in Mn-P have the expected shape characterized by the highest etching rate at the beginning followed by a gradual decrease. As we pointed out earlier (4), this is due not only to the different etching rate of amorphous and crystalline regions, but also to the fact that the etching process is diffusion controlled. We do not understand the detailed etching mechanism and the actual etching agents yet. The analysis of volatile etching products has shown the presence of CO_2 and O_2 in both Mn-S and Mn-P mixtures. This proves that the final stage of polyolefine oxidation proceeds towards CO_2 and H_2O.

EBSCOhost - printed on 2/13/2023 3:45 AM via . All use subject to https://www.ebsco.com/terms-of-use

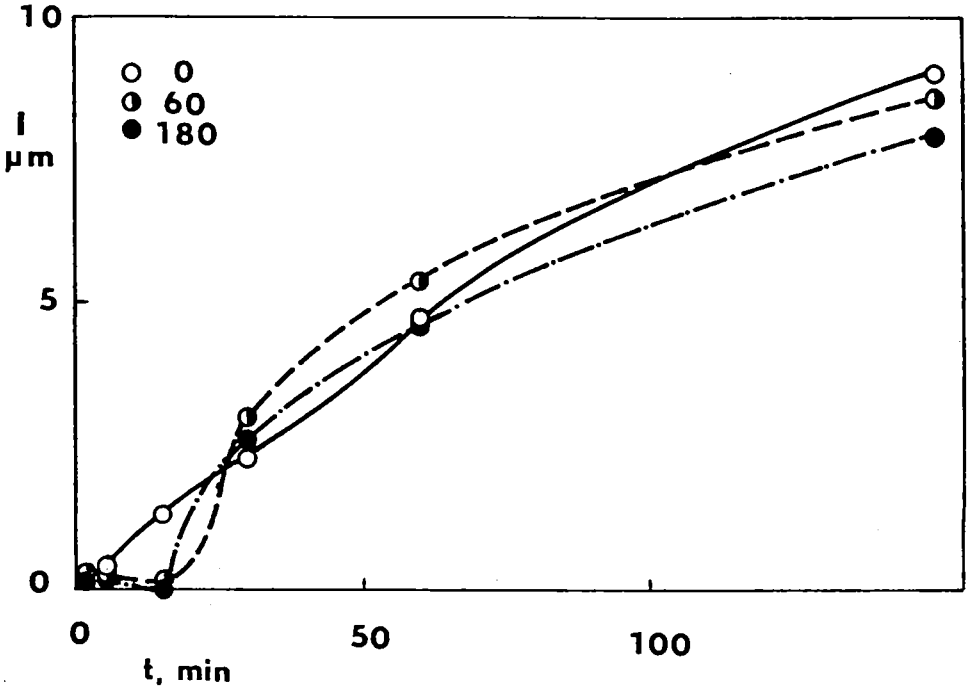

Fig. 1. Etching isotherms of PP-T in 5% Mn-P: 0 - original sample; 60 and 180 - samples preliminary etched 60 and 180 min respectively.

As O_2 evolves also from etching solutions alone, it was not possible to follow the etching course by volumetric methods. On the other hand, this makes it necessary to use fresh etchants. During polyolefin oxidation by Mn-S and Mn-P probably also solid oxidation products are formed on the etched surface which hinder from further etching. This is in agreement with etching isotherms in Fig. 1, where the etching of PP-T at 25°C in 5% Mn-P was performed with original, 60 min and 180 min preliminarily etched samples. The etching curves of preliminarily etched samples show distinct induction periods in contradiction to the original sample. The induction period represents the time necessary to dissolve or overcome the barrier of oxidation products on the etched surface. Evidently, the passivation observed in Mn-S at $KMnO_4$ concentrations over 1% has a different character. In this case, the passivation is connected with a high H_2SO_4 concentration. If this concentration is lowered, e.g., by preparing the 5% $KMnO_4$ solution in 1:1 H_2SO_4 + + o-H_3PO_4 mixtures then the passivation disappears and the etching

EBSCOhost - printed on 2/13/2023 3:45 AM via . All use subject to https://www.ebsco.com/terms-of-use

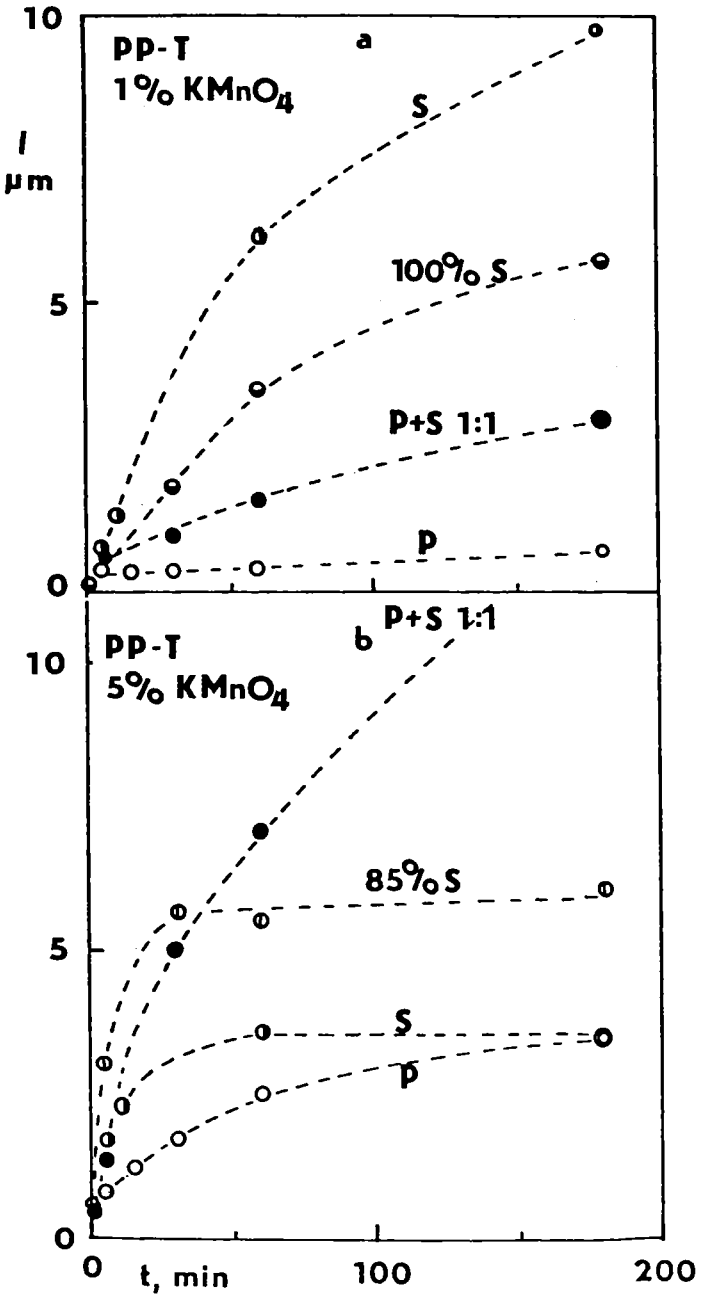

Fig. 2. Etching isotherms of PP-T in 1% (a) or 5% (b) $KMnO_4$ solution in 96% H_2SO_4 (S), 85% H_2SO_4 (85%S), 100% H_2SO_4 (100% S), 85% H_3PO_4 (P) and in 1:1 P + S mixture.

EBSCOhost - printed on 2/13/2023 3:45 AM via . All use subject to https://www.ebsco.com/terms-of-use

efficiency is much higher than in 5% Mn-S alone (Fig. 2). Diluting by water to 50 or 85% H_2SO_4 does not remove the passivation, although the etching efficiency is higher than in 96% H_2SO_4. In 1% Mn-S solution, passivation does not take place. Thus the etching course and efficiency for 1:1 mixture of H_2SO_4 and o-H_3PO_4 lie, as expected, between those of the pertinent acids (Fig. 2a).

Etching of polyethylene. Plots in Figs 3 and 4 show the thickness of the removed surface layer l versus the etching time for lPE-T and bPE-T samples at 25°C in Mn-P and Mn-S with various $KMnO_4$ content. The general picture of the etching course is qualitatively identical with that for the PP samples (4). Again, one can see the marked difference between etching by Mn-P and Mn-S with passivation at higher $KMnO_4$ content. Otherwise, we have observed the expected trend of greater etching for quenched samples. When comparing different polymers the situation is complicated. Generally, the etching efficiency of Mn-S and Mn-P differs for lPE, bPE and PP, where the etching efficiency is not simply connected with the content of amorphous or disordered phase. Thus, in Mn-P, the etching grows in order PP, lPE, bPE. Using Mn-S with $KMnO_4$ content less than 1% (no passivation effect), the rank of order for increasing etching extent is bPE, lPE and PP. This is illustrated in Fig. 5, showing the thickness of the surface layer etched off after 180 min for bPE-T, lPE-T and PP-T. A similar picture was found with quenched samples, the only difference being somewhat higher l_{180} values.

The results show two important facts:

1) Although there are differences in etching action of Mn-S and Mn-P, this does not hinder one from achieving selectivity.

2) The etching efficiency is proportional, for the same polymer, to its amorphous content, but this is not true in comparing different polymers. Thus, e.g., lPE is etched in Mn-S to a greater extent than bPE and in Mn-P is PP etched less than lPE. Only finding a typical etching course, as shown, e.g., in Fig. 1-4, does not prove selectivity of etching. This is demonstrated for bPE, where the etching by Mn-S is not selective. Here, the morphology shows markedly damaged lamellar texture, contrary to lamellar texture revealed by Mn-P etching (Fig. 6).

EBSCOhost - printed on 2/13/2023 3:45 AM via . All use subject to https://www.ebsco.com/terms-of-use

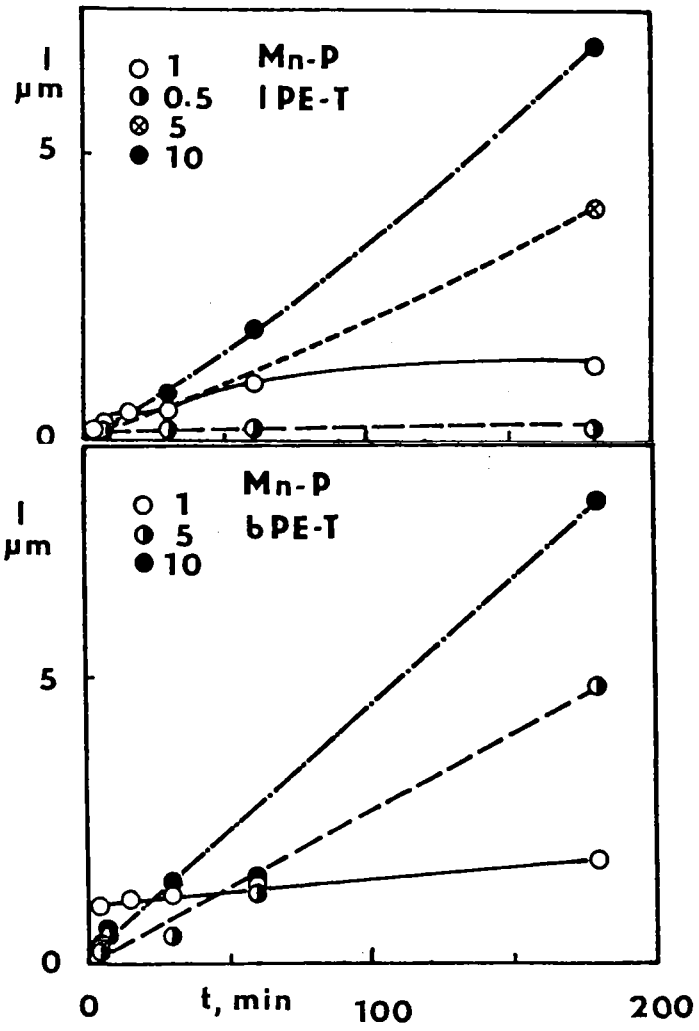

Fig. 3. Thickness of the etched off surface layer l against the etching time at 25°C in Mn-P for lPE-T and bPE-T samples.

Conclusions

It is possible to reveal details of polyolefin lamellar organization by selective etching using Mn-S, Mn-P or combinations of these etchants. For most cases, it is sufficient to etch shortly (1 min) at room temperature with low $KMnO_4$ concentration (1% or less). The thickness of the removed surface layer may be controlled

EBSCOhost - printed on 2/13/2023 3:45 AM via . All use subject to https://www.ebsco.com/terms-of-use

by $KMnO_4$ concentration and etching time. The etching curves are of two types. In Mn-P at all $KMnO_4$ concentrations (to 10%) and in Mn-S with $KMnO_4$ 1% and less, the shape of the etching isotherms corresponds with a diffusion controlled process. The gradually increasing etching barrier consists probably of oxidation products formed on the etched surface. Etching curves in Mn-S with high $KMnO_4$ content have a different shape. Here, after very fast initial etching, the etching process essentially stops. With growing $KMnO_4$ content, the thickness of the etched layer even decreases, contrary to the situation in Mn-P. The unusual etching course in concentrated Mn-S

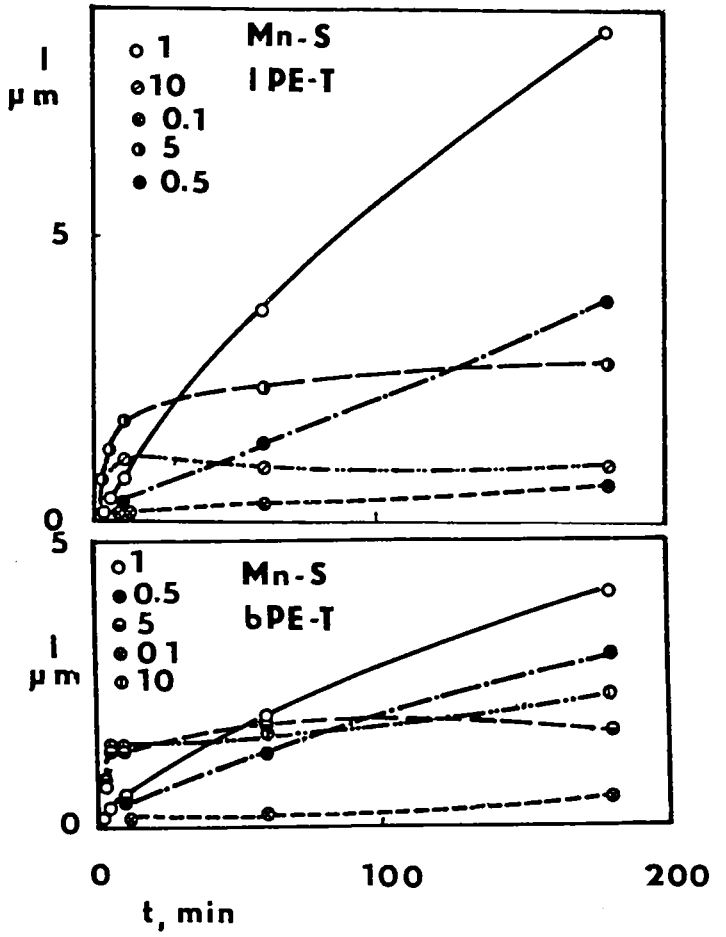

Fig. 4. Thickness of the etched off surface layer l against the etching time at 25°C in Mn-S for lPE-T and bPE-T samples.

EBSCOhost - printed on 2/13/2023 3:45 AM via . All use subject to https://www.ebsco.com/terms-of-use

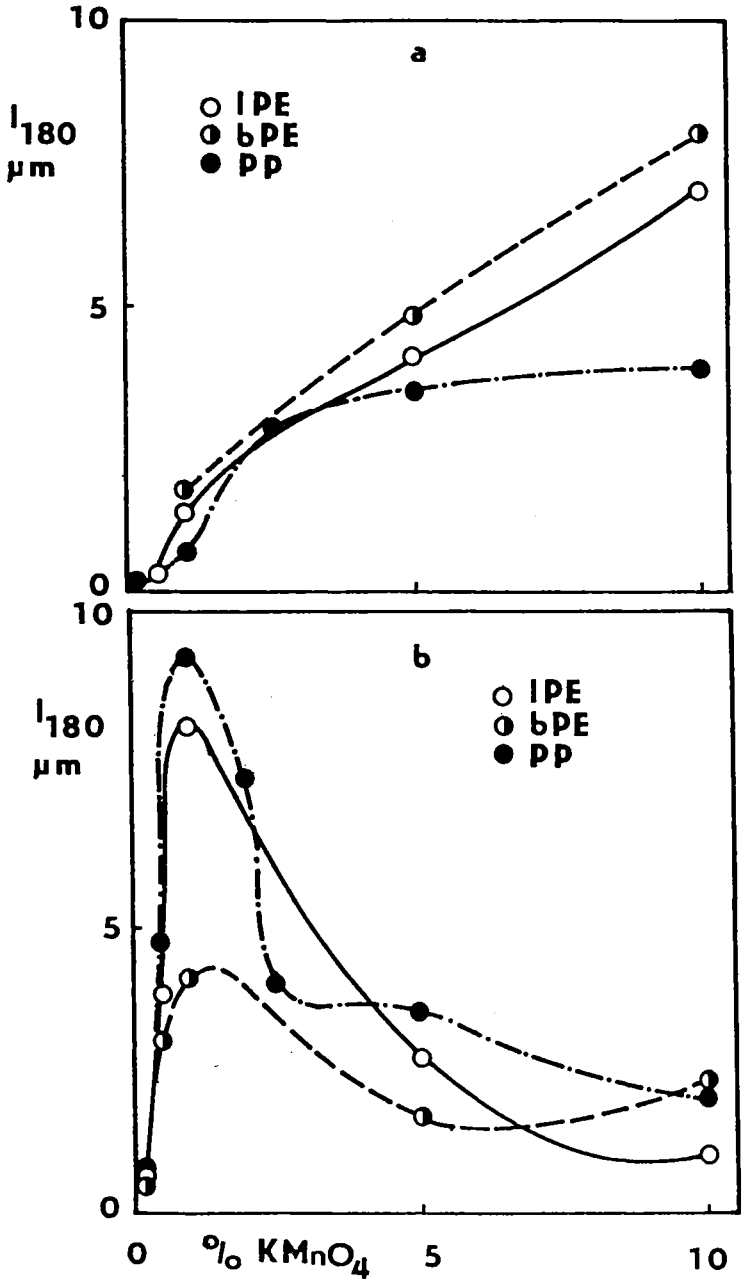

Fig. 5. Thickness of the etched off surface layer after 180 min etching of lPE, bPE and PP samples against $KMnO_4$ concentration in Mn-P (a) and Mn-S (b).

EBSCOhost - printed on 2/13/2023 3:45 AM via . All use subject to https://www.ebsco.com/terms-of-use

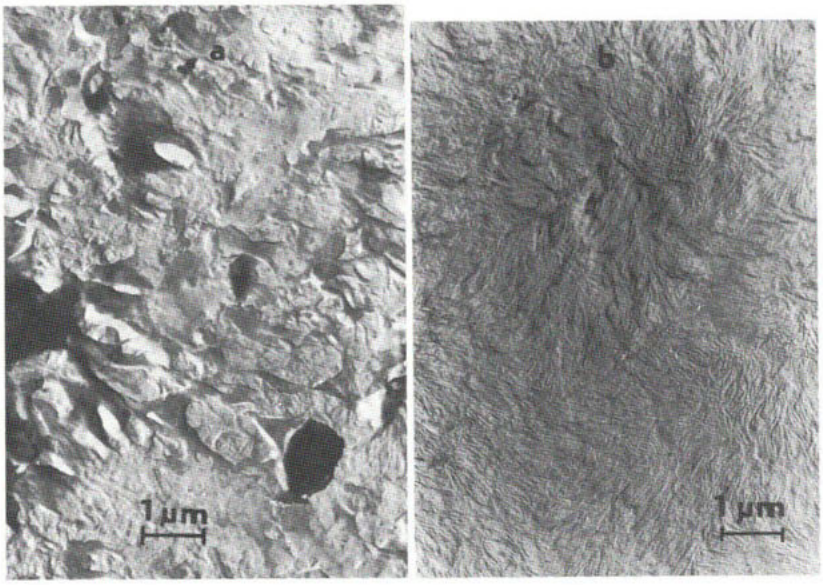

Fig. 6. Morphology of bPE etched in 1% Mn-S (a) and 1% Mn-P (b).

could be explained by H_2SO_4 passivation, because it disappears by diluting H_2SO_4 with e.g. o-H_3PO_4. Such a combined etchant behaves in a similar way as Mn-P. The extent of etching decreases for the same polymer with increasing crystallinity and crystalline order. In etching different polyolefines, one cannot find a direct correlation between the extent of etching and the content of amorphous and disordered structures. The differences in etching of individual polyolefines are due to different etching mechanisms in Mn-S and Mn-P and to various molecular configuration and supermolecular organization.

References

1. Olley, R.H., et al 1979. J.Polym.Sci., Phys. 17, 627
2. Olley, R.H., D.C. Basset. 1982. Polymer 23, 1707.
3. Barnes, S.R. 1980. Polymer 21, 723.
4. Rybnikář, F. 1985. J.Appl.Polym.Sci. 30, 1949.
5. Rybnikář, F. 1982. Plasty Kauc. 19, 321.
6. Rybnikář F. 1982. J.Appl.Polym.Sci. 27, 1497.

EBSCOhost - printed on 2/13/2023 3:45 AM via . All use subject to https://www.ebsco.com/terms-of-use

EBSCOhost - printed on 2/13/2023 3:45 AM via . All use subject to https://www.ebsco.com/terms-of-use

STRUCTURE AND DEFORMATION OF POLYETHYLENE SPHERULITES

Kaoru Shimamura
School of Engineering, Okayama University
Tsushima, Okayama 700, Japan

Introduction

Linear polyethylene (PE) forms spherulites during growth from unperturbed melts and these are composed of lamellar crystals (1,2). Structure of the spherulites and their deformation have been studied by various methods. Among these, the electron microscopical observation have given many instructive data on the lamellar organization within individual spherulites. The usual procedures for studying the polymer morphology by electron microscopy are by observing directly the bulk surface (SEM), by replicating the surface and by preparing very thin films (TEM). While the surfaces and the thin films form good analogies to the lamellar organization in various solids, some care must be taken in extending the findings into polymers in bulk state, because the surface morphology is generally very different from the internal morphology, especially in polymer solids. Some researchers have used ion- (4) or nitric acid (4,5) etchings or solvent extraction (6) techniques for removing the surface region. However, there have been always the danger of introducing artefacts by these treatments. If a specimen is fractured without the inherent plastic deformation, the exposed surface will be more appropriate for the electron microscopy. It is well known that polymer solids treated with some acids lose their ductility and become brittle. It has been proved that this effect is useful for exposing the internal morphology, free from the confusing effects of additional plastic deformation by fracture (7).

In the present work we have undertaken a study of structure of polyethylene spherulites and their deformation in order to provide information about how and where the mechanical inferiors come from into the uniaxially drawn fibers.

Morphology of Polymers
© 1986 Walter de Gruyter & Co., Berlin · New York - Printed in Germany.

EBSCOhost - printed on 2/13/2023 3:45 AM via . All use subject to https://www.ebsco.com/terms-of-use

Experimental

Materials used were a fractionated PE (NBS1475) with a molecular mass of M_w = 52000; M_w/M_n = 2.9 and an unfractionated PE (Sholex 6009, MI = 9). These PEs were melted in vacuo at 160°C for 1 h, then crystallized at 118°C for 2 h, at 125°C for 6 h and 129°C for 5 days. The resultant spherulite aggregates were drawn uniaxially in polyethylene glycol at temperatures of 0 and 100°C at a speed 1 cm/min. The samples were then immersed in fuming nitric acid for 10 h at 80°C, subsequently fractured by lightly touching the samples with a knife. The fracture surfaces were coated with gold of thickness ca. 200 Å. Specimens were observed using a scanning electron microscope (HITACHI S-310). Mechanical data were obtained using a tensile tester.

Results and Discussion

Structure of PE spherulites

It has been generally approved that banded spherulites consist of radiating arrays of continuously twisted helicoidal ribbons with

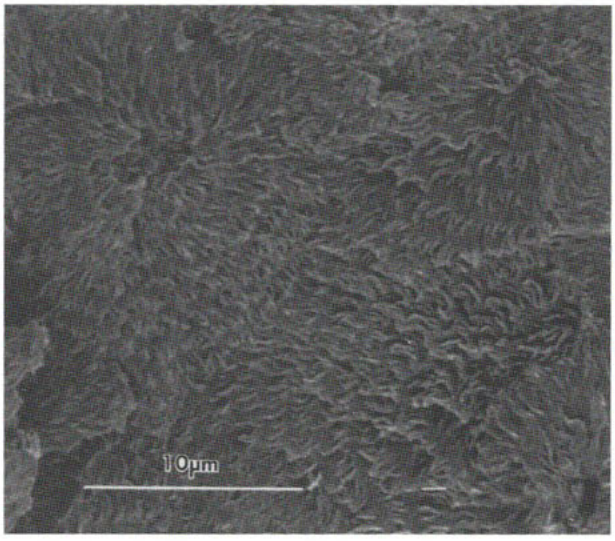

Fig.1. Banded polyethylene spherulites crystallized at 118°C.

EBSCOhost - printed on 2/13/2023 3:45 AM via . All use subject to https://www.ebsco.com/terms-of-use

b-axis on the spherulite radius (1,2). However requirement of space filling was hardly satisfied with the twisted lamellar model. Fig.1 shows an electron micrograph of banded spherulites of diameter ca. 15 μm, crystallized at 118°C. Closer inspection revealed that the lamellar crystals take the shape of parts of coiled helices. The morphology implies that the lamellar crystals grew spiraled and turned ca. two thirds until the growing fronts collided with a neighboring lamellae whose growth were simultaneously proceeding. After the collision and/or during the growth of the crystal, secondary nuclei were born on them, probably on (201)

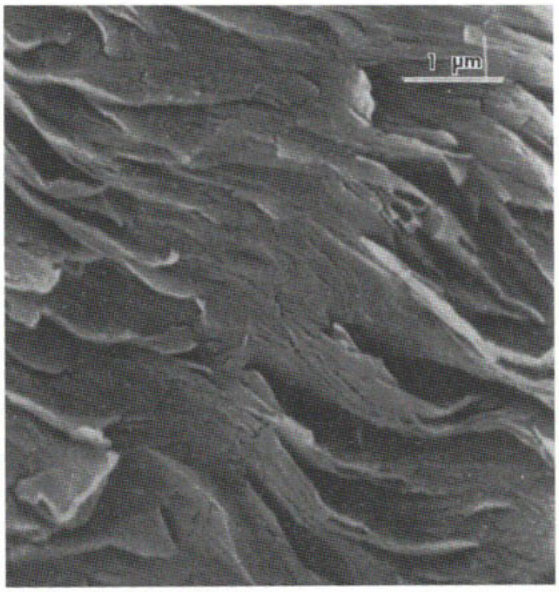

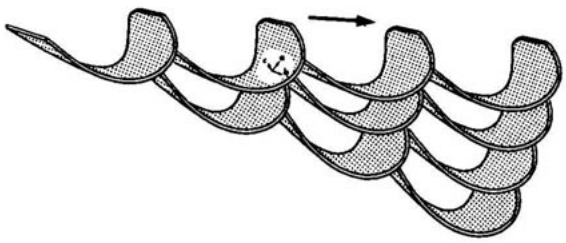

Fig.2. Lamellae in the banded spherulite.

EBSCOhost - printed on 2/13/2023 3:45 AM via . All use subject to https://www.ebsco.com/terms-of-use

facets (8), and grew in the similar way, and finally formed the helicoidal lamellae. Thus the branches continue to advance in a direction shown by an arrow in Fig.2. Electron diffraction from the spherulite fragments suggests that the b-axis is not consistent with the advance direction. This mechanism agrees with a observation that spherulites are often fractured conically and the surfaces of the cones appear to be terraced. Electron micrographs of the organization looking down along the radius have revealed that the spaces between those bent crystals are filled with subsidiary crystals born on (h01) facets of the already formed helicoidal lamellae. This banded feature is generally observed in PEs crystallized at temperature lower than ca. 123°C, increasing the band period with the crystallization temperature. In the sample prepared at 125°C, there are well developed radiating lamellae with fewer branches and without helicoidal bending. These may correspond to the "dominant S-shaped crystals" found by Bassett et al. (3,5).

At high crystallization temperatures, crystal growth proceeds very slowly and the resultant PE solid, e.g., crystallized at 129°C, consists of several bricks developed from one growth center

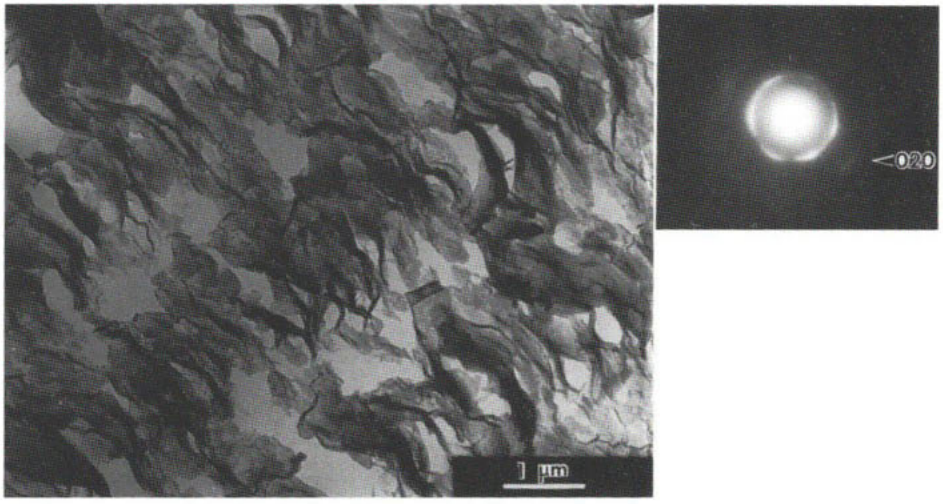

Fig.3. Transmission electron micrograph and electron diffraction of fragments of the banded spherulite.

EBSCOhost - printed on 2/13/2023 3:45 AM via . All use subject to https://www.ebsco.com/terms-of-use

(Fig.4). Within the individual bricks, there are several tens of well developed planar sheets stacked parallelly, with continuity of the observable over 10 μm. The difference in organization caused by crystallization temperature suggests that at lower temperatures, crystals grow preferably in a direction close to <110>, but at higher temperatures the growth along <010> becomes predominant.

Deformation of spherulites

There is a distinct difference in the deformation mechanism between cold drawing and hot drawing. Fig. 5a shows deformed

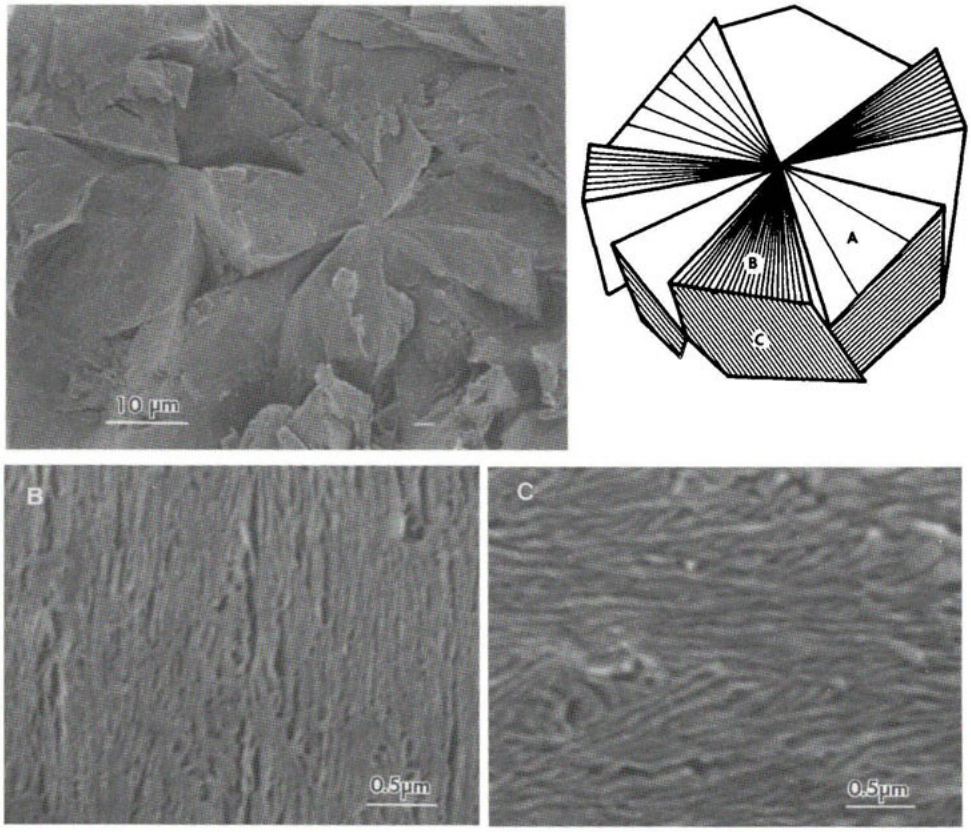

Fig.4. Polyethylene spherulites crystallized at 129°C.

EBSCOhost - printed on 2/13/2023 3:45 AM via . All use subject to https://www.ebsco.com/terms-of-use

spherulites elongated ca. 2 times uniaxially. By the cold drawing of the spherulite, the polar region (P in Fig.6) where lamellae directed comparatively parallel to the draw direction, starts to deform (Fig.5). The overall change in the shape is close to that proposed by Wang´s model (9). On the contrary, by the hot drawing, elongation starts in the equatorial region (E in Fig.6) where lamellae align on average normal to the draw direction. In this case, the deformation mode is similar to Wilchinsky´s affine deformation (10). SEM observation of the deformed lamellae in the elongated spherulite viewed along and perpendicular to the draw direction showed that lamellar parts originally almost parallel to the drawing direction (DD) tend to orient in the DD at the beginning of deformation but remnant ones are squeezed and subject to complex deformation. Fig.6 summarizes the deformation mechanism of spherulites drawn at 0°C or 100°C, which were depicted based on the SEM observation.

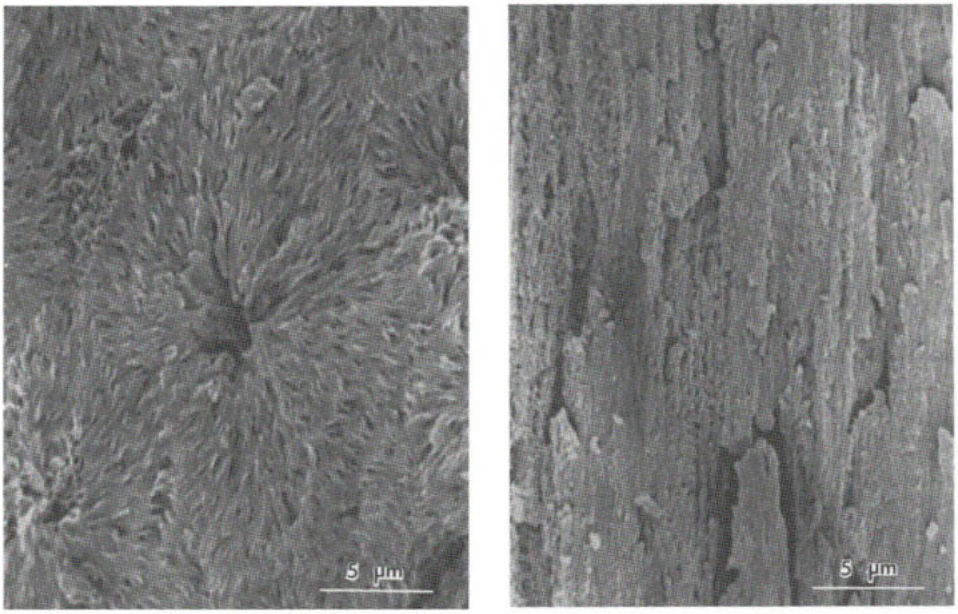

Fig.5. (a) Polyethylene spherulite elongated ca. 2x at 0°C.
(b) Polyethylene fiber prepared from spherulite aggregates at 0°C.

EBSCOhost - printed on 2/13/2023 3:45 AM via . All use subject to https://www.ebsco.com/terms-of-use

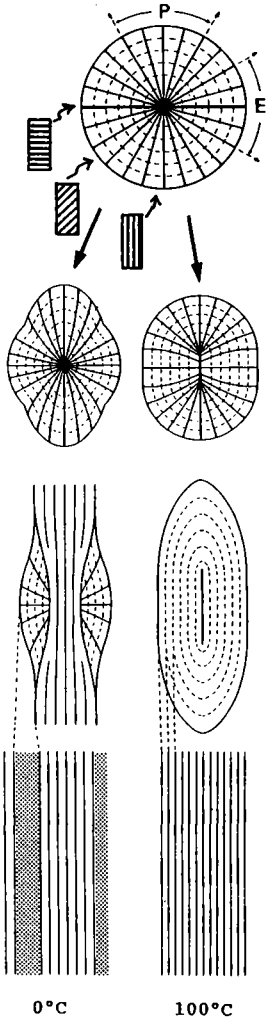

Fig.6. Deformation mechanism of polyethylene spherulites.

A PE spherulite has radially developing lamellae, and the radius is along the crystallographic b-axis. However, spherulites are so tiny that it is difficult to analyse the deformation behavior. It is well known that the extruded-blown film is composed of lamellar crystals stacked in the extrusion direction and the mechanical characteristics are easily measurable on macroscopic scale as a function of lamellar anisotropy. In order to simulate the

EBSCOhost - printed on 2/13/2023 3:45 AM via . All use subject to https://www.ebsco.com/terms-of-use

deformation mechanisms of the spherulite aggregates, we adopted the deformation data of the film and assumed as follow; in the spherulite, lamellae deform like those in the extruded-blown film depending on the angle between the lamellar normal and the DD. For example, lamellae in the polar region behave in the similar manner as the EB film which is under elongation transverse to the extrusion direction. Although the spherulite aggregate seems to obey macroscopically uniform extension, detailed examination clearly revealed the deformation is much complex microscopically. Here we assume each entity bears same stress though the strain is strongly dependent on the lamellar direction to DD. Although there are a variety of spherulite boundaries, here we analyse one special case where the boundary is flat and orients at an angle of 45° to the DD. For simplicity we divide a spherulite into 5 strips all of which contain lamellae of various orientations. The drawability (λ) of each portion is dependent on the angle between DD and the lamellar normal (Fig.7). The deformation of the strip starts at the lamellae with the least yield stress, and the portion stops elongation when the draw ratio reaches its λ. Then the next weak portions begin to be elongated. Once all the

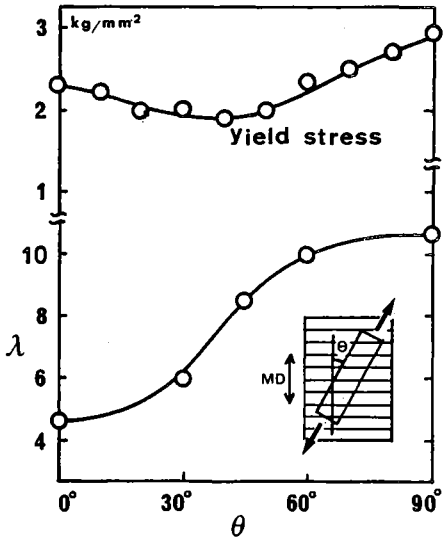

Fig.7. Mechanical characteristics of extruded-blown film.

EBSCOhost - printed on 2/13/2023 3:45 AM via . All use subject to https://www.ebsco.com/terms-of-use

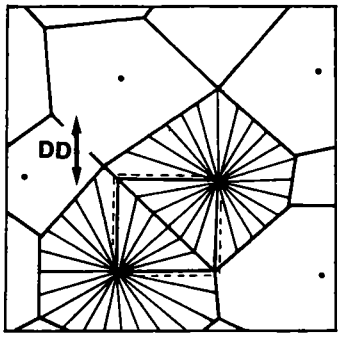

Fig.8. Model of spherulite aggregate.

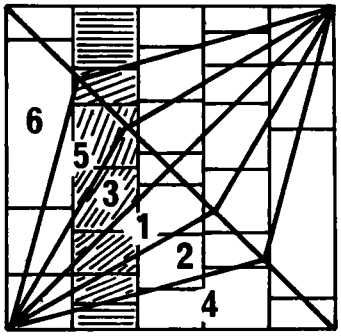

Parts of spherulite for elongation calculation: thin lines represent lamellar direction.

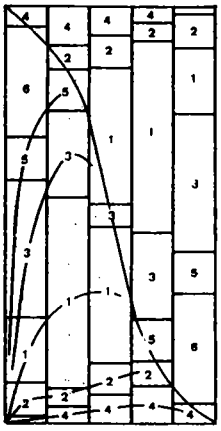

Fig.9a. Deformed spherulite. Draw ratio = 2.

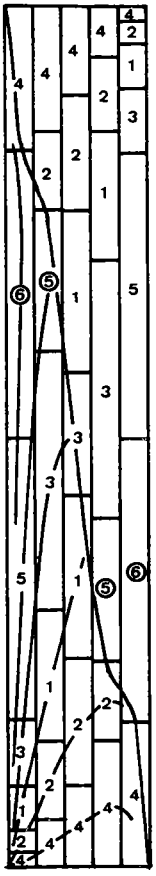

Fig.9b. Fiber structure: Portions of circled numbers are imperfectly drawn.

EBSCOhost - printed on 2/13/2023 3:45 AM via . All use subject to https://www.ebsco.com/terms-of-use

portions in one strip are stretched in full, neighboring strips stop deformation at the same time, even when they still have some portions undrawn or imperfectly stretched. Fig. 9a shows the deformed spherulite at the draw ratio 2. The spherulite boundary is in good agreement with that observed (Fig.5a). Fig. 9b is the calculated fiber structure, where the center strip is drawn to ca. 6 times in full, i.e., the macroscopic draw ratio is estimated to be 6, the value of which is consistent with the general phenomenon of cold drawing of the spherulite aggregates. In addition, the estimation suggests that there remain imperfectly drawn portions, which can be actually found in the fiber (Fig.5b).

References

1. Geil, P.H.. 1969. Polymer Single Crystals. Interscience, New York, Chapter IV.

2. Bassett, D.C. 1981. Principles of Polymer Morphology. Cambridge Univ.Press, Cambridge.

3. Hay, I., Keller, A. 1965. Kolloid-Z. 204, 43; Kobayashi, K., Nagasawa, T. 1966. J.Polym.Sci. C 15, 163; Allan, P., Bavis, M. 1976. Electron Microscopy 1976, 341.

4. Breedon, J.E., Jackson, J.F., Marcinski, M.J., Taylor, M.E.,Jr. 1973. J.Mater.Sci. 8, 1071; Fotherringham, D., Parker, B. 1976. J.Mater.Sci. 11, 979.

5. Bassett, D.C., Hodge, A.M., Olley, R.H. 1979. Faraday Discuss. Chem.Soc. 68, 216; Bassett, D.C., Hodge, A.M. 1978. Polymer 19, 469.

6. Winram, M.M., Grubb, D.T., Keller, A. 1978. J.Mater.Sci. 13, 791.

7. Shimamura, K., Murakami, S., Tsuji, M., Katayama, K. 1978. J.Soc.Rheology, Japan, 7, 42; Tagawa, T., Shimamura, K. 1979. 28, 314.

8. Keller, A., Sawada, S. 1964. Makromol.Chem. 74, 190.

9. Wang, T.T. 1974. J.Polym.Sci. 12, 145.

10. Wilchinsky, Z.W. 1961. Polymer 5, 271.

EBSCOhost - printed on 2/13/2023 3:45 AM via . All use subject to https://www.ebsco.com/terms-of-use

INFLUENCE OF MOLECULAR STRUCTURE ON THE MORPHOLOGY OF SEMI-CRYSTALLINE POLYMERS

G.H. Michler, I. Naumann

Wissenschaftliches Forschungs- und Koordinierungszentrum im Kombinat VEB Chemische Werke Buna, 4212 Schkopau, German Dem. Rep.

1. Introduction

Electron microscope investigations have essentially pushed forward the knowledge of the morphology of semi-crystalline polymers. In these polymers structures of the most different sizes are distinguished: from the interior structure of the crystalline elements (e.g. the lamellae) and the shape and size of the lamellae up the largest superlamellar structures, e.g. the spherulites of diameters up to more than 100 µm. For investigating these structures over a range of more than 5 orders of magnitude several different preparation methods have to be used.

In the following some general methods based on ultramicrotomy are briefly described, followed by some results on the influence of the molecular structure on the morphology of semi-crystalline polymers.

2. Summary of Preparation Techniques and Investigation Methods

In general, for the electron microscope study of semi-crystalline polymers both surfaces (low temperature fracture surfaces or selectively etched surfaces) and ultramicrotomed thin sections can be investigated, but the techniques based on ultramicrotomy are more widely applicable. This is shown schematically in Figure 1.

Polymers investigated are polyethylenes of high and low density (HDPE, LDPE) in the range of branching degree (V) of 0.3 to

Morphology of Polymers
© 1986 Walter de Gruyter & Co., Berlin · New York - Printed in Germany.

EBSCOhost - printed on 2/13/2023 3:45 AM via . All use subject to https://www.ebsco.com/terms-of-use

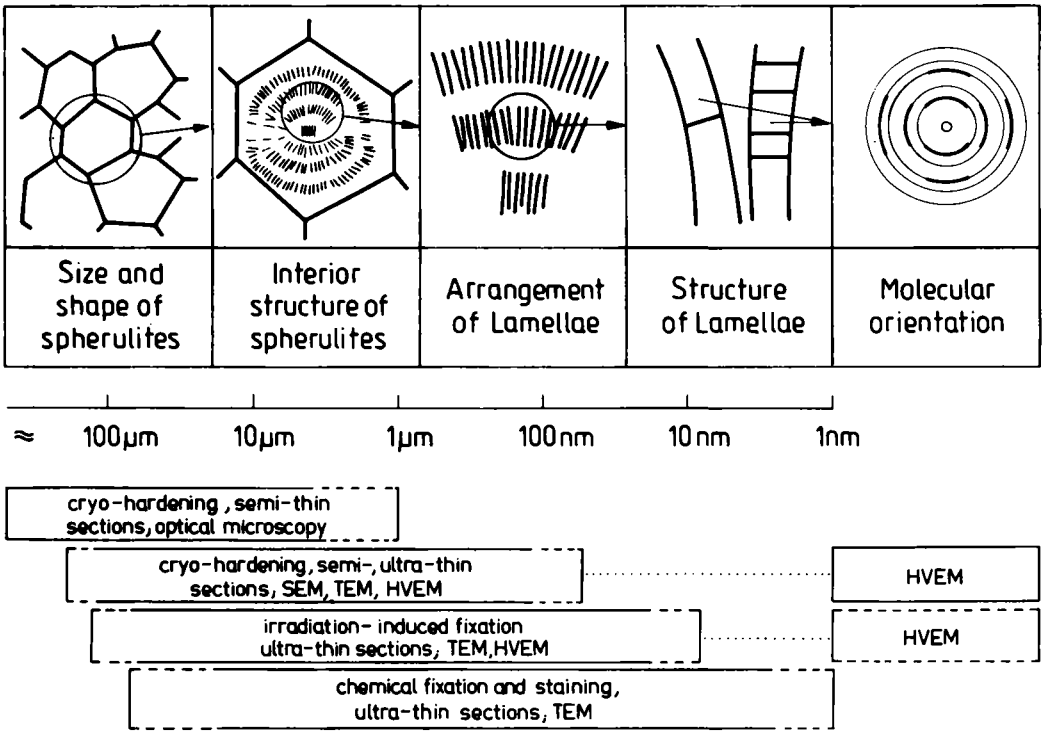

Fig. 1. Scheme of structural details of different size in semi-crystalline polymers (e.g. polyethylenes) and of the different preparation techniques and electron microscopic methods applied.

3 CH_3/100 C and of molecular weight ($\bar{M}_w$) of about 10^3 to 6 x 10^5, and segmented polyurethanes (sPU).

3. Results

3.1. Characteristic structural elements

Structural elements of different kind and size, characteristic of HDPE, LDPE, and sPU, are compared in Figure 2. Larger superlamellar structures are bundles of lamellae, sheaf-like structures (e.g. in HDPE), spherulites with an interior structure of concentric rings (LDPE) or radial lines (sPU (1)) - Figure 2a. Crystalline elements usually are lamellae varying in shape, thickness, and interior structure. The lamellae often contain boundary layers, distinguishable from the crystalline interior of the lamellae and the interlamellar, amorphous regions - Figure 2b. The molecular orientation inside the lamellae varies between neighboured lamellae (LDPE) or is in special cases

EBSCOhost - printed on 2/13/2023 3:45 AM via . All use subject to https://www.ebsco.com/terms-of-use

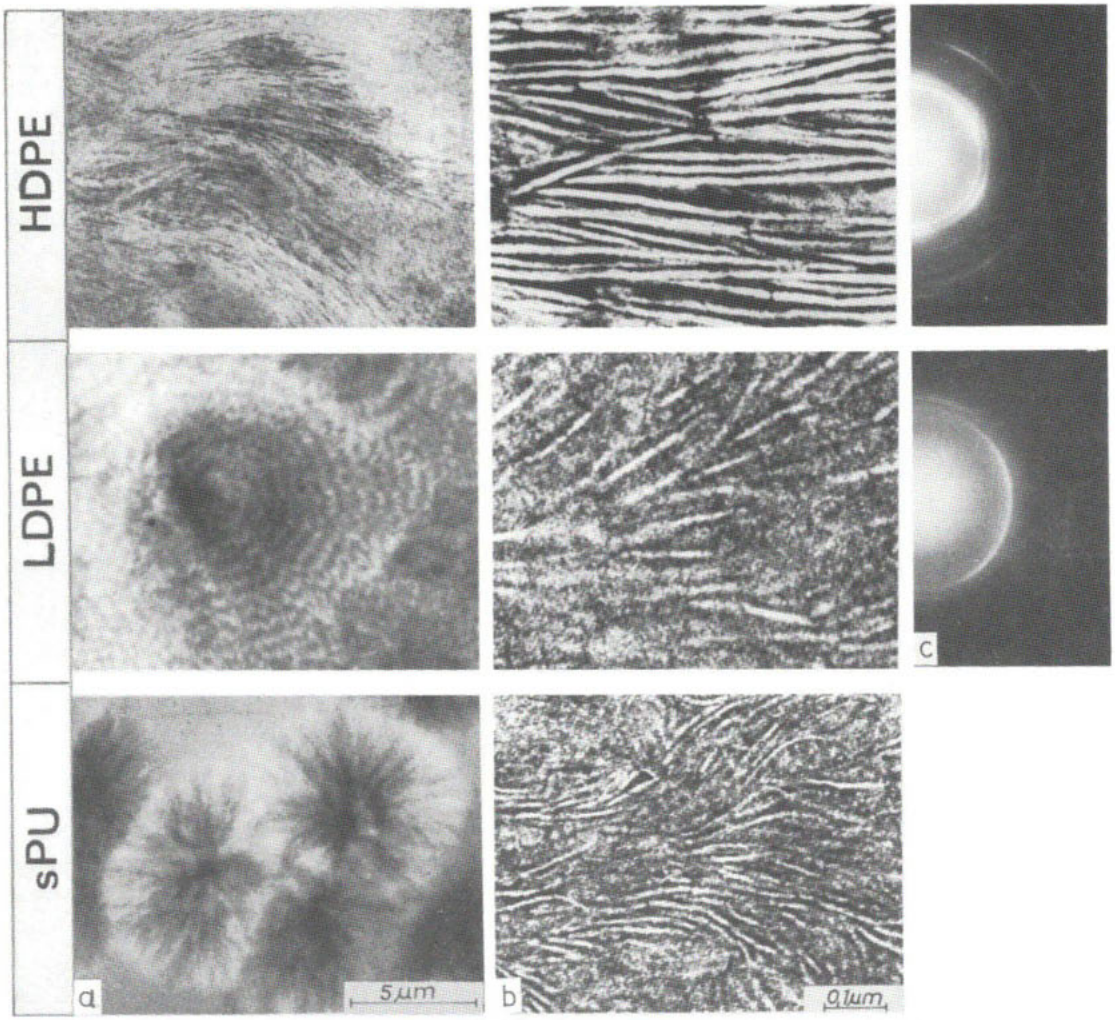

Fig. 2. Structural elements of different size, characteristic of HDPE, LDPE, and sPU (cryo-thin sections, chemically stained sections; TEM, HVEM).

constant over many lamellae in a larger area (HDPE) - Figure 2c. Structures comparable with those in Figure 2 were found in other semi-crystalline polymers, too (e.g. in polyamides). This confirms the model character of PE for semi-crystalline polymers.

3.2. Influence of branching degree

The branching degree strongly influences the size and interior structure of lamellae and also the large superlamellar structures. Changes of the lamellae are shown in Figure 3. In general, with increasing branching degree does the number of

EBSCOhost - printed on 2/13/2023 3:45 AM via . All use subject to https://www.ebsco.com/terms-of-use

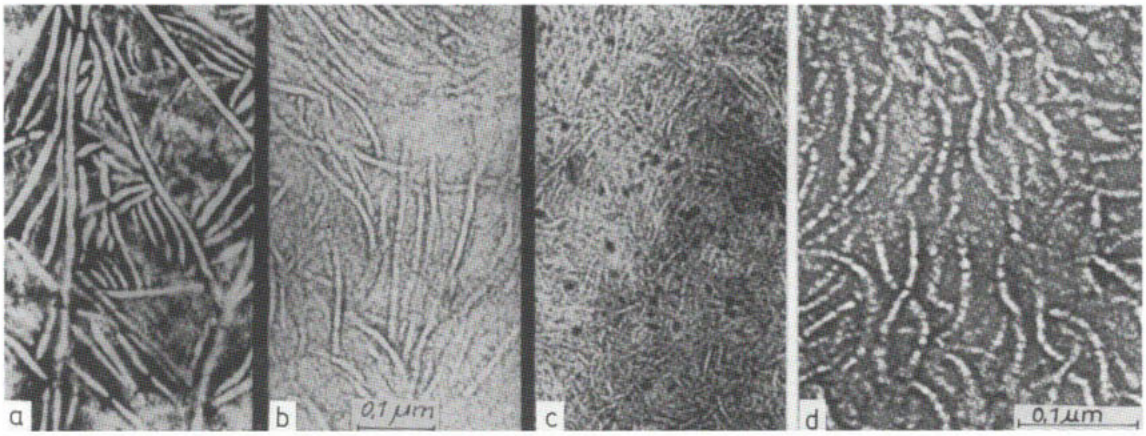

Fig. 3. Influence of branching degree on size and arrangement of lamellae;
branching degree V [CH_3/100 C]:
a) 0.3, b) 2.5, c) 7,
d) 2.5; improved visibility of the defect layers and crystalline blocks inside the lamellae using an effect of contrast enhancement by combined influence of chemical staining and electron- or γ-irradiation (2, 3).

intralamellar defect layers also increase, whereas the size of the crystalline blocks between these layers as well as the length L_{max} and thickness D_i of the lamellae decrease. The crystalline blocks correspond to micro-paracrystals (4).

For quantitative correlations one has to consider also the strong influence of the molecular weight on the lamellar structure. Therefore, the role of branching degree was studied using fractions of both linear and branched polyethylenes of constant molecular weight and narrow molecular weight distributions (5). Three series were investigated each having nearly the same molecular weight $\bar{M}_w$:
series I : $\bar{M}_w \approx 6 \times 10^5$, series II: $\bar{M}_w \approx 6 \times 10^4$
series III: $\bar{M}_w \approx (7...9) \times 10^3$.
The thicknesses D_i of the crystalline interior of the lamellae are compared with the calculated "mean free chain lengths" l_f between short-chain branchings (where the short-chain branchings are assumed to be statistically distributed along the chain and to have a content of about 90 % of the total branching degree), s. Table. For short-chain branching degrees above 1.4 the mean free chain length l_f is smaller than the minimum thickness D_i. Branching molecules can therefore be assumed to be incorporated

EBSCOhost - printed on 2/13/2023 3:45 AM via . All use subject to https://www.ebsco.com/terms-of-use

Table 1. Polymer Chains and Thickness of Lamellae

Branching degree V CH_3/100 C total	short-chain	Thickness D_i, nm (interior of lamellae)	Mean free chain length l_f, nm	Content (%) of incorporated branches
0.3	0.3	14 - 16	42	-
1.35	1.22	9 - 16	10.5	-
1.70	1.53	9 - 14	8.3	8
1.96	1.76	8 - 17	7.2	10
2.03	1.87	8 - 16	6.8	15
2.28	2.05	8 - 17	6.2	22
7.5 (EVAc)	6.8	3 - 9	1.9	38

into the lamellae. This content was calculated and quoted in the last column of the table. This result agrees qualitatively with conclusions from X-ray measurements (e.g. (6)).

3.3. Influence of molecular weight

With decreasing molecular weight the trend both of HDPE and LDPE is a change from short lamellae, which are irregularly distributed (HDPE) or arranged in concentric rings inside spherulites (LDPE), to long lamellae, which are parallely arranged in sheaf-like structures - Figure 4. The parallel arrangement of the lamellae is connected with a well-pronounced

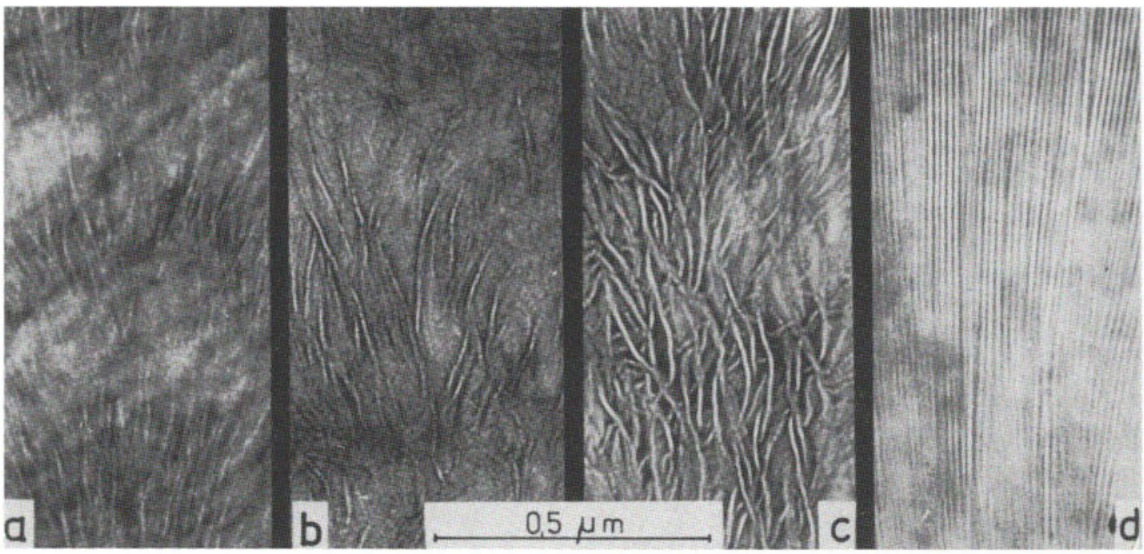

Fig. 4. Influence of the molecular weight on the lamellar structure of branched polyethylene; fractions of molecular weight $\bar{M}_w$:
a) 466000, b) 66100, c) 45100, d) 7600.

EBSCOhost - printed on 2/13/2023 3:45 AM via . All use subject to https://www.ebsco.com/terms-of-use

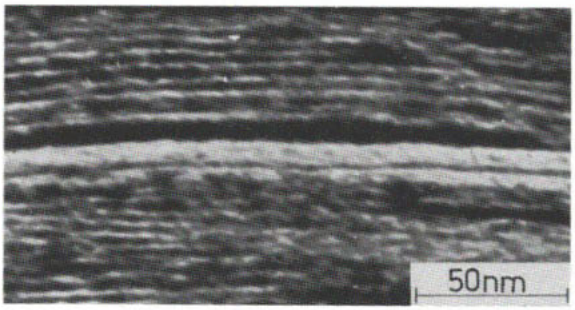

Fig. 5. Lamellae in a fraction of very low molecular weight ($\bar{M}_w$ = 3600).

molecular orientation (orientation of the straight parts of the macromolecules inside the lamellae) over a relatively large area of the sheaf-like structures - which has been shown by electron diffraction using HVEM (cf. (8)). This effect of a long-range order indicates the existence of a strong contact between the molecules of neighboured lamellae.

Fractions of molecular weights smaller than 10^3 show lamellae relatively thin but, in general, comparable with the lamellae in the samples of higher molecular weight (9) - Figure 5. Here the calculated stretched length of the macromolecules is only slightly larger than the total thickness of the lamellae (e.g. for a fraction of M_w = 725 the stretched length of a linear molecule of PE is about 6.5 nm, and the mean thickness of lamellae is 5 nm). The molecules can therefore pass the lamellae only once (comparable with the extended-chain crystals of HDPE after high-pressure crystallization) and are not folded (as it is assumed for the lamellae of samples of higher molecular weight). The changes in both the superlamellar structure and in length and thickness of the lamellae with varying molecular weight are discussed in more detail in ref. (5).

3.4. Conclusions

In PE samples very different forms and sizes of lamellae and superlamellar structures have to be produced by suitably choosing molecular weight and branching degree. As a further important parameter the thermal treatment has to be considered. From the detailed investigation of the influence of the molecular structure on the lamellar structure conclusions have been drawn on the arrangement of macromolecules inside the lamellae

EBSCOhost - printed on 2/13/2023 3:45 AM via . All use subject to https://www.ebsco.com/terms-of-use

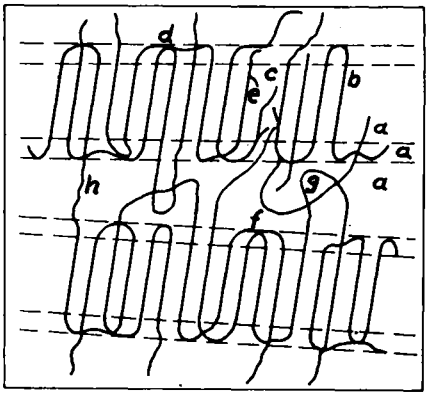

Fig. 6. Model of arrangement of macromolecules in the lamellae and in the amorphous regions as it agrees with conclusions from electron microscope investigations of the PE structure; (see a-h in the text).

and between the lamellae in the amorphous regions. These conclusions coincide with a "modified folded-chain model" - Figure 6. It contains several elements of the well-known switchboard model (10) and the regularly folded-chain model (11) and has the following characteristics:

a) existence of three phases (crystalline interior of lamellae, boundary layers of lamellae, and interlamellar amorphous regions);
b) oblique chains inside the lamellae having deviation angles between 5 and 20°;
c) defect layers and small crystalline blocks inside the lamellae;
d) non-crystallizable parts of the macromolecules accumulated in the boundary and defect-layers;
e) short-chain branchings built into crystallites (about 10 to 20 % of all short-chain branchings);
f) folded chains in the boundary layers;
g) entanglements in the amorphous regions;
h) tie-molecules connect neighboured lamellae.

Due to the similarity of characteristics of the morphology of PE and other semi-crystalline polymers the main characteristics of this model may refer not only to PE.

EBSCOhost - printed on 2/13/2023 3:45 AM via . All use subject to https://www.ebsco.com/terms-of-use

Acknowledgement

We are indebted to Professor Dr. H. Bethge for the provision of research facilities in the Institute of Solid State Physics and Electron Microscopy of the Academy of Sciences of GDR in Halle/S.

References

1. Foks, J., G.H. Michler: J. Appl. Polym. Sci. (in press).
2. Michler, G.H., K. Gruber. 1980. Acta Polymerica 31, 771.
3. Michler, G.H. 1984. Ultramicroscopy 15, 81.
4. Hosemann, R. 1967. J. Polymer Sci. Polymer Symp. 20, 1.
5. Michler, G.H., E. Brauer. 1983. Acta Polymerica 34, 533.
6. Čačkovic, H., J. Loboda-Čačkovic, R. Hosemann, D. Weick. 1974. Colloid & Polym. Sci. 252, 812.
7. Martinez de Salazar, J., F.J. Balta-Calleja. 1980. J. Crystal Growth 48, 283.
8. Michler, G.H., this issue.
9. Michler, G.H., K. Gruber. 1981. Acta Polymerica 32, 323.
10. Flory, P.J. 1962. Americ. Chem. Soc. 84, 2857.
11. Keller, A. 1959. Kolloid-Z. 165, 34.

EBSCOhost - printed on 2/13/2023 3:45 AM via . All use subject to https://www.ebsco.com/terms-of-use

MORPHOLOGY IN CROSSLINKED POLYETHYLENE

U.W. Gedde

Department of Polymer Technology, The Royal Institute of Technology, S-100 44 Stockholm, Sweden.

Introduction

The supermolecular structure in crystalline polymers has been studied by various methods, e.g. polarized light microscopy, scanning electron microscopy (SEM) of solvent-etched samples (1-5) and of samples etched with degrading agents such as $KMnO_4$-H_2SO_4 (6), and small-angle light scattering (SALS) (7-9). Studies of supermolecular structure in crosslinked polyethylene (XLPE) have been problematic for a number of different reasons. A major cause of these problems is the small size of the spherulites in XLPE. Polarized light microscopy, which is a suitable method for the study of larger spherulites, becomes intriguing when applied to XLPE. Solvent etching using refluxing CCl_4 vapor, a successful method for LDPE, was found to give a quilt-like surface texture with no correlation to the spherulite structure (10). After etching with $KMnO_4$(7% wt/vol)-H_2SO_4 nodular structures were revealed by SEM (10,11). These structures were later shown to be artefacts due to the precipitation of manganese salts which led to a non-homogeneous etching (10-12). Successful modifications of this type of etching to prevent the formation of artefacts have recently been reported (11,12).

This paper describes morphological studies of XLPE samples of low density, high pressure grades of the kind used for insulation in power cables. Results from polarized microscopy, SEM of selectively solvent-etched samples and of samples etched with $KMnO_4$-H_2SO_4 and SALS, are compared.

Morphology of Polymers
© 1986 Walter de Gruyter & Co., Berlin · New York - Printed in Germany.

EBSCOhost - printed on 2/13/2023 3:45 AM via . All use subject to https://www.ebsco.com/terms-of-use

Experimental

Five different XLPE samples (referred to as TOT), described in Table 1, were studied. Further details about four of the samples (insulation in power cables) are given in refs. 13 and 14. The sample denoted PX was compression moulded and crosslinked while being kept in the mould at 453 K for 15 minutes and finally cooled at a rate of 20 K/min to room temperature.

From each TOT sample, a soluble (SOL) and an insoluble (GEL) fraction could be isolated. For details, see refs. 13 and 14.

Films (5 μm) for polarized light microscopy and SALS were prepared either by compression moulding (PX TOT, BASIC and SOL samples) or by microtoming at 130 K (PG, PS, SA and SN TOT). Samples obtained by microtoming were annealed to relax stresses caused by the sectioning.

The samples were investigated by the following methods:

1. Polarized light microscopy using a Leitz Ortholux microscope equipped with crossed polarizers. Melting and crystallization were followed in the microscope using a Mettler Hot Stage FP 82.

2. SALS using a He-Ne laser and crossed polarizers revealing H_v scattering patterns which were recorded photographically with a Polaroid camera.

3. SEM of samples treated with $KMnO_4$-H_2SO_4 according to Naylor and Phillips (12). Samples with planar surface and minimum smearing-out effects were obtained by microtoming at 130 K ("freeze polishing"). The samples were washed with acetone, treated with a solution 0.9% (w/w) $KMnO_4$-concentrated H_2SO_4 for 1.5 hours at 300 K in an ultrasonic bath, and washed at 300 K in the ultrasonic bath with three different solutions: 2 parts H_2SO_4 and 7 parts H_2O for 90 seconds, H_2O for 90 seconds, acetone for 90 seconds. The procedure was repeated twice for each sample. After being

EBSCOhost - printed on 2/13/2023 3:45 AM via . All use subject to https://www.ebsco.com/terms-of-use

etched,the samples were dried, gold sputtered and examined in an ISI Super Mini SEM.

4. SEM of samples treated with hot p-xylene. In order to determine the optimum temperature for solvent etching, the following studies were made: TOT samples (5 mg) were treated with 15 ml p-xylene at different temperatures (T_e) for 24 hours, separated from the solution, washed with fresh solvent at the same temperature, dried to constant weight in vacuum and analysed with a Perkin-Elmer DSC-2 scanning from 280 to 430 K. For each sample an optimum T_e was established, see discussion. The material removed from the samples at optimum conditions, i.e. low temperature melting SOL, were analysed in the DSC to verify the selectivity of the extraction and by GPC (Dr. S. Holding, RAPRA, G.B.) to determine the molecular weight distribution of this material. "Freeze polished" samples were treated with p-xylene at optimum T_e for 24 hours, separated from solution, washed with fresh solvent at the same temperature, dried under vacuum, gold-sputtered and examined in the scanning electron microscope.

Table 1. Samples Investigated

Code	Crosslink. process	$\bar{M}_n$ [a] $\times 10^{-3}$	$\bar{M}_w$ [a] $\times 10^{-3}$	$\%CH_3$ [b]	W_{GEL} [c]	$\bar{M}_c$ [d] $\times 10^{-3}$
PX	peroxide	13.8	74.9	1.4	0.78	-
PG	"	"	"	"	0.755	6.9
PS	"	"	"	"	0.78	7.0
SA	sioplas	12.6	126	1.6	0.735	5.9
SN	monosil	11.6	106	-	0.68	6.1

a) by GPC for polymer prior to crosslinking (BASIC).
b) content of methyl groups by ^{13}C-NMR and IR.
c) gel content by extraction with p-xylene at 405 K.
d) average molecular weight of chains between adjacent crosslink points, details are available in ref. (13).

EBSCOhost - printed on 2/13/2023 3:45 AM via . All use subject to https://www.ebsco.com/terms-of-use

Results and Discussion

Samples subjected to solvent extraction show a bimodal melting when analysed by DSC (Fig. 1). The low temperature peak is associated with swelled material, mainly low melting GEL, which crystallizes after the isothermal solvent treatment at a lower temperature than T_e. The high temperature peak is associated with the material remaining crystalline at T_e, which is both GEL and SOL. The low temperature peak increases at the expense of the high temperature peak as T_e is increased (Figs. 1 and 2-curve C). For the particular sample shown, the high temperature peak has disappeared at 349 K. Curve D of Fig. 2 shows that about 10 % of the original SOL is still present in the sample after treatment at this temperature. A very interesting point worth noting is the shift of the high temperature peak towards higher temperatures with increasing T_e (Fig.2-curve A).

An optimum temperature of solvent treatment, unique for each sample, was chosen on the basis of plots of W_{ltp} and $\Delta W/W_{SOL}$ vs. T_e (symbols are defined in Fig.2). The idea is that "enough" material should be removed from the sample to produce an etched surface but without the formation of artefacts due to swelling. This is achieved by having a significant amount of material in the crystalline state at T_e to hinder large-scale restructurations of sample due to swelling. A value of W_{ltp} for the samples studied of about 0.6 was found to be a reasonable compromise.

The selectivity of extraction at the chosen optimum T_e was checked by isolation of the dissolved material. This material was melted and then crystallized in the DSC at 10 K/min cooling. The DSC trace of the melting of the sample treated in this way in comparison with that of the solid residue demonstrates the high selectivity of the extraction (Fig. 3). Fig. 4 shows that the material dissolved at the optimum T_e is low molecular weight material compared with the corresponding entire SOL fraction. The low molecular weight SOL crystallizes at low temperatures whereas the high molecular weight SOL is the part of the entire TOT sample

EBSCOhost - printed on 2/13/2023 3:45 AM via . All use subject to https://www.ebsco.com/terms-of-use

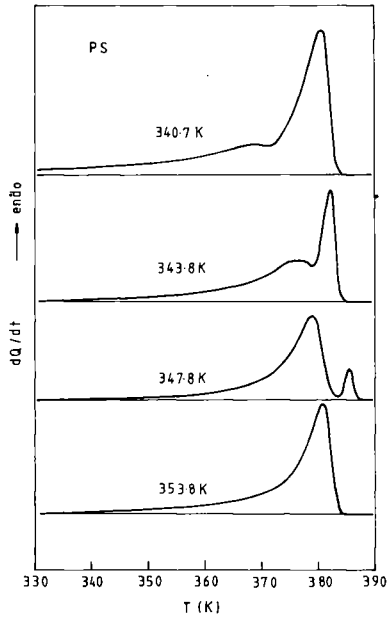

Fig. 1. Melting thermograms of PS treated with p-xylene at different temperatures as indicated in the figure.

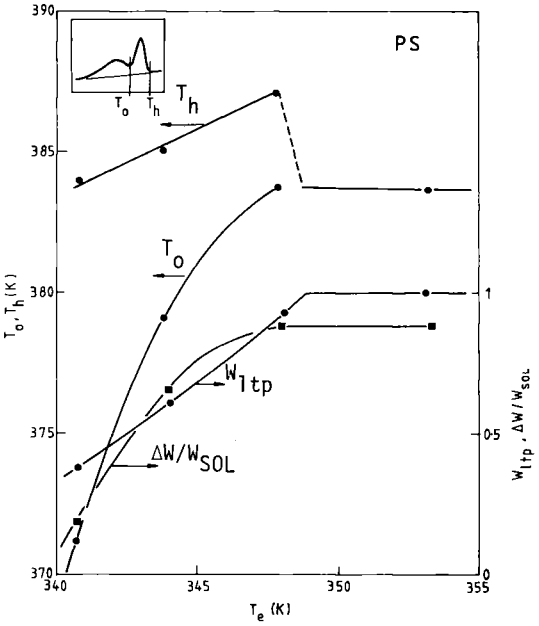

Fig.2. Temperatures T_o and T_h (def. in the inset fig.), the relative size of the low temp. peak (W_{ltp}) and the weight reduction normalized with respect to SOL content ($\Delta W/W_{SOL}$), plotted vs. temperature of extraction (T_e).

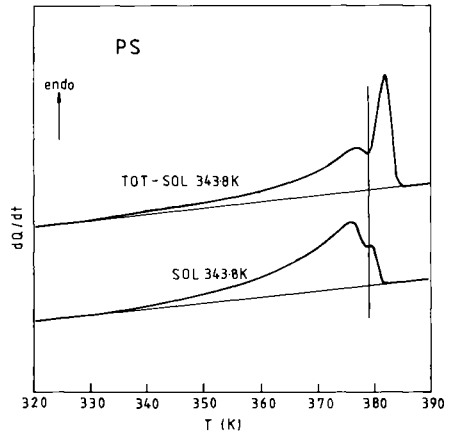

Fig.3. Melting endotherm of soluble fraction and solid residue obtained at optimum T_e. Sample: PS.

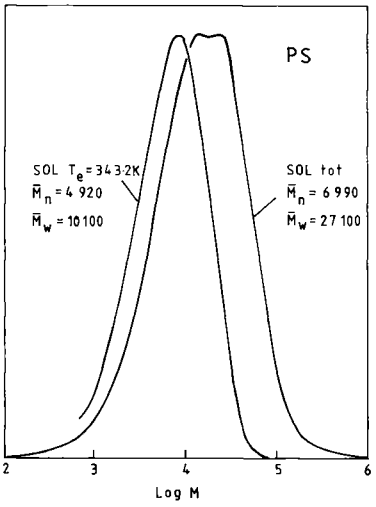

Fig.4. MWD for soluble fraction at optimum T_e and entire SOL. Sample: PS.

EBSCOhost - printed on 2/13/2023 3:45 AM via . All use subject to https://www.ebsco.com/terms-of-use

that crystallizes at the highest temperature,(see ref. 14). Thus, this selective solvent treatment removes low molecular SOL which has crystallized at a late stage in the solidification process at relatively low temperatures.

Fig. 5 shows that the surface texture of the etched samples differ considerably from that of the samples prior to etching. A nodular structure with an characteristic dimension approximately of 2 μm is observed in the micrographs of the etched samples. The removed material seems to form a network not dissimilar to that formed by the peripheral parts of spherulites. SA TOT seems in addition to these nodules to have a finer textured structure. Fig. 6 presents data on the distribution in nodule size for the sample shown. These data are transferred to Table 2 and there compared with spherulite size data obtained by SALS and polarized light microscopy.

Etching with $KMnO_4$-H_2SO_4 was unsuccessful in revealing possible spherulites in the TOT samples, with one exception: SA TOT. Less well-developed ringed patterns were observed in this sample (Fig. 7). Similar structures have been observed in both linear PE and linear low-density PE by Naylor and Phillips (12). For SA the diameter of such a spherulite-like formation is 2-3 μm.

Fig. 8a shows the SALS-H_v pattern for PX TOT. Such a clover-leaf pattern is indicative of a spherulite morhology. The spherulite diameter (D_s) was determined according to the expression derived by Stein and Rhodes (7):

$$D_s = 4.09\lambda/(2\pi n \sin(\theta_{max}/2))$$

where λ= wave length in vacuum = 632.8 nm, n= refractive index = 1.5 and θ_{max}= scattering angle at maximum intensity of scattered light for an azimuthal angle equal to 45^{o}. For this particular sample, D_s is equal to 2.0 μm, which is about the same value as that obtained from polarized light microscopy, Fig. 8b: Maltese cross patterns with a diameter of about 3 μm are observed.

The D_s values from polarized light microscopy are generally somewhat larger than those obtained from SALS (Table 2). It is

EBSCOhost - printed on 2/13/2023 3:45 AM via . All use subject to https://www.ebsco.com/terms-of-use

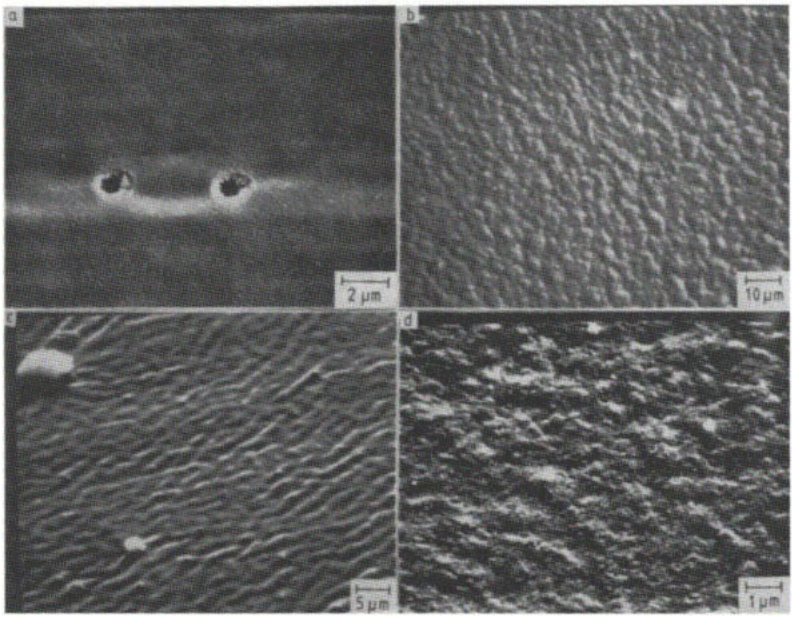

Fig.5. Scanning electron micrographs of (a) sample prior to etching (b) PX TOT, solvent-etched at 343.2 K (c) PG TOT, solvent-etched at 343.2 K (d) SA TOT, solvent-etched at 348 K.

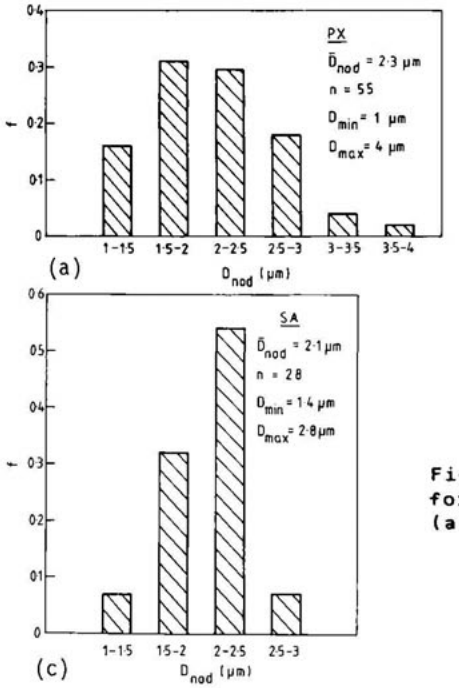

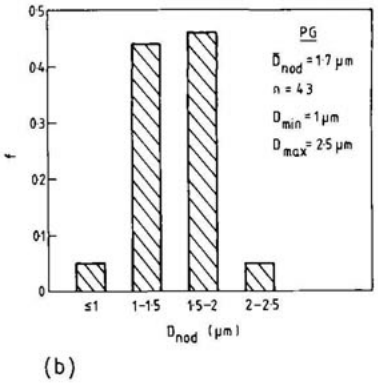

Fig.6. Nodule size distributions for solvent-etched samples of (a) PX TOT (b) PG TOT (c) SA TOT

EBSCOhost - printed on 2/13/2023 3:45 AM via . All use subject to https://www.ebsco.com/terms-of-use

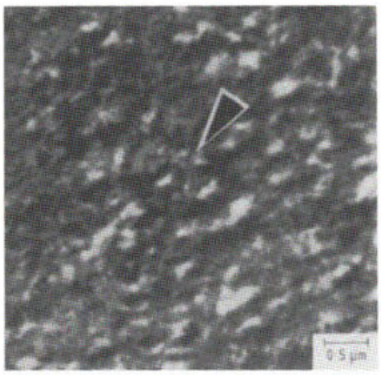

Fig.7. Scanning electron micrograph of SA TOT etched with $KMnO_4$-H_2SO_4.

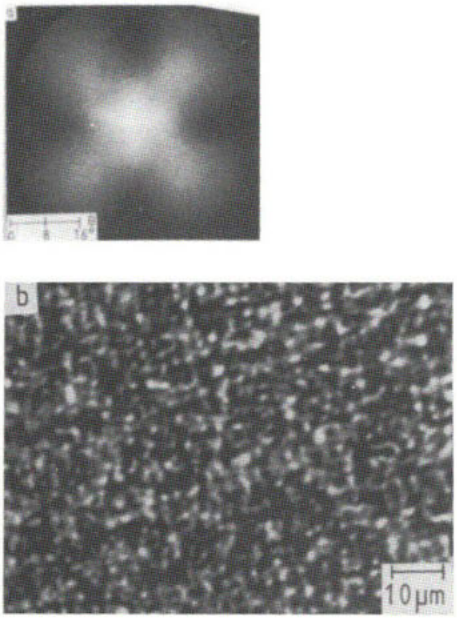

Fig.8. (a) SALS-H_v pattern and (b) polarized light micrograph of PX TOT.

possible that larger spherulites are over-represented in the statistical sample from polarized light microscopy. Fair agreement is obtained between the size of spherulites from SALS and polarized light microscopy and the size of the nodules in the solvent etched samples (Table 2). This fact can be regarded as an indication that the low melting SOL is localized primarily in the peripheral parts of the small spherulites in the TOT samples.

Table 2 also shows that the polymer seems to have slightly larger spherulites prior to crosslinking than after crosslinking and that the SOL samples have 2-3 times larger spherulites than the corresponding TOT sample.

None of the techniques used provides information that indicates a bimodal spherulite size distribution indicative of a phase separation of SOL and GEL in the melt prior to crystallization. Instead, a unimodal spherulite size distribution seems to be present in agreement with earlier findings by Gedde (14).

EBSCOhost - printed on 2/13/2023 3:45 AM via . All use subject to https://www.ebsco.com/terms-of-use

Table 2. Data from Morphological Studies

Sample code	SALS pattern	D_s[a] (μm)	D_s[b] (μm)	$\bar{D}_{nod}$[c] (μm)	D_s[d] (μm)
PX TOT	clover-leaf	2.0	3.0	2.3	-[e]
PG TOT	"	1.9	2-3	1.7	-[e]
PS TOT	-	-	2-3	1-3[f]	-[e]
SA TOT	-	-	3	2.1	2-3
SN TOT	-	-	3	1-2[f]	-
PX/PG/PS BASIC	clover-leaf	2.2	3.8	-	-
SN BASIC	"	1.6-3.1	3.7	-	-
PG SOL	"	5.7	7	-	-
SA SOL	"	5.3	7	-	-

a) spherulite diameter by SALS.

b) spherulite diameter by polarized light microscopy.

c) average size of nodules in solvent-etched samples.

d) size of "ring-pattern structures in samples etched with $KMnO_4$-H_2SO_4.

e) method was not successful.

f) results difficult to interpret.

Hot stage studies of the melting and crystallization of PX TOT also supports the idea of a uniform spherulite structure.

Acknowledgements

These studies have been sponsored by the Swedish Natural Science Research Council (NFR) - grant no. K-RT 1910-100.

EBSCOhost - printed on 2/13/2023 3:45 AM via . All use subject to https://www.ebsco.com/terms-of-use

References

1. F.P. Reding and E.R. Walter. 1959. J. Polym. Sci. 38, 141.

2. J.S. Mackie and A.J. Rudin. 1961. J. Polym. Sci. 49, 407.

3. G.W. Bailey. 1962. J. Polym. Sci. 62, 241.

4. M.M. Winram, D.T. Grubb and A. Keller. 1978. J. Mater. Sci. 13, 791.

5. U.W. Gedde and J-F. Jansson. 1984. Polymer 25, 1263.

6. S.R. Barnes. 1980. Polymer 21, 723.

7. R.S. Stein and M.B. Rhodes. 1960. J. Appl. Phys. 31, 1873.

8. J. Maxfield and L. Mandelkern. 1977. Macromolecules 10, 1141.

9. T. Pakula, M. Kryszewski and Z. Soukap. 1976. Eur. Polym. J. 12, 41.

10. S. Bamji, A. Bulinski, J. Densley and A. Garton. 1983. IEEE Trans. Electr. Insul. EI-18, 32.

11. R.H. Olley and D.C. Bassett. 1982. Polymer 23, 1707.

12. K.L. Naylor and P.J. Phillips. 1983. J. Polym. Sci, Polym. Phys. Ed., 21, 2011.

13. U.W. Gedde. 1985. Polymer, submitted.

14. U.W. Gedde. 1985. Polymer, submitted.

EBSCOhost - printed on 2/13/2023 3:45 AM via . All use subject to https://www.ebsco.com/terms-of-use

POLYPROPYLENE MORPHOLOGY IN BLENDS WITH POLYETHYLENE

M. Plešek, Z. Maláč
Rubber and Plastics Technology Research Institute, Gottwaldov 764 22, Czechoslovakia

Introduction

The morphology and properties of PP/PE blends have been studied intensively for some time. Detailed analysis of the blends on the basis of PP including those with LDPE was performed by Martuscelli (1) and Galeski et al. (2,3). Their observations revealed that these blends were heterogenous two-phase systems, the components of which crystallized separately. The occlusions of the dispersed LDPE do not influence significantly the formation and growth of PP spherulites, but the nucleation density is decreased.
As for PP/HDPE blends there is a certain controversy in the results by different authors. Wenig and Meyer (4) proved that these blends also segregated into two discrete phases with a negligible influence of the PE phase on the crystallization behaviour of PP. On the other hand, Lovinger and Williams (5) reported on the nucleation activity of HDPE in the PP matrix, Noel and Carley (6) arrived at similar conclusions, an important contribution on the temperature dependence of the crystallization kinetics was presented by Eder and Wlochowicz (7). Their results establish for the isothermal crystallized blends that HDPE decreases the rate of PP crystallization above 122 ^{o}C and increases it below this temperature.
In the present work the morphology of the blends of isotactic polypropylene and polyethylene are described. Of special interest was determining a dependence of the PP morphology on the PE type and its melt history.

Morphology of Polymers
© 1986 Walter de Gruyter & Co., Berlin · New York - Printed in Germany.

EBSCOhost - printed on 2/13/2023 3:45 AM via . All use subject to https://www.ebsco.com/terms-of-use

Experimental

The isotactic polypropylene used was Mosten 55212 (density 0.907 and MFI 0.7 g/10´), polyethylenes were LDPE Bralen FB 2-17 (0.923 and 2), HDPE Liten FB 29 (0.952 and 0.12) and HDPE Marlex 6050 (0.967 and 5). The results yielded were essentially the same for both types of HDPE, therefore no further comments are given concerning their type.
Pieces of either homopolymer or blends were crystallized in Perkin - Elmer Differential Scanning Calorimeter. After melting (10 min at 200 ^{o}C) in nitrogen atmosphere samples were crystallized non-isothermally at a cooling rate ranging from 0.5 to 64K/min. Thin sections of samples were viewed in the polarizing light microscope. Microtomed surfaces were etched using the permanganic acid and examined in the electron scanning microscope after Au - sputtering.

Results and Discussion

Figure 1 presents dependences of T_{max} values (temperature of the exotherm peak) of DSC scans for homopolymer on the cooling rate. The values of T_{max} are much lower for LDPE than for PP. This fact results in the observation of two distinct peaks on the thermogram for the PP/LDPE blend at all cooling rates (Figure 2a). For the PP/HDPE blend the same conclusion holds only for the lowest cooling rates (0.5 and 1 K/min). For higher cooling rates the values of T_{max} for HDPE homopolymers is higher than for PP. In these cases the overlapping of the crystallization peaks appears on the PP/HDPE thermograms (Figure 2b).
The above results can be correlated with the morphology of the blends. The difference between the thermograms at 16 K/min entails different morphological behaviour of PP on the interface (cf.Figs. 3,4). The transcrystalline morphology is induced only by HDPE surface. A consequence of this nucleating activity is the very

EBSCOhost - printed on 2/13/2023 3:45 AM via . All use subject to https://www.ebsco.com/terms-of-use

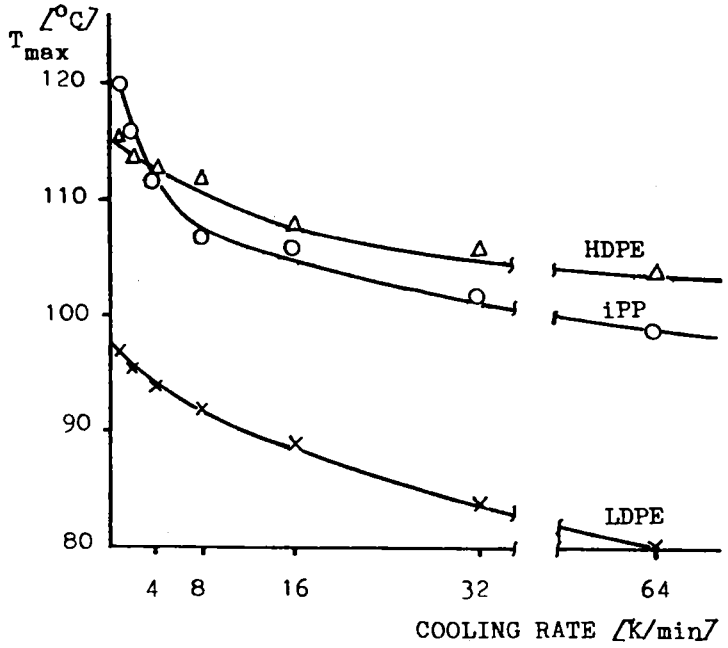

Fig. 1. Temperatures T_{max} of the DSC peaks for homopolymers crystallized at various cooling rates.

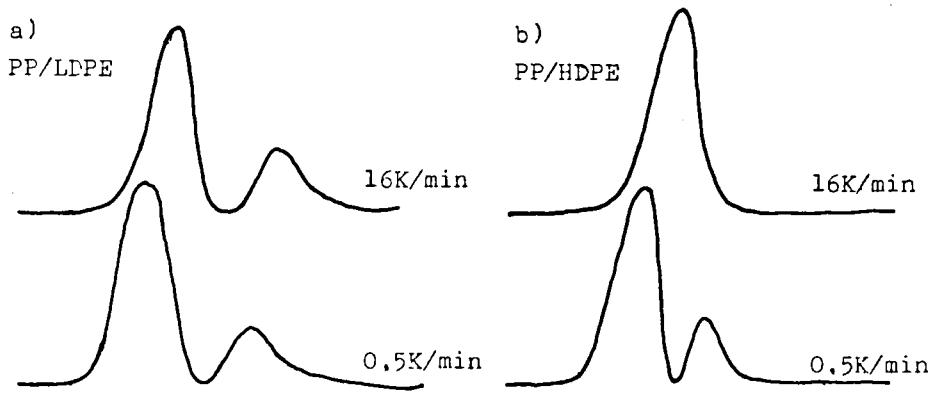

Fig. 2. Influence of the cooling rate on the DSC crystallization thermograms of the blends.

EBSCOhost - printed on 2/13/2023 3:45 AM via . All use subject to https://www.ebsco.com/terms-of-use

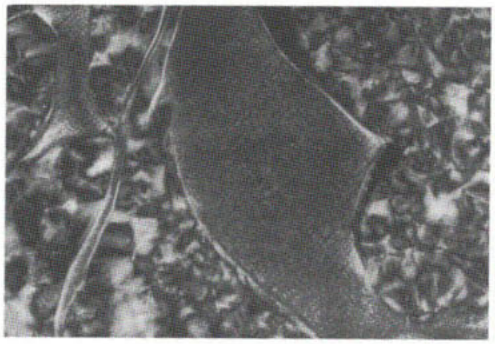

Fig. 3. Polarizing micrograph of the PP/LDPE boundary crystallized at the cooling rate 16 K/min.

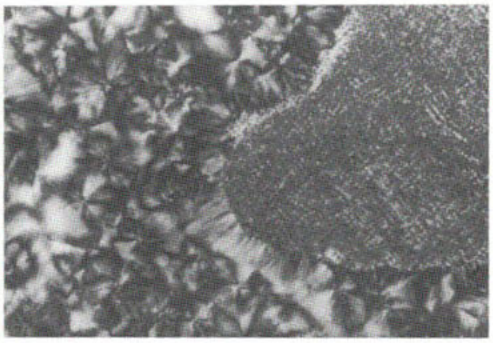

Fig. 4. Polarizing micrograph of the PP/HDPE boundary crystallized at the cooling rate 16 K/min.

Fig. 5. Polarizing micrograph of the PP/HDPE (97/3) blend crystallized at the cooling rate 16 K/min .

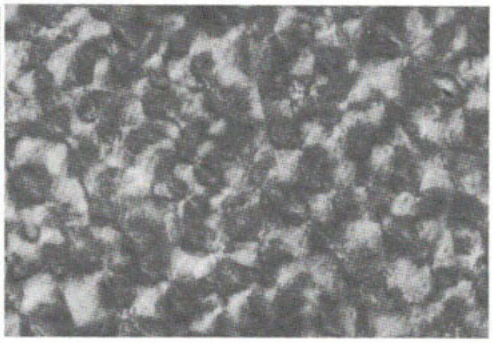

Fig. 6. Polarizing micrograph of the PP/LDPE (80/20) blend crystallized at the cooling rate 16 K/min.

EBSCOhost - printed on 2/13/2023 3:45 AM via . All use subject to https://www.ebsco.com/terms-of-use

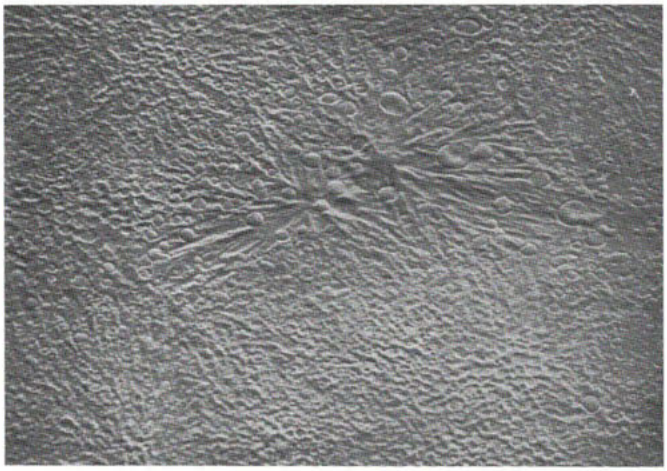

Fig. 7. Scanning electron micrograph of the etched surface of the PP/LDPE blend ecrystallized at coolig rate 16 K/min. (500x)

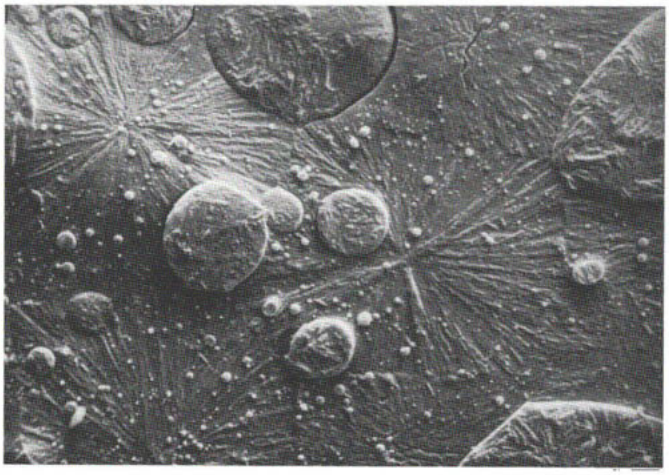

Fig. 8. Scanning electron micrograph of the etched surface of the PP/HDPE blend crystallized at the cooling rate 0.5 K/min. (500x)

EBSCOhost - printed on 2/13/2023 3:45 AM via . All use subject to https://www.ebsco.com/terms-of-use

fine spherulite morphology of the blend even at low content of HDPE, which must, of course, be finely dispersed (Fig. 5). On the other hand, no activity was observed for LDPE (Fig. 6) at all cooling rates used.

The nucleating activity of HDPE can be connected with the above mentioned overlapping of the crystallization exotherms. If there is no overlapping for the PP/HDPE blend, i.e. at low cooling rates, HDPE loses its activity. In this case the morphology of both PP/HDPE and PP/LDPE blends has similar appearance. The PE occlusions are trapped within PP spherulites with a negligible influence on the crystallization behaviour of the PP phase (Figs.7,8). These results are taken to mean that PE exhibits the nucleating activity only if crystallized.

This conclusion suggests an interpretation in terms of the surface energies. Based on the data from Wu (8) the surface tensions for homopolymers at a crystallization temperature can be estimated. In aproximative consideration the surface tensions of LDPE and HDPE are taken as the same. At the temperature of 120°C estimated surface tension values expressed in mN/m are as follows : 24 and 29 for PP and PE melt respectively, 34 and 64 for PP and PE crystalline surface respectively. Using the relation for the interfacial surface tension (8)

$$\gamma_{12} = \gamma_1 + \gamma_2 - 4\frac{\gamma_1 \gamma_2}{\gamma_1 + \gamma_2}$$

the data as shown below are obtained :

γ(PP melt / PE melt) = 0.5
γ(PP melt / PE cryst) = 18
γ(PP cryst / PE melt) = 0.4
γ(PP cryst / PE cryst) = 9

From these values it is clear that the transition

PP melt / PE cryst ⟶ PP cryst / PE cryst

is energetically preferred. Thus the PE crystalline surface acts as the nucleating agent for PP. On the contrary the PP surface cannot be active for the crystallization of PE. This conclusion is in agreement with the above observations.

EBSCOhost - printed on 2/13/2023 3:45 AM via . All use subject to https://www.ebsco.com/terms-of-use

References

1. Martuscelli, E.. 1984. Polym. Eng. Sci. 24, 563.

2. Galeski, A., M. Pracella, E. Martuscelli. 1984. J.Polym.Sci.: Polym.Phys.Ed. 22, 739.

3. Galeski, A., Z. Bartczak, M. Pracella. 1984. Polymer 25, 1323.

4. Wenig, W., K. Meyer. 1980. Coll.Polym.Sci. 258, 1009.

5. Lovinger, A.J., M.J. Williams. 1980. J.Appl.Polym.Sci. 25,1703.

6. Noel, O.F., J.F. Farley. 1984. Polym.Eng.Sci. 24, 488.

7. Eder, M., A. Wlochowicz. 1984. Acta Polymerica 35, 548.

8. Wu, S. 1982. Polymer Interface and Adhesion. Marcel Dekker Inc., New York.

EBSCOhost - printed on 2/13/2023 3:45 AM via . All use subject to https://www.ebsco.com/terms-of-use

EBSCOhost - printed on 2/13/2023 3:45 AM via . All use subject to https://www.ebsco.com/terms-of-use

SPIN DIFFUSION STUDIES ON MORPHOLOGY OF LINEAR POLYETHYLENE

L. Deutschbein, B. Walter, T. Willing
Pädagogische Hochschule Erfurt/Mühlhausen, Sektion Mathematik/Physik, DDR 5060 Erfurt

1. Introduction

Solid polymers are structurally heterogeneous. They contain regions (domains) having different local order and therefore differing degrees of mobility of polymer chains. Understanding the physical properties of such materials requires the determination of the structure of various regions. In addition to common methods such as x-ray diffraction, electron microscopy or Raman scattering, ^1H nuclear magnetic resonance (NMR) can also be used to characterize the morphology of polymeric systems (1,2). The usefulness of NMR is based upon two facts:

- the different mobility of chains in the amorphous and crystalline domains leads to multicomponent line shapes and spin lattice relaxation rates;
- spin diffusion, induced by the dipolar interaction between neighbouring protons provides magnetization transfer between several domains.

The study of the spin diffusion process which depends on the domain size gives information on the domain structure (3,4).

2. Diffusion Model

The semicrystalline polymeric system is described by a simplified one - dimensional model with two regions: amorphous (A) and crystalline (C) (Fig.1). The regions A and C have characteristic spin diffusion coefficients D_A and D_C. The thickness of the regions are l_A and l_C, respectively. It is further assumed that the spatial distribution of magnetization ($m_A = m_A(x,t)$, $m_C = m_C(x,t)$) is initially inhomogeneous. It is well-known that mutual spin flip - flop transitions, caused by the dipolar

Morphology of Polymers
© 1986 Walter de Gruyter & Co., Berlin · New York - Printed in Germany.

EBSCOhost - printed on 2/13/2023 3:45 AM via . All use subject to https://www.ebsco.com/terms-of-use

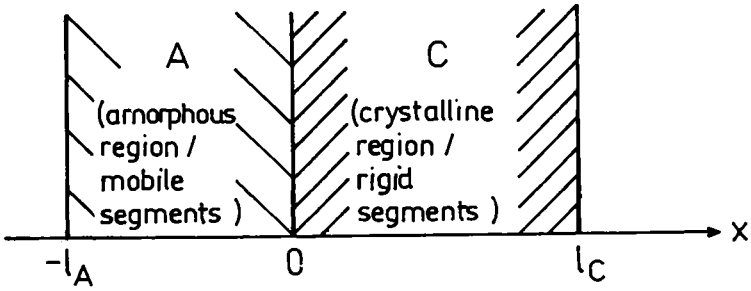

Fig. 1. One-dimensional two-region model.

coupling of neighbouring protons, smooth local magnetization differences.

Since the transport of magnetization connected with spin processes can be described by a diffusion equation, we can set up the following relationships for the development of magnetization in both regions, neglecting spin lattice relaxation processes,

$$\frac{\partial}{\partial t} m_A (x,t) = D_A \frac{\partial^2}{\partial x^2} m_A (x,t)$$

$$\frac{\partial}{\partial t} m_C (x,t) = D_C \frac{\partial^2}{\partial x^2} m_C (x,t) \qquad (1)$$

The solutions of both differential equations are related through the boundary conditions

$$m_A (0,t) = m_C (0,t) \qquad (2)$$

$$D_A \frac{\partial}{\partial x} m_A (x,t)\Big|_{x=0} = -D_C \frac{\partial}{\partial x} m_C (x,t)\Big|_{x=0} \qquad (3)$$

The equations (1) may be solved for the following set of initial conditions $m_A(x,0) = 0$, $m_C(x,0) \neq 0$
or $m_A(x,0) \neq 0$, $m_C(x,0) = 0$ (4)

Results of numeric calculation represented in Fig. 2 demonstrate, that the total magnetic moments of the individual regions

$$M_A(t) = \int_{-l_A}^{0} m_A(x,t)\, dx$$

or

$$M_C(t) = \int_{0}^{l_C} m_C(x,t)\, dx$$

EBSCOhost - printed on 2/13/2023 3:45 AM via . All use subject to https://www.ebsco.com/terms-of-use

increase with $t^{1/2}$ for small times. According to analytical approximate solutions, the recovery of magnetic moments depends on both the diffusion coefficients and on the thickness of the regions l_A and l_C, respectively,

$$R_A(t) = \frac{M_A(t)}{M_A(\infty)} = \frac{4}{\pi^{1/2}} \cdot \frac{M_C(0)}{M_C(\infty)} (D_A^{-1/2} + D_C^{-1/2})^{-1} \, l_A^{-1} \, t^{1/2}$$

$$R_C(t) = \frac{M_C(t)}{M_C(\infty)} = \frac{4}{\pi^{1/2}} \cdot \frac{M_A(0)}{M_A(\infty)} (D_A^{-1/2} + D_C^{-1/2})^{-1} \, l_C^{-1} \, t^{1/2} \qquad (5)$$

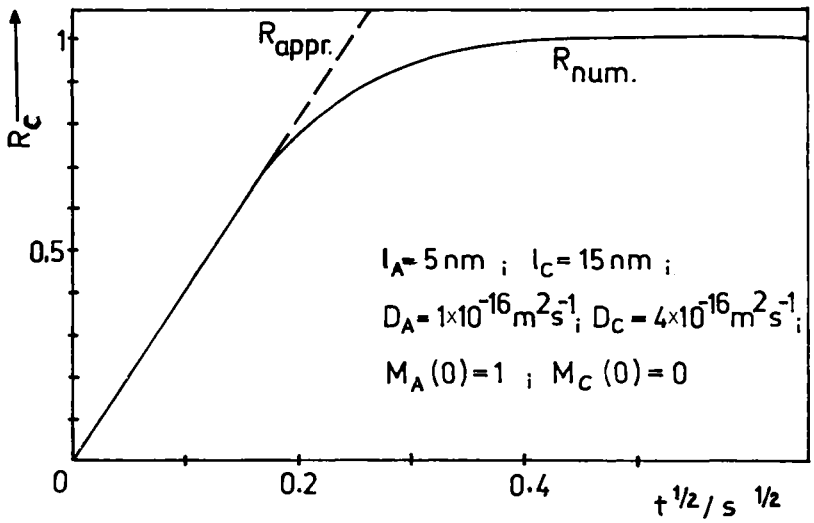

Fig. 2. Theoretical curves of recovery of magnetization are based on Eqs. (1) and (5).

3. Measurement of Proton Spin Diffusion Rate

In the case when transverse magnetic relaxation times of the domains $T_{2,A}$ and $T_{2,C}$ differ considerably ($T_{2,C} \ll T_{2,A}$), the Goldman - Shen experiment (5) can be used successfully to study spin diffusion (3). The three-pulse sequence is shown schematically in Fig. 3a. The first two pulses are used to prepare the nuclear spin system so that the magnetization in the various domains is different. The fixed interval t_o is chosen so that the magneti-

EBSCOhost - printed on 2/13/2023 3:45 AM via . All use subject to https://www.ebsco.com/terms-of-use

zation in the crystalline domains decays nearly to zero ($t_o \gtrsim 3\ T_{2,C}$), while there is still sufficient magnetization remaining in the amorphous domains. Spin diffusion occurs in the period t_d. The registered free induction decay (FID) after the third pulse reflects the distribution of the magnetization. The presence of a fast decaying component in the signal indicates magnetization transfer back into the crystalline domains. The progress of magnetization transport can be measured by observing the increase in this component.
However, if the spin lattice relaxation times $T_{1\rho}$ in the rotating frame are sufficiently different ($T_{1\rho,A} \ll T_{1\rho,C}$), a modified version of the Goldman-Shen experiment is preferred (Fig.3b). This involves the application of a spin locking pulse sequence instead of the initial $\pi/2$ - pulse.

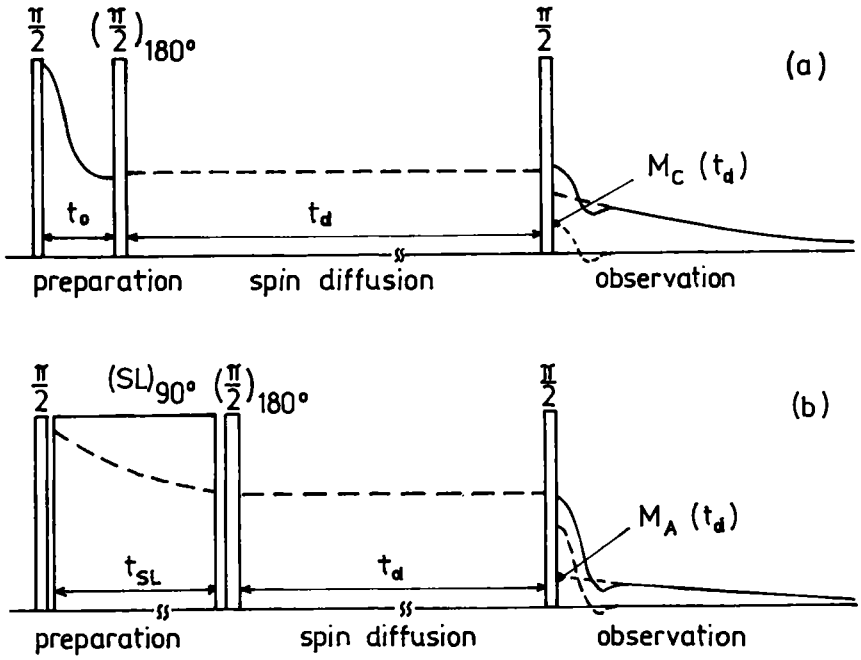

Fig. 3. Pulse sequences used to study the proton-proton spin diffusion: (a) Goldman-Shen experiment, (b) spin locking modified version.

EBSCOhost - printed on 2/13/2023 3:45 AM via . All use subject to https://www.ebsco.com/terms-of-use

With a suitable choice of the spin locking period ($t_{SL} \gtrsim 3\ T_{1\rho,A}$) the magnetization associated with amorphous domains disappears whereas magnetization does still exist in the crystalline regions. In this experiment the transfer of magnetization is reversed, occurring from the crystalline to the amorphous domains. The diffusion rate can therefore be found by recording the increase in the slow decaying signal component.

4. Experimental

NMR measurements: ^{1}H-NMR experiments were made at room temperature using a pulsed spectrometer operating at 60 MHz. The rf field strength used was B_1 = 3 mT. The signals were recorded many times with a fast transient recorder (time resolution: 100 ns). The computer analysis of the free induction decay was carried out with the regression function

$$G(t) = G_A(t) + G_C(t) \tag{6}$$

where $$G_A(t) = G_A(0) \times \exp(-B_A\, t) \tag{7}$$

is the signal component belonging to protons in the amorphous region, and the Abragam-function

$$G_C(t) = G_C(0) \times \exp(-B_C t^2) \times \sin(b_C t)/b_C t \tag{8}$$

is the crystalline signal component.

Polymeric materials: The measurements were made on two solid samples of linear polyethylene (PE) containing ordered lamellar structural units and disordered interlamellar regions. The degree of crystallinity (α), the lamellar thickness (l_c) and the thickness of amorphous region (l_A), obtained by means of x-ray studies, are given in Table 1.

Table 1. X-ray Characterized Structural Data of PE Samples

Sample	α	l_C(nm)	l_A(nm)
PE 1	0.82	21.8	4.8
PE 2	0.82	17.6	3.9

EBSCOhost - printed on 2/13/2023 3:45 AM via . All use subject to https://www.ebsco.com/terms-of-use

5. Results

The FID of a PE sample is shown in Fig. 4, as well as its components. The transverse magnetic relaxation time and the second moment, which characterize the decay of the signal components, amount to $T_{2.A} = B_A^{-1} = 41\ \mu s$
and $\overline{(\Delta\omega)^2} = 2B_C + 1/3\ b_C^2 = 1.72 \times 10^{10}\ s^{-2}$

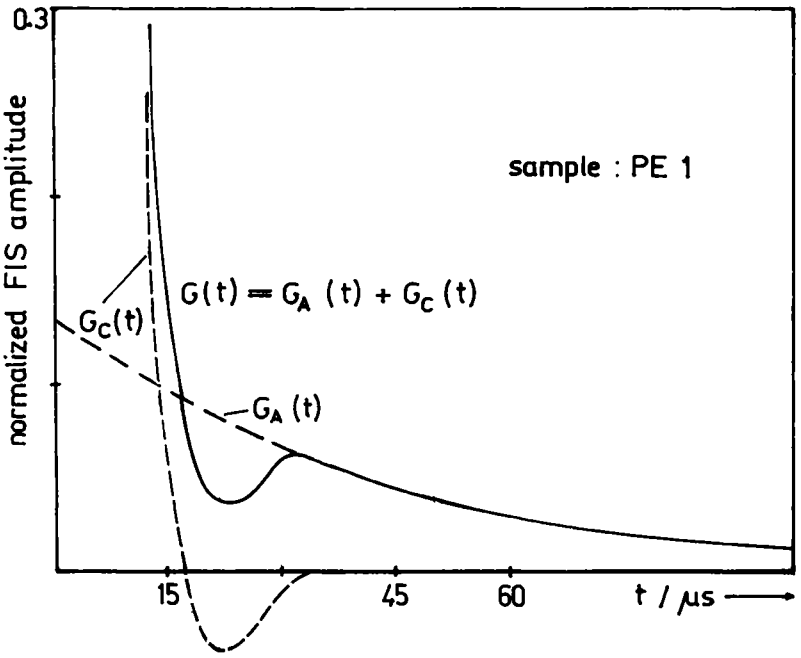

Fig. 4. Free induction decay of sample PE1
($G_A(0) = 0.13$, $B_A = 2.46 \times 10^4\ s^{-1}$; $G_C(0) = 0.87$, $B_C = 2.81 \times 10^9 s^{-2}$, $b_C = 1.86 \times 10^5\ s^{-1}$).

The measured spin lattice relaxation in the rotating frame (Fig.5) and the FID (Fig.4) consist of two components and therefore confirm our assumption of a two-region structural model.
Fig. 6 shows the results of the Goldman-Shen experiment and its modified version with the spin locking pulse sequence and, also, demonstrates that, for short time period, the magnetization increases with $t^{1/2}$ according to the above theoretical considerations.

EBSCOhost - printed on 2/13/2023 3:45 AM via . All use subject to https://www.ebsco.com/terms-of-use

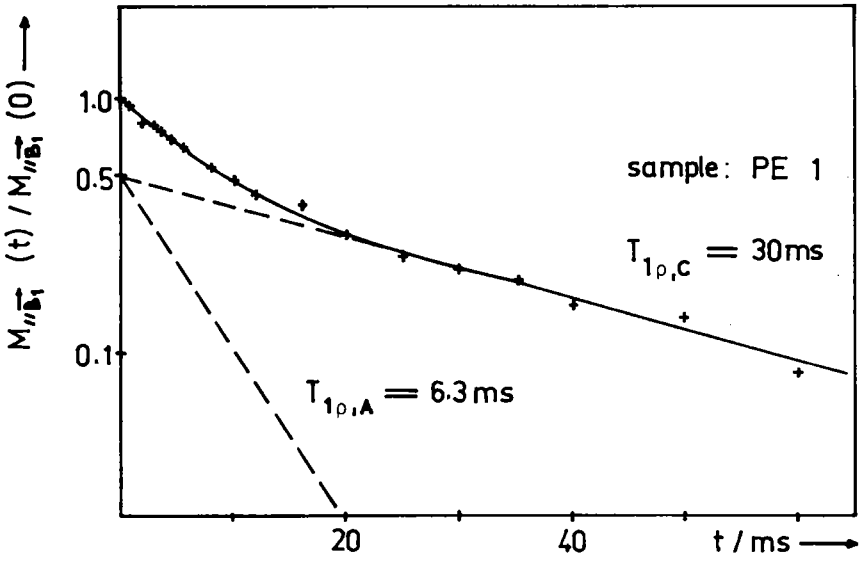

Fig. 5. ^{1}H spin lattice relaxation in the rotating frame.

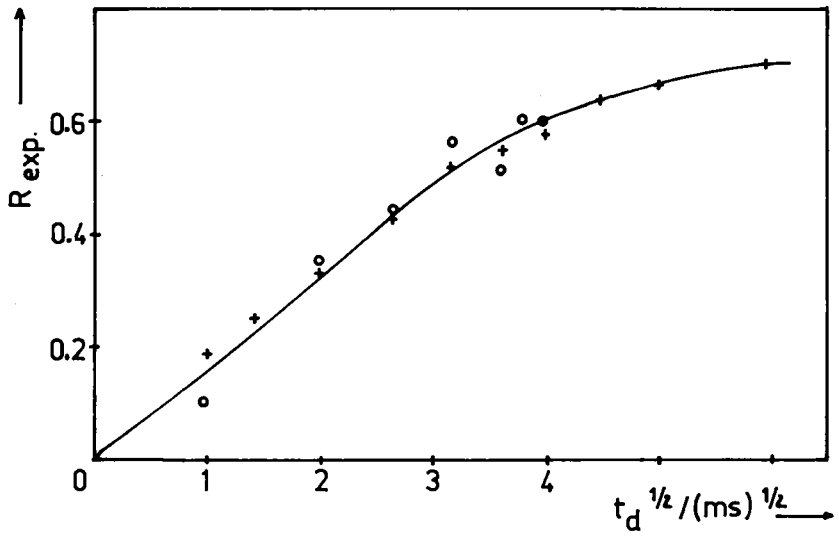

Fig. 6. Recovery of the crystalline region (+) and amorphous region (o) magnetizations.

EBSCOhost - printed on 2/13/2023 3:45 AM via . All use subject to https://www.ebsco.com/terms-of-use

By fitting the experimental data to relations (5) the values $(D_A^{-1/2} + D_C^{-1/2})^{-1} l_A^{-1}$ and $(D_A^{-1/2} + D_C^{-1/2})^{-1} l_C^{-1}$ can be obtained. Using the following expressions to evaluate the spin diffusion coefficients

$$D_A = q\, a^2/T_{2,A} \qquad \text{and} \qquad D_C = q\, a^2 \left[\overline{(\Delta\omega)^2}\right]^{1/2} \qquad (9)$$

where a is the mean distance between neighbouring protons and q a factor, it is possible to estimate the thickness of the various domains. With the resulting data of $D_A = 0.8 \times 10^{-16}$ $m^2 s^{-1}$ and $D_C = 4.2 \times 10^{-16}$ $m^2 s^{-1}$, calculated using the values of $q = 0.05$ and $a = 2.5 \times 10^{-10}$ m, the following data are obtained for the domain structures of the PE samples under investigation ($\alpha = G_C(0)$):

Table 2: ^1H NMR characterized structural Data of PE Samples

Sample	α	l_C(nm)	l_A(nm)
PE 1	0.86	20.8	3.2
PE 2	0.84	18.7	3.0

It is found that the values obtained from these spin diffusion studies are in accordance with the x-ray data.

Acknowledgement

The authors wish to thank colleagues of the TH Merseburg WB Experimentalphysik I for providing the samples and the x-ray data.

References

1. Kitamaru, R., F. Horii. 1978. Advances in Polymer Science 26, 139.
2. Mc Brierty, V.J., D.C. Douglass. 1980. Phys.Reports 63, 61.
3. Cheung, T.T.P., B.C. Gerstein. 1981. J.Appl.Phys. 52, 5517.
4. Packer, K.J., J.M. Pope, R.R. Yeung, M.E.A. Cudby. 1984. J.Polym.Sci.Polym.Phys.Ed. 22, 589.
5. Goldman, M., L. Shen. 1966. Phys.Rev. 144 ,321.
6. Bloembergen, N. 1949. Physica 15, 386.

EBSCOhost - printed on 2/13/2023 3:45 AM via . All use subject to https://www.ebsco.com/terms-of-use

HETEROGENEITY OF LINEAR LOW DENSITY POLYETHYLENE AS STUDIED BY FRACTIONATION AND DSC

V.B.F. Mathot, H.M. Schoffeleers, A.M.G. Brands, M.F.J. Pijpers

DSM Research and Patents
P.O. Box 18, 6160 MD Geleen, Netherlands

Heterogeneity of Comonomer Distribution

Crystallization and melting of LLDPE cover large temperature ranges, and DSC curves often show, Fig. 1, several peaks (1,2,3). This suggests that an LLDPE sample is not uniform in composition as regards the number, shape and degree of perfection of its crystallites. A possible cause of the non-uniformity in crystallization behaviour might be a heterogeneous distribution of comonomer elements (4,5,6), Fig. 2, leading to a multi-peak ethylene sequence length distribution.

In contrast, homogeneous copolymers (7,8,9), Fig. 2, produce a single-peak DSC curve, Fig. 1, the shape of which is dependent on the ethylene sequence length distribution. Also LDPE gives a single-peak DSC curve.

As a start, it is hypothesized that for LLDPE the low temperature peak (up to c. 115 °C, see Fig. 1) in the DSC heating curve reflects the presence of strongly branched chain segments, whilst the high temperature peak (from c. 115 °C) reflects the presence of weakly branched chain segments. Consequently, it is assumed that, unlike the homogeneous EP copolymer, LLDPE has an ethylene sequence length distribution showing at least two peaks. The split-up in the high temperature peaks in the DSC heating curve is caused by recrystallization effects and will here be left out of consideration.

For throwing light on the structure of LLDPE use is made of fractionation techniques of fairly different character.

Morphology of Polymers
© 1986 Walter de Gruyter & Co., Berlin · New York - Printed in Germany.

EBSCOhost - printed on 2/13/2023 3:45 AM via . All use subject to https://www.ebsco.com/terms-of-use

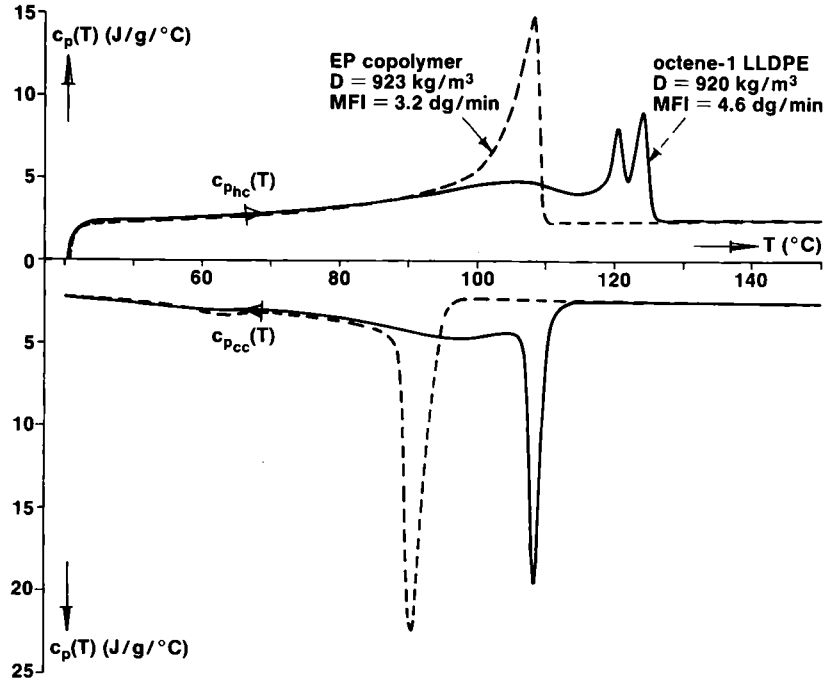

Fig. 1. DSC-2 continuous heat capacity curves for cooling ($c_{p_{cc}}$) at 5 K/min from 200 °C to 40 °C and subsequent heating ($c_{p_{hc}}$) at 5 K/min. Isothermal stays of 5 min, sample weights 4.870 mg (EP) and 4.976 mg (LLDPE).

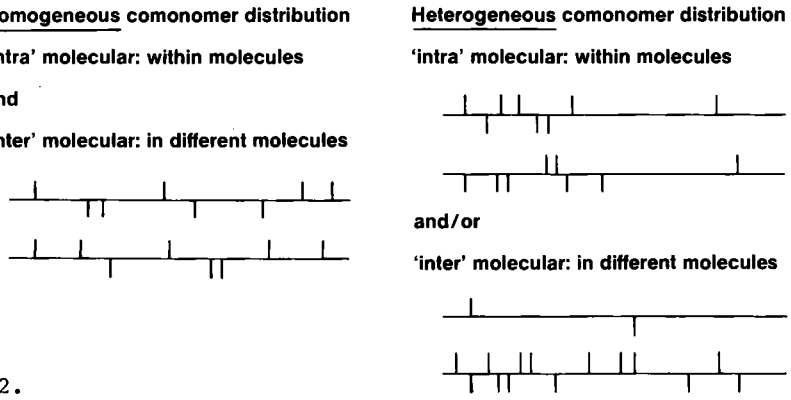

Fig. 2.

EBSCOhost - printed on 2/13/2023 3:45 AM via . All use subject to https://www.ebsco.com/terms-of-use

Fractionation by the Direct Extraction Method

With the direct extraction method (10,11) a good separation according to molar mass is achieved, which opens up the possibility to study the comonomer content as a function of molar mass. As can be seen in Fig. 3, the comonomer content of the fractions increases strongly as $[\eta]$, or the molar mass, decreases. The fractions of the octene-1 LLDPE (solution process) contain less comonomer over the whole of the molar mass range than the fractions of the butene-1 LLDPE (gas-phase process). This is seen also in the starting products, although they are equal in density. That causes other than side-chain length also play a role is seen in the same figure, in comparing the gas-phase butene-1 LLDPE with a high-pressure butene-1 LLDPE.

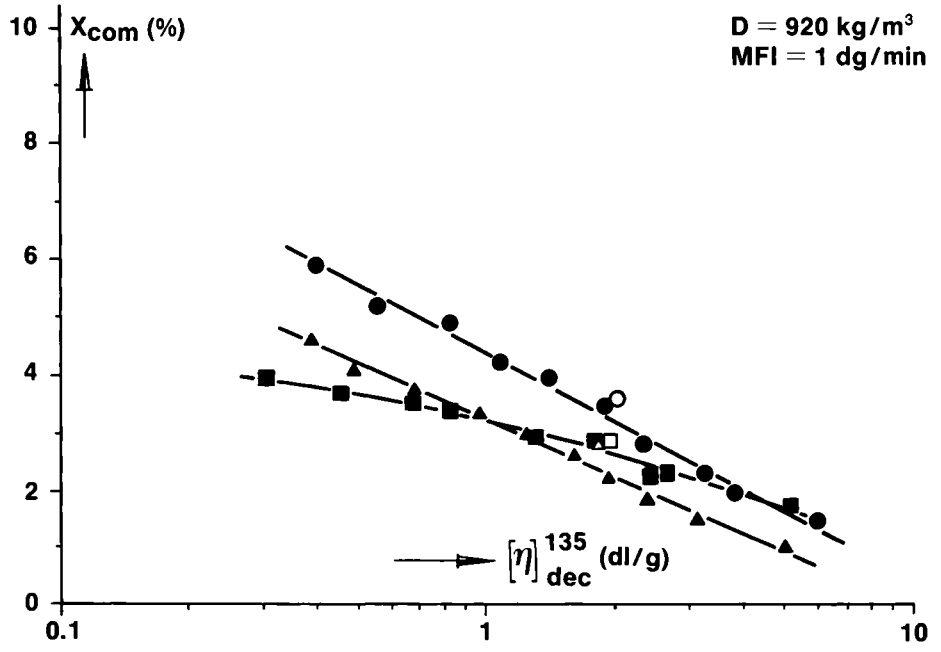

Fig. 3. Mole percentages of comonomer and intrinsic viscosities for a gas-phase C_4-LLDPE (o), a high-pressure C_4-LLDPE (□) and a solution C_8-LLDPE (Δ) and direct extraction fractions thereof (●, ■ and ▲, resp.).

EBSCOhost - printed on 2/13/2023 3:45 AM via . All use subject to https://www.ebsco.com/terms-of-use

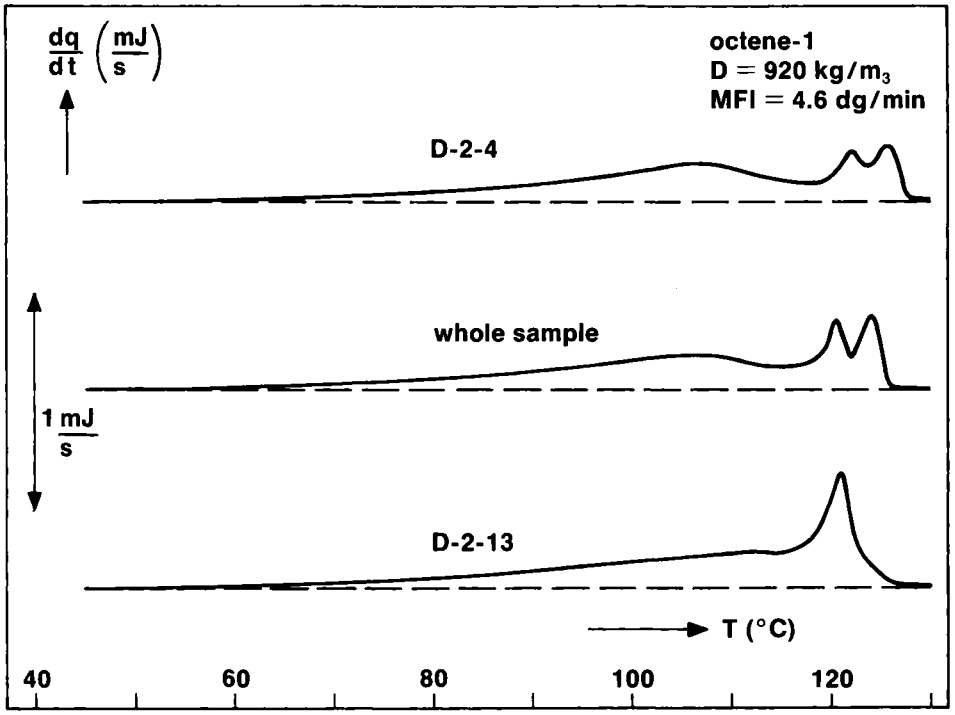

Fig. 4. DSC curves for heating at 5 K/min after cooling from 150 °C at 5 K/min. Sample weight 0.8 mg.

Fig. 4 shows that a low molar mass fraction (D-2-4) and a high molar mass fraction (D-2-13) of an octene-1 LLDPE still possess the characteristic long melting ranges. The DSC curves suggest that for each direct extraction fraction in Fig. 3, the comonomer content still is an average, which means that there is heterogeneity of comonomer distribution over the whole of the molar mass distribution. This implies that if one wants to compare different LLDPEs - as in Fig. 3 - the heterogeneity at each molecular length must be taken into account.

Fractionation by a Crystallization/Dissolution Method

One may try to make a division into strongly branched and weakly

EBSCOhost - printed on 2/13/2023 3:45 AM via . All use subject to https://www.ebsco.com/terms-of-use

branched chains, leaving aside for the moment the lengths of these chains. A method that offers a good chance of success is crystallization of the LLDPE in solution followed by drainage of dissolved material at elevated temperature (11,12,13,14). Fig. 5 shows (diagrammatically) that this, indeed, leads to fractions giving single-peak DSC curves, varying from material suggestive of polyethylene of very low density, with a maximum in the melting curve at about 80 °C, to HDPE-like material, with a peak temperature of 132 °C. The mere fact that it is possible to obtain fractions producing such DSC curves strongly argues for intermolecular heterogeneity of the comonomer distribution. The molar mass distributions, as revealed by GPC, are broad; still there is evidence of fractionation having taken place according to molar mass as well.

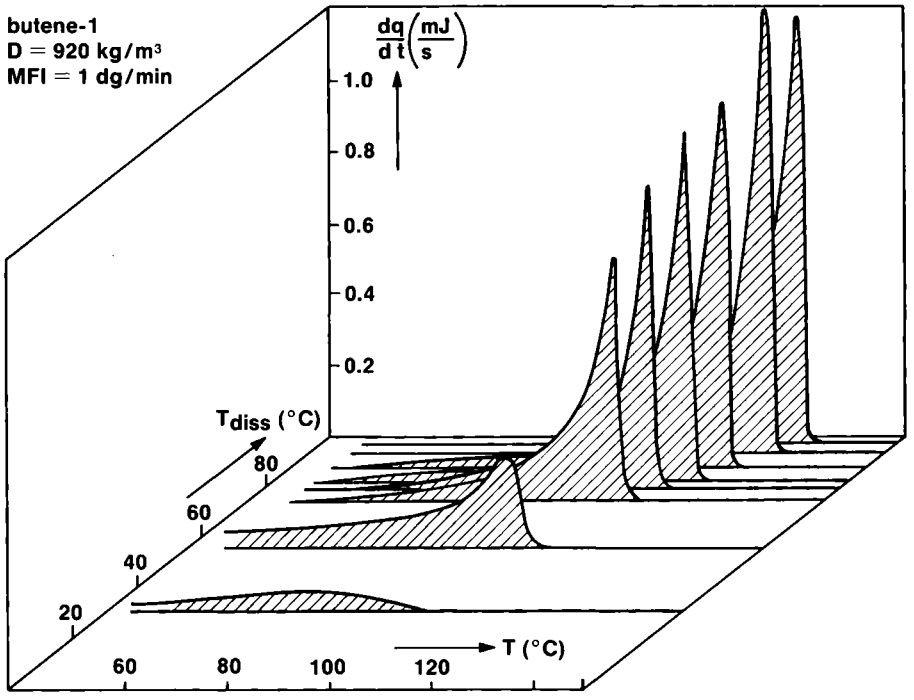

Fig. 5. Diagram showing DSC heating curves for fractions obtained by the crystallization/dissolution method. DSC as in Fig. 4.

EBSCOhost - printed on 2/13/2023 3:45 AM via . All use subject to https://www.ebsco.com/terms-of-use

Cross Fractionation

Fig. 6 shows the results of both fractionation methods for the same butene-1 LLDPE. The conclusion that can be drawn is that with any length of chain there are molecules containing much comonomer as well as molecules containing little.
It was an obvious step to try to find corroboration for this by means of cross fractionation (15). To this end an octene-1 LLDPE was separated according to molecular mass by the direct extraction method, after which a low molar mass fraction and a high molar mass fraction were further separated by a flocculation-crystallization/dissolution method. The fractions have a narrow molar mass distribution, and the corresponding IR results, Fig. 7, in combination with the DSC curves show that additionally a separation by comonomer content was obtained.

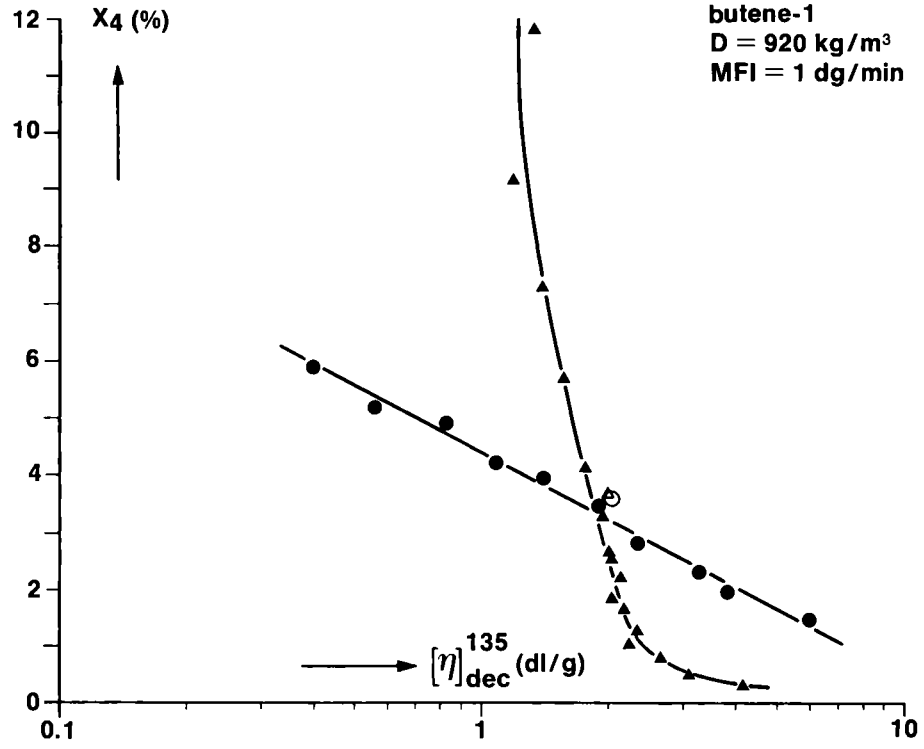

Fig. 6. Results for fractions obtained by the direct extraction method (●) and the crystallization/dissolution method (▲), o and Δ refer to summated fractions.

EBSCOhost - printed on 2/13/2023 3:45 AM via . All use subject to https://www.ebsco.com/terms-of-use

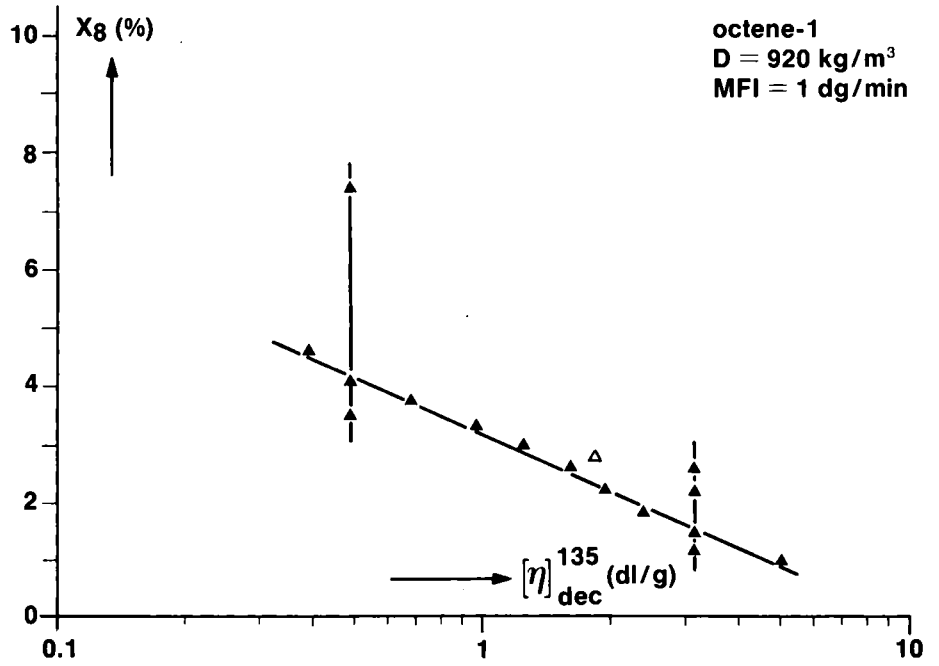

Fig. 7. Cross fractionation by crystallization/dissolution treatment after direct extraction.

Conclusions

LLDPE is a blend of molecules with different comonomer contents. There is intermolecular heterogeneity of comonomer distribution over the entire range of the molar mass distribution. Molecules with the same length are found to differ in comonomer content, the range extending from molecules suggestive of very low density polyethylene to molecules resembling HDPE. In the LLDPEs studied, the average comonomer content rises as the molar mass decreases.

Acknowledgement

The authors are indebted to Dr. L. Kleintjens for his advice on the crystallization fractionation and Mr. A. Veermans and co-workers for the IR measurements.

EBSCOhost - printed on 2/13/2023 3:45 AM via . All use subject to https://www.ebsco.com/terms-of-use

References

1. Gray, A.P., K. Casey. 1964. Polymer Letters 2, 381.

2. Shirayama, K., S.I. Kita, H. Watabe. 1972. Makromol. Chem. 151, 97.

3. Bubeck, R.A., H.M. Baker. 1982. Polymer 23, 1680.

4. Elston, C.T.. March 2, 1967. Can. Pat. No. 984,213.

5. Axelson, D.E.. 1982, J. Polym. Sci. Polym. Phys. Ed. 20, 1427.

6. Mathot, V.B.F.. 1984. In: Polycon '84 LLDPE. The Plastics and Rubber Institute, London, pp. 1-18.

7. Casey, K., C.T. Elston, M.K. Phibbs. 1964. Polymer Letters 2, 1053.

8. Mathot, V., M. Pijpers, J. Beulen, R. Graff, G. van der Velden. 1981. In: Proceedings of the Second European Symposium on Thermal Analysis (D. Dollimore, ed.). Heyden, London, pp. 264-267.

9. Hunter, B.K., K.E. Russell, M.V. Scammell, S.L. Thompson. 1984. J. Polym. Sci. Polym. Chem. Ed. 22, 1383.

10. Holtrup. W.. 1977, Makromol. Chem. 178, 2335.

11. Mathot, V.B.F., M.F.J. Pijpers. 1984. Polymer Bulletin 11, 239.

12. Constantin, D., M. Hert, J.P. Machon. 1978. Makromol. Chem. 179, 1581.

13. Hert, M., D. Constantin. 1982. In: Proc. 6e Conférence Européene des Plastiques, II-2-1.

14. Wild, L., T.R. Ryle, D.C. Knobeloch, I.R. Peat. 1982. J. Polym. Sci. Polym. Phys. Ed. 20, 441.

15. Motooka, M.. April 18, 1984. Jap. Pat. Appl. Discl. No. 59-68307.

EBSCOhost - printed on 2/13/2023 3:45 AM via . All use subject to https://www.ebsco.com/terms-of-use

THE FORMATION OF PVC MORPHOLOGY AND ITS IMPORTANCE DURING SUBSEQUENT PROCESSING

M Clark

ICI Petrochemical and Plastics Division, P O Box No 8,
The Heath, Runcorn, Cheshire, WA7 4QD, UK

Introduction

Polyvinyl chloride (PVC) is manufactured commercially, almost exclusively, by one of three processes as shown in the following Table.

Table 1. Manufacturing Processes for PVC

Process	Proportion of Total (%)
Suspension	80
Mass	10
Emulsion/Microsuspension	10

In this paper I shall deal only with Suspension PVC which is easily the largest proportion of the total although much will also apply to the mass process and product. The suspension process produces PVC grains of average size about 130 µm. The grains themselves are generally porous with their interior consisting of particles (called primary particles) having a diameter of about 1 µm clustered and fused together to form a rigid structure containing various levels of voidage. A single grain of PVC cut open to reveal its internal structure is shown in Figure 1.

Morphology of Polymers
© 1986 Walter de Gruyter & Co., Berlin · New York - Printed in Germany.

EBSCOhost - printed on 2/13/2023 3:45 AM via . All use subject to https://www.ebsco.com/terms-of-use

Figure 1. A Single Grain of PVC

(a) Cut open and viewed by SEM.

(b) Embedded in epoxy resin, microtoned and observed by Optical Microscopy.

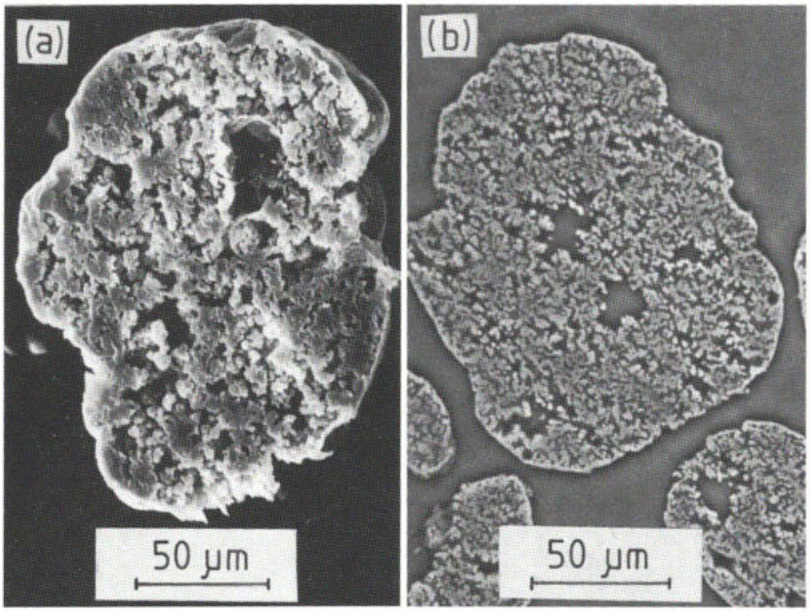

The level of voids/porosity can be controlled within limits during the polymerisation process.

This paper will describe the morphology of PVC and present a possible mechanism of formation. Two important features of PVC processing are its interaction with plasticiser and the gelation mechanism most particularly in rigid applications. The importance of PVC morphology in these two processes is briefly described under separate headings.

EBSCOhost - printed on 2/13/2023 3:45 AM via . All use subject to https://www.ebsco.com/terms-of-use

Morphology Formation

Early stages of polymerisation

The suspension process involves the dispersion of vinyl chloride droplets in a continuous water phase by the use of a combination of vigorous agitation and steric stabilisers. Within these droplets, which are usually about 40 μm in diameter, a free radical initiator is dissolved. When the complete mixture is heated to the desired temperature polymerisation commences within the monomer droplets. Individual PVC molecules grow rapidly and precipitate from the monomer in which they are insoluble. As they precipitate a few such molecules cluster together to form microdomains which is the name given to the smallest (ca 10-20 nm) particulate feature observed in PVC. The microdomains are, however, only the first stage of a series of agglomeration steps that eventually result in the final PVC grain structure. In the full conversion product it is difficult to identify the various morphological features that have contributed to the final structure and it is possible that some do in fact lose their separate identity as polymerisation proceeds. However by performing very slow polymerisations the various stages of morphology formation have been identified as they occur (1). Slow rates of polymerisation have not only made observation easier but accentuate morphological features.

Commercial polymerisation of vinyl chloride uses high initiation rates resulting in a high concentration of microdomains occurring at the very earliest stages of polymerisation. This high concentration of microdomains results in a high collision frequency and rapid agglomeration to form domains which have a diameter of 100-200 nm. This is followed by a short period of growth before further agglomeration occurs. This process is so rapid that it is complete to form the primary particles observed in the final product by less than 0.1% conversion. From this point the primary particles follow a pattern of uninterrupted growth and by the time conversion has reached even a few percent they appear spherical with no outward sign of the constituent subparticles. When, however, low initiation rates are used the concentration of microdomains is very much lower and so the agglomeration steps occur later with longer growth periods. This means that the microdomains and domains are of larger size before they agglomerate and it is possible, at low conversions, to see their presence in primary particles. It is from

EBSCOhost - printed on 2/13/2023 3:45 AM via . All use subject to https://www.ebsco.com/terms-of-use

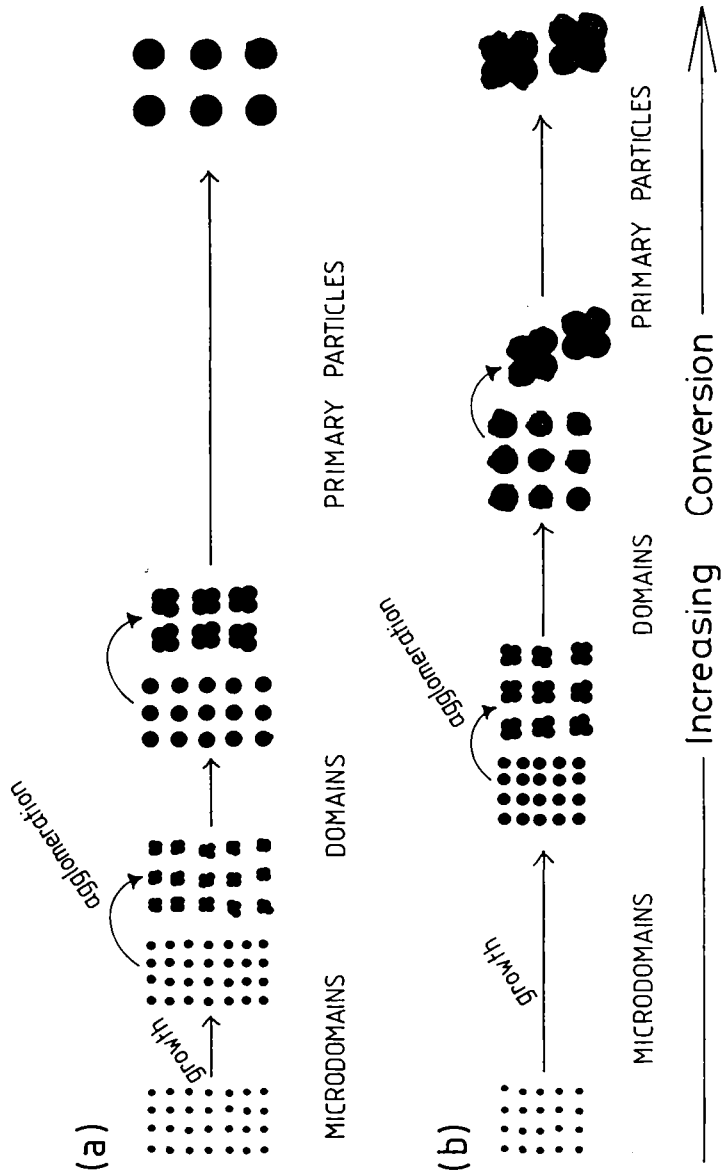

Figure 2. Primary Particle Formation

(a) High Initiation Rate
(b) Low Initiation Rate

EBSCOhost - printed on 2/13/2023 3:45 AM via . All use subject to https://www.ebsco.com/terms-of-use

Figure 3. TEM Photo-Micrographs of Primary Particles

(a) at high initiation rate, conversion 4.8%

(b) at low intiation rate, conversion 2.5%

(a)

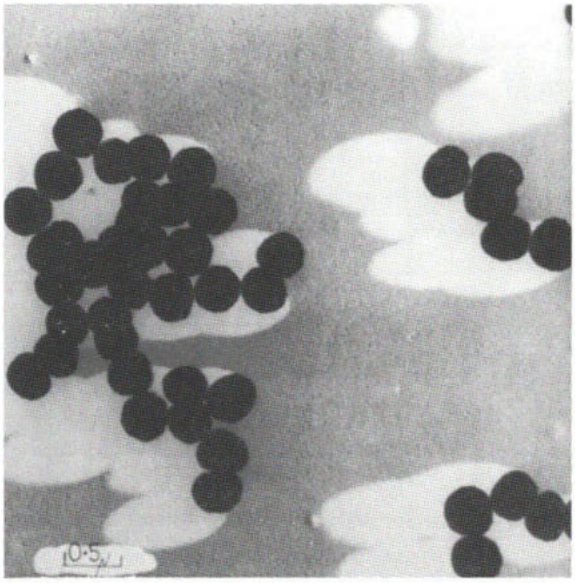

(b)

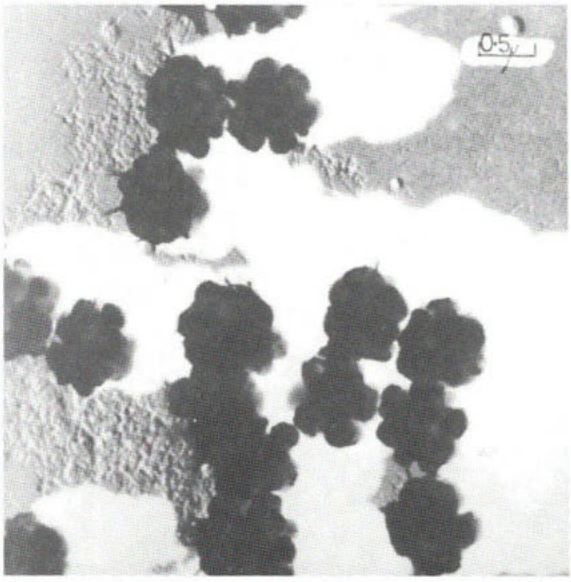

EBSCOhost - printed on 2/13/2023 3:45 AM via . All use subject to https://www.ebsco.com/terms-of-use

observation of the events occurring at low initiation rates that the sequence of events described above has been deduced. The situations are compared diagramatically in Figure 2. The appearance of primary particles at a few percent conversion is shown for the two situations by the photomicrographs in Figure 3.

The primary particles are smaller for high initiation rates as at each stage in the agglomeration process the concentration of agglomerating entities was larger. They are near spherical due to the smaller size of the microdomains and domains at the time of agglomeration and the very early conversion of agglomeration allowing subsequent polymerisation to overlay and thereby disguise them. Commercially produced PVC relates very much to the fast initiation process both in terms of the size of primary particles and by having no outward sign of the agglomeration process.

Development of morphology during polymerisation

Beyond 0.1% conversion the primary particles grow uniformly with conversion such that they are about 1 μm in diameter at full conversion. They do, however, undergo limited agglomeration into clusters and networks that give the final PVC grains their strength. Within the primary particles distinct crystalline regions form which together account for the approximately 10% crystallinity seen in commercial PVC. A diagrammatic representation of how these crystallites are probably arranged is given in Figure 4 based on work by Summers (2). Although only representing 10% of the product these regions of crystallinity are of great importance in contributing to the physical properties of PVC both in rigid and plasticised applications.

Coincidental with the formation of the internal morphology described most suspension polymerisation processes also involve an agglomeration of the initially formed 40 μm vinyl chloride droplets to give the final 130 μm polymer grains. Presumably the polymerisation process increases the water/vinyl chloride interfacial tension such as to make coalescence thermodynamically favourable. It is thought that this usually occurs between 3% and 10% conversion and is largely responsible for the final grain shape and distribution. Evidence for this droplet agglomeration is clearly seen in the photomicrograph of a single PVC grain shown in Figure 5.

EBSCOhost - printed on 2/13/2023 3:45 AM via . All use subject to https://www.ebsco.com/terms-of-use

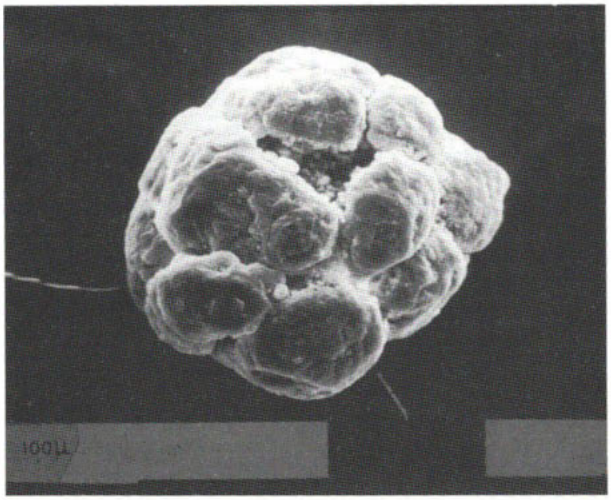

Figure 4. Crystallites Within the Mircrodomain

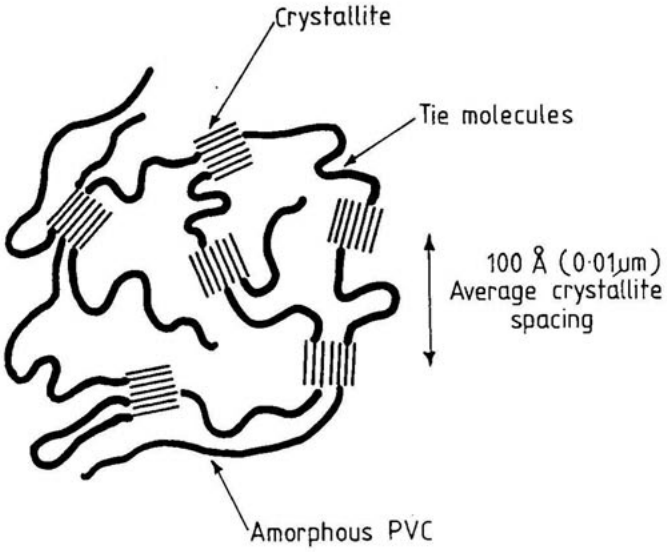

Figure 5. Single Grain of Suspension PVC by SEM

EBSCOhost - printed on 2/13/2023 3:45 AM via . All use subject to https://www.ebsco.com/terms-of-use

Plasticiser Absorption

The incorporation of plasticiser into the PVC grains is the necessary first step to PVC processing in all flexible applications. If mixing is carried out at ambient temperatures plasticiser will be absorbed into the grains to the extent of the available pore volume of that particular resin. As temperature is raised towards the glass transition temperature of PVC (ca 80°C), as is done in modern high speed mixers, the plasticiser is absorbed into the primary particles themselves. The level of porosity is important in both situations, in the first controlling the physical limit of absorption while in the second being the means of access to the primary particles. In the case of elevated temperatures the degree of agglomeration of the primary particles will also be important as this will influence the specific surface area available for diffusion of the plasticiser.

Within the primary particles the plasticiser will almost certainly be absorbed in the amorphous regions between the crystallites (see Figure 4). The presence of the tie molecules are of importance in preserving physical strength of the plasticised PVC.

Gelation of Rigid PVC

The gelation process is of fundamental importance to the processing of rigid PVC. This is especially so in the extrusion of pressure pipe where the physical properties are strongly influenced by the degree of gelation in the finished article. The mechanism by which the grains of PVC are transformed into the fused form has been extensively described by Allsopp (3). In this paper it is shown that, except in a few cases where processing involves the use of high shear/aggressive mixing equipment, the mechanism of gelation is by a process of densification and compaction rather than comminution (breakdown) of the grains. This process of densification can commence at the high speed mixing 'dry blend' stage if temperatures are raised sufficiently high (> 120°C). To obtain information on the mechanism of gelation during extrusion, machines were stopped and stripped down as rapidly as possible to obtain samples of the whole extruder profile. Microscopic examination of samples taken along the complete length of the screws shows densification

EBSCOhost - printed on 2/13/2023 3:45 AM via . All use subject to https://www.ebsco.com/terms-of-use

starting at the grain surface and rapidly developing. Although possibly becoming elongated in shape the grain boundaries remain as intergrain and intragrain porosity is eliminated. By the time the PVC has reached the screw ends the degree of fusion is quite high but memory of grain boundaries can still be in evidence. It appears that it is often not until after passage through adaptor and head regions that inhomogeneity finally disappears.

References

1 Murray, E.J., M Clark. 1981. Unpublished work carried out in the Laboratories of BP Chemicals Limited, Sully, Penarth, South Wales.

2 Summers, J.W. 1981. J. of Vinyl Technology, Vol 3, No. 2.

3 Allsopp M.W. 1982. In : Manufacture and Processing of PVC (ed. R. H. Burgess). Applied Science Publishers Ltd., London. P.183.

EBSCOhost - printed on 2/13/2023 3:45 AM via . All use subject to https://www.ebsco.com/terms-of-use

EBSCOhost - printed on 2/13/2023 3:45 AM via . All use subject to https://www.ebsco.com/terms-of-use

THE EFFECT OF PROCESSING ON MORPHOLOGY OF HETEROGENEOUS POLYMER SYSTEMS

M.Kozłowski and J.Pigłowski
Institute of Organic and Polymer Technology, Technical University of Wrocław, 50-370 Wrocław, Poland

Introduction

The toughness of a polymer blend is one of the major factors deciding on its practical value. An impact - modified poly(vinyl chloride) (PVC) is usually a multiphase system consisting of the PVC and an elastomeric component. The heterogeneous character of such a system and the interfacial adhesion between the components determine its impact strength. Thus, the thoughness is directly related to the composition, morphology and processing condition (1-7).

The concentration of a modifier in a PVC composition determines its morphology and therefore the impact strength. This is a consequence of the heterogeneity of the system. At a certain PVC/modifier ratio even the phase inversion can be observed. A considerable effect upon the mechanical properties of modified PVC has the presence of additives used in preparation of test samples. For PVC this factor is particularly important; the additives contain many components usually combined to provide a synergistic effect.

The processing conditions affect the morphology and properties of PVC/modifier system to a considerable extent. The effect of temperature, time and shear stress on the morphology depends on the kind of modifier used and the stability of phase structures formed.

Well-known high-impact PVC compositions containing ABS or MBS terpolymer are two-phase systems in which the elastomeric component is distributed throughout the PVC matrix in the form of small spheres. The size of the elastomer particles and their stability against shear forces can be controlled already at the stage of the modifier synthesis (1). The ABS and MBS modified PVC compositions, however, have the disadvantage of not being

Morphology of Polymers
© 1986 Walter de Gruyter & Co., Berlin · New York - Printed in Germany.

EBSCOhost - printed on 2/13/2023 3:45 AM via . All use subject to https://www.ebsco.com/terms-of-use

suitable for an outdoor use. The modifiers recommended for such applications are

- copolymers of ethylene and vinyl acetate (EVA)
- chlorinated polyethylene (CPE)
- polyacrylates

In our earlier studies, it has been found that the impact strength of PVC modified with an acrylic modifier of the graft copolymer type (AGM) depends on the processing conditions (2). In this work, the effect of time and temperature of processing on the mechanical properties of PVC/AGM compositions is investigated and the results related to the morphology of products.

Experimental

PVC S-64 (Tarvinyl - Poland) modified with a grafted type acrylic modifier was used. A graft PVC-EVA (10% EVA) copolymer was also used as a reference modifier. The compositions of the samples studied are listed in Table 1.

Table 1. Compositions of PVC/Modifier Systems

Formulation	Composition I	Composition II
S-PVC	40	70
S-PVC-EVA	60	-
AGM	-	30
Ergoterm BTGO	3.8	3.4
Ergowax GS	3.8	3.4

The polymer components were homogenized in a two-roll mill. The temperature and time of rolling were changed and the effect of these parameters determined by measuring the impact resistance. Notched impact strength was determined by the Charpy method using a hammer with the work range of 1 J. The morphology of the samples was observed in a transmission electron microscope (ultrathin specimens were stained with osmium tetroxide). The EM301 Electron Microscope (Philips-The Netherlands) with resolving power better than 5AU was used.

EBSCOhost - printed on 2/13/2023 3:45 AM via . All use subject to https://www.ebsco.com/terms-of-use

Results and Discussion

The impact strength of the samples are shown in Table 2 and 3. The value for unmodified PVC is 2.7 kJ/m^2.

Table 2. The Notched Impact Strengths of Composition I (PVC-EVA), kJ/m^2

Time	Homogenization Temperature, °C		
min	160	170	180
3	-	-	25.1
5	-	-	13.3
7	6.4	7.8	9.2
10	-	-	10.5

The results shown in Table 2 indicate a considerable dependence of the impact strength of EVA containing compositions on the processing conditions. Optimal for the high impact strength, the 'honeycomb' structure of PVC-EVA (or PVC-CPE) systems where the primary PVC grains are joined together with this layers of modifier (Fig.1A) is destroyed by the shear stress as the time of rolling increases (Fig.1B). As a result, the impact strength decreases.

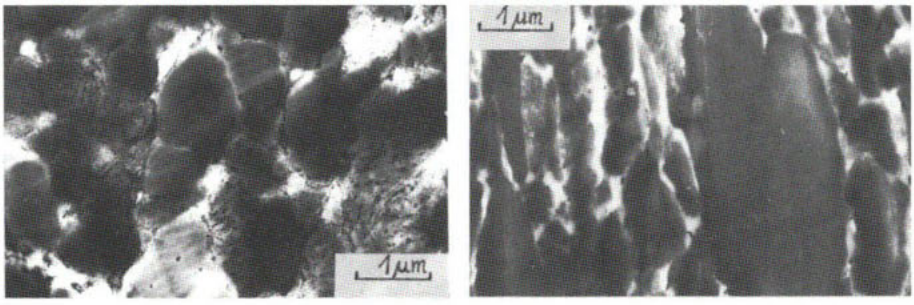

Fig.1. Transmission electron micrographs of PVC-EVA blends milled for 3 minutes (A) and for 5 minutes (B).

EBSCOhost - printed on 2/13/2023 3:45 AM via . All use subject to https://www.ebsco.com/terms-of-use

The composition containing in addition a flow modifier (FM) developed in this laboratory has the impact strength 43.2 kJ/m^2. The modifier reduces the viscosity of melt and therefore reduces the effective shear stress acting upon the multicomponent system. The morphology of the resulting material (Fig.2) provides better dissipation of an impact energy.

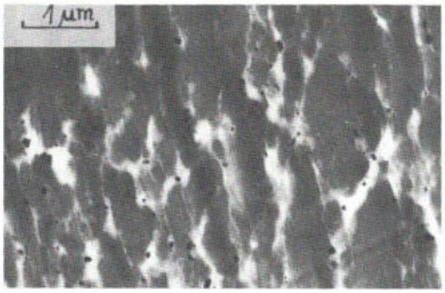

Fig.2. Electron micrograph of PVC-EVA-FM blend milled for 5 minutes.

The impact resistance of PVC modified with the acrylic modifier AGM is much less sensitive to variations in processing conditions.

Table 3. The Notched Impact Strength of Composition II (PVC-AGM), kJ/m^2

Time, min	Homogenization Temperature, °C		
	160	170	180
3	–	–	7.5
5	–	–	42.6
7	34.2	32.4	38.3
10	–	–	42.6

Except for the shortest time of homogenization (3 min) which seems not to be sufficient to produce the characteristic 'island' structure (Fig.3), all PVC/AGM samples have relatively high impact strength.

EBSCOhost - printed on 2/13/2023 3:45 AM via . All use subject to https://www.ebsco.com/terms-of-use

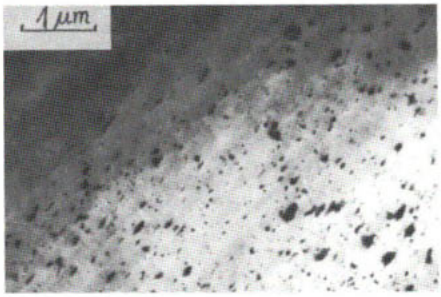

Fig.3. Electron micrograph of PVC-AGM blend milled for 7 minutes

An addition of the flow modifier further increases the impact strength to the value of 54.2 kJ/m^2.

The results presented above demonstrate the effect of the degree of agglomeration or dispergation of modifier particles upon the impact properties of modified PVC. For the EVA modifier, the size of particles and the degree of dispergation is determined to a large extent by the processing conditions; the morphology depends on the shear stress and processing temperature. On the other hand, the PVC compositions containing the acrylic modifier are less sensitive to processing conditions and their structure is more stable.

References

1. Bucknall, C.B. 1977. In: Toughened Plastics. Applied Science Publishers, London.
2. Kozłowski, M., J.Pigłowski. 1984. In: Proceeding of 6th IUPAC Conference 'Modified Polymers' Bratislava 1984, vol.2, pp. 57-61.
3. Deanin,R.D., N.A.Shah. 1983. J. of Vinyl Technol.5, 167.
4. Leps, G., J.Bohse, R.Stephan, J.Sachse. 1983. Plaste u. Kautsch. 30, 458.
5. Röhrl, E. 1980. Kunststoffe 70, 41.
6. Rabinovic, I.S. 1983. J. of Vinyl Technol. 5 (4).
7. Terselius, B., B.Ranby. 1981. Pure Appl.Chem. 53, 421.

EBSCOhost - printed on 2/13/2023 3:45 AM via . All use subject to https://www.ebsco.com/terms-of-use

EBSCOhost - printed on 2/13/2023 3:45 AM via . All use subject to https://www.ebsco.com/terms-of-use

LAMELLAR TEXTURES IN MELT-CRYSTALLIZED POLYSTYRENE

A. S. Vaughan, D. C. Bassett & R. H. Olley

J. J. Thomson Laboratory, University of Reading, Reading, U. K.

Introduction

It is now generally recognized that melt-crystallized polymers are lamellar solids in which the lamellae are themselves organized into spherulites. Although spherulites have been much studied with the polarizing microscope, it has not generally been possible to study details of their internal lamellar organization. This is because their scale, with thicknesses often of the order of 10nm, requires transmission electron microscopy for its resolution, but direct examination of melt-crystallized polymers in this way has been severely restricted by radiation damage. In this communication we are able to report in detail on the lamellar organization within spherulites of isotactic polystyrene. This has been made possible by development of the technique of permanganic etching (1-3). The observations support a pattern of construction also observed in polyethylene (4-6) and isotactic polypropylene (7) but different from that based on the concept of cellulation due to segregated 'impurities' (8, 9).

Experimental

Samples, in the form of discs ~ 10mm in diameter and ~ 3mm thick, were isothermally crystallized from the melt in an atmosphere of oxygen-free nitrogen before being quenched into cold water. From these, internal surfaces were carefully exposed using a microtome, in such a way as to

Morphology of Polymers
© 1986 Walter de Gruyter & Co., Berlin · New York - Printed in Germany.

EBSCOhost - printed on 2/13/2023 3:45 AM via . All use subject to https://www.ebsco.com/terms-of-use

minimise deformation, and etched with a 1% solution of $KMnO_4$ in a mixture of sulphuric acid, orthophosphoric acid and water in the ratio of 5:2:2 by volume. The etched surfaces were then replicated using a two stage process. In this an initial impression was formed in cellulose acetate softened with acetic acid. When dry the acetate cast was stripped from the sample and shadowed with a gold/palladium alloy before being coated with carbon. Finally the cellulose acetate was dissolved in acetone in a refluxing apparatus so as to leave the shadowed carbon replica on an electron microscope grid. Such replicas were examined in a Philips EM301 transmission electron microscope.

Results

Figure 1 shows a sample of isotactic polystyrene crystallized at 210°C. The objects displayed can be described as different views of 'axialites', i.e. arrays of hexagonal lamellae splaying apart in three dimensions but with the major axis of splay connecting opposite corners of a hexagonal lamella. Such structures show three characteristic appearances, corresponding to three orthogonal viewing directions of the structure in three orthogonal planes. These characteristic appearances are labelled A, B and C in figure 1 and have been termed sheaf-like, hexagonal and edge-on respectively (3). Examination of the lamellar growth tips of an object in the sheaf-like projection shows an approximately regular array of individual lamellae separated from one another by regions of melt from which other lamellae subsequently crystallize. The first forming lamellae, which grow out into the melt and by branching and splaying apart dictate the form of the resulting structure, are termed dominant. The later-crystallizing lamellae, which can be seen to be filling-in the pre-established dominant framework ~ 1μm behind the growth tips in object A in figure 1, are termed subsidiary.

Structures such as those described above for crystallization at 210°C have been observed in the range of crystallization temperatures 220°C to 200°C. Varying the crystallization temperature in this range has two major effects.

EBSCOhost - printed on 2/13/2023 3:45 AM via . All use subject to https://www.ebsco.com/terms-of-use

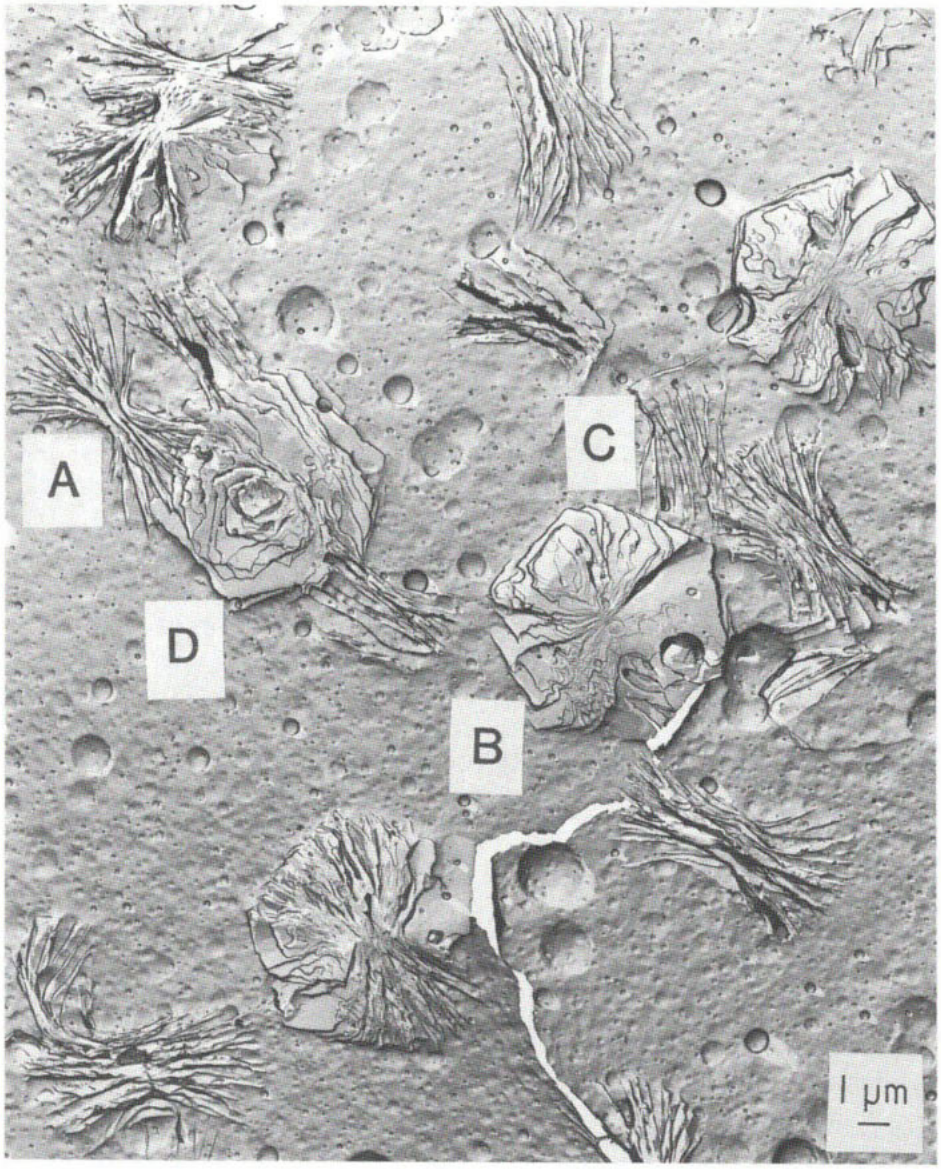

Figure 1. Electron micrograph of a sample crystallized at 210°C showing axialites in random orientations intersecting the etched surface. A, B and C show the structure of an axialite in 3 orthogonal planes and these characteristic views are termed sheaf-like, hexagonal and edge-on. D shows that lamellae splay apart in three dimensions.

EBSCOhost - printed on 2/13/2023 3:45 AM via . All use subject to https://www.ebsco.com/terms-of-use

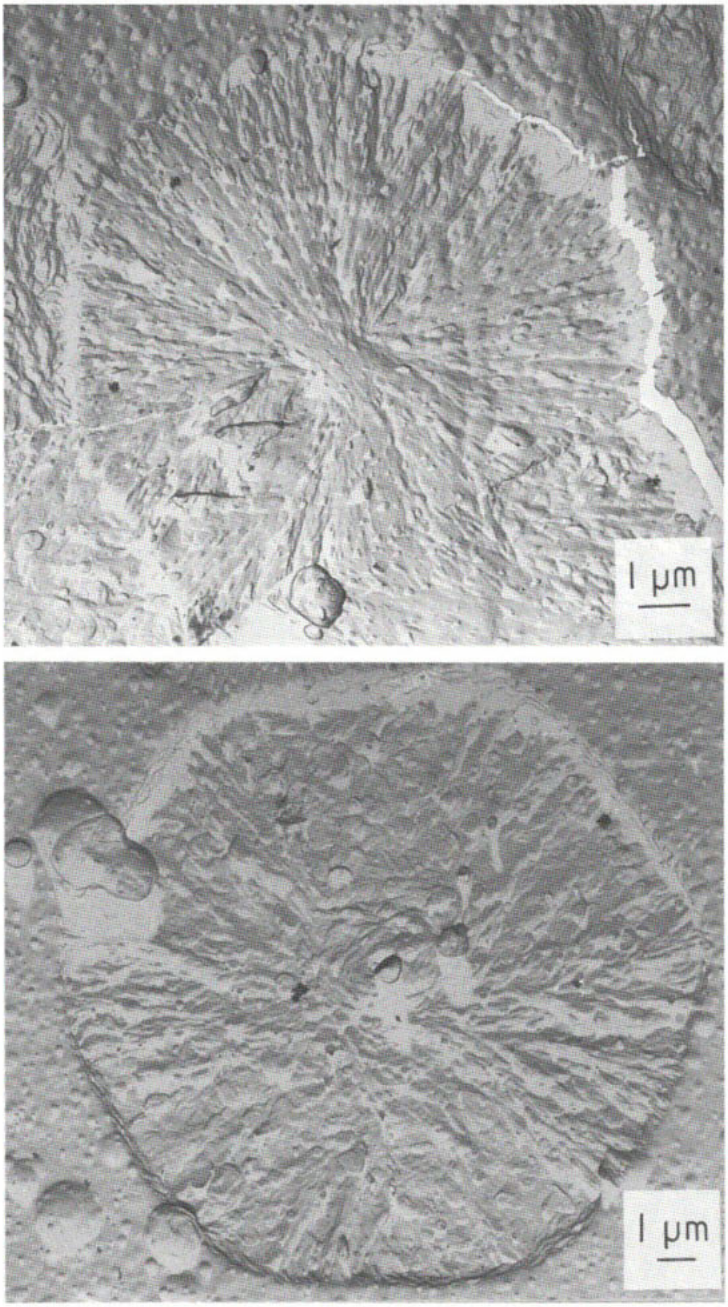

a

b

Figure 2.

EBSCOhost - printed on 2/13/2023 3:45 AM via . All use subject to https://www.ebsco.com/terms-of-use

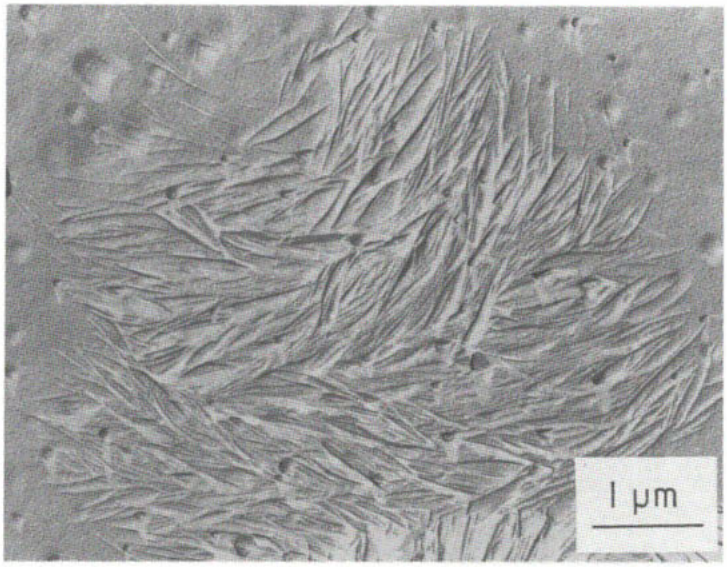

c

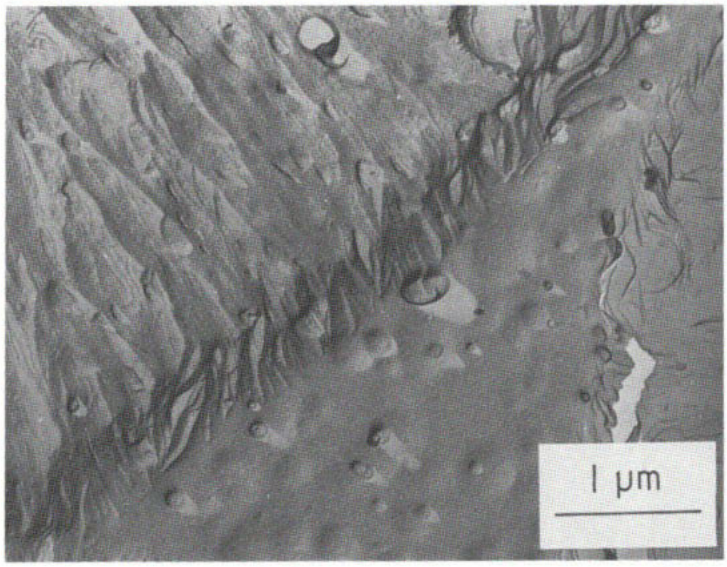

d

Figure 2. Electron micrographs of isotactic polystyrene crystallized at 190°C, showing spherulites in, 4a, sheaf-like, 4b, hexagonal and 4c, edge-on views. Figure 4d shows the array of dominant lamellae at the edge of the structure.

EBSCOhost - printed on 2/13/2023 3:45 AM via . All use subject to https://www.ebsco.com/terms-of-use

Firstly, as the temperature is reduced so the axialites become more compact. That is, the separation of adjacent dominant lamellae, and the distance between the dominant tips and the mass of later crystallizing subsidiary lamellae are both reduced. Secondly, the dominant lamellae branch and splay apart more in three-dimensions as the temperature is reduced such that the aggregates become less like a classical axialite (lamellae splaying apart about a single common axis (10)) and more like a spherulite (equivalent lamellae grow within a spherical envelope with the same radial direction). The tendency for lamellae to splay apart at all their growth faces can be seen in object D in figure 1, where the appearance of the structure resembles a rose, the lamellae of the axialite corresponding to the petals of the flower.

Reducing the crystallization temperature below the above range to 190°C yields mature objects whose envelope is approximately spherical. However, these spherulites have many features in common with the axialites discussed above. As shown in figures 2a to 2c they possess three characteristic appearances analogous to those of axialites. Examination of the growth tips (figure 2d) shows that growth proceeds by the same dominant/subsidiary mechanism as at 210°C. Also the lamellae grow in the form of inherently planar hexagonal sheets with growth faces of a length commensurate with spherulitic dimensions. At no time at 190°C were elongated ribbon-like lamellae observed of the type inferred by Keith and Padden, despite the fact that the size of the constituent lamellae substantially exceeds the characteristic length δ, which under these conditions is of the order of 0.5 nm (11).

Addition of atactic polystyrene to the melt is observed optically to produce more open structures composed of coarse fibrous units (8). Electron micrographs of a sample crystallized at 190°C and composed of 50% isotactic and 50% atactic polystyrene are shown in figure 3. From 3a it can be seen that the spherulites are made up of bundles of lamellae separated from one another by regions of non-crystalline material. Examination of the growth tips (figure 3b) shows that development again proceeds by the initial formation of an array of individual dominant lamellae. From the regions of interstitial melt the isotactic material then crystallizes leaving the atactic material incorporated within the structure. It is found experimentally that the separation of dominant lamellae is a well defined quantity which can be measured as a function of crystallization conditions. This parameter has been termed λ. From figure 4a it can be seen that at 190°C and over the limited range of composition

EBSCOhost - printed on 2/13/2023 3:45 AM via . All use subject to https://www.ebsco.com/terms-of-use

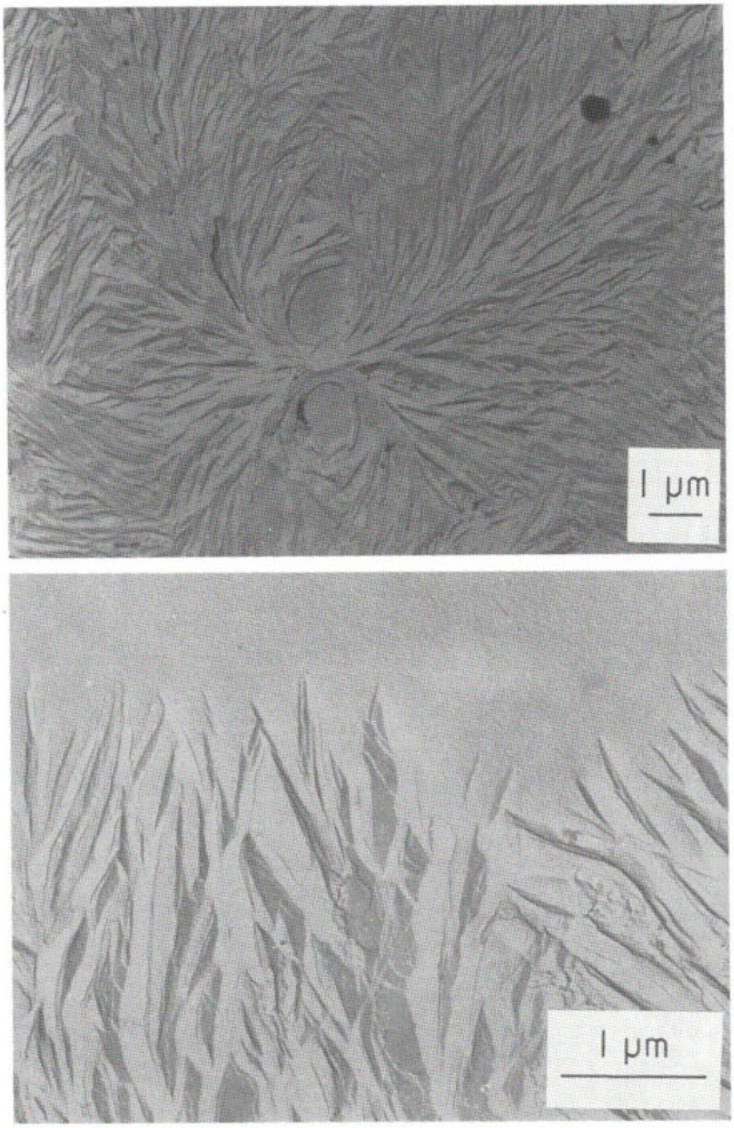

a

b

Figure 3. Electron micrographs of a sample crystallized at 190° C from a melt composed of 50% isotactic and 50% atactic polystyrene. Figure 3a shows the atactic material to be incorporated within the spherulites such that under these circumstances they are composed of bundles of lamellae separated from one another by non-crystalline regions. However, the dominant subsidiary growth mechanism is still operative (figure 3b).

EBSCOhost - printed on 2/13/2023 3:45 AM via . All use subject to https://www.ebsco.com/terms-of-use

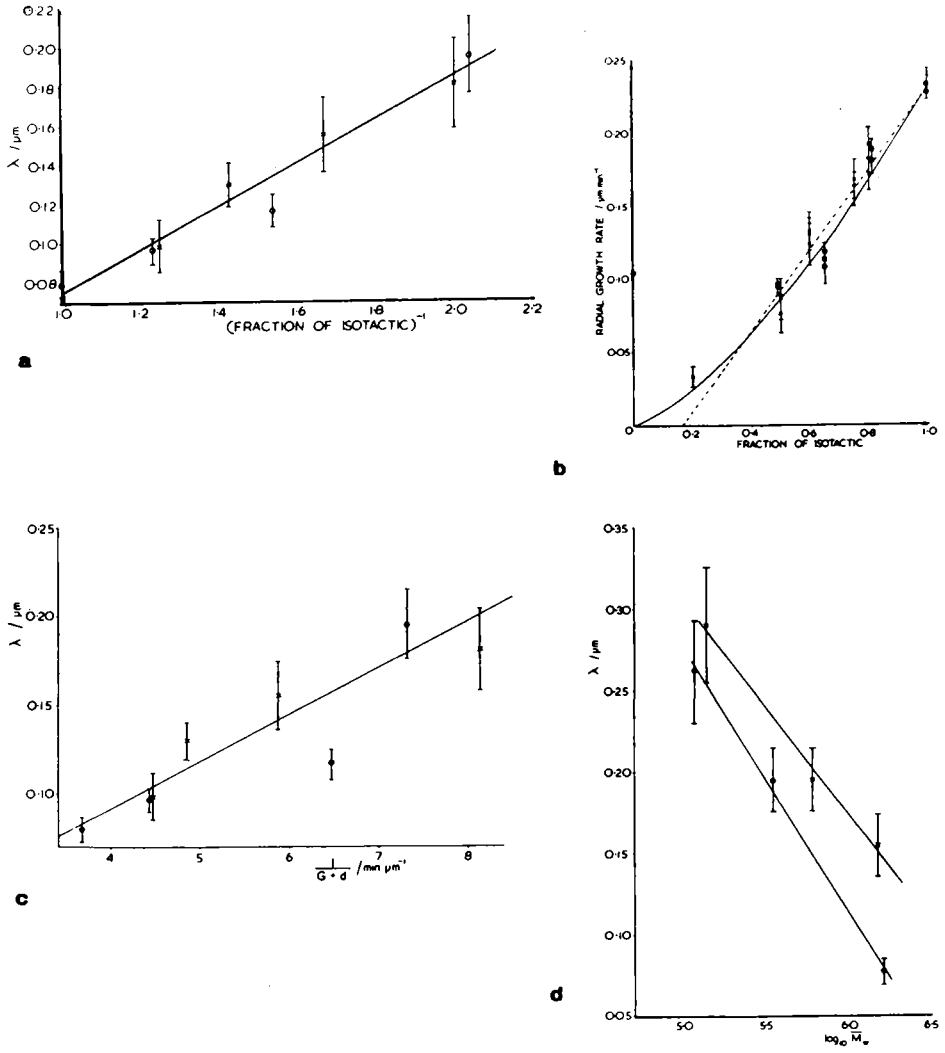

Figure 4. Figures 4a and 4b show the variation of dominant lamellar separation and spherulite growth rate with melt composition. 4c shows that by combining these results, λ varies with growth rate approximately as G^{-1}. The variation of λ with molecular mass of isotactic (upper line) and atactic (lower line) components of a number of blends of equal masses of each stereo-isomer is shown in 4d.

EBSCOhost - printed on 2/13/2023 3:45 AM via . All use subject to https://www.ebsco.com/terms-of-use

0% to 50% atactic polymer λ varies with composition nearly as I^{-1}, where I is the fraction of isotactic polystyrene present in the melt. Over the same range of composition the spherulite growth rate varies linearly with I, as shown by the dashed line in figure 4b. Therefore, combining these results it can be concluded that over the restricted range of composition 0% to 50% atactic polymer, where mature spherulites have been observed, λ varies with growth rate approximately as G^{-1} (figure 4c). At very high impurity concentrations spherulites tend to break down into simpler structures, in agreement with Keith (12) who reported the growth of single crystals at 190°C from a melt containing 90% low molecular mass atactic polystyrene.

Figure 4d shows the results obtained at 190°C by varying the molecular mass of each component in a number of blends made up of equal masses of the isotactic and atactic stereo-isomers. In this the upper and lower lines show the effect of varying the isotactic and atactic components respectively, the value of M_w in each case being as indicated. From these plots it can be seen that the effect of increasing the molecular mass of either component from $\sim 10^5$ to $\sim 2 \times 10^6$ is to reduce λ by a factor of about 3. However, over the same range the diffusion coefficients, and consequently δ, fall by some 3½ orders of magnitude. Thus λ, unlike δ, is insensitive to variations in D.

Although the morphologies reported above, based on individual dominant and infilling subsidiary lamellae are different from expectations based on fibrillation due to cellulation, significant changes are observed at lower crystallization temperatures. Superficially at least, the result of crystallization at 162°C (figures 5a, 5b) does suggest that there is an additional level of order involving several lamellae, since at this temperature no spherulites were observed with a hexagonal outline and the lamellae do appear to show a radially elongated habit. If one considers whether these effects may arise as a result of some kind of cellulation, superimposed onto the basic dominant/subsidiary mechanism (which can still be seen to be operative (figure 6)), then it is noteworthy that the scale of this additional ordering, being of the order of several microns, is many orders of magnitude greater than that predicted (13, 14). For these samples the parameter $\delta = D/G$ is ~ 0.02 nm.

Thus even at 162°C the observations are in accord with the view that

EBSCOhost - printed on 2/13/2023 3:45 AM via . All use subject to https://www.ebsco.com/terms-of-use

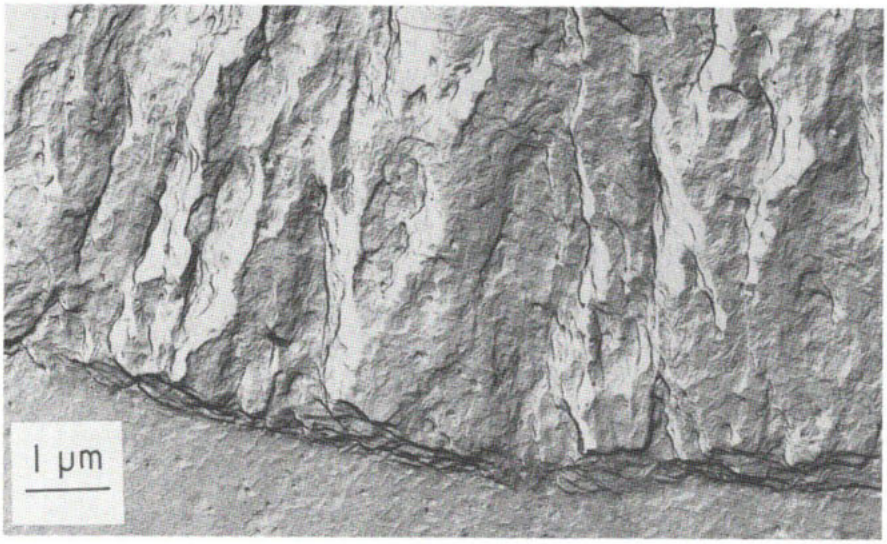

a

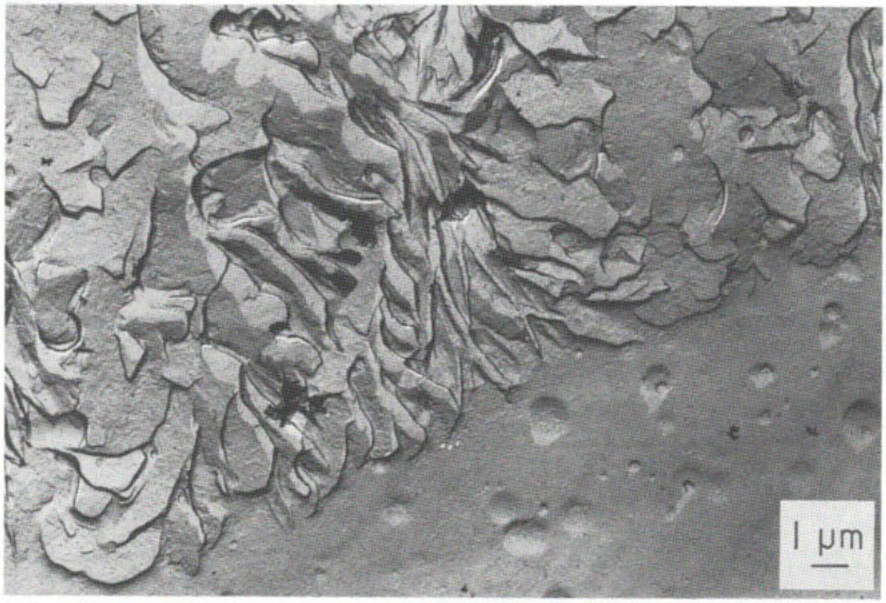

b

Figure 5. Electron micrographs of samples crystallized at 162°C from melts containing. 5a. 100% isotactic polystyrene and 5b. 20% isotactic 80% atactic polystyrene showing the additional scale of ordering observed at this crystallization temperature.

EBSCOhost - printed on 2/13/2023 3:45 AM via . All use subject to https://www.ebsco.com/terms-of-use

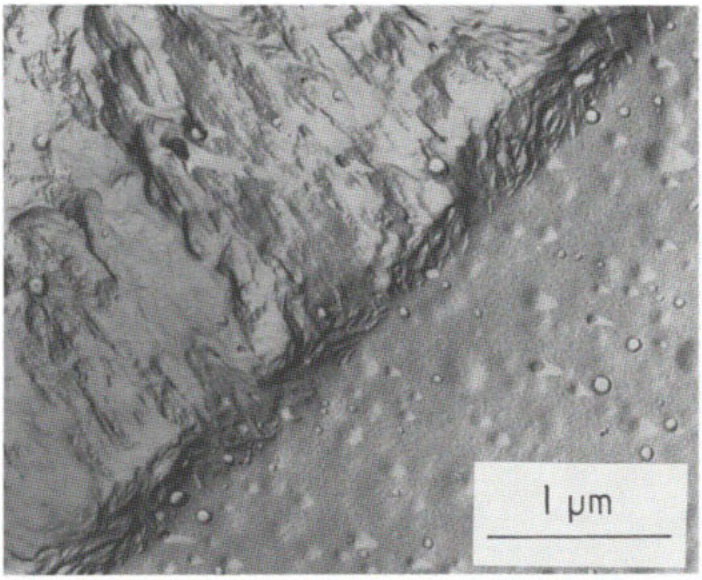

a

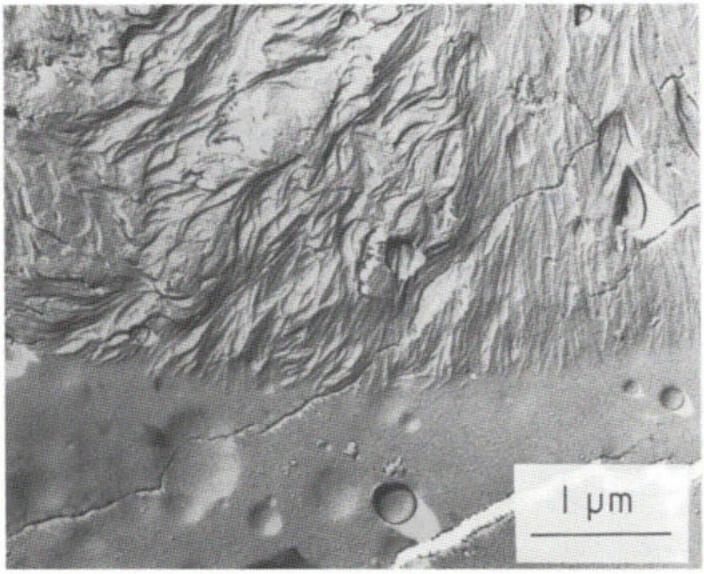

b

Figure 6. Electron micrographs showing dominant/subsidiary growth at 162°C from melts containing 6a 0% and 6b 50% atactic polystyrene.

EBSCOhost - printed on 2/13/2023 3:45 AM via . All use subject to https://www.ebsco.com/terms-of-use

spherulites arise through the frequent branching and splaying apart of dominant lamellae followed by subsidiary crystallization, the lamellar elongation merely being superimposed onto this growth mechanism rather than being of fundamental to the spherulite's development.

References

1. Olley, R. H., A. M. Hodge, D. C. Bassett. 1979. J. Pol. Sci: Pol. Phys. Ed. 17, 627.
2. Olley, R. H., D. C. Bassett. 1982. Polymer 23, 1707.
3. Bassett, D. C., A. S. Vaughan. 1985. Polymer 26, 717.
4. Bassett, D. C., A. M. Hodge. 1981. Proc. R. Soc. Lond. A377, 25.
5. Bassett, D. C., A. M. Hodge, R. H. Olley. 1981. Proc. R. Soc. Lond. A377, 39.
6. Bassett, D. C., A. M. Hodge. 1981. Proc. R. Soc. Lond. A377, 61.
7. Bassett, D. C., R. H. Olley. 1984. Polymer 25, 935.
8. Keith, H. D., F. J. Padden. 1964. J. Appl. Phys. 35, 1270.
9. Keith, H. D., F. J. Padden. 1964. J. Appl. Phys. 35, 1286.
10. Bassett, D. C., A. Keller, S. Mitsuhashi. 1963. J. Pol. Sci: A, 1, 763.
11. Otsuka, S., H. Ueno, A. Kishimoto. 1979. Angew. Makromol. Chem. 80, 69.
12. Keith, H. D., R. G. Vadimsky, F. J. Padden. 1970. J. Pol. Sci: A-2, 8, 1687.
13. Bachus, R., R. Kimmich. 1983. Polymer 24, 964.
14. Fleischer, G. 1983. Polymer Bulletin, 9, 152.

EBSCOhost - printed on 2/13/2023 3:45 AM via . All use subject to https://www.ebsco.com/terms-of-use

THE DIFFERENT TSL BEHAVIOUR OF STATISTICAL AND BLOCK BUTADIENE – STYRENE COPOLYMERS

J. Pospíšil, A. Havránek
Department of Polymer Physics, Faculty of Mathematics and Physics, Charles University, 180 00 Praha, Czechoslovakia

Introduction

The block and statistical butadiene-styrene copolymers were tested by thermostimulated luminescence (TSL) and by other relaxation methods. The main attention was devoted to the changes of the TSL spectra caused by the difference between statistical and block copolymers and by other modifications of the polymer structure. The adequacy of the TSL method as the relaxation analytical method has been checked by comparing its results with results obtained by standard relaxation methods, namely with results of viscoelastic measurements, differential thermal analysis (DTA), and thermally stimulated depolarization (TSD) current measurements.

Experimental

The TSL method consists in the ionization of a sample at low temperature and its subsequent heating during which trapped charges are released. These charges after recombination emit light. The result of this experiment is the glow curve, i.e. the temperature dependence of the luminescence intensity. Our samples were excited in an evacuated cryostat by X-ray irradiation at 77 K. The heating rate was 0.1 K/s.
Viscoelastic measurements were performed by the torsion pendulum in the temperature region from 140 K to 360 K, the frequency was maintained at 1 Hz. DTA measurements were made by the Bruel equipment. TSD measurements were performed by the method described in ref.(1).
The samples are various butadiene-styrene copolymers. The samples 1 and 2 are commercial products: the sample 1 is Krylene 1509,

Morphology of Polymers
© 1986 Walter de Gruyter & Co., Berlin · New York - Printed in Germany.

EBSCOhost - printed on 2/13/2023 3:45 AM via . All use subject to https://www.ebsco.com/terms-of-use

the statistical copolymer with 23.5 % bound styrene made by Polysar Corp., the sample 2 is Solprene 411, the block star-like copolymer with 30 % bound styrene made by the Phillips Petroleum Co. The samples 3 to 6 are laboratory prepared block copolymers with the block dimensions given in Table 1. All these laboratory prepared samples have an elevated content of 1,2-addition, namely 50 % to 60 % in samples 3 to 6 in comparison with approximately 10 % in sample 2 (Solprene).

Table 1. Block Dimensions of the Laboratory Prepared Samples

Sample	S	B	S	Modification
3	9 000	33 000	9 000	
4	28 000	42 000	28 000	
5	13 000	60 000	13 000	oil added
6	13 000	60 000	13 000	oligo-butadiene added

The dimensions of the styrene (S) and butadiene (B) blocks are specified by their number average relative molecular masses $\bar{M}_n$.

Results

The glow curves and other relaxation characteristics of the statistical copolymer (sample 1) are given in Fig.1, the same characteristics of a typical block copolymer (sample 2) are given in Fig.2

The statistical copolymer exhibits a broad relaxation region (labeled β) between 140 K and 180 K, and a sharp maximum (labeled α) at approximately 220 K. The block copolymer exhibits a sharp peak β at 160 K and a shoulder (labeled α') on the high temperature side of the β maximum localized at approximately the same temperature where the corresponding G" curve has its polybutadiene glass transition maximum. The correspondence between the measured relaxation characteristics is quite good.

EBSCOhost - printed on 2/13/2023 3:45 AM via . All use subject to https://www.ebsco.com/terms-of-use

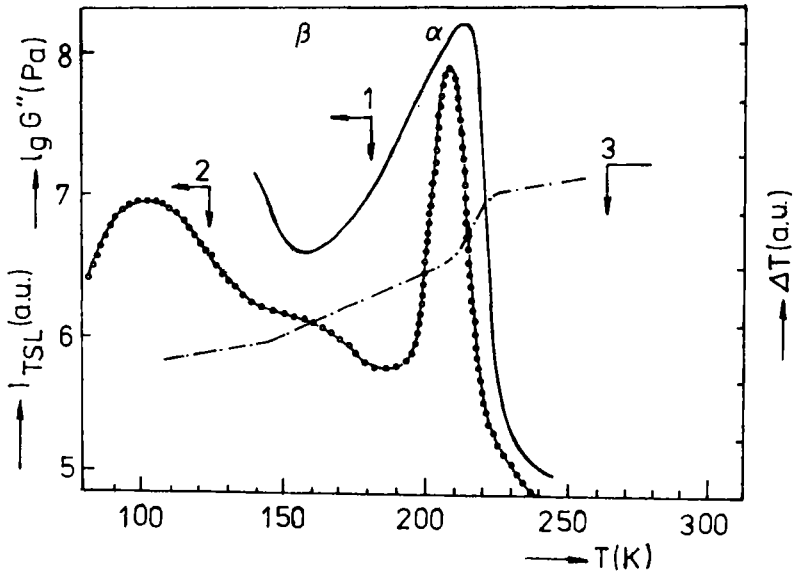

Fig. 1. The statistical copolymer (sample 1). The temperature (T) dependence of the luminescence intensity (I) (the glow curve -o-o-o-), DTA shift ΔT (—·—), imaginary part G''(——) of the complex shear modulus.

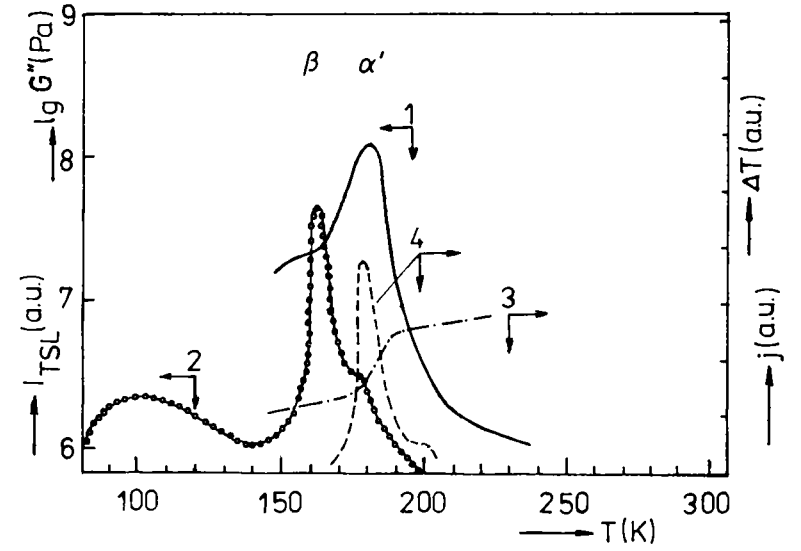

Fig. 2. The block copolymer (sample 2). The temperature (T) dependence of the luminescence intensity (I) (the glow curve -o-o-o-), DTA shift ΔT (—·—), imaginary part G'' (——) of the complex shear modulus, and TSD current j (– – –).

EBSCOhost - printed on 2/13/2023 3:45 AM via . All use subject to https://www.ebsco.com/terms-of-use

The glow curves of the various measured block copolymers are given in Fig.3 . The temperature positions (about 160 K) of the β maxima are very nearly the same for all the samples, intensities and widths of the maxima differ considerably. Sharp maxima have the samples 2 and 4 with large styrene block, weak maxima the sample 3 with small styrene block and the samples 5 and 6 with additives. The α' maxima are well separated from the maxima for the samples 3 to 6 as the higher 1,2-addition butadiene content causes the increase in the α' temperature position from 180 K for the sample 2 to approximately 220 K for the other four samples. The α' maximum forms especially high peak in the samples 5 and 6 with additives, a well detectable peak in the sample 4, and a weak maximum in the sample 3. In the samples with high glow curve maxima (samples 2,5,6) all the TSL intensity is emitted at low temperatures whereas in the samples 3 and 4 glow curve maxima are detectable to high temperatures.

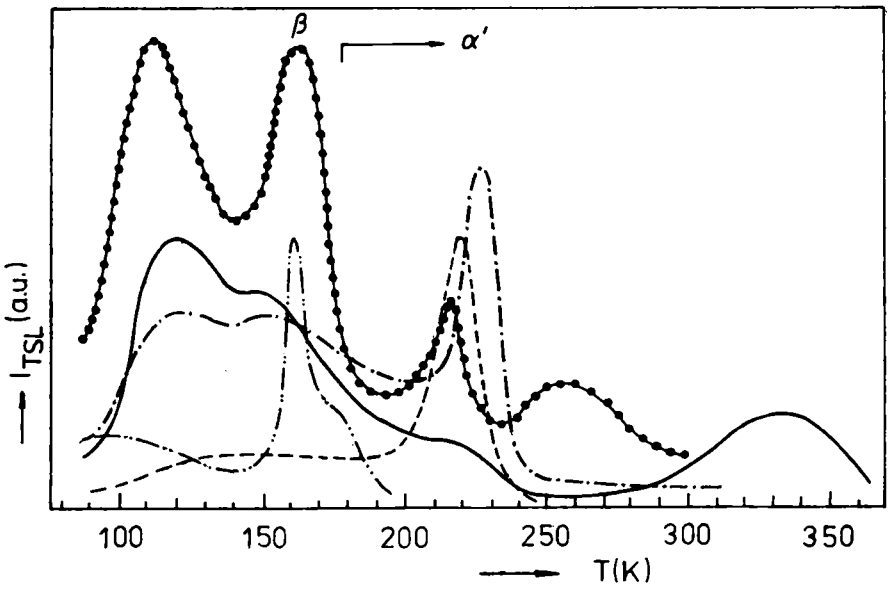

Fig. 3. The glow curves of the samples 2 (—··—), 3 (——), 4 (•••), 5 (– – –), and 6 (—·—).

EBSCOhost - printed on 2/13/2023 3:45 AM via . All use subject to https://www.ebsco.com/terms-of-use

Discussion

The glow curves (TSL spectra) well reflect the usual relaxation regions of the tested copolymers and may therefore be utilized as an analytical tool of detecting their mobility. The highest temperature to which the method may be used is that temperature at which all the TSL intensity is already emitted.

We suppose that the β relaxation at 160 K corresponds to the restricted rotation of the phenyl groups (2), i.e. to the generally (3) γ labeled relaxation region. We believe that the variation in the width of this relaxation region may be explained by the degree of uniformity in the neighbourhood of styrene monomers in the samples, the higher this degree the narrower the β maximum.

If we compare the presented glow curves with the results of viscoelastic and DTA measurements performed on the same samples and also with the generally known results (e.g.(3)) we may nearly uniquely attribute the α glow curve maximum to the glass transition of the statistical copolymer and the α' glow curve maxima to the glass transition of the butadiene blocks of the copolymers. The increase in the α' peak temperature of the samples with higher 1,2-butadiene addition content reflects the well-known (4) increase in the glass transition temperature T_g with the increase of this content.

The additives (samples 5 and 6) act as softening agents and cause the release of the α' relaxation (the glow curve intensity and the G'' peak values are very large) and its shift to higher temperatures.

The high temperature glow curve maximum of the sample 3 situated at 330 K may be in connection with the polystyrene block melting region which is reflected in the G'' curve as a maximum at approximately 360 K.

The applicability of the TSL as an analytical tool for the detection of polymer relaxation processes may be explained by the assumption that the motion of macromolecular chains or their parts helps to release the trapped charges, the radiative recombination of which is detected as the glow curve. The glow curve maxima created by relaxation processes exhibit extremely high activation energies and frequency factors if the usual method of the glow

EBSCOhost - printed on 2/13/2023 3:45 AM via . All use subject to https://www.ebsco.com/terms-of-use

curvē evaluation is used. The above mentioned assumption may be used to explain this anomaly (5).

References

1. Bakule, R., J. Nedbal, P. Štrof. 1985. In: Europhysics Conference Abstracts, Vol. 9 E - Morphology of Polymers (S. Methfessel and G. Thomas, eds.). European Physical Society, Geneva and ÚMCH ČSAV, Prague, abs. P 84.

2. Takayanagi, M.. 1963. Mem. Fac. Eng. Kyushu Univ., 23, No 1., p. 41.

3. Mc Crum, N.G., B.E. Read and G. Williams. 1967. Anelastic and Dielectric Effects in Polymeric Solids. Wiley, New York·London.

4. The Stereo Rubbers. 1977. (W.M. Saltman ed.). Wiley, New York·London. pp. 591-593.

5. Pospíšil, J., A. Havránek and I.A. Tale. 1985. In: Physical Optics of Dynamic Phenomena and Processes in Macromolecular Systems (B. Sedláček, ed.). Walter de Gruyter, Berlin·New York, pp. 245-250.

EBSCOhost - printed on 2/13/2023 3:45 AM via . All use subject to https://www.ebsco.com/terms-of-use

MORPHOLOGIC CHARACTERISTICS OF PRODUCTS OF STYRENE-BUTADIENE 1,3´-POLYBUTADIENE COPOLYMERIZATION IN THE PRESENCE OF $ZnCl_2$ AND A NETWORK REAGENT

D. Kechajov
Petroleum Research Institute, Ec Neftochim, Burgas 8104, Bulgaria

Introduction

Large-scale application of impact polystyrene (IPS) in various technical fields and nowadays living style dictate to enlarge its utilization and to solve adequately the "indexes-prime cost" relation of the polystyrene plastomers (1,2).
Therefore, our Institute was committed to study the copolymerization process between styrene, butadiene 1,3´ and polybutadiene rubber with the purpose to synthesize IPS with considerably lower basic elastomer content, and enlarge usable range of product properties. Data on such polymerization study were probably not published until now. The only known fact is production of transparent impact polybutadiene-styrene thermoplastic in commercial plant (3).

Results

Block-suspension copolymerization of the predissolved polybutadiene rubber "Buna-cis-132" in styrene and added, after that butadiene-1,3 was prepared in steel reactor, under continuous agitation as described in ref. (4). Mass-precopolymerization was carried out at 87°C in the presence of initiators as azobis-isobutyronitrile (AIBN), benzoyl peroxide (BPO) and the regulator tert-dodecylmercaptane (TDM), and components given in Table 1. Precopolymer (conversion 33-63%) was dispersed and suspension copolymerization was carried out until 99.85-99.95% conversion was reached (5). Produced plastomer product was then washed, dried and extruded.

Morphology of Polymers
© 1986 Walter de Gruyter & Co., Berlin · New York - Printed in Germany.

EBSCOhost - printed on 2/13/2023 3:45 AM via . All use subject to https://www.ebsco.com/terms-of-use

Table 1. Components used and their concentrations

Components/Samples	1	2	3
Rubber "Buna-cis-132", %	4.0	2.5	1.0
Butadiene-1,3, mmol/dm^3	252	499	771
Zink chloride, mmol/dm^3	3.33	13.30	19.90
2-merkaptobenzothiazole, mmol/dm^3	0.671	0.440	

Morphologic features of precopolymer and the final product were studied by means of an optical microscope "Beck Kassel" with phase-contrast appliance, and a transmission electron microscope Y MB-100K, according to the methods shown in ref. (6). The conversion was determined from dry substance of the precopolymer, according to the formula given in ref. (7). Dynamic viscosity of precopolymer was measured using a rotational viscosimeter (type RN-211).

At the complex-radical precopolymerization (Table 1, sample 1) higher conversion was reached (17-18%) and phase inversion was delayed, having a strange nature which could be defined as "quasi-net inversion" (Fig.1a). Postinversion conditions of the heterophase polymer-polymer system is also very specific. Part of the elastomer phase had a "cloud" appearance while dispersed rubber particles have irregular shape (Fig.1b). A part of the finally dispersed particles have unusual shape and could be defined as "small elliptical" particles (Fig.1c).

The presence of "small elliptical" particles which are similar to "cord"-type particles requires to complete the system by Echte (8). According to Echte, the dispersed "cord"-phase is formed in the copolymerization of styrene and butadiene-styrene block copolymer which has a fixed composition (Bu:St = 50:50%). So, we can suppose that "small elliptical" particles (found in this study) are formed as a result from block-copolymer formation during the copolymerization process.

"Quasi-net inversion" and "small elliptical" particles described in the present study supplement the morphologic types of IPS summarized by Echte.

EBSCOhost - printed on 2/13/2023 3:45 AM via . All use subject to https://www.ebsco.com/terms-of-use

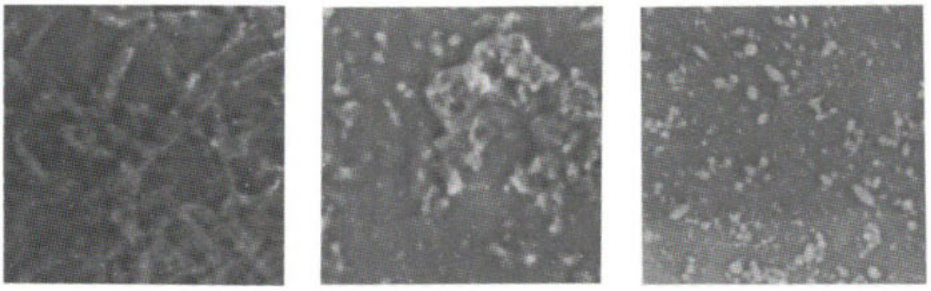

a b c

Fig.1. Morphologic types of heterophase copolymerizing system at different conversion (the elastomer phase is bright): (a) 17-18%, (b) 22-23%, and (c) 28-29% and 99.95%. Enlargement 1250x.

Complex-radical precopolymerization was studied under the same conditions and ingredients (Table 1, sample 2) except that the complexing agent concentration ($ZnCl_2$) varies in the range of 3.33 to 19.90 mmol/dm^3. It was found that the higher the $ZnCl_2$ concentration, the faster the increase in conversion which is still not proportional to $ZnCl_2$ concentration increase (Fig.2). In this way the data shown in refs. (9-11) are confirmed. According to them, the use of complexing agents (especially $ZnCl_2$) brings about a significant increase in the copolymerization rate and decrease in the activation energy of the process. $ZnCl_2$ determines also the repeated increase in the dissociation constant of the initiators which leads to the increase in the initiation rate (9,10). It was also established that the increase in $ZnCl_2$ concentration results in a precopolymer dynamic viscosity decrease which favours mass- and heat-exchange in the copolymerizing system.

In this study, the following special features are witnessed: when the phase inversion is completed, the particles of the dispersed phase aim to reach their equilibrium state (their final mode) for quite a long time. The duration of this process and the dimensions of the macrogel particles thus formed depend on $ZnCl_2$ concentration. Increase in $ZnCl_2$ concentration results in duration increase of the quasi-stable condition of the dispersed particles, and in some temporary dimension increase. Finally, an unusual morphology is formed as shown in Fig.3; particles with a diameter from 0.8 to 1.2 μm do prevail, while particles with a diameter of

EBSCOhost - printed on 2/13/2023 3:45 AM via . All use subject to https://www.ebsco.com/terms-of-use

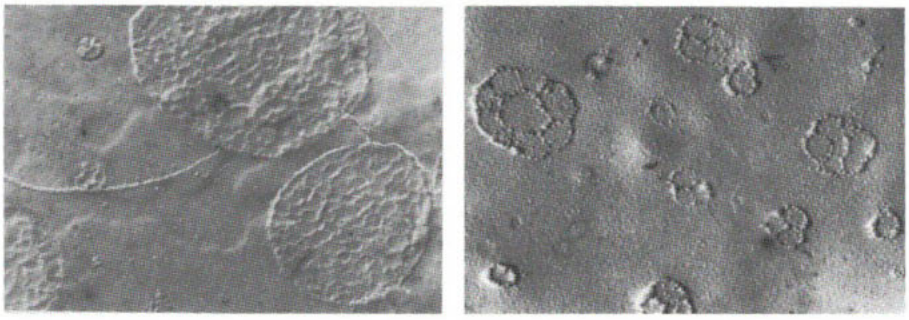

a b

Fig.4. Electron micrographs of copolymer synthetized according to the conditions of (a) sample 1 (12 000x), (b) sample 3 (12 000x).

holds the grafting copolymer formation right after phase inversion. As proof we refer to the fact that precopolymerization velocity obviously decreases in the presence of a network agent with concentration above 5.60 mmol/dm^3.

Electron microscopy studies of the copolymer show, when butadiene and $ZnCl_2$ concentration increases together with a decrease in the elastomer content (Table 1, samples 1-3), that the diameter of dispersed elastomer particles decreases while the diameter of the occlusions increases (Fig.4a,b). Copolymers of sample 2 and, especially, sample 3 are semitransparent.

Without claiming thoroughness, the results of the present study show that varying the components concentration and their ratio in copolymerization system "styrene-butadiene 1,3-$ZnCl_2$-network reagent", intentional influence can be exercised: on the velocities of precopolymerization and on the formation of dispersed elastomer particles; increase in conversion in precopolymer dynamic viscosity; morphology nature of the copolymer and the dispersed elastomer phase. So, real possibility exists for synthesis of impact styrene copolymers with wide useful range of properties.

EBSCOhost - printed on 2/13/2023 3:45 AM via . All use subject to https://www.ebsco.com/terms-of-use

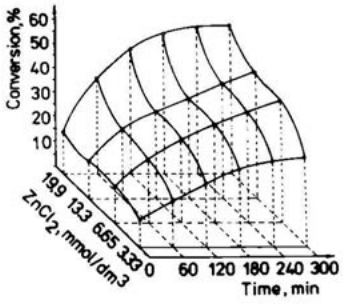

Fig.2. Kinetic dependence of conversion on $ZnCl_2$ concentration.

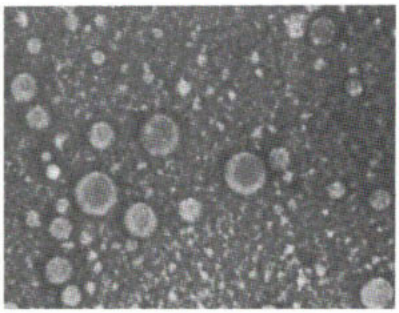

Fig.3. Morphology of copolymers with conversion 99.95% (Sample 2, 1250x).

2-5 and 5-8 μm are randomly located between them and their relevant number slightly increases when $ZnCl_2$ content exceeds 6.65 mmol/dm^3. An explanation of this picture could be given as due to the relatively low dynamic viscosity favouring partial diffusion of the occlusions out of the disperse elastomer phase. Also, effect of delayed grafting after phase inversion because of $ZnCl_2$ presence has to be considered. This statement can be proved reliably by the prolonged period required for final formation of the disperse phase. Specific irregular distribution of the macrogel particles (Fig.3) is probably caused by heterophase nature of the copolymerization process and by inhomogeneous distribution of the complexing agent in plastomer and elastomer phases.

Physico-mechanical tests seem to prove that the morphology, as shown in Fig.3, favours the copolymer strength characteristics. Reasons for this can be seen in the fact that elastomer particles (0.8-1.2 μm), covering a relatively great part of the surface, initiate formation of crazes, while particles (2-5 μm and 5-8 μm) distributed among them increase the possibility of their collision with the cracks. In this way, the cracks are delayed or stopped for a moment.

It was found that slight concentration of network reagent (like ZnO or other) during the precopolymerization results in a quick stabilization of disperse elastomer particles which do not change anymore to the end of this process. The quick stabilization of the disperse phase can be explained with a low inhibition level which

EBSCOhost - printed on 2/13/2023 3:45 AM via . All use subject to https://www.ebsco.com/terms-of-use

References

1. Kirkland, C. 1983. Plast.Technol. 29, 49.

2. Kossoff, R.M., A.E.Plitt. 1976. 2, 13.

3. Mater.plast.elast. 1974. No.8, 634.

4. Kechajov, D.D., M.A.Natov. Author´s Rights, People´s Republic of Bulgaria, Cl. C 08 F 2/20, No.28489. Published on May 26, 1980.

5. Kechajov, D. 1979. Angew.Makromol.Chem. 81, 1.

6. Galperin, W. 1975. Metody issledovaniya udaroprochnykh polistirolov, p.60.

7. Molau, G.E. 1965. J.Polym.Sci. 3, 1267.

8. Echte, A. 1977. Angew.Makromol.Chem. 58/59, 175.

9. Lachinov, M.B. et al. 1977. J.Polym.Sci.,Polym.Chem.Ed. 15, 1777.

10. Kuznetsov, A.A., U.S.Zaitsev. 1976. Report of the Academy of Sciences of USSR, 8, 433.

11. Zaitsev, U.S. et al. 1979. Vysokomol.Soedin. A21, 2163.

EBSCOhost - printed on 2/13/2023 3:45 AM via . All use subject to https://www.ebsco.com/terms-of-use

THE EFFECTS OF MOLECULAR WEIGHT ON THE MORPHOLOGY AND CRYSTALLIZATION OF CIS-1,4-POLYBUTADIENE

Enle Zhou, Guiping Jing, Huizhen Hu, Xuemei Xu and Hong Li
Changchun Institute of Applied Chemistry, Academia Sinica
Changchun

Introduction

It is known that cis-1,4-polybutadiene (PB) synthesized with nickel catalyst has high cis-content, and can crystallize in bulk state easily and rapidly at suitable low temperatures. The dependence of its morphological structure and growth rates of spherulites on the degree of molecular regularity was published in literature (1,2). But the relationship between its crystallization behavior and molecular weight (MW) has not been yet reported. This paper gives the results of our microscopic examination of nucleation and growth rates of spherulites of PB with molecular weights range from 0.45×10^5 to 13.69×10^5 and under different crystallization conditions. The mechanism of crystallization is discussed.

Experimental

1. Specimen

Two samples of cis-1,4-PB polymerized with nickel catalyst were used in this study. The cis-content and the other structure data of PB are listed in Table 1. The samples were fractionated by precipitation (toluene/methanol) into a number of fractions. The intrinsic viscosity and molecular weight of some selected fractions are given in Table 2.

Cis-content was determined by IR spectroscopy (Perkin-Elmer 599B). Weight-average molecular weight $\bar{M}_w$, number-average molecular weight $\bar{M}_n$ and distribution index $\bar{M}_w/\bar{M}_n$ were determined by GPC. Intrinsic viscosity $[\eta]$ was determined with toluene solution at 25°C by viscometer. Average-viscosity molecular weight $\bar{M}_\eta$ was obtained using

Morphology of Polymers
© 1986 Walter de Gruyter & Co., Berlin · New York - Printed in Germany.

EBSCOhost - printed on 2/13/2023 3:45 AM via . All use subject to https://www.ebsco.com/terms-of-use

Table 1. The Structure Data of PB

Sample	Micro-structure(%)			$\bar{M}_\eta$ x10^{-4}	$\bar{M}_w/\bar{M}_n$	$\bar{\lambda}$x10^5	Gel(%)
	$C_{1,4}$	$V_{1,2}$	$T_{1,4}$				
PB-1	96.5	1.1	2.4	32.9	4.6	0.086	2.48
PB-2	96.6	1.8	1.6	53.9	3.6	0.09	0.48

Table 2. The Characterization Data for Fractions of PB

Sample fraction	PB11	PB12	PB13	PB14	PB15	PB21	PB22	PB23	PB24
$[\eta]$, dl/g	8.57	4.46	3.79	2.94	1.32	5.21	3.13	1.90	0.72
$\bar{M}_\eta$ x10^{-5}	13.96	5.56	4.44	3.13	1.04	6.90	4.20	1.34	0.45

the following equation (3):

$$[\eta] = 3.05 \times 10^{-4} M_w^{-0.725} \qquad \text{(dl/g, toluene, 25°C)}$$

For the characterization of branched polymers, the degree of long chain branching $\bar{\lambda}$ was evaluated by the GPC coupled Automatic Viscometer technique.

2. Preparation of specimens for electron microscopic observation

Solution-cast films were made for electron microscopy by dissolving the polymer in toluene to form a 0.05 wt % solution. Films were casted onto a glycerine surface at room temperature; when all the solvent was evaporated, the films were floated off on distilled water and picked on electron microscope grids. The thickness of film was about 400 Å. Films were quickly transferred to a crystallization bath set at predetermined fixed temperature T_c, controlled to 0.1° C. The isothermal crystallization studies were carried out at a temperature in the range from -10°C to -30 C, depending on molecular weight. After crystallization, the films were stained with OsO_4 at the same temperature for two hours. The change of morphological state of the OsO_4 stained film specimen crystallized at a given temperature after different time intervals was observed with electron microscope (Hitachi H-500) at room temperature.

EBSCOhost - printed on 2/13/2023 3:45 AM via . All use subject to https://www.ebsco.com/terms-of-use

Results and Discussion

1. Effects of molecular weight on the nucleation rates

Recently much attention has been paind to the effects of MW on crystallization of polymers, some results have been reported for polyethylene and nylon, but different results have been given in literature. This fact is not suprising due to the different crystallization mechanism.

Fig. 1 is the electron microphotograph of the morphology of PB-1-2 crystallized at $-30^{\circ}C$, for 4, 8 and 20 min. The spherulite radius R increases linearly with time for all the temperatures investigated.

Induction time preceeding the appearance of the first nucleus has been observed for PB-1 crystallized at $-30^{\circ}C$. The induction time τ passed through a maximum at $\bar{M}_{\eta} = 5 \times 10^{5}$, with the increasing of molecular weight (Fig. 2a).

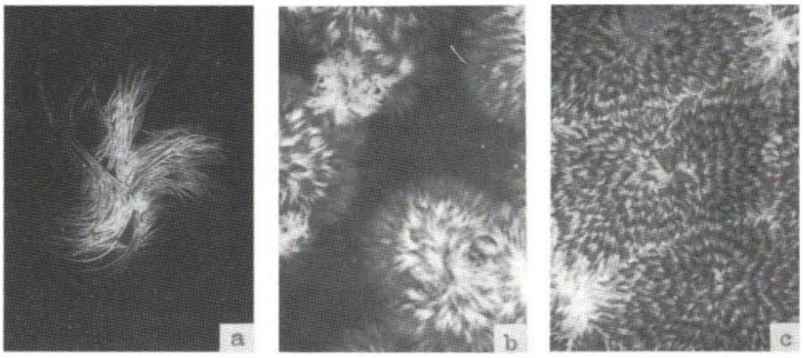

Fig. 1. The growth of spherulites of PB-1-2 crystallized at $-30^{\circ}C$. (a) 4 min, 20000x; (b) 8 min, 3000x; (c) 20 min, 1500x.

EBSCOhost - printed on 2/13/2023 3:45 AM via . All use subject to https://www.ebsco.com/terms-of-use

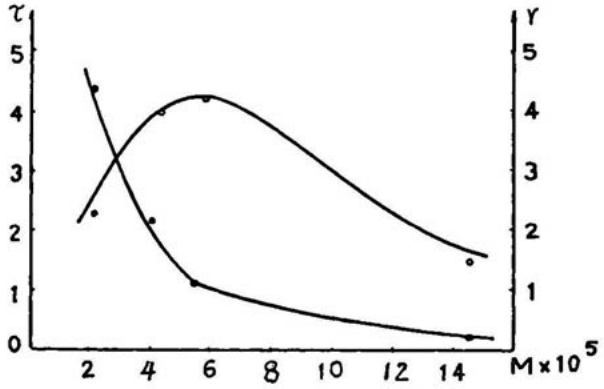

Fig. 2. Molecular weight dependence of PB-1.
(a) induction time τ (min); (b) radial growth rate r(μm/min) of spherulites.

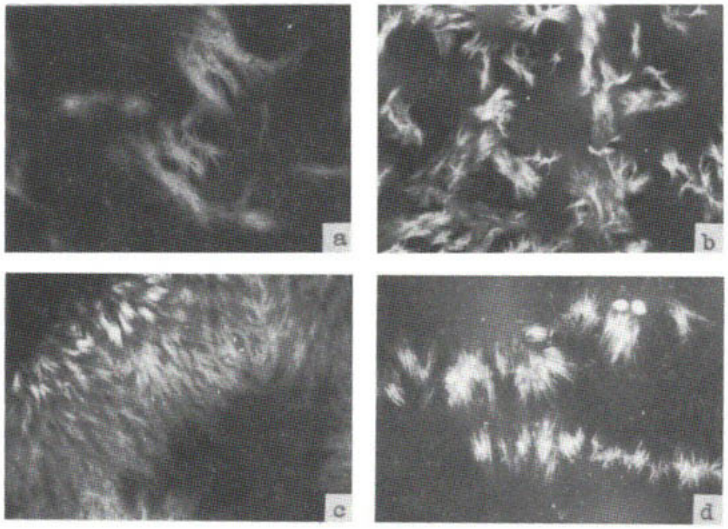

Fig. 3. Nucleus of PB-2 spherulites with different MW, crystallized at -30°C.
(a) PB-2-1, M_η =6.9x10^5, 4 min, 5000x,
(b) PB-2-2, M_η =4.2x10^5, 20 min, 8000x,
(c) PB-2-3, M_η =1.34x10^5, 20 min, 2000x,
(d) PB-2-4, M_η =0.45x10^5, 40 min, 15000x.

EBSCOhost - printed on 2/13/2023 3:45 AM via . All use subject to https://www.ebsco.com/terms-of-use

Due to the fact that the gel content of PB-1 is more that 2.48%, there should be more aggregates of entangled molecules than in the case of PB-2 (with 0.48% gel content). The aggregates of entangled molecules may act as nuclei, at which will develope spherulites. Therefore, nucleation rate of PB-1 is much faster than PB-2.

Shown in Fig. 3 are the nuclei of PB-2 spherulites with different molecular weight crystallized at -30°C. As indicated, for sample PB-2-1 with high MW (M_η =6.9x10^5) τ is 4 min while for low MW fraction (M_η =0.45x10^5) PB-2-4 τ is 40 min. The nucleation rate of PB-2-1 is almost ten times faster than that of PB-2-4.

2. Influence of MW on the morphology and growth rates of spherulite

Electron microscopy has also been much used to study the growth rates of spherulites. EM observation was made on all MW fractions of PB-1. The spherulite size decreased with increasing MW as shown in Fig. 4. However the growth was faster for low MW fractions than for high MW fractions (Fig. 2b). The growth rate of PB crystallized at -30°C can vary from 0.7μm/min (for PB-1-1) to the 5μm/min for PB-1-5); for sample of $\bar{M}_\eta$=2x10^5 it is about five times faster than that of the sample of $\bar{M}_\eta$=1.4x10^6. This may be attributed to the fact that lowering the molecular weight lowers the viscosity and hence increases the molecular mobility.

In the case of high MW fraction, nucleation was very fast, but lamellar growth very slow. As a result, small spherulites or random lamellae were formed (Fig. 4a). For fractions of MW lower than critical entanglement molecular weight M_e, crystals grow from the edges of copper grid and the cracks in foreign particles, as there is no molecular entanglements. The rate of nucleation is very slow; but once formed the nuclei, from which the lamellae grow relatively much faster, then a few large spherulites will result (Fig. 4f). It is evident that there are two modifications of spherulitic texture for cis-1,4-PB.

Specimens of MW below M_e form not entangled lamellae, while that of MW above M_e, lamellar entanglements developed during crystallization, as shown in the electron microscopic graphs (Fig. 5).

The effects of MW on the crystallization behavior of the polymer are rather complicated, and the morphology depends on the relationship between nucleation rate and growth rate.

EBSCOhost - printed on 2/13/2023 3:45 AM via . All use subject to https://www.ebsco.com/terms-of-use

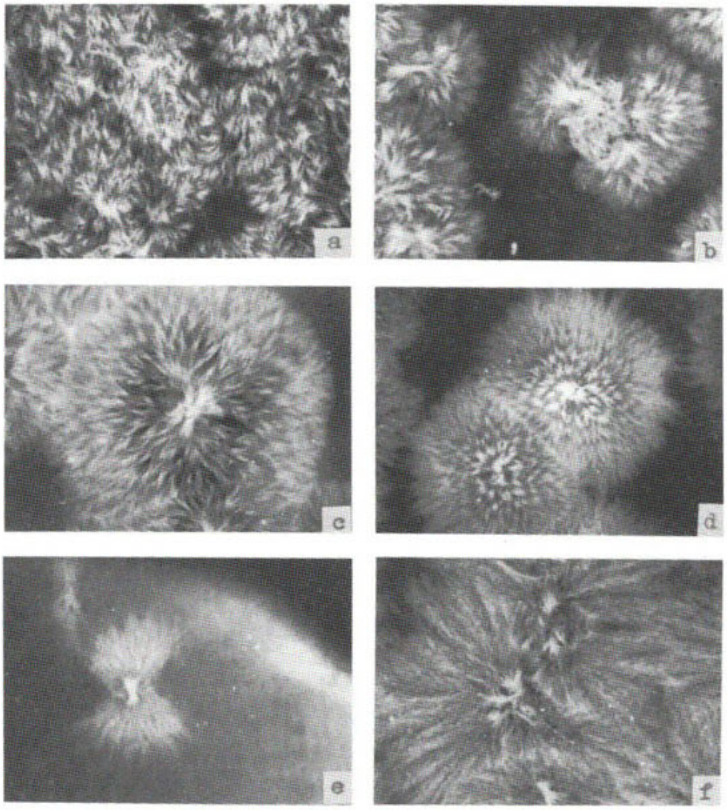

Fig. 4. Morphology and spherulite growth of PB-1 with different MW, crystllized at -30°C.

(a) PB-1-1, M_η =13.69x10^5, 8 min, 3000x;
(b) PB-1-2, M_η = 5.56x10^5, 8 min, 3000x;
(c) PB-1-3, M_η = 4.44x10^5, 8 min, 2500x;
(d) PB-1-4, M_η = 3.13x10^5, 4 min, 1500x;
(e) PB-1-4, M_η = 3.13x10^5, 4 min, 1500x;
(f) PB-1-5, M_η = 1.04x10^5, 8 min, 3000x.

EBSCOhost - printed on 2/13/2023 3:45 AM via . All use subject to https://www.ebsco.com/terms-of-use

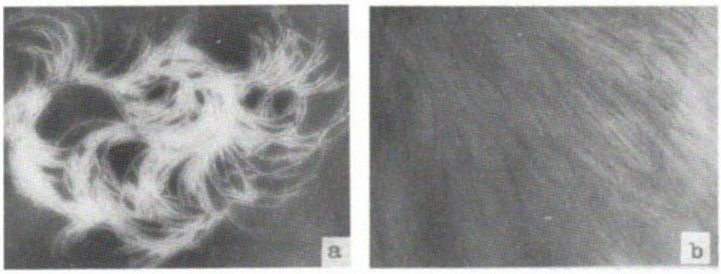

Fig. 5. Lamellar structure of PB-1 crystallized at -30°C.
(a) $M_\eta = 4.44 \times 10^5$, 8 min, 15000x;
(b) $M_\eta = 1.04 \times 10^5$, 8 min, 30000x.

3. The effects of temperature on crystallization behaviour of PB

The variation of crystallization rate with temperature typically takes the form with a maximum, which is discussed in detail in literature (4). The characteristic shape is a consequence of growth being slowed by increasing viscosity at lower temperature and

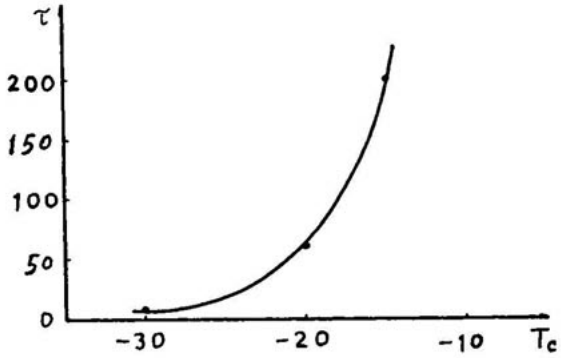

Fig. 6. Induction time τ (min) of PB-2-1 ($M_\eta = 6.9 \times 10^5$) plotted against crystallization temperature T_c (°C).

EBSCOhost - printed on 2/13/2023 3:45 AM via . All use subject to https://www.ebsco.com/terms-of-use

by diminishing thermodynamic drive as the melting point is approached. The temperature of the fastest crystallization rate of PB is -56 C°(2).

Fig. 6 is a plot of induction time of PB-2-1 against crystallization temperature. The higher the crystallization temperature the longer the induction time τ is for the range of temperatures investigated by us. τ is 4 min at -30°C, but it is 150 min at -15°C.

Fig. 7 and Fig. 8 are the EM photographs of growth of spherulites and their lamellar structure respectively, crystallized at -20°C.

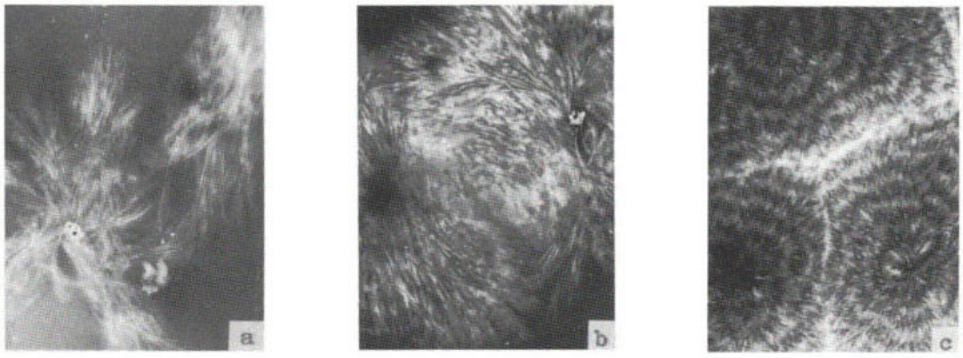

Fig. 7. The spherulite growth of PB-2-1 (M_η =6.9x10^5) crystallized at -20 C.
(a) 20 min, 10000x; (b) 40 min, 10000x; (c) 90 min, 1500x.

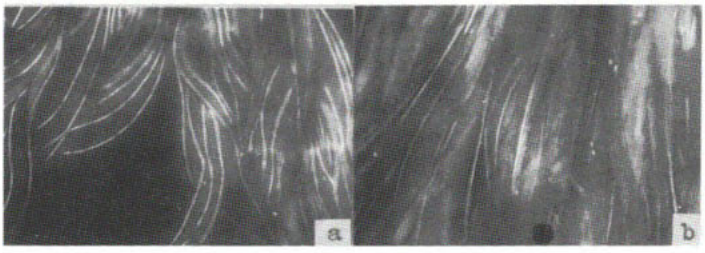

Fig. 8. The lamellar structure of PB-2-1 (M_η =6.9x10^5).
(a) at -20°C, 20 min, 10000x;
(b) at -15 C, 150 min, 50000x.

EBSCOhost - printed on 2/13/2023 3:45 AM via . All use subject to https://www.ebsco.com/terms-of-use

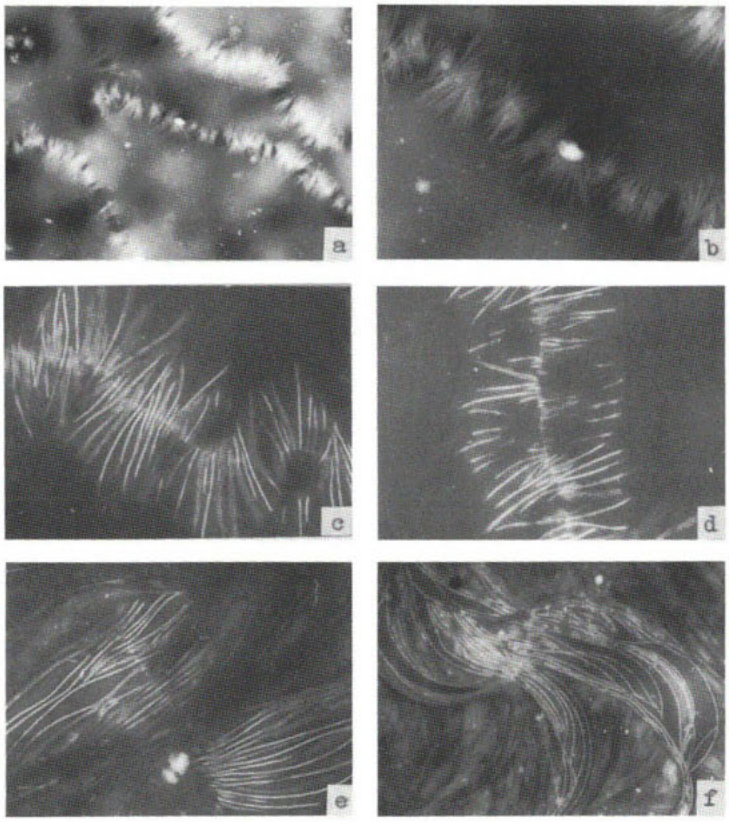

Fig. 9. "Shish kebab" structure of PB formed at different temperatures.

(a) at -30°C, 8000x; (b) at -30°C, 24000x;
(c) at -20°C, 30000x; (d) at -20°C, 30000x;
(e) at -15°C, 40000x; (f) at -15°C, 20000x.

Classical spherulite with fibers of helical arrangement in radial direction could be obtained by crystallization at -30°C. However for spherulites crystallized at -20°C and -15°C the fibers are thicker being formed from cylindrical fibrils, as shown in Fig. 8.

4. "Shish kebab" morphologies of PB

It is interesting to point out that "Shish kebab" structure may

EBSCOhost - printed on 2/13/2023 3:45 AM via . All use subject to https://www.ebsco.com/terms-of-use

be obtained by crystallization at different temperatures and, at the same time, applying small strain to the film specimens, as shown in Fig. 9. It looks like that the lamellae are strung together with a "Thread". We consider that the "Thread" acts as a nucleus, on which the lamellae grow. Sharing a common thread-like nucleus, the lamellae could grow only in the direction perpendicular to the "Thread" and line up in a row, thus forming the "Shish kebab" structure.

Acknoledgement

The authors wish to express thanks to Prof. Zhiliu Feng for her discussion and help in the preparation of this manuscript.

References

1. Zhou Enle, Bailing Xu. 1982. Polymer Communications (China). 3, 178.
2. Bukhina, M.F. 1973. Kristallizatsiya kauchukov i rezin. Izdatelstvo Khimiya, Moscow.
3. Qian Baogong et al., 1982. Scientia Sinica. B, 5, 297.
4. B. Wunderlich. 1973. "Macromolecular Physics". Vol. 1. Academic press, New York.
5. Xu Yang et al., 1984. Chinese Jornal of Applied Chemistry 1, 4, 51.

EBSCOhost - printed on 2/13/2023 3:45 AM via . All use subject to https://www.ebsco.com/terms-of-use

MORPHOLOGICAL STUDY OF THE MELTING OF POLYCAPROLACTONE/POLY (STYRENE-CO-ACRYLONITRILE) BLENDS USING SYNCHROTRON RADIATION

M. Vandermarliere, G. Groeninckx, H. Reynaers
Laboratory of Macromolecular Structure Chemistry, University of Leuven, Belgium

C. Riekel
Institut für Technische und Makromolekulare Chemie, Universität Hamburg, F.R.G.

M.H.J. Koch
EMBL Outstation Hamburg, F.R.G.

Introduction

Blends of poly-ε-caprolactone (PCL) with poly(styrene-co-acrylonitrile (SAN, 28 wt.% AN) are miscible throughout the whole composition range (1,2). In these blends PCL is able to crystallize under well defined conditions of temperature and composition; the question of miscibility is concerned with the remaining amorphous phase.
The semi-crystalline morphology of PCL/SAN blends was studied by time-resolved small-angle (SAXS) and wide-angle(WAXS) X-ray scattering using synchrotron radiation, under the same conditions as the melting behaviour monitored by differential scanning calorimetry (DSC).

Materials

Polycaprolactone flakes (T_g= -52°C, T_m° = 64°C, $\bar{M}_w$ = 30,500 and $\bar{M}_n$ = 17,000) were mixed with SAN pellets (T_g = 120°C, $\bar{M}_w$ = 158,000, $\bar{M}_n$ = 65,000 and acrylonitrile content : 28 wt.%) in the following compositions by weight : 80/20, 60/40, 50/50 and 40/60.
The blends were prepared by melt mixing in a Brabender Plasticor-

Morphology of Polymers
© 1986 Walter de Gruyter & Co., Berlin · New York - Printed in Germany.

EBSCOhost - printed on 2/13/2023 3:45 AM via . All use subject to https://www.ebsco.com/terms-of-use

der : 55 g of the dried materials were mixed at ±220°C for 10 min at 100 rpm.

Experimental Technique

Time-resolved scattering experiments were performed using the X-13 camera of the European Molecular Biology Laboratory (EMBL) Outstation at the storage ring DORIS of the Deutsches Elektronen Synchrotron in Hamburg, F.R.G. Changing from wide-angle to small-angle experiments was done by increasing the distance between the sample in the oven and the one-dimensional position sensitive detector. The melting behaviour was investigated using a Perkin-Elmer differential scanning calorimeter DSC-2C.

Results and Discussion

In the DSC scans of the PCL/SAN blends dynamically crystallized from the melt two melting endotherms have been observed (Fig. 2). What causes this phenomenon is not yet known but the classical reorganization processes such as partial melting and recrystallization or solid state transformations can be ruled out. If this was the case, an increase in the heating rate would lead to a decrease of the area of the higher temperature peak and an increase of the area of the lower one, since only a smaller fraction of the material can reorganize. For the given PCL/SAN blends, the ratio of the areas of the two endotherms remains constant, although they overlap more, when the heating rate is increased.
When the PCL content is increased, the maximum of the first peak remains constant at 53°C while the second peak is shifted to higher temperatures. At the same time the area of the first peak decreases and that of the second one increases.

As shown in Figures 1 and 2, the area under the principal WAXS peak at room temperature is proportional to the total area under the melting endotherms and can thus be regarded as a rough probe of the degree of crystallinity of the blend. The WAXS intensity decreases when the crystalline PCL starts melting and vanishes at the end of the DSC melting trace.

EBSCOhost - printed on 2/13/2023 3:45 AM via . All use subject to https://www.ebsco.com/terms-of-use

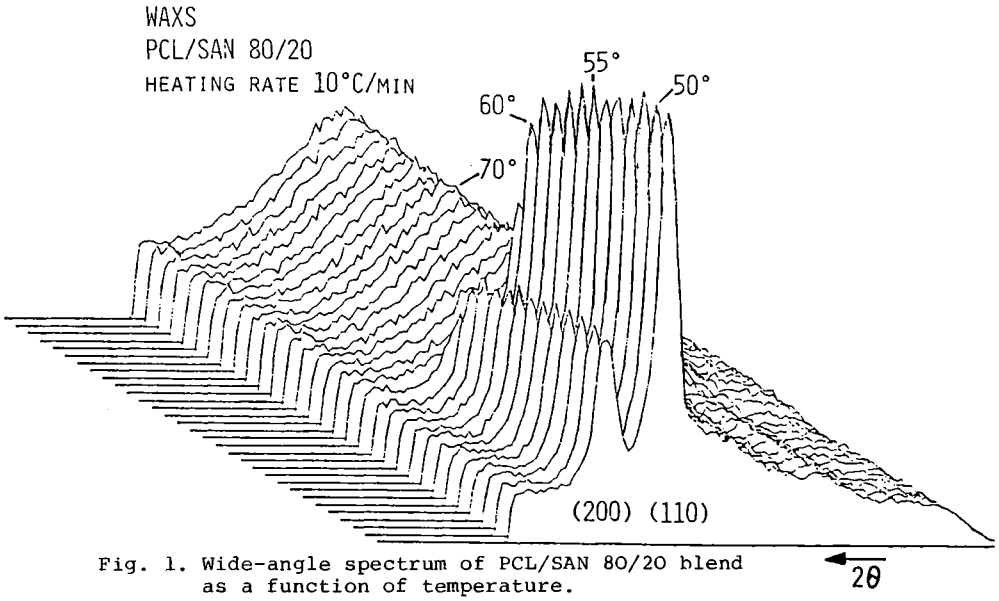

Fig. 1. Wide-angle spectrum of PCL/SAN 80/20 blend as a function of temperature.

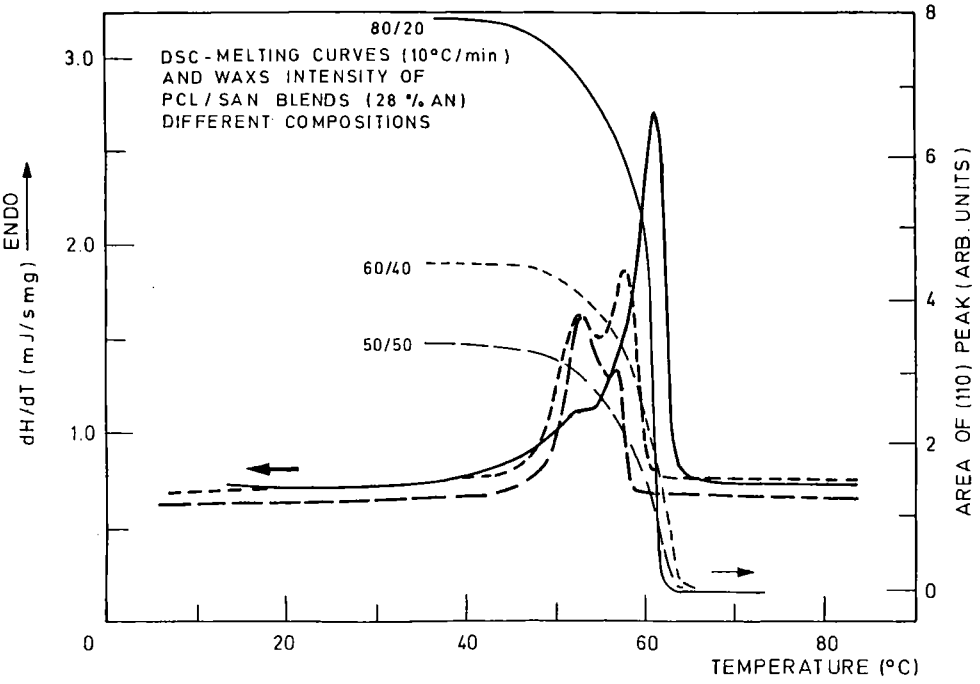

Fig. 2. DSC scans and WAXS intensities of PCL/SAN blends as a function of temperature.

EBSCOhost - printed on 2/13/2023 3:45 AM via . All use subject to https://www.ebsco.com/terms-of-use

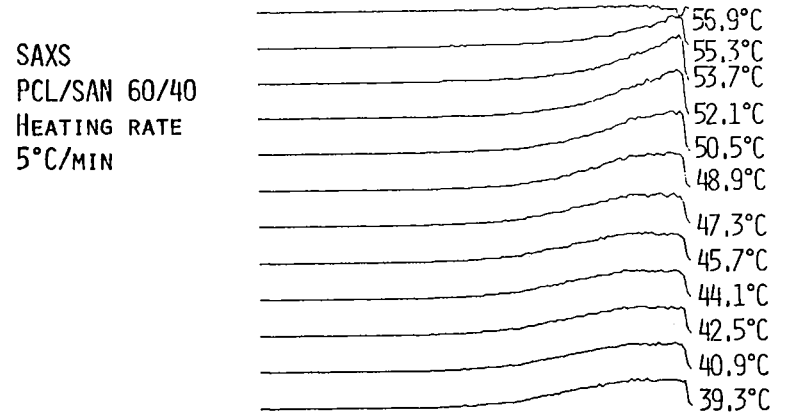

Fig. 3. Small-angle spectrum of PCL/SAN 60/40 blend as a function of temperature.

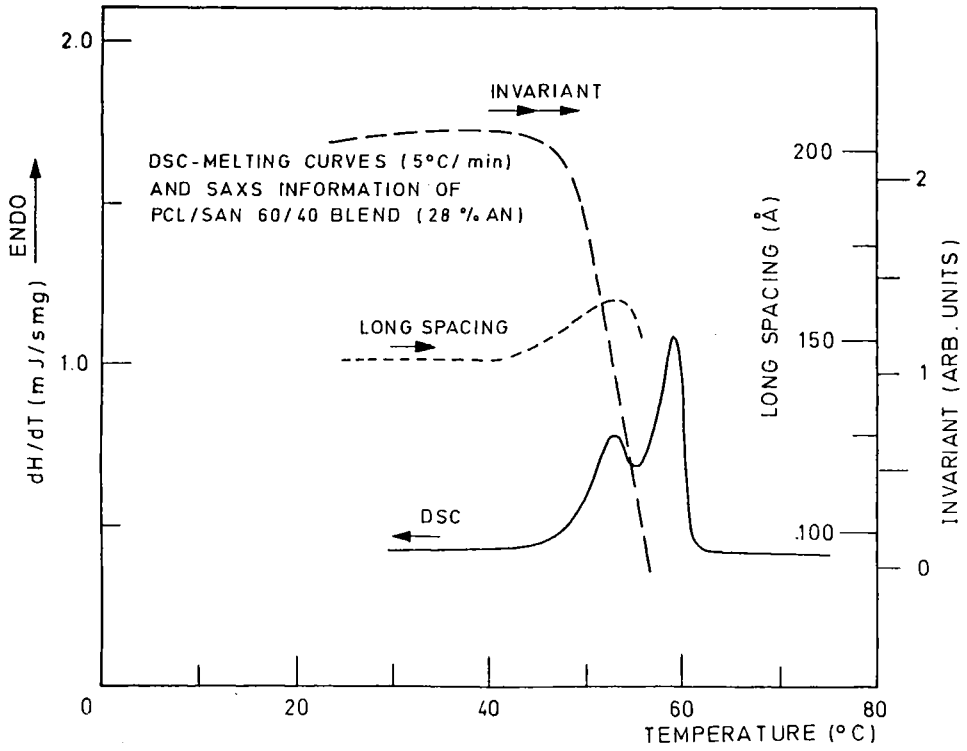

Fig. 4. DSC scan and small-angle data of PCL/SAN 60/40 blend as a function of temperature.

EBSCOhost - printed on 2/13/2023 3:45 AM via . All use subject to https://www.ebsco.com/terms-of-use

As far as the long spacing is concerned (Figures 3 and 4), an increase is apparent as soon as the first melting is observed in the DSC. This is accompanied by a sharpening of the SAXS diffraction peak, indicating the melting of the smaller crystals within the lamellar structure.

The SAXS invariant or scattering power Q is proportional to the averaged squared electron density difference $\langle \eta^2 \rangle$ and reflects the degree of crystallinity since for a semi-crystalline two-phase system :

$$Q = K\langle \eta^2 \rangle = K \, \phi_c (1 - \phi_c) \, (\rho_c - \rho_a)^2$$

where ϕ_c represents the volume fraction of the crystalline phase, $\rho_c - \rho_a$ the electron density difference between the crystalline and amorphous phases and K is a constant depending on the geometry of the scattering instrument.

For the blends the invariant increases slightly with temperature (see Fig. 4) as one may expect from the difference in expansivities of the crystalline PCL phase and the miscible amorphous phase of PCL and SAN. The decrease in scattering power coincides with the first endothermic peak. The height of the SAXS peak varies in the same way as the invariant.

The SAXS observations at the beginning of the melting, viz. the gradual increase in long spacing, the narrowing of the scattering maximum and the change in the invariant, all indicate that the initially broad distribution of lamellar thicknesses is effectively sharpened by the melting out of the smaller crystals.

After the disappearance of the small-angle information, there are still traces of persisting crystalline order at the molecular level as observed by WAXS.

From the study of the melting behaviour of these blends by the combined observations of DSC traces and time-resolved small-angle and wide-angle X-ray scattering profiles, it can be concluded that the three techniques, within the limits of the actual performance of the scattering equipment at the synchrotron, are in good agreement as to the temperature at which melting starts. Furthermore, the superstructural order as revealed by SAXS disappears before the maximum of the second melting endotherm is reached, but

EBSCOhost - printed on 2/13/2023 3:45 AM via . All use subject to https://www.ebsco.com/terms-of-use

crystallinity in the form of unstacked crystals is still present as shown by the WAXS intensity.

Moreover, this study clearly demonstrates the potential of this new experimental approach for the examination of the complex phase transition behaviour inherent to many polymeric systems.

Acknowledgements

M. Vandermarliere thanks the Phillips Petroleum Chemicals Company for the research fellowship. Financial support of the Belgian Science Foundation (NFWO) is also gratefully acknowledged.

References

1. Groeninckx, G., M. Vandermarliere. 1984. In : Polymer Alloys : Structure and Properties. Proceedings of the 16th Europhysics Conference on Macromolecular Physics, Brugge, Belgium, June 1984. p. 70.

2. Vandermarliere, M., G. Groeninckx. 1984. In : IUPAC Polymer Chemistry Meeting, Leuven, Belgium, September 1984. p. 94.

3. Vandermarliere, M., C. Riekel, M. Koch, G. Groeninckx, H. Reynaers. 1985. In : Rolduc Polymer Meeting, April 1985. In press.

EBSCOhost - printed on 2/13/2023 3:45 AM via . All use subject to https://www.ebsco.com/terms-of-use

SYNTHESIS, MORPHOLOGY AND PROPERTIES OF RUBBER MODIFIED POLY(ε-CAPROLACTAM) BY FAST IN SITU-POLYMERIZATION

G.C.Alfonso, G. Dondero, S.Russo, A.Turturro

Centro Studi Chimico-Fisici di Macromolecole Sintetiche e Naturali, C.N.R., C.so Europa, 30, 16132 Genoa, Italy

Introduction

In the last years, we have suggested the activated anionic polymerization of ε-caprolactam, CL, in presence of various additives (inorganic salts, red phosphorous, elastomers, etc.) as a method to prepare directly poly(ε-caprolactam), PCL, with some modified and/or improved physical properties (1,2,3,4,5).
At present, special activity is addressed to improve impact resistance of PCL at low temperatures by using melt blending technique to prepare mixtures of PCL with a suitable elastomeric component. We are studying in detail the fast "in-situ" polymerization of CL in presence of rubber or elastoplastic copolymers because this process may be very interesting for the reaction injection molding (RIM) technology. In this communication, we report some results concerning synthesis, morphology and properties of nitrile rubber modified PCL.

Experimental

Butadiene-acrylonitrile rubbers and ε-caprolactam used were supplied by Enichem Elastomers.
Three copolymers of Europrene family with different acrylonitrile, AN, content and average molecular mass were taken into consideration (Table 1).

Morphology of Polymers
© 1986 Walter de Gruyter & Co., Berlin · New York - Printed in Germany.

EBSCOhost - printed on 2/13/2023 3:45 AM via . All use subject to https://www.ebsco.com/terms-of-use

Table 1. Some Chemical and Physical Characteristics of Butadiene-Acrylonitrile Copolymers

Sample	AN,% by w.	$\bar{M}_v \times 10^{-4}$	T_{g_1},°C	T_{g_2},°C
E 3325	33	10.7	-29	-20
E 3345	33	14.4	-27	-20
E 3945	39	14.0	--	-16

The activated anionic polymerization of ε-caprolactam was performed in bulk under adiabatic conditions. Sodium-caprolactamate and N-acetyl-ε-caprolactam were used as initiator and activator, respectively, of polymerization; the concentrations of both catalytic species were 0.6 mol %.

Nitrile rubber, up to 10% by weight, was dissolved in CL at the initial polymerization temperature of about 150°C under dry nitrogen and controlled stirring conditions, in order to assure good mixing between the media containing the active species.

A more detailed description of the experimental procedure was reported elsewhere (1).

Polymerization rate was followed by recording the temperature increase of reaction medium; the time of the end of polymerization, t_p, was assumed to be that corresponding to the maximun rise in temperature.

High-polymer yield, A , was determined by extraction of monomer and oligomers with boiling water in a jacketed soxhlet apparatus for 48 h.

The rubber component, extracted with acetone from blends after polymerization, was analyzed by IR spectroscopy (IR Perkin-Elmer mod. 680).

Thermal behaviour of mixtures was determined with a DSC 2 calorimeter (Perkin-Elmer DSC); heating and cooling rates of 20 and 10K/min

EBSCOhost - printed on 2/13/2023 3:45 AM via . All use subject to https://www.ebsco.com/terms-of-use

respectively, were used.

Morphological observations were performed by scanning electron microscopy (SEM - Cambridge Stereoscan 250 MK2) on cold fractured surfaces coated with Au.

In order to better elucidate the complex morphology of blends, fracture surfaces were etched with acetone (solvent of rubber) or hexafluorobutanol (solvent of polyamide), before examination by SEM.

Results and Discussion

In Table 2 are reported results concerning some synthesis conditions, polymerization kinetics and high-polymer yields.

Table 2. Data of Synthesis Conditions, Polymerization Kinetics and High-Polymer Yields

Sample	Stirring Time s	t_p, min	Λ , %
PCL/E 3345			
95/5	10	12	87.9
90/10	10	35	89.9
95/5	240	8	94.2
PCL/E 3945			
95/5	10	8.5	91.0
90/10	10	21.0	91.3
PCL/E 3325			
95/5	60	16.5	89.9
90/10	300	18.5	91.3

EBSCOhost - printed on 2/13/2023 3:45 AM via . All use subject to https://www.ebsco.com/terms-of-use

Polymerization rate is affected by several parameters: t_p increases with increasing rubber content, but decreases when AN amount goes from 33 up to 39% by weight in the rubber copolymer.
Also, the high polymer yield is enhanced when rubbers with higher AN content or longer stirring time are used.
Generally, monomer conversion and polymerization rates are to some extend reduced with respect to PCL formation from the neat monomer. But, with proper choice of both initiator and activator type and concentration, as well as of rubber molecular mass and AN content, conversion yields higher than 95% can be obtained in rather short polymerization times. Potential applications of the above process to the reaction injection molding technology can be envisaged.
By selective extraction we have deduced that the polymerization reaction in presence of the uncrosslinked elastomer gives a product constituted of PCL homopolymer, nitrile rubber and a third component insoluble in acetone or hexafluorobutanol.
IR and calorimetric data support its identification as crosslinked nitrile rubber, formed "in-situ" by anionic crosslinking mechanism.
DSC analysis shows also that both glass transition and melting temperatures of the PCL are largely unaffected by the presence of the rubber up to 25% by weight; T_g of the elastomer is slightly increased, due to the crosslinking effect.
All these results indicate a phase separation between the two components.
In Fig. 1 (a,b) blends morphologies of PCL/E 3325 and PCL/E 3945 95/5 are shown. They reveal the presence of composite particles from 20 to 100 μm in diameter, each containing numerous sub-inclusions; particle average diameter increases up to 200-300 μm when rubber amount reaches 10% by weight in blend. The structures formed are similar to those observed in other systems, such as styrenated polyester resins containing poly(vinyl acetate) (6).
By changing synthesis conditions, such as reducing the stirring time, PCL matrix disappears, as we can see in Fig. 2 for the PCL/E3345

EBSCOhost - printed on 2/13/2023 3:45 AM via . All use subject to https://www.ebsco.com/terms-of-use

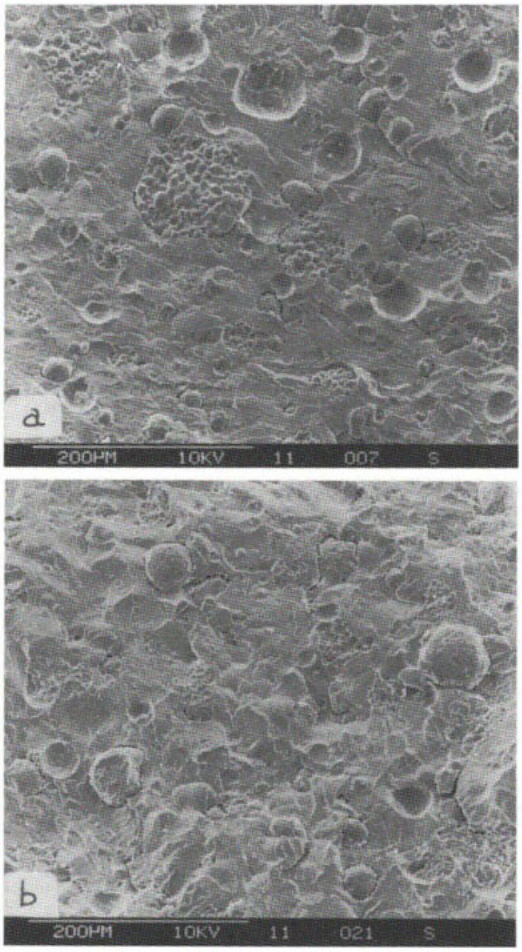

Fig. 1. SEM of fracture surfaces of PCL/nitrile rubbers 95/5 blends. (a) PCL/E 3325; (b) PCL/E 3945.

95/5 sample: we obtain a structure built up of small domains of PCL similar to the aforementioned sub-inclusions, embedded in rubbery matrix.

Deeper insight into the morphologies reported in Fig. 1 (a,b) has

EBSCOhost - printed on 2/13/2023 3:45 AM via . All use subject to https://www.ebsco.com/terms-of-use

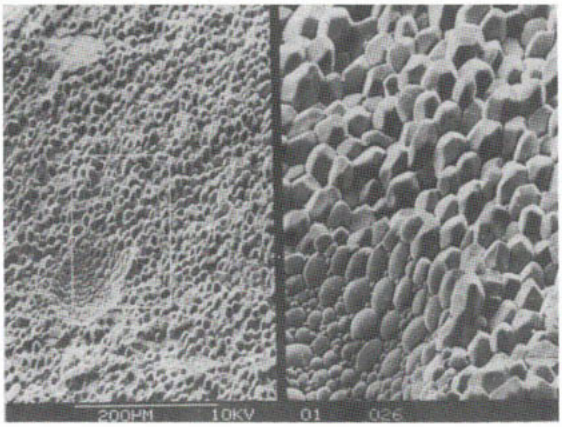

Fig. 2. - SEM of fracture surface of PCL/E 3345 95/5 blend prepared with short time of stirring.

been achieved by etching techniques, namely with acetone (Fig.3 a) and subsequent extensive etching with hexafluorobutanol (Fig.3 b). Both figures refer to the same blend, PCL/E 3325 95/5, and reveal that a fraction of the rubber is crosslinked, the rest fraction being soluble and removable.

Morphologies shown in Figures 1 and 3 are two peculiar examples which can be obtained by "in-situ" polymerization of CL in presence of a typical nitrile rubber: the first one improves impact resistance of polyamide and the second corresponds to a material with very poor mechanical properties.

To sum up, butadiene-acrylonitrile rubbers can easily be dissolved in ε-caprolactam monomer at temperatures around 150°C. Even in presence of relatively large amounts of rubber, fast polymerization of

EBSCOhost - printed on 2/13/2023 3:45 AM via . All use subject to https://www.ebsco.com/terms-of-use

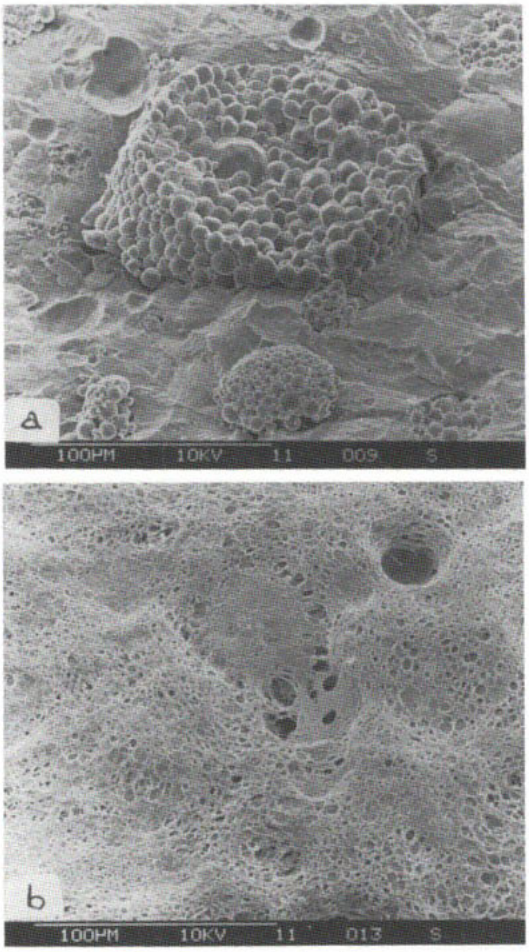

Fig. 3. SEM of fracture surface of PCL/E 3325 95/5 blend. (a) Etched with acetone; (b) after subsequent etching with hexafluorobutanol.

caprolactam by activated anionic mechanism can be achieved and high conversion yields obtained.

With proper choice of both initiator and activator types and con-

EBSCOhost - printed on 2/13/2023 3:45 AM via . All use subject to https://www.ebsco.com/terms-of-use

centration, as well as of stirring time, very peculiar morphologies can be obtained, which characterize materials with good or very poor mechanical properties.

Acknowledgement

This research was sponsored by Progetto Finalizzato Chimica Fine e Secondaria - Sottoprogetto Materiali Polimerici - C.N.R. (Italy).

References

1. Alfonso, G.C., G.Bontà, S.Russo, A.Traverso. 1981. Makromol.Chem. 182, 929.

2. Alfonso, G.C., E.Pedemonte, S.Russo, A.Turturro. 1981. Makromol. Chem. 182, 3519.

3. Alfonso, G.C., G.Cirillo, S.Russo, A.Turturro. 1983. Eur.Polym. J. 19, 949.

4. C.N.R., It.Pat. 21912A/83; Eur.Pat. 84106053.6.

5. C.N.R., It.Pat. 21950A/83; Eur.Pat. 84105456.2.

6. Bucknall, C.B., P.Davies, I.K. Partridge. 1985.Polymer 26, 109.

EBSCOhost - printed on 2/13/2023 3:45 AM via . All use subject to https://www.ebsco.com/terms-of-use

MORPHOLOGY AND PHASE TRANSITIONS OF CRYSTALLINE POLYPHOSPHAZENES

M. Kojima
Chisso Corporation, 2-7-3, Marunouchi, Chiyoda-ku, Tokyo, Japan

J. H. Magill*
Max-Planck-Institut für Polymerforschung, Universität Mainz, 6500 Mainz, F.R.G.

Summary

Solution-grown crystals of poly[bis(trifluoroethoxy)phosphazene]-(PBFP) and poly[bis(phenoxy)phosphazene]-(PBPP) were prepared from dilute solution. Plate-like PBFP crystals are grown and three polymorphic forms and one mesoform are found depending upon the crystallization conditions. When PBFP crystals are heated through the thermotropic T(1) transition a structural transition occurs. This transformation involves the formation of a chain extended morphology from a chain folded one, and it is irreversible after cooling from above T(1). PBPP crystals are also transformed from monoclinic to orthorhombic by heating through T(1). Thus phase transformations are common in crystalline thermotropic polyphosphazenes even though they have not been recognized until recently.

Spherulite formation and fracture surface morphology in PBFP have been investigated from the melt and from solution over a relatively wide crystallization and annealing range. The fracture surface of spherulitic PBFP films was studied too. Spherulitic aggregates consisting of a cospherical platelet morphology appear not to alter upon heating up through T(1) even though the discrete long period disappears above T(1). This cospherical morphology of PBFP may be related to that encountered in PPT (Kevler).

* Permanent address : Metallurgical and Materials Engineering Department, School of Engineering, University of Pittsburgh, Pittsburgh, PA 15261 USA

Morphology of Polymers
© 1986 Walter de Gruyter & Co., Berlin · New York - Printed in Germany.

EBSCOhost - printed on 2/13/2023 3:45 AM via . All use subject to https://www.ebsco.com/terms-of-use

Introduction

Linear polyphosphazenes are a generic class of interesting polymers that have undergone considerable growth and development over the past two decades. Despite the early discovery (1) of poly(dichlorophosphazene) more than 80 years ago, significant progress in producing linear, hydrolytically stable high-molecular weight macromolecules (2) did not occur until the mid 1960's. Linear homopolymers (3,4) with alkyl, aryl, amide groups attached to the phosphorus backbone via oxygen have been made and co-

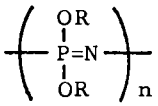

polymers (5) with more than one kind of substituent are also known. Recently substituents have been connected directly to the phosphorus (6). Characterization has included molecular (7), thermodynamic (8,9), thermolysis (10,11), flammability (12), toxicological (13,14), biomedical (15-17), conformational (7,18) and x-ray structure analysis (19,20), solid state and engineering property assesment (21,22) as well as radiochemical (23) and morphology-property (24,25) investigations. Even so, much remains to be learned about these new macromolecules which are devoid of carbon in the backbone. Their chain flexibility (7) has been demonstrated and it compares favorably with that noted in polysiloxanes (27). Variations in the side group chemistry enables them to span a wide range of temperature with glass temperature approaching -100°C and melting points (26, 28) well in excess of 300°C in some systems. In this and other respects they have brought a new dimension to the study and uses of macromolecules. The additional bonus derived from their thermotropic or liquid crystal forming ability introduces another element to their thermotropic nature which may lead to exploitation in many fabrication processes (29) (fiber spinning and extrusion and so on). The present paper is devoted to acquiring a better understanding of the morphology-property characteristics of a few selected polyphosphazenes that have potential commercially.

Although much of the research is concerned with unfractionated materials, some basic principles have been established and complications associated with polymorphism have been recognized (30). The effect of enviromental conditions on the general behavior of these polyphosphazenes has been established. So that other progress will follow particularly in regard to their

EBSCOhost - printed on 2/13/2023 3:45 AM via . All use subject to https://www.ebsco.com/terms-of-use

thermotropic nature and future expectations as potentially useful polymers. Some of these points have been mentioned recently in recent reviews of the polyphosphazenes (31,32).

Experimental

Materials. Poly[bis(trifluoroethoxy)phosphazene], PBFP, and poly[bis-(phenoxy)phosphazene], PBPP, mostly broad molecular weight distributions ($M_w/M_n \geq 10$) have been used in this investgation.
Films. Both thin (100 nm) and relatively thick (5-50 μm) films have been cast from solutions of >0.1 % w/w and several % w/w respectively.
Solution grown crystals. These were prepared from dilute solution typically about <0.03 % w/w. PBFP crystals were made by dissolving the polymer in THF or ethyl acetate solvents. Xylene was used for PBPP.
Electron microscopy. Bright field and electron diffraction investigation were made at 120 kV using a JEOL JEM-100 U and a 100 kV JEM-100 CX microscope. Specimens were often metal shadowed to enhance imaging.
Scanning electron microscopy. Specimens were coated with Pd/Au alloy and examined in a JEOL JSM-T200 microscope at 15 kV.
Optical microscopy. Crystallized polymer films were examined with a Leitz Ortholux research microscope fitted with a 35 mm Leitz camera.

Results and Discussion

Solution grown crystals. Several polymorphic forms and mesophase have been found for PBFP and PBPP homopolymers depending upon the molecular mass, solvent and fabrication conditions. The transformation to the thermotropic state occurs at about 70°C and 130°C respectively. The phase change has been investigated by DSC (8,33,34), dilatometry (24), birefringence (33,34), creep (24) and other methods (22,32). However it is very nicely detected by electron microscopy (26,30) or with x-ray diffraction (8,25). Figure 1 (a) shows the morphology of the monoclinic α-form of PBPP initially cast from xylene (0.015 % w/w) and its corresponding electron diffraction pattern is shown in Fig. 1 (a) (insert). After heating and annealing the crystals on the electron microscope grid at 150°C (2h.) a new modification (γ-orthorhombic) is found at room temperature. The new morphology is seen in Fig. 1 (b) and the diffraction pattern is shown in Fig. 1 (b)

EBSCOhost - printed on 2/13/2023 3:45 AM via . All use subject to https://www.ebsco.com/terms-of-use

(insert). Note that the crystals have thickened after being heated up to the thermotropic transition T(1) and held here.
PBFP crystals exhibit similar behavior (26) upon heating and annealing the well developed monoclinic form obtained from THF solution.

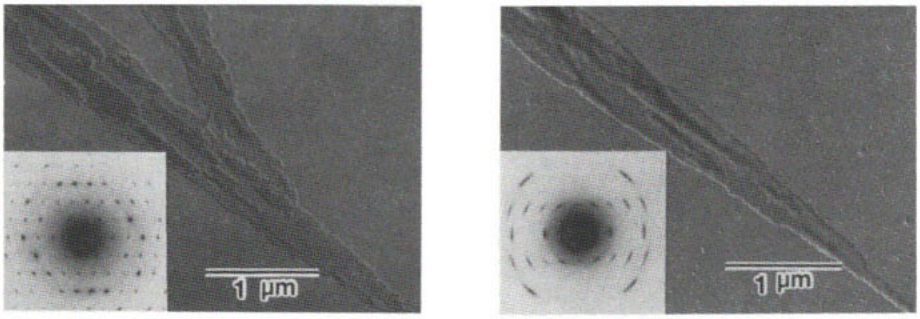

(a) (b)

Fig. 1. (a) Electron micrograph of monoclinic (α-form) PBPP prepared from 0.015 % w/w in xylene and its electron diffraction pattern at 120 kV (insert).
Monoclinic PBPP crystals after heating in nitrogen at 150°C (2 h) transforms into a new γ-orthorhombic modification. (b) Electron micrograph of orthorhombic (γ-form) PBPP and its electron diffraction pattern (insert).

The mesophase structure for both polyphosphazenes is believed to be hexagonal (nematic) having 2D order. The actual phase transformation from the chain-folded solution cast PBFP morphology has been followed in the electron microscope as the specimen undergoes heating and crosslinking during irradiation (see Fig.8, ref.25). The trend is clearly seen in Fig.2 for PBPP. These features are intriguing and point to the complexity of PBFP which forms three polymorphs and one mesophase. The sequence of events during the transformation are illustrated in Fig.2 (a) through (d) for PBPP solution

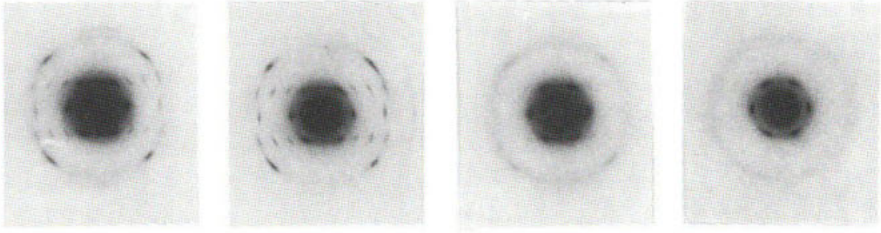

(a) (b) (c) (d)

Fig. 2. Changes in the electron diffraction pattern of PBPP single crystals (a) through (d) recorded at 100 kV under minimum available dosis conditions in our instrument at about 20 s intervals. The crystal was originally annealed at 150°C for 2 h.

EBSCOhost - printed on 2/13/2023 3:45 AM via . All use subject to https://www.ebsco.com/terms-of-use

grown crystals annealed at 150°C for 2 h. Under electron bombardment at 100 kW and low beam intensity, the changes noted for PBPP mimic those found for PBFP (25). Naturally, beam damage is also taking place during bombardment but this is less for PBPP than PBFP (36).

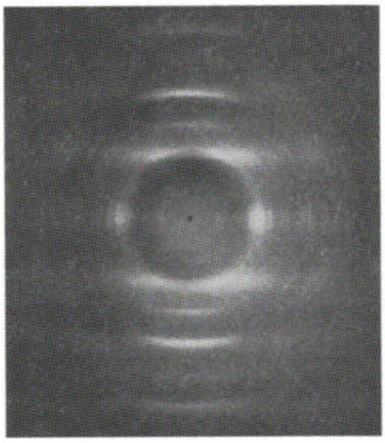

Fig. 3. Electron diffraction pattern of PBPP film. PBPP film was cast from cyclohexanone on water at 30°C, stretched at room temperature and annealed at 160°C (15 min) before cooling to room temperature.

Whenever PBPP is cast directly from solution in water at 30°C and highly drawn before annealing at 160°C (15 min), a very well developed electron diffraction pattern is obtained (see Fig. 3). Here the first layer line is either absent or simply obscured. Interestingly c is estimated as 9.70 Å for PBPP which differs from the value c=4.91 Å reported by Stroh (34). Anyhow, it seems that the transformation from a chain-folded to a chain-extended morphology can only occur after the specimens have passed into the thermotropic state, and it is independent of the route taken.

The temperature interval T(1) to Tm appears to be a pathway to the chain-extended morphology without the use of high pressure.

Twinned crystals. Besides well developed solution grown crystals of more than one kind of PBFP also exhibits well developed twinning when grown as thin films cast from THF (0.1 % w/w), fused at 250°C (5 min), isothermally crystallized at 70°C (60 min) and finally cooled to room temperature. A typical bright field micrograph is shown in Fig. 4 (a). The electron diffraction pattern is identified as the γ-form. Figure 4 (c) is a reciprocal net which corresponds the the diffraction pattern shown in Fig. 4 (b). Other crystalline habits of PBFP have already been reported and indexed (25,36).

EBSCOhost - printed on 2/13/2023 3:45 AM via . All use subject to https://www.ebsco.com/terms-of-use

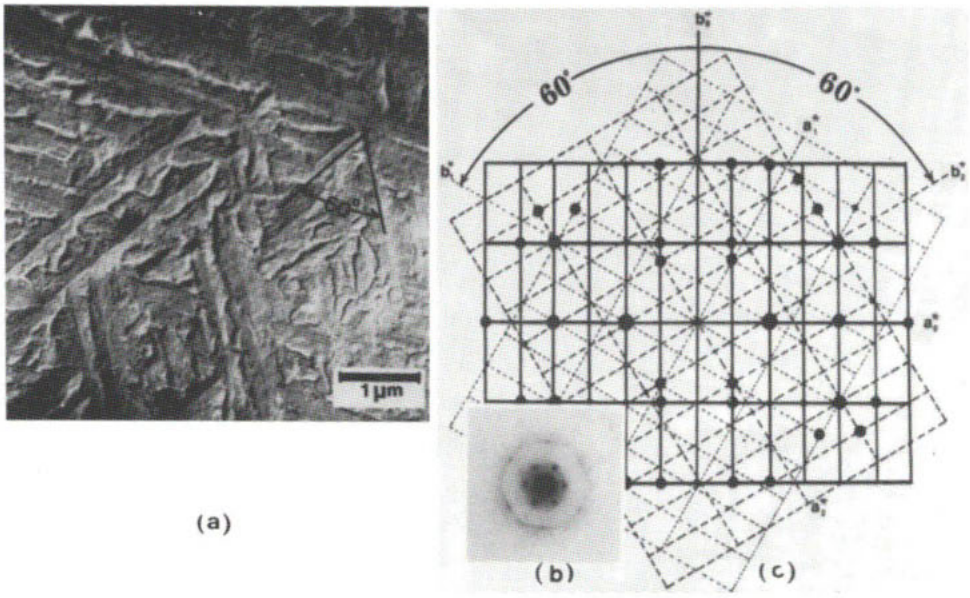

Fig.4. (a) Electron micrograph of PBFP crystals (γ-form) prepared from THF solution followed by fusion at 250°C (5 min), isothemal crystallization at 70°C (60 min) and cooling to room temperature for inspection.
(b) Electron diffraction pattern of (a).
(c) Reciprocal net of (b) showing the a*b* 60° relationship in these twinned crystals in line with 4 (a).

Spherulitic morphology. The spherulite texture of PBFP and PBPP is fibrillar. The sperulitic texture of PBPP is nicely illustrated using scanning electron microscopy in Fig. 5 (a). At higher magnifications using surface replication with poly(acrylic acid) clearly shows that intertwining fibrils merge and overlap in peripheral regions [Fig. 5 (b)].

One can therefore conclude that the spherulitic morphology of PBFP and PBPP are related morphologically when crystallization occurs from THF solution. From the melt, textures are much more numerous and complicated and depend strongly upon the preparation conditions which are not easy to control not far below Tm. Spherulites, aggregates, needlelike crystals and low birefringent structures and other dendritic shapes occur which are associated with rapid transformations and thermotropic phases already cited in the literature (38,39,40).

EBSCOhost - printed on 2/13/2023 3:45 AM via . All use subject to https://www.ebsco.com/terms-of-use

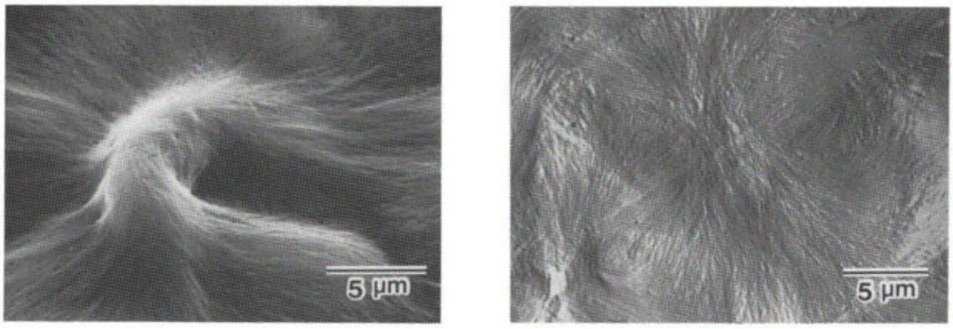

(a) (b)

Fig. 5. (a) Scanning electron micrograph of PBPP spherulite cast from THF solution in the form of a film.
(b) Fibrillar texture of PBPP spherulites cast from THF as a film and then replicated with polyacrylic acid/water.

Fracture surface morphology. PBFP specimens crystallized from THF solution exhibit a spherulitic morphology which can be accentuated by ion-etching which reveals a cospherical morphology [Fig. 6 (a)] with the [c] axis direction perpendicular to the spherulite radius. After heating specimens through T(1) and holding them at 150°C (1 h), they appear unchanged at the SEM magnification seen in Fig. 6 (b). However, the polyphosphazene does become embrittled (but not degraded). Other x-ray and electron diffraction evidence (39) indicate that the crystallinity and crystallite size increases

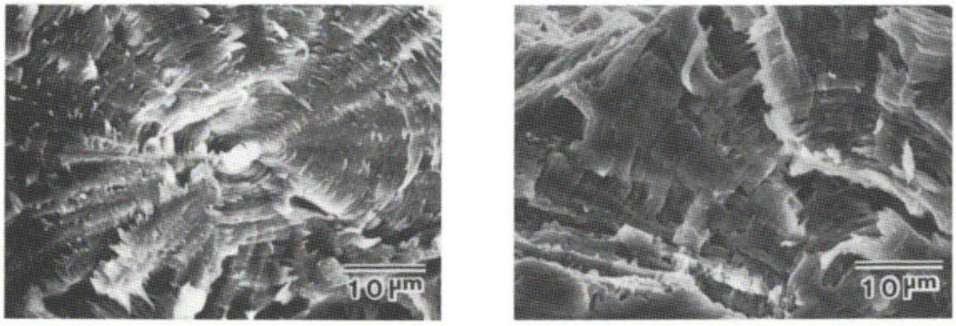

(a) (b)

Fig. 6. (a) Scanning electron micrograph of a fracture surface of PBFP spherulitic film prepared from THF solution (several % w/w) at room temperature.
(b) Fracture surface of film similar to 6 (a) that has been annealed at 150°C (1 h) and cooled to room temperature and fractured.

EBSCOhost - printed on 2/13/2023 3:45 AM via . All use subject to https://www.ebsco.com/terms-of-use

Fig. 7. Surface morphology of PBFP obtained from the melt at 250°C (5 min) followed by crystallization at 70°C (28.5 h).

substantially after heating above T(1). Whenever PBFP polymer is melted (>Tm = 245°C) a crystalline aggregate-like morphology evolves (Fig. 7). These aggregates nucleate and tend to grow spherically whenever possible. The specimens are also brittle or friable and have high crystallinity.

Liquid crystal forming ability. Compared to low molecular weight liquid crystals (L.C.), in polymeric materials, because of their relatively high viscosity morphological and other transformations tend to be more sluggish. Consequently macromolecular polydispersity, chain complexity and melt viscosity are anticipated in many cases to retard or attenuated their L.C. forming capacity. However chain flexibility of the kind experienced in polyphosphazenes and polysiloxanes must off-set these process to some degree in these thermotropic systems. Certainly, the fact that PBFP has not been quenched to the glassy state (25) attests to its molecular flexibility. A glass temperaure Tg of -66°C and a Mark-Houwink-Sakurada exponent of 0.6 approximately in dilute solution supports this claim even though L.C. forming ability is normally associated with chain stiffness (41).
Of course, PBPP with a Tg ≃ 6°C and less flexible side groups tends to be "stiffer" and perhaps not as likely to exhibit polymorphism (even though two crystalline forms are reported in this paper). Perhaps most polyphosphazenes with oxy substituents (unless very large like naphthoxy) will exhibit more than one crystal form (in addition to an L.C. phase).
For this reason accurate x-ray structure analysis will prove difficult unless the conditions necessary for the isolation of a single phase for structure determination is established.
Nevertheless, the thermotropic phase(s) in polyphosphazenes are interesting and merit closer study. Indeed, it seems that the L.C. "structure"

EBSCOhost - printed on 2/13/2023 3:45 AM via . All use subject to https://www.ebsco.com/terms-of-use

requires closer inspection at these elevated temperatures between T(1) and Tm since cooling down the specimen for inspection at room temperature gives rise to yet another morphology (25). Hot stage electron microscopy will be used for this purpose using their films and polyphosphazene crystals.

The mesophase in PBPP and PBFP provides a pathway to chain extended 3D polymer crystals of higher stability than their solution cast analogue. Superficially, the morphology of the hexagonal structure in polyethylene which provides an anabaric route to extended chain orthorhombic crystals, bears a close resemblance in function, entropy and texture* to the anathermic mesophase (identified in PBFP as δ -hexagonal by us); compare for example Fig. 8 with Figs. 7, 8 (b), ref. 43. It is difficult to make a direct thermodynamic assesment based upon comparable physical

Fig. 8. Needle-like crystals formed in PBFP cast from cyclohexanone on glycerol solution above T(1) transition temperature of the polymer.

measurements in these two examples, but from a mechanical properties viewpoint the friability and physical changes of the polymer after fusion or heating in the mesophase region strongly suggest that chain extension has taken place. Extended chain polyethylene is also brittle (43).

In this paper we have tried to present some morphological observation for two polyphosphazenes, emphasizing similarities and differences in physical behavior primarily associated with side group chemistry. The similarity between the siloxane and the polyphosphazene skeleton has already been emphasized (25) and now there are similarities in the L.C. forming abilities of these two "inorganic" classes of polymers which embody a broad range of physical properties, many of which have considerable technological potential.

* Needle-like crystals are also formed when PBFP or PBPP is cast on a hot liquid surface above the T(1) temperature of the respective polymer.

EBSCOhost - printed on 2/13/2023 3:45 AM via . All use subject to https://www.ebsco.com/terms-of-use

Glass formation in polyphosphazenes. Few Tg values have been established using an unambiguous procedure (42) and discrepancies also arise from the polydispersity and molecular mass distribution of most systems studied. However, it is still appropriate to try and establish some useful correlations between Tg, T(1) and Tm for these thermotropic polymers in so far as the side group and backbone chemistry plays an important role in determining these simple, but very important parameters. The values used for this correlation were selected from literature references (8,33). Following minor modifications to reduction procedures used earlier (46) for homopolymers, some tests were made in order to establish trends in the macromolecular behavior of polyphosphazenes (including PBFP and PBPP). One of these is shown in Fig. 9 where a linear interdependence is suggested by the majority of the data analysed.

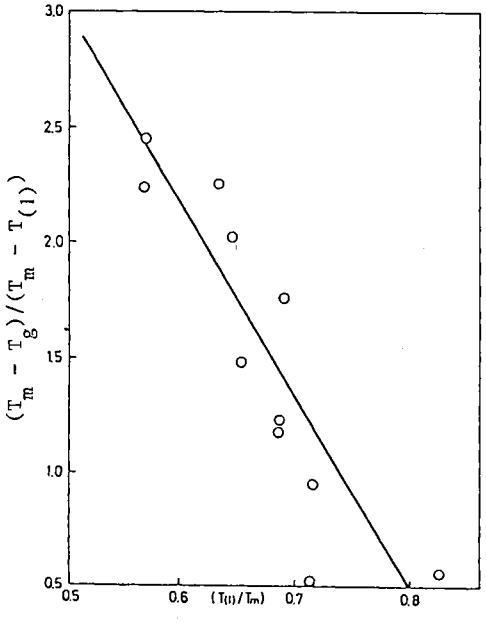

Fig.9. Plot of reduced parameters for polyphosphazenes of the form $(Tm - Tg)/(Tm - T(1))$ vs. $T(1)/Tm$ where Tg, T(1), and Tm are the glass temperature, thermotropic transition temperature and melting point (clearing temperature) respectively.

Correlations are known between Tg, T(1), and Tm, and these serve only as useful empirical relationship. For instance there exists $Tg \simeq 2/3\ Tm$ for macromolecules (44) and $Tg \simeq 0.74\ Tm$ for small molecules (45,46). For polyphosphazenes it seems that $Tg/Tm \simeq 0.42$ is a representative factor obtained from $\ln(Tg/T(1))$ vs. $\ln(T(1)/Tm)$ or their corresponding linear ratios. The straight line also shown in Fig. 9 between $(Tm-T(1))/(Tm-Tg)$ vs. $T(1)/Tm$, serves to indicate how the thermotropic temperature range in

EBSCOhost - printed on 2/13/2023 3:45 AM via . All use subject to https://www.ebsco.com/terms-of-use

polyphosphazenes scales when normalized with respect to the Tm, Tg limits and T(1). Although side group chemistry is very important in determining the polymer chain stiffness in homopolymers, it seems to be equally significant in determining T(1)*, which appears to correlate with Tm and sample history, rather than on the measurement technique as has been suggested in the literature (32).

Conclusion

1. Solution grown crystals of PBFP and PBPP form chain folded crystals from dilute solution and their morphology is discussed.
2. Polymorphic crystalline forms occur in PBFP and PBPP.
3. The c value of PBPP crystals was estimated as 9.70 Å which differs from the value c = 4.91 Å reported previously.
4. Whenever polyphosphazene crystals are annealed below T(1), no crystal thickening takes place, but at temperatures above T(1) and below Tm, erratic thickening occurs as chain extension.
5. Twinned crystals are formed in PBFP thin films cast from the THF, fused at 250°C, isothermally crystallized at 70°C and finally cooled to room temperature.
6. PBFP and PBPP fibrillar spherulites are formed from solution. From the melt, textures of PBFP spherulites appear to be much more complicated and the morphology depends strongly upon the preparation conditions.
7. Solution cast spherulitic aggregates of PBFP consist of cospherical platelets. The morphology does not alter upon heating the PBFP through T(1).
8. Correlation between Tg, T(1) and Tm for polyphosphazenes were established. The side group and backbone chemistry plays an important role in determining these parameters.

* Molecular weight and molecular distribution variables not withstanding.

EBSCOhost - printed on 2/13/2023 3:45 AM via . All use subject to https://www.ebsco.com/terms-of-use

Acknowledgment

Thanks are expressed to the National Science Foundation (Polymer Program) for partial support of this work. One of us (JHM) wishes to acknowledge a Senior Award from the Alexander von Humboldt Foundation which made this presentation possible. The authors wish to express their hearty thanks to Mr. H. Satake and Miss K. Hirano of Chisso Corporation for their generous assistance in this work.

References

1. H. N. Storkes, J. Am Chem. Soc., 19 782 (1897).
2. H. R. Allcock and R. L. Kugel, J. Am. Chem. Soc., 87, 4216 (1965).
3. H. R. Allcock, Science, 193, 1218 (1976).
4. R. E. Singler, N.S, Schneider, and G. L. Hagnauer, Poly. Eng. Sci., 15, 321 (1975).
5. D. P. Tate and T. A. Antkowiak, Kirk-Othmer, Encyclopedia Chem. Technology (3rd Edition) Wiley Interscience, Chap. 10, 936 (1980).
6. H. R. Allcock, Makromol. Chem. Suppl., 4, 3 (1981).
7. A. L. Andrady and J. E. Mark, Polymer J., 17 323 (1981).
8. N. S. Schneider and C. R. Desper in "Liquid Crystalline Order in Polymers" (Ed. A. Blumstein) Acad. Press, Chap. 9,, p. 299 (1978).
9. J. E. Mark and C. Y. Yu, J. Polymer Sci., Polym. Phys. Ed., 15, 371 (1977).
10. S. Futamura, J. K. Valaitis, K. A. Lucas, J. W. Fieldhouse, T. C. Cheng, and D. P. Tate, J. Polymer Sci. Polym. Phys. Ed., 18, 767 (1980).
11. S. V. Peddada and J. H. Magill, Macromolecules, 16, 1258 (1984).
12. E. J. Quinn and R. L. Dieck, J. Fire Flammability, 7, 358 (1976).
13. K. Sebata, J. H. Magill, and Y. C. Alarie, J. Fire Flammability, 9, 50 (1978).
14. P. J. Lieu, J. H. Magill, and Y. C. Alarie, J. Combustion Toxicology, 8, 242 (1983).
15. P. May and L. Guerra, U. S. Patent 4,251,215.
16. H. R. Allcock, Angew. Chem. (English Ed.) 16, 147 (1977).
17. C. E. Carrahar, Jr., in "Organic Coatings and Plastics Chem., 42, 427, 179th Nat. ACS Meeting, Houston, Texas, March 23-28 (1980).

EBSCOhost - printed on 2/13/2023 3:45 AM via . All use subject to https://www.ebsco.com/terms-of-use

18. H. R. Allcock, R. W. Allen, and J. J. Meister, Macromolecules, 9, 950 (1976).
19. H. R. Allcock, R. A. Arcus, and E. G. Stroh, Macromolecules, 13, 919 (1980).
20. C. W. Burkhart, P. C. Gillette, and J. B. Lando, J. Polymer. Sci. Polym. Phys. Ed., 21, 2349 (1983).
21. A. H. Gerber, Amer. Chem. Soc., Organic Coatings and Plastics Chem., 41, 81 (1979).
22. R. E. Singler, G. L. Hagnauer, and R. W. Sica, ACS Symp. #193 (J. E. Kark and J. Lal Ed) Chap. 11, p.229 (1982).
23. S. Yanai, V. T. Staunett, D. R. Squire, G. L. Hagnauer, and R. L. Singler, Rad. Phy. Chem., 19, 1 (1982).
24. T. Masuko, R. L. Simeone, J. H. Magill, and D. J. Plazek, Macromolecules, 17, 2857 (1984).
25. M. Kojima and J. H. Magill, Makromol. Chem., 186, 649 (1985).
26. M. Kojima, W. Kluge, and J. H. Magill, Macromolecules, 17, 1421 (1984).
27. K. H. Gardner , J. H. Magill, and E.D.T. Atkins, Plymer, 19, 370 (1978).
28. D. P. Tate, J. Polymer Sci. Polym. Symp. # 48, 33 (1974).
29. D. Egler and J. H. Magill, (unpublished).
30. M. Kojima and J. H. Magill, Polymer Comm., 24, 329 (1983).
31. H. R. Allcock, Chem. and Eng. News, pp 22-36, March (1985).
32. S. V. Vinogradov , D. R. Tur and I. I. Minosyanto, Russ. Chem. Rev. (English Trans.) 53, 103 (1984).
33. G. Allen, C. J.Lewis, and S. M. Todd, Polymer, 11, 44 (1970).
34. I. C. Choy and J. H. Magill, J. Appl. Polymer Sci., 19, 2495 (1981).
35. E. G. Stroh, PhD. Thesis, Penn State University (1972).
36. J. H. Magill, J. Petermann, and U. Rieck, Paper presented at the Fruhjahrstagung March 18-20 Lausanne 1985; Manuscript to be submitted to J. Colloid and Polymer Sci., May 1985.
37. M. N. Alexander, C. R. Desper, R. L. Sagalyn, and N. S. Schneider, Macromolecules, 10, 721 (1977).
38. W. R. Krigbaum and J. Wanatase, Polymer, 24, 1299 (1983).
39. J. H. Magill, G. McManus, and M. Kojima, (unpublished results)
40. M. Kojima and J. H. Magill, Polymer (submitted).
41. P. J. Flory, Polymer Liquid Crystals, 103 (1982).
42. M. J. Richardson and N. G. Savill, Polymer 16, 753 (1975).

EBSCOhost - printed on 2/13/2023 3:45 AM via . All use subject to https://www.ebsco.com/terms-of-use

43. D. C. Bassett, "Principles of Polymer Morphology", Chap. 7, p. 177 Cambridge U. Press (1981).

44. D. W. Van Krevelen, in "Properties of Polymers", p. 130 Elsevier Pub. Co. (1972).

45. J. H. Magill and D. J. Plazek, J. Chem. Phys., 46, 3757 (1967).

46. J. H. Magill, H-Mo Li, and A. Gandica, J. Crystal Growth, 19, 361 (1973).

EBSCOhost - printed on 2/13/2023 3:45 AM via . All use subject to https://www.ebsco.com/terms-of-use

MORPHOLOGY OF POLYCARBONATE CRYSTALLIZED UNDER THE INFLUENCE OF SOLVENT VAPOURS

I.Daniewska, E.Kocinska
Department of Chemistry, Technical University, Warszawa, Poland

Z.Dobkowski
Institute of Industrial Chemistry, Warszawa, Poland

Introduction

Bisphenol A polycarbonate (PC) represents engineering thermoplastics of unique set of mechanical, thermal and electrical properties. Therefore it is widely applied in many industries (1-3).

It is known that application characteristics of plastics depend, among other things, on the morphological structure of the material. PC as a polymer of symmetric molecular structure is able to crystallize, however, its thermal crystallization is hindered due to the stiffness and low mobility of macromolecules as manifested by its relatively high glass transition temperature T_g (about 145-150°C) and a small extent between the melting point and T_g (about 100°C). However, PC can easily be crystallized under the influence of solvents (1,4-7). Therefore, the phenomena of swelling and solvent induced crystallization are decisive for PC parts exposed to organic solvent vapours. The crystallization of PC induced by organic solvents was investigated mainly from the kinetics point of view (4-7), the morphology of PC has not been taken into account.

In this work the influence of solvents on the morphology of PC crystallized in the solvent vapour atmosphere is investigated. The results are discussed in terms of solubility parameters of solvents and PC.

Morphology of Polymers
© 1986 Walter de Gruyter & Co., Berlin · New York - Printed in Germany.

EBSCOhost - printed on 2/13/2023 3:45 AM via . All use subject to https://www.ebsco.com/terms-of-use

Experimental

Polymer. Three samples of PC of different molecular weight M but of similar polydispersity degree, M_w/M_n, were investigated. Their characteristics are shown in Table 1.

Table 1. Characteristics of PC

Bisphenol A polycarbonate (PC)	M_w	M_w/M_n
Makrolon 2405 (Bayer, FRG)	25 900	2.5
Bistan RT-491 (ICHP, Poland)	39 200	2.5
Bistan AF (Zachem, Poland)	71 800	2.9

Molecular weights and polydispersity degrees were determined by the gel permeation chromatography method (8). The values of solubility parameter of PC were taken from literature data, i.e. total δ_o = 19-22 $MPa^{1/2}$ (9.3-10.6 $cal^{1/2}cm^{-3/2}$), dispersion δ_d = 19.4 $MPa^{1/2}$ (9.5 $cal^{1/2}cm^{-3/2}$) and polar δ_p = 0.8 $MPa^{1/2}$ (0.4 $cal^{1/2}cm^{-3/2}$) (9-11). Single value of δ_o was taken as 9.9 $cal^{1/2}cm^{-3/2}$.

Solvents. Solvents were chosen according to their solubility parameters in comparison with those of PC, and they are shown in Table 2.
Dispersion (δ_d), polar (δ_p) and hydrogen-bond (δ_h) forces (interactions) were taken into account as the components of total solubility parameter (δ_o), (9,100). (Cf. Table 2.)

Preparation of samples

PC in the form of pellets or powder was dried at 110°C during 24 hours and formed into films by the compression moulding technique. Then the films were cooled rapidly by dipping into a water bath at 5°C to obtain amorphous structure. The conditions for preparation of samples are shown in Table 3. The measured density of amorphized films is consistent with that of amorphous PC.

EBSCOhost - printed on 2/13/2023 3:45 AM via . All use subject to https://www.ebsco.com/terms-of-use

Table 2. Solubility Parameters δ ($cal^{1/2}cm^{-3/2}$) of Solvents Used for Crystallization of PC

Solvents	Total		Dispersion	Polar	Hydrogen-bond	
	δ_o	$\Delta\delta_o$	δ_d	δ_p	δ_h	$\Delta\delta_h$
Hexane	7.24	2.66	7.24	0	0	2.8
Carbon tetrachloride	8.65	1.25	8.65	0	0	2.8
Toluene	8.91	0.99	8.82	0.7	1.0	1.8
Benzene	9.15	0.75	9.95	0.5	1.0	1.8
Chloroform	9.21	0.69	8.65	1.5	2.8	0
Trichloroethylene	9.28	0.62	8.78	1.5	2.6	0.2
Tetrahydrofuran	9.52	0.38	8.22	2.8	3.9	1.1
Acetone	9.77	0.13	7.58	5.1	3.4	0.6
Dioxane	10.00	0.10	9.30	0.9	3.6	0.8
Acetic acid	10.50	0.60	7.10	3.9	6.6	3.8
Nitromethane	12.30	2.40	7.70	9.2	2.5	0.3
PC	9.9	-	9.5**	0.4**	2.8*	-

*Calculated in this work, **ref. 11.

Table 3. Preparation of PC Film Samples

Bisphenol A polycarbonate (PC)	Compression temperature	Moulding time	Film characteristics Thickness	Density
	°C	min	μm	g/cm^3
Makrolon 2405	230-240	30	50-90	1.2028
Bistan RT-491	260	10	150-180	1.2019
Bistan AF	270	5	150-180	1.2024

Film strips of 1x3 cm were hanged in the atmosphere of a given solvent vapour during 7 days in a glass vessel closed with a polyethylene cover (not hermetic).

EBSCOhost - printed on 2/13/2023 3:45 AM via . All use subject to https://www.ebsco.com/terms-of-use

All solvents given in Table 2 were used for Makrolon 2405 films, while only five selected solvents, i.e. benzene, chloroform, acetone, dioxane and nitromethane, were used for Bistan RT 491 and Bistan AF.

Methods of morphological investigations

Samples, after exposure to solvent vapours, were investigated by the following methods:

- x-ray diffraction using a Micrometa diffractometer,
- optical microscopy using a MPI (PZO, Poland) polarizing microscope,
- small angle light scattering (SALS) using the He-Ne laser as a light source.

The mean radius of spherulites (R), was calculated from SALS H_v patterns using the following formula (12)

$$R = 4.1\ \lambda/4\pi\ \sin(\theta_{max}/2)$$

where $\lambda = 0.6328$ μm is the light wavelength, and θ_{max} is the angle of maximum scattered light intensity.

Results and Discussion

Under the influence of solvent vapours, all PC films, except those exposed to vapours of hexane, carbon tetrachloride and acetic acid, were hazed. By microscopic investigations it was found that hazed samples exhibit crystalline spherulitic structures; the size of spherulites and the perfection of their structure (estimated from the distinctness of patterns) depend on the kind of solvent. It was also confirmed by SALS technique that the obtained H_v patterns are typical of spherulitic structures (13). The calculated values of mean radius of spherulites are shown in Table 4. Two types of diffractograms were obtained from the x-ray studies (Fig.1): type a (Fig.1a) for amorphized PC samples and for PC films exposed to vapours of hexane, carbon tetrachloride and acetic acid, and type b (Fig.1b) for PC films exposed to all other solvent vapours which induce the formation of spherulites. The number of diffraction peaks was different for various solvents

EBSCOhost - printed on 2/13/2023 3:45 AM via . All use subject to https://www.ebsco.com/terms-of-use

Table 4. The Mean Radius of Spherulites R (μm)

Solvent	Makrolon 2405	Bistan RT-491	Bistan AF
Toluene	6.3	-	-
Benzene	10.6	3.4	2.0
Chloroform	13.9	2.9	1.9
Trichloroethylene	7.2	-	-
Tetrahydrofuran	7.4	-	-
Acetone	3.9	2.4	2.3
Dioxane	7.9	3.8	2.4
Nitromethane	2.2	2.7	1.9

and the reason of this fact is not explained as yet.
Generally it is considered that the solvent interacts with the polymer if the total solubility parameters of both are similar (9,14). Unfortunately, there are exceptions from this rule observed also in our work. E.g. the relatively small difference

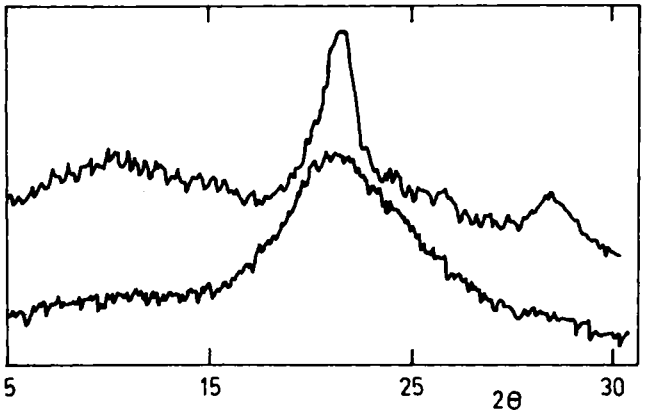

Fig.1. Diffractograms of PC: (a) amorphous PC; (b) crystallized PC (Makrolon 2405) under the influence of tetrahydrofuran vapours

EBSCOhost - printed on 2/13/2023 3:45 AM via . All use subject to https://www.ebsco.com/terms-of-use

$\Delta\delta_o = |\delta_o - \delta_{o,PC}|$ of about 0.6 is observed for acetic acid by which the crystallization is not induced, and for trichloroethylene which induce the crystallization of PC. Similarly, the relatively high value of $\Delta\delta_o$ (about 2.5) is observed for hexane which does not induce the crystallization of PC, and for nitromethane which induce the formation of spherulites. Therefore, component interactions of physical and chemical nature should be taken into account. Thus the three-component Hansen solubility parameters seemed to be useful for this purpose (9,10), cf. Table 2, where $\delta_o^2 = \delta_d^2 + \delta_p^2 + \delta_h^2$ (subscripts o, d, p and h denote the total, dispersion, polar and hydrogen-bonding solubility parameters, respectively).

The values of δ_d for all investigated solvents are similar and probably δ_d is not a decisive parameter in this case. As to the values of δ_h, it is observed that the crystallization of PC is not induced by vapours of the solvent with extreme values of δ_h, i.e. $\delta_h = 0$ for hexane and carbon tetrachlorides, and $\delta_h = 6.6$ for acetic acid. Thus it can be said that the crystallization is induced by solvent vapours if $\Delta\delta_h = |\delta_h - \delta_{h,PC}|$ is below 2 $cal^{1/2} cm^{-3/2}$. It means that hydrogen bond interactions are needed for the solvent vapour induced crystallization. However, the radius of spherulites does not depend on δ_h (cf. Tables 2 and 4).

It has been found that the radius of spherulites R depends on the values of δ_p, especially for Makrolon 2405 (Fig.2). The higher the polar components of solubility parameter, the lower the values of R. It is known that the size of spherulites depends on the ratio of nucleation rate to the growth rate. Thus small spherulites are formed at high nucleation rates if the growth rates are similar. Therefore it can be suggested that the strong polar interactions of solvent vapours enhance the nucleation of crystallizable polymer and high amounts of spherulites of small R are formed. The dependence of R on δ_p is not so distinct for Bistan RT 491 and, in fact, it does not exist for Bistan AF, see Fig.2, due to increasing M (cf. Table 1). It is known that the crystallization rate, mainly the growth rate, decreases with increasing M (15). In the case of Bistan AF of relatively high M, spherulites of small R (about 2 μm) are formed independently of δ_p. Hence, even for solvents of weak polar interactions, the growth rate is lowered, due to the increase in M, in such an extent that the high

EBSCOhost - printed on 2/13/2023 3:45 AM via . All use subject to https://www.ebsco.com/terms-of-use

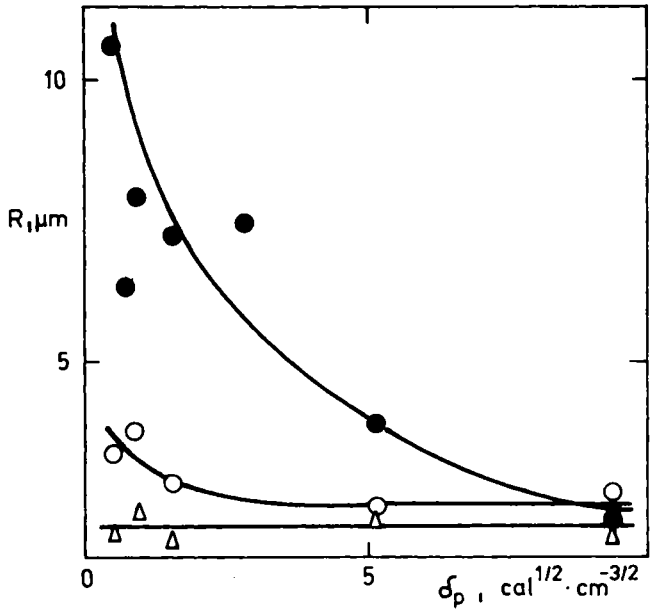

Fig.2. Dependence of spherulite radius R of crystallized PC on the polar solubility parameter δ_p of solvents. 1 ● Makrolon 2405, M_w = 25900, 2 o Bistan RT-491, M_w = 39200, 3 Δ Bistan AF, M_w = 71800.

amount of nuclei can be formed, and as a result the size of spherulites is small.

Therefore, it can be concluded that for the solvent vapour induced crystallization of PC the size of spherulites depends on the kind of solvent, especially on its polar interactions, as well as on the molecular characteristics of the polymer, i.e. on its M. However, at the correspondingly high M, the radius of spherulites, R, is independent of polar solubility parameters δ_p. On the other hand, the crystallizability of PC depends on the hydrogen bond interactions between solvent vapours and the polymer, i.e. on $\Delta\delta_h$.

EBSCOhost - printed on 2/13/2023 3:45 AM via . All use subject to https://www.ebsco.com/terms-of-use

References

1. Christopher, W.F., D.W.Fox. 1962. Polycarbonates. Reinhold, New York.

2. Schnell, H. 1964. Chemistry and Physics of Polycarbonates. Interscience, New York.

3. Krajewski, B. 1971. In: Poliweglany, WNT, Warszawa.

4. Kambour, R.P., F.Karasz, J.M.Daane. 1966. J.Polym.Sci. A-2, 4, 327.

5. Mercier, J.P., G.Groeninckx, M.Lesne. 1967. J.Polym.Sci. C, 16, 2059.

6. Turska, E., W.Benecki. 1979. J.Appl.Polym.Sci. 23, 3489.

7. Ware, R.A., S.Tirtowidjojo, C.Cohen. 1981. J.Appl.Polym.Sci. 26, 2975.

8. Dobkowski, Z., J.Brzezinski. 1981. Eur.Polym.J. 17, 537.

9. Burrel, H. 1975. In: Polymer Handbook (J.Brandrup and E.H.Immergut, eds.). Wiley, New York.

10. Barton, A.F.M. 1984. In: Polymer Yearbook (H.G.Elias and R.A.Pethrick, eds). Harwood Academic Publ., Chur.

11. Shaw, M.T. 1974. J.Appl.Polym.Sci. 18, 449.

12. Mandelkern, L., S.Go, R.Prud´Homme, R.Stein. 1974. J.Polym. Sci.,Polym.Phys.Ed. 12, 1485.

13. Stein, R.S., M.B.Rhodes. 1960. J.Appl.Phys. 31, 1973.

14. Makarewicz, P.J., G.L.Wilkes, Y.Budnitsky. 1978. J.Polym.Sci., Polym.Phys.Ed. 16, 1545.

15. Mandelkern, L.1964. Crystallization of Polymers. McGraw Hill, New York.

EBSCOhost - printed on 2/13/2023 3:45 AM via . All use subject to https://www.ebsco.com/terms-of-use

CRYSTALLIZATION BEHAVIOUR OF POLY(ETHYLENE TEREPHTALATE) GLASSES WITH DIFFERENT ORIENTATION

Ch. Bechev
Higher Institute of Chemical Technology, BG-1156 Sofia, Bulgaria

L.L. Chapoy
Technical University of Denmark, DK-2800 Lyngby, Denmark

J. Mishinev
"Dimitar Dimov" Chemical Works, BG-8603 Jambol, Bulgaria

Introduction

Numerous studies of isothermal melt crystallization of polymers have been reported (1). The currently accepted model is that nuclei appear randomly in the supercooled melt, and subsequently grow at a constant rate in one, two or three dimensions. The picture of crystallization kinetics of polymer glasses, i.e. the crystallization from the amorphous solid state, is not so clear, even though it has been extensively studied by differential scanning calorimetry (DSC). The crystallization under isothermal conditions cannot be practically investigated with sufficient precision, especially to study the crystallization kinetics of polymer glasses with different orientation. On the other hand, isothermal conditions for crystallization are rarely used in practice. Therefore, nonisothermal crystallization was deemed desirable to be studied by DSC. Ozawa (2) has extended the Avrami equation (3) to the nonisothermal kinetics of preexisting nuclei, assuming that the amorphous polymers are heated or cooled at a constant rate, and the mathematical derivation of Evans (4) is valid. According to Ozawa theory the degree of conversion, C, at temperature T is given by:

$$-\ln(1-C) = X_e(T)/\phi^n \qquad (1)$$

Morphology of Polymers
© 1986 Walter de Gruyter & Co., Berlin · New York - Printed in Germany.

EBSCOhost - printed on 2/13/2023 3:45 AM via . All use subject to https://www.ebsco.com/terms-of-use

where ϕ is the heating rate and $X_c(T)$ is a heating crystallization function (4). This function is dependent on temperature and independent of heating rate. The integer n has a value between 1 and 4, depending on whether nucleation is instantaneous or sporadic, and the number of dimensions in which growth occurs. The Ozawa equation (1) has been tested (5) for poly(ethylene terephtalate), PET, precooled melt at different constant cooling rates. In this paper the nonisothermal crystallization of amorphous, solid PET at different constant heating rates and the effect of molecular orientation were studied by DSC.

Experimental

Materials. The samples used throughout this investigation were PET undrawn fibres with different orientation. The melt spinning process at spinning speeds in the range of 800 to 2000 m/min was applied to prepare the samples. The PET polymer used in melt spinning had a relative viscosity of 835 measured in dichloracetic acid. It is well known (6) that undrawn fibres so obtained are practically amorphous when they are produced at these spinning conditions. The average molecular orientation was evaluated by three different parameters: birefringence, n, water shrinkage, S, and natural draw ratio, DR_n. The results are summarized in Table 1.

Methods. The measurements of birefringence were carried out using a POL-D Zeiss Jena microscope with Bereck optical compensation technique (7). The shrinkage was evaluated by relative change of filament lengths after 10 min treatment in boiling water. The natural draw ratio was estimated from the stretch-elongation curves of filaments by the usual method (8). Observation of dynamic heating crystallization of the oriented PET samples reported here was carried out with a Du Pont 900 differential scanning calorimeter. The samples were heated at a constant rate of 2, 4 and 8 deg/min. The degree of conversion at different temperatures was estimated as previously described (9).

EBSCOhost - printed on 2/13/2023 3:45 AM via . All use subject to https://www.ebsco.com/terms-of-use

Table 1. Average Molecular Orientation of PET Glasses Studied

Sample N	n	S	DR_n
1	0.0040	42.2	2.92
2	0.0081	50.8	2.56
3	0.0155	60.9	2.12
4	0.0240	66.7	1.74

Results and Discussion

The experimental data obtained can be analysed in terms of the Ozawa equation. From equation (1) it follows that:

$$\log[-\ln(1-C)] = \log X_c(T) - n \log \phi \qquad (2)$$

According to this relation the DSC curves of crystallization were converted to integral curves of C vs T as shown in Fig.1. Assuming the validity of Ozawa theory, a plot of the left side of equation (2) against log ϕ at a given temperature gives a straight line. Typical plots of log -ln(1-C) against log ϕ are shown in Fig.2, where straight lines with slope 3 are drawn. Similar plots were obtained from measurements on the other PET glasses with different orientation. Therefore, we conclude that the Ozawa theory can be used for investigation of the effect of orientation on the crystallization of undrawn PET fibres. The values of the exponent n in eq. (1), and regression coefficients, R, for plots of several of the samples studied are given in Table 2. The values of n were estimated by the least squares method to be approximately three. It can be concluded that the predetermined nuclei exist in the samples studied before heating in the calorimetric cell and that the crystallites grow three-dimensionally. The origin of the nuclei, however, is not elucidated in this investigation. Turning our attention to the effect of degree of orientation we note that the integer n decreases with increasing orientation to about two. The heating function $X_c(T)$ for two of the samples studied was found

EBSCOhost - printed on 2/13/2023 3:45 AM via . All use subject to https://www.ebsco.com/terms-of-use

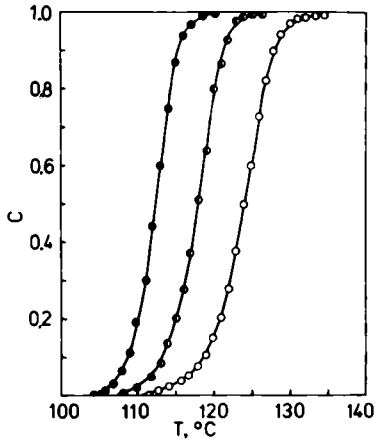

Fig.1. Relations of crystallized fraction versus temperature obtained at different cooling rates for the sample with $\Delta n = 0.0040$: o 2 C/min; ◐ 4 C/min; ● 8 C/min.

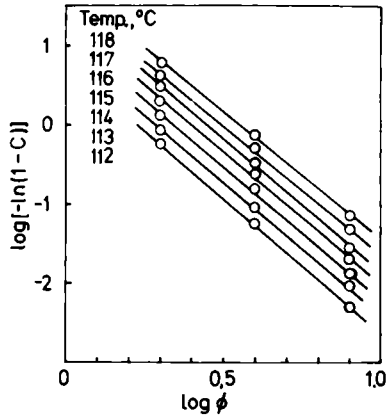

Fig.2. Plots of log[-ln(1-C)] vs. log ϕ at given temperatures for the sample with $\Delta n = 0.0040$.

EBSCOhost - printed on 2/13/2023 3:45 AM via . All use subject to https://www.ebsco.com/terms-of-use

Table 2. Estimated Values of n and R

Temp.	Δn = 0.0040		Δn = 0.0081		Δn = 0.0155		Δn = 0.0240	
°C	n	R	n	R	n	R	n	R
108	-	-	-	-	-	-	1.9	0.9509
109	-	-	-	-	-	-	1.9	0.9564
110	-	-	-	-	3.6	0.9937	1.8	0.8633
111	-	-	-	-	3.3	0.9957	1.7	0.9666
112	3.5	0.9996	2.8	0.9915	3.1	0.9965	1.6	0.9684
113	3.5	0.9999	3.1	0.9995	3.0	0.9971	1.5	0.9711
114	3.3	0.9997	3.2	0.9955	2.8	0.9980	1.4	0.9778
115	3.4	0.9990	3.2	0.9922	2.6	0.9980	-	-
116	3.3	0.9994	3.0	0.9928	2.6	0.9995	-	-
117	3.2	0.9995	2.8	0.9916	-	-	-	-
118	3.1	0.9992	2.7	0.9902	-	-	-	-

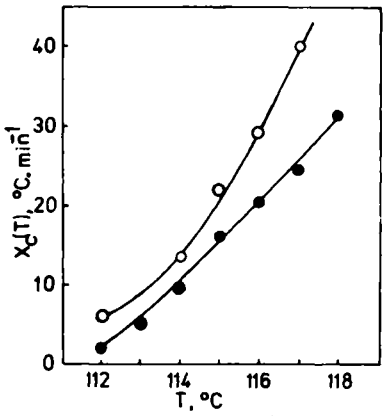

Fig.3. Heating crystallization functions for oriented PET glasses; birefringences are: 0.0040 (o); 0.0081 (●).

EBSCOhost - printed on 2/13/2023 3:45 AM via . All use subject to https://www.ebsco.com/terms-of-use

as shown in Fig.3. The appearance of the curves is dependent on the degree of orientation of PET glasses but does not yield any clear trends. With oriented PET glasses the crystallization is complicated by an additional slow process, referred to as secondary crystallization (1), which is thought to involve an increase in the degree of crystallinity. According to Ozawa (5), the theory and method of analysing DSC curves neglect secondary crystallization. Moreover, it is possible that asymmetric predetermined nuclei exist in the volume of oriented PET glasses and that the mechanism of two dimensional growth is valid. However, it is necessary to obtain more data about the crystallization behaviour of oriented PET glasses using methods in addition to DSC.

References

1. Wunderlich, B. 1976. Macromolecular Physics, Part 2: Crystal Nucleation, Growth, Annealing. Academic, New York.
2. Ozawa, T. 1984. Bull.Chem.Soc.Jpn 57, 639.
3. Avrami, M. 1939. J.Chem.Phys. 7, 1103.
4. Evans, R.U. 1945. Trans.Farad.Soc. 41, 365.
5. Ozawa, T. 1971. Polymer 12, 150.
6. Jacob, I., H.R. Schoder. 1980. Chemiefasern/Textilind, N2, 114; N3, p. 228.
7. Urbanczyk, G.W. 1970. Fizika wlokna. WNT, Warszawa.
8. Eder, M., A.Wlochowicz. 1983. Polymer 24, 1593.
9. Marshal, I., A.B. Thompson. 1954. J.Appl.Chem. 4, 145.

EBSCOhost - printed on 2/13/2023 3:45 AM via . All use subject to https://www.ebsco.com/terms-of-use

RING SPHERULITE STRUCTURE IN POLYETHYLENE ADIPATE

J. Foks, H. Janik, J. Osipiuk, Z. Głowacki
Technical University, Institute of Organic and Food Chemistry and Technology, 80-952 Gdańsk, Poland

Introduction

Polyethylene adipate is frequently used as a raw material in the synthesis of segmented polyurethanes (1,2). It reacts with diisocyanates to form the so-called "soft" segment. Knowledge of the crystalline structures of its component elements helps solve problems related to polyurethanes. There is abundant literature dealing with polyester morphology, but the results adduced in it do not always agree with one another (3,4). The present paper is an effect of the authors' own studies of the adipic acid polyester and ethylene glycol (PEA) made by Zachem, Bydgoszcz.

Results

The morphology of the PEA sample was considerably affected by the crystallization temperature. Seven types of spherulites were observed. Spherulites arising at low temperatures ranging from -20 to +3°C reveal, seen through a polarization microscope, the characteristic Maltese cross and outlines of borders between the spherulites (Fig.1a, area A). Distinct radial elements as described in the literature are absent. The spherulite shows negative birefringence and is similar to the spherulite of type III described in polypropylene (5,6). The interference pattern of spherulites crystallized at a higher temperature reveals no Maltese cross ; fibrillar, radial elements are distinctly outlined (Fig.1b). They are mixed forms with intermingling areas of positive and negative birefringence.
Already at 12°C, and still more distinctly at 14-17°C, there are formed the radial spherulites with positive birefringence (Fig.1c) described in other polymers as type I. Similar spherulites pre-

Morphology of Polymers
© 1986 Walter de Gruyter & Co., Berlin · New York - Printed in Germany.

EBSCOhost - printed on 2/13/2023 3:45 AM via . All use subject to https://www.ebsco.com/terms-of-use

viously observed in the polyester were ascribed both to positive and negative birefringence (3,4).

Within the 23-35°C temperature range are obtained the ring spherulites (Fig.1d) known to be present in polymers (7,8). Intermediate forms between radial and ring spherulites arise at temperatures ranging from 18 to 20°C and from 35 to 39°C. In these conditions the rings become irregular and take zig-zag form (Fig.1e). Polymers crystallized at lower or higher temperatures have different melting temperatures. Positive radial spherulites are formed again (Fig.1f) after further increase in crystallization temperature.

The characteristic features of some of the morphological forms are particularly striking in preparations crystallized successively under various conditions. E.g. a preparation transferred from 43°C to 23°C shows not only forms characteristically appearing at these temperatures, but also transient zig-zag forms with considerably higher birefringence (Fig.1i). Gradual warming of preparations crystallized at various temperatures permits to observe differences in melting temperatures (Fig.1h and Fig.1g).

Radial spherulites with positive birefringence crystallized at temperatures ranging from 12 to 20°C and from 37 to 48°C differ from one another in birefringence value and free surface morphology. According to literature data, these spherulites crystallize in various crystallographic systems (4). The beta form crystallizes at low temperatures of up to 20°C, the alpha form at temperatures of above 40°C. At intermediate temperatures, the two forms crystallize simultaneously, a fact that might account for the presence of the ring structures. It is to be assumed that a polymer crystallizes periodically in the two crystallographic systems and that a different optical sign corresponds to each of the systems in the spherulite.

The above hypothesis has been confirmed by the fact that a spherulite with "forced" rings was obtained (9). After a series of crystallizations performed at 40 and 19°C, the authors obtained a spherulite in which the spacing between the rings were considerably wider than in spherulites crystallized at constant temperature.

We have obtained similar "forced" ring spherulites (Fig.1k). We can, however, not accept the hypothesis discussed above, because the spherulites obtained by us at 19°C and 40°C were characterized

EBSCOhost - printed on 2/13/2023 3:45 AM via . All use subject to https://www.ebsco.com/terms-of-use

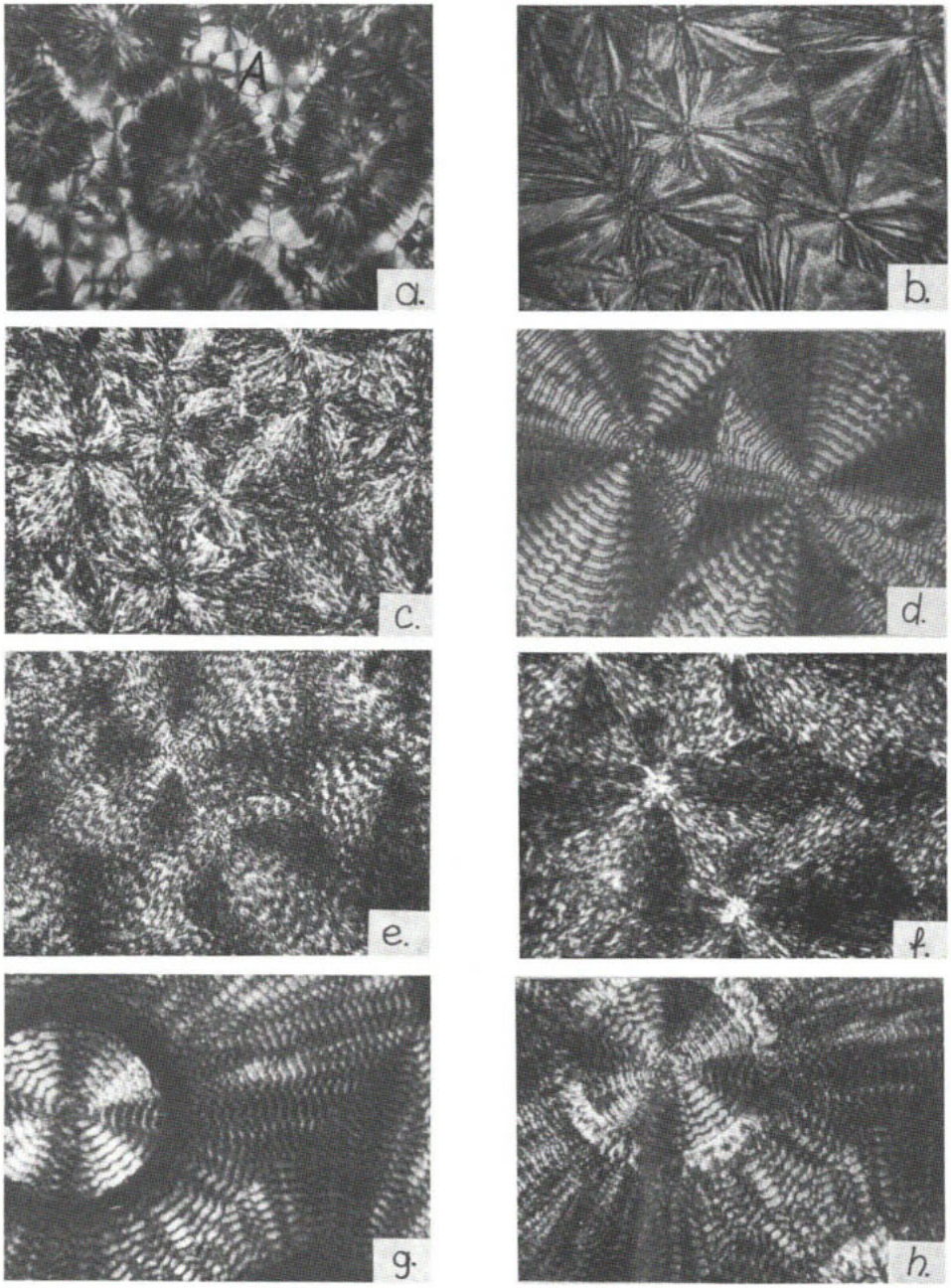

EBSCOhost - printed on 2/13/2023 3:45 AM via . All use subject to https://www.ebsco.com/terms-of-use

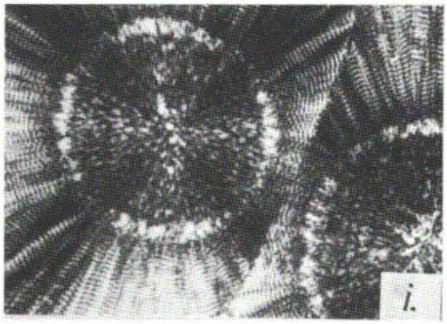

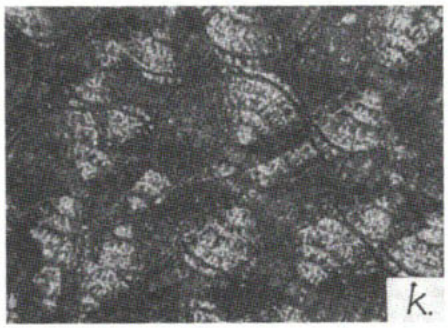

Fig.1. Typical micrographs of the polyethylene adipate sample crystallized at various temperatures: a. -10 and 5°C, b. 8°C, c. 14°C, d. 23°C, e. 19°C, f. 48°C, i. 43 and 23°C, h. 23 and 18°C, g. 23 and 18°C melting at 40°C, k. alternating 40 and 19°C.

by positive birefringence. It must be emphasized that obtaining "forced" spherulites is not merely a matter of crystallization at two different temperatures. At a higher temperature there may occur partial melting, while at a lower temperature crystallization may be considerably accelerated owing to the process of "enhanced self-nucleation" (10), and there may occur crystallization of transient zig-zag forms.

We have found that one single change from 40°C to 19°C in the crystallization temperature results in obtaining a narrow ring with negative birefringence. It is therefore not the fact of performing the crystallization at a given temperature, but the change in temperature that is responsible for the formation of a ring with different birefringence.

According to what was said above, a change in crystallization time may merely influence the width of a ring with positive birefringence. It is this kind of birefringence that prevails in a "forced" ring spherulite, whereas negative birefringence prevails in a spherulite crystallized at constant temperature. In the latter case, the spacing between rings was found to depend on crystallization temperature.

The influence of crystallization temperature on the spacing between rings has been noticed in other polymers also (7,8). The character of the change is different in the polyester studied by us. The spacing at first increases along with temperature increase to reach a maximum at 26°C, but decreases with further temperature

EBSCOhost - printed on 2/13/2023 3:45 AM via . All use subject to https://www.ebsco.com/terms-of-use

increase. Results of direct measurements on micrographs and results obtained with SALS agree with one another.

References

1. Foks, J., H. Janik, S. Winiecki. 1982. J.Appl.Polym.Sci. 27, 645-647.
2. Keroza, J.J. 1979. Fizicheskaya Khimiya Poliuretanov. Kiev. Naukova Dumka.
3. Tarasova, A.I., T.A. Sinicina, V.N. Serebrakova, A.G. Surovcev. 1975. Vysokomol.Soed. 17, 176-178.
4. Tetelbaum, B.J., N.N. Polichov, L.I. Maklakov, N.P. Anoshina, I.O. Murtazina, V.I. Kovalenko. 1967. Vysokomol.Soed. 9, 1672-1676.
5. Rabek, J.F. 1980. Experimental Methods in Polymer Chemistry. John Willey. New York. p.455.
6. Padden, F.J. and H.D. Keith. 1959. J.Appl.Phys. 30, 1479-1484.
7. Daniewska, I., T. Hashimoto, A. Nakai. 1984. Polymer J. 16, 49-60.
8. Basset, D.C. and A.M. Hodge. 1978. Polymer. 19, 469-472.
9. Tetelbaum, B.J. and N.A. Palichov. 1970. Vysokomol.Soed. 12, 3-5.
10. Chivers, R.A., P.J. Barham, J. Martinez-Salazar, A. Keller. 1982. J.Polym.Sci. 20, 1717-1732.

EBSCOhost - printed on 2/13/2023 3:45 AM via . All use subject to https://www.ebsco.com/terms-of-use

EBSCOhost - printed on 2/13/2023 3:45 AM via . All use subject to https://www.ebsco.com/terms-of-use

FULLY ORIENTED CRYSTALLINE POLYACETYLENE OF NON-FIBROUS MORPHOLOGY

G.Leising, O. Leitner and H. Kahlert
Institut f. Festkörperphysik, TU Graz,
A-8010 Graz, Petersgasse 16,AUSTRIA.

Abstract

A large number of investigations on the conducting polymer polyacetylene has been performed on polymer films prepared by the Shirakawa or Luttinger method, which result in a polymer with a complex fibrillar morphology causing a variety of problems both what concerns the measurement of various properties (optical density, electrical conductivity etc.) as well as their physical interpretation. We report on the development of a route to prepare fully oriented non-fibrous crystalline polyacetylene utilizing a precursor polymer, which is converted to polyacetylene under applied stress. Morphology and structure are probed by scanning electron microscopy, X-ray diffraction and electron diffraction.

Introduction

Polyacetylene, $(CH)_x$, is presently regarded to be a model organic polymer for a whole new class of polymers which exhibit fascinating electrical and electrochemical properties (1,2). Because of its chemical and structural simplicity it was expected that an explanation of the unusual properties of conjugated polymers is easier than for more complex systems like eg. polyparaphenylene, polypyrrole or polythiophene. However, $(CH)_x$ prepared according to the standard procedure (3) could not be compared to usual semiconductors or metals in a straightforward manner, since all samples of this kind showed neither a single crystal nor a polycrystalline morphology but consist of randomly entangled partially crystalline fibres, which are in contact with each other but also have a lot of empty space in-between them. Therefore,it was suspected that many observed physical properties do not reflect intrinsic properties of the

Morphology of Polymers
© 1986 Walter de Gruyter & Co., Berlin · New York - Printed in Germany.

EBSCOhost - printed on 2/13/2023 3:45 AM via . All use subject to https://www.ebsco.com/terms-of-use

$(CH)_x$-chains but are a consequence of the peculiar morphology. Consequently, great effort has been put in investigations of this morphology and its changes under certain conditions and treatments (4,5,6,7). In 1980, Edwards and Feast developed a new synthesis of polyacetylene (8) utilizing a metathetical polymerization of a suitable monomer to a precursor polymer, which subsequently can be converted to $(CH)_x$ by heat treatment under appropriate conditions. The $(CH)_x$ derived by this route exhibits a compact morphology and a rather low degree of crystallinity (9,10). We have further developed this route: By applying mechanical stress on the precursor polymer film during the conversion reaction to $(CH)_x$, we succeeded to yield fully oriented crystalline $(CH)_x$-films or fibres (11,12). The aim of this work is to compare $(CH)_x$ prepared by this new route to the widely used Shirakawa-$(CH)_x$ concerning the morphology and to give proofs for the high crystallinity of our samples. As $(CH)_x$ is expected to be a quasi-one-dimensional system, this should result in a strong anisotropic behavior of its physical properties.

Results

1. Morphology of fibrous Shirakawa-polyacetylene

Polyacetylene is a well known material since a long time. But only in 1974 Shirakawa (3) reported a simultaneous polymerization and formation of a free standing polyacetylene film on the surface of concentrated soluble Ziegler-type catalyst solution. These polymer films have a metallic silvery appearance, whereas morphological investigations by scanning electron micrography (SEM) showed that these films consist of an irregular arrangement of fibres (see Fig. 1), with diameters ranging from about 5 to 100 nm depending on

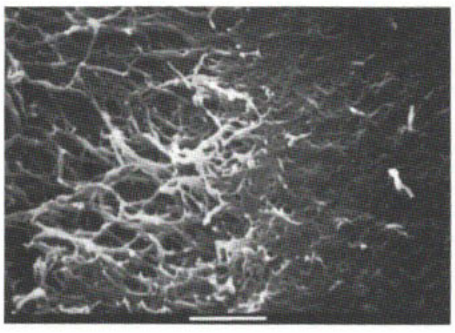

Figure 1. SE-micrograph of $(CH)_x$ prepared by the Shirakawa-procedure (the white bar corresponds to 1 micrometer).

EBSCOhost - printed on 2/13/2023 3:45 AM via . All use subject to https://www.ebsco.com/terms-of-use

the preparation conditions. The SE-micrograph in Fig. 1 shows a selected part of a Shirakawa-type sample, where one can see a rather compact surface on the right half of the picture as well as an insight into the bulk on the left half with the above mentioned fibrillar morphology. A question open to controversial discussions was the kind of the $(CH)_x$ chain orientation inside the fibrils. High-energy electron-diffraction (HEED) on appropriate thin networks of $(CH)_x$ fibres in an transmission electron microscope (TEM) gave circular patterns characteristic for polycrystalline material, with a dominating ring related to the 020/110 crystal planes. Using the dark-field TEM mode to form an image from electron scattered from the 020/110 planes one gets a direct evidence for the chain orientation parallel to the fibre direction (13). Since $(CH)_x$ was expected to exhibit anisotropic behavior of its optical and transport properties in the doped and even in the undoped state, the aim was to produce oriented films in a shear flow field during the polymerization (14,15) or by mechanically stretching the already prepared $(CH)_x$ films (16). Although an anisotropy of the electrical

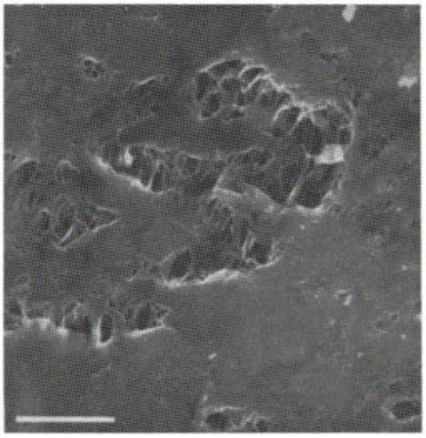

Figure 2. Stress-induced holes in the surface of a 36% strained Shirakawa-type $(CH)_x$ film (SE-micrograph, the white bar corresponds to 4 micrometers).

conductivity has been observed on mechanically stretched films (16), reliable interpretations concerning the intrinsic anisotropic transport properties of polyacetylene could not be drawn since mechanical stretching complicates the already complex morphology by the introduction of voids and fractures in the polymer film. A SE-micrograph of a $(CH)_x$ film which was stretched for about 36 % is shown in Fig.2.

EBSCOhost - printed on 2/13/2023 3:45 AM via . All use subject to https://www.ebsco.com/terms-of-use

2. Morphology of fully oriented crystalline polyacetylene

The basic idea for the new synthesis of polyacetylene is to produce a precursor polymer, which can be purified to a high extent and then is converted to $(CH)_x$ by the elimination of a volatile substance, which can be removed under dynamic vacuum. The preparation route is outlined in Fig. 3. A monomer containing a cyclobutene ring, in our case 7,8-bis-(trifluoromethyl)-tricyclo-[4.2.2.0]-deca-3,7,9-triene (BTFM-TCDT) is synthesized via a Diels-Alder reaction of hexafluoro-2-butene and cyclooctotetraene. The catalyst system WCl_6-$(CH_3)_4Sn$

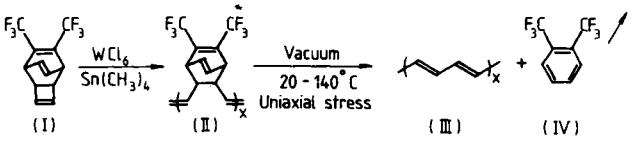

Figure 3. Preparation route for $(CH)_x$ by ring-opening metathesis.

(molar ratio 1:2) is dissolved in chlorobenzene and when the monomer is introduced, the mixture becomes viscous as the polymerization occurs. The reaction is terminated by the addition of methanol. The precursor polymer is filtered and dried under vacuum, then dissolved in absolute acetone or chloroform and precipitated by the addition of methanol. This purification is repeated several times and yields a precursor polymer of high purity what concerns catalyst residues, which are a serious problem of the Shirakawa synthesis, because remaining catalyst groups cannot be removed and act as defect states in the polyacetylene system. The precursor polymer is stored at low temperature until use. Films were cast onto glass substrates from a saturated solution of the precursor polymer in acetone, dried under argon gas flow and mounted in a stretching apparatus. By applying dynamical vacuum at temperatures between 40 and 80 °C, the precursor polymer is converted to polyacetylene under continuous mechanical stress. After the completion of the elimination reaction the stretched polymer film is heated up to 140 °C to yield pure trans-$(CH)_x$. Drawing ratios up to 20 times the initial length of the precursor polymer are attainable with tensile load of about 60 kg/cm^2. Polyacetylene films prepared by this route have a

EBSCOhost - printed on 2/13/2023 3:45 AM via . All use subject to https://www.ebsco.com/terms-of-use

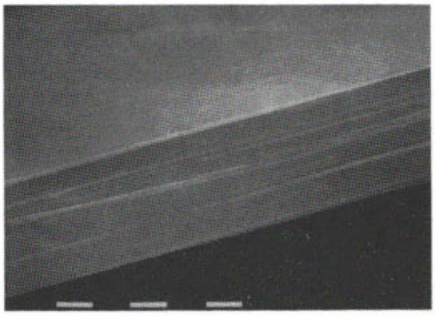

Figure 4. SE-micrograph of the edge of a polyacetylene film. The edge was produced by cleaving a film along the c-axis. (The white bars correspond to 1 micrometer).

compact morphology and a nearly perfect order of the polymer chains parallel to the stretching direction (which coincides with the crystallographic c-axis); therefore they can easily be cleaved in this direction. A SE-micrograph of a cleaved edge is shown in Fig.4. If one looks closer into the cleaved edge with higher magnification (Fig. 5) the compact non-fibrous morphology is clearly seen.

Figure 5. SE-micrograph of the cleaved edge of Fig. 4. Even at highest magnification no individual fibres can be seen. (The white bar corresponds to 1 micrometer.)

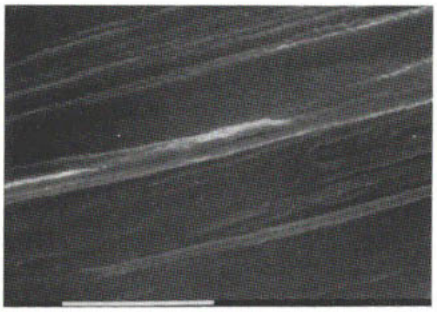

For optical measurements homogeneous bulk and high-quality surfaces are of great importance, particularly if one plans to deduce the optical constants. The surface of our films has a rather high reflectivity with a strong anisotropy (17). The quality of the film surface is demonstrated in Fig. 6, which shows a SE-micrograph at high magnification. The irregularities in the surface are negligible for optical measurements for wavelengths greater than 200 nm.
To examine the degree of alignment of the polymer chains parallel to the stretching direction we performed X-ray diffraction experiments. With Cu-K_α radiation and the incident beam perpendicular to the chain axis we got diffraction patterns shown in Fig. 7. From the almost negligible off-equatorial extension of the (hk0) reflections a nearly perfect alignment of the $(CH)_x$ chains is

EBSCOhost - printed on 2/13/2023 3:45 AM via . All use subject to https://www.ebsco.com/terms-of-use

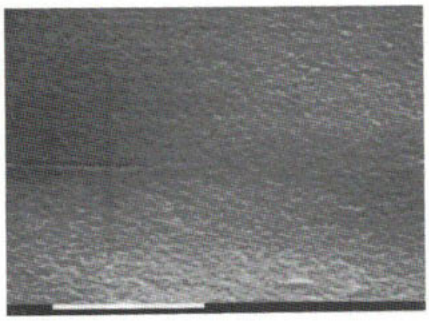

Figure 6. SE-micrograph of the surface of the $(CH)_x$ film from Fig. 4 at higher magnification. (The white bar corresponds to 1 micrometer.)

Figure 7. X-ray diffraction pattern of oriented trans-$(CH)_x$. (Cu-K_α radiation, cylindrical film.)

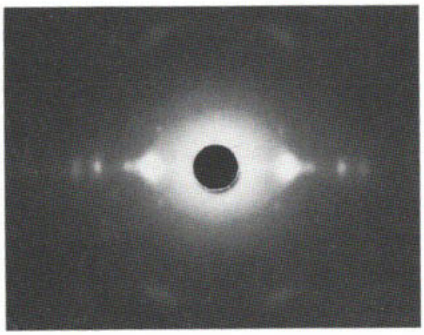

evidenced. Based on the results of X-ray and HEE-diffraction (Fig.8) we were able to calculate the structural parameters for trans-$(CH)_x$ (18,19). The unit cell was found to be monoclinic and the space group $P2_1/a$, which implies that the C-C double bonds on neighbouring chains are in phase.

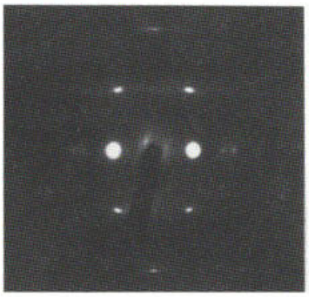

Figure 8. HEED-pattern (120 keV) of a very thin ($d < 1000$ Å) $(CH)_x$-film.

Conclusion

We have demonstrated the compact, non-fibrous morphology of fully oriented crystalline polyacetylene prepared by a route (11,20) based on a synthesis using a processable precursor polymer (8).

EBSCOhost - printed on 2/13/2023 3:45 AM via . All use subject to https://www.ebsco.com/terms-of-use

Optical investigations from the visible to the infrared region and electrical transport measurements (21,22) allow to deduce the strong anisotropy of many physical properties like the conductivity, the refractive index, the optical absorption coefficient, and of the IR-active and Raman active lattice modes, as expected from the quasi-one-dimensionality of polyacetylene.

Acknowledgements

The SEM work was done at the Zentrum für Elektronenmikroskopie of the Technical University, Graz. The authors are indebted to Ing. H.C. Waltinger for his assistance. This work was supported by the Austrian Science Research Fund under the project Nr. 5175.

References

1. Chien, J.C.W. 1984. Polyacetylene. Academic Press, New York.

2. Simon, J. and J.J. Andre. 1984. In: Molecular Semiconductors. Springer-Verlag, Berlin-Heidelberg-New York, pp. 150-192.

3. Ito, T., H. Shirakawa and S. Ikeda. 1974. J. Polymer Sci. Polym. Chem. Ed. 12, 11.

4. Shirakawa, H. and S. Ikeda. 1979/80. Synth. Met. 1, 175.

5. Epstein, A.J., H. Rommelmann, R. Fernquist, H.J. Gibson, M.A. Druy and T. Woerner. 1982. Polymer 23, 1211.

6. Karasz, F.E., J.C. Chien, J.C.W. Galkiewicz, R. Wnek, A.J. Heeger and A.G. MacDiarmid. 1979. Nature 282, 236.

7. Enkelmann, V., G. Lieser, W. Müller and G. Wegner. 1981. Chem. Scr. 17, 141.

8. Edwards, J.E. and W.J. Feast. 1980. Polymer Commun. 21, 595.

9. Bott D.C., C.K. Chai, J.H. Edwards, W.J. Feast, R.H. Friend and M.E. Horton. 1983. J.d. Phys. 44/C3, 143.

10. Leising, G., F. Stelzer and H. Kahlert. 1983. J.d.Phys. 44/C3, 139.

11. Leising, G. 1984. Polymer Bull. 11, 401.

12. Leising, G. 1984. Polymer Commun. 25, 201.

EBSCOhost - printed on 2/13/2023 3:45 AM via . All use subject to https://www.ebsco.com/terms-of-use

13. White, D., D.C. Bott, R.H. Weatherhead. 1983. Polymer 24, 805.

14. Meyer, W.H. 1981. Mol.Cryst.Liqu.Cryst. 77, 137.

15. Chien, J.C.W., F.E. Karasz, M.A. Shen and Y. Yamashita. 1983. Macromol. Chem. Rapid Commun. 4, 5.

16. Park, Y.W., M.A. Druy, C.K. Chiang, A.G. Mac Diarmid, A.J. Heeger, H. Shirakawa and S. Ikeda. 1979. J. Polym. Sci. Polym. Lett. Ed. 17, 195.

17. Leising, G. and B. Ankele. 1985. Solid State Commun. (to be published).

18. Leising, G., O. Leitner and H. Kahlert. 1985. Mol. Cryst. Liqu. Cryst. 117, 67.

19. Leising, G., H. Kahlert and O. Leitner. 1985. In: Springer Series on Solid State Sciences 63. Springer-Verlag, Berlin-Heidelberg-New York, p. 56.

20. Kahlert, H. and G. Leising. 1985. Mol. Cryst. Liqu. Cryst. 117, 1.

21. Leising, G., R. Uitz, B. Ankele, W. Ottinger, F. Stelzer. 1985. Mol. Cryst. Liqu. Cryst. 117, 327.

22. Kahlert, H., G. Leising, O. Leitner, R. Uitz and F. Stelzer. 1985. In: Proceedings of the 17th International Conference on the Physics of Semiconductors, San Francisco 1984. (J.D. Chadi and W.A. Harrison, eds.). Springer-Verlag, Berlin-Heidelberg-New York, p. 1453.

EBSCOhost - printed on 2/13/2023 3:45 AM via . All use subject to https://www.ebsco.com/terms-of-use

MORPHOLOGICAL CHANGES IN THE COPOLYMER OF TRIOXAN WITH PHENYLGLYCIDYL ETHER

R. Mateva, G. Sirashki, M. Krasteva

Institute of Chemical Technology, Sofia, Department of Technology of Plastics
University of Sofia "Kliment Ohridski", Faculty of Physics, Department of General Physics, Sofia 1126, "A.Ivanov" street 5

Introduction

The copolymerization of trioxan (TO) and phenylglycidyl ether (PhGE) is a typical example how crystallizing and non-crystallizing monomers may be combined. The first studies of the copolymerization of TO and PhGE were carried out in 1970 (1). They deal with the conformational changes of the block copolymers obtained with very small quantities of PHGE (weight up to 0.02%) built in the POM chain. The investigation of the morphological changes of TO/PhGE copolymers prepared in a solution of nitrobenzene, at PhGE content ranging within wide limits from 1% to 50 mol%, was of interest. The polymerization of TO and PhGE proceeds according to ref.(2) and the purification of the copolymers is described in ref.(1).

Experimental

The WAXS investigations were carried out with usual X-ray equipment. A Karl Zeiss apparatus with a phase contrast was used for visual microscopic characterization of samples.
For electron microscopy measurements a Philips 300 was used. A one-step replica was prepared of the samples which were covered with C/Pt. The removing of the replicae was made with concentrated HCl acid and a following wash. The micrographs were taken on Philips 300 at 80 kV and scanning was carried out on Jeol.
The DSC thermograms were taken on Perkin Elmer in hermetically sealed pans. The degree of crystallinity was determined according to

Morphology of Polymers
© 1986 Walter de Gruyter & Co., Berlin · New York - Printed in Germany.

EBSCOhost - printed on 2/13/2023 3:45 AM via . All use subject to https://www.ebsco.com/terms-of-use

Hermans (3) and the size of the mosaic blocks was established the method of Sherer.

Results

In Fig.1 wide-angle X-ray diagrams of the two series of samples are shown: 1st series represents the copolymerization proceeding at low rate $[C_{cat}] = 10^{-4}$ and the 2nd series that at high rate $[C_{cat}] = 10^{-3}$ mol/mol.

As it should be expected in both of the series the inclusion of non-crystallizing units in the chain results in defects of the crystal lattice (4,5). At low polymerization rate these defects create first of all a size decrease of the mosaic blocks (Fig.2). The degree of crystallinity, even at high PhGE concentration, remains very high (over 90%). At the same time when the polymerization proceeds at a high rate even very small quantities of PhGE units cause changes in the crystal lattice. This is proved by the splitting of the 100-010 reflection which means an occurrence of a difference between a and b axes and, consequently, a decrease in the symmetry. The melting peaks of DSC-thermograms are an indication that new lattices are formed. Along with the basic

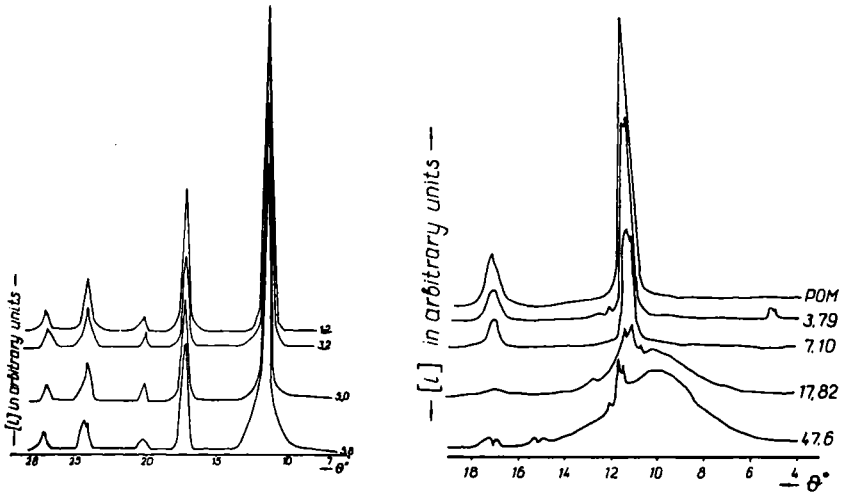

Fig.1. WAXS of PhGE/TO copolymers at a signed PhGE content respectively: a) $[C_{cat}] = 10^{-4}$mol/mol; b) $[C_{cat}] = 10^{-3}$mol/mol.

EBSCOhost - printed on 2/13/2023 3:45 AM via . All use subject to https://www.ebsco.com/terms-of-use

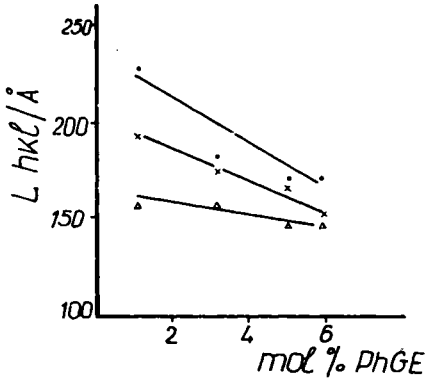

Fig.2. Dependence of the mosaic block size (L_{hkl}) on PhGE per cent content in directions perpendicular to the planes: O [100], [010]; × [105],[015]; Δ [108],[018].

maximum corresponding to the melting temperature of POM, another wider peak at higher temperatures is also observed. With the increase in PhGE content this peak moves towards higher temperatures while the area beneath it decreases. The first peak decreases in intensity and gradually disappears (Fig.3). At PhGE concentrations

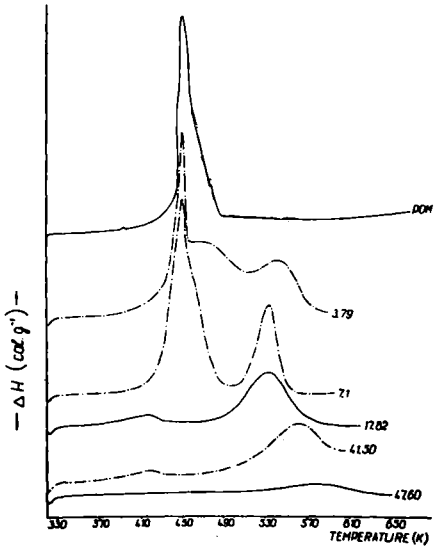

Fig.3. DSC thermograms of PhGE/TO copolymers at the signified PhGE contents, W_{scan} = 20°C/min.

EBSCOhost - printed on 2/13/2023 3:45 AM via . All use subject to https://www.ebsco.com/terms-of-use

higher than 10% a considerable increase in the amount of the amorphous material is observed. The position of the reflections is changed and new reflections appear. More elaborate studies on the crystal lattice changes of these copolymers are in progress.
The alternation of the degree of crystallinity with the increase in PhGE content in the 2nd series is shown in Fig.4. The curve can be divided in three intervals: Up to 7% concentration of the non-crystallizing copolymer, the degree of crystallinity remains almost constant. At higher concentrations a sudden change in the degree of crystallinity up to C_{PhGE} = 18% is observed. At concentrations greater than 18%, the crystallinity again remains essentially constant.
The peculiar course of these dependences may be explained in different ways. Since the sequence distribution of the non-crystallizing segments along the chain is not well established such arguments must be speculative in character.
The change of the supermolecular structural organization on the level of lamellae and lamellar aggregates is shown in Fig. 6. It can be seen from the figure that the hexagonal formations are predominant in pure POM (Fig. 6a). They are built of regularly arranged lamellar crystals grown probably according to a screw dislocational mechanism. Such POM structures have been time and again observed with an introduction of small quantities of PhGE in the chain; the hexagonal nature of the structures is preserved but the walls become more irregular and the angles gradually round off

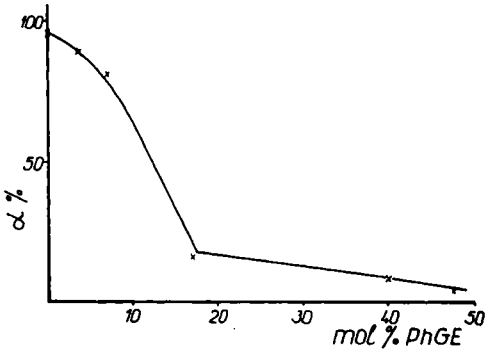

Fig. 4. Dependence of the degree of crystallinity (according WAX) on the % PhGE.

EBSCOhost - printed on 2/13/2023 3:45 AM via . All use subject to https://www.ebsco.com/terms-of-use

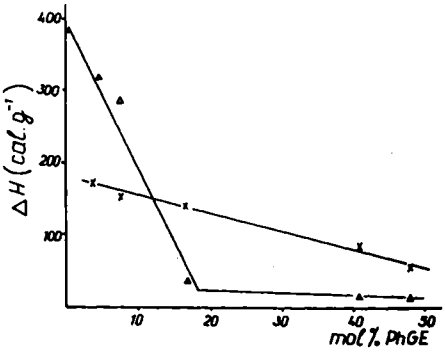

Fig. 5. Dependence of the melting enthalpy $\Delta H(\text{cal g}^{-1})$ on the % PhGE; Δ 1st, X 2nd peak from Fig.3.

(Fig. 6 b1, d1-e1). It becomes noticeable in the scanning electron microscopy that the lamellae are no longer parallel to one another but that every new layer is bent towards the preceding one at a certain angle (Fig. 6,b2).

This type of structure resembling a rose blossom is characteristic of almost all PhGE concentrations with the exception of the highest ones ($C_{PhGE} = 40\%$). Their peculiar form is probably due to the higher rate of crystal growth on the periphery of the aggregate rather than on its centre.

In almost all samples electron diffraction pattern of both monocrystal (Fig. 6, c2) and polycrystal (Fig. 6, e2) type are observed with the monocrystal diffraction being predominant at small concentrations and the Debye-rings - at the higher ones. With increasing the PhGE concentration the spots of the electron diffraction pattern become larger. At high polymerization rates and at high concentrations a considerable amorphous dispersion halo is also observed (Fig. 6, e2). All the same the presence of distinct reflections is surprising and unexpected. It shows a certain microheterogeneity of the sample even though the degree of crystallinity in it is very small (Fig. 1, b5). It is possible, because of the different exhaustion rate of the monomers in the polymerization, that the end of the polymerization is enriched in trioxan and more perfect lamellae are formed. This cause a monocrystal diffraction

EBSCOhost - printed on 2/13/2023 3:45 AM via . All use subject to https://www.ebsco.com/terms-of-use

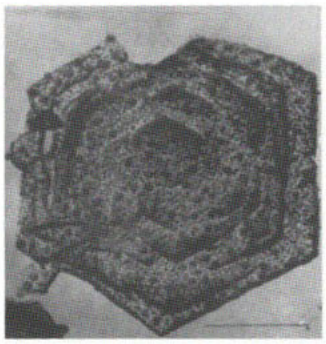

a - EM

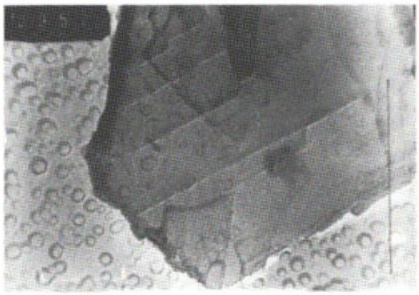

b1 - EM

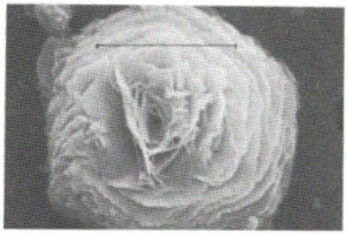

b2 - SEM

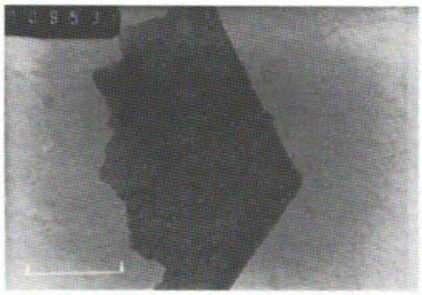

c1 - EM

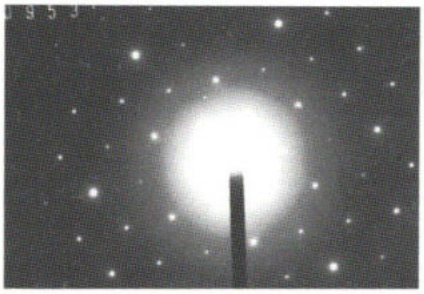

c2 - Diffraction

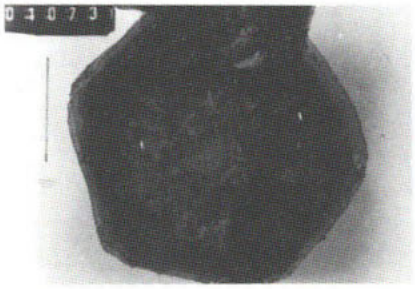

d1 - EM

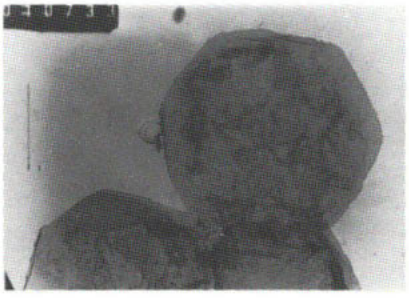

d2 - SEM

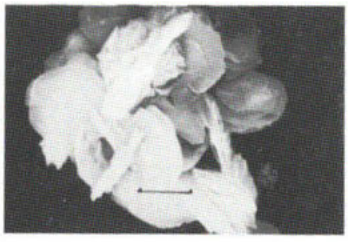

d3 - EM

EBSCOhost - printed on 2/13/2023 3:45 AM via . All use subject to https://www.ebsco.com/terms-of-use

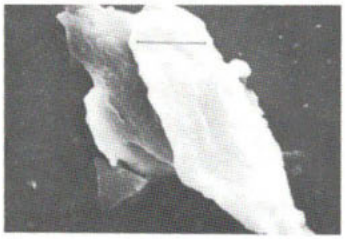

e1 - SEM

e2 - EM

Fig. 6. Morphology of the crystallites and electron diffraction at: (a) pure PTO-EM, $[C_{cat}] = 10^{-4}$ mol/mol; (b) PhGE = 1.3%, (c) 3.8%, (d) 10.7%, (e) 41.5%, $[C_{cat}] = 10^{-4}$ mol/mol.

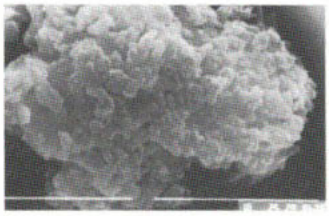

a - SEM

b - EM

Fig. 7. (a) SEM for PTO, [C] = 10^{-3}mol/mol and (b) PhCE = 10.7%, [C] = 10^{-4} mol/mol.

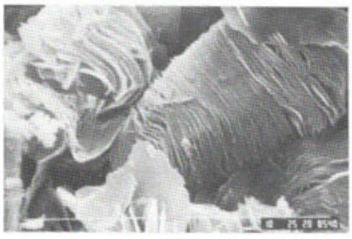

a - SEM

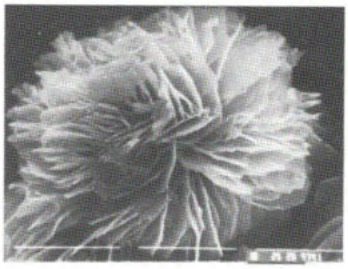

b - SEM

c - SEM

Fig. 8 SEM of samples: (a) PhGE = = 1.5%; (b) PhGE = 5.9%, $[C_{cat}]$ = = 10^{-3} mol/mol; (c) PhGE = 9.8%, [C] = 10^{-4} mol/mol.

EBSCOhost - printed on 2/13/2023 3:45 AM via . All use subject to https://www.ebsco.com/terms-of-use

but their quantity, as the last product formed, is insignificant. Figure 7 shows the great influence of the polymerization rate on the morphology. Even the pure POM at high polymerization rates forms minute and imperfect crystal structures (Fig.7a). Meanwhile, even with a considerable PhGE content but low polymerization rates the screw dislocational mechanism of growth is distinctly observed on the surface of the lamellar crystal (Fig. 7b). Along with these forms, most often occurring at high polymerization rates, a dendritic growth mechanism of the aggregates is observed along with an increase in the speed of the crystal growth on the edges (Fig. 8a). Similar structures are probably due to the great quantity of secondary nuclei on the base of the lamellae, from which secondary lamellae grow in all directions. The cylindrical layered structures consisting of parallel lamellae grown up one upon the other are an interesting morphological form, characteristic of the lower polymerization rates (Fig. 8b). It is also possible for the constituent lamellae to have grown up extended epitaxially from a common monocrystal (8). We consider it more probable that one or several long folds of the preceding lamella serve as a nucleus for every following one.

On the basis of the experimental results stated above we may suggest the following model for the supermolecular structural organization of the TO and PhGE copolymers (Fig. 9). At low PhGE concentration, because of the high crystallizing ability of POM, the tendency to build in copolymeric segments as point defects in POM crystal lattice is strongly favoured. Since the point defects have the ability to generate dislocations (8), both screw and edge dislocations appear on the surface of the basic lamella. They serve as secondary nuclei for growth of new lamellae. In this way the

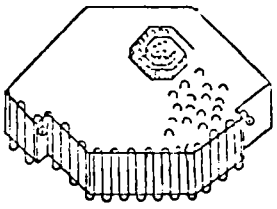

Fig. 9a. Model of growing of POM crystals.

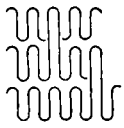

Fig. 9b. Model of growing of a crystal of TO/PhGE copolymer.

EBSCOhost - printed on 2/13/2023 3:45 AM via . All use subject to https://www.ebsco.com/terms-of-use

hedritic hexagonal structures are formed (Fig. 6, b1,c1). At higher concentrations PhGE segments are pushed out into the intramosaic blocks and in the long folds of the lamellae because of this there is a size diminution of the areas with coherent dispersion (Fig.2), although the dislocational mechanism of growth is preserved. In the later stages of polymerization and crystallization, when the monomer access to the interior of the aggregates is hampered, a radial gradient of crystal growth speed is created. This leads to a hindering of the lateral growth of the lamellae - axialites are formed.

When the growth speed is equal along the diameter of the increasing surface and there are no other aggregates nearby which can hamper the lamellar spatial growth, conditions for formation of large cylindrical layered structures are created (Fig. 8c). When the growth speed is high in all directions, conditions of growing of spherulites are formed (Fig. 8b). When the PhGE concentration along the chain becomes higher, the pushing out under lamella comonomeric segments of the form of long folds, or whole amorphous ends of chains, predominates. It is possible that the long folds are formed at the simultaneous polymerization and crystallization according to the mechanism suggested by Mateva and Wegner (6). These long folds may serve as secondary nuclei for the growth of new lamellae. The "pushing" of the non-crystallizing component into the intralamellar spaces results in a tightening of the layer structures (Fig. 6, e2). The PhGE concentration at which the separation of PhGE segments in the amorphous areas becomes predominant, depends on the polymerization rate. At low rates the copolymer is able to build into its lattice a considerable quantity of voluminous segments in the form of defects. At a high polymerization rate the reduction in the degree of crystallinity occurs at considerably lower PhGE concentrations (over 8%) (Fig. 1 a,b).

References

1. Mikhailov, M., L. Terlemezyan. 1974. Dokl.Akad.Nauk 8, 1, 61.

2. Mateva, R., G. Sirashki. J.Polym.Sci. (in press).

3. Chala, J., P.H. Herman, A. Weidinger. 1961. Makromol.Chem. 44, 24.

EBSCOhost - printed on 2/13/2023 3:45 AM via . All use subject to https://www.ebsco.com/terms-of-use

4. Dröscher, M., K. Hertwig, K. Reiman, G. Wegner. 1976. Makromol. Chem. 177, 1695.

5. Michnev, B., R. Mateva. 1985. Makromol.Chem. 239, 240, 241.

6. Mateva R., G. Wegner, G. Lieser. 1973. J.Polym.Sci., Lett.Ed. 369, 11.

7. Munöz-Escahim, A., S.J. Gnerro. 1976. Makromol.Chem. 2169, 177.

8. Wunderlich B. 1979. Macromol.Phys., v. 1. Mir, Moscow (in Russian).

EBSCOhost - printed on 2/13/2023 3:45 AM via . All use subject to https://www.ebsco.com/terms-of-use

RECENT WAXS- AND TEM-RESULTS ON PHASE TRANSITION OF CELLULOSE

H.-P. Fink, H.J. Purz, B. Philipp

Academy of Sciences of the GDR, Institute of Polymer Chemistry "Erich Correns", 1530 Teltow-Seehof, Kantstraße 55, German Democratic Republic

Introduction

Cellulose processing is closely connected with the physical structure of this natural polymer, particularly with polymorphism and lattice transitions (1). Here, the lattice transition cellulose I ⟶ sodium-cellulose ⟶ cellulose II, due to reaction between native cellulose with aqueous alkali and subsequent neutralization, plays an important part. In the recent years phase transitions in connection with the alkalization reaction of cellulose have been investigated by us on the different levels of the physical structure of cellulose (2-8).

This contribution summarizes some of our recent results on cellulose I ⟶ cellulose II phase transition, centering on changes in the supermolecular structure detected by wide angle x-ray scattering (WAXS) and on changes in fibrillar morphology revealed by transmission electron microscopy (TEM), and compares the effects of aqueous and ethanolic solutions of NaOH on the physical structure of cellulose.

Experimental

As starting materials mainly an acetate grade cotton linters (DP = 1600) and additionally a bacterial cellulose from Acetobacter xylinum (NC IB 8034, DP = 2000) as well as a commercial spruce sulphite dissolving pulp (DP = 470) were used. Treatment with aqueous alkali of different NaOH-concentration up to 18 wt.-% was performed with the air-dry samples at liquid-to-solid ratio of 50 during 2 h at 20 °C. The alkali-treated samples

Morphology of Polymers
© 1986 Walter de Gruyter & Co., Berlin · New York - Printed in Germany.

EBSCOhost - printed on 2/13/2023 3:45 AM via . All use subject to https://www.ebsco.com/terms-of-use

were separated from adhering lye by pressing, and neutralized after desintegration, washed and air-dried. Steeping with an ethanolic solution of NaOH was carried out with different cellulose samples by using a 10 wt.-% NaOH solution in an ethanol/water mixture (volume ratio 80:20) at liquid-to-solid ratio of 500 at 20 °C and varying the steeping time between 2 and 72 h.

Washing of the alkalized samples to neutral p_H was performed with an ethanol/water mixture of the same proportion.

For taking the WAXS pattern, the samples were placed between polyester foils on tne sample holder of a horizontal diffractometer, employing symmetric transmission technique with stepwise registration. The CuK_α-radiation used was monochromatized by means of a Ni-filter and pulse-hight-analyser. Intensities registered in the angular range $4^\circ \leq 2\vartheta \leq 104^\circ$ were corrected for parasitic scattering including that of the foil, absorption and polarization.

For taking EM micrographs (TEM-technique, 60 kV), a surface replica and a suspension technique were used for preparation. Surface replicae were obtained by oblique shadowing with Pt/Ir/C, subsequent treatment with H_2SO_4/H_2O mixtures of increasing H_2SO_4 concentration for desintegration and dissolution of the cellulose, and washing with water to neutral p_H. For suspension preparation, a dilute aqueous cellulose suspension was distributed on a carbon film covered gold grid, preferentially using an ultrasonic technique. The cellulose samples obtained in this way were then treated with the appropriate steeping lye in situ, washed to neutral p_H and dried. Subsequently, also these specimens were shadowed with Pt/Ir/C for contrast enhancement.

Results

Structural changes after treatment with aqueous alkali

As demonstrated in Fig. 1, the lattice transition from cellulose I to cellulose II considered here is a multi-step process proceeding via Na-cellulose I and water-cellulose as intermediates. For a qualitative phase analysis, the position of the first interference can be considered as a suitable criterion. By means

EBSCOhost - printed on 2/13/2023 3:45 AM via . All use subject to https://www.ebsco.com/terms-of-use

of a method of quantitative phase analysis established by us (2), the transition from cellulose I to Na-cellulose I and subsequently to cellulose II was investigated. From the curves in Fig. 2 it can be concluded that within the range of lattice transition the amount of Na-cellulose formed exceeds that of cellulose II finally obtained, thus indicating a partial reversibility of the step cellulose I ⇄ Na-cellulose I.

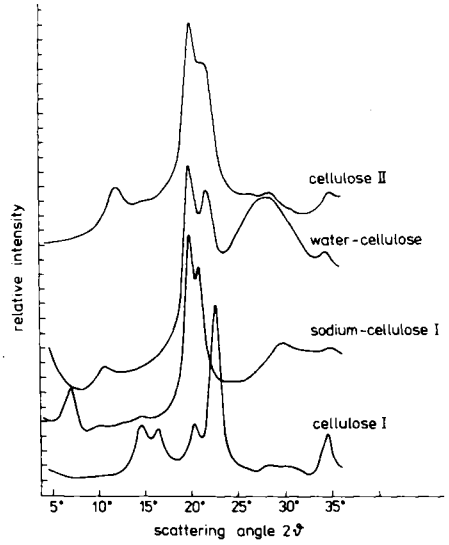

Fig. 1. WAXS-curves of cellulose modifications obtained by alkalization (18 % aqueous NaOH) and regeneration of isotropic samples.

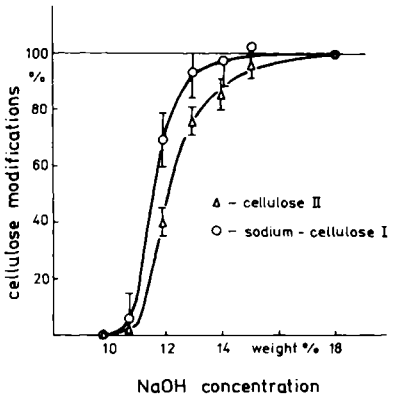

Fig. 2. Lattice conversion from cellulose I to Na-cellulose I and cellulose II versus steeping lye concentration.

In dependence on the steeping lye concentration, changes in the supermolecular structure of cellulose can be characterized by a degree of crystallinity and by the average size and perfection of order of the crystallites. The degree of crystallinity as well as a disorder parameter of the crystallites was assessed according to Ruland (9), using the computerized version of Vonk (10). This method is based on the separation of scattering I_c of crystalline peaks from background scattering which can appropriately be achieved in an $I \cdot s^2$ plot (I-intensity, $s = \frac{2}{\lambda} \sin\vartheta$, λ - wave length of x-rays) of WAXS. The experimentally obtained ratio of integrals

EBSCOhost - printed on 2/13/2023 3:45 AM via . All use subject to https://www.ebsco.com/terms-of-use

$$R(s_p) = \int_{s_o}^{\tilde{p}} I \cdot s^2 \, ds \Big/ \int_{s_o}^{s_p} I_c \cdot s^2 \, ds \qquad (1)$$

is fitted by the linear equation

$$R(s_p^2) = \frac{1}{x_c} + \frac{k}{2x_c} \, s_p^2 \qquad (2)$$

thus providing the degree of crystallinity x_c and the disorder-parameter k. As a result, with increasing concentration of NaOH, x_c as well as k decrease (Fig. 3), i.e. the state of order in the remaining crystalline regions is enhanced as compared to the original value. This decrease in x_c and k is found to start already at a concentration of NaOH significantly lower than that of the lattice transition range.

An estimation of lateral dimension of the crystallites was performed via peak width at half the maximum height of the crystalline peaks. To this end, background scattering was eliminated in the same way as for determination of x_c. Overlapping crystalline peaks found especially with samples containing both cellulose I and II, were separated by means of Pearson-VII-functions (comp. (7))

$$P(2\vartheta) = I_{max} \; 1+4 \, ß^{-2} \, (2\vartheta - 2\vartheta_{max})^2 \, (2^{1/m} - 1)^{-m} \qquad (3)$$

with ß as half the maximum width and m as a parameter influencing the shape of the curve in the transition range from Gauss to Lorentz type. Peak separation is demonstrated in Fig. 4, with cellulose I crystalline peaks. The influence of lattice distortions of the second kind was neglected, as it was estimated to amount to less than 10 % of the particle dimensions thus obtained. An average number of lattice planes queued up across the crystalline regions was calculated using the well known interplanar spacings (Fig. 5). The number of lattice planes as a yard-stick of lateral crystallite dimensions is definitely of advantage in comparing different polymorphs of cellulose, as the influence of differing unit cell sizes is eliminated. By alkali treatment, the average number of lattice planes queued up in the cellulose I crystallites increases with c_{NaOH} of the steeping lye. After complete phase transition to cellulose II, the number of (101) as well as ($10\bar{1}$) lattice planes is about the same as in

EBSCOhost - printed on 2/13/2023 3:45 AM via . All use subject to https://www.ebsco.com/terms-of-use

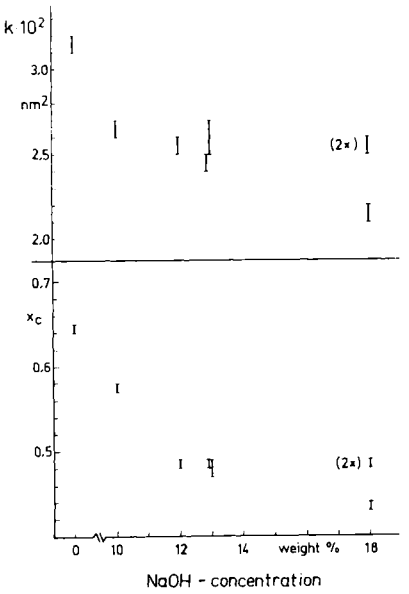

Fig. 3. Degree of crystallinity x_c and disorder parameter k in dependence on NaOH-concentration.

the original state.

If a sample completely transformed to cellulose II is treated a second time with 18 % aqueous NaOH, recrystallization occurs as shown by the increase in x_c (comp. Fig. 3). In this case the number only of the $(10\bar{1})$ and not of the (101) planes increases (Fig. 5), it may be assumed that additional polymer chains are mainly places within the (101)-planes.

The effect of NaOH treatment with increasing lye concentration on the microfibrillar morphology of cellulose linters is demonstrated by the TEM-micrographs in Fig. 6. Significant changes occur within the concentration range of lattice transition. After complete phase transformation to cellulose II, very small and slender microfibrils are dominant. Even more drastic morphological transition were found with other types of cellulose (5).

EBSCOhost - printed on 2/13/2023 3:45 AM via . All use subject to https://www.ebsco.com/terms-of-use

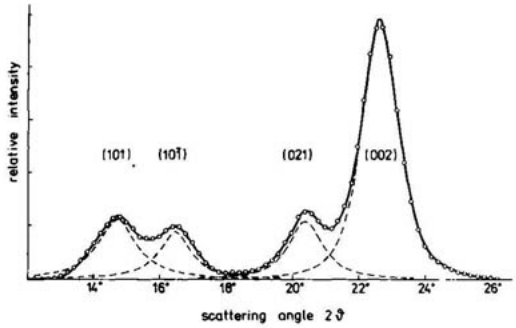

Fig. 4. Peak separation of a cellulose I scattering curve (circles) by means of Pearson-VII-functions (dotted lines).

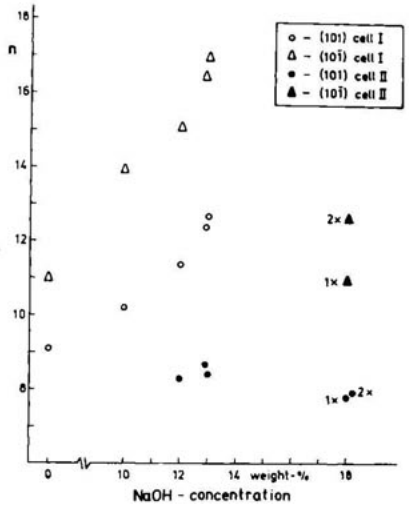

Fig. 5. Averaged number n of lattice planes as a measure for lateral crystallite sizes versus NaOH-concentration.

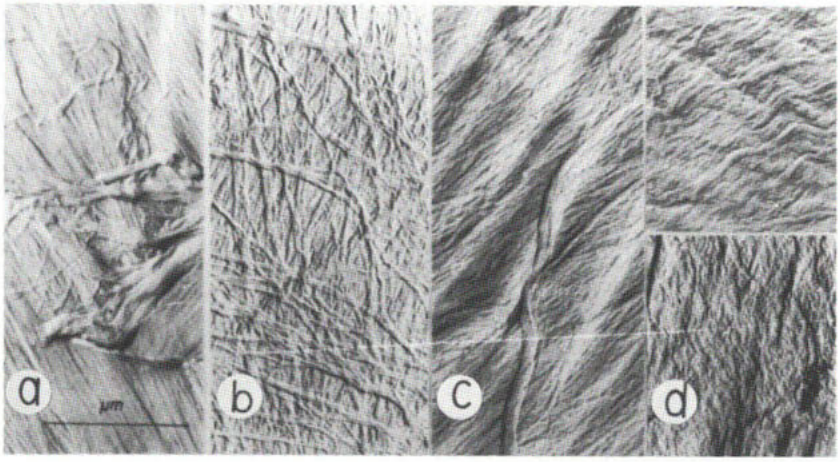

Fig. 6. Effect of aqueous NaOH treatment with increasing lye concentration on the microfibrillar morphology of cotton linters (1 h at 20 °C, neutralization, air-drying), surface replica. a) untreated cotton linters, b) 12 % NaOH, c) 15 % NaOH, d) 25 % NaOH.

EBSCOhost - printed on 2/13/2023 3:45 AM via . All use subject to https://www.ebsco.com/terms-of-use

Structural changes after treatment with ethanolic NaOH-solution

According to (12), a significantly changes phase transition behaviour may be expected by employing ethanol instead of water as the reaction medium in alkali treatment. As shown for the first time by Chanzy (13), formation of a shish-kebab-like structure may occur with cellulose in ethanolic alkali, if a prehydrolyzed sample and appropriate conditions of treatment are employed.

From our own work on cellulose alkalization with ethanolic NaOH the question of shish-kebab formation in dependence on sample-type and time of treatment will be the main point in this context in order to discuss the generalizability of Chanzy's findings. As seen from Table 1 our cellulose samples differ significantly in degree of order, which nevertheless is generally lower than that of Valonia cellulose employed by Chanzy.

Table 1. Supermolecular Order of Different Cellulose Types

Sample	Degree of crystallinity x_c %	Disorder parameter k 10^{-2} nm^2
Bacterial cellulose	73 - 79	3.3 - 3.9
Cotton linters	64 - 65	3.1 - 3.2
Spruce wood pulp	46 - 52	1.8 - 2.1

Treatment with ethanolic NaOH (10 % NaOH in a 80:20 vol.% ethanol/water mixture) resulted in a gradual decrease in x-ray crystallinity, arising at a nearly amorphous cellulose after sufficient long times of treatment. Also a significant decrease in DP was found. The partial reversibility of Na-cellulose formation already mentioned in connection with aqueous alkali proved to be much more pronounced with the ethanolic lye.

The influence of treatment time on fibrillar morphology, especially on shish-kebab formation, is demonstrated in Fig. 7 with a prehydrolyzed sample of bacterial cellulose (DP = 750) still showing an intact microfibrillar structure (Fig. 7a). After about 14 h of treatment a well-developed shish-kebab structure has grown on fibrillar backbones (Fig. 7b).

A prolonged treatment leads to a degradation of the lateral lamellae, and finally, after 24 h or still longer times of treat-

EBSCOhost - printed on 2/13/2023 3:45 AM via . All use subject to https://www.ebsco.com/terms-of-use

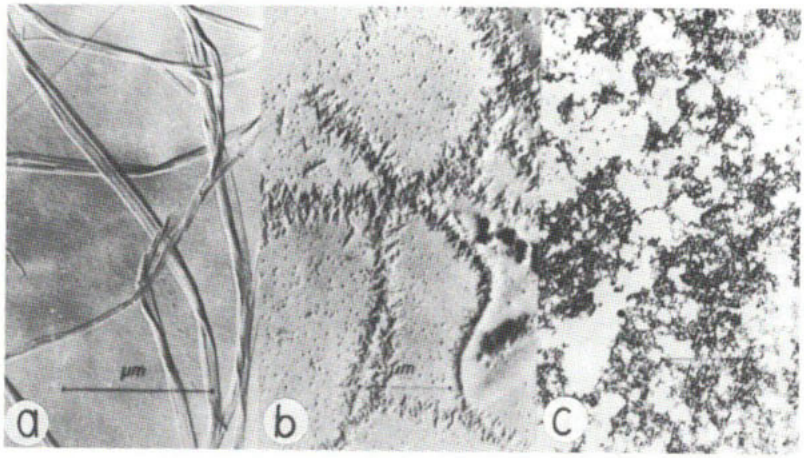

Fig. 7. Effect of time of treatment with an ethanolic NaOH-medium (10 % w/v) on prehydrolyzed bacterial cellulose (hydrolysis: 1:1 mixture of glacial acetic acid and 70 % perchloric acid in H_2O for 7 h at 20 °C, DP = 750), neutralization in a mixture of 80 % ethanol and 20 % water, suspension preparation;
a) prehydrolyzed bacterial cellulose,
b) 18 h treatment,
c) after 24 h or longer times of treatment.

ment to a total disintegration of the strand structure. Totally disoriented, single or agglomerated globular particles are remaining then as a residue of the original morphology (Fig. 7c). Obviously, shish-kebab formation passes through an optimum with time of treatment.

To decide whether a hydrolytic pretreatment is a prerequisite of shish-kebab formation, a native sample of bacterial cellulose (DP≈2000) was treated for 18 h with ethanolic NaOH. The appropriate EM-micrograph shows a shish-kebab-like structure (Fig.8a); from the x-ray diagram a rather low degree of order with mainly cellulose II as the crystalline phase can be concluded. Also with this sample, the destruction of the shish-kebab structure after prolonged times of treatment (72 h) is confirmed (Fig.8b), accompanied by a drastically reduced state of order nearly down to amorphity. Thus prehydrolysis of the sample obviously is not a prerequisite of shish-kebab formation, while some kind of decrease in DP, in our case by alkaline-oxidative degradation, may be necessary to ensure a sufficient high mobility of chains or

EBSCOhost - printed on 2/13/2023 3:45 AM via . All use subject to https://www.ebsco.com/terms-of-use

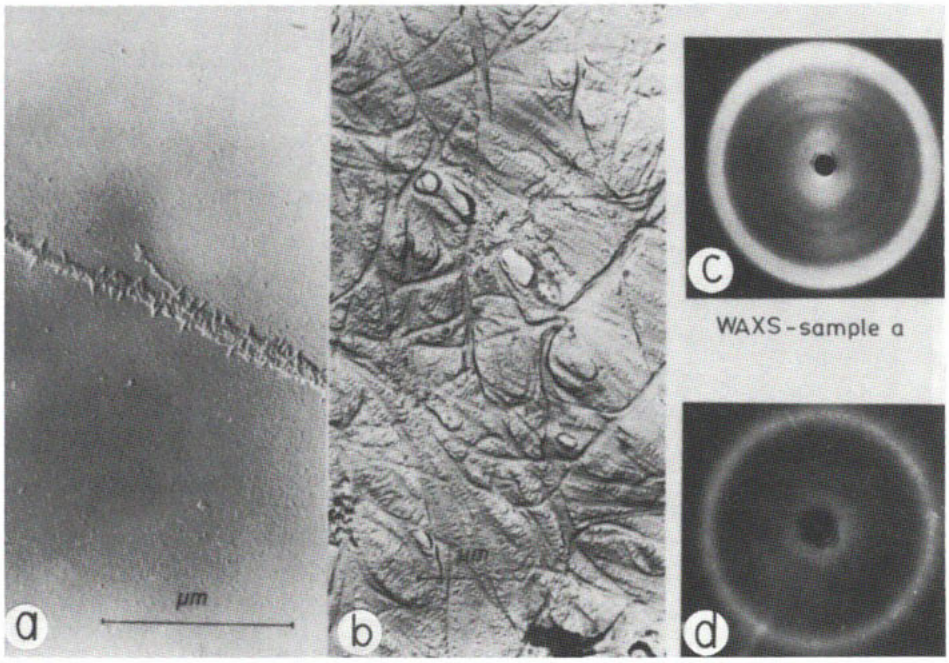

Fig. 8. Shish-kebab-like structures. Treatment of initial bacterial cellulose (DP: 2000) with ethanolic NaOH, preparation as in Fig. 7.
a) 18 h treatment, suspension technique,
b) 72 h treatment, surface replica technique,
c) WAXS diagram of sample a),
d) WAXS diagram of sample b).

chain fragments.

We also succeeded in obtaining shish-kebabs from spruce wood pulp (Fig. 9), but not from linters (Fig. 10). With the latter, globular morphological elements were found after sufficient long times of treatment, resembling in their mutual position the habitus of the original microfibril. Considering the ranking of the different samples in degree of crystallinity, it may be concluded from our and Chanzy's findings, that no integral order parameter can be discussed as a decisive criterion of shish-kebab formation. Besides a sufficiently low DP, special morphological features of the samples, which will be discussed later, have to be taken into account as a necessary prerequisite for the formation of this special morphological structure in cellulose.

EBSCOhost - printed on 2/13/2023 3:45 AM via . All use subject to https://www.ebsco.com/terms-of-use

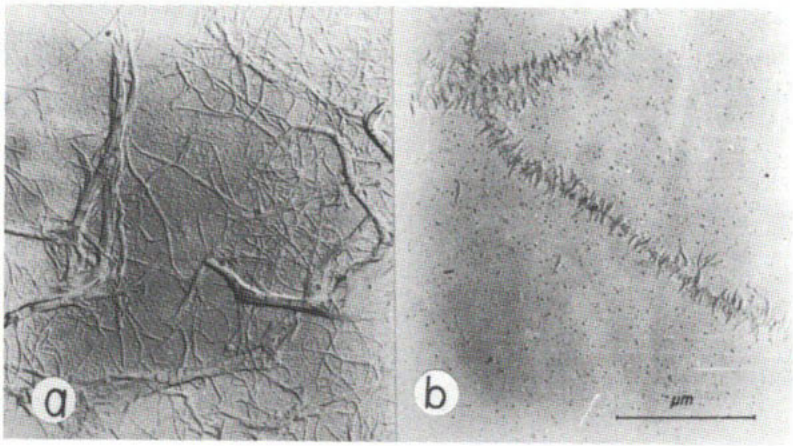

Fig. 9. Shish-kebab structures. Effect of treatment of prehydrolyzed spruce wood pulp (hydrolysis: 45 % H_2SO_4, 30 s) with ethanolic NaOH, preparation as in Fig. 7.
a) Microfibrils of untreated spruce wood pulp.
b) 14 h treatment with ethanolic NaOH.

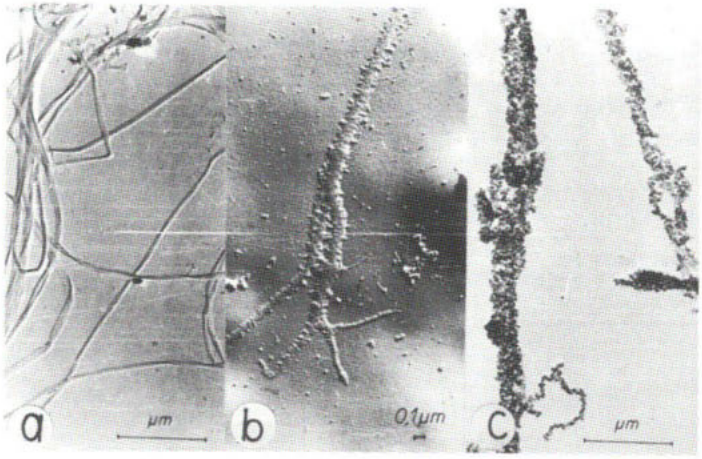

Fig. 10. Effect of treatment of an acetate grade cotton linters with ethanolic NaOH, preparation as in Fig. 7.
a) Microfibrils of untreated cotton linters.
b) 18 h treatment.
c) 18 h treatment of hydrolyzed cotton linters (hydrolysis: 45 % H_2SO_4, 30 s).

EBSCOhost - printed on 2/13/2023 3:45 AM via . All use subject to https://www.ebsco.com/terms-of-use

Discussion and Conclusion

From the numerous physical and chemical aspects and open problems of cellulose I ⟶ cellulose II phase transition via Na-cellulose the changes in supermolecular structure and in microfibrillar morphology in dependence on alkali concentration and reaction medium (water-ethanol) have been chosen as the topic of this contribution. For an interpretation of the results presented here it seems appropriate to refer to a critical survey of current models of cellulose physical structure given by us recently (8), and arriving at the conclusion that a fringed fibrillar model according to Hearle (14) with non-folded cellulose chains might provides the most suitable basis for a tentative discussion of all of our experimental results obtained so far on this topic.

Fig. 11 gives an impression of a refined version of this model, which may be considered as some kind of schematized insight into a microfibril on a sub-EM level. The decisive point of this model is the assumption of the existence of ordered fibrillar regions of different lateral dimensions and different degree of mutual branching, and also of disordered regions.

First we shall discuss the action of aqueous lye in dependence on the NaOH-concentration c_{NaOH} as it was found mainly employing cotton linters. At low c_{NaOH} the chains in the disordered regions are reached, followed with increasing c_{NaOH} by small and poorly ordered crystallites, which are decrystallized during the reaction. With further increasing lye concentration, larger and larger crystallites are attacked and transformed to cellulose II. Thus it can be explained that with increasing c_{NaOH} the average lateral dimensions of the cellulose I crystallites still persisting do increase steadily. If finally also these largest and relatively most perfect crystallites are attacked by a lye of sufficiently high concentration, their chemical transformation to Na-cellulose is accompanied by a disintegration to smaller morphological units. This lateral disintegration probably proceeds along preformed lattice distortions connected with an internal structural stress. Thus, the increase in order of the remaining crystallites (Fig. 3) becomes clear. From this

EBSCOhost - printed on 2/13/2023 3:45 AM via . All use subject to https://www.ebsco.com/terms-of-use

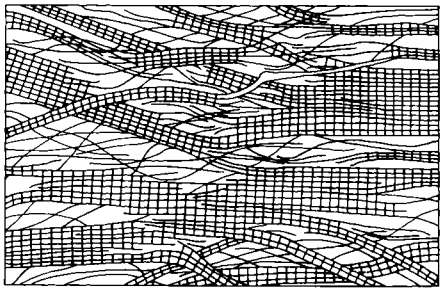

Fig. 11. Fringed fibrillar model of cellulose supermolecular structure.

point of view, the simultaneous gradual peeling off of all the cellulose I crystallites, as discussed in (15), seems to be rather improbable. According to our model consideration, a cellulose I crystallite of given lateral dimensions is either completely transformed or not at all at a given lye concentration.

Thus, from our experiments mainly performed with aqueous solution of NaOH it can be concluded that the decisive factor governing the changes in supermolecular structure during cellulose I ⟶ cellulose II transition via Na-cellulose is the lateral dimension of the crystalline strands. On the other hand, the different degree and distribution of branching of these strands may be responsible for the different behaviour of the various cellulose samples with regard to weakening or disintegration of the microfibrillar structure. It may be suggested that, depending on the type of branching, the microfibrils can be stabilized or disintegrated to smaller fibrillar elements. From this the contradictory findings in the literature (16, 17) with regard to an elementary fibril with lateral dimensions in the same range as that of the crystallites become clear. Considering the action of ethanolic NaOH-solution as compared with aqueous NaOH a modified phase transition behaviour is confirmed. The phase transition occurs at lower c_{NaOH} and generally a remarkable decrease in order is found. On the microfibrillar morphological level shish-kebab formation can accompany lattice transition, depending on cellulose provenience. According to our model consideration the degree and/or type of branching of the original microfibrillar strands may be the decisive point in the formation process of this special morphology. In dependence on the

EBSCOhost - printed on 2/13/2023 3:45 AM via . All use subject to https://www.ebsco.com/terms-of-use

length of unbranched ordered strands and of the number and mutual order of interfibrillar tie-chains single backbone fibrillae may be individualized, thus inducing growth of a shish-kebab by recrystallization of chain fragments of sufficient mobility onto this backbone. Thus shish-kebab formation might be considered as a balanced competition between backbone individualization, chain degradation and recrystallization. It may be mentioned here that according to our model shish-kebab formation cannot be considered as a suitable criterion for the existence of chain folding of cellulose, as short chain segments exist in a sufficient number indicated by the decrease in DP.

In our opinion the thickness of laterally crystallized lamellae is determined by the length of extended chain fragments and not by the folding-length of long chain molecules.

Finally, we should like to emphasize that further progress in solving the numerous open problems of the complex transition reaction cellulose I ⟶ Na-cellulose ⟶ cellulose II requires a synoptic consideration of the different structural levels of this polymer and joint efforts of chemistry and physics. With the WAXS and TEM results presented here and their interpretation based on a branched fringe-fibrillae model a more appropriate explanation of cellulose I ⟶ II phase transition has been achieved at least for aqueous systems. In this case, from our quantitative results concerning phase transition process depending on c_{NaOH} a concept of "reactive structural fractions" of cellulose could be developed (18). Resulting consequences with regard to alkali uptake and chemical composition of alkali cellulose are evident as some kind of positive feedback from polymer physics to polymer chemistry.

References

1. Philipp, B. 1985. Österreichische Chemiezeitschrift 86, 96.

2. Fink, H.-P., D. Fanter, F. Loth. 1982. Acta Polymerica 33, 241.

3. Philipp, B., H.-P. Fink, J. Kunze, H.J. Purz. 1983. Internat. Diss. Spec. Pulps Conf., Boston, TAPPI Proceedings p. 199.

EBSCOhost - printed on 2/13/2023 3:45 AM via . All use subject to https://www.ebsco.com/terms-of-use

4. Philipp, B., J. Kunze, A. Brandt. 1983. J. Appl. Polymer Sci.: Appl. Polymer Symposium 37, 393.

5. Purz, H.J., H.-P. Fink. 1983. Acta Polymerica 34, 546.

6. Purz, H.J. 1984. Dissertation B, AdW der DDR.

7. Fink, H.-P., D. Fanter, B. Philipp. 1985. Acta Polymerica 36, 1.

8. Fink, H.-P., B. Philipp: J. Appl. Polymer Sci. (in press)

9. Ruland, W. 1961. Acta Cryst. 14, 1180.

10. Vonk, C.G. 1973. J. Appl. Cryst. 6, 148.

11. Haase, J., R. Hosemann, B. Renwanz. 1973. Kolloid-Z. u. Z. Polymere 251, 871.

12. Jeffries, R., J.O. Warwicker. 1969. Text. Res. J. 39, 548.

13. Chanzy, H.D., E.J. Roche. 1975. J. Polymer Sci.: Polymer Phys. Ed. 13, 1859.

14. Hearle, J.W.S. 1958. J. Polymer Sci. 28, 432.

15. Sarko, A., T. Okano, H. Nishimura. 1983. Internat. Diss. Spec. Pulps Conf., Boston, TAPPI Proceedings p. 225.

16. Mühlethaler, K. 1960. Beih. Z. Schweiz. Forstver. 30, 55.

17. Fengel, D. 1978. Holzforsch. 32, 37.

18. Fink, H.-P., H. Dautzenberg, J. Kunze, B. Philipp: Polymer, submitted

EBSCOhost - printed on 2/13/2023 3:45 AM via . All use subject to https://www.ebsco.com/terms-of-use

AGEING OF ORIENTED AND NON-ORIENTED CELLULOSE TRIACETATE UNDER HEAT TREATMENT

M.K.Kurbanaliev, Kh.M.Abdullaev, V.A.Mirzoeva
Tajik V.I.Lenin State University
Dushanbe, 734016, USSR

Introduction

This paper deals with the orientation of rigid polymers, and of cellulose triacetate (CTA) in particular. The choice of stretching regime, essentially a strengthening of CTA, is of great practical interest. It has been shown (1,2) that the mechanism of heat ageing is quite different in non-oriented and oriented polymers. High stability of properties of oriented polymers enables the durability to be increased by modifying their orientation. The aim of this investigation is a comparative estimation of the heat stability of the non-oriented and oriented samples of CTA.

Experiments

The experiments were carried out under a wide variety of conditions: orientation temperature of 403-473 K, degree of stretching (20-95%) and rate of stretching (2.8×10^{-6} - 4.2×10^{-3} m/s). The degree of the specimen orientation was estimated from the data of birefringence (Δn) and the average angle of crystallites disorientation ($\Delta \varphi$). The destruction under heat treatment was estimated from relative changes in the tensile strength (σ) and intrinsic viscosity $[\eta]$.

Results

The tensile strength of CTA depends on temperature and degree of polymer stretching (Figs 1 and 2). As can be seen from Fig.1, under the constant temperature (403 K) and with increasing degree of stretching from 20 to 80%, CTA strength increases from

Morphology of Polymers
© 1986 Walter de Gruyter & Co., Berlin · New York - Printed in Germany.

EBSCOhost - printed on 2/13/2023 3:45 AM via . All use subject to https://www.ebsco.com/terms-of-use

140 to 180 MPa, respectively. With further increase in the degree of stretching (to 95%), σ decreases. Such analogy is observed at 423 and 443 K; however the strength values are decreased to some degree.

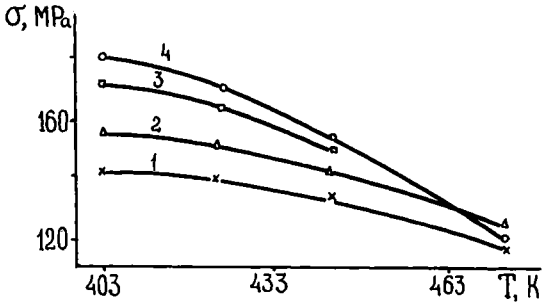

Fig.1. The dependence of CTA strength on the orientation temperature. Sample stretching: 1-20, 2-40, 3-95, 4-80%.

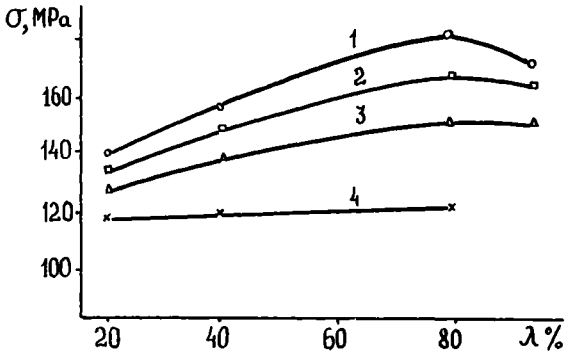

Fig.2. The dependence of CTA strength on the stretching degree λ(%) of samples oriented at the temperatures: 1-403, 2-423, 3-443, 4-473 K.

When plotted against stretching degree (Fig.2), the tensile strength initially increases and then falls, the rate of both processes being dependent on temperature and stretching degree. At 473 K, no lengthening of CTA can be observed at all stretching degrees, and σ appoaches values for not oriented polymers.

It is interesting to note, that the stretching leads to an increase in strength up to λ=80%; then, σ either remains nearly constant (423 and 443K) or decreases (403 K), when rising λ to

EBSCOhost - printed on 2/13/2023 3:45 AM via . All use subject to https://www.ebsco.com/terms-of-use

95%. The stretching at 473 K is not adequate because of the sample destructions. As can be seen, the above-mentioned methods of orientation do not lead to a significant lengthening of CTA, even under such broad variations of stretching conditions. Strength of samples oriented in such regimes increases to 130 - 180 MPa (this value is equal to 8-50% of the initial strength).

It was pointed out earlier (3) that the durability of non-oriented CTA films at $T > T_g$ is related to stress applied to the sample. At $\sigma > \sigma'$, where σ' is the stress corresponding to the break point on the dependence $\ln\tau$ vs σ, the sample destroys before lengthening and, at $\sigma < \sigma'$, the orientation stretching precedes destruction of the polymer, which leads to a considerable increase in its durability. This effect can be used to find a suitable regime for CTA orientation. From the durability isotherm of CTA at 473 K (Fig.3), we can see that $\sigma' = 41$ MPa. When the sample is exposed to a stress of 30 MPa (condition $\sigma < \sigma'$) for one hour, polymer strength increases to 260 MPa (at 473 K) i.e. 110% of the initial value. Sample orientation at 443 K and lower σ (10 MPa) leads to lower strengths (210-225 MPa). However, it is not difficult to show that this strength is much higher than that of the sample oriented in rapid regime. These data indicate that the durability isotherms of CTA contain an important information about relaxation and destruction processes in the polymer, which can be used for preparing highly durable samples.

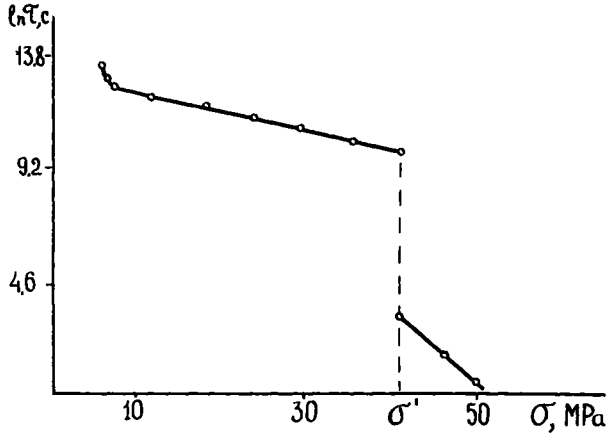

Fig.3. Logarithmic dependence of CTA durability vs stress at 473 K.

EBSCOhost - printed on 2/13/2023 3:45 AM via . All use subject to https://www.ebsco.com/terms-of-use

The structure investigation have also shown that in regimes of CTA stretching the orientation, crystallization and thermo-oxidative degradation processes are developed. For samples oriented in the slow regime (1st method), the value of birefringence is $(2.1 - 2.3) \times 10^{-9}$ m and, for samples oriented in the rapid regime (2nd method), it is $(5.2 - 5.3) \times 10^{-9}$ m. The high degree of polymer chains orientation obtained by the 2nd method, leading to a greater durability of samples in comparison with those oriented by the 1st method, should be explained. However, the main reason of strength difference of samples oriented in various regimes does not consist in this fact. Really, the annealing of CTA films oriented by the 1st method during one hour at 473 K leads to the increase in their birefringence approximate to the respective values for the samples oriented by the 2nd method. Despite this fact their strength does not vary considerably.

The degree of the CTA destruction stretched in the slow regime as compared to the rapid one, is even higher (0.7 and 0.82 respectively). It points out to the fact, that the CTA strength properties are not determined by the transformations on the molecular level.

Physico-mechanical properties of polymers are determined to a great extent by the character of their supermolecular structure (4). Accordingly, also the tenacity of CTA films oriented under different conditions seems to be determined by some peculiarities of the supermolecular structure formation. This statement has been confirmed by electron microscopy investigations.

In the slow regime of stretching, supermolecular structure elements are merged in the particles of larger sizes, and tightly packed particles oriented in the direction of stretching appear (Fig.4). This leads to a significant increase in the CTA strength oriented by the 2nd method.

In the rapid regime of stretching, there is not such variation in density and sizes, although supermolecular structure elements possess some orientation in the direction of stretching (Fig.5). A non-significant increase in strength, as compared with the initial value of CTA, corresponds to this structure.

EBSCOhost - printed on 2/13/2023 3:45 AM via . All use subject to https://www.ebsco.com/terms-of-use

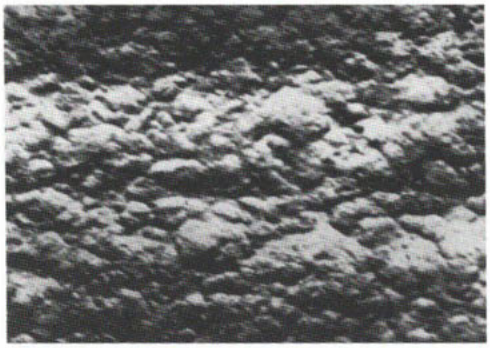

Fig.4. Electron micrographs of CTA supermolecular structure oriented in the slow regime (24750x).

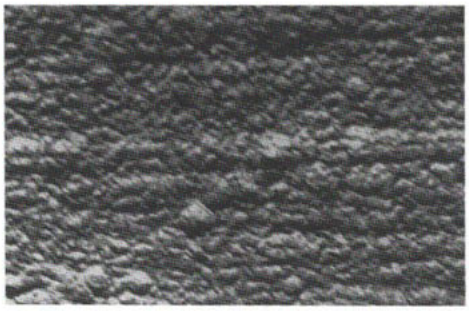

Fig.5. Electron micrographs of CTA supermolecular structure oriented in the rapid regime (24750x).

So, the durability of oriented CTA are not defined by their degree of stretching, as demonstrated by Δn and $[\eta]$. The specimen oriented under different regimes possesses various supermolecular structures, and its durability is defined by the character of supermolecular structure formed after the orientation.

The main processes of heat ageing of CTA are the crystallization and thermal-oxidative degradation. For both, the non-oriented and oriented specimens, the degree of destruction (demonstrated by a decrease in $[\eta]$) is the most essential during the first period of annealing ($t < 6$ hours). Under such conditions, however, the durability of specimen even increases (by 10-20 MPa) and remains stable during 24 hours (Fig.6). At $t > 24$ hours, the strength of all specimens decreases, despite the stability of the values Δn and $\Delta\varphi$.

EBSCOhost - printed on 2/13/2023 3:45 AM via . All use subject to https://www.ebsco.com/terms-of-use

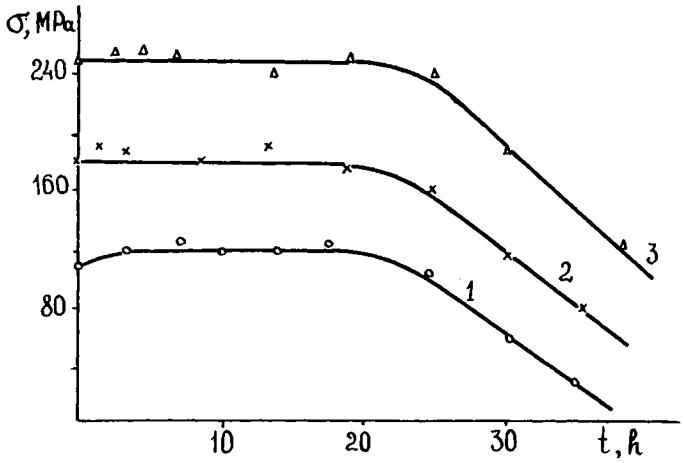

Fig.6. Strength dependence on the annealing time at 473 K for CTA: non-oriented (1), and oriented in the rapid (2) and slow (3) regimes.

The observed dependence of $\sigma(t)$ seems to be connected with the improvement of the CTA structure, the increase in the crystallinity degree, and the orientation of crystallites and chains during the first hours of annealing. These processes prevail over the destruction processes in this stage. Further decrease in strength is due to the destruction of the amorphous intercrystallite regions.

The stretching increases the initial strength of CTA which, under constant rate of destruction, leads to an increase in the durability.

References

1. Rapoport N.Ya., S.I.Berulava, A.L. Kovarskii and others. 1975. On the connection between the kinetics of thermal-oxidative degradation and the structure and the molecular mobility in oriented polypropylene. Vysokomolek. Soed. A 17, 2521-2527.
2. Emanuel N.M. 1980. The structural-kinetics aspects of ageing and stabilization of polymers. Vysokomolek.Soed. A 20 , 2653-2661.
3. Narzullaev B.N., Kh.M.Abdullaev and V.A. Mirzoeva. 1979. The

EBSCOhost - printed on 2/13/2023 3:45 AM via . All use subject to https://www.ebsco.com/terms-of-use

study of temperature-time dependence of cellulose triacetate strength at temperatures close to that of its degradation.Vysokomolek.Soed. A 21, 603-607.

4. Kargin V.A. and G.L. Slonimskii. 1967. Essays of physico-chemistry of polymers. Khimiya, Moscow. p. 232.

EBSCOhost - printed on 2/13/2023 3:45 AM via . All use subject to https://www.ebsco.com/terms-of-use

EBSCOhost - printed on 2/13/2023 3:45 AM via . All use subject to https://www.ebsco.com/terms-of-use

A STUDY ON CRYSTALLINE STRUCTURE OF POLYGLYCINE I AND II AT LOW TEMPERATURE

J. Garbarczyk

Politechnika Poznańska, Instytut Technologii i Inżynierii Chemicznej, Pl.Skłodowskiej-Curie 2, 60-965 Poznań, Poland

Introduction

This work is a continuation of our earlier studies of the crystalline structure of polymers under extreme thermal conditions. It has been determined previously that during lowering of temperature, changes in crystal lattice of polyamide-6 (αPA6) take place only in the direction perpendicular to the planes with intermolecular hydrogen bonds (1). Analysis of these results in the light of pleated structure of PA6 proposed by Stepaniak et al. (2) suggested that magnitude of such an anisotropic shrinkage can be connected with the length of methylene part between amide groups. To prove this hypothesis we have undertaken investigation of polyglycine (PG), one methylene group of which contrasts well with five-membered chain in PA6.

Experimental

In our study we have used polyglycine (M.W. 3000) consisting of a mixture of monoclinic (PGI) and hexagonal (trigonal) (PGII) modifications. The samples examined were in the form of a powder. The investigation was carried out in temperature range of 303-93 K on a horizontal diffractometer HZG-3 equipped with attachment KRN-190, using Ni-filtered CuK_{α} radiation. Liquid nitrogen was used as a cooling agent. Each sample was kept at determined temperature (step 40°C) for 15 min, and subsequently X-ray measurement was carried out. The X-ray diffraction pattern in the angle region of 5-25° (θ) was analysed.

Morphology of Polymers
© 1986 Walter de Gruyter & Co., Berlin · New York - Printed in Germany.

EBSCOhost - printed on 2/13/2023 3:45 AM via . All use subject to https://www.ebsco.com/terms-of-use

Results and Discussion

The results obtained have shown that in monoclinic phase (PGI), changes occur only in the direction perpendicular to (001) planes, while distance between (200) planes remain unchanged (Fig.1). According to Lotz (3) polyglycine I has a sheet structure of hydrogen-bonded chains. The distance between chain axes within such a sheet (4.77 Å) corresponds to that between (200) planes.

Table 1. Relative Changes of Interplanar Spacing in Reference to Distances Observed at Temperature 303 K before Cooling

Planes	Values of relative changes at temperatures					
	253 K	213 K	173 K	133 K	93 K	303 K After cooling
A.Monoclinic						
200	-0.005	-0.005	-0.005	-0.005	-0.005	-0.001
001	-0.005	-0.005	-0.008	-0.011	-0.012	-0.000
B.Hexagonal						
010	-0.006	-0.010	-0.015	-0.019	-0.025	-0.002
100						
101	-0.013	-0.020	-0.025	-0.030	-0.035	-0.001

The fact that the latter does not change with decreasing temperature (Table 1) indicates that structural stability of a sheet, similarly as in PA6 (1), is determined by hydrogen bonds. On the other hand, the distance between (001) planes (3.40 Å) concerns the intersheet region and structural data (3) indicate that the sheets are bonded only by van der Waals forces. In the light of the above, the stability of PGI lattice in the direction perpendicular to the sheets depends on their density packing. In other words, the magnitude of the shrinkage is connected with sheet pleating and with arrangement of methyl group in relation to the plane passing through chain axes. The influence of the arrangement of methylene part on stability of intersheet structure is clearly

EBSCOhost - printed on 2/13/2023 3:45 AM via . All use subject to https://www.ebsco.com/terms-of-use

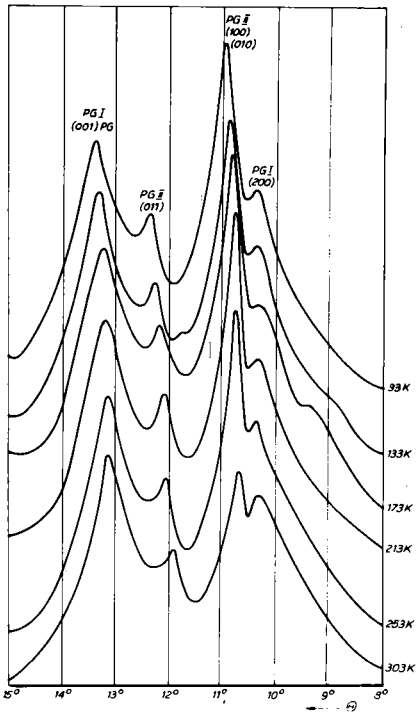

Fig.1. Changes in X-ray diffraction patterns of PGI and PGII during lowering of temperature.

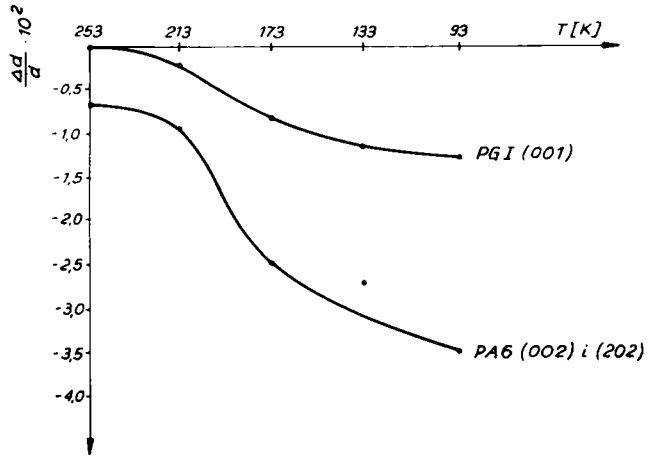

Fig.2. Relative changes of interplanar distances in PGI and PA6 vs. temperature.

EBSCOhost - printed on 2/13/2023 3:45 AM via . All use subject to https://www.ebsco.com/terms-of-use

seen when comparing results presented in this paper with those obtained earlier for polyamide-6 (1). The last compound can exist as a pleated sheet structure (2), as in case of PGI. Diagrams of relative changes of distances between corresponding planes in lattice of PGI and PA6 as a function of temperature (Fig.2) indicate that in both cases the course of phenomenon is similar. Threefold larger changes in PA6 suggest that magnitude of the shrinkage is connected not only with length of paraffinic part but also with its pleated or twisted structures. A similar suggestion was put forward by Miyasaka et al. on the basis of their investigation of oriented PA6 at low temperatures (4). They have found that parameters of unit cell along chain axes increase with decreasing temperature.

The examination of PG samples after increasing temperature back to 303 K has shown the recovery of the structure to the previous state; this fact indicates that observed changes are a result of reduction in amplitudes of oscillation and rotation of atoms rather than of phase transition. The mentioned decrease in amplitudes concerns particularly carbon atoms from methylene part because the remaining ones are more rigid due to H-bonds. The confirmation of this hypothesis can be found in paper by Kawaguchi et al. who established that the shrinkage of polyethylene unit cell perpendicularly to chain axes and a simultaneous extension towards these axes are a result of a limitation of thermal motions of atoms at low temperatures (5). Diagrams given in Fig.1 show, moreover, that in hexagonal (trigonal) modification (PGII) during decrease in temperature both observed reflections are shifted towards higher angles and the changes are larger than in PGI (Table 1). Unfortunately, these reflections have not univocal indices: at $\Theta = 10.67^{\circ}$ it can be (100) or (010), and at $\Theta = 11.89$ - (101) or (011). Therefore, the observed changes can be interpreted as a shrinkage in x, y and z directions. On the other hand, helical conformation of chains and hydrogen bonds arranged in different directions in relation to chain axes (6), prevent from the determination of the role of methylene group in stability of PGII lattice. To solve this problem a detailed structural investigation of oriented samples giving richer diffraction pattern is required.

EBSCOhost - printed on 2/13/2023 3:45 AM via . All use subject to https://www.ebsco.com/terms-of-use

Acknowledgements

The author gratefully acknowledges Dr B.Lotz of Centre de Recherches sur les Macromolécules, Strasbourg (France) for polyglycine sample and Mr. J.Witkowski of Politechnika Poznańska (Poland) for his help in X-ray measurements. These study were supported in part by Polish Academy of Sciences, Project MRI9.

References

1. Garbarczyk, J., P.Florysiak. 1981. 27th IUPAC Symposium on Macromolecules, Strasbourg 6-9 July.

2. Stepaniak, R.F., A.Garton, D.J.Carlssen, D.M.Wiles. 1979. J.Polym.Sci.,Phys.Ed. 17, 987.

3. Lotz, B. 1974. J.Mol.Biol. 87, 169.

4. Miyasaka, K., T.Isomoto, H.Koganeya, K.Uehara, K.Ishikawa, N.Ogata. 1980. J.Polym.Sci.,Phys.Ed. 18, 1047.

5. Kawaguchi, A., R.Matsui, K.Kobayashi. 1977. Bull.Inst.Chem.Res. Kyoto Univ. 55(2), 217.

6. Crick, F.H.C., A.Rich. 1955. Nature 176, 780.

EBSCOhost - printed on 2/13/2023 3:45 AM via . All use subject to https://www.ebsco.com/terms-of-use

EBSCOhost - printed on 2/13/2023 3:45 AM via . All use subject to https://www.ebsco.com/terms-of-use

THERMOTROPIC MAIN-CHAIN POLYESTERS

L.Makaruk, H.Polańska
Department of Chemistry, Technical University (Politechnika)
Noakowskiego 3, 00-664 Warsaw, Poland

B.Ważyńska
Institute of Materials Science and Engineering, Technical
Univeristy (Politechnika), Narbutta 85, 02-524 Warsaw, Poland

Introduction

The diversity of liquid-crystalline polymers, which have been synthesized over past few years, has focused the attention of scientists on the studies of structure-properties relationship, for it is well known that the chemical as well as spacial arrangement of the macromolecules affect the liquid-crystalline properties of polymer. In the present paper the thermal analysis data for thermotropic main-chain polyesters having the following structure of the repeating unit:

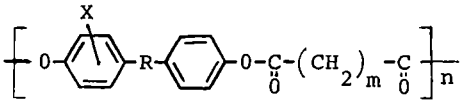

where: R = $-\overset{\overset{O}{\|}}{C}-$, $-\overset{\overset{O}{\|}}{C}-\text{Ø}-\overset{\overset{O}{\|}}{C}-$, $-\overset{\overset{O}{\|}}{C}-NH-$, $-\overset{\overset{}{\|}}{C}-$ with CCl_2

X = none or CH_3

m = 6 or 8

are reported. The studies were performed with the aim to correlate the liquid-crystalline characteristics, that is the transition temperatures, enthalpies and entropies of transitions, and temperature range of mesomorphic phase, with the structure of mesogenic and flexible segments of the macromolecules.
Polymers were obtained from the appropriate bisphenols and aliphatic dicarboxylic acid dichlorides by means of the interfacial polycondensation. The preparation of polymers and their characterization (molecular weights or η_{inh}) are described elsewhere (1-4).
The existence of liquid-crystalline phase in polymer samples was confirmed by DSC measurements and visual observations of the texture in polarized microscope. According to these studies, the polymers form nematic phase within the temperature range indicated in Table 1.

Morphology of Polymers
© 1986 Walter de Gruyter & Co., Berlin · New York - Printed in Germany.

EBSCOhost - printed on 2/13/2023 3:45 AM via . All use subject to https://www.ebsco.com/terms-of-use

Results

Table 1 summarizes the transition temperatures (from crystal to mesophase, T_m, and from liquid-crystalline phase to isotropic liquid, T_i), as well as the enthalpies and entropies of both transitions for a number of polyesters. All data were obtained from DSC measurements at the heating rate of 10°C/min. Enthalpies and entropies were estimated from DSC peak area and recalculated per mole of the repeating unit of the polymer.

Table 1. Thermodynamic Properties of Polyesters Derived from Bisphenols and Dicarboxylic Acid Dichlorides

No	Bisphenol R	Bisphenol X	Dichloride m	T_m K	T_i K	ΔH_m kJ/mol	ΔH_i kJ/mol	ΔS_m J/mol.K	ΔS_i J/mol.K
1	-C(=O)-	-	6	399	437	1.59	10.97	3.98	25.08
			8	399	416.5	8.76	7.33	21.90	18.38
2	-C(=O)-Ø-C(=O)-	-	6	498	524	1.38	9.21	2.81	17.33
			8	470	505	2.09	16.54	4.35	32.74
3	-C(=O)-NH-	-	6	491	535.5	0.96	5.78	2.01	10.67
			8	468	544	0.42	3.93	0.92	7.32
4	-C(=O)-	-	6	-	336[x]	-	2.60[x]	-	8.20[x]
	CCl_2		8	-	318[x]	-	1.78[x]	-	5.29[x]
5	-C(=O)-	m-CH_3	6	327	368	1.13	4.35	3.48	11.80
			8	331	373	3.18	3.85	9.59	10.30
6	-C(=O)-	0-CH_3	6	-	325[x]	-	2.18[x]	-	6.69[x]
			8	323	341	2.18	6.53	6.74	19.39

x Melting

As it is seen, the modification of polyester, derived from aliphatic acid dichlorides and bisphenol 1, by introducing more rigid group as in bisphenol 2 or group capable of forming the hydrogen bonds between the macrochains (bisphenol 3) increases both T_m and T_i. What is interesting yet that on increasing T_m of polyesters the effect of stiffness of the group linking the aromatic rings together or the effect of formation of the hydrogen bonds is more or less the same.

In the neighbourhood of isotropisation temperatures, however, where the hydrogen bonds are less effective, this is the molecular packing which becomes the main parameter controlling T_i. Therefore, the

EBSCOhost - printed on 2/13/2023 3:45 AM via . All use subject to https://www.ebsco.com/terms-of-use

macromolecules containing relatively more flexible amide groups (bisphenol 3) as compared to terephthaloyl ones (bisphenol 2) can be arranged more densily and the increase in T_i is more pronounced. It is worth to note that polyesters prepared from bisphenol 4 (having dichloroethylene group between the aromatic rings) do not reveal the liquid-crystalline properties at all, though studies performed on molecular models indicated that this linkage should be more rigid as compared to ketone one (bisphenol 1). We believe that in this case, the strong interactions between polar chlorine atoms restrict the ordering of macrochains and instead of two-step transition (crystal-nematic-isotropic liquid) only melting occurs.
Contrary to previously described polyesters, modification of bisphenol 1 by lateral substitution of its aromatic ring with CH_3 group leads to polymers of lowered T_m and T_i. Moreover, the decrease in both temperatures depend strongly on the position of CH_3 group in the aromatic ring and is more pronounced for ortho-substituted derivatives (even up to the disappearance of the liquid-crystalline behaviour for polyester derived from suberyl dichloride, m = 6).
As the temperature range of mesophase ($\Delta T = T_i - T_m$) is concerned the broadening of ΔT as much as twice or four times (comparing to polyester of bisphenol 1) for polyesters based on bisphenol 2 and 3 and sebacyl dichloride was observed. In the case of suberyl dichloride series, only a slight increase in ΔT was noticed for bisphenol 3 containing polyester.
The parallel situation occurred for polyesters of laterally modified bisphenols (samples 5 and 6), though the broadening of ΔT for sebacyl dichloride polyesters was not so drastic. In view of these results one can say, that for suberyl dichloride derivatives the alteration of the mesogen fragment has minor effect on ΔT as compared to sebacyl dichloride polyesters.
In Table 1 the results of ΔH and ΔS of both transitions for all polymers are also reported. One has to have in mind, however, that they were obtained for samples which might differ in degree of crystallinity (or liquid-crystalline phase). They have, therefore, little absolute significance, although we use them for the comparison of the degree of molecular order in the respective phases, assuming that the samples do not differ substantially in phase content. As it is known, the mesophase-isotropic liquid transition is governed largely by entropy. For this transition the expected value of entropy is about 15 - 45 J/K.mol (5), but usually it is much smaller, indicating that the orientational order in liquid-crystalline phase is rather imperfect. Since ΔS_i represents the difference between the entropy of fully isotropic liquid and mesophase, the higher this value the higher molecular order in mesophase. As it is seen from ΔS_i data in Table 1, the values obtained for the polymers studied are close to those usually found in the literature, though lower than predicted by theory (5).
For polyesters of sebacyl dichloride as flexible segment, ΔS_i is higher for the polymer containing bisphenol 2 in the macromolecule than bisphenol 1 or 3. It is very likely then to assume that the rigidity of bisphenol 2 molecule enables the macromolecules to pack regularly in liquid crystalline state, since the positioning of stiff molecules is easier than those which still exhibit certain mobility (as in bisphenol 1 or 3). The values of ΔH_i for those three polyesters are also in favour of such explanation.
For polyesters with laterally substituted mesogens (bisphenol 5 and 6) both ΔS_i and ΔH_i are lower than for polyester containing

EBSCOhost - printed on 2/13/2023 3:45 AM via . All use subject to https://www.ebsco.com/terms-of-use

a non-modified bisphenol (sample 1), except for the one obtained from bisphenol 6 and sebacyl dichloride. It is then very likely that for this group of polymers the steric hindrances caused by the lateral substituents restrict the ordering of the macromolecules in regular manner. Such substituents are also expected to decrease the packing density of polyesters.
This result is somehow in contradiction with those reported by Lenz et al. (6) for polyesters containing three aromatic rings in the repeating unit (with the middle one substituted by CH_3 group). The authors have observed the increase in ΔS_i for this polyester and explained it by interlocking of lateral CH_3 groups on the adjacent polymer chains which reduced the molecular mobility of the chains. The discrepancy in behaviour of both systems might be due to differences in molecular conformation, which could be responsible for various portions of free volume in the close vicinity of each molecule.
The influence of the length of the aliphatic spacer on the molecular order of polyesters having the same mesogenic unit can also be discussed. From the comparison of the entropies and enthalpies it can be concluded that our polyesters of shorter aliphatic segments (m = 6) generally exhibit the higher degree of order in the liquid-crystalline state.
In view of the results presented above, it is justified to say that by selecting the appropriate molecular structure of the mesogen and the flexible spacer one can control the characteristics of liquid-crystalline thermotropic polymers in order to obtain the material of desirable properties. This paper presents some structure-properties relationships and offers an attempt for explanation of their physical origin.

Acknowledgement

The authors are grateful to Polish Academy of Sciences for the support of this work. We wish to express our appreciation to Dr.Irena Daniewska of Warsaw Technical University and Dr.Andrzej Wasiak of Polish Academy of Sciences for their helpful suggestions during the course of this study and preliminary discussion of this paper.

References

1. Makaruk, L., H.Polańska. 1984.Liq.Cryst.Ordered Fluids 4, 154.
2. Makaruk, L., H.Polańska, B.Ważyńska. 1983.Polym.Prepr.(Am.Chem. Soc.Div.Polym.Chem.)24(2), 260.
3. Makaruk, L.,H.Polańska,B.Ważyńska.1985. In: Polymeric Liquid Crystals (A.Blumstein, ed.). Plenum Press, New York and London,p. 265.
4. Makaruk,L.,H.Polańska,B,Ważyńska: Polymer J.(in press).

EBSCOhost - printed on 2/13/2023 3:45 AM via . All use subject to https://www.ebsco.com/terms-of-use

5. Wunderlich, B., J. Grębowicz. 1984. Advances in Polymer Science 60/61, 1.

6. Lenz, R.W., J.I. Jin. 1984. Liq. Cryst. Ordered Fluids 4, 347.

EBSCOhost - printed on 2/13/2023 3:45 AM via . All use subject to https://www.ebsco.com/terms-of-use

EBSCOhost - printed on 2/13/2023 3:45 AM via . All use subject to https://www.ebsco.com/terms-of-use

THE ROLE OF MESOMORPHIC STATE IN THE FORMATION OF STRUCTURE AND PROPERTIES OF POLY(URETHANE METHACRYLATES)

L.A. Sukhareva

Technology Institute of Meat and Milk Industry, Talalikhina 33, 109818 Moscow, USSR

Z. Pelzbauer

Institute of Macromolecular Chemistry, Czechoslovak Academy of Sciences, 162 06 Prague 6, Czechoslovakia

Introduction

Oligourethane methacrylates of regular structure form polymers noted for their high space network density and physico-mechanical characteristics (1). The formation of coatings from these systems is, however, accompanied by the onset of significant internal stresses comparable with their adhesion strength (2).
The present paper is concerned with the effect of mesomorphic state on the process of melting of oligourethane methacrylates and their polymerization, and on the structure and properties of the polymers obtained.

Results and Discussion

The oligomers studied were aromatic and aliphatic oligourethane methacrylates (OUM) of the general formula (3)

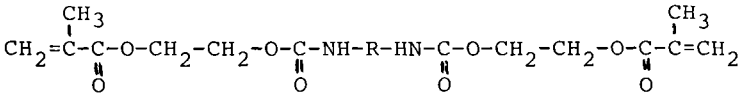

where R = $-(CH_2)_2-$ OUM-1; $(CH_2)_6$ - OUM-2; $(C_6H_5-CH_2-C_6H_5)$ - OUM-3.

Oligomer block flexibility was evaluated by the proton paramagnetic resonance (PMR) technique. As can be seen from the PMR spectra,

Morphology of Polymers
© 1986 Walter de Gruyter & Co., Berlin · New York - Printed in Germany.

EBSCOhost - printed on 2/13/2023 3:45 AM via . All use subject to https://www.ebsco.com/terms-of-use

the oligomers under examination can be arranged in the following series in terms of oligomer block flexibility: OUM-2 > OUM-1 > OUM-3. Depending of the length and flexibility of the oligomer block, crystallization from melts and solutions in poor solvents yields lamellar structures, radial and annular spherulites. The temperature range of melting and melting point increase with the increased supermolecular organization, crystal size and non-uniformity of crystal size and structure.

The OUM-2 oligomer yields the most homogeneous crystals in terms of their size and morphology. This oligomer is characterized by the lowest melting point (74°C) and a narrow melting temperature range of 2-3°C. When increasing the rigidity of an oligomer block, particularly by incorporation of aromatic fragments into the chain, melting points rise to 100°C and melting temperature range expands to 20°C (Fig.1).

Structural transformations during oligomer melting exert a marked effect on the polymerization rate, and the structure and properties of space network polymers. Oligomers that crystallize from melts and yield radial and annular spherulites undergo melting via the step of smectic and nematic mesophases formation (Fig.2), which

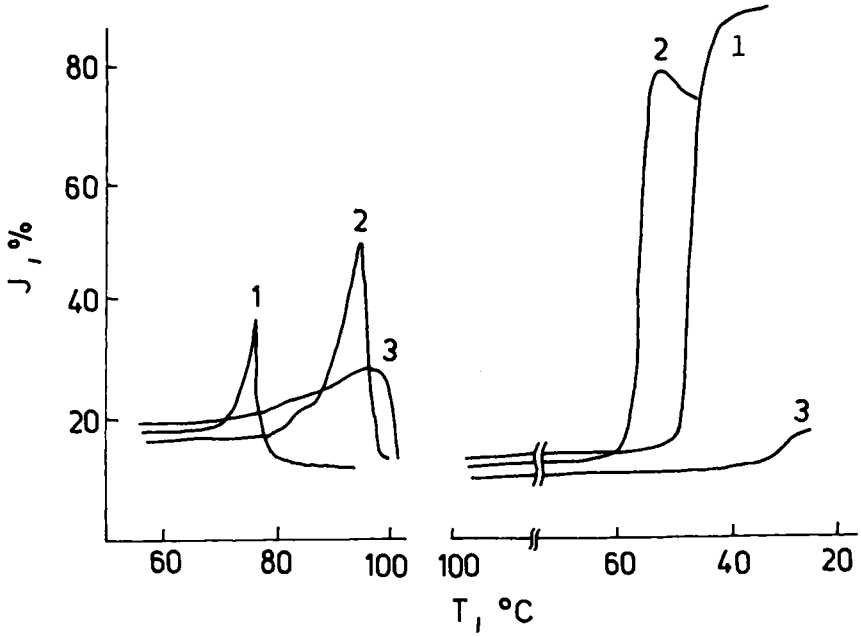

Fig.1. Melting and crystallization kinetics of OUM-2 (1), OUM-1 (2), OUM-3 (3) oligomers.

EBSCOhost - printed on 2/13/2023 3:45 AM via . All use subject to https://www.ebsco.com/terms-of-use

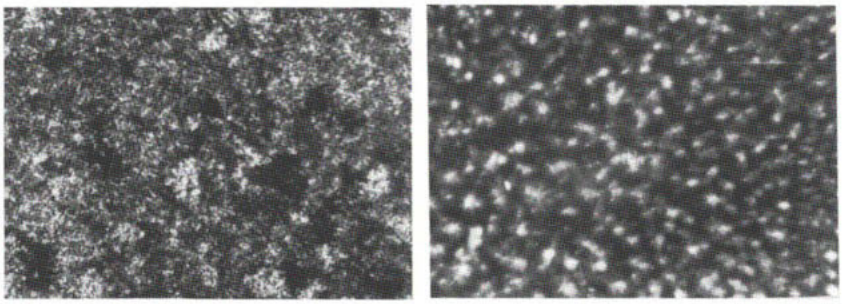

Fig.2. Mesomorphic structures formed during melting of OUM-1(a) and OUM-2(b) crystals.

leads to significant acceleration of the polymerization process, causing it to proceed to high conversion level (Fig.3).
When oligomer block rigidity is enhanced by incorporation of aromatic fragments into the chain, the oligourethane methacrylate crystallization yields structures of a higher supermolecular organization comprising parallel plates stacked so as to form parallelepipeds and pyramids. In the course of melting of such structures the polymerization proceeds very slowly, preferably at the interphase, the conversion being low.

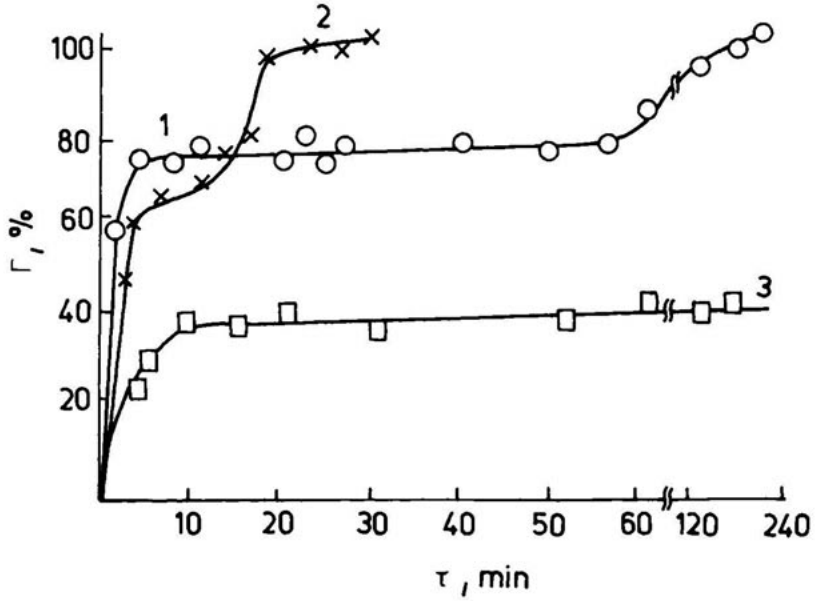

Fig.3. Polymerization kinetics of OUM-1(1), OUM-2(2) and OUM-3(3) obtained by crystallization from a poor solvent.

EBSCOhost - printed on 2/13/2023 3:45 AM via . All use subject to https://www.ebsco.com/terms-of-use

The level of crystal organization and the kinetics of oligomer polymerization during melting are markedly affected by the nature of the solvent used to carry out oligomer crystallization. When the crystals are formed from oligomer solutions in good solvents, the sequence of oligomer order, as regards the rate and degree of polymerization is reversed with respect to the series of oligourethane methacrylates studied (Fig.4). In this case, the OUM-2 oligomer polymerization proceeds at the slowest rate and to a low conversion. The aromatic oligomer (OUM-3) having a higher supermolecular organization and crystallized out of a good solvent polymerizes at a much faster rate and to a higher conversion than does the OUM-2 oligomer.

The crystals obtained from the solutions of oligomers in good solvents were shown by scanning optical microscopy to possess a lower level of supermolecular organization. Accordingly, the ability of

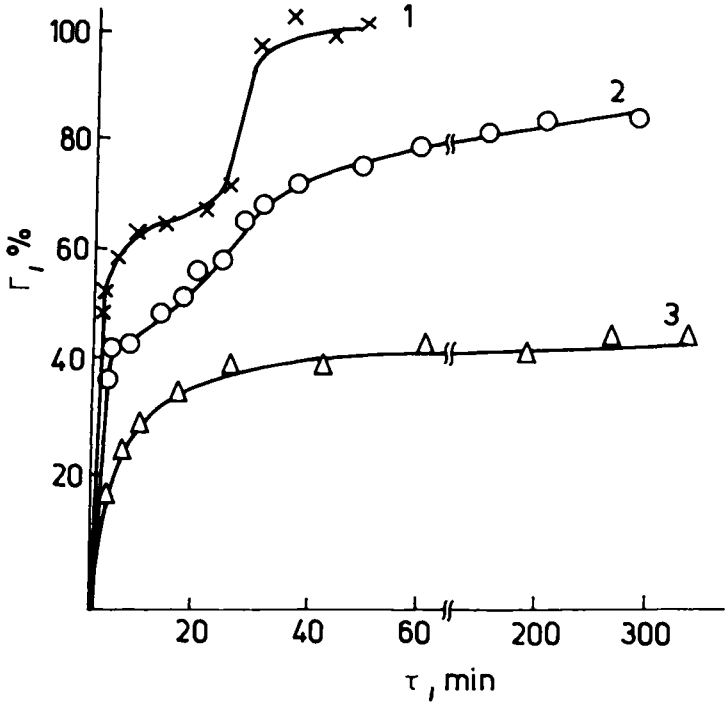

Fig.4. Polymerization kinetics of OUM-3(1), OUM-2(2) and OUM-1(3) obtained by crystallization from benzene solutions.

EBSCOhost - printed on 2/13/2023 3:45 AM via . All use subject to https://www.ebsco.com/terms-of-use

crystals to form mesophases during the oligomer melting manifests itself exclusively in the case of oligourethane methacrylates with more rigid oligomer blocks.

Hence, varying the quality of solvents used in the oligomer crystallization exerts different effects on the kinetics of polymerization depending on the supermolecular organization level of oligomers. For oligourethane methacrylates having more flexible oligomer blocks, crystallization from solutions in a good solvent results in a sharp decrease in the polymerization rate and final conversion. In the case of oligomers with more rigid oligomer blocks and a high supermolecular organization formed under the same crystallization conditions, the rate and degree of polymerization are much higher compared to the polymerization from solutions in an inferior solvent used to obtain crystals.

The structure of oligomer crystals and the crosslinking polymerization during their melting exert an enhanced effect on the properties of coatings. Thus, the melting of crystals obtained from oligomer solutions in poor solvents results in the formation of a homogeneous globular structure (structural size element of 20-30 nm) from the OUM-2 oligomer. With increased supermolecular organization of the crystals and their greater inhomogeneity in terms of morphology and size, OUM-1 and OUM-3 coatings have been found to display an imperfect heterogeneous structure comprising globules and aggregates and incorporating fragments of incompletely molten crystals. It is feasible to obtain in the OUM-1 and OUM-2 oligomer coatings a homogeneous ordered structure by carrying out the oligomer crystallization from solutions in good solvents.

The nature of structural transformations in the formation of coatings from crystalline oligourethane methacrylates exerts a marked effect on the magnitude and kinetics of the build-up internal stresses (Fig.5). Where use is made of oligourethane methacrylates crystallized from a poor solvent, the greatest internal stresses arise in the OUM-3 coatings having a non- uniform heterogeneous structure. The minimal internal stresses are observed in coatings obtained from the OUM-2 noted for its narrow temperature range of melting and crystal homogeneity as to the size, morphology and supermolecular organization.

A significant reduction in internal stresses, viz. one with at least 1,5-fold diminution, occurs in the case of coating formation

EBSCOhost - printed on 2/13/2023 3:45 AM via . All use subject to https://www.ebsco.com/terms-of-use

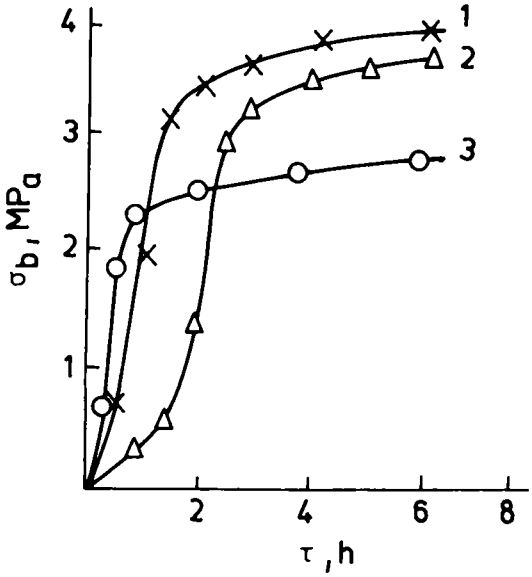

Fig.5. Growth kinetics of internal stresses during the formation of OUM-3(1), OUM-1(2) and OUM-2(3) coatings.

from the OUM-1 and OUM-3 samples crystallized from solutions in good solvents.

As can be seen from the above data, the crystallization of oligomers under specific conditions makes it possible to obtain oligourethane methacrylates having the optimum supermolecular organization of crystals homogeneous in size and morphology. When melting crystals this structure goes through the mesomorphic state, which is being accompanied by a marked acceleration of the polymerization process, internal stress reduction, and improvement in the strength characteristics of the polymers.

References

1. Berlin, A.A., T.Ya. Kefeli, G.V. Korolev. 1967. Polyesteracrylates. Moscow, Nauka P.H. p. 372 (in Russian).

2. Sukhareva L.A. 1984. Longevity of Polymer Coatings. Moscow, Khimiya P.H. p. 240 (in Russian).

3. Sukhareva L.A., N.G. Taraskina, T.Ya. Kefeli, et al. In: 7th Discussion Conference "Polymer Networks", Karlovy Vary 1980,C3-1.

EBSCOhost - printed on 2/13/2023 3:45 AM via . All use subject to https://www.ebsco.com/terms-of-use

A ONE POLYMER COMPOSITE POLYETHYLENE FILM: FAILURE MORPHOLOGY

R. Hirte[+], V. Hnát, J.P. Melior[+], Z. Pelzbauer, M. Raab, E. Schulz[+], and D. Zenke[+]

Institute of Macromolecular Chemistry, Czechoslovak Academy of Sciences, 162 06 Prague 6, Czechoslovakia

[+]Institute of Polymer Chemistry "Erich Correns", Academy of Sciences of the German Democratic Republic, 1530 Teltow, GDR

Introduction

There are several ways how to prepare fibres with nearly perfect crystalline extended-chain structure and extreme mechanical properties from linear polyethylene (1). Ultra-high strength and high modulus (UHSHM) fibres are especially promising as reinforcing fibres for polymer composites. Their perfect crystalline structure imparts them also unusual thermal properties: They show higher resistance to shrinkage than common-grade polyethylenes and could be shortly overheated at least by 20°C above the usual polyethylene melting temperature. This makes possible to use them as reinforcing fibres not only for polyester and epoxy matrices (2), but also for thermoplastics, including polyethylene itself (3). In composites with a thermoplastic matrix the lower thermal resistance of the fibres as compared with glass or carbon fibres is not necessarily a limiting factor.

Another interesting property of UHSHM fibres is the sensitivity of mechanical properties to the loading rate. With decreasing test speed the tensile strength decreases, on the one hand, but the extensibility increases, on the other. This impairs the long-term strength of the composite, but can increase its toughness and enables a positive reinforcing effect even with a very low volume fraction of fibres. In this communication we have denoted this behaviour as the "plantain effect" by analogy with some natural composites.

Morphology of Polymers
© 1986 Walter de Gruyter & Co., Berlin · New York - Printed in Germany.

EBSCOhost - printed on 2/13/2023 3:45 AM via . All use subject to https://www.ebsco.com/terms-of-use

Experimental

Material

The reinforcing fibres (4) were prepared by flow-induced crystallization from dilute (<1%) solutions of high molecular weight (M_w >10^6) polyethylene (Hoechst GUR).

The electron microscopy revealed that the fibres had a nearly rectangular elongated cross-section. Their widths varied from 70 to 120 μm and thicknesses were between 10 and 25 μm. These values of the cross-section area and their variability were also confirmed by precise weighing of short (~ 50 mm) fibre sections using a digital microbalance.

The film was a common-grade linear polyethylene produced by blow-extrusion technology. Its thickness was about 110 μm. Composite films were prepared (5) by laminating a parallel array of ultra-high-strength polyethylene fibres between two sheets of the polyethylene film in a heated press. The temperature was about 150°C and the pressing time was about 60 seconds. This resulted in a firm junction of the film layers and at the same time preserved the identity and properties of the reinforcing fibres. Typically, the specimen contained 18 fibres within a width of 10 mm.

Stress-strain measurement

Mechanical measurements of both fibres and films were performed in the air at 24 ± 1 °C on an Instron TM Tester. Typically, the gauge length was 22.5 mm and the test speed was 0.167 mm s^{-1} (test rate 7.41×10^{-3} s^{-1}). Moreover, the effect of test rate on the fibre and matrix material behaviour was studied in a range from c. 10^{-4} s^{-1} to c. 10^{-1} s^{-1}. The film specimens were strips 10 mm wide, some contained an artificial single-edge razor cut 1 mm deep. Their gauge length was also 22.5 mm.

Sonic measurements

The sonic velocity along the fibres and composite films was tested by the Pulse Propagation Meter R-5 (manufactured by H.M. Morgan, Inc., USA) at room temperature. The measuring frequency was 5000 Hz.

Microscopy

The morphology of reinforcing fibres and composite films was stud-

EBSCOhost - printed on 2/13/2023 3:45 AM via . All use subject to https://www.ebsco.com/terms-of-use

ied by a Reichert optical microscope and scanning electron microscope Tesla BS 300. (We are indebted to Mr. W.Dietz, Medical Academy, Erfurt, GDR for preparing the SEM micrographs.)
For observation of various stages of crack propagation by optical microscopy, a simple grip (8) was used which allowed to photograph the crack region in the deformed state.

Shrinkage
Shrinkage and melting of reinforcing fibres were investigated using an optical microscope equipped with a hot stage. The sample was heated at a rate of 2°C min^{-1}, the temperature range was 25 - 180°C.

Results and Discussion

Fibres
The cross-section morphology of a fibre prepared by "flow-induced crystallization" from a solution of an ultra-high molecular weight polyethylene is shown in Fig.1. The elongated cross-section of the fibre corresponds to the spinning conditions at the surface of a rotating cylinder. For the application in a composite, two pro-

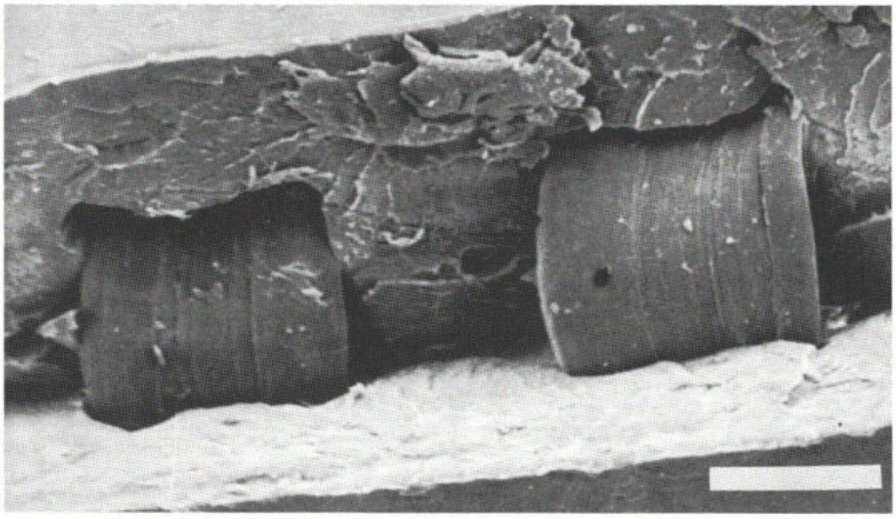

Fig. 1a. Scanning electron micrograph of composite polyethylene film broken in liquid nitrogen; bar = 50 µm.

EBSCOhost - printed on 2/13/2023 3:45 AM via . All use subject to https://www.ebsco.com/terms-of-use

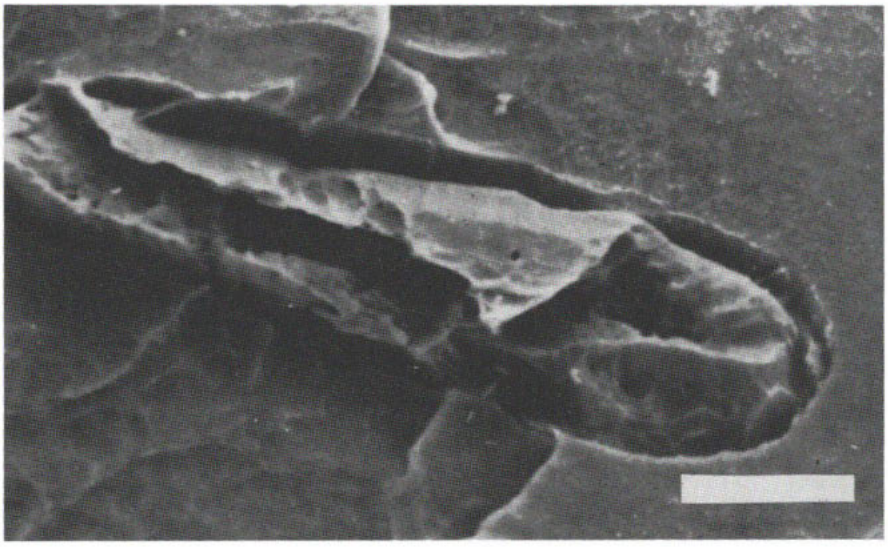

Fig. 1b. Another scanning electron micrograph of fracture surface of the composite film broken in liquid nitrogen showing elongated cross-section of a reinforcing fibre; bar = 20 μm.

perties are of importance, viz., strength and thermal properties. The effect of temperature on the shrinkage of the fibre is compared with a common-grade high-density polyethylene behaviour in Fig. 2. A very good thermal stability of the fibre up to 140°C can be seen. On the other hand, the shrinkage of the common oriented polyethylene film starts at a substantially lower temperature and is less pronounced in absolute terms (broken line in Fig. 2). Microscopical observations also revealed that the high-strength fibres can shortly be overheated up to about 175°C. In Fig. 3, stress-strain curves are shown for the reinforcing fibres at different test rates. Two features can be noted. First, the ultimate strength of the fibres is about 90 times higher and Young's modulus is about 50 times higher than the values of the matrix material under the same test conditions. Second, with decreasing test rate, the ultimate (yield) stress and the stiffness markedly decrease while the elongation at break and the energy up to break increase.

Composite

Despite the dramatic difference in the absolute stiffness and strength values, the polyethylene matrix and the polyethylene rein-

EBSCOhost - printed on 2/13/2023 3:45 AM via . All use subject to https://www.ebsco.com/terms-of-use

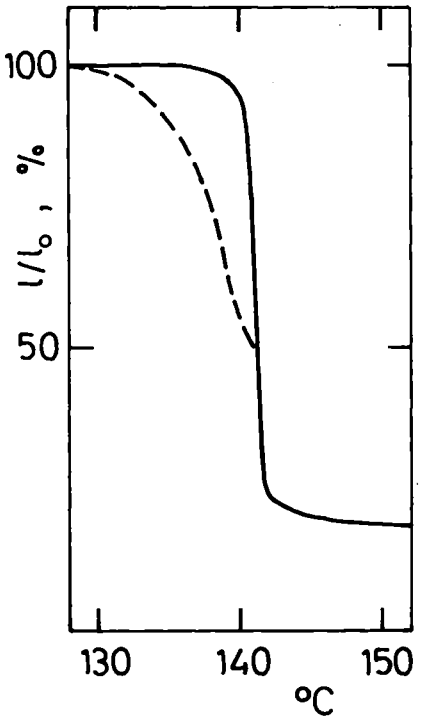

Fig. 2. Change in shrinkage of a common-grade HDPE film (dashed line) and the reinforcing fibres (solid line).

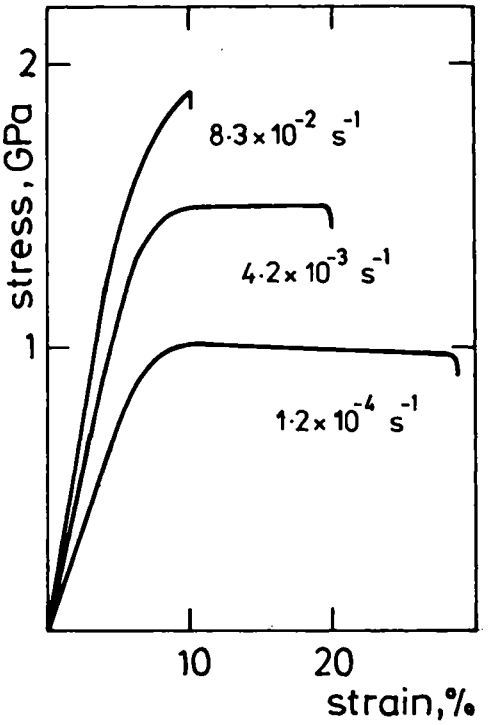

Fig. 3. Stress-strain curves of high strength polyethylene fibres at various strain rates (marked on the curves).

forcing fibres show some general similarities in their mechanical behaviour. This, in turn, imparts unusual properties to the one--polymer composite:

(i) The yield strain values of the matrix and fibres are very close to each other. For example, at a test speed 0.167 mm s^{-1} we obtained $\varepsilon_y = 10.5 \pm 0.5\%$ and $\varepsilon_y = 11 \pm 2\%$ for the matrix and fibres, respectively. Under such conditions, the longitudinal strength of the unidirectional fibrous composite is not a purely fibre-dominated property, but the strength of the matrix, too, could be fully manifested. Fig. 4 shows in a diagram that the load at failure of a film specimen reinforced by 18 fibres is approximately given as a sum of strength values of the matrix and individual fibres. (In fact, we have observed a slight increase in the strength of the composite.) The cooperative effect of the matrix and the rein-

EBSCOhost - printed on 2/13/2023 3:45 AM via . All use subject to https://www.ebsco.com/terms-of-use

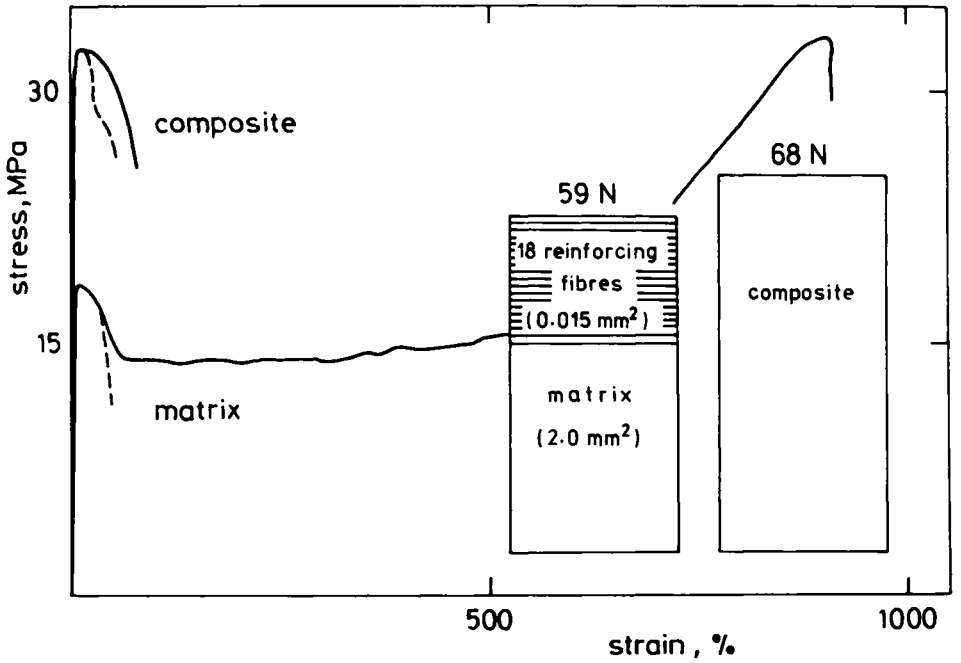

Fig. 4. Stress-strain curves of the neat matrix and the composite film. The solid lines represent behaviour of defect-free specimens and the dashed lines specimens with razor cuts. The schematic shows additive contributions of matrix and fibres to the longitudinal composite strength.

forcing fibres during a stress-strain test of the composite film is also shown in Fig.4 for specimens with and without an artificial razor cut 1 mm deep. Again, the stress-strain traces show that the matrix contributes significantly to the longitudinal mechanical behaviour.

(ii) Both the matrix and the fibres show a marked strain-rate dependence of strength. In a semilogarithmic plot the dependences are linearly decreasing and show remarkable similarity in relative terms (Fig.5). (In such a sense the dependence of the mechanical behaviour on the strain rate is not "larger" for the fibres than that for the matrix material (6).) Consequently, the mechanical properties of the composite, too, show a pronounced time sensitivity. This, however, does not necessarily mean poor mechanical performance as decreasing the test rate simultaneously reduces the strength of the fibres but raises its strain at break considerably, thus even slightly raising its toughness (work up to break).

EBSCOhost - printed on 2/13/2023 3:45 AM via . All use subject to https://www.ebsco.com/terms-of-use

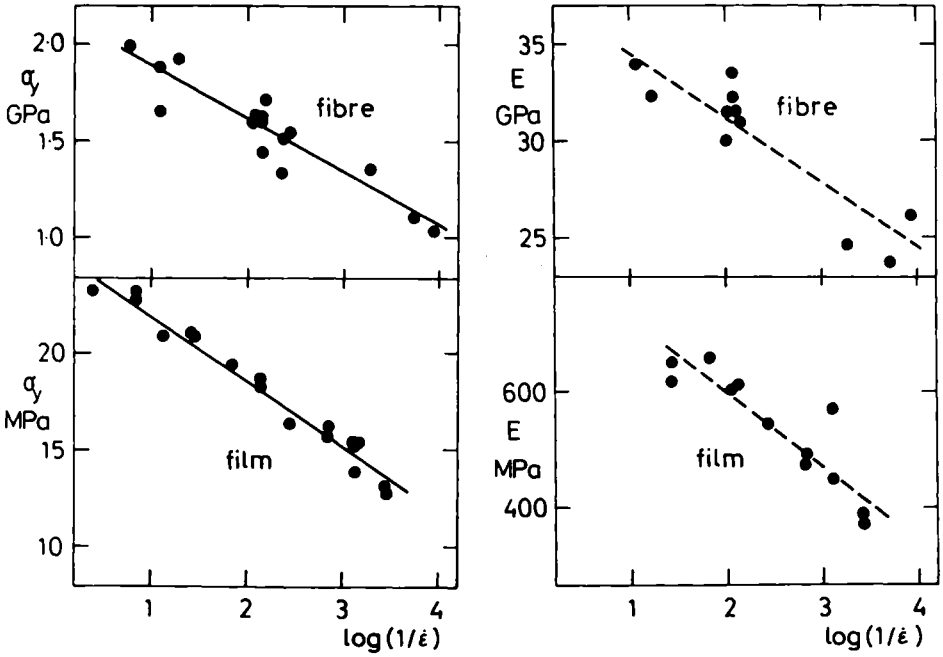

Fig. 5. Effect of strain rate ($\dot{\varepsilon}$,s^{-1}) on the yield stress σ_y and modulus E for reinforcing fibres and starting polyethylene film in the machine direction.

We observed that also Young's modulus of the fibres and the matrix as determined from the initial parts of stress-strain traces increased significantly with increasing test rate. However, for the fibres we never reached a value comparable with the extremely high moduli reported in the literature (1). Even the upper limit of the elasticity modulus as given by the sonic Pulse Propagation Meter was "just" 50 ± 20 GPa. It is interesting to note that the Pulse Propagation Meter also detected a relatively large and reproducible variation of the sonic velocity along the fibre.

Crack propagation

Polyethylene films possess an effective mechanism of self-protection against crack propagation (7) due to the geometrical crack blunting and strain-strengthening of the material ahead of the crack root. It is important that the incorporation of high-modulus fibres brings additional barriers against the crack propagation

EBSCOhost - printed on 2/13/2023 3:45 AM via . All use subject to https://www.ebsco.com/terms-of-use

into the film, while at the same time allowing the matrix material to develop its own natural protection by plastic deformation in the crack zone. This is partly due to the strain capacity of the fibres, but also to a moderate interfacial adhesion. In Figs. 6 and 7 the morphologies of crack regions are shown for an unreinforced film and a polyethylene/polyethylene composite. It can be seen that the presence of the high-modulus fibres does reduce the necking of the composite film to a narrow zone, but a considerable plasticity still occurs, even in the close vicinity of the reinforcing fibres. The protective role of plasticity against the crack growth is also manifested in the stress-strain traces: up to the yield point no effect of notch could be detected for both the neat and reinforced films (Fig. 4).

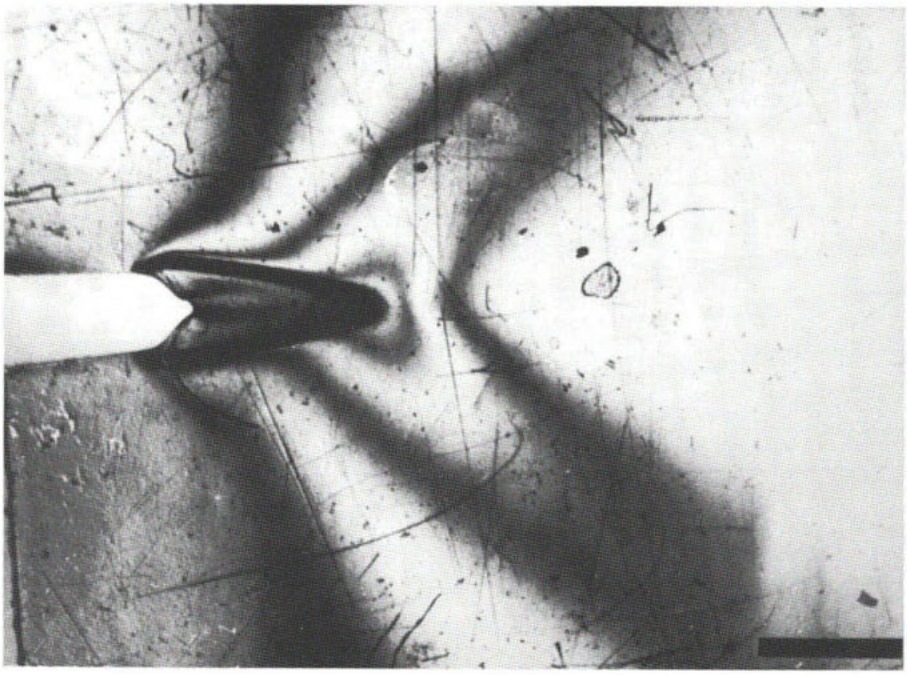

Fig. 6. Optical micrograph in polarized light of starting polyethylene film loaded to yield and then relaxed showing large plastic zone surrounding the crack tip. Bar = 1 mm.

EBSCOhost - printed on 2/13/2023 3:45 AM via . All use subject to https://www.ebsco.com/terms-of-use

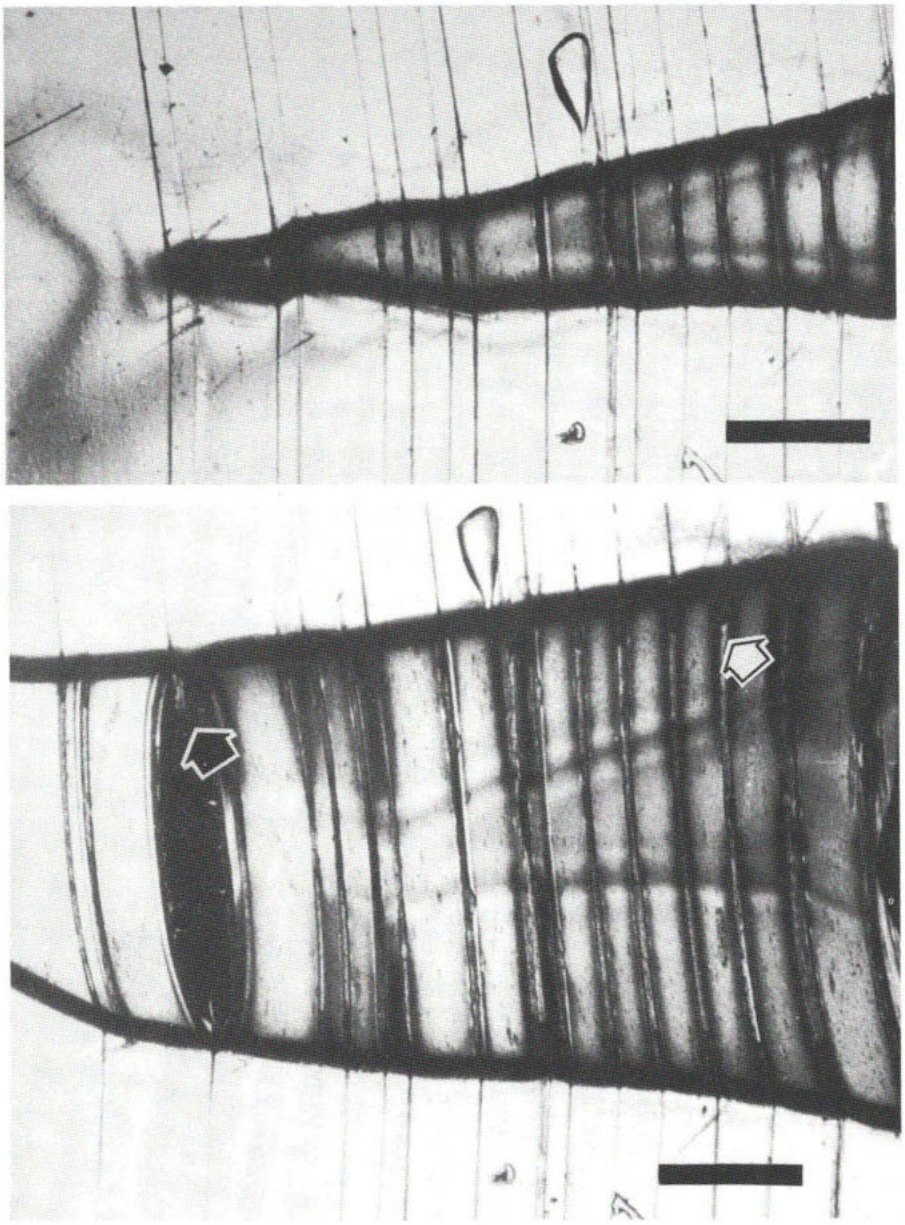

Fig. 7. Localized neck preceding a crack growth in composite film, (a) initial stage, (b) advanced stage (arrows indicate broken fibre ends). Bars = 1 mm.

EBSCOhost - printed on 2/13/2023 3:45 AM via . All use subject to https://www.ebsco.com/terms-of-use

The plantain effect

From Fig. 4 it follows that the longitudinal tensile strength σ_{bc} of the unidirectional polyethylene/polyethylene composite is approximately given by a simple law of mixtures

$$\sigma_{bc} = \sigma_{bf} v_f + \sigma_{ym}(1 - v_f)$$

where σ_{bf} is the tensile strength of fibres, σ_{ym} is the yield stress of the matrix and v_f is the volume fraction of the fibres. This is another particular feature of our one-polymer composite. In fibre composites reinforced with stiff but brittle fibres, deviations from law of mixtures occur at low-fibre concentrations. If the composite does not fracture when all the fibres are broken, a critical volume fraction v_{fc}, below which there is no reinforcing effect, can be calculated (8):

$$v_{fc} = (\sigma_{ym} - \sigma_m)/(\sigma_{bf} - \sigma_m)$$

here, σ_m is the stress in the matrix at the ultimate fibre stress. A general relationship between the composite tensile strength and fibre concentration is shown in Fig.8 (9). For our one-polymer

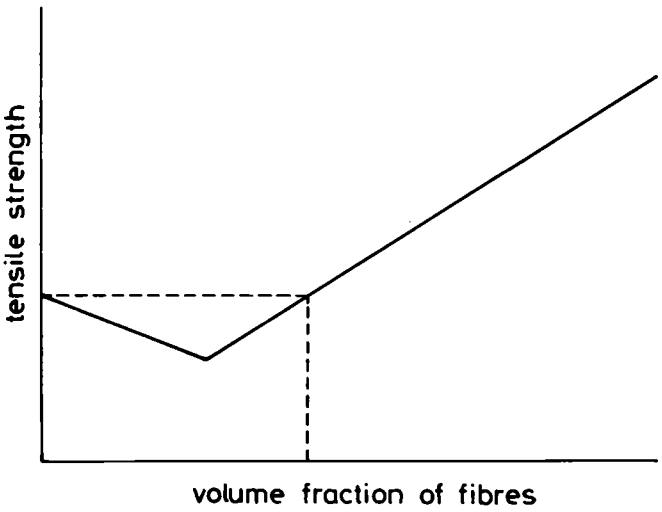

Fig. 8. General relation between tensile strength and volume fraction of fibres in unidirectional continuous fibre-reinforced composite.

EBSCOhost - printed on 2/13/2023 3:45 AM via . All use subject to https://www.ebsco.com/terms-of-use

composite, the values σ_{ym}, σ_m are very close. For example, at a strain rate $7.41 \times 10^{-3}\ s^{-1}$, $\sigma_{ym} \triangleq \sigma_m \triangleq 18$ MPa and $\sigma_{bf} \triangleq 1500$ MPa. Thus $v_{fc} = 0$. As a consequence, even one single fibre has a positive reinforcing effect on the film. (The volume fraction v_f in our model specimens was about 1%.)

It is interesting that some natural composites show a strikingly similar behaviour. A typical example is a leaf of the broad-leaved plantain *(Plantago major)*, which is reinforced with only 6 or 7 strong fibres, but the extensibility of the fibres even exceeds that of the "matrix" material. The longitudinal stress-strain behaviour of a plantain leaf is illustrated in Fig. 9 together with an example of its fracture morphology. It is also seen that the moderate fibre-matrix adhesion allows mutual slippage before final fracture. This mechanism absorbs mechanical energy and imparts toughness to the composite. The advantage of extensible reinforcing fibres applied by mother Nature after long natural selection is obviously also worth of application in man-made composites. (By analogy to plantain leaves, we denote the behaviour of a composite with extensible fibres and zero critical fibre concentration as *the plantain effect*.)

The adhesion problem

At low strain values the deformation behaviour of our composite film is nearly *isostrain*, i.e. strains in the matrix and fibre are approximately equal. After the yield point of the matrix has been reached, however, the fibres cannot follow the cold drawing of the matrix and begin to break. The occurrence of large fibre pull out in the crack zone as seen in Fig. 7b is an indication of a weak interface. A weak fibre-to-matrix contact is also suggested by sonic measurements. The high velocity of sound along a single fibre (7.2 ± 1.4 km s^{-1}) was no more detectable after embedding the fibre into the matrix: The longitudinal sonic velocity of the composite (1.33 ± 0.04 km s^{-1}) was about the same as that of the neat film (1.35 ± 0.08 km s^{-1}). The interfacial adhesion is, however, not crucial for the longitudinal strength behaviour of the uniaxial long-fibre composite, where stress is directly transferred to the fibres. Moreover, the fibre-matrix slippage could be beneficial to some extent furnishing an additional mechanism of mechanical energy dissipation and providing a better fit between the fibre and matrix behaviour.

EBSCOhost - printed on 2/13/2023 3:45 AM via . All use subject to https://www.ebsco.com/terms-of-use

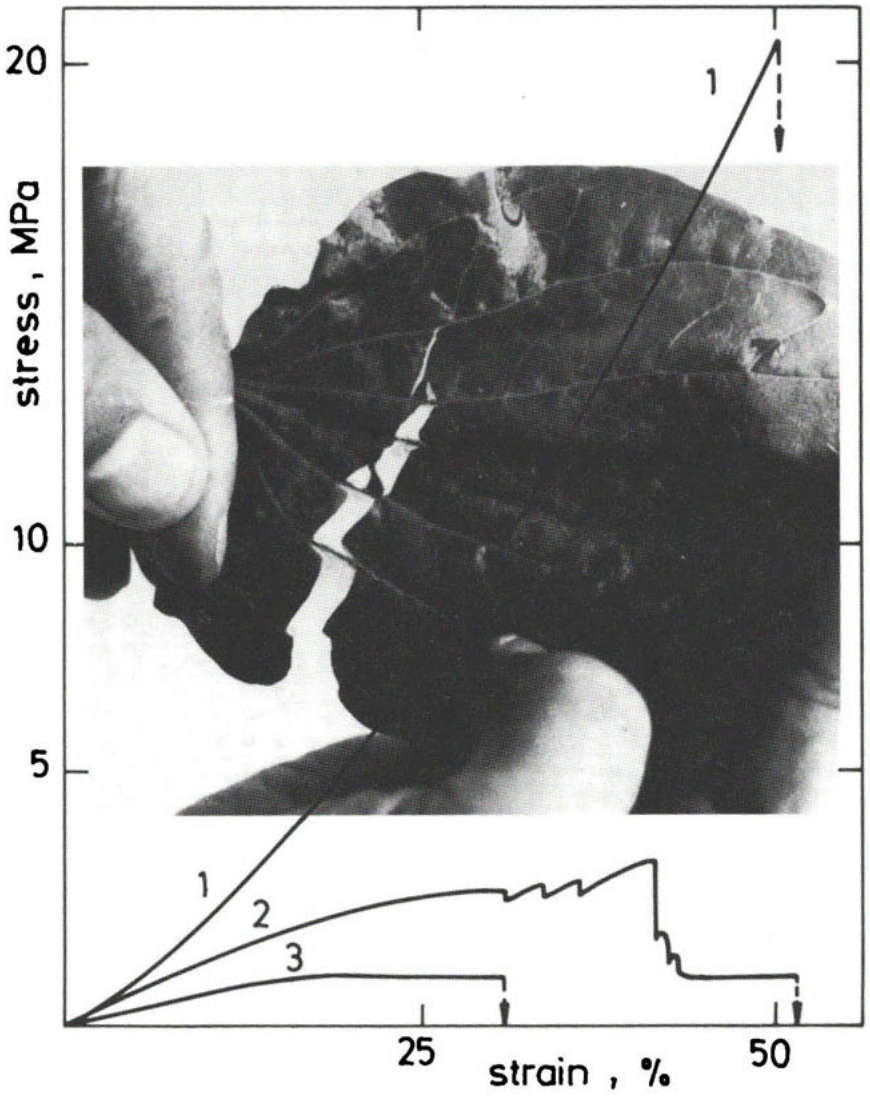

Fig. 9. Stress-strain behaviour of a plantain leaf (Plantago major), (1) reinforcing fibre, (2) whole leaf, (3) basic leaf tissue. The photograph of a crack in a plantain leaf shows extensibility of reinforcing fibres and weak interfacial adhesion.

EBSCOhost - printed on 2/13/2023 3:45 AM via . All use subject to https://www.ebsco.com/terms-of-use

On the other hand, the adhesion between fibres and matrix is an important factor controlling the behaviour of a composite during *off-axis loading*. An investigation of the mechanical behaviour of multilayer polyethylene/polyethylene composites in a more complex geometry and of possibilities of influencing the interfacial adhesion is the subject of our further study.

Conclusions

It appears that the incorporation of ultra-high-strength and high-modulus polyethylene fibres into a common-grade polyethylene film improves substantially its longitudinal mechanical behaviour. Due to the extremely high strength and a relatively large extensibility of the reinforcing fibres, a considerable effect is obtained even with a very low fibre concentration. All mechanical characteristics of the composite film show a large strain-rate sensitivity.

References

1. Ciferri, A. and I.M. Ward (eds.). 1979. Ultra High Modulus Polymers. Applied Science Publishers, London.

2. Ward, I.M. 1985. In: 28th Prague Microsymposium on Macromolecules "Polymer Composites", Prague.

3. Capiati, N.J., R.S. Porter. 1975. J.Mater.Sci. 10, 1671.

4. Zwijenburg, A., A.J. Pennings. 1976. Colloid and Polymer Sci. 254, 868.

5. GDR Patent WPB 32 B/ 2682057.

6. Woods, D.W., W.K. Busfield, I.M. Ward. 1984. Polymer Communs. 25, 298.

7. Zamfirova-Ivanova, G., M. Raab, Z. Pelzbauer. 1981. J.Mater.Sci. 16, 3381.

8. Williams, T. 1973. J.Mater.Sci. 8, 59.

9. Sheldon, R.P. 1982. Composite Polymeric Materials. Applied Science Publishers, London. p. 80.

EBSCOhost - printed on 2/13/2023 3:45 AM via . All use subject to https://www.ebsco.com/terms-of-use

EBSCOhost - printed on 2/13/2023 3:45 AM via . All use subject to https://www.ebsco.com/terms-of-use

POSSIBILITIES OF THE ESTIMATION OF POLYMER MORPHOLOGY FROM FRACTURE SURFACES

F. Lednický

Institute of Macromolecular Chemistry, Czechoslovak Academy of Sciences, 162 06 Prague 6, Czechoslovakia

Introduction

A rapid record is the main advantage of the fracture surface method used to reveal the inner supermolecular structure of polymeric materials in the solid state by the transmission (TEM) and scanning (SEM) electron microscopy. Fracture surfaces are often available with samples which have been mechanically tested. Disadvantages consist in difficulties of replica preparation for TEM (completely eliminated if SEM is used), and mainly in artefacts caused by deformation processes during fracture (Fig.1).

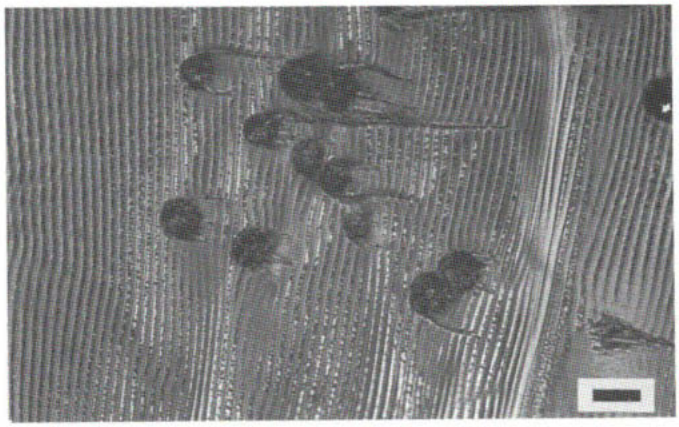

Fig.1. Interference of the inner structure (spherulites) and the fracture deformation structure (lines perpendicular to the fracture direction - a stick-slip behaviour). Polycarbonate annealed for 6 days at 190°C; visible light reflection microscopy. Bar scale 20 μm.

Morphology of Polymers
© 1986 Walter de Gruyter & Co., Berlin · New York - Printed in Germany.

EBSCOhost - printed on 2/13/2023 3:45 AM via . All use subject to https://www.ebsco.com/terms-of-use

These artificial deformation structures may sometimes be eliminated or, in turn, their existence may prove useful when studying the mechanism of sample fracturing. The aim of this paper is to compare the common morphological features of several different polymers and reveal the possibilities and limitations of the estimation of polymer morphology from their fracture surfaces.

Fracture Deformation Processes and Fracture Surface Morphology

Plastic deformation observed during the fracture process is a characteristic feature of most polymeric materials, even with those materials which are brittle regarding their mechanical behaviour. An evidence of such deformation occurring in a thin layer (crazing) prior to fracture may be seen in the appearance of interference colours on fracture surfaces of poly(methyl methacrylate)fractured in liquid nitrogen (1).

The fracture surface is smoothest in the region of its first formation (mirror region); its roughness increases with the distance from the primary fracture centre. Rough relief is caused by mutual interaction of different fracture cracks spreading in different levels. Their contact borders form fracture curves (Fig.2). From a theoretical analysis (2) it is obvious that structures formed in this way do not reflect the inner structure of the material. (Although the process of fracture curves formation is quite different from that of spherulitic crystallization, the shapes of fracture curves sometimes resemble the shapes of spherulites. The similarity resulting from coalescence processes is reported elsewhere (3)).Formations in the centres of secondary fractures need not reflect the real structures either (Fig.3).

The smoother relief of the fracture surface of amorphous polymers can be ascribed to different mechanisms. E.g., the origin of "hills" has been interpreted by the relaxation of filaments drawn out during the adiabatic deformation (4), and that of filaments has sometimes been ascribed to cleavage (5); the origin of humps has been explained as the local retardation of the spreading crack, etc.

In heterogeneous materials, the fracture process itself is influenced by their structure. The resulting fracture surface morpho-

EBSCOhost - printed on 2/13/2023 3:45 AM via . All use subject to https://www.ebsco.com/terms-of-use

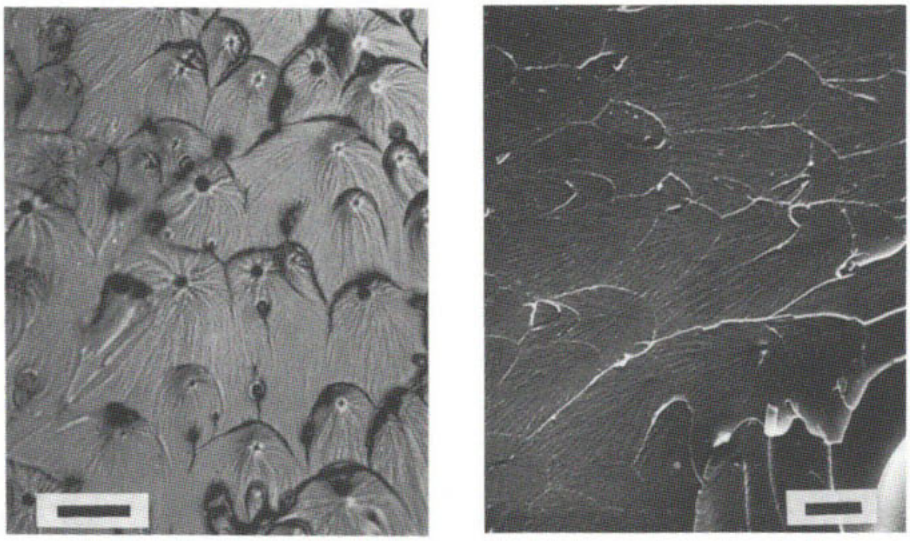

a b

Fig.2. Fracture curves on the fracture surface of commercial polystyrene (a) and epoxy resin modified by rubber (b). Visible light reflection microscopy of Al coated sample (a); SEM (b). Bar scale 20 μm (a) and 10 μm (b).

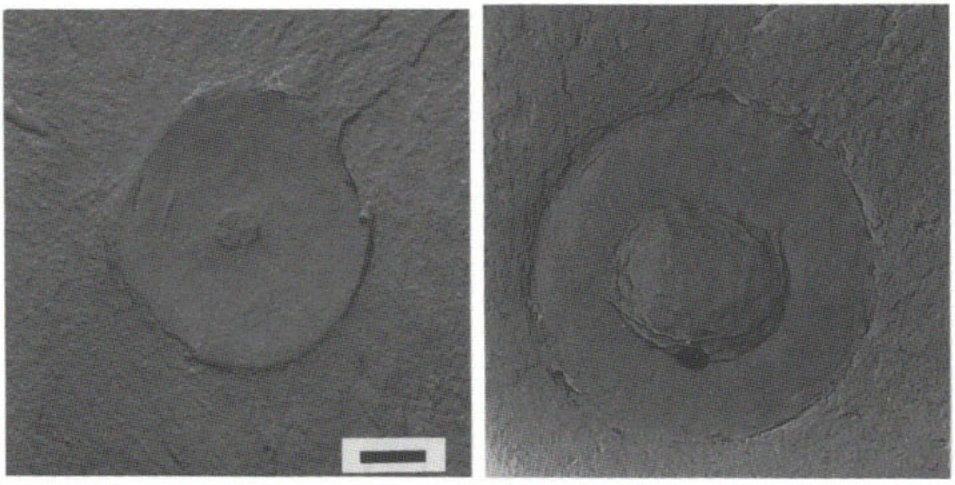

Fig.3. Formations in secondary fracture centres of amorphous poly(methyl methacrylate). They do not correspond to inner morphology; their origin is connected with the mechanism of deformation. TEM, primary carbon replica, preshadowed by Pt-SiO. Bar scale 0.5 μm.

EBSCOhost - printed on 2/13/2023 3:45 AM via . All use subject to https://www.ebsco.com/terms-of-use

logy is given by superposition of the fracture surface of amorphous material and the relief dependent on the supermolecular structure. It is obvious that this interference is least pronounced in the mirror region. For this reason, one is justified to examine the region close to the primary fracture centre in order to visualize the inner morphology.

Material Heterogeneity and Fracture Surface Morphology

The inner morphology is best visualized when the path of the crack is influenced mainly by the heterogeneity of the material components. This is the case with the system of a soft matrix and hard particles (Fig.4).
A hard matrix gives the clearest picture of supermolecular structure of multicomponent systems when the interfacial adhesion is low. The crack path then follows the phase boundaries, particles are usually nondeformed and are peeled out (Fig.5). An equal number of particles and holes remaining after the peeled-out particles is characteristic for such a system. When the interfacial adhesion is

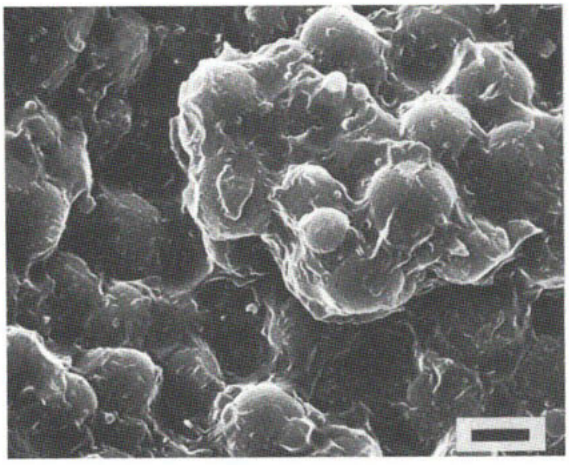

Fig.4. Fracture surface of the system with a soft matrix and hard particles. Epoxy resin modified by rubber; SEM. Bar scale 10 µm.

EBSCOhost - printed on 2/13/2023 3:45 AM via . All use subject to https://www.ebsco.com/terms-of-use

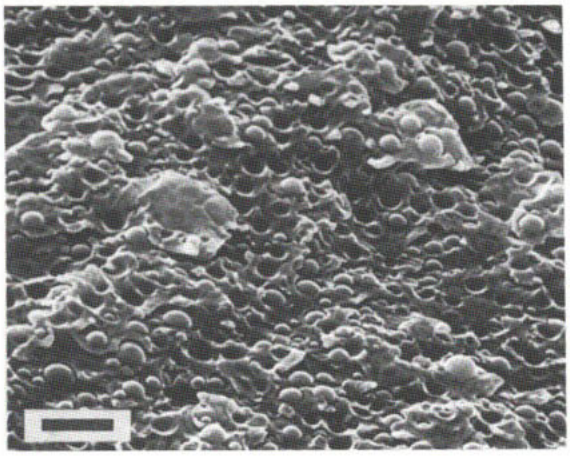

Fig.5. Fracture surface of a system with low interfacial adhesion between a hard matrix and soft particles. Epoxy resin modified by rubber; SEM. Bar scale 5 μm.

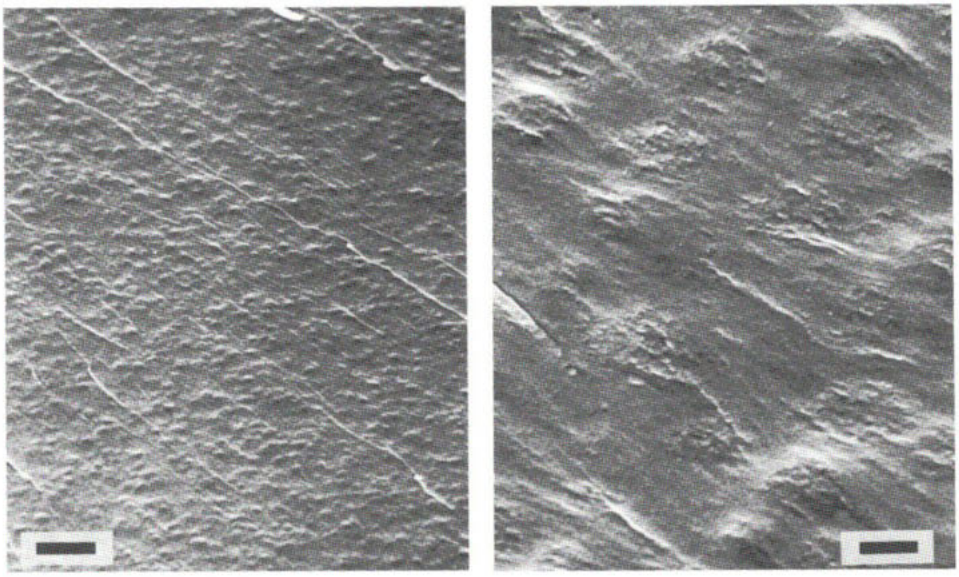

a b

Fig.6. Fracture surface of a system with high interfacial adhesion. Epoxy resin modified by rubber; SEM. Bar scale 10 μm (a) and 1 μm (b).

EBSCOhost - printed on 2/13/2023 3:45 AM via . All use subject to https://www.ebsco.com/terms-of-use

higher, the two phases are outlined less clearly. The crack path does not follow the phase boundaries; the arrangement of particles within the matrix is reflected only in a different character of the fracture surface of the matrix and included particle areas (Fig.6).

Interference of Structure and Deformation Process

With respect to the material properties, the most favourable polymer systems are such where the interfacial adhesion is as high as possible. A morphological evaluation of the supermolecular structure from fracture surfaces is the least suitable in this case. The crack path is very much influenced by the material structure: its composition is adjusted so that the spreading crack is stopped, e.g., by rubber particles or so that preferential crazing takes place (ABS polymers, high-impact polymers). The fracture crack "chooses" its path through the material, and hence the quantitative analysis of the supermolecular structure from fracture surfaces is very unreliable or even quite impossible (Fig.7). In such case it is necessary to estimate the supermolecular structure in another independent way (e.g., from ultrathin section); fracturing of a supercooled material does not yield good results under given conditions.
Another advantage of the investigation of the fracture surface morphology is making visible such formations (structures) which reduce the strength characteristics despite their negligible concentration in the material. These formations become the weak points in which the material breaks preferentially; they are found in secondary fracture centres (Fig.8).

Conclusions

In order to interpret the fracture surface morphology adequately, it is necessary to separate the influence of the structure from that of deformation processes. A clear two-phase structure suggests weak interfacial adhesion. High interfacial adhesion usually allows us to investigate only the mechanism of fracturing

EBSCOhost - printed on 2/13/2023 3:45 AM via . All use subject to https://www.ebsco.com/terms-of-use

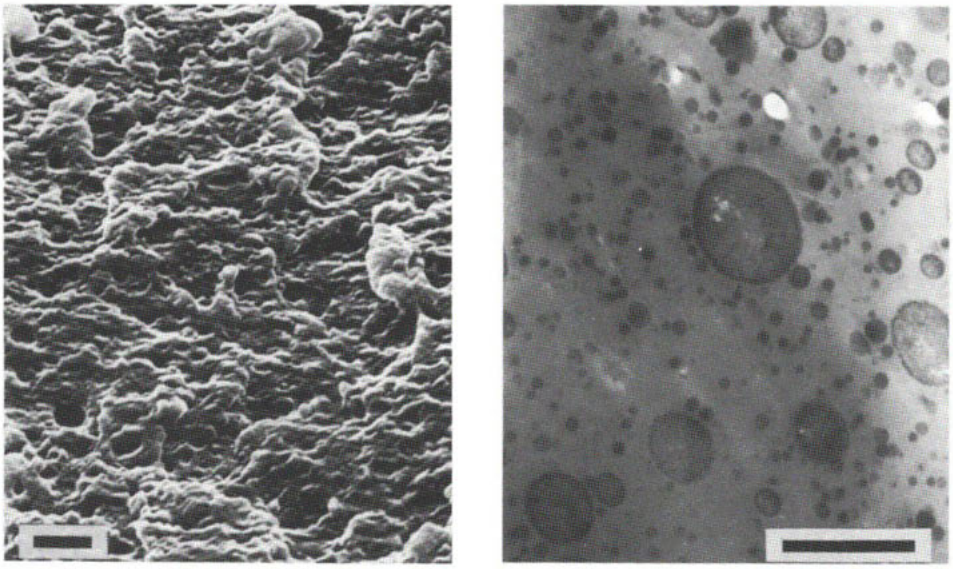

a b

Fig.7. Comparison between the fracture surface morphology (a) and the inner morphology (b) of ABS polymers. Sample Novodur PZT; SEM (a) and TEM of ultrathin sections of the sample stained by OsO_4 (b). Bar scale 1 μm.

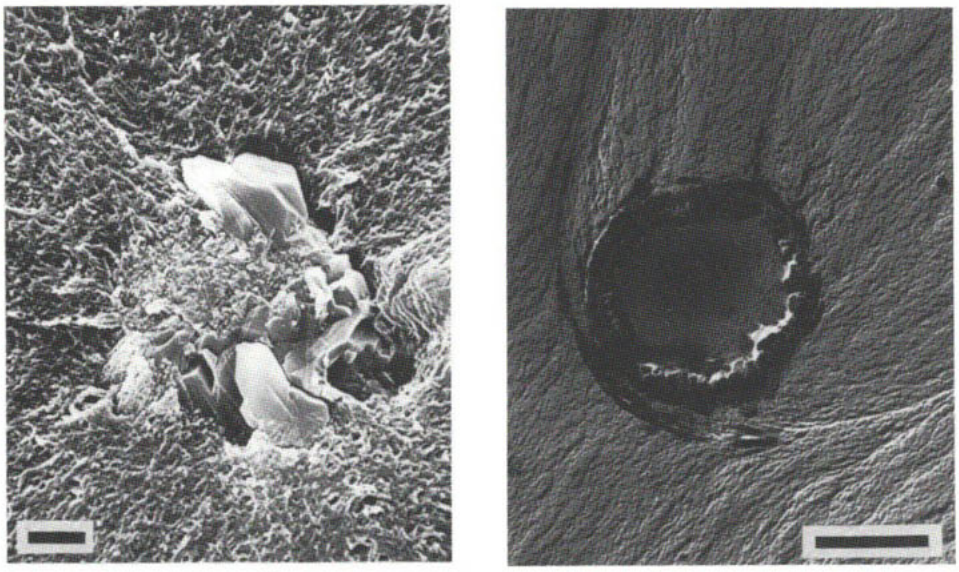

a b

Fig.8. Heterogeneous inclusions reducing the strength of the material. Inorganic crystals in ABS polymer (a), SEM of the fracture surface; bubble in a sample of poly(methyl methacrylate) (b), TEM, carbon replica of the fracture surface. Bar scale 5 μm (a) and 1 μm (b).

EBSCOhost - printed on 2/13/2023 3:45 AM via . All use subject to https://www.ebsco.com/terms-of-use

from fracture surfaces. Most information on the supermolecular structure can be obtained from the first steps of fracture surface formation.

References

1. Berry, J.P. 1965. J.Polym.Sci. A, 3, 2027.
2. Lednický, F., Z.Pelzbauer. 1972. J.Polym.Sci. C, 38, 375.
3. Lednický, F. 1977. J.Cryst.Growth 38, 353.
4. Haward, R.N., I.Brough. 1969. Polymer 10, 724.
5. Jacoby, G., C.Cramer. 1968. Rheol.Acta 7, 23.

EBSCOhost - printed on 2/13/2023 3:45 AM via . All use subject to https://www.ebsco.com/terms-of-use

THE ANALYSIS OF POLYURETHANE FRACTURE SURFACE BELOW ITS GLASS TRANSITION

H. Janik, J. Foks

Technical University, Institute of Organic and Food Chemistry and Technology, 80-952 Gdańsk, Poland

Introduction

Urethane elastomers (UE) represent a peculiar class of polymers which constitute the interesting utility properties. They may be changed in wide range depending on composition, parameters of synthesis as well as thermal treatment.

In our recent works we studied the morphology of urethane elastomers in microtomed thin sections, solvent cast thin films and manually fractured samples in liquid nitrogen (1-4).

It has been found that the UEs have a different morphology in dependence on the chemical composition and synthesis conditions (5-7). The electron microscopic studies show that the polymers have continuous and dispersed phases. Furthermore, the continuous phase on the fracture surface as well as the dispersed one have a diversified structure.

Study of UEs with a growing share of hard segment revealed an increase in the content of the dispersed phase. Parallel studies conducted in polarized light have established the presence of the crystalline phase corresponding to the size of the dispersed phase (8,9).

In the investigation which is reported in this paper we have examined the morphology of fracture surfaces in tensile tested specimens of UEs below its glass transition. The purpose of these studies is to clear up the nature of the continuous phase. We have chosen the sample in which the morphological elements of the continuous phase were sufficiently large to be studied by means of optical metallographic microscope.

Morphology of Polymers
© 1986 Walter de Gruyter & Co., Berlin · New York - Printed in Germany.

EBSCOhost - printed on 2/13/2023 3:45 AM via . All use subject to https://www.ebsco.com/terms-of-use

Results

A urethane elastomer studied in this paper was obtained from poly-adipate ethylene, p,p'-diphenylmethyl diisocyanate and 1,4-butan-diol at a 5% molar excess of the NCO groups (8).
The samples of the polymer were in the form of dumb-bell-shaped test pieces. A series of tensile tests were performed using testing machine with cross-head speed varying between 0.096 mm/min and 87.3 mm/min. Experiments were conducted at -133K in an atmosphere of gaseous nitrogen. The temperatures of the specimens were measured with a copper-constantan thermocouple during the tests.
In general three different characteristic fracture surface features have been observed on the macro scale (Fig. 1 - 3): the mirror area (zone A), the lined area (zone B, Fig.4) and the rough area (zone C, Fig.5). The most obvious change in fracture surface on this scale was the proportion of the fracture surface occupied by mirror area. The smallest and the most smooth area was observed for the highest cross-head speed (Fig.3). These large changes in fracture surface appearance were accompanied by changes on a finer scale.
Fig.6 shows fine characteristic feature of the initiation regions for samples tested with lower cross-head speeds.
The surface contains many secondary fractures consisting of a central point from which lines radiate. It is not apparent from this micrograph where the main crack initiated. This type of fracture surface morphology has not been observed in zone A for the sample tested with the highest cross-head speed (Fig.7).
Fig.8 is a typical zone B and C under higher magnification for specimen tested with lower cross-head speed. Again the surface contains many secondary fractures but in these regions they are intersected by cracks.
Contrary to this feature,Fig.9 represents patch or mound-depression morphology (so far called by us as two mutually penetrating phases) characteristic for zone B and C for the specimen tested with 87.3 mm/min.
The above results show that the nature of the continuous phase on the fracture surface depends on the type of fracture mechanism which in turn is affected by the conditions of the test.

EBSCOhost - printed on 2/13/2023 3:45 AM via . All use subject to https://www.ebsco.com/terms-of-use

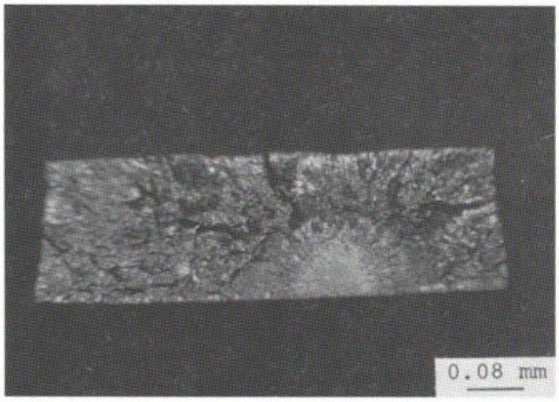

Fig.1. Optical micrograph of a tensile tested specimen (cross-head speed 0.096 mm/min).

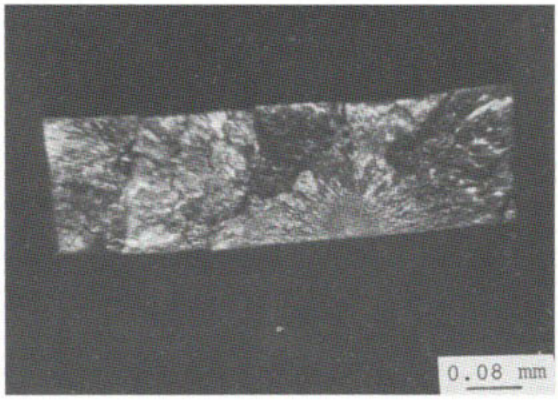

Fig.2. Optical micrograph of a tensile tested specimen (cross-head speed 0.895 mm/min).

Fig.3. Optical micrograph of a tensile tested specimen (cross-head speed 87.3 mm/min).

EBSCOhost - printed on 2/13/2023 3:45 AM via . All use subject to https://www.ebsco.com/terms-of-use

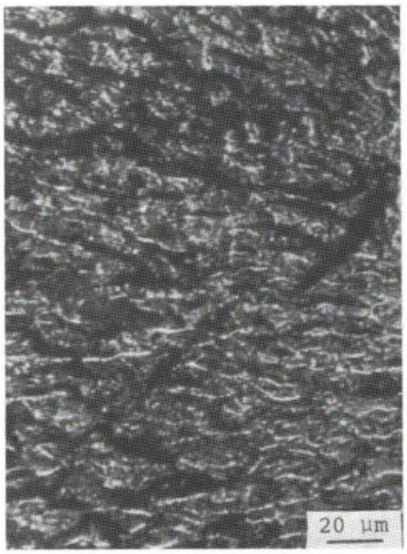

Fig.4. Typical fracture surface illustrating zone B (low magnification).

Fig.5. Typical fracture surface illustrating zone C (low magnification).

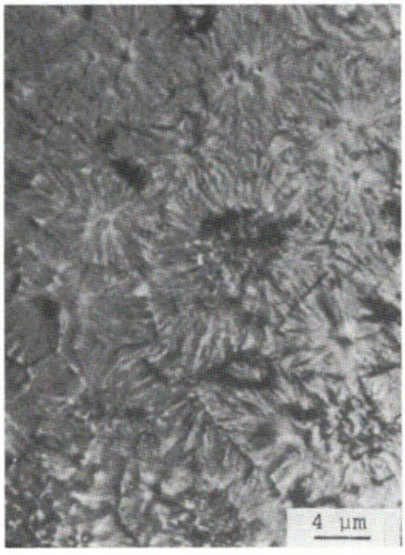

Fig.6. Optical micrograph of zone A (lower cross-head speeds).

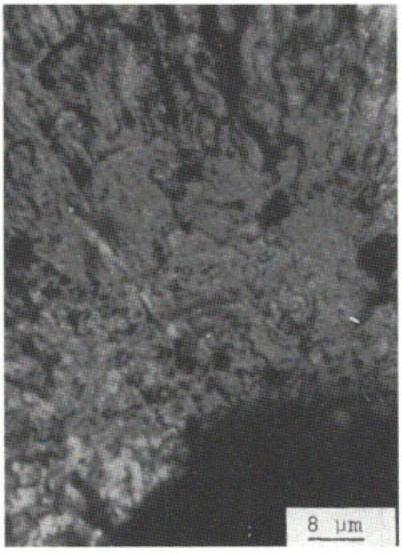

Fig.7. Optical micrograph of zone A (higher cross-head speed).

EBSCOhost - printed on 2/13/2023 3:45 AM via . All use subject to https://www.ebsco.com/terms-of-use

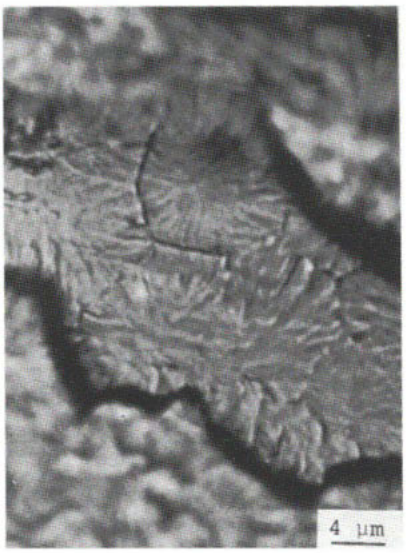

Fig.8. Optical micrograph of zone B and C of specimens fractured with lower cross-head speeds (higher magnification).

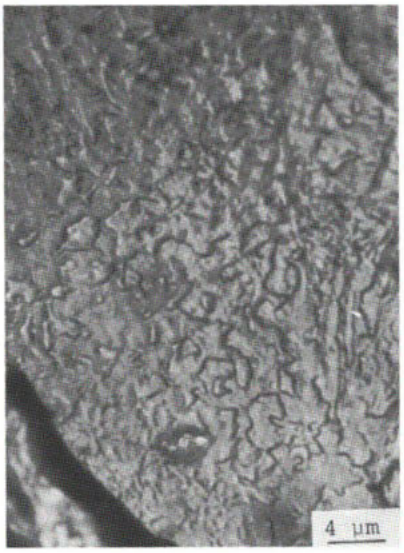

Fig.9. Optical micrograph of zone B and C of a specimen fractured with 87.3 mm/min (higher magnification).

References

1. Foks, J., H. Janik, A. Potocki. 1977. Proc. 15th Czechoslovak Conf. on Electron Microscopy, Prague, p.491.

2. Foks, J., H. Janik, S. Winiecki. 1983. Structure and Properties: IUPAC MACRO'83, Sec.IV, p.529.

3. Janik, H., J. Foks. 1980. Polimery 25, 410-412.

4. Foks, J., G. Michler. 1985. J.Appl.Polym.Sci. in press.

5. Balas, A., G. Palka, J. Foks, H. Janik. 1984. J.Appl.Polym.Sci. 29, 2261-2270.

6. Janik, H., J. Foks. 1979. Modified Polymers: 5th Bratislava IUPAC - sponsored International Conference, Vol.2, p.204-206.

7. Foks, J., H. Janik. 1981. Proc. 27th International Symp. on Macromol., Strasbourg, p.923-926.

8. Foks, J., H. Janik. 1982. 6th European Polymer Conference, Paris, p.V-9.

9. Foks, J., H. Janik. 1984. 16th Europhysics Conference on Macromolecular Physics, Brugge, p.106-107.

EBSCOhost - printed on 2/13/2023 3:45 AM via . All use subject to https://www.ebsco.com/terms-of-use

EBSCOhost - printed on 2/13/2023 3:45 AM via . All use subject to https://www.ebsco.com/terms-of-use

FRACTURE SURFACE MORPHOLOGY OF CARBON/EPOXY COMPOSITES

A. Krsová, M. Jirouš, Z. Sucharda
National Research Institute for Materials, Prague, Czechoslovakia

Introduction

Carbon fibre reinforced composites are usually manufactured by processing of the so-called prepreg, i.e. a fibrous reinforcement covered by resin in B stage (when the rate of resin-hardener network formation is reduced to the minimum).
The time of B stage stability at a given temperature is an important technological characteristic of resin-curing agent mixture. After application of elevated temperature and pressure, the mixture is able, during this period, to form a network structure with advantageous mechanical properties of the product. This ability determines the prepreg processing time available in the production of composites from epoxy matrix and carbon fibre reinforcement, nevertheless the prepreg is able to give moldings without visible defects and with required mechanical properties.
The description of fracture surface morphology of loaded composite body is well established at present (1). Typical shapes of fracture surface and correlation of their origin with loading conditions are widely studied (2-6). It results that the onset of composite damage is connected with resin-fibre interphase which depends on the composite composition, mode of specimen loading and, especially, on the matrix used (5). The goal of this work is to find whether the shear loading of epoxy/carbon fibre composite specimens can initiate such a fracture surface formation, which would indicate that this type of composite damage is a process governed by the matrix.

Morphology of Polymers
© 1986 Walter de Gruyter & Co., Berlin · New York - Printed in Germany.

EBSCOhost - printed on 2/13/2023 3:45 AM via . All use subject to https://www.ebsco.com/terms-of-use

Experimental

Specimen materials

Commercially available is the carbon/epoxy prepreg Fibredux 914 C with the matrix resin system of high melt viscosity and with a nominal fibre content of 58% by weight in the uncured condition (8). Fibredux 914 C is an unidirectional prepreg suitable for making reinforced composite components and laminates for application within the range of -60 to 180°C; especially, it is suitable for processing by medium or high-pressure laminating and moulding techniques.

The prepreg delivered was divided into two parts for experimental works differing by storage conditions. Parts A and B of the prepreg were stored in air and darkness for thousands of hours at temperature between 15 and 30°C, and for hundreds of hours at -18 ± 5°C, respectively. Thermooxidative ageing of the prepreg at elevated temperature (80 ± 2°C) was then used to determine its ability and adaptability for processing cycle.

Specimen preparation

Test specimens were obtained by cutting of plates consisting of 16 prepreg plies with 0° orientation. The plates were molded at 170°C and pressure 0.7 MPa, with cooling to 120°C before releasing pressure. The cutting was made in a lengthwise direction parallel with the fibre reinforcement.

Methods

Interlaminar shear strength (ILSS) using short beam test method (see ASTM D 2344-76); flexural loading, span:thickness ratio max. 5, temperature 23 ± 2°C, dimensions of specimens 10x12 mm. After the ILSS value was determined, morphology of fracture surfaces was investigated by using scanning electron microscopy (SEM) and JEOL 3 XA-50A equipment.

In order to reach the goal of our work, the specimens for SEM method were selected with respect to the shape of the prepreg ageing time dependence of the ILSS, shown in Fig.1. The ILSS values used for material B (stored at -18°C) are higher than those for A material at the beginning of the ageing experiment; they decrease with time of ageing and achieve the level for A values

EBSCOhost - printed on 2/13/2023 3:45 AM via . All use subject to https://www.ebsco.com/terms-of-use

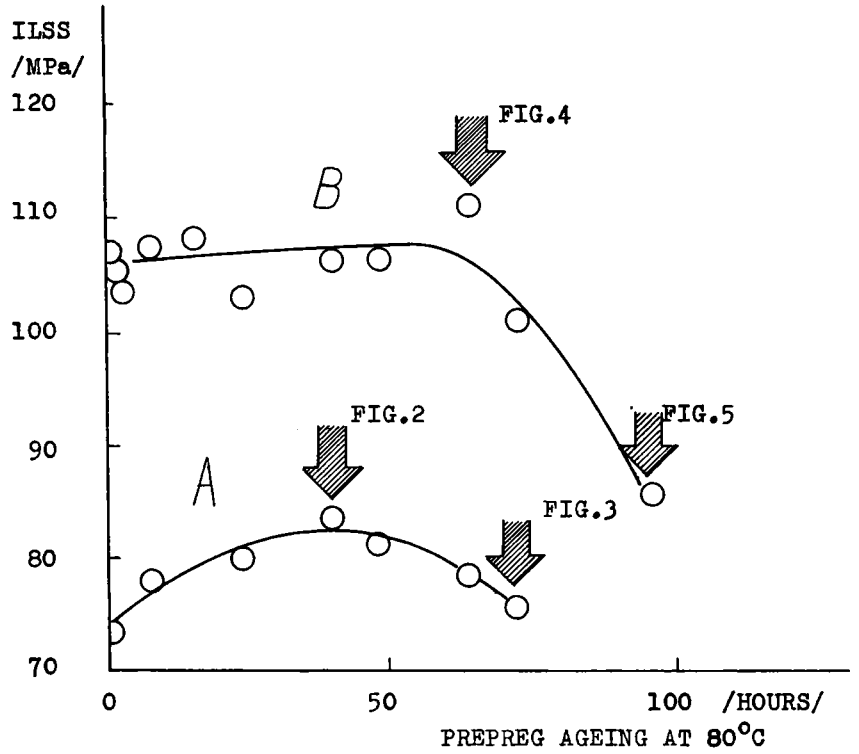

Fig.1. The dependence of interlaminar shear strength (ILSS) on the time of prepreg ageing for parts A and B. Samples further illustrated by micrographs (Figs 2-5) are indicated by arrows (ageing time) and numbers of the respective figures.

(the prepreg stored at 15 to 30°C) after ca. 100 h of ageing. Microscopically analyzed specimens are denoted by arrows on the curves in Fig.1 for both materials examined. The thermooxidative ageing serves as a tool for achieving differentiation in resin structure before molding of specimen.

EBSCOhost - printed on 2/13/2023 3:45 AM via . All use subject to https://www.ebsco.com/terms-of-use

Results and Discussion

All micrographs (Figs 2-5) show typical morphological features occurring on the fracture surfaces, which were obtained by the ILSS method (cf. Fig.1) using magnification of 100x (a-figures) and 1000x (b-figures).

Fig.2a. Morphology of the fracture surface obtained by ILSS method. Material A, ageing of 40 h at 80°C. Magnification 100x. No bare fibres on the fracture surface are visible.

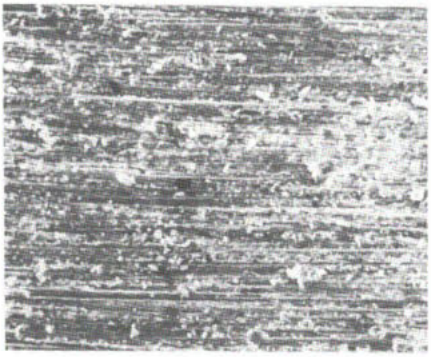

Fig.3a. Morphology of the fracture surface obtained by ILSS method. Material A, ageing of 74 h at 80°C. Magnification 100x. No bare fibres on the fracture surface are visible.

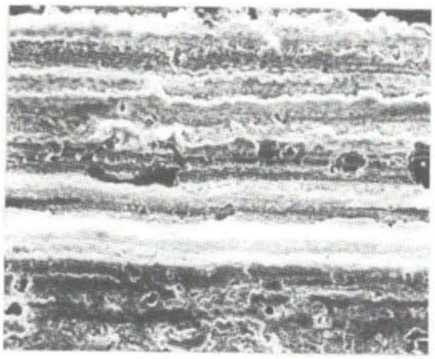

Fig.2b. Detail from Fig.2a. Magnification 1000x. Cleavage and laceration are visible.

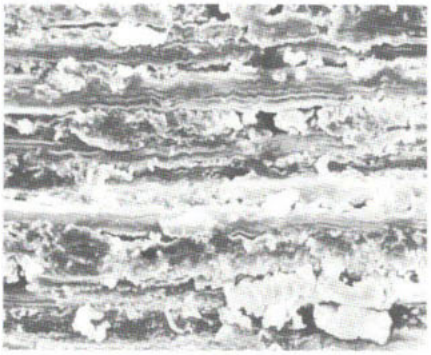

Fig.3b. Detail from Fig.3a. Magnification 1000x. Matrix debris is visible.

EBSCOhost - printed on 2/13/2023 3:45 AM via . All use subject to https://www.ebsco.com/terms-of-use

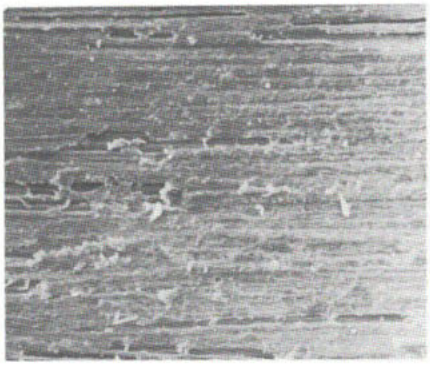

Fig.4a. Morphology of the fracture surface obtained by ILSS method. Material B, ageing of 65 h at 80°C. Magnification 100x. No bare fibres on the fracture surface are visible.

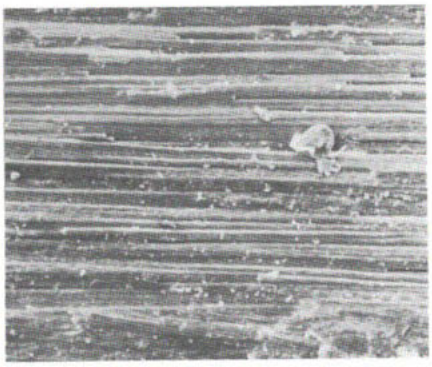

Fig.5a. Morphology of the fracture surface obtained by ILSS method. Material B, ageing of 96 h at 80°C. Magnification 100x. (Larger number of bare fibres apparently observed on the fracture surface.)

Fig.4b. Detail from Fig.4a. Magnification 1000x. Cleavage, laceration and exceptional matrix debris are visible.

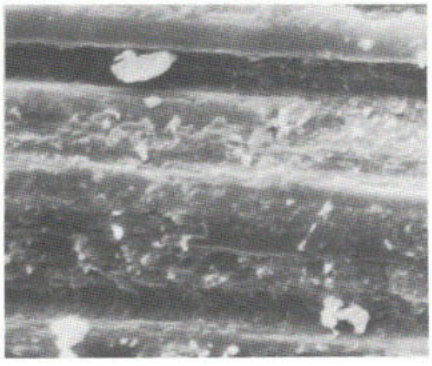

Fig.5b. Detail from Fig.5a. Magnification 1000x. Cleavage, laceration, and exceptional matrix debris are visible.

All micrographs show areas of damaged matrix with isolated places disclosing bare reinforcing fibres. Typical phenomena of the matrix damage are cleavage and laceration of the matrix and matrix debris (loose isolated parts of the matrix). The fraction of bare fibres in the whole plane is relatively small. The damage of

EBSCOhost - printed on 2/13/2023 3:45 AM via . All use subject to https://www.ebsco.com/terms-of-use

matrix is better discernible at larger magnifications (see Figs 2b-5b). Fig.5 may serve as an example, where at smaller magnification (Fig.5a) a larger number of bare fibres can be seen, but at larger magnification one observes only a continuous layer of resin on the fibre surface (Fig.5b). Laceration and cleavage of matrix appears predominantly at shorter ageing times of the prepreg (cf. Figs 1, 2b and 4b). The origin of matrix debris on the fracture surface is connected with longer times of prepreg ageing especially by inconvenient storage (see material A, Figs 1 and 3b). From comparison of Figs 3b and 4b we may conclude that at nearly identical time of ageing, there are differencies in the time period of the prepreg B stage existence, which influence properties of the matrix resulting in a great variation of fracture surface morphology (matrix debris; cleavage and laceration of matrix), corresponding to the values of interlaminar shear strength (75 and 110 MPa).

Comparison of Figs 2b and 5b shows almost equal morphology of the fracture surfaces (cleavage and laceration of matrix and, in the case of Fig.5b, small volume of matrix debris) with nearly the same ILSS value (about 85 MPa). This indicates that, by molding the plates of two materials (A and B) exposed to different storage and ageing conditions, the same resin structure is reached.

The stage of fracture surface of the composite after determination of interlaminar shear strength by short beam test method, i.e. the fracture surface with cleavage and laceration of matrix, matrix debris, and practically without bare fibres, leads to the assumption that the failure (crack) passes with priority in the matrix phase, when the composite is overloaded and reaches its failure by exceeding the limiting shear stress. The phenomenon is obviously controlled by the matrix phase distribution in the composite and by chemical and physical structures of the matrix. The morphology of the cured composite fracture surface obtained by ILSS method is determined by storage and ageing conditions of the prepreg. These conditions seem to be decisive for determination of the level of interlaminar shear strength. The value of ILSS is therefore presented as a matrix dominated property of material.

EBSCOhost - printed on 2/13/2023 3:45 AM via . All use subject to https://www.ebsco.com/terms-of-use

References

1. Richards-Frandsen R., Y.Naerheim. 1983. J.Compos.Mater. 17, 105.

2. Bailey J.E., A.Parvizi. 1981. J.Mater.Sci. 16, 649.

3. Miller A.G., A.L.Wintergest. 1979. ASTM STP 696, 223.

4. Morris G.E. 1979. ASTM STP 696, 274.

5. Kobec L.P., V.V.Michajlov, O.N.Nadjezina. 1983. Mechanika komp.materialov 8, 275.

6. Johanesson P., P.Sjöblom. 1984. J.Mater.Sci. 19, 1171.

7. Waddoups M.E. 1975. Polymer Engng Sci. 15, 160.

8. Instruction Sheet No. FTA 49b. 1975. CIBA-GEIGY.

EBSCOhost - printed on 2/13/2023 3:45 AM via . All use subject to https://www.ebsco.com/terms-of-use

EBSCOhost - printed on 2/13/2023 3:45 AM via . All use subject to https://www.ebsco.com/terms-of-use

EFFECT OF MORPHOLOGY ON THERMOOXIDATION PROCESS OF SEMICRYSTALLINE POLYMERS

M. Mucha

Polymer Institute of Technical University, Żwirki 36,
90-924 Lódź, Poland

Introduction

A gas penetration into semicrystalline polymers having spherulitic morphology occurs mainly through lower packed amorphous phase which is located both on spherulite boundaries and inside spherulites (so-called interspherulitic and intraspherulitic amorphous phases). The distribution and the size of individual amorphous phases can be modified by different conditions of sample preparation, leading to various morphological structures of polymers.
The thermooxidation process of semicrystalline polymers is initiated by oxygen penetrating into amorphous phases. The rate of the process depends not only on volume fraction of the amorphous content but also on morphological structure of the polymer under study (1-5).

Morphological Aspects of Thermooxidation of Semicrystalline Polymers

The analysis of previous results (1) allows us to divide the thermooxidation process into two processes simultaneously occurring with different rates. The first process is a rapid polymer chain scission resulting from oxidation of the interspherulitic amorphous region which is more easily accessible to oxygen. The second process is related to slower oxidation of the intraspherulitic amorphous region between lamellae.
The process is controlled by oxygen diffusion into spherulites. It is assumed that the oxygen does not penetrate the crystalline phase (lamellae) at all.

Morphology of Polymers
© 1986 Walter de Gruyter & Co., Berlin · New York - Printed in Germany.

EBSCOhost - printed on 2/13/2023 3:45 AM via . All use subject to https://www.ebsco.com/terms-of-use

The rate of polymer chain scission in the amorphous-crystalline interfaces is predicted to be lower than that inside the amorphous phases, due to lower mobility of radicals and higher probability of their recombination (6).
Chain strains in the polymeric phases and interfaces caused by sample preparation processes (e.g. quenching and deformation) are quickly relaxed during heating process and a fast decrease in T_g is to be observed (3).
According to the above assumptions, the rate of polymer chain scission, dS/dt, per mass unit of polymer can be described (7) with some simplifications as follows:

$$dS/dt = K_{exp} = K_{exp1} + K_{exp2} = K_a W_{a1} C_1 + K_1 W_{a2} F_c \qquad (1)$$

where K_{exp1}, K_{exp2} are the rates of polymer chain scission in interspherulitic and intraspherulitic phases, respectively; K_a is the complex rate constant of polymer chain scission in interspherulitic amorphous phase, C_1 is the equilibrium oxygen concentration in interspherulitic amorphous phase, K_1 is a constant; $F_c = n_r F$ is the rate of oxygen uptake by spherulitic samples in steady conditions, and F is that of a spherulite, n_r being the spherulites number per mass unit of the polymer proportional to $1/r_o^3$, and r_o their radius, W_{a1}, W_{a2} are the interspherulitic and intraspherulitic amorphous phase fractions, respectively, and $W_{a1} + W_{a2} = 1 - C_x$, C_x being the mass degree of crystallinity.
An example of a complex process of polymer chain scission, $S = f(t)$, for two samples of isotactic polypropylene is presented in Fig.1. The curves obtained at 145°C have shown the meaning of K_{exp1} and K_{exp2}.
The values of W_{a1} and W_{a2} can be calculated from the data of linear (C_{x1}) and mass (C_x) degree of crystallinity obtained from density and SAXS studies, respectively. The value of C_x is lower than that of C_{x1} (2,8,9) due to the fact that C_{x1} is related to the alternate crystalline and amorphous regions, i.e. the interspherulitic amorphous phase and defects in crystalline lamellae have not been taken into account.

EBSCOhost - printed on 2/13/2023 3:45 AM via . All use subject to https://www.ebsco.com/terms-of-use

Thus:

$$C_{x1} = \frac{l_c}{\lambda}; \qquad C_x = \frac{m_c}{m_c + m_a} = \frac{\rho_c n\, l_c S}{m_c + m_a}$$

$$W_{a2} = \frac{n(\lambda - l_c)S\rho_a}{m_c + m_a} = \left(\frac{\lambda}{l_c} - 1\right)\frac{\rho_a}{\rho_c} C_x \qquad (2)$$

$$W_{a1} = 1 - C_x - W_{a2}$$

where l_c is the lamella thickness, λ is the long period, ρ_c, ρ_a and m_c, m_a are the densities and mass per volume units, respectively, of crystalline and amorphous phase; S is the average area of lamella surface and n is the average number of lamellae per mass unit.

The process of polymer chain scission is rapid at the beginning of the thermooxidation (1) and it occurs without any induction period. This allows us to assume that it is related to the equilibrium concentration C_1 of oxygen which was dissolved in more easily accessible amorphous phase of W_{a1} fraction.

Considering $K_{exp} = K_{exp1} = (dS/dt)_1$ as initial rate of polymer chain scission, the second process becomes much slower with increasing W_{a1}, according to Eq.(1). This was observed for isotactic polypropylene and the data of $(dS/dt)_1$ were plotted versus $(1-C_x)$ and W_{a1} (Fig.2).

The second process of thermooxidation is much slower than the first one, and it is here considered as being in steady state conditions. Annealing occurring together with thermooxidation leads to a fast increase in crystallinity degree and crystal perfection (1,2). Value of W_{a2} becomes constant and K_{exp2} is mainly affected by the rate of oxygen uptake into spherulitic samples, F_c.

If the diffusing substance is immobilized by an irreversible first-order reaction with rate constant k, then the equation for radical diffusion into spherical spherulite (10), takes the following form in the case of steady state conditions:

EBSCOhost - printed on 2/13/2023 3:45 AM via . All use subject to https://www.ebsco.com/terms-of-use

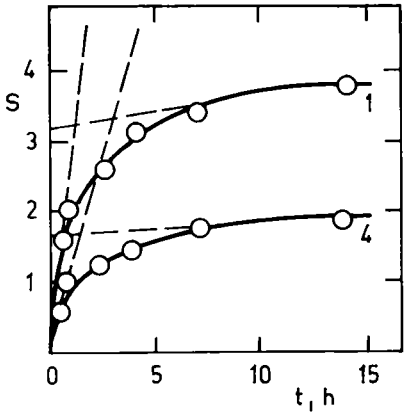

Fig.1. Number of molecular chain scission, S, versus degradation time t at 145°C for two samples obtained at T_c = -70°C (1) and 100°C (4). Slopes determine the K_{exp1} and K_{exp2} values.

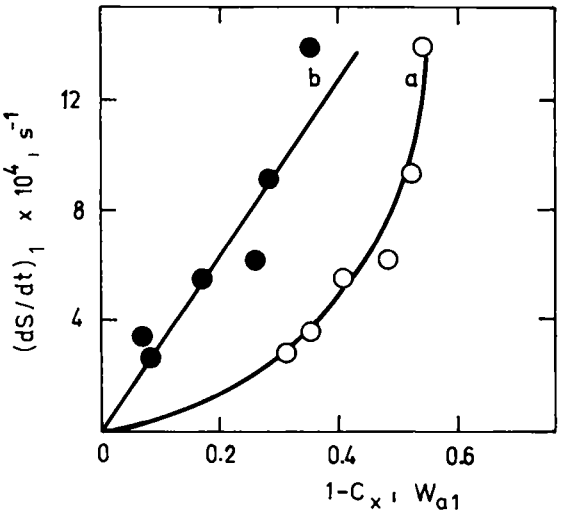

Fig.2. Initial rate of polymer chain scission $(dS/dt)_1$ versus $(1-C_x)$ and W_{a1}.

EBSCOhost - printed on 2/13/2023 3:45 AM via . All use subject to https://www.ebsco.com/terms-of-use

$$\frac{d^2C}{dr^2} + \frac{2}{r}\frac{dC}{dr} - \beta^2 C = 0 \qquad (3)$$

where $\beta^2 = k/D$, k and D being the rate and diffusion constants, respectively, C is the oxygen concentration, and r is the spherulite radius.

Solution of Eq.(3) under the following boundary conditions

$$C = C_o \quad \text{for} \quad r = r_o \quad \text{(at spherulite surface)}$$

$$\frac{dC}{dr} = 0 \quad \text{for} \quad r = 0 \quad \text{(in spherulite center)}$$

takes the form

$$C = C_o \frac{r_o \sinh \beta r}{r \sinh \beta r_o} \qquad (4)$$

Based on Fick´s first law and applied to the flux of diffusant through spherical surface, the rate of oxygen absorption by spherical spherulite can be calculated as follows

$$F = 4\pi r_o^2 D \left(\frac{dC}{dr}\right)_{r=r_o} = 4\pi r_o C_o D(\beta r_o \operatorname{ctgh} \beta r_o - 1) \qquad (5)$$

and the equation for the rate of oxygen uptake into spherulitic samples has the form

$$F_c = n_r F = \frac{4\pi D C_o}{r_o^2} (\beta r_o \operatorname{ctgh} \beta r_o - 1) \qquad (6)$$

The plots $F_c Z$ versus βr_o and $1/\beta r_o$ are presented in Fig.3 ($Z = (4\pi C_o k)^{-1}$).

Assuming constant β for a given polymeric sample and temperature, the character of $F_c(r_o)$ function depends on morphological structure of the samples reflected in different spherulite sizes. This effect is clearly seen for values $\beta r_o > 0.5$.

Experimental plot of $K_{exp2} = (dS/dt)_2$ versus $1/r_o$ obtained for thermooxidation study of isotactic polypropylene is presented in Fig.4.

EBSCOhost - printed on 2/13/2023 3:45 AM via . All use subject to https://www.ebsco.com/terms-of-use

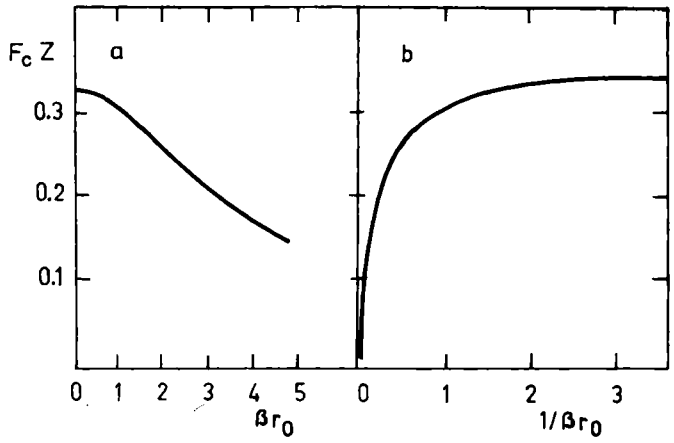

Fig.3. Rate of oxygen uptake by spherulitic sample: $F_c Z = F_c/4\pi C_o k = (\beta r_o \mathrm{ctgh}\ \beta r_o - 1)/\beta r_o^2$ versus βr_o (a), $1/\beta r_o$ (b).

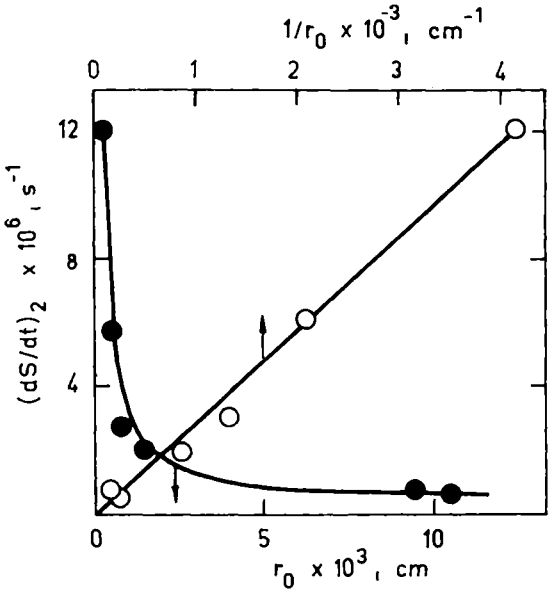

Fig.4. Rate of molecular chain scission $(dS/dt)_2$ versus r_o and $1/r_o$.

EBSCOhost - printed on 2/13/2023 3:45 AM via . All use subject to https://www.ebsco.com/terms-of-use

K_{exp2} increases linearly with increasing $1/r_o$ indicating a good agreement with the above proposed model of thermooxidation process. It also means that the value of βr_o is higher than 0.5. This results from a much higher value of k in comparison with D for isotactic polypropylene at temperature under study (1).

Conclusions

Morphological structures of semicrystalline polymers resulting from various conditions of sample preparation lead to different rates of the sample thermooxidation.
The rate of molecular chain scission is predicted to be much faster in interspherulitic than in intraspherulitic amorphous phase. Thus, the initial rate of polymer chain scission depends on fraction of the interspherulitic amorphous phase. The rate of polymer chain scission in intraspherulitic amorphous phase reflects the oxygen diffusion into spherulites and thus depends on spherulites sizes.

References

1. Mucha, M., M.Kryszewski. 1980. Colloid and Polym.Sci. 258, 743.
2. Mucha, M. 1981. J.Polym.Sci.,Polym.Symp. 69, 79.
3. Mucha, M. 1981. Colloid Polym.Sci. 259, 984.
4. Jellinek, H.H.G. 1975. J.Polym.Sci.,Polym.Chem.Ed. 14, 1249.
5. Michaels S.A., A.J.Bixler. 1961. J.Polym.Sci. 50, 513.
6. Chien, J.C.W., D.S.T.Wang. 1975. Macromolecules 8, 921.
7. Bhateja, S.K., R.J.Young. 1983. J.Polym.Sci.,Polym.Phys.Ed. 21, 523.
9. Hert, H., J.Rault, E.Robelin. 1983. Makromol.Chem. 184, 225.
10. Crank, J. 1975. The Mathematics of Diffusion, Clarendon Press, Oxford.

EBSCOhost - printed on 2/13/2023 3:45 AM via . All use subject to https://www.ebsco.com/terms-of-use

EBSCOhost - printed on 2/13/2023 3:45 AM via . All use subject to https://www.ebsco.com/terms-of-use

TEXTURES

1. Fibres 573-650
2. Films 651-706
3. Other Textures 707-746

EBSCOhost - printed on 2/13/2023 3:45 AM via . All use subject to https://www.ebsco.com/terms-of-use

EBSCOhost - printed on 2/13/2023 3:45 AM via . All use subject to https://www.ebsco.com/terms-of-use

MORPHOLOGY OF POROUS POLYPROPYLENE FIBRES

V. MARCIAN
Research Institute for Man-Made Fibres
Svit 059 21, Czechoslovakia

Introduction

During cold deformation of hard-elastic polypropylene /PP/ fibres a reversible generation of microvoids, oriented perpendicularly to the fibre axis direction, was observed. By means of subsequent heat-setting under isometric conditions it is possible to obtain extended fibres with a permanent microporous structure, characterized by a high volume fraction of microvoids and by a large specific inner surface. These fibres can be used in the textile industry and other industrial and medical areas/1,2/.
Specific physical properties of porous fibres include very good sorption of low surface tension liquids such as oils and other petroleum products, good moisture transport, high gas permeability and excellent heat-insulation properties. Microporous PP fibres can be effectively used in filters for gas and liquid cleaning, for waste water purification, in textiles for inner hygienic layer production, for fabrication of underwear and sportswear with improved moisture transport properties, heat-insulating clothes and sleeping bags.
Microporous hollow fibres are used as membranes in devices for separation processes. They are effective as ultrafilters, membranes for gas separation, reverse osmosis etc., and are successfully applied to pollution control problems, separation of oil/water emulsions, recovery of byproducts, for separation of small molecules such as gases from mixtures or salts from solutions. Microporous hollow fibres are often used in medical/biomedical areas, for haemofiltration and to separate blood proteins from blood/3/.
The formation of microvoids in the fibre, their shape, quantity, size and orientation are determined by special supermolecular structure of hard-elastic precursors and they are dependent upon processing conditions /4/.

Morphology of Polymers
© 1986 Walter de Gruyter & Co., Berlin · New York - Printed in Germany.

EBSCOhost - printed on 2/13/2023 3:45 AM via . All use subject to https://www.ebsco.com/terms-of-use

In this paper, some studies of processing conditions are presented, by estimating morphological and structural parameters, in order to determine optimal conditions for fibres with maximal porosity and specific inner surface which secure the best sorption properties.

Experimental

The initial hard-elastic polypropylene fibre was prepared by means of a high speed melt spinning process from polymer TATREN TE 451, with melt index of 5 and by subsequnt annealing at 142°C. Wind-up speed was 1500 m/min, which corresponds to a draft of 280. A hard-elastic precursor with a tenacity of 0.205 GPa, an elongation of 220 %, an initial modulus of 2.19 GPa and elastic recovery from 100 % extension ER_{100} of 95.5 %, exhibited a slight decrease in ER values depending on the number of extension cycles. In the first cycle, elastic recovery values gradually decrease as a function of extension, until rupture of the fibre /see Fig.1/.

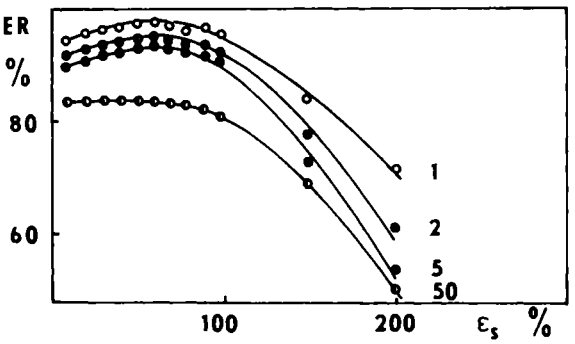

Fig. 1. Dependence of elastic recovery on extension for cycled hard-elastic PP fibre. 1,2,5,50 - number of cycles.

The initial hard-elastic fibre was subjected to single-stage drawing at room temperature with different degrees of deformation then heat-set at 70 - 150°C under dynamic conditions. In order to determine the optimal heat-setting time, the fibre was treated

EBSCOhost - printed on 2/13/2023 3:45 AM via . All use subject to https://www.ebsco.com/terms-of-use

for times ranging from 6 to 600 s.
The supermolecular structure of static-deformed hard-elastic precursor, as well as that of the permanent porous fibres was evaluated by means of WAXS, SAXS and sonic velocity measurement. Morphological features of fibres was evaluated by SAXS, SALS and by scanning electron microscopy /SEM/. Changes of microporous structure parameters in static-deformed and permanent porous fibres was studied by means of SAXS /5,6/.To calculate the microvoid content and to distinguish different microvoid fractions, a computer program in language FORTRAN IV of SAXS analysis was used. By using a liquid immersion technique, discrete reflections due to periodicity of electron density changes between crystalline and non-crystalline regions in axial direction, was separated by microvoids.

Results and Discussion

Morphological features and supermolecular structure of the initial hard-elastic fibre are characterized qualitatively by diffraction patterns as shown in Figure 2.

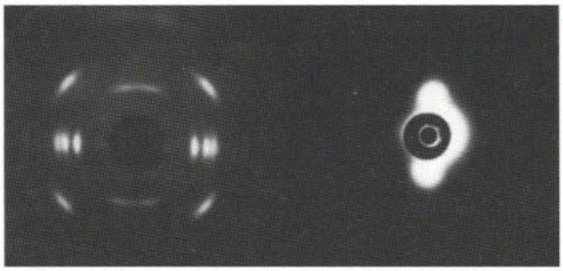

Fig. 2. WAXS and SAXS patterns of hard-elastic precursor.

WAXS studies established the presence of a high content of very well developed crystals of α-monoclinic modification, characterized by sharp spots of /110//040//130//111,041,131/ planes accompanied by a high degree of preorientation. Crystals with distinct crystallographic orientation were evaluated by WAXS. Splitting of /110/ reflections into equatorial and meridional compo-

EBSCOhost - printed on 2/13/2023 3:45 AM via . All use subject to https://www.ebsco.com/terms-of-use

nents as well as of /130/ reflections into equatorial part and in general position one, is due to presence of both a'– and c–axis oriented crystals, respectively. Fractions of a'– and c–axis oriented crystals x_a, x_c , orientation of both crystalline and noncrystalline regions expressed as orientation factors f_c, f_{am} respectively, parameters of crystalline structure as determined by mathematical peak–separation procedure from WAXS profile /7/, together with other parameters are shown in Table 1.

Table 1. Structural Characteristics of Polypropylene Fibres

Fibre	Kp	D_{110}	x_c	x_a,	f_c	f_{am}	f_{am}^s	f_{am}^v	f_{am}^{rtg}	ΔL/L	n/N
	%	nm	%	%							
Initial	65	10.9	89	10	0.96	0.02	0.19	0.25	0.98	0.20	0.032
Deformed	66	11	90	10	0.92	0.41	0.22	0.29	0.99	0.34	0.056
Porous	68	12	96	4	0.89	0.48	0.28	0.36	0.99	0.31	0.050

Two–point fan–like meridional spots SAXS pattern of the initial fibre, shown in Figure 2, suggest a high degree of morphological perfection. Large sized c–axis oriented crystals are packed into row–nucleated lamellar structural units having their planes arranged normal to the fibre axis direction. The large long spacing, lamellar thickness as well as a relative narrow long spacing distribution, as characterized by parameter ΔL/L /8/, quantitatively confirms the high degree of lamellar perfection.

The SAXS analysis offers the low average density value of noncrystalline regions $\bar{\varrho}_{am}$ /9/, suggesting low degree of macromolecular chain perfection in interlamellar space. This supposition is supported by evaluation of average noncrystalline orientation f_{am} and by tie chain orientation f_{am}^s as well as by taut tie chain f_{am}^v in interlamellar space /10/. The content of taut tie chains, characterized by relative fraction n/N /11/, was found very small, as reflected in low fibre tenacity. Related to generally very low axial orientation of macromolecular chains in interlamellar space the parameter n/N, as calculated from sonic velocity measurements, characterizes taut tie chains in mesomorphic regions exhibiting very small transversal dimensions and very high orientation f_{am}^{rtg}. The SAXS pattern exhibits no diffuse scattering

EBSCOhost - printed on 2/13/2023 3:45 AM via . All use subject to https://www.ebsco.com/terms-of-use

indicating the presence of microvoids size 1 to 120 nm. Table 1 lists some morfological and supermolecular parameters of specified hard-elastic fibre subjected to a static deformation from 100 %. In comparison with precursor, crystallinity and crystal size are practically unchanged, whereas the orientation and other parameters do show some changes.

The marked increase upon extension was expected in average noncrystalline orientation by macromolecular chains straightening along the fibre axis direction. The noncrystalline orientation increase was caused by a rise of the tie chain orientation and was accompanied by increase in the taut tie chains fraction n/N. Figure 3 illustrates the strong increase in long-spacing, related to the dry fibre extension and, for comparison, the same relationship in the presence of an immersion liquid.

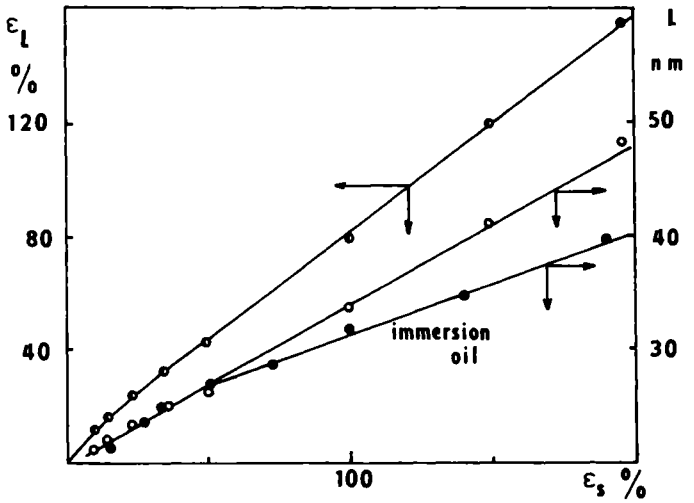

Fig. 3. Dependence of long-spacing /L/ and long-spacing deformation / ε_L/ on extension, for hard-elastic precursor.

From displacement of the diffraction maximum toward longer long-spacings proportional to the extension, the deformation of long-spacing and noncrystalline space was calculated /12/. It is seen that the long spacing deformation corresponds to macrodeformation of the sample approximately to 40 % extension. Since the deformation of crystals can be neglected, the whole macrodeformation of the fibre is caused by enlargement of noncrystalline re-

EBSCOhost - printed on 2/13/2023 3:45 AM via . All use subject to https://www.ebsco.com/terms-of-use

gions.

In Figure 4, ABC show the SAXS patterns of dry hard-elastic precursor subjected to different static deformation levels. A considerable increase in the meridional scattering intensity are seen and increase in equatorial diffuse scattering at higher deformations. Increase in diffuse scattering relates to the drastic drop in the average density of noncrystalline space. Quantitative SAXS analysis established that the increasing in small angle spacing and scattering intensity are caused by transversal microvoid formation in the lamellae separation process. As extension proceeds, a horizontal streak begins to appear on the SAXS patterns. Development of the equatorial diffuse scattering is connected with plastic deformation of the sample, the formation of longitudinal microvoids, and with the fibrillar slip process. These microvoids have their long axis oriented parallel to the deformation direction. Liquid immersion technique have practically no effect on dimension and the deformation behavior of long-spacings, but a strong scattering intensity reduction can be expected by density difference levelling between crystalline regions and noncrystalline ones /see Fig. 4 DEF/.

Figure 4G illustrates reversibility of microvoid formation in dry fibre, after stress relaxation.

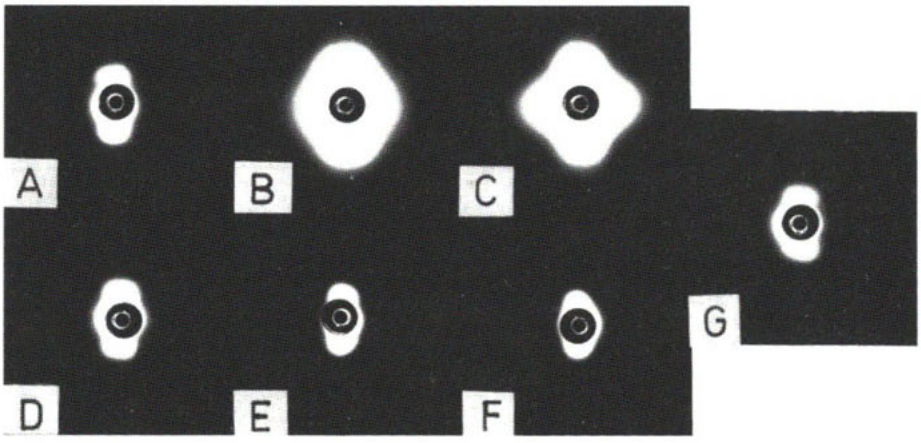

Fig. 4. SAXS patterns of static-deformed hard-elastic precursor A,B,C – dry fibre, D,E,F – in immersion liquid, G – dry fibre after relaxation to zero stress.

EBSCOhost - printed on 2/13/2023 3:45 AM via . All use subject to https://www.ebsco.com/terms-of-use

Figure 5 shows a practically linear change of microvoid size in the fibre axis direction upon deformation.

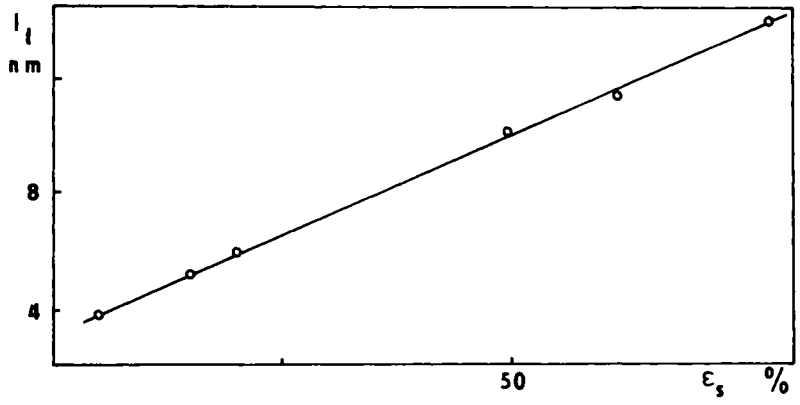

Fig. 5. Calculated microvoid sizes in the fibre axis direction as a function of room-temperature extension.

The shape of equatorial diffuse scattering curves suggests the presence of bimodal oriented microvoids in fibres. The scattering curve registered at low static deformation level, shown in Figure 6, exhibits a single inflection point at very small scattering angles and the area below the curve characterizes the pores of relative large dimensions. In comparison with SAXS patterns it is clear that the fibre contains only transversal microvoids.
A second marked inflection point at larger scattering angles characterizes generation of longitudinal microvoids at higher deformation levels. Curve shape analysis allowed the evaluation of porosity and specific inner surface variations as well as the average dimensions of microvoids in direction perpendicular to the fibre axis, depending on extension /13/.
Figure 7 quantitatively shows strong, almost linear increases in porosity and specific inner surface, respectively, upon extension approximately from 30 %. The next increase of values is slow, until saturated. Variations in dimensions of microvoids perpendicular to the fibre axis exhibits the reverse relationship, probably due both to their elongation and by change of size distribution

EBSCOhost - printed on 2/13/2023 3:45 AM via . All use subject to https://www.ebsco.com/terms-of-use

upon deformation. Some attempts were made to separate the areas below scattering curves into two parts by computer and calculate volume fractions of microvoids perpendicular and parallel to fibre axis.

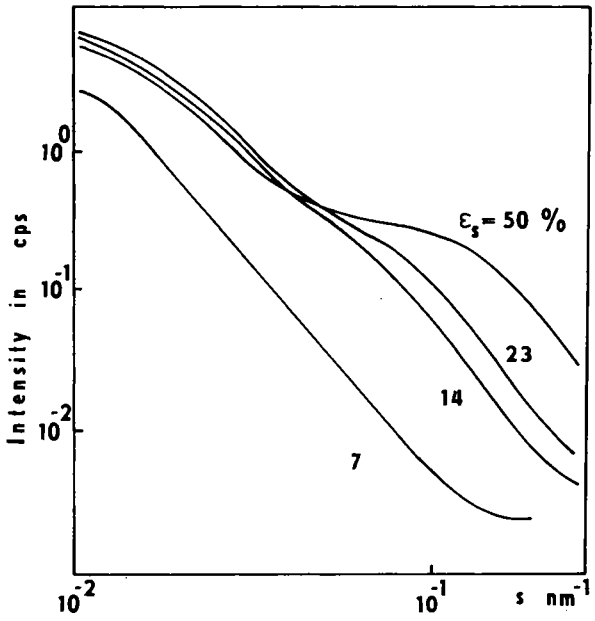

Fig. 6. Equatorial SAXS intensity distribution as a function of extension, for hard-elastic precursor.

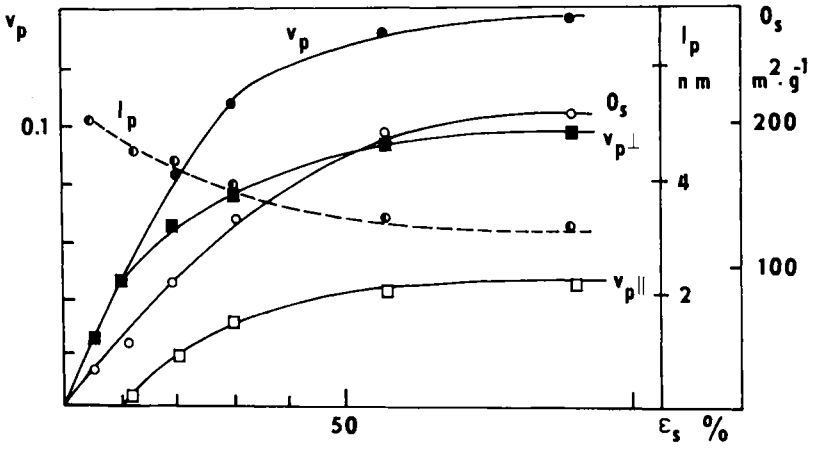

Fig. 7. Dependence of porous structure parameters on extension.

EBSCOhost - printed on 2/13/2023 3:45 AM via . All use subject to https://www.ebsco.com/terms-of-use

It is initially seen in Figure 7 that depending on the extension rise, the content of transversal microvoids increases, whereas the content of vertical microvoids is negligible. With deformations above 10 %, the fraction of vertical microvoids generates as a result of the horizontal microvoid extension, of chain rupture and fibrillar slip.

Figure 8 shows the SAXS patterns of hard-elastic fibre dynamically cold-drawn on different deformation degrees and subsequently heat-set at 140°C. In comparison with static-deformed fibres, the shape differences of diffuse scattering from permanent porous fibres can be seen, as a result of the vertical microvoid fraction increase.

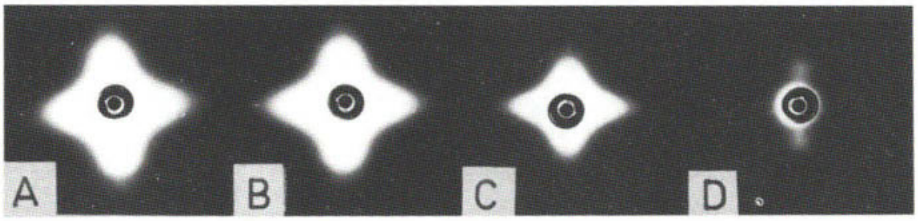

Fig. 8. The SAXS patterns of permanent microporous PP fibres

The SAXS pattern variations seem to be influenced by the collapse of extended horizontal microvoids during heat-setting. This presumption is supported by quantitative evaluation of porous structure from permanent porous fibres /see Fig. 9/.

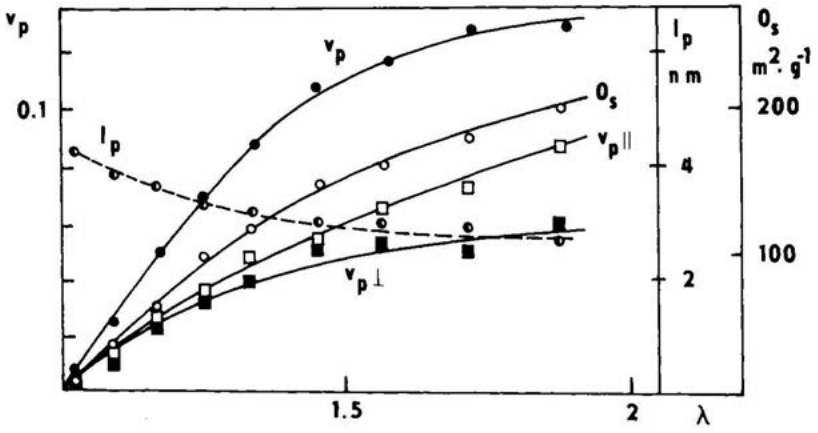

Fig. 9. Porous structure parameters as a function of drawing ratio.

EBSCOhost - printed on 2/13/2023 3:45 AM via . All use subject to https://www.ebsco.com/terms-of-use

At the corresponding deformation degrees, the total porosity and specific inner surface as well as average dimensions of microvoids measured perpendicularly to drawing direction are slightly smaller, whereas the fraction of parallel oriented microvoids is larger. After adding immersion liquid, the complete disappearance of the SAXS diffuse scattering in permanent porous fibres demonstrates the communication of microvoids with both a fibre surface and each other.
Electron micrographs of the extended precursor as well as the permanent microporous fibres exhibit the destroyed fibrillar morphology. No microvoids were observed in fibres by SEM.
SALS analysis does not confirm the presence any anisotropic objects /spherulites, macrovoids/ in the fibres. The horizontal streak can be seen, indicating the diffraction from filament surfaces only.

Conclusions

The presence of high crystalline, row-nucleated lamellar morphology in the starting fibres is a basic condition to obtain such high microvoid content fibres with uniform pore sizes and high specific inner surfaces respectively. Thick, well-packed crystalline lamellae having a large lateral dimension oriented perpendicularly to the fibre axis direction, interlamellar noncrystalline space with very low arrangement of macromolecular chains and the presence of mesomorphic regions with taut tie chains forming a strong connections between lamellae, allow a reversible separation and elastic bending lamellae upon extension accompanied by opening of microvoids in interlamellar regions.
Control of porosity, shape and microvoid size in permanent porous fibre, required for specific types of separation processes is possible by changing conditions such as cold drawing, fibre quenching and heat-setting.

EBSCOhost - printed on 2/13/2023 3:45 AM via . All use subject to https://www.ebsco.com/terms-of-use

References

1. Cannon, S.L., G.B. McKenna, W.O. Statton. 1976. J.Polymer Sci.: Macromolecular Reviews 11, 209.

2. Noether, H.D.. 1979. J.Polymeric Mater. 7, 57.

3. Budnickii, G.A., L.P. Perepechkin, J.A. Kostrov, B.L. Biber. 1976. Khim. Volokna. 6, 9.

4. Samuels, R.J.. 1979. J.Polymer Sci., Polymer Phys.Ed. 17, 535.

5. Fischer, E.W., H. Goddar, G.F. Schmidt. 1968. Makromol.Chem. 118, 144.

6. Marcian, V.. 1982. Chemické vlákna 32, 217.

7. Marcian, V.. 1985. Chemické vlákna 35, 22.

8. Slutsker, L.I.. 1975. Vysokomolek.Soyed. 17A, 262.

9. Ozerin, A.N., J.A. Zubov. 1976. Vysokomolek.Soyed. 18A, 2128.

10. Utevskii, L.E.. 1974. Vysokomolek.Soyed. 16A, 2339.

11. Utevskii, L.E.. 1972. Vysokomolek.Soyed. 14B, 396.

12. Pakhomov, P.M.. 1976. Vysokomolek.Soyed. 18A, 132.

13. Marcian, V.: Chemické vlákna /in press/.

EBSCOhost - printed on 2/13/2023 3:45 AM via . All use subject to https://www.ebsco.com/terms-of-use

EBSCOhost - printed on 2/13/2023 3:45 AM via . All use subject to https://www.ebsco.com/terms-of-use

ENVELOPMENT OF HIGH STRENGTH POLY(ETHYLENE) FIBRES

E. Schulz, R. Hirte

Akademie der Wissenschaften der DDR, Institut für Polymerenchemie "Erich Correns", 1530 Teltow-Seehof, German Democratic Republic

Introduction

Ultra-high strength poly(ethylene) (PE) fibres like surface grown crystals and also fibres of gel-spinning/hot drawing technique (1, 2) possess some disadvantages, as splitting and bending tendencies, limiting applications (Fig. 1).

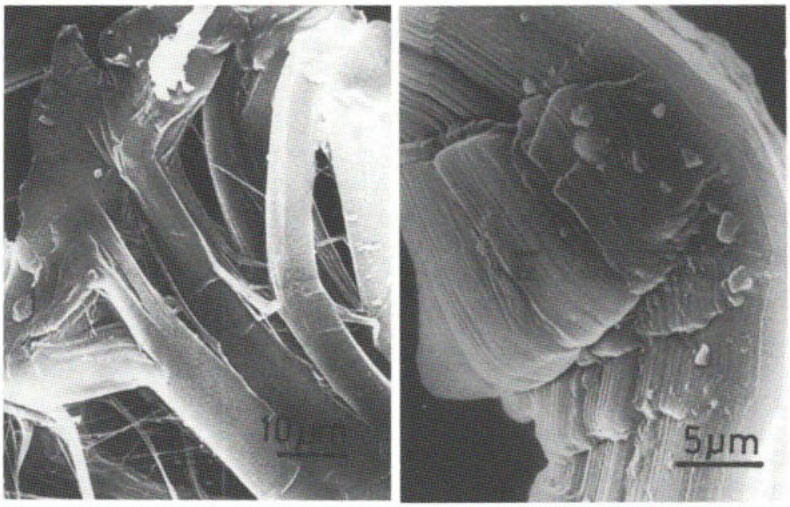

Fig. 1. Surface grown PE crystals.
a) Splitting tendency. b) Bending tendency.

This limitation can be overcome in two possible ways, namely by the volume modification and/or surface modification.
The volume modification, as crosslinking, is connected with changes of the macromolecules themself and generally with changes in the strength of the material (decrease in tensile strength). In contrast to this the physical surface modification implies no direct effect on the molecular and supermolecular structure of

Morphology of Polymers
© 1986 Walter de Gruyter & Co., Berlin · New York - Printed in Germany.

EBSCOhost - printed on 2/13/2023 3:45 AM via . All use subject to https://www.ebsco.com/terms-of-use

the basic fibres and no essential effect on the tensile properties of the material. By means of enveloping the fibre with a polymer layer an improvement can be achieved consisting in reducing the splitting and bending tendencies.
The main objective of this investigation was the improvement of fibres based on physical surface modification. Some questions of enveloping are related to the selection of the deposit polymer and the formation process of the envelope on surface grown PE crystals.
A good enveloping material has to meet the following demands:
- good wetting behaviour of the solution and good adhesion of the envelope to the substrate,
- good thin film forming behaviour,
- nearly the same chemical behaviour.

In our experiments PE, polycaproamide-6 (PA-6) and polyvinylidene fluoride (PVDF) were tested. PA-6 and PVDF proved to be unsuitable for this purpose. Actually, PA-6 formed thin surface films on PE crystals but the adhesion on the substrate was very poor and any mechanical strain causes the thin film to separate from the PE fibre sample. With PVDF globular precipitation structures were obtained; the formation of a coherent envelope was not possible under the chosen preparation conditions. PE itself was found to meet all the demands mentioned.

Experimental

Surface grown PE crystals prepared from ultra-high molecular weight linear PE Hostalen GUR (3) were used as substrate fibres. For enveloping procedures PE with different molecular weight ($M_w \sim 10^6$ and $\sim 10^5$) were applied. The surface films were formed, first, by means of a hot xylene/PE solution (PE concentration was ~ 1 wt.%) and, second, by evaporation technique (4). In the preparation from the solution the crystallization temperature was 105 °C and the sample temperatures in the evaporation experiments were 50 °C and 110 °C. Some of the treated samples were annealed at temperatures above 110 °C for improvement of the coating behaviour. All samples were characterized by SEM.

EBSCOhost - printed on 2/13/2023 3:45 AM via . All use subject to https://www.ebsco.com/terms-of-use

Results

Good adhesive surface coatings from PE are formed on the fibre surface with both techniques. The films show characteristic morphological features depending on the preparation method. The envelope formation from solution is based on crystal growth processes. The crystallization sites are responsible for the characteristic lamellar structure being formed more or less completely according to the local crystallization conditions and the molecular weight of the deposit. The film formation can be described in the following way:

In the first stage epitaxial nucleation and growth result in small surface lamellae arranged perpendicular to the fibre axis at the microfibrils of the PE substrate. This oriented overgrowth of the first molecular layer explains the strong adhesion of the coating at the PE fibre. An optimum fit of deposit and substrate molecules in the nucleation region promoting intermolecular interaction can be supposed. With crystallization propagation lamellar growth was found to proceed and the interlamellar regions of the overgrowing structures were filled in with structureless polymeric material. The surface morphology of the completed film depends decisively on the temperature-time conditions of crystallization. The structure of the enveloping film consisting of lamellae precisely oriented perpendicularly to the fibre axis, can be developed under isothermal conditions and low molecular weight polymer of the deposit (see Fig. 2).

Non-isothermal growing procedures cause a smooth or, by uncoordinated shred growing processes, formed surface films (see Fig. 3). The influence of the molecular weight of the deposit is reflected in a precise lamellar structure of the coating with a low molecular weight deposit while with high molecular deposits the structure formation is less precise.

In contrast to these lamellar structures the envelopes formed by the evaporation technique consist generally of fused globular particles. Here the film formation is based on precipitation of small molecule clusters from the vapour phase, using their mobility and transformation behaviour on the substrate surface. Epitaxial binding of the deposit molecules on the substrate is

EBSCOhost - printed on 2/13/2023 3:45 AM via . All use subject to https://www.ebsco.com/terms-of-use

possible, but occurs at high temperatures (above 90 °C), see Fig. 4.

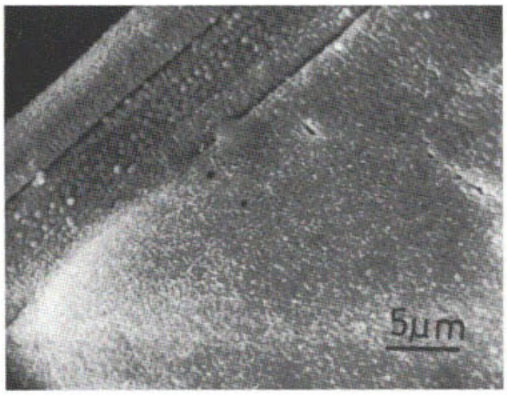

Fig. 4. PE coating of PE fibre prepared by evaporation technique.

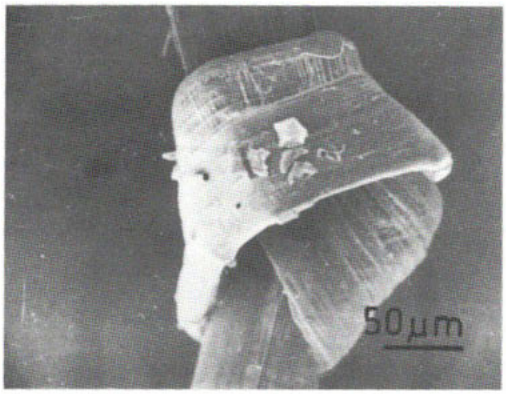

Fig. 5. Knotting test of an enveloped PE fibre.

Annealing procedures at temperatures above 120 °C are able to initiate partial melting processes causing levelling and destruction of the growing structure of the coating.
To test the adhesion and effects improving properties of the envelope the fibres were subjected to a knotting test. In the untreated fibres knotting causes splitting and bending. This behaviour is diminished by coating. Here the forces were absorbed by the enveloping film which shows cracking with bridge forma-

EBSCOhost - printed on 2/13/2023 3:45 AM via . All use subject to https://www.ebsco.com/terms-of-use

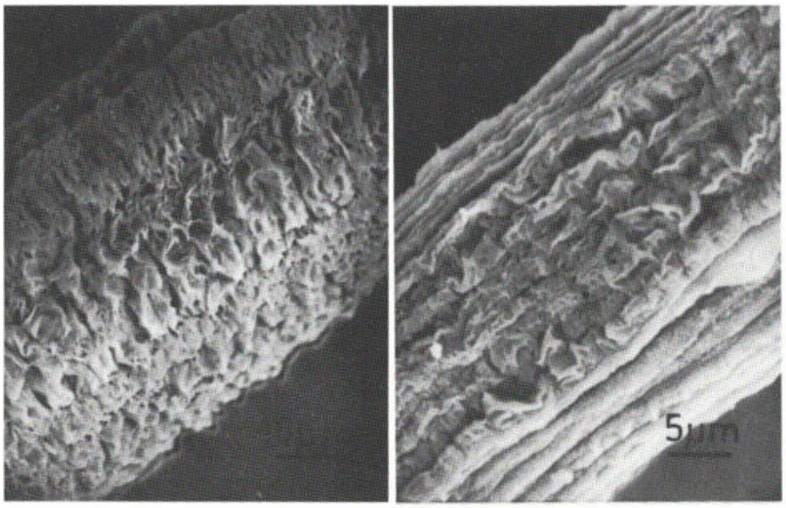

Fig. 2. PE coating on PE fibre prepared under isothermal conditions by solution technique.
a) Low molecular weight deposit. b) High molecular weight deposit.

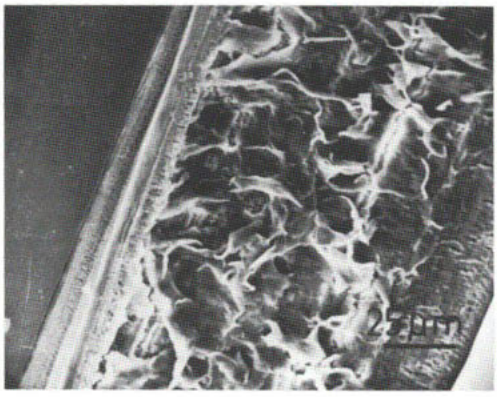

Fig. 3. PE coating on PE fibre prepared by solution technique. Non-isothermal crystallization condition.

EBSCOhost - printed on 2/13/2023 3:45 AM via . All use subject to https://www.ebsco.com/terms-of-use

tion in the coating material of the knot regions. In this way the splitting and bending tendency of the PE fibre will be reduced (see Fig. 5).
More details of the surface film formation and the epitaxial growing process will be described in a following publication. Investigations about the problem of the adhesion between deposit and substrate are in progress.

References

1. Pennings, A.J., Schouteten, C.J.H., Kiel, A.M. 1972. J. Polymer Sci. C 32, 167.

2. Kalb, B., Pennings, A.J. 1980. J. Mater. Sci. 15, 2584.

3. Marichin, V.A., L.P. Mjasnikova, D. Zenke, R. Hirte, P. Weigel. 1984. Vysokomol. Soed. A2, 210.

4. Madorsky, S. 1951. J. Polymer Sci. 9, 133.

EBSCOhost - printed on 2/13/2023 3:45 AM via . All use subject to https://www.ebsco.com/terms-of-use

THE HEAT CAPACITY AND THERMAL EXPANSIVITY OF ANNEALED POLY(ETHYLENE TEREPHTHALATE) FIBERS

G.W. Urbańczyk and G. Michalak
Institute of Fiber Physics and Textile Finishing, Technical University Łódź, Poland

Introduction

The influence of annealing of PET fibers on their heat capacity and thermal expansivity, especially the recognition of the structural background of variation of these thermal characteristics, is still not adequately known. In the present contribution an attempt has been made to extend the knowledge referring to the mentioned properties of PET fibers.

Experimental

Sample preparation

The material under study comprises samples of continuous PET filaments of linear density 220/48 dtex drawn to 4.5 draw ratio. The following samples have been investigated: (a) fibers annealed isothermally at temperatures of 130, 140, 150, 160, 170, 180, 190, 200, and 210°C in air during 2, 5, 10 and 30 min in loose state, and (b) fibers in their initial (unannealed) state for the reason of comparison.
The values of indices characterizing the morphological and fine structures of all considered samples are presented in Table 1.

Measurements

Assuming that the morphological structure of the given fibers is described by the widely accepted fibril-lamellar structure model, the fraction b of taut tie molecules (t.t.m.) has been chosen as a parameter which decisively determines the morphological structure of the examined PET fibers. The t.t.m. fraction has been calculated on the basis of measured fiber Young's modulus $E_{\parallel}$ due to

Morphology of Polymers
© 1986 Walter de Gruyter & Co., Berlin · New York - Printed in Germany.

EBSCOhost - printed on 2/13/2023 3:45 AM via . All use subject to https://www.ebsco.com/terms-of-use

Table 1. Morphological and Fine Structure Parameters of Examined PET Fibers

AT,min	Δn	Δn/d	x,%	t.t.m.	CDT,s	f_a
Without	0.1781	0.1296	36.7	0.120	9	0.50
		Annealing at 130°C				
2	0.1681	0.1209	45.6	0.068	19	0.50
5	0.1615	0.1165	45.8	0.063	25	0.50
10	0.1614	0.1184	45.4	0.065	41	0.47
30	0.1653	0.1189	49.2	0.047	55	0.46
		Annealing at 140°C				
2	0.1645	0.1184	48.1	0.051	40	0.49
5	0.1607	0.1156	48.6	0.057	35	0.49
10	0.1593	0.1146	49.0	0.053	55	0.46
30	0.1670	0.1202	48.8	0.051	74	0.45
		Annealing at 160°C				
2	0.1628	0.1169	50.3	0.046	103	0.47
5	0.1572	0.1129	50.8	0.048	108	0.44
10	0.1628	0.1170	51.3	0.056	106	0.44
30	0.1622	0.1163	52.8	0.041	156	0.44
		Annealing at 180°C				
2	0.1592	0.1139	53.5	0.045	160	0.46
5	0.1610	0.1154	53.1	0.045	150	0.44
10	0.1606	0.1150	54.3	0.047	222	0.44
30	0.1650	0.1180	55.6	0.035	245	0.43
		Annealing at 200°C				
2	0.1637	0.1171	55.5	0.037	240	0.45
5	0.1609	0.1145	55.4	0.038	245	0.44
10	0.1634	0.1167	57.8	0.047	323	0.44
30	0.1663	0.1187	57.9	0.034	383	0.43
		Annealing at 210°C				
2	0.1623	0.1158	58.7	0.030	329	0.44
5	0.1611	0.1150	58.1	0.035	405	0.43
10	0.1573	0.1122	59.5	0.034	703	0.43
30	0.1692	0.1203	62.3	0.029	1417	0.42

AT annealing time; Δn birefringence; Δn/d density reduced birefringence; x volume-percent crystallinity; t.t.m. fraction of taut tie molecules; CDT critical dissolution time of a fiber; f_a orientation function of the amorphous component.

the procedure applied earlier by Prevorsek (1), Misra (2), Mishra (3) and Choy (4) which is in turn attributed to the approximation of the real morphological fiber structure by the Takayanagi (5) model.

As relevant fine structure characteristics of the examined samples, the overall orientation, the molecular orientation of the amorphous

EBSCOhost - printed on 2/13/2023 3:45 AM via . All use subject to https://www.ebsco.com/terms-of-use

component of the fiber, the crystallinity, and the intermolecular cohesion have been chosen. The overall orientation has been evaluated from the density reduced birefringence, $\Delta n/d$. The molecular orientation of the amorphous component has been characterized by means of the orientation function, f_a, calculated from dichroic measurements of standard dyed fiber (6). The crystallinity has been evaluated on the basis of the volume-percent crystallinity using the flotation method in a mixture of n-heptane and carbon tetrachloride. Values of the fiber critical dissolution time (CDT) in the mixture of phenoltetrachlorethan 2:1 at 60°C have been used as a measure of the intermolecular cohesion (7).

The heat capacities of the examined samples were estimated at constant pressure from the DSC diagrams using the relationship

$$c_p = H_s\, m_a\, c_{ap}/H_a\, m_s \qquad (1)$$

where H_s and H_a refer to the amplitude of enthalpy change occurring at the temperature increase from 20 to 25°C, respectively, for fiber sample and reference substance (saphire); m_s and m_a are weights of sample and reference substance, c_{ap} = 775.43 J/kg.K is the heat capacity of the reference substance.

The values of the thermal volume expansivity, α_{25}, were calculated from the hydrostatic weight measurements using n-heptan as a liquid. The sought α_{25} values have been calculated from equation

$$\alpha_{25} = (Q_o - Q_t)/Q_t(t - t_o) \qquad (2)$$

where Q_o and Q_t refer to fiber density at t_o = 19°C and t = 25°C, respectively.

Results and Discussion

Heat capacity

The established c_p values for all examined samples are shown in Fig. 1. The obtained c_p values give evidence that the heat capacity of PET fibers alters essentially as a result of applied heat treatment. The variation in c_p depends on both the annealing temperature and the time of heat treatment; their character is temperature dependent, as all thermal effects of annealing are strictly

EBSCOhost - printed on 2/13/2023 3:45 AM via . All use subject to https://www.ebsco.com/terms-of-use

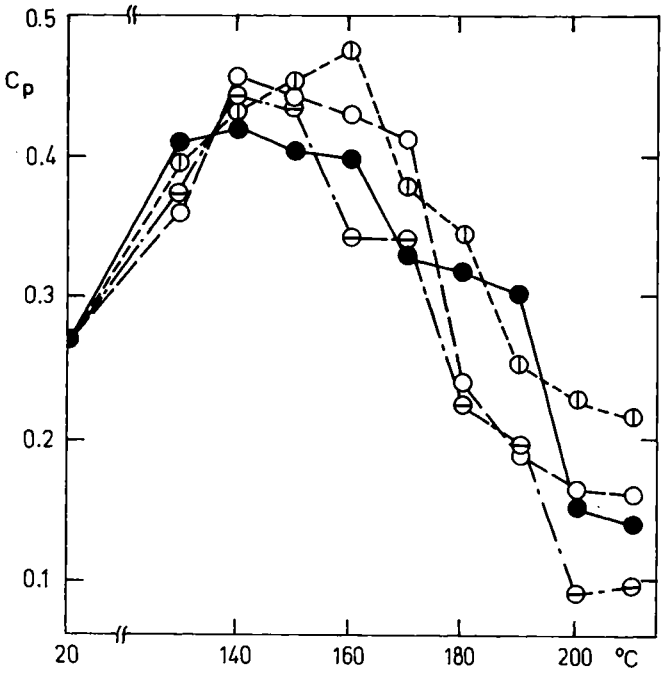

Fig. 1. Heat capacity c_p(cal $K^{-1}g^{-1}$) of annealed PET fibers: ● 2 min, o 5 min, ⊕ 10 min, ⊖ 30 min.

related to heat transfer from the surrounding to fiber. The duration of annealing modifies only the relationship $c_p = f(T_{ann})$. It can be noticed that with increasing time the effects of annealing become stronger pronounced.

The obtained results allow us to conclude that there exist three distinguished temperature intervals of annealing of PET fibers in which c_p attains different level and undergoes alteration different with increasing temperature of annealing.

1st interval corresponds to temperature zone 130-140°C. Within this zone, c_p after annealing is always larger than c_p of unannealed fibers, and the increase in temperature is related to the increasing c_p. 2nd interval refers to temperature zone of 150-170/190°C. Within this zone, c_p of annealed fibers is always larger than that for the initial state, but the value of c_p diminishes with increasing temperature. 3rd interval pertains to temperature zone of 170/190-210°C within which c_p after annealing is always

EBSCOhost - printed on 2/13/2023 3:45 AM via . All use subject to https://www.ebsco.com/terms-of-use

smaller than before and drops with increasing temperature to minimum, and then again reaches higher level for the annealing temperature of 210°C.

It may be noticed that the duration of annealing does not influence the width of the 1st interval, whereas 2nd and 3rd intervals undergo alteration, i.e. the width of the 2nd zone decreases and that of the 3rd interval extends.

Comparing the changes in morphological and fine structure indices with the alterations in c_p, it can be noticed that the change in c_p does not correlate with variation of any separate structure parameters. This leads to conclusion that the ascertained alteration in c_p must be evoked by a complex change in different morphological and fine structure parameters.

A closer examination of the relations enables us to infer that the c_p values of annealed PET fibers are determined by counteracting, mutually competitive influence of particular structure parameters. The level of c_p is always set up by mutual opposite effects involved by the change in t.t.m. fraction and overall orientation, on one side, and the change in crystallinity, on the other side. Heat treatment of fibers causes an increase in their internal energy which demands then smaller amount of heat, i.e., the smaller the value of c_p, the lower the mobility of vibrating groups. This mobility will increase with decreasing t.t.m. fraction, diminishing overall orientation and, on the contrary, will drop with increasing crystallinity.

The annealing within the 1st temperature interval (130-140°C) leads to a relatively strong decrease in the t.t.m. fraction as compared to the increase in crystallinity and simultaneously to a drop in overall orientation. Such changes must cause a noticeably increase in the internal freedom and thus an enhanced mobility of vibrating groups. Within the 2nd temperature interval, the diminishing of t.t.m. fraction as a result of annealing will be compensated by a relatively strong increase in crystallinity. This and additionally the drop in the overall orientation leads to a state of lower internal freedom and thus to lower mobility of the vibrating groups, which yields lower c_p values than those for the 1st interval.

Within the 3rd temperature interval, the decrease in t.t.m. fraction seems to be predominated by the very strong increase in crystallinity. This and the drop in the overall orientation must pro-

EBSCOhost - printed on 2/13/2023 3:45 AM via . All use subject to https://www.ebsco.com/terms-of-use

duce a strong reduction in internal freedom (reduction in vibrating groups mobility) which manifests itself by the low c_p values. The pronounced tendency to a renewed increase in c_p for annealing at 210°C seems to be linked with the conversion of PET fine structure into the so-called mosaic-blocks structure (8,9). It may be supposed that the level of internal freedom, resulting from such rebuilding, becomes higher; as a consequence, this leads to an increase in c_p.

Thermal expansivity

The extablished values of thermal volume expansivity are presented graphically in Fig. 2. The lay-out of received α_{25} values shows that thermal volume expansivity of PET fibers undergoes an essential alteration resulting from annealing. The change in α_{25} depends on annealing temperature and duration of the heat treatment.

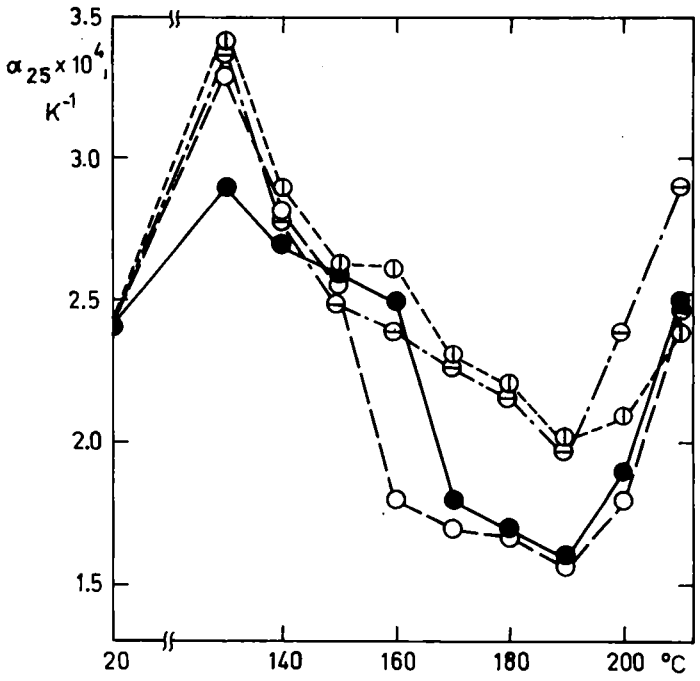

Fig. 2. Thermal volume expansivity coefficient α_{25} of annealed PET fibers: ● 2 min, o 5 min, ⊕ 10 min, ⊖ 30 min.

EBSCOhost - printed on 2/13/2023 3:45 AM via . All use subject to https://www.ebsco.com/terms-of-use

The character of the alterations is attributed first of all to the level of annealing temperature. Annealing time modifies only the range of changes and the α_{25} value, but does not alter the character of the variation. The results obtained allow us to draw a conclusion that there may be distinguished three temperature intervals of annealing in which α_{25} values attain different level and undergo alteration different with increasing annealing temperature. 1st interval refers to the temperature zone of 130-150/160°C within which the α_{25} values are larger than those of unannealed fibers. The growth of annealing temperature involves a monotonic declining of α_{25}. 2nd temperature interval refers to 170-190°C within which the α_{25} values are lower than those of unannealed fibers. With increasing annealing temperature α_{25} diminishes continuously reaching a minimum value at 190°C. 3rd temperature interval pertains to the temperature range of 200-210°C. Within this zone α_{25} increases with annealing temperature reaching a level equal or higher than that of unannealed fibers.

Comparing the changes in structure indices with the alteration in α_{25} values it can be seen that the change in α_{25} does not correlate with variation in any particular structure parameter. This enables us to conclude that the ascertained alteration in α_{25} must be evoked by a complex change in different morphological and fine structure parameters.

The explanation of reason of the ascertained variation in α_{25} is complicated by the intricate essence of the volume expansivity of PET fibers. Similarly to other fibers their thermal expansivity exhibit anisotropy and depends on the fiber crystallinity. Neglecting the influence of orientation and considering a PET fiber simply as a system of anisotropic thermal expanding crystallites dispersed in isotropic thermal expanding amorphous matrix, the thermal volume expansivity of a fiber may be described by the expression

$$\alpha = x\,\alpha_{\parallel}^{c} + 2x\alpha_{\perp}^{c} + 3(1-x)\alpha^{a} \qquad (3)$$

where x refers to the volume-percent crystallinity, $\alpha_{\parallel}^{c}$, $\alpha_{\perp}^{c}$ are the linear thermal expansivity coefficients, respectively, parallel and perpendicular to the direction of molecule axis, and α^{a} is the linear thermal expansivity coefficient of the amorphous component. Attempting to elucidate the alteration in α_{25} resulting

EBSCOhost - printed on 2/13/2023 3:45 AM via . All use subject to https://www.ebsco.com/terms-of-use

from annealing we shall utilize the above equation.
The observed increase in α_{25} within the 1st temperature interval explained in the light of eq.(3) must be connected, first of all, with a strong enhancing of the component $x\alpha_{\parallel}^{c}$ and, to a minor extent, with an increase in the $2x\alpha_{\perp}^{c}$ component. The enhancing of the first term will be a result of increasing crystallinity x and especially, of a very strong increase in $\alpha_{\parallel}^{c}$. The last effect is, as discovered by Choy and coworkers (10,11), to be attributed to the reduction in t.t.m. fraction. The increase in the second term will be, in view of the independence of $\alpha_{\perp}^{c}$ of the t.t.m. fraction changes, only a consequence of increasing crystallinity. It may be assumed simultaneously that the change in the third term $3(1-x)\alpha^{a}$ will be of lesser importance. Indeed, (1-x) becomes smaller even if α^{a} reveals still large values, because the intermolecular cohesion does not increase noticeably. In result, the decrease in the third term as relatively small will be prevailed by the remaining terms of eq.(3).
The observed diminishing of α_{25} within the 2nd temperature interval of annealing, as compared to the 1st interval, may be attributed to the strong diminishing of the component $3(1-x)\alpha^{a}$ and, to a lesser extent, to that of the $2x\alpha_{\perp}^{c}$ term. The reason of the $3(1-x)\alpha^{a}$ term decrease lies in a simultaneous drop in (1-x) and α^{a}. The decrease in α^{a} will be a consequence of the strong growth of intermolecular cohesion which reduces the thermal expansivity of amorphous regions. The increase in intermolecular cohesion can also be recognized as the reason of the $\alpha_{\perp}^{c}$ diminishing.
Analyzing the change in the last term, $x\alpha_{\parallel}^{c}$, it can be concluded that its growth will be relatively small (only small additional diminishing of t.t.m. fraction). The influence of this growth will be overweighed by the decrease in both remaining terms. The explanation of the α_{25} enhancement within the 3rd annealing temperature interval, as compared to the 2nd interval, needs to regard additionally new aspects of the fiber structure changes. As stated by Fischer and Fakirov (8,9) in semicrystalline oriented PET objects a rebuilding of crystalline regions takes place as a result of annealing at temperatures of 200°C. Due to this rebuilding the mosaic-blocks structure is being established. In consequence, the density of crystalline regions decreases. The decrease in density must inevitably involve an essential growth of $\alpha_{\perp}^{c}$. Taking into ac-

EBSCOhost - printed on 2/13/2023 3:45 AM via . All use subject to https://www.ebsco.com/terms-of-use

count the above mentioned as predominant reason of the observed α_{25} increase, there should be recognized the strong increase in $2x\alpha_{\perp}^{c}$ and, simultaneously, the larger values of $x\alpha_{\parallel}^{c}$.

References

1. Prevorsek, D.G., P.J. Harget, R.K. Sharma, D.C. Reimschüssel. 1973. J.Macromol.Sci., Phys. B8, 127.
2. Misra, A., R.S. Stein. 1979. J.Polym.Sci., Phys.Ed. 17, 235.
3. Mishra, S.P., B.L. Deopura. 1982. J.Appl.Polym.Sci. 27, 3211.
4. Choy, C.L., M. Ito, R.S. Porter. 1983. J.Polym.Sci., Phys.Ed. 21, 1327
5. Takayanagi, M., K. Imada, T. Kajiyama. 1966. J.Polym.Sci. C15, 262.
6. Lipp-Symonowicz, B., G.W. Urbańczyk. 1982. Acta Polym. 33, 197.
7. Galil F. 1973. Text.Res.J. 43, 615.
8. Fischer, E.W., S. Fakirov. 1976. J.Macromol.Sci. 11, 1041.
9. Fakirov, S., E.W. Fischer, R. Hoffmann, G.F. Schmidt. 1977. Polymer 18, 1121.
10. Choy, C.L., F.C. Chen, E.L. Ong. 1979. Polymer 20, 1291.
11. Choy, C.L., F.L. Chen, K. Young. 1981. J.Polym.Sci., Phys.Ed. 19, 335.

EBSCOhost - printed on 2/13/2023 3:45 AM via . All use subject to https://www.ebsco.com/terms-of-use

EBSCOhost - printed on 2/13/2023 3:45 AM via . All use subject to https://www.ebsco.com/terms-of-use

STRUCTURAL CHANGES OF PETP FIBRE DURING THE HEAT TREATMENT IN DIFFERENT MEDIA

B. Lipp-Symonowicz

Institute of Fibre Physics and Textile Finishing, Technical University of Lódź, 90-507 Lódź, Poland

Introduction

The fibre properties are largely changed by the integrated factors acting during processing, starting with spinning and ending in the manufacture of ready-made clothes. The changes of the fibre properties result from the mechanical, thermal and chemical treatment of the fibre, which induces its structure alteration. Although a large number of investigations already exist, concerning the influence of the different factors on the structure of polyethylene terephthalate fibre, the problem remains still open.
The results presented concern the structural changes in PETP fibre caused by heat treatment in the media applied usually during its finishing processes, i.e. water, dry air, air containing wet, and superheated steam.
These changes were analyzed on the basis of the average values of such structure parameters, as the degree of crystallinity, the molecular orientation, and the molecular cohesion energy.

Experimental

Fibre

Commercial drawn 5× polyethylene terephthalate, PETP fibre, has been examined. The fibre was isothermally heated with free ends in the following media: water, dry air, air containing wet and superheated steam, according to the time and temperature programme shown in Table 1.

Morphology of Polymers
© 1986 Walter de Gruyter & Co., Berlin · New York - Printed in Germany.

EBSCOhost - printed on 2/13/2023 3:45 AM via . All use subject to https://www.ebsco.com/terms-of-use

Methods

The crystallinity degree of the fibre was estimated by wide angle X-ray scattering (WAXS), and from its density. The WAXS data were obtained, using the DRON-II generator (USSR), at 30 kV and 20 mA, with Ni-filtered CuK_α-radiation. The degree of crystallinity C_X was estimated by the method described in ref.(1). The fibre densities were measured by means of a gradient column with a mixture of carbon tetrachloride and toluene, and the crystallinity index C_D was calculated from these data in a usual way. The following values were found for densities of amorphous and crystalline PET, respectively, $\rho_a = 1.333\ g\ cm^{-3}$ and $\rho_c = 1.455\ g\ cm^{-3}$.

The fibre molecular orientation were analyzed on the basis of the total molecular orientation function of the fibre, f_o, and the molecular orientation function of noncrystalline regions, f_a. The values of f_o were determined (2) from the directional refractive indices, $n_\parallel$ and $n_\perp$, respectively, for the light of wavelength 546 nm using a double refracting interference microscope of Pluta (3). The values f_a were estimated by measuring the fibre infrared dichroism, according to the refs.(4,5), on the basis of the $897\ cm^{-1}$ 'amorphous' band. The spectrophotometer Specord IR-75 (DDR) supported with polarizer was used for this purpose.

The molecular cohesion energy of the fibre was evaluated from the critical dissolution time (CDT) of the fibre in a mixture of phenol/tetrachloroethene (1:1 vol.part) at 45°C.

Results and Discussion

Fibre crystallinity

As shown in Table 1, the heat treatment of the fibre in the media used leads to an increase in its crystallinity degree, proportional to the temperature T_h of the treatment. The rate of this process depends on T_h of such treatment and, to some extent, also on the type of medium applied. The steady-state crystallinity of the fibre for each medium depends only on its temperature. This conclusion follows from both the X-ray and density data. The values

EBSCOhost - printed on 2/13/2023 3:45 AM via . All use subject to https://www.ebsco.com/terms-of-use

Table 1. Crystallinity indices, C_D and C_X, orientation functions, f_o and f_a, and CDT values for the fibre treated in different media at different temperature and time

Medium	Temp. °C	Time min	C_D	C_X	f_o	f_a	CDT
Without	-	-	0.426	0.391	0.7003	0.4567	13
water	100	15	0.435	0.426	0.6710	0.3910	35
		60	0.441	0.461	0.6771	0.3926	42
		240	0.446	0.482	0.6835	0.4107	53
		4320	0.449	0.515	0.6842	0.4171	69
	130	15	0.513	0.512	0.6431	0.2500	180
		60	0.527	0.568	0.6573	0.2790	250
		240	0.534	0.591	0.6635	0.2893	365
Air +	120	5	0.497	0.483	0.6592	0.4065	62
wet steam		15	0.518	0.531	0.6636	0.4059	84
		60	0.520	0.557	0.6548	0.3802	250
	150	5	0.501	0.570	0.6635	0.4314	176
		15	0.559	0.598	0.6664	0.3284	232
		60	0.573	0.618	0.6648	0.3544	463
Air +	120	5	0.491	0.471	0.6678	0.4056	70
superheated		15	0.505	0.525	0.6796	0.4314	100
steam		60	0.513	0.550	0.6836	0.4311	240
	150	5	0.532	0.555	0.6672	0.4314	221
		15	0.567	0.579	0.6723	0.4167	303
		60	0.569	0.610	0.6830	0.4167	482
Dry air	180	0.5	0.596	0.642	0.6613	0.3853	846
		2.0	0.634	0.678	0.6737	0.3284	1188
		15.0	0.641	0.688	0.6768	0.3802	1765
	220	0.5	0.623	0.691	0.6641	0.3802	2467
		2.0	0.663	0.732	0.6746	0.4056	3310
		15.0	0.746	0.785	0.6796	0.3544	-

of the steady-state crystallinity indices, obtained from the methods applied and the dependences C_X and C_D plotted as a function of the heating temperature of the fibre, clearly differ from each other. The WAXS-values are higher. The dependence of C_X on T_h exhibits a linear character over the whole range of the temperatures used. The same seems to hold also for $C_D = f(T_h)$ in the range of lower temperatures (from 100 to 150°C). The linear character of the relationship is lost in the range of higher temperatures. At 220°C, the high increase in the crystallinity index of the fibre appears, resulting from the rapid increase in the density of fibre treated by heat at that temperature.

EBSCOhost - printed on 2/13/2023 3:45 AM via . All use subject to https://www.ebsco.com/terms-of-use

Fibre molecular orientation

The analysis of the molecular orientation changes in the fibre during its heating in different media, using data f_o and f_a shown in Table 1, allows us to formulate the following statements:
The heat treatment of the fibre in the media used leads to a decrease in the total molecular orientation and the molecular orientation of the noncrystalline regions of the fibre.
The former decrease is dependent on the type of medium, and relatively slightly dependent on temperature of the heat treatment. The level of changes is determined by the heat treatment time.
The strongest decrease in the fibre total orientation is observed during its heating in water and air containing wet steam, and reaches its maximum for the short time periods of the fibre heating and gets weaker with the extension of the time periods.
The decrease in the molecular orientation in noncrystalline regions of the fibre is dependent very strongly on the temperature, time and medium used during the treatment. The decrease in f_a as a function of T_h for the longest time of the fibre heat treatment in dry air and air containing superheated steam is proportional to the temperature of treatment. The heat treatment in water and air containing wet steam intensifies the process of molecular disorientation in noncrystalline regions of the fibre. The changes in f_a as a function of the heat treatment time are similar for all media. For the shortest time, there appears the decrease in f_a if related to f_a for non-heated fibre. With the extension of the heat treatment time, further decrease in f_a occurs, followed by its new increase.
The specific effect of water and air containing wet steam on the fibre molecular orientation observed may be explained by the interaction of water with polymer molecules, leading to an increase in the molecular mobility of the latter in noncrystalline regions of the fibre. It would confirm the statement (6) that PETP fibre in water shows the glass transition temperature about 20°C lower than in the medium of dry air.

Molecular cohesion energy of the fibrous polymer

The CDT values (Table 1), characterizing the molecular cohesion energy, reveal its very high increase for the fibre heated in all media used, in relation to the non-heated fibre. They clearly de-

EBSCOhost - printed on 2/13/2023 3:45 AM via . All use subject to https://www.ebsco.com/terms-of-use

pends on the temperature and time of the heat treatment, being affected very slightly by the type of medium.
From the comparison of data collected in Table 1, the following may be concluded: The increase in CDT values as a function of T_h, the simultaneous decrease in f_a values, and the steadiness of f_o values as a function of T_h point out the lack of correlation between the molecular cohesion energy and molecular orientation of the fibre.
On the other hand, there is the linear correlation between the CDT values and the crystallinity indices, C_X and C_D, of the fibre treated at lower temperature in different media. For the fibre treated at higher temperatures (in air), the relationship changes its character: relatively small changes in the fibre crystallinity are accompanied by very large changes in CDT values.

Conclusion

The results obtained demonstrate that the changes in the structural parameters of PETP fibre heated in the media used are determined mainly by temperature.
The type of medium is important only for the changes in molecular orientation of the fibre. The non-proportional increase in CDT values in relation to the changes in the crystallinity degree of the fibre heated in the range of higher temperatures tends to formulate the conclusion that, during that treatment, there occurs the specific rebuilding of the PETP fibre structure which causes very high increase in the molecular cohesion energy of the fibrous polymer. This conclusion corresponds well with the statements by Fakirov and Fischer (7-9). Thus, it may be concluded that the increase in the molecular cohesion energy of the fibrous polymer, reflected in the decrease in the fibre dissolution time, may be justified only by the fact of rebuilding the fibre structure into mosaic block structure.

References

1. Wakelin, J.H., H.S. Wirgin, E. Crystal. 1959. J.Appl.Phys.30, 1654.

EBSCOhost - printed on 2/13/2023 3:45 AM via . All use subject to https://www.ebsco.com/terms-of-use

2. Nobbs, J.H., J. Bower, J.M. Ward. 1976. Polymer 17, 25.

3. Pluta, M. 1982. In: Mikroskopia Optyczna. PWN-Warszawa, p. 778.

4. Fraser, R.B.D. 1958. J.Chem.Phys. 28, 1913.

5. Cunningham, A., J.M. Ward. 1974. Polymer 15, 749.

6. Holfeld, W.T., M.S. Shepard. 1978. Text.Chem. and Col. 10, 18/26.

7. Fischer, E.W., S. Fakirov. 1976. J.Mater.Sci. 11, 1041.

8. Fakirov, S., E.W. Fischer, R. Hoffmann, G.F. Schmidt. 1977. Polymer 18, 1121.

9. Fakirov, S., D. Stahl. 1982. Die Angew.Makromol.Chem. 102, 117.

EBSCOhost - printed on 2/13/2023 3:45 AM via . All use subject to https://www.ebsco.com/terms-of-use

RADIAL STRUCTURE DIFFERENTIATION OF PET FILAMENTS AND ITS INFLUENCE ON THE DYESTUFF DIFFUSION

B. Lipp-Symonowicz

Institute of Fibre Physics and Textile Finishing, Technical University of Łódź, 90-507 Łódź, Poland

Introduction

Polyethylene terephthalate filaments, like the other man-made fibres, may reveal radial structure differentiation (1-3). The polymer layer at the surface of such fibre shows generally a higher molecular orientation than the inner layers of the fibre. The macromolecules in that layer are more closely packed. Due to this, the surface layer of fibres gets hardly penetrable for the molecules of different chemical substances, thus creating a surface barrier (4) to diffusion of these molecules into the fibre. The results presented concern the investigation of the radial structure differentiation of PET filaments and its influence on diffusion of the selected disperse dyestuffs into the fibre.

Experimental

Fibres

Commercial, non-tarnished PET filaments supplied by Chemitex-Elana plant in Toruń have been examined. The radial structure differentiation was additionally determined for the fibre treated with water at 130°C.

Dyestuffs

Two selected disperse dyestuffs, C.I.Disperse Yellow 3/11855 and C.I.Disperse Blue 6/62050, with different diffusion properties due to differentiation in size, shape and polarity of their molecules, have been used. These dyestuffs were both used for investigation of the radial structure differentiation of the filaments, and of

Morphology of Polymers
© 1986 Walter de Gruyter & Co., Berlin · New York - Printed in Germany.

EBSCOhost - printed on 2/13/2023 3:45 AM via . All use subject to https://www.ebsco.com/terms-of-use

the diffusion process.

Methods

The radial structure differentiation of PET filaments has been examined using the following methods:
Method A. Microscopic measurements of visible dichroism of the fibre coloured for different time periods consists in the estimation of the directional optical densities, $D_{\parallel}$ and $D_{\perp}$, respectively, using polarized, monochromatic radiation of wavelength λ = 430 nm. The fibre was dyed in aqueous bath of the dyestuff C.I.Disperse Yellow 3/11855, at 50°C, according to the following dyeing time programme: 15, 30, 60, 120, 180, 360, 600 and 2880 min. Thus, for each sample dyed at a definite time, the distance a of the dyestuff penetration into the fibre, has been determined. For the polymer layer thickness a, the orientation function of the polymer chain segment axis with respect to the fibre axis was calculated from the equation (5):

$$\frac{D_{\parallel} - D_{\perp}}{D_{\parallel} + 2D_{\perp}} = 0.5(3\,\overline{\cos}^2\rho - 1)\;\; 0.5(3\,\overline{\cos}^2\theta - 1)$$

where $0.5(3\cos^2\rho - 1)$ is the orientation function of the dyestuff molecule axis related to the polymer chain segment axis, $0.5(3\cos^2\theta - 1)$ is the orientation function (f_{aD}) of the polymer chain segment axis to the fibre axis, ρ is the angle between the axis of the dyestuff molecule used and the polymer chain segment axis, which was determined for PET as equal to 10° (6).

Method B. Microphotometric measurement of the dyestuff concentration has been made to estimate its distribution along the fibre radius. The concentration curves, reflecting the dyestuff distribution along the fibre radius, were obtained from microphotometric analysis of coloured cross-sections of the fibres, using monochromatic light of wavelength λ = 570 nm.
For revealing the radial structure differentiation of the fibre, samples of the fibre cross-section of 5 μm in thickness were dyed on the microscopic slide, using aqueous suspension of the dyestuff C.I.Disperse Blue 6/62050. The dyeing was carried out at 60°C for 330 min. Then, the dyeing bath was removed and the samples were

EBSCOhost - printed on 2/13/2023 3:45 AM via . All use subject to https://www.ebsco.com/terms-of-use

rinsed with aqueous solution of acetone. Radial structure differentiation of the filament was evaluated in terms of the transmittance T, changing as a function of its radius.

The influence of the fibre radial structure differentiation on the dyestuff diffusion into the fibre can be expressed by the relationship $c_t/c = f(t^{1/2})$, where c_t and c_∞ are the dyestuff concentrations in the fibre after the dyeing times t and t_∞, respectively, t being related to the state of dyeing balance. In the case when the diffusion of dyestuff into the fibre is not disturbed by the existence of the surface structural barrier in the fibre, the relationship given above ought to show the linear character in its initial run (4).
This relationship was analysed for the dyeing process carried out at different temperatures 100, 115 and 130°C, respectively. The fibre was dyed in aqueous bath with a constant concentration of dyestuff, according to the dyeing programme shown in Table 2.

Results and Discussion

The results obtained (Table 1, Fig.1) clearly confirm the radial structure differentiation of PET filament, expressed in terms of the orientation function f_{aD} and the coloured fibre transmittance T, as a function of the fibre radius r. Polymer in the surface layer of the fibre reveals a higher molecular orientation than in the inner layers of the fibre. This confirms the change in f_{aD} and T values as a function of the fibre radius.
Both methods used show clearly the existence of the radial structure differentiation in the filament investigated. Unfortunately, this information is only qualitative, giving a trend of but not real differences in the molecular orientation between successive polymer layers in the fibre.
The obtained picture of the radial structure differentiation of PET filament is deformed, in method A, by the superposition of the f_{aD} value for the surface layer on the f_{aD} values of each successive polymer layer in the fibre and, in method B, by the probable superposition of the differences in the crystallinity degree of such successive fibre layer on the differences in orientation. The last suggestion is in conformance with the different character of

EBSCOhost - printed on 2/13/2023 3:45 AM via . All use subject to https://www.ebsco.com/terms-of-use

Table 1. Radial Structure Characteristics of the Fibre, f_{aD} and T, before (BWT) and after (AWT) Water Treatment

Fibre radius r, μm	Polymer layer thickness a μm	BWT f_{aD}	BWT T,%	AWT f_{aD}	AWT T,%
	0.25	0.1868	88	0.1301	78
	0.32	0.1439	86	0.1305	79
	0.50	0.1409	80	0.1299	76
12.5	0.75	0.1399	73	0.1296	79
	1.15	0.1381	68	0.1299	80
	1.52	0.1358	65	0.1300	77
	2.50	0.1338	64	0.1301	76

Table 2. Dyestuff Concentration c_t and Characteristic Ratio c_t/c_∞ as a Function of Temperature (130, 115 and 100°C) and Dyeing Time 1-9

	°C	1	2	3	4	5	6	7	8	9
					Dyestuff C.I.Disperse Yellow 3/11855					
c_t	130	0.806	0.960	1.145	1.350	1.635	2.060	2.540	2.860	2.920
	115	0.215	0.290	0.352	0.451	0.558	0.650	0.780	0.810	0.835
	100	0.056	0.077	0.096	0.129	0.161	0.190	0.216	0.247	0.307
c_t/c_∞	130	0.276	0.329	0.382	0.462	0.560	0.705	0.870	0.979	-
	115	0.252	0.340	0.413	0.529	0.654	0.726	0.914	0.949	-
	100	0.182	0.251	0.314	0.420	0.524	0.620	0.704	0.805	-
					Dyestuff C.I.Disperse Blue 6/62050					
c_t	130	0.467	0.593	0.733	0.880	1.100	1.420	1.710	1.790	2.030
	115	0.113	0.159	0.196	0.257	0.322	0.387	0.464	0.493	0.610
	100	0.032	0.057	0.068	0.098	0.127	0.152	0.183	0.208	0.295
c_t/c_∞	130	0.230	0.295	0.361	0.433	0.542	0.700	0.842	0.882	-
	115	0.185	0.260	0.322	0.421	0.528	0.635	0.760	0.808	-
	100	0.110	0.193	0.230	0.332	0.430	0.515	0.620	0.699	-

For the dyeing temperature of 130°C, dyeing time 1-9 corresponds to the real time 5, 7, 10, 15, 20, 30, 60, 120, and 600 min, respectively; for the dyeing temperatures of 115°C and 100°C, dyeing time 1-9 corresponds to the real time 10, 15, 20, 30, 45, 60, 90, 180, and 2880 min, respectively.

EBSCOhost - printed on 2/13/2023 3:45 AM via . All use subject to https://www.ebsco.com/terms-of-use

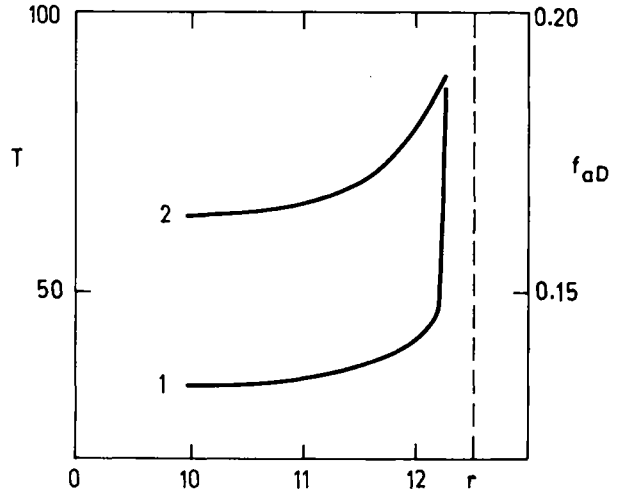

Fig.1. Radial structure differentiation of the fibre investigated: 1 from T-values, 2 from f_{aD}-values.

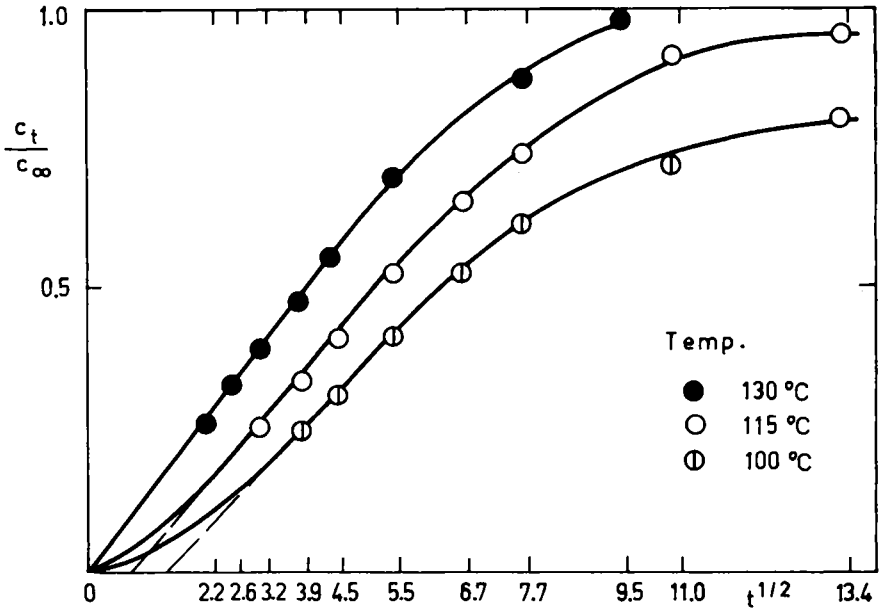

Fig.2. The relationship $c_t/c_\infty = f(t^{1/2})$ (Dyestuff C.I.Disperse Yellow 3/11855).

EBSCOhost - printed on 2/13/2023 3:45 AM via . All use subject to https://www.ebsco.com/terms-of-use

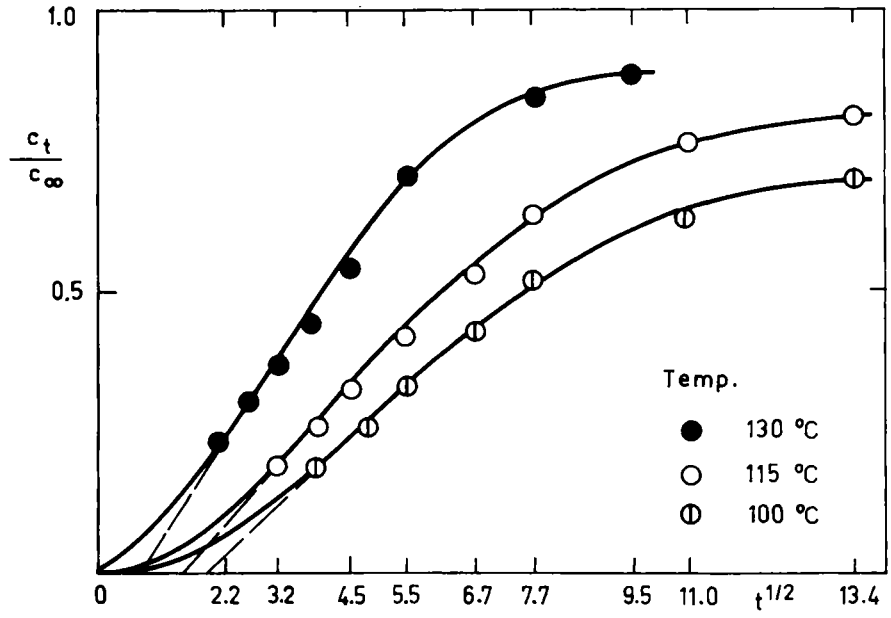

Fig.3. The relationship $c_t/c_\infty = f(t^{1/2})$ (Dyestuff C.I.Disperse Blue 6/62050).

f_{aD}-r and T-r dependences.

The results involving the influence of the radial structure differentiation on the dyestuff diffusion into the fibre, given as c_t/c_∞, have been presented in Table 2 and, shown as a function of $t^{1/2}$, in Figs 2 and 3. From these plots, the following conclusion can be made:

The existence of the radial structure differentiation in PET filaments induces the disturbances in the dyestuffs diffusion at the beginning of the dyeing process. This can explain the deformation of the plot $c_t/c_\infty = f(t^{1/2})$ in its initial run.

The disturbance of the dyeing process is different for individual dyestuff used (differing in their diffusion properties). Disturbances appear stronger for the dyestuff with larger and more space-expanded molecule. The disturbance of the dyestuff diffusion depends on temperature of the dyeing process, being the strongest at the lowest dyeing temperature (100°C). At the highest dyeing temperature (130°C) no such effect appears. This confirms the

EBSCOhost - printed on 2/13/2023 3:45 AM via . All use subject to https://www.ebsco.com/terms-of-use

former observations by the author that, with the increase in dyeing temperature, the radial structure differentiation of the filaments decreases (3). The evaluation of f_{aD} values for the fibre treated with water at 130°C shows that the decrease in the radial structure differentiation results from the decrease in molecular orientation in the surface polymer layer of the fibre (Table 1).

The radial structure differentiation in PET filaments is nearly completely eliminated during 5 min of their water treatment (3).

References

1. Valk, G., G.Jellinek, U.Schröder. 1980. Textile Res.J. 50, 46.

2. Schollmeyer, E., G.Kühnle. 1979. Ber.Bunsenges.Phys.Chem. 83, 322.

3. Lipp-Symonowicz, B., G.Urbańczyk. 1985. Mell.Textilber. 66, 123.

4. Coates, J.A., V.Ellard, I.D.Rattee. 1980. JSDC 96, 14.

5. Lipp-Symonowicz, B., G.Urbańczyk. 1982. Acta Polymerica 33, 197.

6. Lipp-Symonowicz, B. 1979. Zeszyty Naukowe P.Ł.Rozprawy Naukowe No.16.

EBSCOhost - printed on 2/13/2023 3:45 AM via . All use subject to https://www.ebsco.com/terms-of-use

EBSCOhost - printed on 2/13/2023 3:45 AM via . All use subject to https://www.ebsco.com/terms-of-use

MORPHOLOGY OF PET FIBRES IN A RANGE OF SPINNING SPEEDS

O.Ďurčová, M.Mitterpachová
Research Institute for Man-Made Fibres,05921 Svit,ČSSR

M.Jambrich
Slovak Technical University,Faculty of Chemical Enginnering,
81237 Bratislava,ČSSR

Abstract

The formation of oriented superstructures in melt spinning of poly(ethylene terephthalate) fibres in connection to their physical properties has been studied. The IR analysis of orientational changes and the macromolecular segment conformations of as-spun fibres has been shown to provide useful direct evidence for the structural states. The transition which occurs in the morphological level in the range of spinning speeds 2000 - 3750 $m.min^{-1}$ has been observed. The experimental results have been explained in agreement with recent studies of the strain-induced crystallization in an oriented precursor.

Introduction

Poly(ethylene terephthalate) is an important clothing material and extensive studies have reported organic liquid-induced crystallization/1/,thermal history /2/, DSC analysis of cold crystallization /3/ and dyeing of textile fibres /4/. Several properties of as-spun PET fibres are known to show pronouced changes in the range of spinning speeds 1500 - 4500 $m.min^{-1}$. For example, the shrinkage of undrawn fibres increases progressively up to the spinning speeds of $\sim$ 3000 $m.min^{-1}$, but then shows a dramatic decrease to low values around of 4500 $m.min^{-1}$. Generally, the as-spun PET fibres are non-crystalline but exibit some degree of molecular orientation along the fibre axis as

Morphology of Polymers
© 1986 Walter de Gruyter & Co., Berlin · New York - Printed in Germany.

EBSCOhost - printed on 2/13/2023 3:45 AM via . All use subject to https://www.ebsco.com/terms-of-use

measured by optical birefringence /5/ . In this state prepared PET fibres are highly deformable and their strength is low. They must be exposed to a drawing operation to convert them to an useful form. The molecular orientation and formed morphological structure developed in the threadline during the spinning process are very important parameters in determining the physical and mechanical properties of final yarn.
In our paper we discuss the experimental results of several physical properties and corresponding morphological structure of as-spun PET fibres in relation to increasing spinning speeds. From the microscopic point of view we paid attention to the crystalline and amorphous orientations in connection with the macroscopic morphological studies.

Experimental

Poly(ethylene terephthalate) was a commercial material for the production of yarn , $[\eta] = 83.2\ ml.g^{-1}$. As-spun fibres were extruded at 290°C and quenched in a cold air stream. The filaments were wound into a godet at a take-up device with surface speeds ranging from 2000 to 3750 $m.min^{-1}$.
Infrared spectra of the fibres were obtained on a double-beam spectrophotometer UR-20 (Carl Zeiss Jena) using a KBr pallet technique.For the study of the gauche - trans transformation four bands near 1337, 1370, 2890 and 2910 cm^{-1} were considered / 6,7 /. The 1337 and 2910 cm^{-1} bands increase in intensity when spinning speeds increase . They are assigned to the trans conformation of the glycol moiety of the polymer structural unit. Two other bands are assigned to the gauche conformation of the glycol moiety. The trans index / I_{trans} / and gauche index / I_{gauche} / are the ratios of the measured peak absorbances :

$$I_{trans} = \frac{A_{1337}}{A_{1370}} \qquad I_{gauche} = \frac{A_{2890}}{A_{2910}}$$

A are measured absorbances at absorption maximum of above mentioned bands.

EBSCOhost - printed on 2/13/2023 3:45 AM via . All use subject to https://www.ebsco.com/terms-of-use

Infrared polarization spectra of PET fibres were obtained by using Se - polarizer. The fibres were wound up on the frames and parafinic oil was used as an immersion liquid. The dichroic ratio R and dichroic function DF were calculated for the absorption bands at 437 and 502 cm^{-1}, which have been assigned to the crystalline and amorphous regions / 8 /. The used relations are as follows :

$$R = \frac{A_{//}}{A_{\perp}} \qquad DF = \frac{A_{//}/A_{\perp} - 1}{A_{//}/A_{\perp} + 2}$$

$A_{//}$ resp. $A_{\perp}$ are measured absorbances by using the base - line method at the absorption maximum of polarized light parallel and perpendicular to the fibre axis direction.
The PET fibres were then investigated by several rheo - optical techniques, viz. optical microscopy / OM /, small - angle light scattering / SALS / and scanning electron microscopy / SEM /. The OM studies were carried out on a Zetopan polarizing microscope. The SALS studies were carried out on an optical difractometer equipped with He - Ne laser Model TKG 203 / Tesla CSSR / as the light source in H_v conditions. The H_v patterns were recorded photographically. SEM studies were conducted on a Jeol JSM - 35 / Jeol , Japan /. The fibre samples were coated with a thin layer of Cu to prevent charging. The density was measured at 20°C by flotation in a carbon tetrachloride / isopropanol. Birefringence measurements were carried out on a Zeiss microscope equipped with Berek compensator.

Results and Discussion

The observed evolution of the supermolecular structure during PET solidification along the threadline is the most interesting result of the present work. We have considered mainly the molecular orientation and the morphology of the filaments versus spinning speeds. Figure 1 shows the birefringence of the fibres against spinning speeds. The birefringence and molecular orientation of PET fibres show considerable increase in the dependence of spinning speeds.

EBSCOhost - printed on 2/13/2023 3:45 AM via . All use subject to https://www.ebsco.com/terms-of-use

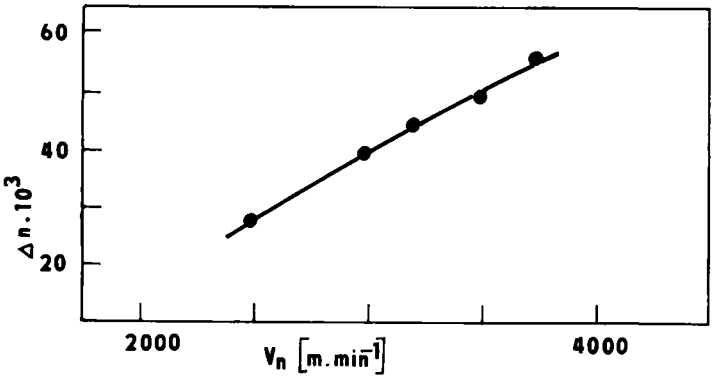

Fig.1. Birefringence of PET fibres as a function of spinning speed.

The orientational behavior of PET fibres can also be discussed in terms of the dichroic function as measured by infrared dichroism in order to obtain more detailed information. The transition moment of the absorptin band which occurs at 437 cm^{-1} and is assigned to the crystalline regions takes a positive value with increasing extension ratio / 8 /. The transition moment of the amorphous band at 502 cm^{-1} shows the reverse behavior. Therefore, the orientation measured by infrared dichroism of the above mentioned bands indicates the molecular orientation in crystalline or amorphous regions, respectively. As can be seen in Figure 2 the crystalline molecular orientation increases in the whole range of spinning speeds. It is interesting to note that the crystalline orientation reaches the negative values for fibres prepared at $V_n < 3000$ m.min^{-1}. It means that the preferential orientation of the crystalline macromolecular segments is perpendicular to the fibre axis. The next increase of spinning speeds results in the transformation from the negative to the positive values of DF_{437}. The smaller differences can be seen in the case of the amorphous molecular orientation estimated by DF_{502}. The abrupt decrease in DF_{502} in the middle range of spinning speeds can be affected by increasing the active mobility of the macromolecular segments in amorphous regions .

EBSCOhost - printed on 2/13/2023 3:45 AM via . All use subject to https://www.ebsco.com/terms-of-use

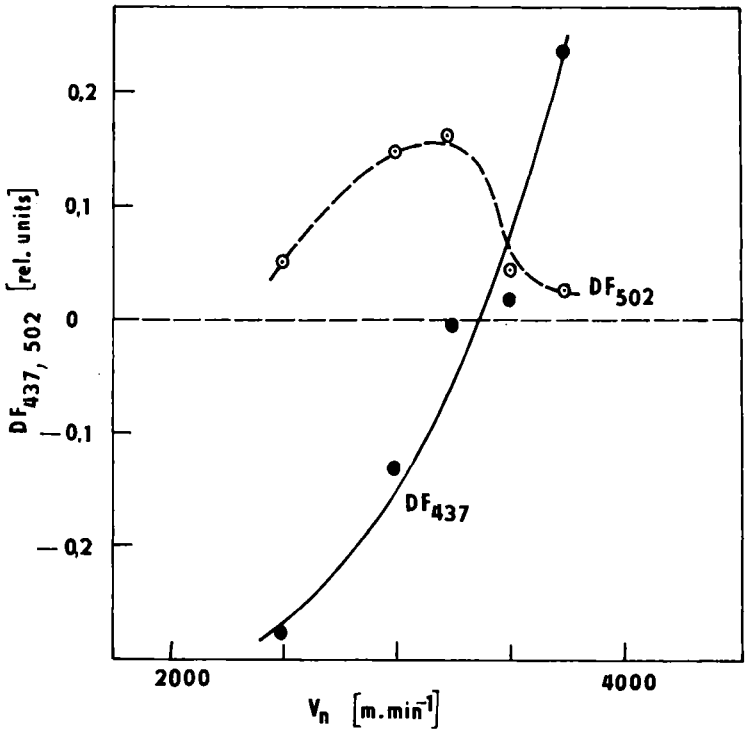

Fig.2. Dichroic function / spinning speed - plot of the 437 cm^{-1} /●/ and 502 cm^{-1} /○/ absorption bands.

This phenomenon is probably a consequence of a turn in the growth direction of the crystalline macromolecular segments from perpendicular into parallel to fibre axis.
To understand the crystallization behaviour of the particularly oriented PET fibres we estimated the density and the trans - gauche conformations of the macromolecular segments. In the case of infrared analysis I_{trans} increases while I_{gauche} decreases at higher spinning speeds. It means that the gauche conformations of the macromolecular segments gradually convert to the trans. Apart from the observed trans - gauche transformations in PET fibres the density values are nearly unchanged and could not have been used for structural analysis. Figure 3 shows these results. Therefore, the infrared measurements have the advantage of revealing small changes in the crystalline re-

EBSCOhost - printed on 2/13/2023 3:45 AM via . All use subject to https://www.ebsco.com/terms-of-use

gions, which are impossible to detect on the basis of the density by flotation.

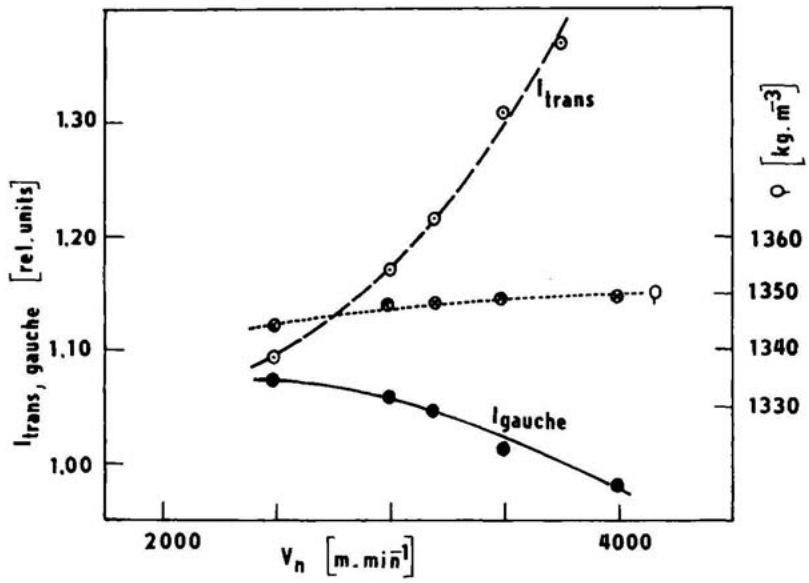

Fig.3. I_{trans} , I_{gauche} and density versus spinning speeds for as-spun PET fibres.

From the above considerations we can state that because of the different conformations there are different modes of crystallization that result in different morphological features. The scanning electron microscope comparison between the individual PET fibres confirms a more homogeneous morphological structure

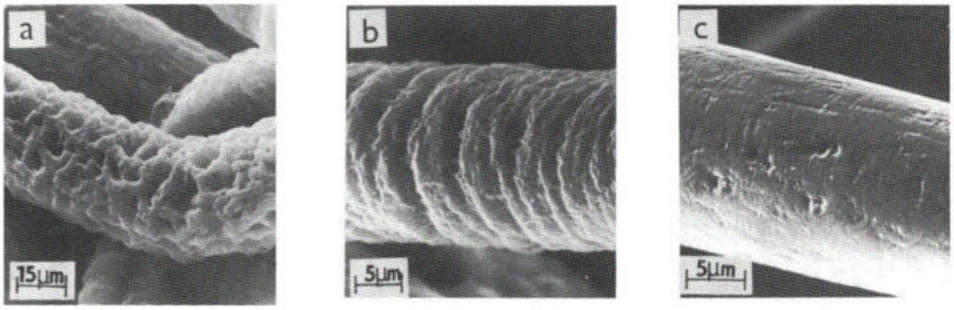

Fig.4. SEM micrographs of PET fibres after treatment in chloroform : /a/ V_n = 2000 m.min^{-1}, /b/ V_n = 3000 m.min^{-1}, /c/ V_n = 3750 m.min^{-1}.

EBSCOhost - printed on 2/13/2023 3:45 AM via . All use subject to https://www.ebsco.com/terms-of-use

for fibres prepared at higher spinning speeds. Figure 4 shows representative SEM's of the fibre surfaces after treatment in chloroform (-26°C, 10 min). It is clear, that the distinct spherulitic texture is observed on the surface of PET fibres prepared at V_n = 2000 m.min^{-1}. More oriented fibres have the lamellar morphological structure as can be seen in Figure 4b. The lamellae are regularly arranged perpendicularly to the fibre axis.The most oriented PET fibres do not show expressive differences in the surface morphological features.
SALS, however, reveals that internal supermolecular structure is evidenced in these fibres following the liquid treatment. Figure 5 shows characteristic SALS patterns obtained from the filaments immersed in monochlorbenzene/polystyrene mixture.

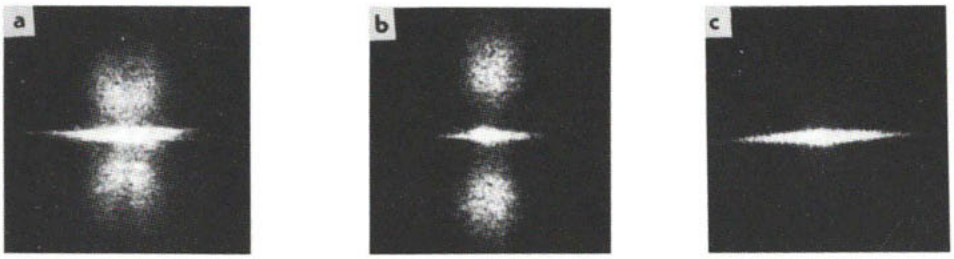

Fig.5. SALS H_v patterns of PET fibres : /a/ V_n = 2000 m.min^{-1}, /b/ V_n = 3000 m.min^{-1}, /c/ V_n = 3750 m.min^{-1}.

The first point to note is that the spinning process of PET fibres at speeds of $\sim$ 2000 m.min^{-1} induced poorly-defined spherulitic-like superstructure.The H_v pattern shows some slight distortion of the spherical symmetry of the crystallite aggregation (deformed spherulites). . Next can be also noted that with increasing spinning speeds the corresponding fibre H_v pattern changes qualitatively too. The elongated four-leaf-clover pattern converts into two-leaf-clover pattern (see Fig.5b).
It means that scattering objects have lamellar-like shape with the cylindrically-symmetric crystallite aggregations. These scattering lamellae formations are oriented perpendicularly to the fibre axis. The SALS data for the PET fibres formed in the threadline at speed of $\sim$ 3750 m.min^{-1} show no scattering maxima indicating that fibrillar morphology is appeared (see Fig. 5c).

EBSCOhost - printed on 2/13/2023 3:45 AM via . All use subject to https://www.ebsco.com/terms-of-use

OM studies verify that these superstructures are really formed in the PET fibres during the high spinning process in the range of V_n = 2000 - 3750 $m.min^{-1}$ (see Fig. 6a,b,c).

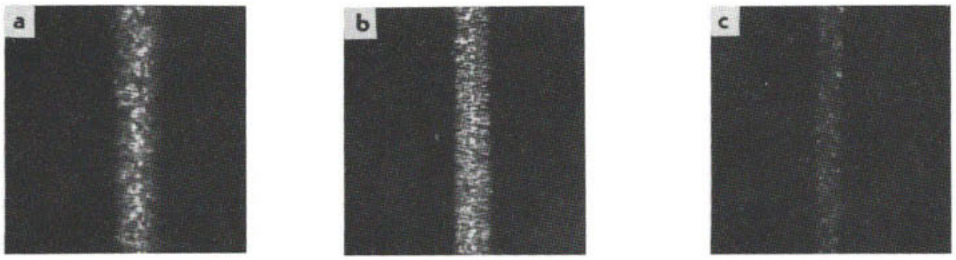

Fig.6. Representative optical micrographs of as-spun PET fibres immersed in monochlorbenzene/polystyrene mixture : /a/ V_n = 2000 $m.min^{-1}$, /b/ V_n = 3000 $m.min^{-1}$, /c/ V_n = 3750 $m.min^{-1}$.

Conclusions

Analysis of the supermolecular structure of PET fibres formed along the spinning path within the range of speeds 2000 - 3750 $m.min^{-1}$ lead to the following conclusions.

PET fibres prepared within the low-speed range, $V_n \leq 2500$ $m.min^{-1}$, are characterized by a low level of anisotropy and a low level of the macromolecular segments in the crystallizable trans conformations. They have spherulitic morphology.

PET fibres prepared in the middle - speed range, V_n = 2500 - 3000 $m.min^{-1}$, have increasing molecular orientation and the high trans content. The preferential crystalline orientation changes from perpendicular into parallel to the fibre axis. The morphological features can be characterized as the lamellar crystalline aggregations.

The high - speed range, V_n = 3200 - 3750 $m.min^{-1}$, is accompanied by the highest anisotropy and the highest trans content in the fibres. The PET fibres prepared at such conditions have the typical fibrilar morphology.

We think that the above mentioned combination of several physical methods can be useful for detection of the structure changes brought about by spinning PET at different speeds.

EBSCOhost - printed on 2/13/2023 3:45 AM via . All use subject to https://www.ebsco.com/terms-of-use

References

1. Makarewicz, P.J.and G.L. Wilkes. 1978. Structural Rearrangements in the Liquid - Induced Crystallization of Cold - Drawn Poly (Ethylene Terephthalate) . Textile Res.J. 48, 136 - 143 .

2. Hamidi, A., Abhiraman, A.S. and Pravin Asher . 1983. Melt Spinning of Poly(Ethylene Terephthalate) - Structural Transitions in a Range of Spinning Speeds. 1983. J. Appl. Polym. Sci. 28, 567 - 578.

3. Bragato, G. and G. Gianotti. 1983. High speed spinning of poly(ethylene terephthalate) - II. Eur. Polym. J. 19, 803 - 809.

4. Gulrajani, M.L., Saxena, R.K. and A.K. Sengupta. 1980. Dye-Induced Structural Changes and Mechanical Properties of Polyethylene Terephthalate Fibres. Textile Res. J. 50 , 589 - 591.

5. Davis,G.W., Everage, A.E. and J.R. Talbot. 1984. Polyester fibres : High speed melt spinning. Fiber producer 12, 22 - 28.

6. Galli, R., Canetti, M., Sadocco, P., Seves, A and L.Vicini. 1983. Preoriented Poly (Ethylene Terephthalate) Yarns : Influence of the Gauche - Trans Transformation on Crystallization. J. Polym. Sci. Polym. Phys. Ed. 21, 717 - 723 .

7. Koenig, J.L. 1979. In : XXI Colloquium Spectroscopicum Internationale. Cambridge. Heyden, London Philadelphia. pp. 16 - 22 .

8. Dechant, J. 1972. Ultrarotspektroskopische Untersuchungen an Polymeren. Akademie - Verlag. Berlin. pp. 354 - 355 .

9. Siesler, H.W. 1984. Recent Advances in Rheo - optical FTIR spectroscopy of Polymers. Polymer Preprints 25, 165 - 166.

EBSCOhost - printed on 2/13/2023 3:45 AM via . All use subject to https://www.ebsco.com/terms-of-use

EBSCOhost - printed on 2/13/2023 3:45 AM via . All use subject to https://www.ebsco.com/terms-of-use

MORPHOLOGY AND VISCOELASTIC PROPERTIES OF HIGHLY DRAWN POLYETHYLENE TEREPHTHALATE TEXTILE FIBRES

B. Košková

Department of Textile Materials, College of Mechanical and Textile Engineering, 461 17 Liberec, Czechoslovakia

Introduction

The textile fibres consist of semicrystalline polymers with oriented linear macromolecular chains. The physical and end-use properties of the textile fibres depend strongly on their supermolecular structure which is influenced by the way of their production and processing. Drawing and setting are important processing operations. From the physical point of view drawing is a uniaxial deformation which causes orientation of macromolecules in the direction of the applied force, i.e. along the fibre axis. The setting balances the internal stress whose source is the drawing and causes the shrinkage resistance of the fibres. The structure of the fibre ought not to change if it is heated only to its setting temperature.

The viscoelastic properties of these fibres are complicated with regard to great variety of their morphological structure. From the structural point of view we can consider them as the two-phase material which exhibits, in general, thermorheologically complex behaviour. However, it is possible to delimit time and temperature range when the degree of crystallinity and orientation of structure does not undergo significant changes. Then we can apply a shifting procedure along the time axis on the curves of the viscoelastic functions and hence the material behaves as thermorheologically simple.

At present we can find very different results in literature (7,8, 9) regarding PET fibres, namely their fulfilling the thermorheological simplicity and the shape of the shift function. Our experiments contribute to the characterization of the viscoelastic behaviour of the fibres in dependence on the time, temperature and deformation.

Morphology of Polymers
© 1986 Walter de Gruyter & Co., Berlin · New York - Printed in Germany.

EBSCOhost - printed on 2/13/2023 3:45 AM via . All use subject to https://www.ebsco.com/terms-of-use

Materials and Methods

Morphology and viscoelastic properties of the Czechoslovak textile fibre TESIL 12 were studied using the commercially produced unmodified PET fibre drawn in two steps with drawing ratios $\lambda_1 = 3.8$ and $\lambda_2 = 1.2$. The structure of fibres (18-22 μm in diameter) was heat-setted at 130°C.

The fibre morphology was studied by means of a scanning electron microscope TESLA BS 300. The surface structure of fibres is usually different from their internal structure (so-called skin-core effect). For this purpose the peeling technique has been used (1, 2,3). A few fibres are pasted on the holder and placed on the stage of the optical stereomicroscope. Using the magnification of 100 to 200x the upper part of the fibre is nicked with a razor blade and peeled back. The samples prepared in this way are shadowed with gold and studied by the scanning electron microscopy.

The viscoelastic properties of the fibres were studied on an INSTRON apparatus in the quasistatic tensile relaxation experiment at various constant strains, $\varepsilon_o = 1,3,5$ and 10%, in the temperature range of 80 to 180°C, the relative humidity being 0%.

From the amount of experiments studying the relation of polymer morphology and properties it follows that the nonlinear viscoelastic behaviour of the filamentous materials is due to their oriented structure (6). The behaviour of such fibres may be described phenomenologically, for example by the method of reduced variables (4,5,6). This method is known as the time-temperature superposition if we are interested in the dependence of the viscoelastic properties on temperature. For this purpose the relaxation modulus at an arbitrary time t defined as a ratio

$$E(t) = \sigma(t)/\varepsilon_o$$

is reduced to a reference temperature T_o, according to the relation

$$E_r(t) = E(t)T_o/T \quad ,$$

where T is arbitrary experimental temperature.

EBSCOhost - printed on 2/13/2023 3:45 AM via . All use subject to https://www.ebsco.com/terms-of-use

Results and Conclusions

The degree of crystallinity and the glass transition temperature gave us the first indication what type of morphological structure and properties can be expected. The degree of crystallinity determined by the flotation method was 40%. The glass transition temperature T_g, frequently published in literature (4-8), is 80°C for PET in general. For our fibres T_g = 92°C, as determined from dynamic viscoelastic measurements on a RHEOVIBRON instrument. The structure of the fibres is fibrillar, their order size width being 0.1 µm. The arrangement of fibrils into the flat ribbons and the cross ties between adjacent fibrillar ribbons may be seen in Fig.1. This Figure shows clearly the skin-core effect. Using small strains (below 5%) no changes of the fine fibrillar structure have been found up to the heat-setting temperature(130°C). The shift procedure has been carried out on the computer EC 1033 (logarithmic scale) for the data related to constant strain. As a result of the reduced curves analysis we obtained the shift factor, log a_T, for each experimental temperature, and the master curve of relaxation modulus (Fig.2) on the graphic output. The experimental data can be superimposed within the temperature region

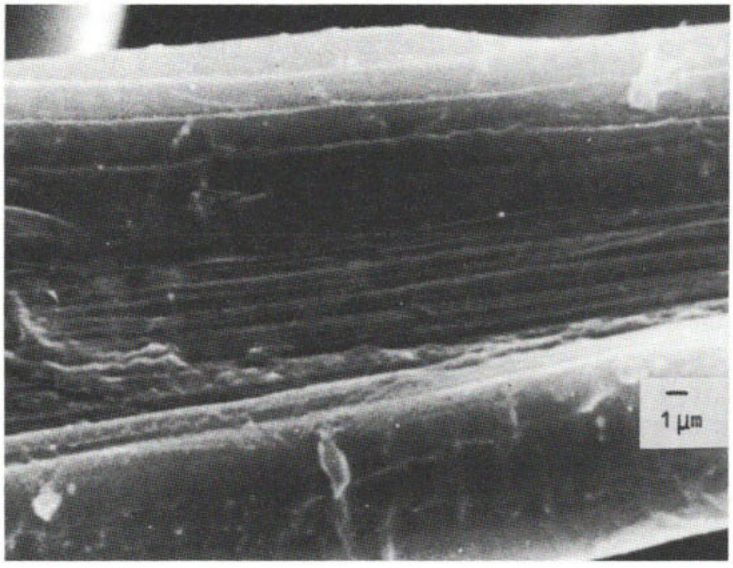

Fig.1. The internal and the surface structure of the fibre.

EBSCOhost - printed on 2/13/2023 3:45 AM via . All use subject to https://www.ebsco.com/terms-of-use

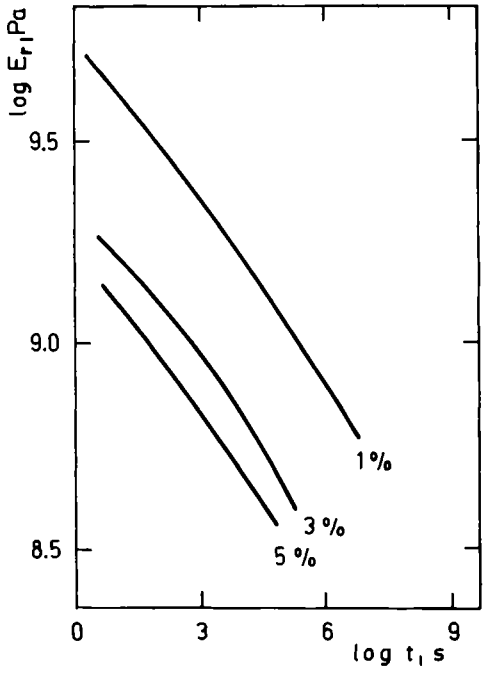

Fig.2. The master curves of relaxation modulus, reduced to the reference temperature T_o = 80°C at various strains. (Percents denote deformation.)

of 80 to 125°C using the strains 1, 3 and 5%. The data obtained at higher temperatures (>125°C) and the strain above 5% cannot be superimposed. This fact indicates a more complicated behaviour above the heat-setting temperature.

The linear shift function of the relaxation modulus is shown in Fig.3. This is in good agreement with the results for uniaxial oriented PET fibre of 48% degree of crystallinity (7). The slope of our shift function does not differ from that reported in ref. (7). On the other hand, the shift function below T_g or for biaxially oriented semicrystalline PET fibre was found to be non-linear (7,8). From these facts it follows that the shape of the shift function is strongly dependent on the orientation. Our shift function does not exactly satisfy the standard form of WLF equation

EBSCOhost - printed on 2/13/2023 3:45 AM via . All use subject to https://www.ebsco.com/terms-of-use

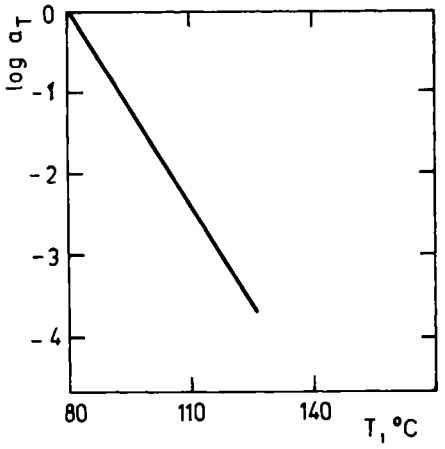

Fig.3. The shift function of the reduced relaxation modulus for strains 1, 3 and 5%.

$$\log a_T = -8.86(T-T_S)/(101.6 + T - T_S)$$

The standard reference temperature T_S determined by the least-squares method is 81°C, which is in good agreement with T_g. The magnitude of the relaxation modulus in Fig.2 decreases with the increasing strain without changing its time dependence. The shift function hence does not depend on strain. The physical interpretation of this fact may be the following: The nonlinearity of the mechanical properties of PET fibres up to the strain of 5% seems to be caused chiefly by elastic nonlinearity, while the viscous properties are linear. Meanwhile, the nonlinearity was rather attributed to the viscous properties. This is the main result of our work, which might be useful, to a certain extent, for better analytical description of the viscoelastic properties of this material.

EBSCOhost - printed on 2/13/2023 3:45 AM via . All use subject to https://www.ebsco.com/terms-of-use

References

1. Scott, R.G. 1959. ASTM Bull. No 257, 121.

2. Van Veld, R.D., Morris, G., Billica, H.R. 1968. J.Appl.Polym. Sci. 12, 2709.

3. Hochman, V. 1973. A review.VÚP, Brno, No 2/3, 81.

4. Ferry, J.D. 1980. Viscoelastic Properties of Polymers. Wiley, New York, Ch. 11.

5. Christensen, R.M. 1971. Theory of Viscoelasticity. An Introduction. Academic Press, New York. Ch. III.

6. Eirich, F.R. 1958. Rheology. Theory and Applications, Vol.2. Academic Press, New York. Ch. 6 and 7.

7. Murayama, T., Dumbleton, J.H., Williams, M.L. 1968. J.Polym.Sci. Part A-2, 6, 787.

8. Hawthorne, J.M. 1981. J.Appl.Polym.Sci. 26, 3317.

9. Wortmann, F.J., De Jong, S. 1985. J.Appl.Polym.Sci. 30, 2195.

EBSCOhost - printed on 2/13/2023 3:45 AM via . All use subject to https://www.ebsco.com/terms-of-use

MORPHOLOGY OF METHYLAMINE-TREATED POLY(ETHYLENE TEREPHTALATE) FIBERS

L. Kudláček, M. Hepner, Z. Kašparová
University of Chemical Technology, Pardubice 53210, ČSSR

Introduction

The effect of alkylámines on the ester bonds in poly(ethylene terephtalate) (PETP) consists in nucleophilic substitution of basic amine-group to ester carbonyl. The consequence of it is chain splitting with the formation of amide end-groups:

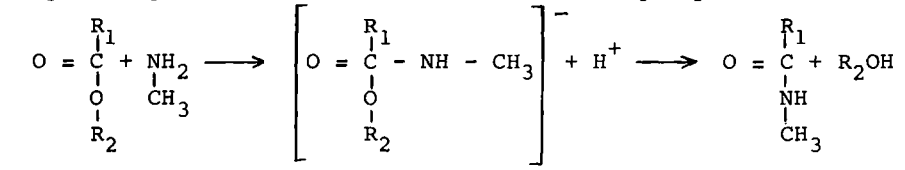

The reaction rate depends on the diffusion rate of amine into the fiber. In principle it may be used for characterization of the accessibility of the fiber structure which was formed under various conditions, thermal and deformational influences. The reaction rate, the changes in polymer and the possibility of separation of the amorphous and crystalline phases were investigated by a number of authors. From the published data it can be concluded that the rate of aminolysis depends on the basicity and steric volume of the amine molecule, the concentration of amine and the fiber morphology (1,2). Most authors found the rate changing from the initial slow phase to a rapid one and a retardation in the end of the reaction. Some authors found a constant reaction rate (2). Separation of the amorphous and crystalline fractions is considered improbable, even though the final product of degradation are crystalline lamellas with thickness corresponding with the long period of original structure (3). The initial microfibrillar structure is destroyed during aminolysis and the destruction starts with formation of cracks in the surface layer (4). The cracks origin is connected with the existence of internal stresses in the fiber structure. The mo-

Morphology of Polymers
© 1986 Walter de Gruyter & Co., Berlin · New York - Printed in Germany.

EBSCOhost - printed on 2/13/2023 3:45 AM via . All use subject to https://www.ebsco.com/terms-of-use

lecular weight of the polymer decreases to a value of 5 - 9 monomeric units and the mechanical properties become worse at the same time(5). The outer skin layer is separated from the central core which is disintegrating gradually to disks. The dimensions of cracks and disks are not consistent with the periodicity of the amorphous and crystalline structures. The aminolysis may be accompanied by the growth in crystallinity caused by amine-induced crystallization of the degraded polymer(2,6,7).

Results

The used PETP fibers served to prove the influence of the spinning rate, drawing ratio, comonomers'kind and content on the rate and morphology of destruction in the course of aminolysis.
The fiber samples were shaked thoroughly with 30 % aqueous methylamine (1 : 150) and kept at 20 °C for a definite period of time in a glass-stoppered bottle. The filtered, washed and dried fibers were used for the weight loss and nitrogen content determinations as well as for scanning electron microscopy. The weight loss is taken for a portion of the sample dissolved in the aqueous amine and/or washing water. For this method an "induction" period is characteristic. The weight loss is relatively low at the beginning of the reaction.
It is probable that owing to their limited solubility the precipitated low-molecular products of degradation are present in the rest after the aminolysis. We proved by the extraction with dioxane that the low-molecular products are formed from the beginning of the reaction and the value of the weight loss reaches more than 90 % during 10-12 hours. Both methods of determination are compared in Fig. 1 for modified PETP fibers.
In the fraction extracted after 15 h of aminolysis the N_2 content was 6-8 %, which agrees with the presence of the oligomers. The theoretical N_2 content in monomeric N,N'-methylamide of terephtalic acid is 14.57 %, its melting point being 316 °C. The N_2 content in the residue approaches the theoretical value 13.5-14 % and the melting point of it is almost the same (310-316°C) as the T_m value for monomeric amide prepared from dimethylterephtalate. The N_2 content in the extracted sample after 5-7 h of aminolysis was only 1-2%.

EBSCOhost - printed on 2/13/2023 3:45 AM via . All use subject to https://www.ebsco.com/terms-of-use

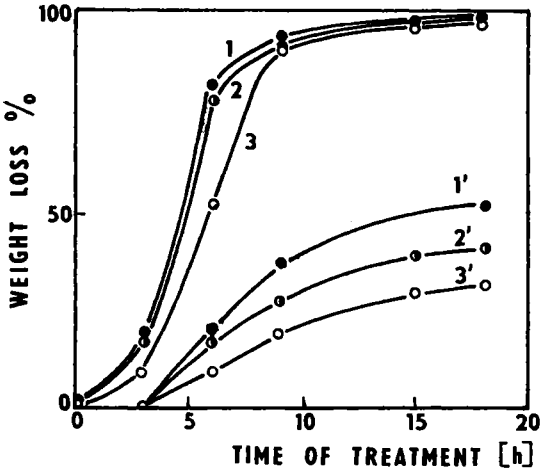

Fig. 1. The weight loss of modified PETP fibers with different content of comonomers (1>2>3) after treatment with 30 % aqueous methylamine; 1', 2', 3',... without extraction; 1, 2, 3,... after extraction with dioxane.

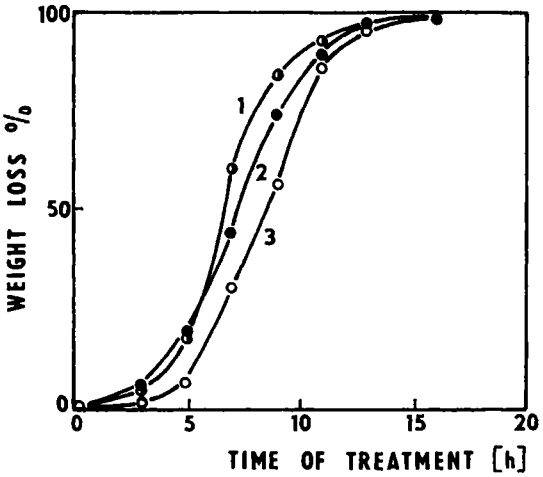

Fig. 2. The weight loss of modified PETP fibers spun with different velocity (1<2<3) after treatment with 30 % aqueous methylamine.

EBSCOhost - printed on 2/13/2023 3:45 AM via . All use subject to https://www.ebsco.com/terms-of-use

The fiber diameter diminishes after 9 h to 46 % of the original value. Approximately at that time the treated samples loose also their fibrous form.

The aminolysis of fibers spun with different spinning velocity and fibers drawn to different draw ratios revealed that the increasing order and crystallinity lowers the rate of degradation (Figs. 2 and 3).

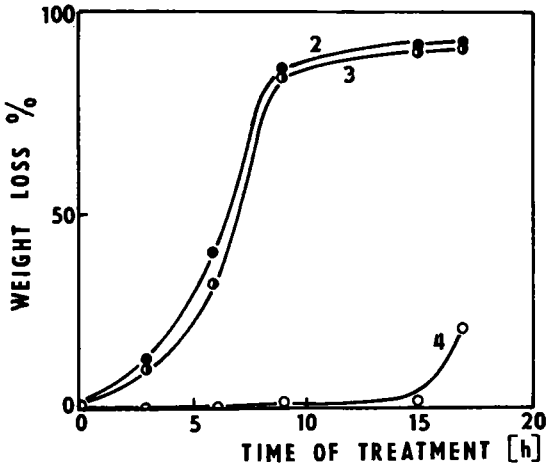

Fig. 3. The weight loss of PETP fibers drawn to various draw ratios after treatment with 30 % aqueous methylamine; figures indicate the draw ratio values.

Fine, gradually growing cracks along and across the fiber or in an oblique direction to the axis are the first morphological changes (Figs. 4 and 5).

These cracks enable the amine to diffuse in the interior. Next there appears the differentiation of skin and core. The surface layer is divided into rectangular pieces which can separate from the core (Fig. 6). The crystals of oligomers and monomer can arise already in the first phases of aminolysis and grow on fiber to the dimensions much greater than the fiber diameter. At the end of fibers there appears fibrillar structure and a distinctly greater extent of core destruction (Fig. 7). The surface cracks become deeper and

EBSCOhost - printed on 2/13/2023 3:45 AM via . All use subject to https://www.ebsco.com/terms-of-use

form wedge incisions around the fiber perimeter, the width of which was 1-3 μm (Fig. 8).

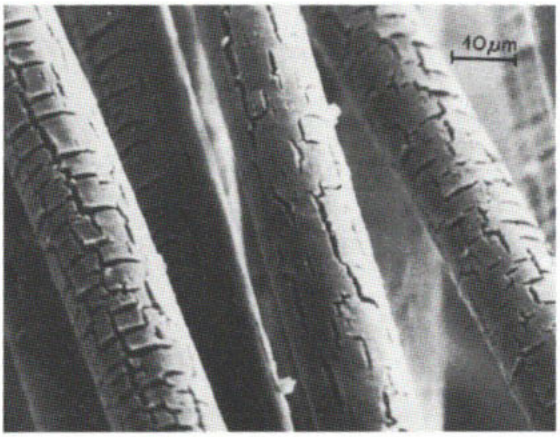

Fig. 4. The modified PETP fibers after 7 h aminolysis with 30 % aqueous methylamine.

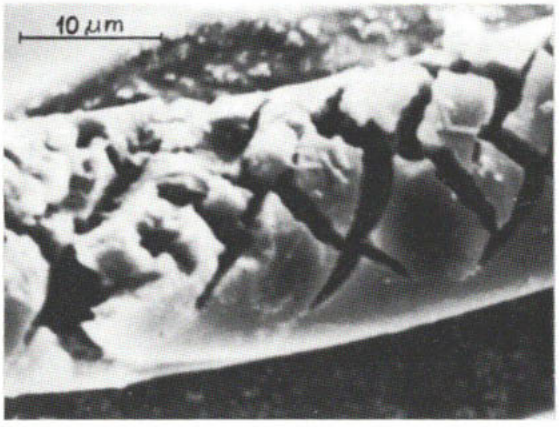

Fig. 5. The modified PETP fibers after 7 h aminolysis with 30 % aqueous methylamine.

EBSCOhost - printed on 2/13/2023 3:45 AM via . All use subject to https://www.ebsco.com/terms-of-use

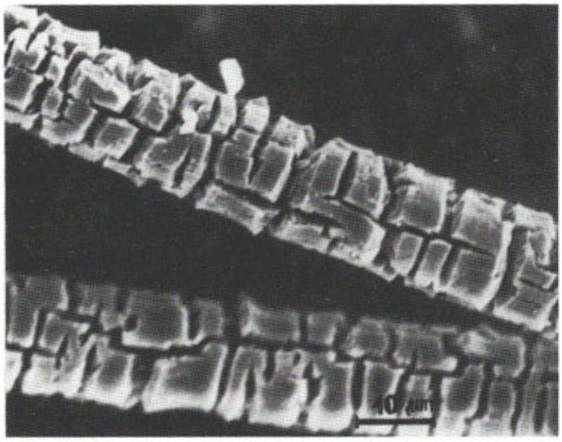

Fig. 6. The PETP fibers after 9 h aminolysis with 30 % aqueous methylamine.

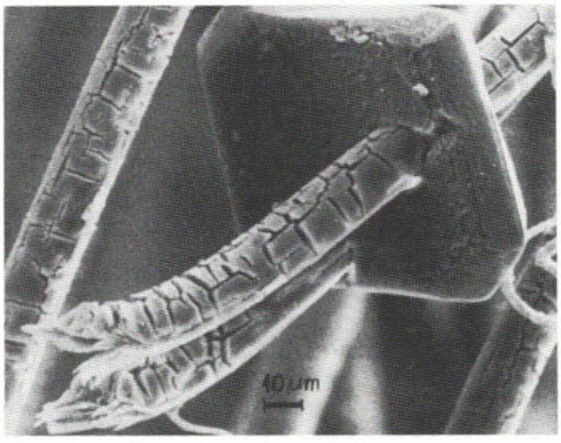

Fig. 7. The modified PETP fibers after 9 h aminolysis with 30 % aqueous methylamine.

EBSCOhost - printed on 2/13/2023 3:45 AM via . All use subject to https://www.ebsco.com/terms-of-use

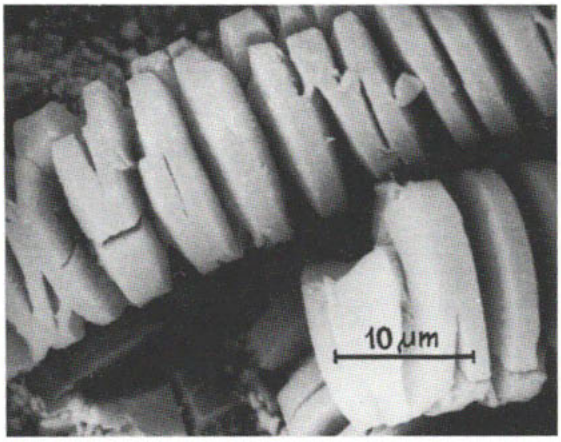

Fig. 8. The modified PETP fibers after 10 h of aminolysis with 30 % aqueous methylamine.

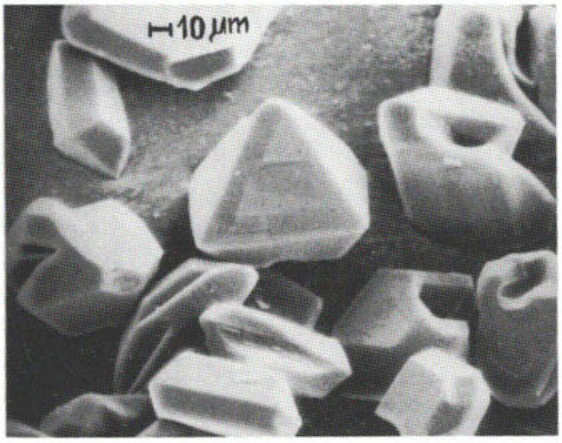

Fig. 9. The product of 15 h aminolysis of modified PETP fibers with 30 % aqueous methylamine.

So, an array of disks held together by the central part of the fiber is formed. The width of disks was 3-9 µm. Some fibers reveal less regular and rather helical pattern of cracks. The last traces of the original fiber structure vanish at the same time. The solid is then represented by a mixture of individual disks, fragments

EBSCOhost - printed on 2/13/2023 3:45 AM via . All use subject to https://www.ebsco.com/terms-of-use

and crystals of oligomers and monomer which prevail at last (Fig. 9). The determination of crystalinity during aminolysis can be misinforming by the presence of these crystals and polymer recrystallization.

It can be concluded that the aminolysis may be useful for relative comparison of accessibility, especially in the phase of the maximum reaction rate, where the sensibility to the structure differences seems to be the greatest. The morphology of destruction is complicated by secondary changes in the structure of fibers.

References

1. Farrow, G., D.A.S. Ravens, I.M. Ward. 1962. Polymer 3, 17.

2. Sweet, G.E., J.P. Bell. 1978. J. Polymer Sci., Polymer Physics 16, 1935.

3. Duong, D.T., J.P.Bell. 1975. J. Polymer Sci., Polymer Physics 13, 765.

4. Murray, R., H.A. Davis, P. Tucker. 1978. J. Applied Polymer Sci., Symp. 33, 177.

5. Hinrichsen, G., A. Iburg, A. Eberhardt, H. Springer, P. Wolbring. 1980. Melliand Textilber. 61, 807.

6. Adams, G.C. 1976. Polymer Eng. Sci. 16, 222.

7. Yamazaki, N., H. Tonami. 1976. Sen-i Gakkaishi 8, T 317 English summary .

EBSCOhost - printed on 2/13/2023 3:45 AM via . All use subject to https://www.ebsco.com/terms-of-use

INFLUENCE OF STRUCTURE ON THE CHANGES DURING HEAT TREATMENT AND PROPERTIES OF ACRYLIC FIBERS

A.I. Stoyanov
Economic Combine "Neftochim", Plant "Bulana", Burgas, Bulgaria

V.P. Krustev
State University, Sofia, Bulgaria

Introduction

The influence of the heat treatment on the structure and properties of acrylic fibers has been extensively studied (1-5). On the other hand, the structure of fibers before heat treatment depends on coagulation variables, extrusion rate, stretching and other technological parameters (6,7).
However, it seems that the relation between their structure before heat treatment, with additional changes during that process, and properties of the finished fibers received little attention as yet. In this communication the results of our investigation of this problem will be reported.

Experimental

The acrylic fibers were prepared by the wet-spinning process. The protofibers were washed, stretched and treated consecutively in the presence of steam at about 100°C, and dried at 125°C. Fibers having different structure before heat treatment were prepared by variation of molecular weight, coagulation bath composition and temperature, and polymer concentration in spinning solution. The data on structure and mechanical properties were measured by usual methods (8).

Morphology of Polymers
© 1986 Walter de Gruyter & Co., Berlin · New York - Printed in Germany.

EBSCOhost - printed on 2/13/2023 3:45 AM via . All use subject to https://www.ebsco.com/terms-of-use

Results and Discussion

Light changes in molecular weight, coagulation variables and dope concentration exert influence on the density, perfection of structure and weak orientation of fibers after stretching (cf. Tables 1-3).

Table 1. Effect of Molecular Weight on Fiber Properties and Shrinkage During Heat Treatment

Fiber properties and shrinkage		Molecular weight, $\eta_{sp}^{0.5}$			
		1.65	1.74	1.90	1.98
X-Ray orientation, H°	1*	39.8	39.0	37.5	37.5
	2	41.8	40.8	39.5	39.4
	3	43.7	42.5	41.1	40.9
Perfection of structure, B°	1	1.25	1.19	1.09	1.03
	2	1.23	1.18	1.10	1.03
	3	1.25	1.18	1.10	1.03
Dyeability, %	1	15.9	15.0	14.0	11.8
	2	25.4	24.0	22.0	19.3
	3	14.7	14.0	12.9	11.2
Density, g/cm^3		0.30	0.32	0.35	0.40
Shrinkage after thermosetting, %, time 15 min		26.9	26.8	26.5	24.9
Shrinkage after drying, %, T=125°C, without thermosetting		22.3	22.0	20.0	16.1
Shrinkage after thermosetting, %, time 2 min		20.6	19.5	18.9	14.5
Shrinkage after thermosetting, %, time 2 min, drying 125°C		25.0	24.8	24.8	21.9

* 1 - after stretching; 2 - after thermosetting; 3 - after drying.

After heat treatment the orientation is somewhat lower in comparison with that of the same fibers after stretching. This could be explained with slight disorientation of the macromolecules and fibrils. In the same time the heat treatment does not disturb the perfection of the structure.

EBSCOhost - printed on 2/13/2023 3:45 AM via . All use subject to https://www.ebsco.com/terms-of-use

Table 2. Effect of the Coagulation Bath Composition and Temperature on the Fiber Properties and Shrinkage During Heat Treatment

Fiber properties and shrinkage		Coagulation variables		
		A*	B	C
X-Ray orientation, H°	1**	42.5	36.9	37.9
	2	46.0	40.0	41.3
	3	46.8	40.8	41.8
Perfection of structure, B°	1	1.23	1.10	1.14
	2	1.23	1.11	1.12
	3	1.21	1.10	1.12
Dyeability, %	1	16.5	13.9	14.6
	2	24.6	20.6	22.0
	3	13.8	12.0	12.6
Density, g/cm^3		0.30	0.36	0.35
Shrinkage after thermosetting, %, time 15 min		25.5	26.5	27.0
Shrinkage after drying, %, T=125°C, without thermosetting		14.5	20.0	20.5
Shrinkage after thermosetting, %, time 2 min		13.5	19.0	20.0
Shrinkage after thermosetting, %, time 2 min, drying 125°C		23.5	25.0	25.0

* A - Dimethylformamid(DMF):water, %, 37:63; T = 40°C; B - DMF:water, 52 : 48 %, T = 25°C; C - DMF : water, 63:37%, T = 15°C.

** 1 - after stretching; 2 - after thermosetting; 3 - after drying.

It is well known that the heat treatment leads to a decrease in tension and to elimination of the internal microvoids between the fibrils as a result of a retraction of the stretched molecules into a helical conformation and restructuring of the network (3-5). Regarding this, it is logical to expect considerable changes in dyeability after heat treatments.

The observed changes in orientation, perfection and dyeability as a result of the heat treatment are the same, independently of molecular weight, dope concentration and coagulation variables (in

EBSCOhost - printed on 2/13/2023 3:45 AM via . All use subject to https://www.ebsco.com/terms-of-use

Table 3. Effect of Dope Concentration on Fiber Properties and Shrinkage During Heat Treatment

Fiber properties and shrinkage		Dope concentration, %			
		24.0	25.5	27.0	28.8
X-Ray orientation, H°	1*	37.5	37.1	37.2	37.6
	2	40.9	40.0	39.9	40.5
	3	41.8	41.0	41.0	41.2
Perfection of structure, B°	1	1.14	1.09	1.10	1.13
	2	1.15	1.09	1.08	1.13
	3	1.14	1.08	1.08	1.13
Dyeability, %	1	15.1	14.2	14.0	15.5
	2	24.0	22.8	22.6	24.8
	3	13.2	12.3	12.5	13.5
Density, g/cm^3		0.31	0.37	0.37	0.32
Shrinkage after thermosetting, %, time 15 min		25.9	26.4	25.0	23.2
Shrinkage after drying, %, 125°C, without thermosetting		20.2	20.8	18.9	17.0
Shrinkage after thermosetting, %, time 2 min		19.7	20.1	18.5	16.5
Shrinkage after thermosetting, %, time 2 min, drying 125°C		24.2	24.9	23.0	21.9

*1 - after stretching; 2 - after thermosetting; 3 - after drying.

the regions studied).

The phenomenon termed "collapse" is related to the shrinkage of the fibers. The influence of the structure on the shrinkage during thermosetting is slight; this is probably due to high mobility of the structural elements in the presence of water molecules. However, when the fibers are dried directly without thermosetting, the shrinkage depends on the structure in great extent. If the fibers are coagulated at high temperature and low concentration of the solvent the shrinkage decreases. These fibers possess very large voids and defects in the network (9) and the structural rearrangement is probably inhibited. It was shown in our previous work (10) that the very high or very low dope concentrations lead

EBSCOhost - printed on 2/13/2023 3:45 AM via . All use subject to https://www.ebsco.com/terms-of-use

Table 4. Effect of Heat Treatments on the Variation Coefficients of Ultimate Tensile Properties[a] of the Fibers

Heat treatments	C_v,% of[a]	Molecular weight, $\eta_{sp}^{0.5}$			Coagulation variables			Dope concentration, %	
		1.65	1.90	1.98	A*	B	C	25.5	28.8
1**	TSD	13.9	13.6	14.0	15.4	13.5	14.0	13.5	15.1
	TED	9.0	8.2	8.2	11.5	8.4	8.1	8.4	10.5
2	TSD	16.1	16.0	16.6	19.9	15.1	14.8	14.8	19.6
	TED	10.9	10.3	11.5	15.0	10.3	10.9	10.6	14.0
3	TSD	15.0	14.6	16.0	17.5	14.7	14.5	14.1	19.0
	TED	10.9	9.9	11.0	11.9	9.1	11.0	9.4	11.9

* A - DMF:water 37:63%, T = 40°C; B - DMF:water 52:48%, T = 25°C;
C - DMF:water 63:37%, T = 15°C.

** 1 - after thermosetting 15 min and drying at T = 125°C;
2 - after drying at 125°C, without thermosetting;
3 - after thermosetting 2 min and drying at T = 125°C.

[a]TSD = tensile strength (dry); TED tensile elongation (dry).

to a heterogeneous structure of the protofibers and stretched fibers. Bearing in mind the structural changes occurring within heat treatment it is natural that the shrinkage is the highest at moderate dope concentration (24-26%). When the fibers are produced from polymer with high molecular weight the shrinkage decreases. This may be ascribed to the number of connections and forces acting between the fibrils.

The results confirm the conclusion of Dumbleton, Bell, Sotton and Vialard (3-5) that this rearrangement in the internal structure is not identical in wet and dry atmosphere. The combination of great mobility of the chains and fibrils (thermosetting) and the slow elimination of the voids (drying) will increase the homogeneity of the structure. When the protofibers and stretched fibers possess an irregular structure, the influence of the heat treatment increases. Therefore, the data for unevenness of the ultimate tensile properties are not unexpected (Table 4). In the case of fibers coagulated under "hard" conditions or spun from highly concentrated solution, and dried directly without thermosetting, the

EBSCOhost - printed on 2/13/2023 3:45 AM via . All use subject to https://www.ebsco.com/terms-of-use

variation coefficients of the tensile properties are highest. The same effect is observed when the duration of the thermosetting is short.

The authors wish to express their acknowledgements to Mrs. L.Macheva and Mrs. Y.Raycova for carrying out the tensile tests.

References

1. Takahashi, M., Y. Nukushina. 1962. J.Polym.Sci. 56, S19.
2. Takeda, H., Y. Nukushina. 1964. Text.Res.J. 34, 173.
3. Dumbleton, J.H., J.P. Bell. 1970. J.Appl.Polym.Sci. 14, 2402.
4. Bell, J.P., J.H. Dumbleton. 1971. Text.Res.J. 41, 834.
5. Sotton, M., A.M. Vialard. 1971. Text.Res.J. 41, 834.
6. Craig, J.P., J.P. Knudsen, V.F. Holland. 1962. Text.Res.J. 32, 435.
7. Knudsen, J.P. 1963. Text.Res.J. 33, 13.
8. Stoyanov, A.I., V.P. Krustev. 1979. J.Appl.Polym.Sci. 24, 583.
9. Stoyanov, A.I., V.P. Krustev. 1981. J.Appl.Polym.Sci. 26, 1813.
10. Stoyanov, A.I., V.P. Krustev. 1982. J.Appl.Polym.Sci. 27, 235.

EBSCOhost - printed on 2/13/2023 3:45 AM via . All use subject to https://www.ebsco.com/terms-of-use

INFLUENCE OF RADIATION GRAFTING OF ACRYLIC ACID ON SOME THERMOANALYTICAL CHARACTERISTICS OF POLYAMIDE FIBRES

P. Veselý, D. Provazníková

Textile Research Institute, Centre of Radiation Technologies, Veverská Bítýška, Czechoslovakia

Introduction

Radiation grafting of acrylic acid on polyamide fibres results in improved hydrophilic properties of knitted fabric.
The purpose of this work is to verify the influence of radiation grafting of acrylic acid on the melting temperature T_m and on that of the thermal decomposition of polyamide fibres, T_{in}. Differences stated between the original and modified samples would necessitate influencing the above parameters during the course of continuous operation with on-line electron accelerator.
The authors have not been acquainted with any previous thermoanalytical measurements of materials like the above mentioned composition. It may be anticipated, however, that the grafted copolymerization of acrylic acid will induce a decrease in T_m and T_{in} due to the fact that parameters of polyacrylic acid are lower than those of polyamide. This way of consideration is acceptable, taking into account results of ref.(1) where decrease in T_m of copolyester of tetramethylene terephthalate and tetramethylene sebacate with increasing content of the latter component was measured, whereby T_m of polyethylene terephthalate (222°C) is higher than that of polyethylene sebacate (65°C). Even a reverse case (2) can be cited: by adding fire retardants with higher melting temperature, T_m of polyethylene terephthalate will increase. It has been also shown (3) that PA materials do not differ from PES in their thermoanalytical behaviour.

Morphology of Polymers
© 1986 Walter de Gruyter & Co., Berlin · New York - Printed in Germany.

EBSCOhost - printed on 2/13/2023 3:45 AM via . All use subject to https://www.ebsco.com/terms-of-use

Experimental Part

The starting material was a knitted fabric (made in Jitex Knitting Works, Písek) of following fibre composition (produced by Chemlon Fibre Works, Humenné): 93% of poly-ε-caprolactam, 2 $\pm$ 0.2% of low-molecular components, 1 $\pm$ 0.2% of preparation oil and 4 $\pm$ 0.5% of water. The acrylic acid produced by BASF Works was used for grafting.

For modification process, simultaneous method of irradiation was employed, the knitted fabric being at first impregnated by acrylic acid and subsequently irradiated by means of an electron accelerator. Accelerator characteristics (high-energy pulse linear accelerator Tesla-VÚVET at Nuclear Research Institute, Řež): energy of electron 4 MeV, pulse duration 3 μs, repeating pulse frequency 500 Hz, mean output in deflected beam 1 kW, deflecting width 50 cm, mean dose input 1 $kGy.s^{-1}$. Irradiation was performed in air under normal atmospheric pressure. Optimum irradiation doses were 20 to 35 kGy. Material add-on after grafting was established by weighing. Observation of surface structure of knitted fabric was performed by means of scanning electron microscopy. For thermoanalytical measurements a Derivatograph OD 102 - Paulik system (MOM Budapest) was used. The evaluation of hydrophilic parameters (capillarity, absorptive capacity and humidity content) of the polyamide fabric was performed by means of conventional methods used in textile testing according to the following standards: ČSN (Czechoslovak Standards) 80 0831, 80 0828, 80 0061, 80 0065 and 80 0074.

With the material add-on of 3 to 5% which can be regarded as optimum (according to the achieved results), the capillarity and absorption capacity increase was up to 50% and 20%, respectively.

Results and Discussion

On the basis of hitherto acquired knowledge (4-6), it may be assumed that the given problem - change in thermoanalytical properties of polyamide with increasing add-on of acrylic acid - may be best evaluated by measuring T_m. This value is not influenced by possible recrystallization during the course of irradiation and by heat setting temperature, but it is affected by the copolymeriz-

EBSCOhost - printed on 2/13/2023 3:45 AM via . All use subject to https://www.ebsco.com/terms-of-use

ation component content.

It is known that better results, from the point of view of improved hydrophilicity of synthetic fibres, can be reached e.g. with methacrylic acid or with synergic mixture of methacrylic and acrylic acids (13), or with synergic mixture of acrylic acid and acrylamide (14).

Experiments were carried out in the simplest possible way so that they might be realized in industrial scope without any problems. Even in case when Mohr salt in concentration of 4 g/l was added into the impregnation bath as a homopolymerization inhibitor (7-11), irregular and partly homopolymer deposit of grafted material was not completely excluded, especially at higher material add-on (see Fig.1).

Better results from the point of view of regular deposit of grafted material and minimum homopolymer content can be reached under special conditions, viz. under reduced pressure and nitrogen atmosphere (10,12). When the pilot-plant tests were carried out with a pressure dyeing apparatus being used for impregnation,

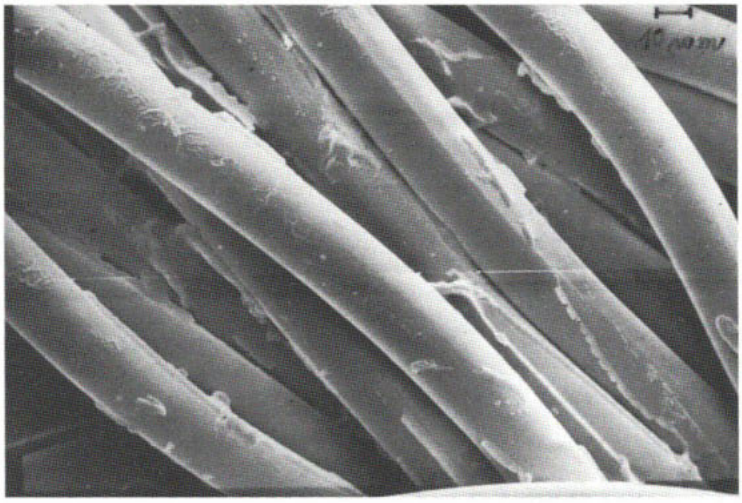

Fig.1. Polyamide 6 + 21% of acrylic acid (micrograph): numerous homopolymer deposits on the knitted fabric.

EBSCOhost - printed on 2/13/2023 3:45 AM via . All use subject to https://www.ebsco.com/terms-of-use

washing and dyeing of polyamide knitted fabric, higher homogeneity of impregnation solution deposit as well as higher homogeneity of dyeing were achieved.

Melting temperature values were evaluated from the endothermal melting peaks on the DTA curve. T_m values after extrapolation to zero heating rate, dependent upon the add-on of acrylic acid, are shown in Table 1.

Furthermore, from thermogravimetric curves the so-called initial temperatures of decomposition were also read off corresponding to the point of intersection of the extrapolated front base line and the tangent drawn through the inflex point of the TG curve. This means the point of intersection of curve gradient with the axis of abscissas at the inflex point. The value of initial decomposition temperature (16) used generally before was defined at the starting point of TG curve deflection from the base line (lower value T_{in}). T_{in} values, after extrapolation to zero heating rate, dependent upon add-on of acrylic acid are shown in Table 1.

Table 1. Temperatures of Melting (T_m) and Decomposition (T_{in}) of Polyamide Fibre

Grafting by acrylic acid (%) %	T_m °C	T_{in} °C
0	221	360
1.2	219	360
5	217	353
9	215	345
35	215	260

Dispersion variance: $\pm$ 2°C (T_m) and 4°C (T_{in}).

When measuring at different heating rates, differences between zero heating rate and 6 K/min heating rate were established (higher values for higher heating rates). An example of this measurement is shown in Fig.2.

The T_m value established for unmodified sample of PA 6 fibre (221 $\pm$ 2°C) is in good coincidence with values reported in the literature (17,18).

EBSCOhost - printed on 2/13/2023 3:45 AM via . All use subject to https://www.ebsco.com/terms-of-use

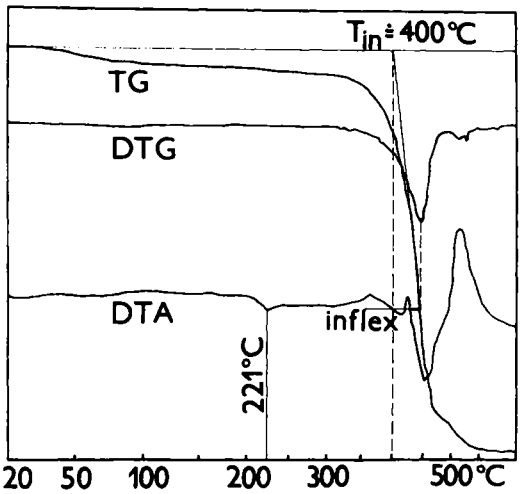

Fig.2. Thermoanalytical record - polyamide 6 + 1.2% of acrylic acid; measurement was done at the heating rate of 6 K/min.

We have ascertained that higher add-ons of grafted acrylic acid affect temperature of decomposition to a greater extent than T_m. Regarding the aim to obtain improved hydrophilic parameters (capillarity, absorption capacity, etc.) and to keep, at the same time, undeteriorated properties, the values of material add-on after modification by 3 to 5% have been found optimum. These values of add-ons being reached, the decrease in decomposition temperature amounts to ~10 K max, and the decrease in T_m to ~4 K (see Table 1). In pilot-plant operation, the heat setting temperature of polyamide fabric was able to reduce from usual 190°C to 170°C after modification by 5% of acrylic acid.

References

1. Marrs, W., R.H.Peters and R.H.Still. 1976. Proc.Eur.Symp.Therm. Anal. 1st, 192.

2. Minčeva, W., S.Wojnova, D.Dimitrov. 1979. Angew.Makromol.Chem. 80, 161.

3. Vaníček, J., M.Berka. 1975. Textil 33, 368.

EBSCOhost - printed on 2/13/2023 3:45 AM via . All use subject to https://www.ebsco.com/terms-of-use

4. Vaníček, J. 1975. Textil 30, 328.

5. Berndt, H.J., A.Bossmann. 1976. Polymer 17, 241.

6. Zemplén, G. 1978. Magyar Textiltechnika 31, 373.

7. Huglin, M.B., B.L.Johnson. 1969. J.Polym.Sci. A-1, 7, 1379.

8. Bonnfis, J.C., J.R.Puig. 1971. J.Appl.Polym.Sci. 15, 553.

9. Rao, M.H., K.N.Rao. 1979. Polym.Bull. 1, 727.

10. Pružinec, J., Š.Varga. 1980. Radiochem.Radioanal.Lett. 43, 147.

11. Pružinec, J., J.Kadlečík. 1983. Chem.vlákna 33, 38.

12. Usmanov, Ch.U., A.A.Yulchibayev, T.Sirlibayev. 1967. Khim. volokna 6, 32.

13. Shim, J.S., H.I.Kim. 1982. Polymer (Korea) 6, 406.

14. Teli, M.D., H.T.Lokhande. 1982. Indian Text.J. 92, 173.

15. Holba, P. 1979. Czechoslovak Seminar on Thermal Analysis and Calorimetry of Polymers. Tábor, pp. 7-12.

16. Barton, J.M., W.A.Lee, W.W.Wright. 1978. Therm.Anal. 13, 85.

17. Grzebieniak. 1973. Polimery-Tworz.Wielkoczast. 18, 336.

18. Strattmann. 1973. Erkennen und Identifizieren der Faserstoffe, Spohr Verlag, Stuttgart.

EBSCOhost - printed on 2/13/2023 3:45 AM via . All use subject to https://www.ebsco.com/terms-of-use

THE INFLUENCE OF THE MORPHOLOGY OF BLOCK COPOLYMERS ON THEIR GAS PERMEABILITY

A. Ferdinand, J. Springer
Institut für Technische Chemie, Fachgebiet Makromolekulare Chemie, TU Berlin, Straße d. 17. Juni 122-128, D-1000 Berlin 12, Germany

Introduction

One of the main characteristic features of block copolymers is the phase separation in the solid state. Indeed this is the source for the multiple special physical properties of these copolymers which can then be modified by changing the degree and kind of phase separation. There are three factors which have to be considered for preparing special microstructures:
- the composition of the block copolymer
- the molecular weight of the single blocks and its distribution
- the solvent which may be involved in preparing the polymer.

In a recently published paper (1) the influence of different solvents on the phase separation of copolymers has been discussed. Furthermore this article also reviewed the influence of the modified microstructure on some physical properties such as thermomechanical behaviour, tensile properties, stress hardening and softening.
Another physical property, the gas permeability, is also very sensitive to changes in the microstructure of an investigated polymer. Therefore the purpose of this paper is to show the influence of the morphology of block copolymers on the gas permeability, especially when investigating the influence of the solvent involved in the preparation.

Theory

Influence of the casting solvent on the microstructure

The behaviour of block copolymers during their phase separation has been investigated extensively so that only the most important factors needed for further discussion are here briefly reviewed.

Morphology of Polymers
© 1986 Walter de Gruyter & Co., Berlin · New York - Printed in Germany.

EBSCOhost - printed on 2/13/2023 3:45 AM via . All use subject to https://www.ebsco.com/terms-of-use

In preparing a block copolymer film or membrane by evaporating the casting solvent one has to differentiate between two kinds of solvents, i.e. the selective and non selective ones. The selective solvent is a good solvent for only one component of the block copolymer while the non selective solvent dissolves all components in the same way, either good or poor. So, for example, considering a block copolymer of styrene (S) and butadiene (B), methyl ethyl ketone (MEK) is a selective solvent for polystyrene (PS) and a poor solvent for polybutadiene (PB). In contrast, benzene is a non selective solvent because it is a good solvent for both styrene and butadiene.
When comparing block copolymers in the solid state prepared from either a selective or non selective solvent one has observed different structures of phase separation (1). So the selective solvent promotes formation of greater regions of the preferred component than does a non selective solvent.

Theories of the permeation through heterogeneous media

Many authors have tried to describe the transport phenomena through heterogeneous media. Whether they considered electricity or heat conduction problems or they wanted to calculate the transport of molecules through solids, all had to pay regard to three factors: the geometry and distribution of the dispersed phase, the composition of the continuum as well as that of the dispersed phase. Many of these theories have been recently discussed (2), (3). Therefore only those models needed for further discussion are briefly reviewed.

1) "Parallel model"

Both phases are arranged lamellarly parallel to the direction of the transport (2).

$$P = \varphi_A P_A + \varphi_B P_B \qquad |1|$$

P permeability coefficient
P_i permeability coefficient of the pure phase i
φ_i volume fraction of the component i

EBSCOhost - printed on 2/13/2023 3:45 AM via . All use subject to https://www.ebsco.com/terms-of-use

2) "Series model" Both phases are arranged lamellarly normal to the direction of the transport.

$$P^{-1} = \varphi_A P_A^{-1} + \varphi_B P_B^{-1} \quad |2|$$

3) "Maxwell model" Maxwell describes the transport through media where isolated, almost impermeable spheres A are imbedded in a continuous matrix B.

$$P = P_B \frac{P_A + 2P_B + 2\varphi_A(P_B - P_A)}{P_A + 2P_B - \varphi_A(P_B - P_A)} \quad |3|$$

4) "Böttcher model" Böttcher considers spheres and ellipsoids A in a continuous matrix B. He derived an equation where the dispersed and continuous phases are interchangeable.
For $P_B \gg P_A$

$$P = P_B(1 - 3/2\,\varphi_A) \quad |4|$$

5) "Bruggeman model" Bruggeman describes elongated particles A in a matrix B. In the case of $P_B \gg P_A$

$$P = P_B\,(\varphi_B)^{3/2} \quad |5|$$

6) "Higuchi model" This model is an empirical one which can be written in the case of $P_B \gg P_A$

$$P = P_B \frac{1.61\,\varphi_B}{1.61 + 1.31\varphi_A} \quad |6|$$

7) "Robeson model" Robeson expands the Maxwell analysis assuming both phases to have continuous and discontinuous characteristics. He suggests an equation where x_i is the proportion of the component i to the continuous phase. $\overline{P_i}$ is the value resulting from eq. |3| when i is regarded as the matrix (4).

EBSCOhost - printed on 2/13/2023 3:45 AM via . All use subject to https://www.ebsco.com/terms-of-use

$$P = x_A \bar{P}_A + x_B \bar{P}_B \qquad |7|$$

8) "Petropoulos model" Petropoulos combines the parallel and series models to describe the contribution f_i of each component i to the continuous phase

$$P = f_A \varphi_A P_A + f_B \varphi_B P_B + \frac{\left|(1-f_A)\varphi_A + (1-f_B)\varphi_B\right|^2}{(1-f_A)\varphi_A/P_A + (1-f_B)\varphi_B/P_B} \qquad |8|$$

Experimental

Materials and film preparation

The polymer used is a styrene-butadiene triblock copolymer referred to hereafter as SBS. SBS is a commercial product "Cariflex TR 1101" (Shell). The characteristics of the polymer are given in Table 1.

Table 1. Characterization of SBS.

Content of styrene	33 wt.%
M_n	78000 g/mol
M_{nS}-M_{nB}-M_{nS}	10000-58000-10000 g/mol
Volume fraction of polybutadiene φ_{PB}	0.62*

*Estimated from electron micrographs

Pure copolymer was dissolved in benzene (BE) and/or methyl ethyl ketone (MEK), both of analytical grade. Polymer solutions were poured onto a clean mercury surface and stored under vacuum (400 mbar) at room temperature. The evaporation of solvents lasted two or three days. The thickness of membranes was 0.05-0.1 cm. According to the solvents used, the membranes will be named as "solvent"-membrane. So, for example, BE/MEK-membrane means a membrane prepared using a sol-

EBSCOhost - printed on 2/13/2023 3:45 AM via . All use subject to https://www.ebsco.com/terms-of-use

vent mixture of 1:1 benzene/MEK.
To characterize the films ultrathin sections were treated with OsO_4. Electron micrographs of such sections show the PB phase as dark regions while the PS phase appears as white regions. Argon (99.995%) and carbon dioxide (99.997%) were used as gases.

Permeability measurements

The differential permeation method was used to determine the parameters of the membrane transport (5). The actual permeation rate was detected by a quadrupole mass spectrometer in a high vacuum apparatus. The resulting curve is a response to a step concentration change. The permeability coefficient P is then evaluated from the steady state signal while the diffusion coefficient D can be obtained by an approximate description of the non-steady state. The solubility coefficient S is then given by the quotient P/D.
The pressure difference at the membrane was 400 mbar for all gases.

Results and Discussion

To demonstrate the influence of the casting solvent on the morphology of copolymers the microstructures of a BE- and MEK-membrane are compared in Fig. 1. Because of the non-selectivity of benzene, the BE-membrane shows a PB-matrix in which spheres and rods of PS

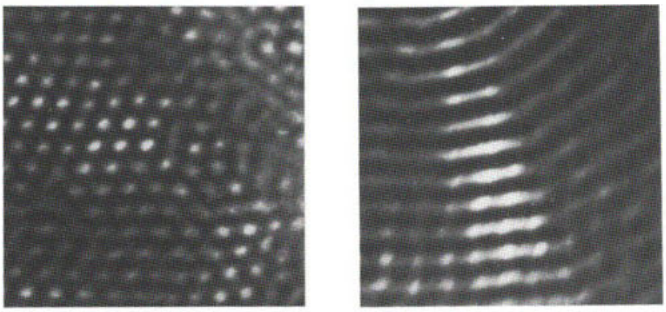

Fig. 1. Microstructure of the BE- (a) and MEK-membrane (b).

EBSCOhost - printed on 2/13/2023 3:45 AM via . All use subject to https://www.ebsco.com/terms-of-use

are imbedded. As stated, the use of the selective solvent MEK enhances the formation of greater regions of PS. The MEK-membrane has a lamellar structure. Thus PB is no longer the main continuous phase but now the PS phase seems to be nearly equivalent.

The influence of the casting solvent on the permeability data is presented in Fig. 2. The temperature dependence of the three main parameters P,D and S can be expressed by Arrhenius' equation which has often been used for description of the gas permeation through polymers.

The effect of changing the casting solvent is rather significant. One can recognize that a higher content of MEK in the order BE, BE/MEK and MEK in the casting solution promotes a greater decrease in the permeability and diffusion while the solubility remains nearly constant.

Qualitatively this result can be discussed as follows. The temperature range investigated (298-333 K) is between the glass temperature T_g of PS (373 K) and that of PB (173 K). It has been observed that, for a given temperature, the permeation rate through polymers having a high T_g is lower than through those having a low T_g (2). Table 2 shows

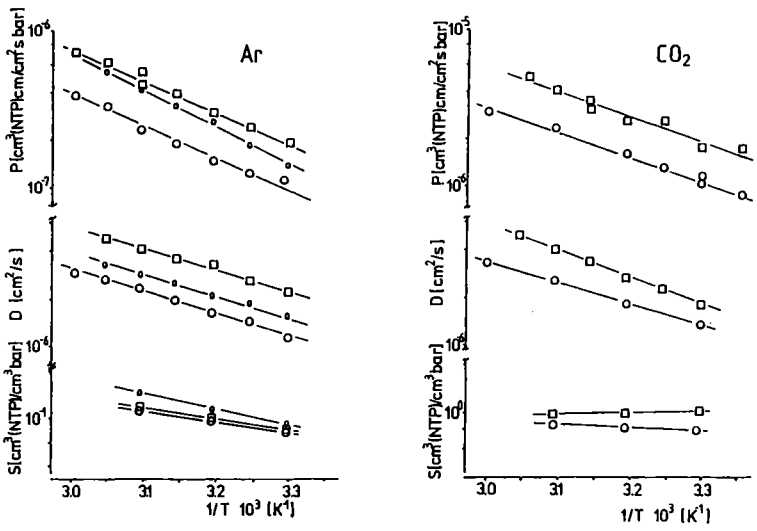

Fig. 2. Temperature dependence of P, D and S : □ BE; ● BE/MEK, ○ MEK.

EBSCOhost - printed on 2/13/2023 3:45 AM via . All use subject to https://www.ebsco.com/terms-of-use

the permeability coefficients given in the literature for PS and PB. The data for PS compared with those of PB are hundred times smaller so that the PS phase might be regarded as impermeable. Now because of the use of MEK greater regions of the impermeable phase are formed. Therefore the gas molecule has a longer way through the MEK-membrane than in the case of the BE-membrane. Here only small regions of spheres and rods hinder the gas transport.

Table 2. Permeability Data (7), (8), (9).
$P \times 10^{-7}$ | cm^3(NTP)cm/cm^2sbar |, T = 298 K

Polymer	Ar	CO_2
PB	3.080	29.61
PS	0.075	0.78

As mentioned before, many authors have tried to describe mathematically the transport phenomena through heterogeneous media. Fig. 3 shows their predictions for the permeability of a heterogeneous system made of PB (continuous matrix) and PS (dispersed phase). The calculations of these plots are based on the equations (1)-(6) and on the data given Table 2.
For further interpretation of these plots the volume fractions of each component are regarded constant even though the casting solvent is changed. This assumption seems reasonable because an analysis of the electron micrographs shows that the relation between the areas of styrene and butadiene proves to be nearly constant.
When comparing the results of SBS with the theoretical predictions the models of Bruggeman and Higuchi fit very well in the case of the

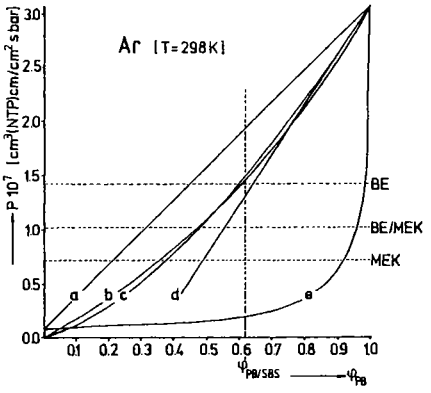

Fig. 3. Theoretical predictions

a : |1|
b : |6|
c : |5|
d : |4|
e : |2|

EBSCOhost - printed on 2/13/2023 3:45 AM via . All use subject to https://www.ebsco.com/terms-of-use

BE-membrane. This statement is valid for both gases.
Barrie and Munday (6) also found the Bruggeman and Higuchi predictions as the best fit for their results. The Bruggeman theory is based on the assumption that elongated particles are imbedded in the matrix. When comparing this assumption with the microstructure (Fig. 1) the Bruggeman model seems to predict the right shape of the dispersed phase.
None of these models describes the permeabilities of the MEK- and BE/MEK membrane in the right way. It has been shown that the dispersed phase changes more and more to a continuous phase by the use of MEK. To determine the contribution of each component to the continuous phase the Robeson and Petropoulos predictions are plotted in Fig. 4 and 5.

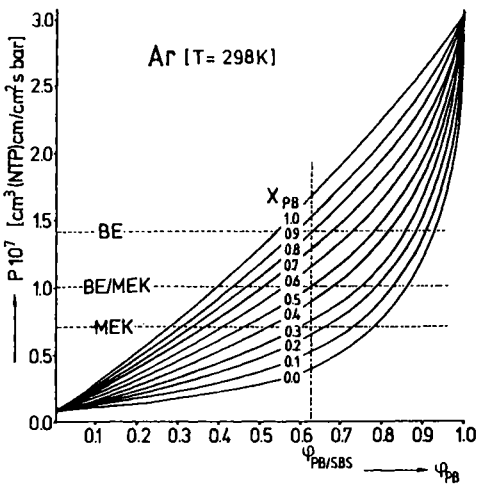

Fig. 4. Predictions of the Robeson model.

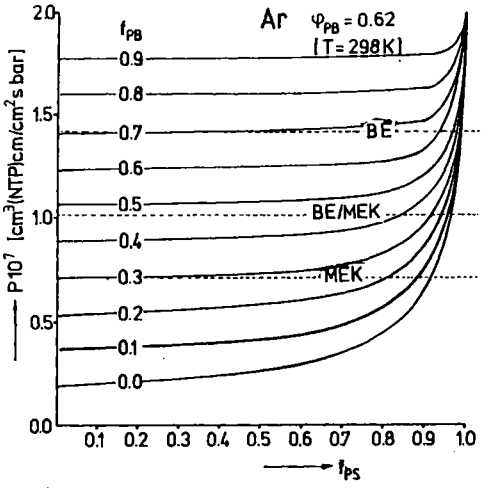

Fig. 5. Predictions of the Petropoulos model.

The interpretation of the permeability data by the help of the Robeson model gives for the BE-membrane a 80% content of the continuous phase contributed by the PB phase. This proportion lowers to 30% while using the selective solvent MEK. About the same results are obtained for CO_2 (Table 3a).
The Petropoulos model is not valid nearby the point $f_A = f_B = 1$. Mathematically this point is not determined because the denominator becomes zero. On the other hand, one can see that the assumption of the small influence of the PS phase on the permeability, as stated

EBSCOhost - printed on 2/13/2023 3:45 AM via . All use subject to https://www.ebsco.com/terms-of-use

earlier, is justified. There are only little changes by increasing the f_{PS} factor, i.e. in calculating a higher contribution of the PS phase to the continuous phase. In contrast, the increase in the f_{PB} factor changes the coefficient P enormously. Table 3b shows the f_{PB} factors which result from Fig. 5.

Table 3. Proportions of the PB phase to the continuous phase calculated by the Robeson (a) and the Petropoulos model (b)

Solvent	a) x_{PB}(Ar)	x_{PB} (CO_2)	b) f_{PB} (Ar)	f_{PB} (CO_2)
BE	0.8	0.9	0.7	0.8
BE/MEK	0.5	-	0.5	-
MEK	0.3-0.4	0.4	0.3	0.4-0.5

When comparing Table 3a and 3b the f_{PB} factor of the Petropoulos model seems to be equivalent to the Robeson x_{PB} factor. Both describe correctly the influence of the casting solvent indicating a change in the structure due to phase separation. Both theories postulate a decrease in the PB phase because of its lower proportion to the continuous phase.

If these results are compared with the microstructure showed in Fig. 1 both models seem to overemphasize the effect of changing the solvent. The models predict a nearly total phase inversion, i.e. the MEK-membrane should have spheres and rods of butadiene imbedded in a styrene matrix. In contrast to these predictions the micrograph shows a lamellar structure. One explanation of this effect might be the formation of interphases. Interphases form the transitions between the pure PS and the pure PB phase containing both components mixed together. A hint for their existence is that the separation between the two phases is not so sharp in the case of the MEK-membrane while in the case of the BE-membrane the transitions are sharper (Fig. 1). Therefore, calculating the proportion of butadiene to the continuous phase one has to consider the formation of interphases besides the change from the matrix phase to the lamellar regions. The proportion to the continuous phase is therefore reduced.

EBSCOhost - printed on 2/13/2023 3:45 AM via . All use subject to https://www.ebsco.com/terms-of-use

Acknowledgement

This work was sponsored by the Deutsche Forschungsgemeinschaft, Bonn. Thanks are due to the Fritz-Haber-Institut, Berlin, for the electron micrographs of the samples.

References

(1) J.M.G. Cowie. 1982. In: Developments in Block Copolymers-1, (I. Goodman, ed.). Applied Science Publishers, London · New York, pp. 1-39.

(2) J.H. Petropoulos. 1985. In: Advances in Polymer Science, Vol. 64 (M. Gordon, ed.). Springer-Verlag, Berlin·Heidelberg·Tokyo, pp. 93-143.

(3) R.M. Barrer. 1968. In: Diffusion in Polymers (J. Crank and G.S. Park, eds.). Academic Press, London New York, 165-219.

(4) L.M. Robeson, A. Noshay, M. Matzner and C.N. Meriam. 1973. Die Angewandte Makromol. Chem. 29/30, 47.

(5) R.M. Felder. 1977. J. Membr. Sci. 3, 15.

(6) J.A. Barrie and K. Munday. 1983. J. Membr. Sci. 13, 175.

(7) H. Odani, K. Taira, N. Nemoto and M. Kurata. 1975. Bull Inst. Chem. Res. Kyoto University 53, 216.

(8) H. Yasuda and Kj. Rosengren. 1970. J. Appl. Polymer Sci. 14, 2839.

(9) R. Cowling and G.S. Park. 1979. J. Membr. Sci. 5, 199.

EBSCOhost - printed on 2/13/2023 3:45 AM via . All use subject to https://www.ebsco.com/terms-of-use

X-RAY STUDY OF FIBRILLATION OF POLYPROPYLENE FILMS

J. Baldrian
Institute of Macromolecular Chemistry, Czechoslovak Academy of Sciences, 162 06 Prague 6, Czechoslovakia

Introduction

Uniaxial drawing of polypropylene films (POP) to a high degree gives rise to long narrow cracks elongated in the direction of the acting force. The films are decomposed to a system of parallel fibres. The procedure is used in the production of film fibres and non-woven textiles. Structural interpretations of fibrillation (1--5) are based on a microfibrillar model suggested by Peterlin (6) who investigated the deformation of polymer single crystals, lamellae and spherulites. High-oriented fibres and films are composed of microfibrils in which crystallites are separated from each other in the direction of deformation by the noncrystalline phase through which they are joined by extended tie molecules. Fibrillation is a consequence of different intra- and interfibrillary interactions. This study is an attempt to contribute to the investigation of structural causes of fibrillation in three-stage drawing by using parameters obtained by small-angle X-ray scattering (SAXS) and wide-angle X-ray scattering (WAXS).

Experimental

Films of isotactic polypropylene were obtained by blown extrusion technology. They were cooled with air and continuously drawn in three stages using a drawing apparatus consisting of five cylinders and a pair of heating bodies on the curved surfaces of which deformation took place. The samples were taken after the individual step (zone) of drawing. Characteristics of the films under study are summarized in Table 1.
WAXS was measured with an automatic Syntex $P2_1$ diffractometer. CuKα radiation monochromatized with a carbon monochromator was

Morphology of Polymers
© 1986 Walter de Gruyter & Co., Berlin · New York - Printed in Germany.

EBSCOhost - printed on 2/13/2023 3:45 AM via . All use subject to https://www.ebsco.com/terms-of-use

Table 1. Preparation of POP Films

Film No.	F45	F50	F54	F60	THB[a]	°C
Velocity[b], $m\,s^{-1}$	0.47	0.43	0.38	0.33		
		Drawing ratios				
1st zone	4.00	4.40	4.87	5.78	106	117
2nd zone	4.12	4.58	5.02	5.95	122	124
3rd zone	4.50	4.94	5.51	6.49	120	130

[a]Temperature of the pair of heated bodies, [b]velocity of film take-away rolls.

employed for the purpose. The radiation was registered with a scintillation counter.

SAXS was measured with a Kiessig and a Kratky camera. The CuKα radiation was used, registered on a film or by means of a proportional counter.

Methods

Profile analysis: Intensity distribution on WAXS fibre diagrams of POP films were approximated in different dirrections by

$$I(x) = ax + b + \sum_{i=1}^{n} P_i(x)$$

i.e., by the sum of profile functions P(x) of the individual reflexions and by the linear background. The profile function Pearson VII

$$P(x) = A[1 + (x-x_o)^2/(ma^2)]^{-m}$$

was used in view of its shape flexibility[7]. A is the value of the profile function in the maximum in position x_o, m is the shape factor, the parameter a is related with the half-width of reflexion. The structural parameters of POP films were determined by using parameters of the profile functions obtained from diffractograms of these films. The dimensions of the unit cell and the density of the crystalline phase were determined from positions of the reflexions. The apparent crystallite sizes, L_{hkl}, were determined

EBSCOhost - printed on 2/13/2023 3:45 AM via . All use subject to https://www.ebsco.com/terms-of-use

from half-widths of the reflexions corrected for experimental broadening. By using the relation (8)

$$\langle\cos^2\Phi_{c,Z}\rangle = 1-1.099\langle\cos^2\Phi_{110,Z}\rangle-0.901\langle\cos^2\Phi_{040,Z}\rangle$$

involving the intensity distributions of the reflexions 110 and 040 in the azimutal direction Φ, the degree of axial orientation of the crystalline phase with respect to the direction of drawing Z was determined (8):

$$F = 0.5(3\langle\cos^2\Phi_{c,Z}\rangle - 1)$$

Film porosity by means of SAXS: Using the Porod theory of scattering from isotropic two-phase systems, it is possible to determine the volume fraction of pores, p, for a porous system by means of the relation

$$p(1-p) = 4\pi Q/i_e N^2 d a P_o \rho^2$$

in which $Q = \int_0^\infty I(s)\,s\,ds$ is Porod invariant, s is the scattering vector, i_e is Thompson's scattering constant, N is the Avogadro number, d is the specimen thickness, a is the specimen-to-receiver distance, P_o is the intensity of the primary beam, ρ is the polymer density, I(s) is the scattered intensity measured with an infinitely high primary beam.

As has been shown (9,10), in the case of systems with a cylindrical symmetry around the fibre axis it is possible to obtain values of Porod invariant, Q, and thus porosity, by a one-dimensional integration of the intensity of scattering in the direction perpendicular to the fibre axis. It is also possible to determine the specific surface area of the phase boundary

$$S = 8\pi p(1-p)k_1/Q$$

where $k_1 = \lim_{s\to\infty} s^3 I(s)$ and the mean length of intersects passing through the pores, l_p, and those passing through the polymer matrix, l_{POP},

$$l_p = Q/2\pi k_1(1-p),\quad l_{POP} = Q/2\pi k_1 p$$

EBSCOhost - printed on 2/13/2023 3:45 AM via . All use subject to https://www.ebsco.com/terms-of-use

Results and Discussion

WAXS patterns showed that undrawn POP films have a very poorly developed preferred orientation. After the first degree of drawing the orientation becomes axial, which is improved by further drawing, as is shown in Fig.1. The effect of drawing on orientation is virtually the same for all films. The maximal change in the orientation takes place in the first step, in accord with the largest drawing ratio (Table 1). The considerably high degree of orientation after the second step of drawing is the reason why its increment in the third step is smaller than in the second, in spite of the fact that the relative drawing ratio is higher in the third drawing zone. In the third step of drawing visible splitting appears in the films, which may lead to a partial loosening of the structure, and thus a decrease in the degree of orientation.

It appeared that the other measured structure parameters change only during the first step of drawing and then remain stable. They are shown in Fig. 2 as a function of the 1st drawing ratio. With increasing drawing ratio, the transverse dimensions of the crystallites, L_{110}, L_{130}, L_{040}, and the long period are reduced, and the density of the crystalline phase, ρ_c, also decreases. Hence, the structure of the crystalline phase of POP films

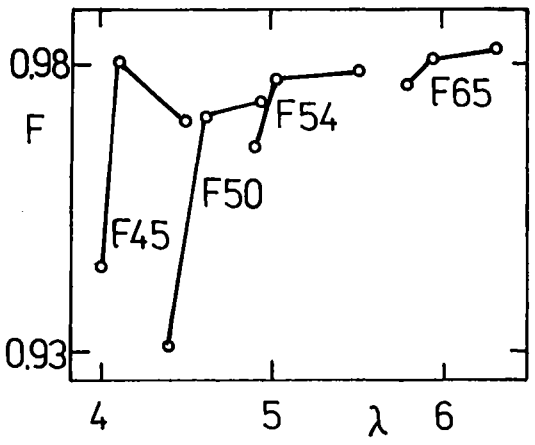

Fig. 1. Dependence of the degree of orientation of POP films on the drawing ratio λ.

EBSCOhost - printed on 2/13/2023 3:45 AM via . All use subject to https://www.ebsco.com/terms-of-use

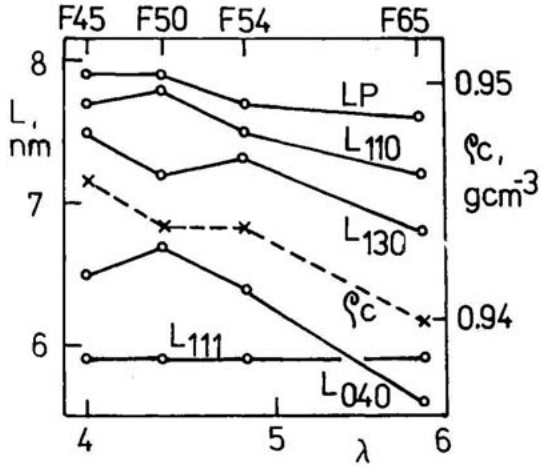

Fig. 2. Dependence of crystallite sizes L_{hkl}, long period LP and of the density of the crystalline phase ρ_c of POP films on the drawing ratio λ in the first zone.

is the more perfect, the smaller the deformation to which it was subjected in the first degree of drawing. The size of crystallites in the direction perpendicular to the 111 plane remains unchanged. It is probable that the size of crystallites remains unchanged also in the direction of deformation. Due to the fact that with increasing drawing ratio the magnitude of the long period decreases, the size of amorphous regions in the fibrils also decreases in the same direction.

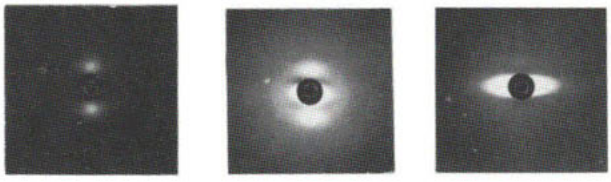

Fig. 3. SAXS pattern of undrawn film (a) and of films after drawing in the second (b) and third (c) zones.

EBSCOhost - printed on 2/13/2023 3:45 AM via . All use subject to https://www.ebsco.com/terms-of-use

Changes in SAXS during the treatment of POP films are shown in Fig. 3. The SAXS pattern of an undrawn film has circular reflexions on the meridian. After drawing, the reflexion is somewhat extended in the direction perpendicular to that of deformation, and an intensive central small-angle scattering extended in the same direction appears (Fig.3b). With proceeding deformation the central scattering is extended still more, and its intensity considerably increases. At the maximal deformation the intensity is higher by an order of magnitude than that of meridian reflexions.
The undrawn film has a supermolecular structure in which the predominant part of the crystallites are arranged in fibrils in the direction of orientation. In the process of drawing the fibrillar structure improves, and the fibril width somewhat decreases. The formation of central small-angle scattering elongated perpendicularly to the direction of deformation and a considerable increase in its intensity with proceeding deformation were interpreted on the basis of formation of narrow long cracks elongated in the direction of deformation. To describe this system quantitatively, the small-angle scattering curve of central scattering in the direction of the equator for the film after third drawing was measured (Fig. 4). Due to the intensity of meridian reflexions

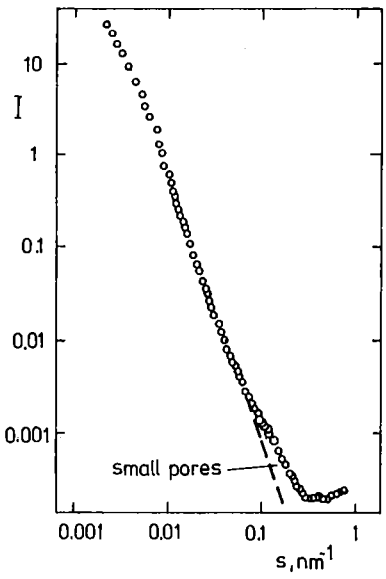

Fig. 4. Central SAXS curve in equatorial direction.

EBSCOhost - printed on 2/13/2023 3:45 AM via . All use subject to https://www.ebsco.com/terms-of-use

being weaker by an order of magnitude, the latter do not affect the measured scattering curve to any major extent. The shape of the scattering curve indicates a bimodal distribution of the sizes of pores arising in POP films during drawing, as illustrated in Fig.4. On the basis of the two-phase structure model (polymer/pores), the overall structure parameters of the porous structure of films and parameters corresponding to microporosity were determined. The results of this assessment are given in Table 2.

Table 2. Porous Structure of POP Films

Pores	Porosity vol.%	Spec.surface area $m^2 cm^{-3}$	l_p nm	l_{POP} nm
All pores	3.3	1.02	103	2988
Microporosity	0.15	2.20	2.7	1817

Conclusions

The structure of undrawn films has very weakly developed preferred orientation; after the first drawing it is transformed into the axial one. The films consist of fibrils, the inner structure of which is so resistant that it does not change with further drawing. The structure is determined by the take-away rolls velocity of the film and by the first step of drawing. At higher degrees of deformation, only the degree of orientation increases. Stiff fibrils become straightened and slide along each other, thus improving their orientation with respect to the direction of the acting force. The mutual sliding of the fibrils gives rise to interfibrillary sliding planes. With increasing deformation the sliding planes are transformed into microcracks elongated in the direction of deformation. Microcracks become elongated, joined, and cracks having the cross-section larger by an order of magnitude are formed. These cracks cause fibrillation of the films.

EBSCOhost - printed on 2/13/2023 3:45 AM via . All use subject to https://www.ebsco.com/terms-of-use

References

1. Peterlin, A. 1979. In: Ultra-High Modulus Polymers (E. Ciferi and J.M. Ward, eds.). Applied Science Publishers, p. 279.

2. Lenz, J., E. Wrentschur. 1982. Colloid Polymer Sci. 260, 663.

3. Polovichina, L.A., H.G. Simko, M.P. Zverev. 1978. Khim. Volokna 12.

4. Hajmasy, T., J. Alberti. 1976. Magy. Textiltechnik 30, 65.

5. Bouriot, P., R. Hagege, M. Sotton. 1976. Bull. Scient. ITF 5, 139.

6. Peterlin, A. 1972. Text. Res. J. 20.

7. Hall, M.M. V.G. Veeraraghavan, H. Rubin, P.G. Winchel. 1977. J.Appl.Cryst. 10, 66.

8. Alexander, L.E. 1969. X-Ray Diffraction Methods in Polymer Science, Wiley-Interscience, pp. 241-250.

9. Porod, O. 1961. In: Advances in Polymer Science, Vol. 2. (J.D.Ferry, C.G. Overberger, G.V. Schulz, A.J. Staverman and H.A. Stuart, eds.). Springer Verlag, Berlin. Götingen . Heidelberg. pp. 363-400.

10. Fischer, E.W., H. Goddar, G.F. Schmidt. 1968. Macromol.Chem. 118, 144.

EBSCOhost - printed on 2/13/2023 3:45 AM via . All use subject to https://www.ebsco.com/terms-of-use

SURFACE MICROSTRUCTURE OF POLYBUTADIENE FILMS DURING DISSOLUTION

S. Tkaczyk, A. Kwiatkowska, J. Świątek
Institute of Physics, Pedagogical University, 42-200 Czestochowa, Poland

Introduction

Thin films (~2 μm) of 1,4 cis-polybutadiene have been investigated with the aim to determine their applicability in the X-ray lithography. It was found that in the process of dissolution in toluene a characteristic cellular structure appeared on the surface area of the irradiated polymer.

Experimental

Thin films of 1,4 cis-polybutadiene (with an average viscosity molecular weight of 2.3×10^5) were formed on a glass substrate by spin coating from a solution in toluene. The films were exposed through a mask in an X-ray tube by 8.34 Å Al K_α line in a vacuum of 5×10^{-4} Pa. Exposure doses were determined as described in ref. (1). In order to develop the exposed pattern, the samples were immersed in toluene at 303 K for a time interval of 3 min which was enough to remove completely unexposed polymer regions, whereas the exposed areas were only partially dissolved due to the polymer crosslinking. Fig. 1 illustrates the influence of X-ray irradiation on solubility. Normalized thickness $d_n = d/d_o$ has been used, where d is the thickness remaining after development and d_o is its value before development in toluene.

Results and Discussion

Polymer areas irradiated with doses in the range from 60 to 170 J/m^2 have shown, after development in toluene, a characteristic cellular microstructure (see Fig. 2) which depends on the

Morphology of Polymers
© 1986 Walter de Gruyter & Co., Berlin · New York - Printed in Germany.

EBSCOhost - printed on 2/13/2023 3:45 AM via . All use subject to https://www.ebsco.com/terms-of-use

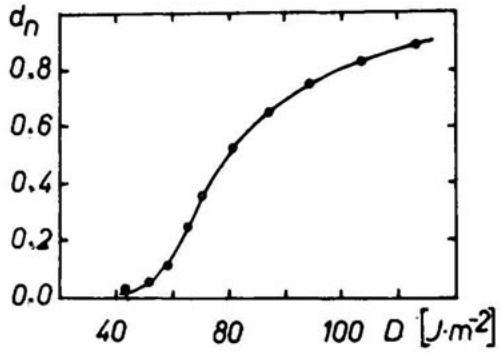

Fig. 1. Normalized thickness d_n as a function of the X-ray dose.

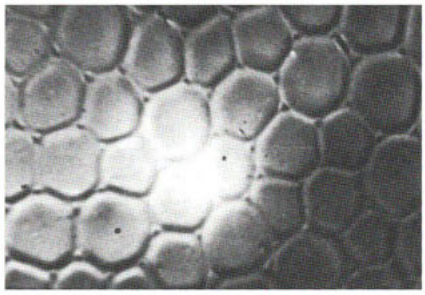

Fig. 2. Cellular structure of the surface of polybutadiene (magnification 330x).

X-ray dose. Changes in cell size are presented in Fig. 3. For doses greater than 170 J/m^2 the microstructure is so small that it could be seen in an optical microscope as a rough surface only. Also, the cell morphology changes with the dose, from flat surface hexagons of irregular boundaries projecting into liquid (at 70 J/m^2) to more regular hexagonal cells with dome-shaped central region and pronounced boundaries having additional maxima at vertices (at more than 100 J/m^2). A cross-section through a cell is shown in Fig. 4.

Interpretation of the observed phenomenon is rather difficult. It is obvious that irradiation causes crosslinking of polybutadiene which leads to an increase in its average molecular weight.

EBSCOhost - printed on 2/13/2023 3:45 AM via . All use subject to https://www.ebsco.com/terms-of-use

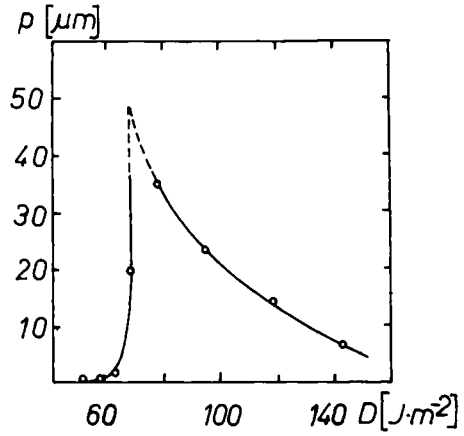

Fig. 3. Average size of cells p as a function of the X-ray dose.

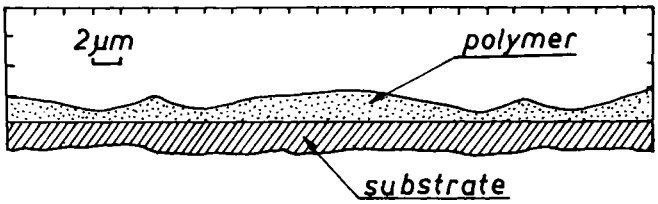

Fig. 4. Cross-section through a cell.

Immersion of such polymer in a solvent creates sometimes conditions under which a planar solid-liquid interface breaks down and dissolution proceeds via formation of cells. Spontaneous order formation that we observe here belongs probably to the group of Bénard-like phenomena (2,3). In this case, polymers as polybutadiene, may be good materials to observe experimentally these interesting phenomena.

References

1. Lenzo, P.V., D.L.Spencer, Appl.Phys.Lett. 24, 289 (1974).
2. Segel, L.A., J.Fluid Mech. 13, 289 (1962).
3. Jackson, K.A., D.J.Hunt, 13, 1212 (1965).

EBSCOhost - printed on 2/13/2023 3:45 AM via . All use subject to https://www.ebsco.com/terms-of-use

EBSCOhost - printed on 2/13/2023 3:45 AM via . All use subject to https://www.ebsco.com/terms-of-use

ELECTRIC FIELD-DEPENDENCE OF CRYSTALLINITY AND DIPOLE ORIENTATION IN POLY (VINYLIDENE FLUORIDE)

A. Janke, W. Künstler, D. Geiss, R. Danz and
W. Stark

Academy of Sciences of the GDR
Institute of Polymer Chemistry "Erich Correns"
1530 Teltow-Seehof, Kantstraße 55,
German Democratic Republic

1. Introduction

Several authors have discussed the change of crystallinity in β-phase poly (vinylidene fluoride) (PVDF) after poling (1,2,3). Latour et al. (1) have described these effects qualitatively using FT-IR-spectroscopy and x-ray techniques. Kepler et al. (2,3) have tried to quantify the change of crystallinity under applied electric field. Their experimental setup was not able to distinguish between intensity due to dipole orientation and that which is due to the variation in crystallinity.
We use x-ray texture analysis to distinguish between these two effects.

2. Experimental

50 µm α-phase PVDF-films (Bemberg G.m.b.H., FRG) for x-ray measurements and 20 µm for piezoelectric measurements were drawn uniaxially by hot zone drawing. Drawing conditions: temperature - 383 K; travel speed of necking zone - 0.5 mm s^{-1}; load - 2.5 kg; draw ratio - 4 (20 µm films) and 4.5 (50 µm films). The sample thickness after drawing was 10 µm or 12 µm. These samples had a β-phase content of $>$ 95 %, measured by IR-technique (4).
Thin aluminium electrodes were then evaporated on both sides of the samples. For piezoelectric measurements samples were poled for 10 s at room temperature. For x-ray measurements the samples

Morphology of Polymers
© 1986 Walter de Gruyter & Co., Berlin · New York - Printed in Germany.

EBSCOhost - printed on 2/13/2023 3:45 AM via . All use subject to https://www.ebsco.com/terms-of-use

were mounted on a special sample holder which allows poling during measurements. Poling took place at room temperature at a range of E = 0 ... 250 MVm^{-1}. According to the duration of x-ray measurements the poling time was 12 or 23 hours.
X-ray texture analysis was made in order to estimate the change of both dipole orientation and crystallinity induced by the electric field. For that reason we chose the (111)-reflex of β-phase PVDF. There is no coincidence with other reflexes (the (201)-reflex intensity is smaller than 4 % of the (111) one). Owing to the drawing process the distribution of the (111)-lattice planes is such that transmission technique (5) is sufficient to estimate it. The measurements were carried out by means of a commercial horizontal x-ray diffractometer HZG 3 (VEB Freiberger Präzisionsmechanik) completed with a φ-circle. We used Cu-K_α radiation (40 kV, 35 mA) monochromatized by a Ni-filter and impulse height analysis. The orientation of the dipoles (crystalline b-axis) was recalculated from the orientation distribution of the (111)-net plane normals. The change in crystallinity was estimated by integration of x-ray intensity over the whole pole sphere. This is assumed to be a first order approximation if the crystal shape does not change extremely.
The piezoelectric strain coefficients d_{31} were determined quasistatically under free-field conditions using a vibrating capacitor electrometer being connected with an external measuring capacitor (charge integration). The voltage of the samples was kept at zero by a compensation-voltage generated by a bootstrap integrator.

3. Results

Two representative pole figures obtained from unpoled and poled (at E = 250 MVm^{-1}) β-phase PVDF films are shown in Figure 1. The (111)-net plane normals lie along a small circle around the machine direction M (= drawing direction). We found a mixture of axial and uniplanar-axial orientation modes (6). The ratio between the orientation modes depends on poling (Table 1).

EBSCOhost - printed on 2/13/2023 3:45 AM via . All use subject to https://www.ebsco.com/terms-of-use

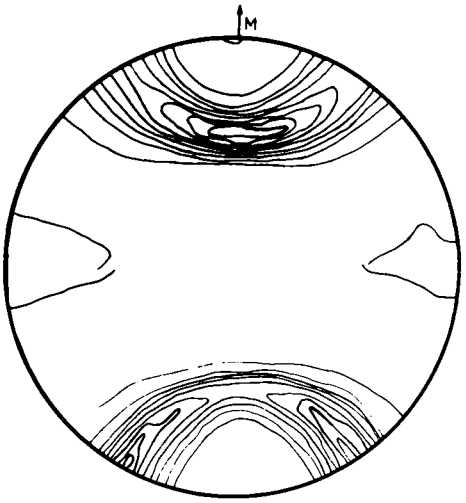

Fig. 1. Pole figures of (111)-net plane normals of an unpoled (below) and a poled (above) (E = 250 MVm-1) β-phase PVDF film.

Table 1: Ratio between the Orientation Modes in PVDF before and after Poling

Orientation mode	before poling	after poling ($E = 250\ MVm^{-1}$)
axial	81 %	71 %
uniplanar-axial	19 %	29 %

Figure 2 shows the dipole orientation distribution along the great circle N-T recalculated from the pole figures depending on the electric field strength. In the unpoled state the part of the dipoles with a uniplanar-axial orientation lies preferably along the transversal direction T parallel to the film plane. The dashed curves show the dipole orientation during electric field application. Above an electric field strength of $E = 100\ MVm^{-1}$ such curves cannot be measured, because the films become wrinkly during electric field application. After switching off the electric field (full curves) the dipoles relax toward the original direction. With increasing electric field strengths the dipoles turn over step by step to the normal direction. If the poling field

EBSCOhost - printed on 2/13/2023 3:45 AM via . All use subject to https://www.ebsco.com/terms-of-use

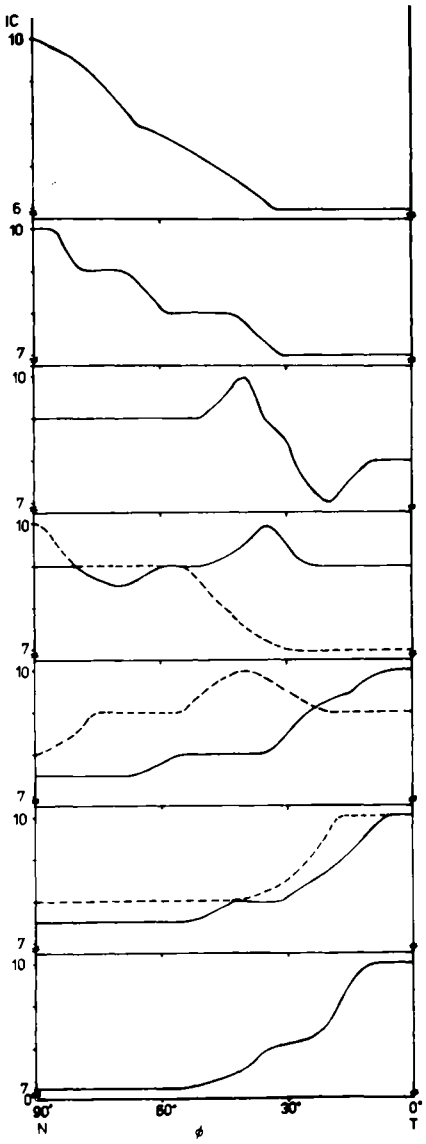

Fig. 2 Dipole orientation distribution along the great circle N - T, N - normal direction, T - transversal direction, ϕ - angular distance, IC - intensity class, - - - with applied poling field, ——— after switching off the field

strengths reach 200 MVm^{-1} or more, the preferred orientation of the oriented part of the dipoles is parallel to the normal direction N (poling field direction). Figure 3 shows the change of the index of crystallinity ε (relative change in x-ray intensity) versus electric field E. The curve with full circles represents measurements with applied electric field, the curve with open circles measurements after switching off the poling field. A significant change in crystallinity can be seen to begin at a field strength of E = 60 MVm^{-1}. The crystallinity increases with increasing field strength. It shows a local maximum at E = 160 MVm^{-1} (ε = 16 %) then it decreases abruptly and slightly increases at higher field strengths. Both curves show the same behaviour, but the crystallinity change without applied poling field is smaller (maximum ε = 6 %).

EBSCOhost - printed on 2/13/2023 3:45 AM via . All use subject to https://www.ebsco.com/terms-of-use

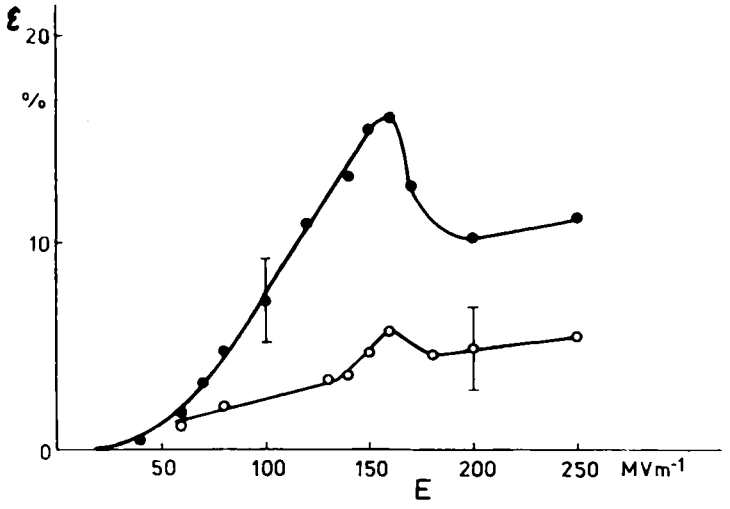

Fig. 3. Index of crystallinity ε versus electric field E, ● applied electric field, o after switching off the poling field.

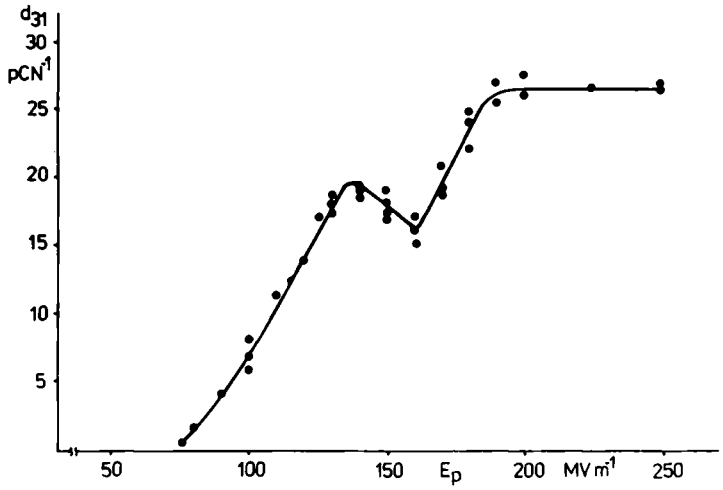

Fig. 4. Piezoelectric strain coefficient d_{31} versus electric field.

EBSCOhost - printed on 2/13/2023 3:45 AM via . All use subject to https://www.ebsco.com/terms-of-use

The results of the piezoelectric measurements are represented in Figure 4. The rising curve of d_{31}-coefficients versus electric field drops into a local minimum at a poling field of E = 160 MVm^{-1}. It rises again before it goes over to saturation at E = 200 MVm^{-1}.

4. Discussion

The results presented above show that both crystallinity and the orientation state change simultaneously during the poling of β-phase PVDF films. We are able to find a measure of crystallinity from the pole figure data.
Both dipole orientation and crystallinity show a significant, but different, dependence on the poling field strength. Below E = 60 MVm^{-1} no changes were observed. The dipole orientation changes during poling field application and relaxes towards the original direction after switching off the field. The orientation distribution of the dipoles corresponds to a mixture of axial and uniplanar-axial orientation modes. The results show that only 30 % of all crystalline dipoles have a uniplanar-axial orientation mode, which is responsible for the remanent macroscopic polarization.

It seems that the turning over of the dipoles goes step by step in dependence on the electric field strength. This behaviour must be discussed in connection with the change in crystallinity, as can be seen in Figure 3. The crystallinity increases with increasing applied electric field, probably due to the emergence of new crystallites or the growth of existing crystallites. The peaks in the crystallinity-curves (Fig. 3) correspond to the local minimum in the d_{31}-curve (Fig. 4). The decrease of piezoelectricity seems to be related to an increase in stiffness which is joint with the change in crystallinity. In our opinion, there are two counteracting effects that could be responsible for the peak in the crystallinity-curve:
1. New crystallites emerge from noncrystalline regions.
2. Existing crystallites are destroyed by rotation of dipoles.

EBSCOhost - printed on 2/13/2023 3:45 AM via . All use subject to https://www.ebsco.com/terms-of-use

At low field strengths the first effect is predominant, which up to an electric field strength of E = 100 MVm^{-1} corresponds to the increase in x-ray intensity near the normal direction N without a significant decrease in intensity near the transversal direction T, as can be seen in Figure 2. With increasing poling field strength the second effect becomes stronger and predominant at a range of E = 160 ... 200 MVm^{-1}. The difference between the curves in Figure 3 shows that in this range of electric field strength the dipoles cannot find a stable crystalline position during field application. Obviously, above ca. E = 200 MVm^{-1} the dipoles find new crystalline positions resulting in a significant change in orientation after switching off and in a slight increase in crystallinity caused by the first effect.

References

1. Latour, M., H. Abo Dorra, J.L. Galigué, J. Polym. Sci., Polym. Phys. Ed. 22 (1984), 345-56.

2. Kepler, R.G., R.A. Anderson, R.R. Lagasse, Ferroelectr. 57 (1984), 151-8.

3. Kepler, R.G., R.A. Anderson, Mol. Cryst. Lign. Cryst. 106 (1984), 345-59.

4. Danz, R., Polym. Bull. 7 (1982), 497-504.

5. Bunge, H.J., C. Esling, Quantitative Texture Analysis, Deutsche Gesellschaft f. Metallkd., Oberursel, 1982.

6. Geiss, D., Ch. Ruscher, U. Kofer, Acta Polymerica 34 (1983), 12-5.

EBSCOhost - printed on 2/13/2023 3:45 AM via . All use subject to https://www.ebsco.com/terms-of-use

EBSCOhost - printed on 2/13/2023 3:45 AM via . All use subject to https://www.ebsco.com/terms-of-use

INFLUENCE OF THE CRYSTALLINITY ON THE CHARGE CARRIER PHOTOGENERATION IN POLY(N-VINYLCARBAZOLE)

S. Nešpůrek, V. Cimrová

Institute of Macromolecular Chemistry, Czechoslovak Academy of Sciences, 162 06 Prague 6, Czechoslovakia

B. Klein-Szymanska

Warsaw Technical University, Warsaw, Poland

Introduction

The dependence of the photocarrier yield on the electric field, temperature and photon energy was established in various organic solids, among them, in poly(N-vinylcarbazole) (PVCA). In this material, the photogeneration efficiency is strongly dependent upon the electric field and, at high fields, the field dependence is in agreement with predictions based on the Onsager theory (1). From the variation of the quantum efficiency with the electric field, separation distances, r_o, of the bound electron-hole pairs were reported as 2.2 and 3.0 nm for excitation into the first (λ = 345 nm) and third (λ = 260 nm) excited singlet states, respectively. The primary quantum yield, η_o, was determined as 0.14 and independent of wavelength. Later on, Borsenberger and Ateya (2) gave precision to these values on amorphous PVCA films as 2.6 and 3.0 nm with η_o = 0.11 at 296 K, completed the values of r_o for the second excited singled state (λ = 295 nm), r_o = 2.8 nm, and determined the dependence of η_o on temperature. η_o can be described by an exponential dependence on reciprocal temperature with an activation energy of 0.05 eV. The thermalization distance was independent of temperature. Thus far, measurements on crystalline PVCA have not been performed, and therefore the relation of r_o to molecular parameters could not be determined. In this paper, we present the results of an investigation of the field dependence of the photogeneration efficiency at two excitation wavelengths, λ = 254 and 355 nm, for amorphous and crystalline PVCA films with the aim to determine the difference in the thermalization dis-

Morphology of Polymers
© 1986 Walter de Gruyter & Co., Berlin · New York - Printed in Germany.

EBSCOhost - printed on 2/13/2023 3:45 AM via . All use subject to https://www.ebsco.com/terms-of-use

tances and the primary quantum yields and to relate r_o to structural parameters.

Experimental

PVCA (m.w. 9.6×10^5) was obtained by the radiation polymerization (3). Amorphous films were cast from a cyclohexane-benzene polymer solution on a nickel substrate. To obtain a crystalline material, the amorphous films were heated to 573 K in the vacuum of 10^{-3} Pa for 3 hours. The X-ray diffraction curve is given in Fig.1.
The photogeneration efficiency η was determined from the rate of change of the surface charge density which is equal to the product of the photoinduced discharge quantum efficiency η' (which in turn is equal to η provided (i) the Schubweg is comparable to the

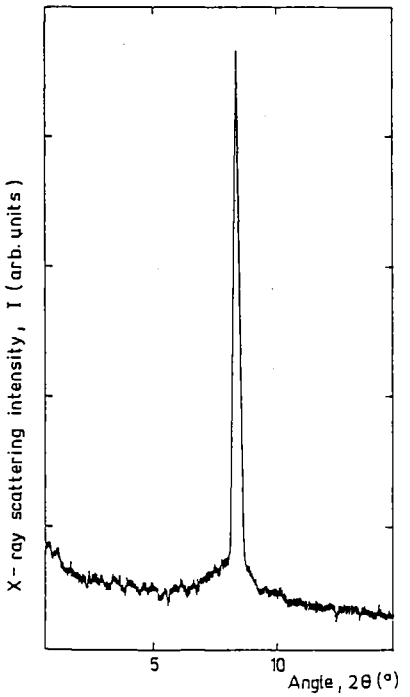

Fig.1. X-ray scattering curve from crystalline PVCA.

EBSCOhost - printed on 2/13/2023 3:45 AM via . All use subject to https://www.ebsco.com/terms-of-use

sample thickness and (ii) the emission-limited conditions (4) hold), the absorbed photon flux density and the magnitude of the unit charge at the onset of irradiation (5). With this technique, a sample is charged by a corona and then discharged by radiation. The surface potentials were measured with a rotary electrodynamic condenser electrometer (6) with a time resolution of 20 ms. The measurements were performed with both strongly (254 nm) and weakly (355 nm) absorbed radiation incident upon the positively charged surface. To ensure the emission limited conditions, the discharge was measured with photon fluxes as low as possible (c. $6x10^{17}$ photons m^{-2} s^{-1} for 254 nm light and $4x10^{18}$ photons $m^{-2}s^{-1}$ for 355 nm light). Light-induced discharge rates were corrected for the penetration depth of light, the dark discharge rate and the rest surface charge.

Results

Decay of the surface potential under irradiation may be characterized as the emission-limited case in the initial phase of the discharge, whereas at longer times a transition to the space-charge-perturbed discharge took place.

The shape of the quantum efficiency-electric field relationships at room temperature for 254 nm irradiation (intrinsic photogeneration) of amorphous (a) and crystalline (c) samples are shown in Figs 2 and 3, for 355 nm irradiation (extrinsic photogeneration) in Figs 4 and 5. Over the accessible range of electric fields the results are consistent with predictions of the Onsager theory of geminate recombination (7). The best theoretical fits according to the Onsager relation (8) - full lines (ε = 3.0) - have been obtained with the following parameters of the effective charge carrier separation lengths r_o (nm) and the primary quantum yields of autoionization η_o (charges per photon): Fig.2, λ = 254 nm, a-PVCA, r_o = 2.9, η_o = 0.11; Fig.3, λ = 254 nm, c-PVCA, r_o = 2.5, η_o = 0.13; Fig.4, λ = 355 nm, a-PVCA, r_o = 2.7, η_o = 0.04; Fig.5, λ = 355 nm, c-PVCA, r_o = 2.4 nm, η_o = 0.04. The photogeneration quantum efficiency for the zero electric field was: $1.6x10^{-4}$ charges per photon (λ = 254 nm, a-PVCA), $7.1x10^{-5}$ (λ = 254 nm, c-PVCA), $3.9x10^{-5}$ (λ = 355 nm, a-PVCA) and $1.6x10^{-5}$ (λ = 355 nm, c-PVCA).

EBSCOhost - printed on 2/13/2023 3:45 AM via . All use subject to https://www.ebsco.com/terms-of-use

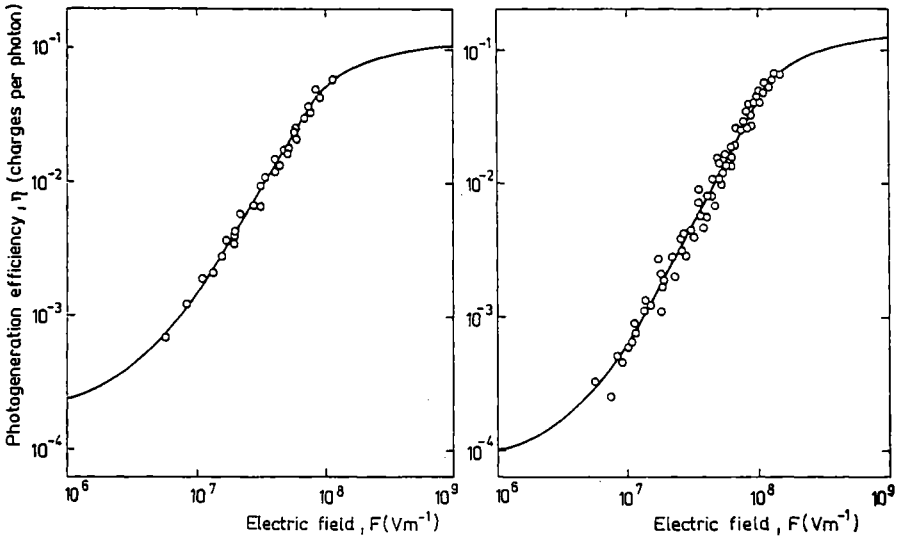

Figs 2 and 3. Field dependences of the photogeneration efficiency in amorphous (Fig.2) and crystalline (Fig.3) PVCA for 254 nm irradiation. The solid curves are calculated from the Onsager theory with $\varepsilon = 3$, and $r_o = 2.9$ nm, $\eta_o = 0.11$ (Fig.2) and $r_o = 2.5$ nm, $\eta_o = 0.13$.

Discussion

Intrinsic photogeneration could be depicted as a multistage process (Fig.6) which involves (i) photoexcitation to a neutral molecular electronic state, (ii) autoionization of the excited state, resulting in the creation of a localized hole and a hot electron, (iii) thermalization of the hot electron due to fast inelastic scattering leading to the formation of a Coulomb field-bound geminate electron-hole pair (so-called charge-transfer (CT) state), and (iv) thermal dissociation of the electron-hole pair into free carriers by Brownian motion subject to the combination of Coulomb and applied fields. The fraction of absorbed photons that result in bound thermalized pairs is the primary quantum yield η_o (assumed to be independent of the applied field). Under this assumption the overall field dependence of the photogeneration is governed by the efficiency of the dissociation step (iv)

EBSCOhost - printed on 2/13/2023 3:45 AM via . All use subject to https://www.ebsco.com/terms-of-use

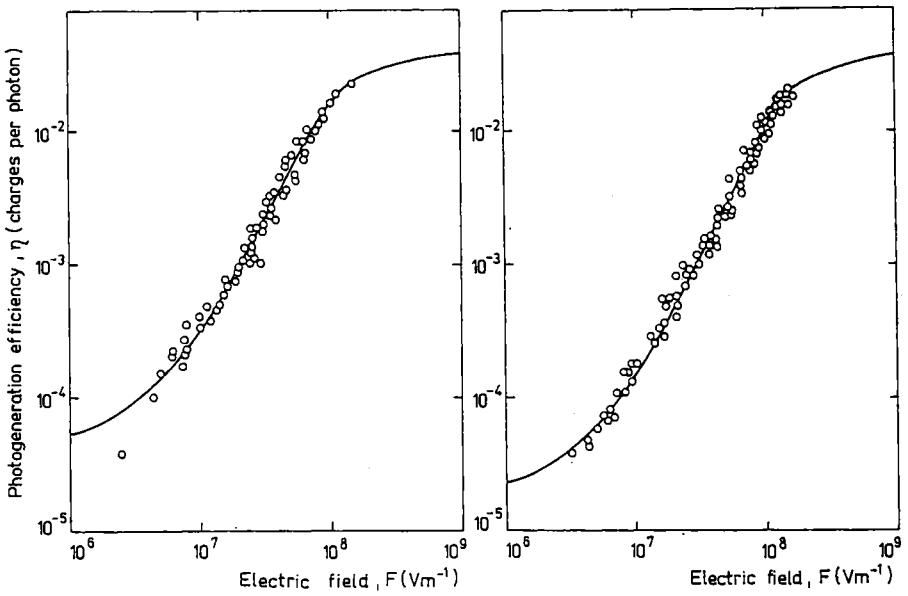

Figs 4 and 5. Field dependences of the photogeneration efficiency in amorphous (Fig.4) and crystalline (Fig.5) PVCA for 355 nm irradiation. The solid curves are calculated from the Onsager theory with $\varepsilon = 3$ and $r_o = 2.7$ nm, $\eta_o = 0.04$ (Fig.4) and $r_o = 2.4$ nm, $\eta_o = 0.04$ (Fig.5).

which may be described using the solution of the Smoluchowski equation given by Onsager (7). The experimental results have shown that the Onsager model (assuming that the distribution of the bound pairs is an isotropic δ function, i.e. all pairs are separated by the same distance r_o) provides a good description of the photogeneration process. We also checked the possibility of fitting our results to the Poole-Frenkel model that might be taken into account. However, the experimental field dependences of the photogeneration efficiency cannot be fitted to formula of this type. If the photogeneration proceeded via an autoionization step, one should suppose the overall electric field dependence of the quantum yield to be a superposition of a field dependence of the autoionization and that of the thermal dissociation. These features were incorporated in a modification of the Onsager model presented by Noolandi and Hong (9). However, the description of

EBSCOhost - printed on 2/13/2023 3:45 AM via . All use subject to https://www.ebsco.com/terms-of-use

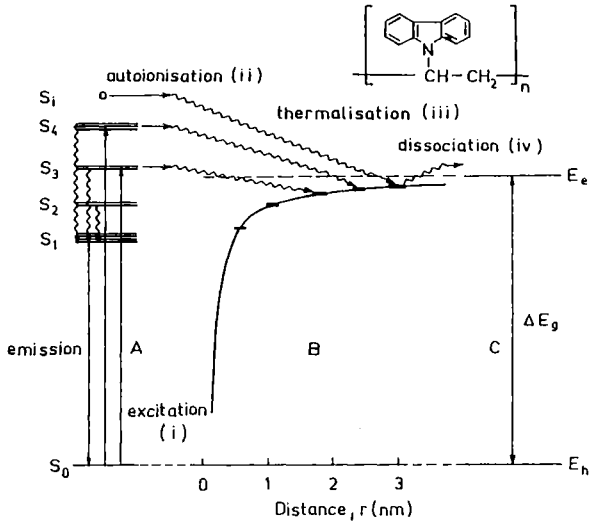

Fig.6. Photogeneration steps according to the ballistic model. A neutral electronic states, B bounded charge pairs, C ionized states. Inset: molecular structure of PVCA.

the thermal dissociation step in both the original Onsager model and its modifications follows basically the same pattern. Thus, experimental results obtained in this work were treated within the framework of the classical Onsager model. Our obtained parameters r_o = 2.9 nm and η_o = 0.11 charges per photon for a-PVCA are in a very good agreement with the data published by Pfister and Williams (1), and Borsenberger and Ateya (2). As it could be expected, the average separation distances were found shorter in the ordered (crystalline) material by c. 14%. The value of η_o changed imperceptible from 0.11 to 0.13 charges per photon. The most effective CT states for the photogeneration of charge carriers are those in the direction of the electric field. According to Griffiths (10), the crystalline films form a lamellar structure with the chain axis normal to the film plane, the lamellar thickness being approximately 70 to 80 nm from the substrate. However, the top layers of the thick films have the chain axis orientation parallel to the film plane. Since the penetration depth of 254 nm light is 50 nm only (sample thickness varied from 1 to 5 μm), the "parallel" case is responsible for the intrinsic charge carrier

EBSCOhost - printed on 2/13/2023 3:45 AM via . All use subject to https://www.ebsco.com/terms-of-use

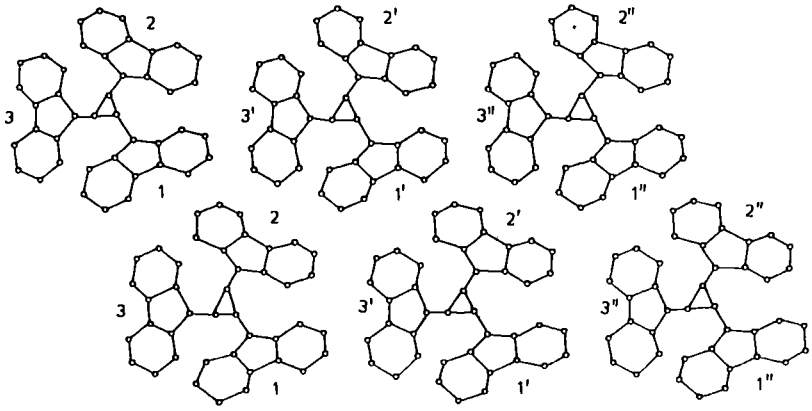

Fig.7. Structure model for crystalline PVCA.

photogeneration. The important separation distance is given by carbazole units 1-1" and 1-2" (2.4 and 2.5 nm respectively, see Figure 7), i.e. by units over one chain.
In the extrinsic photogeneration case the separation distances obtained experimentally, r_o = 2.7 nm for a-PVCA and shorter for c-PVCA by 11% (r_o = 2.4 nm), are very close to those obtained in the region of intrinsic photogeneration. Thus, in both cases the direct charge carrier precursors are not the nearest-neighbour states. But from the energetic point of view in the extrinsic case (the excitation energy is lower than the gap) the condition for the thermalization on the long distances is not fulfilled. Therefore, another process has to be assumed for this type of photogeneration, e.g., a slow gradual occupation of the adjacent CT states with longer radii. This process results in a decrease of the primary quantum yield from 0.11 to 0.04.

Conclusions

The Onsager model is adequate for an explanation of experimental electric field dependences of the quantum photogeneration efficiency. The same values of the primary quantum yield and shorter separation distances of electron-hole pairs in crystalline material

EBSCOhost - printed on 2/13/2023 3:45 AM via . All use subject to https://www.ebsco.com/terms-of-use

both for intrinsic and extrinsic photogeneration process suggest the lower efficiency of charge carrier photogeneration at low electric fields. Here, the direct charge carrier precursors are not the nearest-neighbour states, but states with a diameter of about 2.5 nm (in the low field approximation) which are formed by carbazole units over one chain.

References

1. Pfister, G., D.J.Williams. 1974. J.Chem.Phys. 61, 2416.
2. Borsenberger, P.M., A.I.Ateya. 1978. J.Appl.Phys. 49, 4035.
3. Daniewska, I., B.Klein-Szymanska, A.Wasiak. 1982. Polymer 23, 1842.
4. Mort, J., I.Chen. 1975. In: Applied Solid State Science. Academic Press, New York. p. 77.
5. Chen, I., J.Mort, M.D.Tabak. 1972. IEEE Trans. ED-19, 413.
6. Nešpůrek, S., K.Ulbert. 1975. Čs.čas.fyz. 25A, 144.
7. Onsager, L. 1938. Phys.Rev. 54, 554.
8. Mozumder, A. 1974. J.Chem.Phys. 60, 4300.
9. Noolandi, J., K.H.Hong. 1979. J.Chem.Phys. 70, 3230.
10. Griffiths, C.H. 1975. J.Polym.Sci. 13, 1167.

EBSCOhost - printed on 2/13/2023 3:45 AM via . All use subject to https://www.ebsco.com/terms-of-use

CHARGE TRANSPORT IN THIN FILMS OF POLYVINYLCARBAZOLE N-VINYLCARBAZOLE

I. Chudáček

Department of Polymer Physics, Charles University, V Holešovičkách 2, Praha 180 00, Czechoslovakia

G. Naumenko

Faculty of Physics, State University Saratov, USSR

J. Urban

Institute of Macromolecular Chemistry, Czechoslovak Academy of Sciences, Praha 160 00, Czechoslovakia

Introduction

The drift mobility μ_D of charge carriers is a quantity which best characterizes the transport of carriers. In polymeric systems the value of μ_D is very low in comparison with ordered systems. Of big impact on charge transport was the idea that continuous time random walk treatement of Scher and Montroll (1) can be applied to disordered polymeric systems. But recent work by Pfister and Griffith (2) on polyvinylcarbazole (PVCa) showed considerable temperature dependence in the dispersion of the hole transport not expected by CTRW model. Tahmasbi et al. (3) showed that the hole transport in PVCa is trap-controlled and Tiedje and Rose (4) demonstrated that an exponential distribution of trap levels gives also observed dispersion. Marshall (5) argues that the dispersion given by spatial disorder alone should vanish after a time of carrying through a macroscopic sample. The aim of this contribution is to find what is the influence of monomer doping on carrier mobility. The change in the concentration of traps or the creation of new types of traps in our system occurs with the enhancement of the concentration of N - vinylcarbazole molecules (NVCa). In this way it is possible to study the role of traps in the charge car-

Morphology of Polymers
© 1986 Walter de Gruyter & Co., Berlin · New York - Printed in Germany.

EBSCOhost - printed on 2/13/2023 3:45 AM via . All use subject to https://www.ebsco.com/terms-of-use

riers transport.

Experimental

In present work we utilize for PVCa the product of BASF Luvican M170, which was three times precipitated in metanol. The mean molecular mass is $\overline{M}_w = 1.6 \times 10^6$. The low molecular NVCa was added to the polymer in pulver form. The homogenized mixture was dissolved in solution of toluene : cyclohexane = 4 : 1 and it was applied on metalic sheet after perfect dissolution. After drying the samples were covered with a thin layer of gold by vacuum evaporation.

The thickness of PVCa : NVCa layers was measured by Talystep (USA) with an error of 1 - 2%.

The measurement of dielectric properties and of the transit time was accomplished in vacuum 10^{-2} - 10^{-3} Torr in a metalic home-made cryostat. The measurement of the permitivity was done by the Tesla bridge BM - 484 at 1.592 kHz with an error lower than 5%.

The charge carrier mobility was determined by the measurement of the time of flight, t_F, between the electrodes. Packets of photoholes were generated under the gold semitransparent electrode by electric spark discharge in air. The time duration of photogeneration pulses was 1 - $3x10^{-7}$ s and it was smaller than t_F.

The number of photogenerated holes was so small that the charge of electric field topology did not occur. The measurement was performed in the regime of constant electric field. In this case the load resistance R on which we measure in the screen of a memory osciloscope the voltage response U_R (t), is substantially smaller than the sample resistance in the dark, r_D, minus the photoinduced change in the sample resistance, Δr_{ph} ($R \ll r_D - \Delta r_{ph}$). For sample of thickness d and area S we obtain for the photoconductivity the equation:

$$\sigma_{ph} = \frac{U_R(t)\, d}{U_o\, RS}$$

where $U_o \neq U_o(t)$ is the voltage across the sample. Under these conditions between t_F and drift mobility of holes, μ_D, is ful-

EBSCOhost - printed on 2/13/2023 3:45 AM via . All use subject to https://www.ebsco.com/terms-of-use

filled the relation

$$\mu_D = \frac{d^2}{t_F U_o}$$

which shows the importance of the thickness. Five types of samples with different NVCa concentrations were prepared. The parameters of the samples are in Table 1.

Table 1. Parameters of Samples

Sample No	NVCa concentration (weight ratio)	(%)	Thickness (μm)
0	0 : 1	0	5.7
1	1 : 8	11	8.3
2	1 : 2	33	-
3	1 : 1	100	8.5
4	2 : 1	200	8.5

Experimental Results

We have measured the temperature dependence of the real and imaginary parts ε' and ε'' of the permitivity at the frequency of 10 kHz. The results are shown in Figs. 1 and 2, respectively. Therefore, it follows that samples 1, 2 and 3 have similar behaviour comparable with that of the pure polymer. The sample 4 with 200% concentration of NVCa has another course: ε' and ε'' have peaks at the same temperature, $\varepsilon''_4(T)$ does not link to $\varepsilon''_{1,2,3}(T)$. We have calculated temperature dependences of the drift mobility $\mu_D(T)$ and photoconductivity σ_F at the transit time t_F. From these two values it is possible to determine the concentration of holes, p_F, coming to the opposite electrode at the transit time

$$\sigma_F = e \mu_D p_F$$

In Fig. 3 we show the typical temperature dependence at NVCa concentration of 30% for μ_D, σ_F and p_F. We can see

EBSCOhost - printed on 2/13/2023 3:45 AM via . All use subject to https://www.ebsco.com/terms-of-use

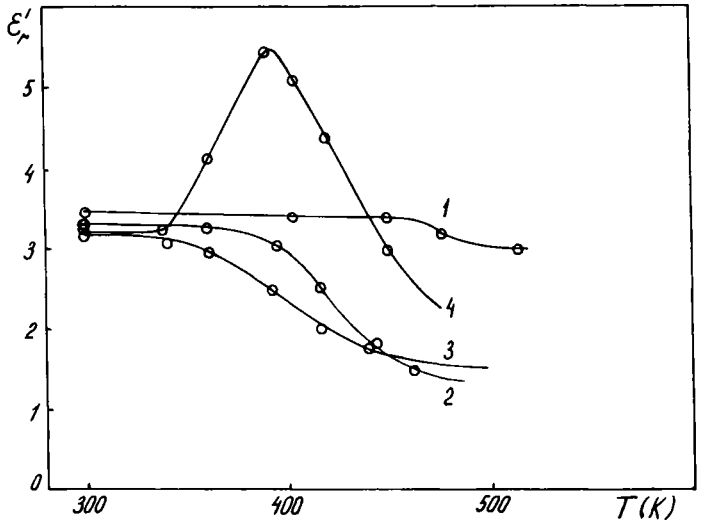

Figure 1. The temperature dependence of ε' .

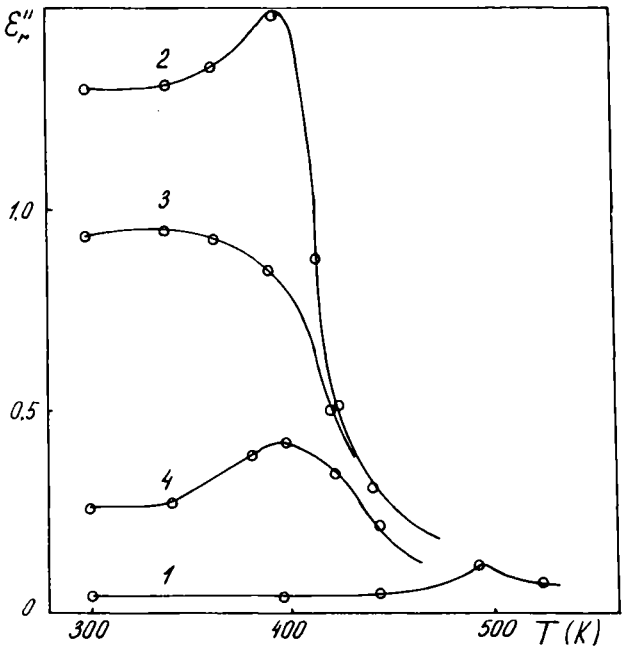

Figure 2. The temperature dependence of ε'' .

EBSCOhost - printed on 2/13/2023 3:45 AM via . All use subject to https://www.ebsco.com/terms-of-use

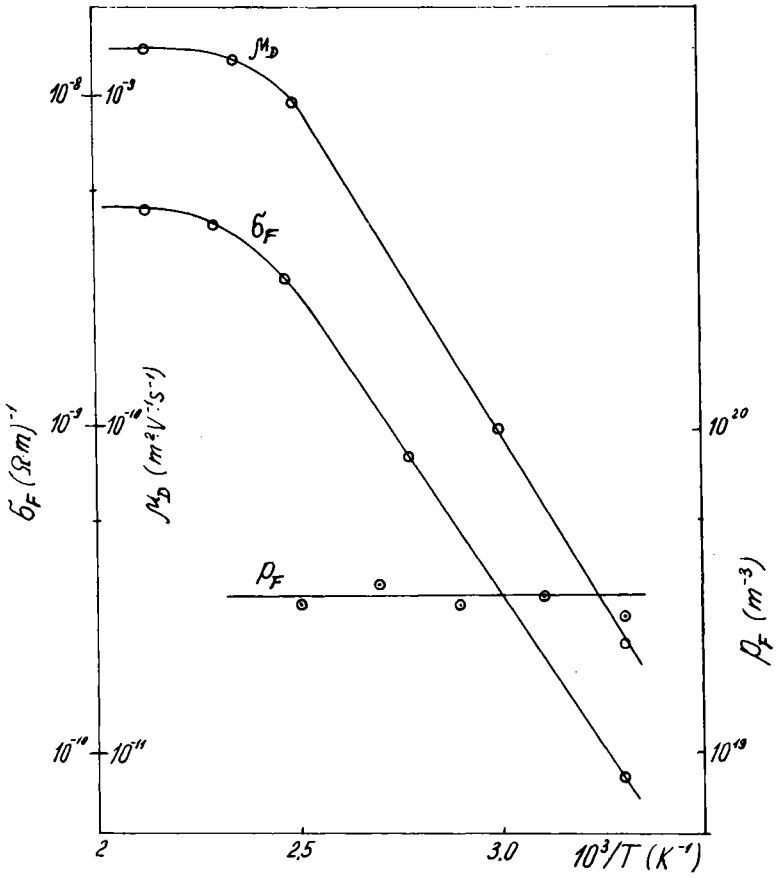

Figure 3: Typical temperature dependence of μ_D, σ_F and p_F for 30% NVCa.

that μ_D and σ_F have similar temperature dependence and p_F is temperature independent.
In Figs. 4 and 5 the measured dependences of σ_F and μ_D on NVCa concentration for different temperatures are illustrated. The experimental points are connected for better comprehension of the results.

Discussion

We have carefully measured the dependence of μ_D on the elect-

EBSCOhost - printed on 2/13/2023 3:45 AM via . All use subject to https://www.ebsco.com/terms-of-use

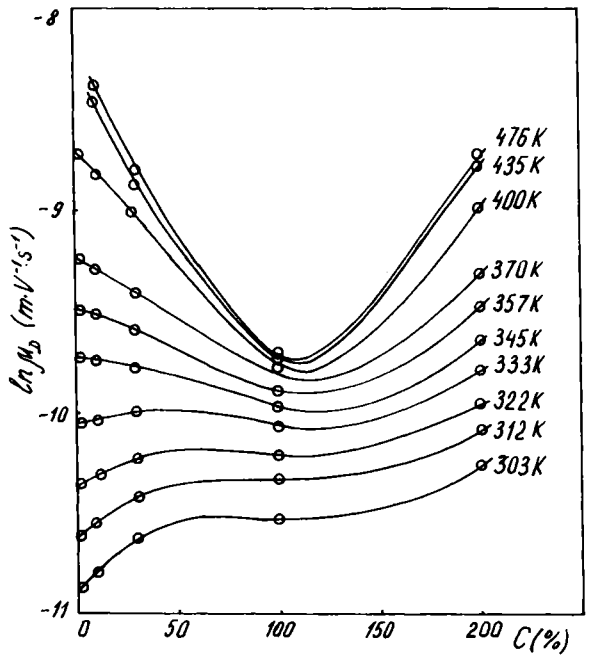

Figure 4. Dependences of μ_D on NVCa concentration for different temperatures.

ric field intensity E at room temperature. In Fig. 6 we have plotted ln μ_D versus $\sqrt{E}$. One can see that this dependence is linear and for this reason it seems that the charge carriers transport in PVCa - NVCa system is governed by traps.

When we add VCa molecules at any temperature enhancement of the photoconductivity (see Fig. 5) occurs. We interpret this so that the number of traps falls and the traps in pure PVCa are of such a type that NVCa annihilate them. Since low molecular NVCa preferentially diffuses into the empty volume, the original traps in PVCa are connected with it. Between 10% and 30% the filling of these traps occurs (see Fig. 5), because at 30% the photoconductivity is lower than that at 10%.

If we assume that the bundle model is suitable for PVCa, it is possible to accept the hypothesis that the traps are the interfaces between bundles where occurs the change in compression of the structure, which produces a change in polarization

EBSCOhost - printed on 2/13/2023 3:45 AM via . All use subject to https://www.ebsco.com/terms-of-use

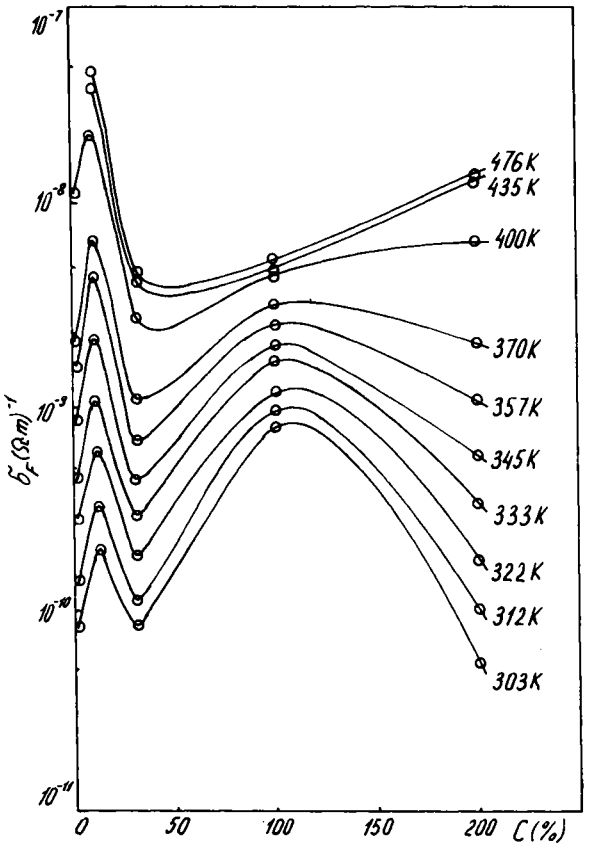

Figure 5. Dependences of σ_F on NVCa concentration for different temperatures.

energy. In many materials it was theoretically and experimentally demonstrated (8, 9) that the change in polarization energy leads to the creation of traps for charge carriers. In Fig. 7 we show a photograph from electron microscope (with a magnification of 45000x) of a rupture surface. One can see a fibre structure with the diameter of the order of 70 nm. We shall calculate the ratio of the volume occupied by a bundle to the volume between bundles. In the case of cubic or hexagonal arrangement of bundles we obtain 0.21% and 0.10%, respectively. The drift mobility with NVCa concentration also rises for low temperatures up to 330 K. This is in connection with the fact that the mean distance R between nearest Ca groups diminishes

EBSCOhost - printed on 2/13/2023 3:45 AM via . All use subject to https://www.ebsco.com/terms-of-use

with temperature, too.

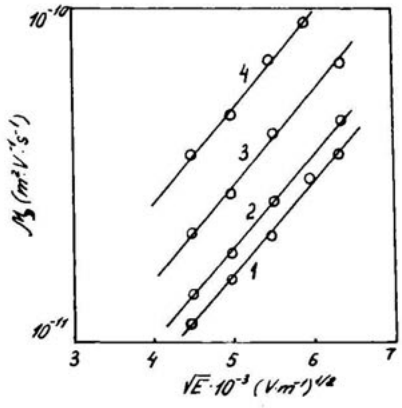

Figure 6. The dependence of μ_D on the electric field intensity E.

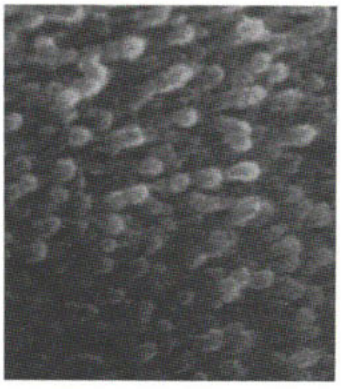

Figure 7. Photograph of a rupture surface of PVCa. Magnification 45000x.

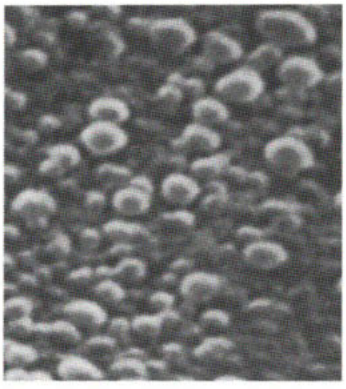

Figure 8. Photograph of a rupture surface of PVCa : NVCa = 1 : 2. Magnification 45000x.

In hopping mechanism of charge transport the following relation is known

$$\mu_D \approx R^2 \exp(-R^2 / R_o)$$

where R_o is the delocalization radius of the hopping charge. At higher temperatures VCa molecules between PVCa bundles act

EBSCOhost - printed on 2/13/2023 3:45 AM via . All use subject to https://www.ebsco.com/terms-of-use

as hole gas, which can diminish the delocalization radius R_o and enhance the hopping distance R as a consequence of large thermal motions of the bundles.

After the next enhancement of NVCa concentration the photoconductivity falls. We suppose that it is in connection with the creation of NVCa pairs or small clusters. They are the principal kinetic units which produce the main absorption of electromagnetic energy (see Fig. 2).

At higher VCa concentrations the photoconductivity grows, temperature and drift mobility falls. The structure of the samples becomes homogeneous and for this reason vanishes the interface of structural compressions followed by the diminution of the number of traps. The photoconductivity rises. On the other hand, the distance between the nearest Ca groups grows, which leads to the fall in the carriers mobility.

For free NVCa concentrations higher than the concentration of Ca groups in polymeric chains the crystalline state arises (see Fig. 8). In this case a straight interface between amorphous and crystalline state is created which produces a new type of traps (9). For this reason the photoconductivity falls. The drift mobility for all temperatures grows, because we have an ordered structure with small hopping distance R between transport groups in the crystalline state.

In conclusion we can say that the charge carrier transport in the system PVCa - NVCa is governed by different types of traps. These traps are closely connected with the suprastructure of the system.

References

1. Sher, H., E. W. Montroll, 1975. Phys. Rev. B12, 56.
2. Pfister, G., C. H. Griffith. 1978. Phys. Rev. Lett., 40, 659.
3. Tahmasbi A. R., J. Hirsch, J. Z. Koledowicz. 1978. Solid State Commun. 29 , 847.
4. Tiedje, T., A. Rose. 1981. Solid State Commun., 37, 49.
5. Marshall J., 1983. Phil. Mag., B 47, 323.
6. Bässler H.,1984. Phil. Mag., B 50, 9.
7. Pechhold W. E. W. Sautter, v. Soden, P. H. Grossmann, B. Stoll

EBSCOhost - printed on 2/13/2023 3:45 AM via . All use subject to https://www.ebsco.com/terms-of-use

1979. Macromol. Chem. Suppl., 3, 247.
8. Silinsch, E. A., 1980. Organic Molecular Crystals. Their Electronic States, Springer Verlag. Berlin.
9. Nešpůrek S., D. Slavínská, M. Šorm. 1981. Czech. J. Phys. B 31, 1144.

EBSCOhost - printed on 2/13/2023 3:45 AM via . All use subject to https://www.ebsco.com/terms-of-use

THE INFLUENCE OF PHYSICAL STRUCTURE ON THE POLARIZATION CURRENTS IN POLY(ETHYLENE TEREPHTHALATE)

K.-L. Voß, W. Neumann, H. Hänsel
Pedagogical University "Karl Liebknecht", Am Neuen Palais,
1500 Potsdam, DDR

Introduction

Usually, the production and application of polymer foils is combined with stretching and annealing processes. A change in d.c.conductivity and charge carrier mobility is caused by such preparation for instance (1,2). But it is also interesting to know how can be changed the dielectric properties by these processes. The electric polarization was investigated in poly(ethylene terephthalate) (PETP) in dependence on crystallinity and birefringence because annealing and stretching processes change these parameters (3).

Methods used for varying the polymer structure

Isothermal and thermally stimulated depolarization currents were observed in poly(ethylene terephthalate). The equipment used is described in detail in ref.(4). The foils were X-ray amorphous and unstretched at the beginning of the investigations. Isothermal crystallization and stretching in one direction were used to modify the structure of the samples. The main crystallization process is finished when the foils are annealed for 10 min at 140°C (5). The orientation of the samples was regulated by stretching the foils in ethylene glycol. The annealing temperature ϑ_T, the annealing time t_T, the ratio l of the lengths of the samples after and before stretching, the birefringence Δn, and the degree of crystallinity, α, are shown in Table 1.

Morphology of Polymers
© 1986 Walter de Gruyter & Co., Berlin · New York - Printed in Germany.

EBSCOhost - printed on 2/13/2023 3:45 AM via . All use subject to https://www.ebsco.com/terms-of-use

Table 1. Some Characteristics of the Foil Samples

Structure	ϑ_T, °C	t_T, min	l	$\Delta n \times 10^3$	α
A	-	-	1	<1	0
B	140	10	1	<1	0.27
C	140	10	4	153	0.28
D	76	1	5.5	153	0.18

Δn was measured using a polarization microscope; α was estimated from the density of the samples. It was very difficult to prepare an oriented foil having a low degree of crystallinity. This was only possible at low temperatures (see Table 1) using the low crystallization velocities in this temperature region. The stretch velocity was 800 %/min for all foils. In this way foils B and C were stretched in the plastic deformation region (6), whereas sample D was stretched in the region of forced elasticity. At temperatures below 67°C the stretch of the samples causes cracks in the foils. Furthermore, we get not the same structure, when first we stretch the sample and after this the annealing process takes place or vice versa.

Isothermal depolarization currents

The isothermal depolarization currents were measured in the ohmic region of the electric field strength E. The log I vs. log t plots are linear in sections for all samples measured. The charge Q was estimated from the current-time curves. If the polarization time and the time of depolarization are sufficiently long it is advantageous to use the Q values for characterizing the experimental results. In this case Q depends on the temperature only. Figure 1 shows the log Q vs. 1/T plot for four structures of the samples. The measurements were done with increasing temperatures.

EBSCOhost - printed on 2/13/2023 3:45 AM via . All use subject to https://www.ebsco.com/terms-of-use

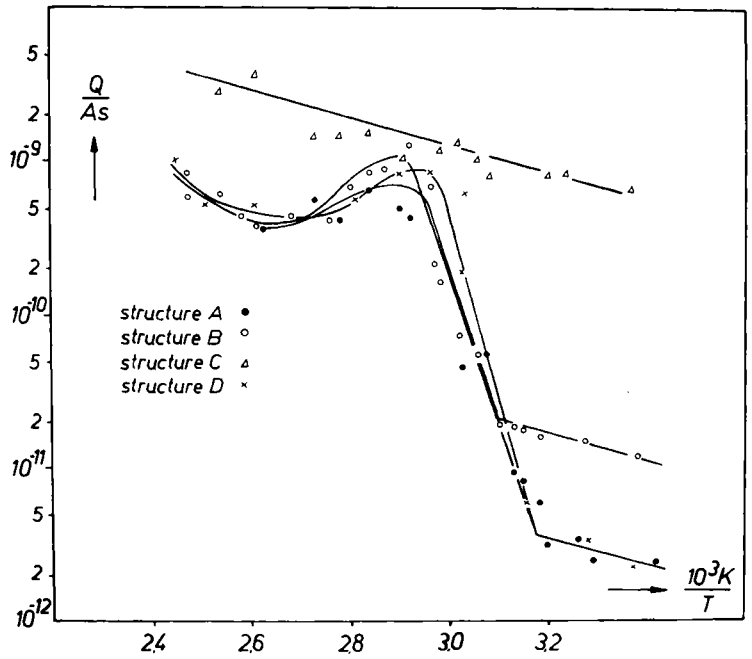

Fig. 1. Storage charge versus temperature (measured by isothermal depolarization method).

As can be seen from Fig. 1, the storage charge for structure C is about two orders of magnitude greater at temperatures below 40°C than for the other structures. Furthermore, Q increases relatively slowly with temperature over the whole temperature region. Contrary to this, Q increases drastically in the other structures for temperatures above 40°C. Moreover, the storage charge Q is approximately the same for all structures at the glass transition temperature T_g (about 75°C). It was shown by infrared absorption measurements (7,8,9) that both isothermal crystallization and stress cause an increase in the trans-contents and a decrease in the gauche-contents in the monomers. Thereby the increase in the trans-contents takes place predominantly in the crystalline regions. Connection should be expected between these changes of conformation and the measurements of the depolarization currents. Consequently, long-time annealing used

EBSCOhost - printed on 2/13/2023 3:45 AM via . All use subject to https://www.ebsco.com/terms-of-use

for the measurements, shown in Figure 1, changes the polarization properties of the sample C at temperatures below 40°C. The results obtained suggest that the spherulites become oriented through the formation of the crystalline-oriented structure C.

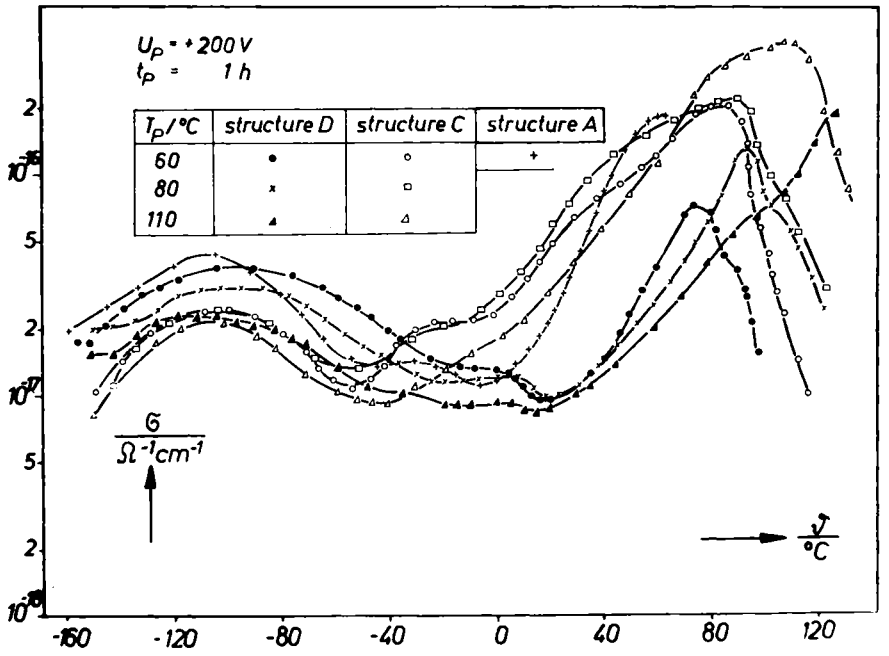

Fig. 2. TSD - measurements (parameter T_P).

Thermostimulated depolarization currents (TSD)

Figure 2 shows thermostimulated depolarization currents for the foil structures A, C and D at different polarization temperatures. The conductivity $\sigma = j/E$ was used instead of the current density because of the varying sample thickness. All structures show a distinct β- and α- maximum. The β- maximum is nearly identical for all structures. Contrary to this, the storage

EBSCOhost - printed on 2/13/2023 3:45 AM via . All use subject to https://www.ebsco.com/terms-of-use

charge estimated from the α- maximum is dependent on the structure. Figure 3 A shows the dependence of the magnitude of the α - maximum on the polarization temperature. This is in agreement with the results shown in Figure 1. Figure 3 B shows the magnitude of the α - maximum as a function of the polarization time t_p. It can be seen that very high time constants appear for the structures A, B and C. Figure 4 shows TSD-measurements for one and the same sample. The first measurement was done with the structure D. After this, the sample was annealed at 110°C and for 10 min at 140°C. Then the other measurements was carried out. Obviously, the crystalline-oriented structure C cannot be obtained in this way.

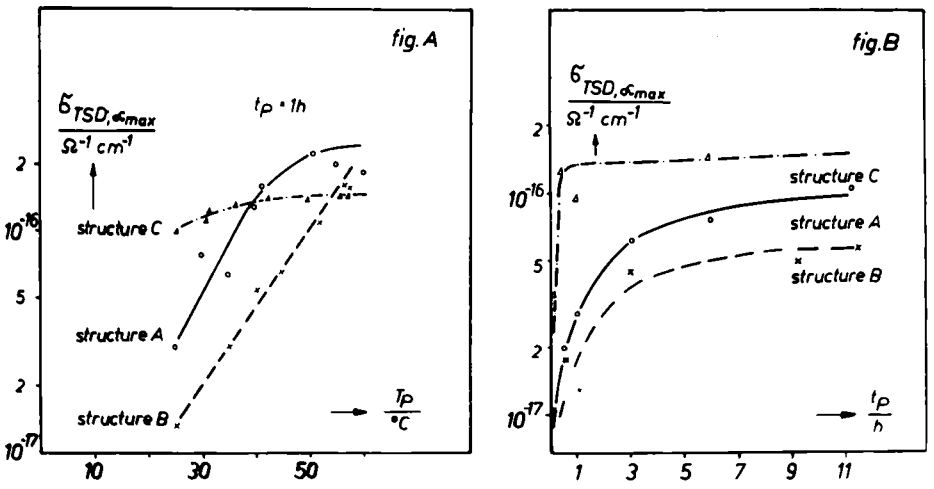

Fig. 3. $\sigma_{TSD,\alpha}$ plotted versus T_p and t_p ($\sigma_{TSD,\alpha}$ corresponds to the α - maximum of the TSD-curve).

EBSCOhost - printed on 2/13/2023 3:45 AM via . All use subject to https://www.ebsco.com/terms-of-use

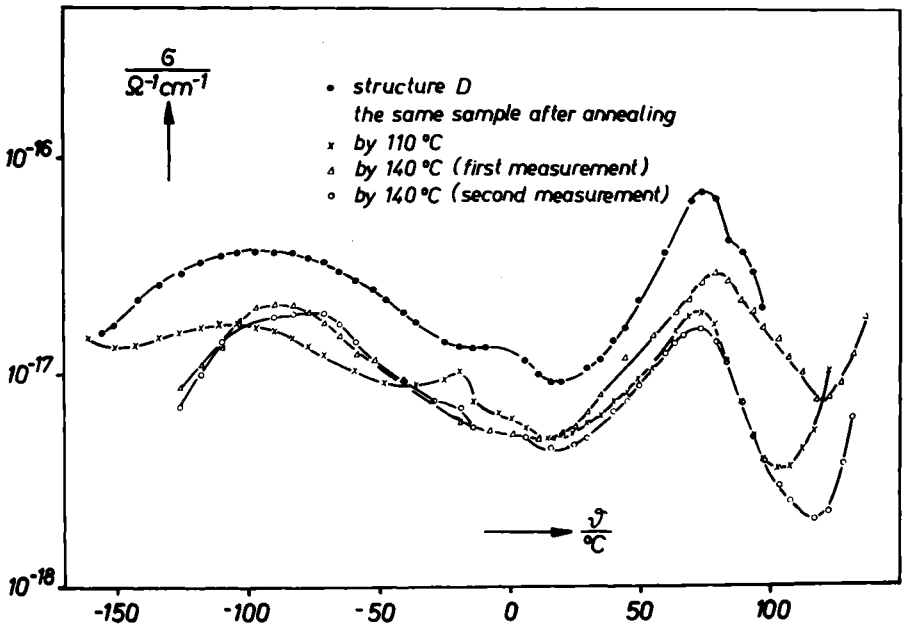

Fig. 4. TSD - measurements (parameters T_p=60°C and t_p=1h).

Conclusions

The depolarization currents in poly(ethylene terephthalate) are **influenced by the physical structure. Measurements of the isothermal and thermally stimulated depolarization give the same results. The storage charge for the isothermally crystallized and simultaneously stretched foil is greater at temperatures below T_g than for amorphous or unstretched structures, and does not depend much on temperature. The differences of the storage charge were observed only in the α - region.**

EBSCOhost - printed on 2/13/2023 3:45 AM via . All use subject to https://www.ebsco.com/terms-of-use

References

1. Stroloke, W., W. Neumann, H. Hänsel. 1982. Polymer Bull. 8, 527.
2. Hanspach, J., H. Hänsel, M. Kryszewski, R. Gaulke. 1985. Acta Polymerica 36, 234.
3. Schick, C., L. Krämer, W. Mischok. 1985. Acta Polymerica 36, 47.
4. Frübing, P.. 1978. Thesis A, Ped. Univ. Potsdam.
5. Gaulke, R.. 1982. Thesis A, Ped. Univ. Potsdam.
6. Vlasov, S.V., V.N. Kuleznev. 1983. Vysokomol. Soed. A 25, 2357.
7. Rietsch, F., B. Jasse. 1984. Polym. Bull. 11, 287.
8. Baranova, S.A., S.A. Gribanov, B.N. Kljusnik, P.M. Pachomov, M.V. Sablygin. 1980. Vysokomol. Soed., Serija A 22, 536.
9. Baranova, S.A., S.A. Gribanov, B.N. Kljusnik, P.M. Pachomov, V.E. Geller, M.V. Sablygin. 1983. Vysokomol. Soed. A 25, 290.

EBSCOhost - printed on 2/13/2023 3:45 AM via . All use subject to https://www.ebsco.com/terms-of-use

EBSCOhost - printed on 2/13/2023 3:45 AM via . All use subject to https://www.ebsco.com/terms-of-use

PROBLEMS IN QUANTITATIVE TEXTURE INVESTIGATIONS OF POLYMERS AND AVERAGED PHYSICAL PROPERTIES

J. Ganster, D. Geiss

Academy of Sciences of the GDR
Institute of Polymer Chemistry "Erich Correns"
1530 Teltow-Seehof, Kantstraße 55,
German Democratic Republic

1. Introduction

Semicrystalline polymeric materials contain anisotropic constituent parts (crystallites), which, in general, cause anisotropic sample properties, if the crystallites are non randomly distributed, i.e. certain crystallite orientations are preferred. This fact is referred to as texture.
An analytical description of the texture is provided by the orientation distribution function (ODF) of the crystalline phase (sec. 2), which can be calculated from X-ray or neutron diffraction experiments (1, 2).
The first determination of this function for a non-axially symmetrical sample was done by Krigbaum et al. for biaxially oriented polyethylene (3). A recently published ODF for polyethylene terephthalate can be in ref. (4).
The ODF can be used to average anisotropical crystallite properties and thus to predict macroscopical properties of the sample. Of course, this is a drastic simplification of the complex morphological problem (5) (shape of crystallites, tie molecules, preferred orientation in amorphous regions), but a welldefined and complete description of one aspect and thus a first step towards a quantification of anisotropic material behaviour.
In this paper we study how far a certain lack of information in the ODF (6, 7), occurring in 10 crystal classes due to experimental conditions, exerts influence on the average of anisotropical properties in the simple average approximation (ODF-average).

Morphology of Polymers
© 1986 Walter de Gruyter & Co., Berlin · New York - Printed in Germany.

EBSCOhost - printed on 2/13/2023 3:45 AM via . All use subject to https://www.ebsco.com/terms-of-use

2. The Orientation Distribution Function of the Crystalline Phase

For defining the orientation distribution function (ODF) (1) we fix a coordinate system $K_B(x)$ (x-position in the sample) in an identical way to each of the N unit cells in the crystalline regions. The orientation of $K_B(x)$ towards a coordinate system K_A fixed to the sample is expressed by a rotation g(x), usually parametrized by the Eulerian angles. The ODF f(g) is then given by the probability density with which a unit cell of orientation g is found in the sample, i.e. $N \cdot f(g)dg$ is the number of unit cells having an orientation between g and g+dg.
Obviously the position x does not appear in this function and therefore neither the shape and dimensions, nor the mutual arrangement of crystallites are covered by f(g). Assuming equal (or similar) shape and dimensions of all crystallites, f(g) becomes also the corresponding probability density of crystallite orientation.
In case of polymers it is useful not to choose the unit cell or the crystallite as the structural unit, but a certain "unit element" comprising both crystalline and amorphous material (8). For equal unit elements the ODF will represent their orientation. Again, the linkage of the elements is not reflected by the ODF (provided they are not linked with crystall bridges (5) large enough to be detected by the X-rays or neutrons).
In the calculations presented in sections 5 and 6, f(g) can be understood as the orientation probability density of any structural unit, but it has to be obtained experimentally. The almost exclusively used experiment -pole figure measurement- provides the unit cell ODF and we shall use the term ODF (f(g)) in this sense.

3. Pole Figures for Reproducing the ODF of Polymers

There is no simple experiment allowing the ODF to be measured in a direct manner with reasonable accuracy. One is thrown upon the so-called pole figures, certain integrals of the ODF, which depend on only two angular variables, whereas the ODF itself depends on three angles (sec. 2). One of the central tasks of the

EBSCOhost - printed on 2/13/2023 3:45 AM via . All use subject to https://www.ebsco.com/terms-of-use

classical quantitative texture analysis consists in reproducing the ODF from experimental pole figures (1). Until the late seventies this problem had been thought to be solved, but a reinvestigation started in connection with "ghost phenomena" (see below) (9). Experimental pole figures are obtained by X-ray or neutron diffraction with Bragg angle θ fixed and the position of the sample towards the goniometer being variable. In such a way the whole solid angle range is scanned and the orientation distribution of a certain set of net planes in recorded. The fixed θ selects all those net planes whose net plane distance d is equal to $\lambda/(2\sin\theta)$, according to Bragg's law (λ -wave length of the radiation). From these, all the planes having their normals parallel to a given direction scatter in the same direction so that the intensity per solid angle gives the orientation distribution of the net plane normals. Orientations perpendicular to the normals are not differentiated and more than one pole figure (the lower the crystal symmetry, the more) are necessary to construct the complete ODF.

Besides, specific problems for polymers arise from semicrystalline structure, small crystallite size and imperfection of crystal lattice. One is faced with difficulties in substracting the amorphous contribution from the scattered intensity. Owing to broad and overlapping reflexes as well as accidental coincidences the number of utilizable pole figures decreases. Accidental coincidences (due to unit cell dimensions) occur if inequivalent sets of net planes have similar Bragg angles, since in this case the intensity of all these planes is detected simultaneously. More important are the intrinsic coincidences produced by physically different sets of net planes having exactly the same θ due to crystal symmetry. They cause a considerable loss of information in the experimental pole figures, which has intensively been investigated (6, 7). Only the "even" part of the ODF can always be reconstructed unambiguously (ghost phenomena). The "even" ("odd") part means the components of f(g) with even (odd) l in the expansion of the ODF in generalized spherical harmonics $D_{mn}^{(l)}(g)$:

$$f(g) = \sum_{l=0}^{\infty} \sum_{m,n=-l}^{l} C_l^{mn} \, D_{mn}^{(l)}(g) \qquad (1)$$

EBSCOhost - printed on 2/13/2023 3:45 AM via . All use subject to https://www.ebsco.com/terms-of-use

Whereas for the crystal classes C_s, C_{2v}, S_4, C_{4v}, D_{2d}, C_{3v}, C_{3h}, C_{6v}, D_{3h} and T_d the "odd" part of the ODF cannot be obtained, this is possible for the remaining 22 classes but only with additional (quite natural) assumptions. The consequences of this loss of information will be studied in section 5 after the introduction of simple averages for physical properties.

4. The Simple Average Approximation for Physical Properties

A polycrystalline (semicrystalline) material can have, in principle, all the physical properties shown by a single crystal. By physical property we mean any material-dependent relation between two measurable physical quantities (10), for instance strain and stress related by mechanical compliance.
We write in a general form (1) the local relation

$$Y(x) = E(x)\ X(x) \qquad (2)$$

where x is again the position in the sample, X and Y are the measurable quantities (tensors of appropriate rank) and E is the corresponding property (a tensor of rank r = rankX + rankY). An effective material property $\langle E \rangle$ would be the tensor relating $\overline{X}$ and $\overline{Y}$ with

$$\overline{Y} = \langle E \rangle\ \overline{X}$$

and

$$\overline{X} = \frac{1}{V} \int X(x)\ d^3x\ , \quad \overline{Y} = \frac{1}{V} \int Y(x)\ d^3x$$

$\overline{E}$ is defined analogically. Now we split X(x), Y(x) and E(x) into volume average and fluctuation

$$X(x) = \overline{X} + \Delta X(x), \quad Y(x) = \overline{Y} + \Delta Y(x), \quad E(x) = \overline{E} + \Delta E(x)$$

and average (2) ($\overline{\Delta X(x)} = \overline{\Delta Y(x)} = \overline{\Delta E(x)} = 0$)

$$\overline{Y} = \overline{E}\ \overline{X} + \frac{1}{V} \int \Delta E(x)\ \Delta X(x)\ d^3x$$

$\overline{E}$ is now taken as an approximation for $\langle E \rangle$, the so-called simple average approximation, not taking into account the detailed field X(x), i.e. the boundary conditions.

EBSCOhost - printed on 2/13/2023 3:45 AM via . All use subject to https://www.ebsco.com/terms-of-use

E(x) will be different in amorphous ($E^a(x)$) and crystalline ($E^c(x)$) regions:

$$\bar{E} = \frac{1}{V} \int_{am} E^a(x)\, d^3x + \frac{1}{V} \int_{cryst} E^c(x)\, d^3x$$

For completely amorphous (= isotropic) regions $E^a(x)=E^a=$const. is valid. For the single crystal, E^c is a constant tensor and the position dependence reduces to an orientation dependence (anisotropy). Using the ODF and the crystallinity $\varphi = V^{cryst}/V$ we thus have for the second integral

$$\bar{E}^c = \varphi \int f(g)\, E^c(g)\, dg \qquad (3)$$

In the unit-element-model mentioned in sec. 2, $\bar{E}$ becomes

$$\bar{E} = \int f(g)\, E^{a,c}(g)\, dg$$

with $E^{a,c}(g)$ as the unit element property composed of amorphous and crystalline contributions.
The question if integrals of type (3) can be evaluated despite the loss of information, discussed in section 3, will be answered in the following sections.

5. Simple Average and Loss of Information

The tensor property of E^c (r-th rank) means that the components $E^c_{i_1 i_2 \ldots i_r}$ obey the following transformation law (sum convention for tensor indices)

$$E^c_{i_1 \ldots i_r}(g) = T_{i_1 j_1}(g) \ldots T_{i_r j_r}(g)\, E^c_{j_1 \ldots j_r} \qquad (4)$$

$E^c_{i_1 \ldots i_r}$ and $E^c_{i_1 \ldots i_r}(g)$ are the components of E^c in K_B and K_A, respectively (see sec. 2). T(g) is the orthogonal rotation matrix, transforming K_B into K_A.
Inserting (4) and (1) into (3) we find

$$\bar{E}^c_{i_1 \ldots i_r} = \sum_{l=0}^{\infty} \sum_{m,n=-l}^{l} C_l^{mn} \int T_{i_1 j_1}(g) \ldots T_{i_r j_r}(g)\, D^{(l)}_{mn}(g)\, dg\, E^c_{j_1 \ldots j_r} \qquad (5)$$

EBSCOhost - printed on 2/13/2023 3:45 AM via . All use subject to https://www.ebsco.com/terms-of-use

In order to simplify this expression we will utilize some results of group theory (11). Formula (4) can be interpreted as a tensor representation of the rotation group, which is decomposable into irreducible parts. In other words, the products of $T_{ij}(g)$ can be expressed linearly by the (complex conjugated) harmonics $D^{(l)*}_{mn}(g)$ with $l \leq r$.

Taking into account the orthogonality of the $D^{(l)}_{mn}(g)$

$$\int D^{(l)}_{mn}(g)\, D^{(l')*}_{m'n'}(g)\, dg = \frac{1}{2l+1}\, \delta_{ll'}\, \delta_{mn'}\, \delta_{nn'} \qquad (6)$$

we see that the sum in (5) becomes finite with $l \leq r$. Beyond that, the tensors of physical properties often possess intrinsic symmetries (12) concerning the permutation of indices (e.g. dielectric constant ε: $\varepsilon_{ij} = \varepsilon_{ji}$). These symmetries form a group P of, say, N_P elements, so that (4) can be considered to be the "symmetrized power" of the tensor representation on P-invariant tensors (11). In the following it will be demonstrated how to find out which $D^{(l)*}_{mn}(g)$ further drop out in the decomposition of $T_{i_1 j_1}(g) \ldots T_{i_r j_r}(g)$ and hence which C^{mn}_{l} occur in (5) (cf. (6)).

The character $\chi_o(g)$ of our representation is given by (for $\chi^{(1)}(g)$ see below)

$$\chi_o(g) = \frac{1}{N_P} \sum_{p \in P} \chi^{(1)}(g^{q_1})\ \chi^{(1)}(g^{q_2}) \ldots \chi^{(1)}(g^{q_\sigma}) \qquad (7)$$

where $q_1, \ldots, q_\sigma$ are the lengths of the cycles of $p \in P$. (Every permutation can be ordered in σ cycles, where the q_i objects within the i-th cycle transform among each other ($q_1 + \ldots + q_\sigma = r$). For an example see sec. 6.

On the other hand, the (equivalent) decomposed form of our representation yields

$$\chi_o(g) = \sum_{l=0}^{r} \mu_l\ \chi^{(l)}(g) \qquad (8)$$

with unknown μ_l and the characters $\chi^{(l)}(g)$ of the unitary irreducible representations of the rotation group

$$\chi^{(l)}(g) = \sum_{m=-l}^{l} D^{(l)}_{mm}(g) = \frac{\sin((l+1/2)\alpha)}{\sin(\alpha/2)} \qquad (9)$$

α is simply the rotation angle of the rotation g. For all l, $\chi^{(l)}(g)$ is a polynomial in $\cos\alpha$, especially for l = 1

EBSCOhost - printed on 2/13/2023 3:45 AM via . All use subject to https://www.ebsco.com/terms-of-use

we have from (9) $\chi^{(1)}(g) = 1 + 2\cos\alpha$. Therefore, successively comparing the powers of $\cos\alpha$ in (7) and (8) one obtains the unknown μ_l (starting with $l = r$), i.e. the frequencies how often $D^{(l)*}_{mn}(g)$ occur in the decomposition of $T_{i_1 j_1}(g) \ldots T_{i_r j_r}(g)$. If $\mu_l = 0$ for a given l, the corresponding texture component C^{mn}_l does not influence the average (5). This is almost trivially the case for all $l > r$, but nontrivially for some $l \leq r$ depending on r and P. The example in the next section will illustrate the general method outlined above.

6. Mechanical Properties as an Example

The tensor of mechanical compliance S_{ijkh} (or stiffness C_{ijkh}) possesses the symmetries $S_{ijkh}=S_{jikh}=S_{ijhk}=S_{khij}$ (12). From these permutations, $N_p=8$ elements of the whole symmetry group P are generated:

$$P = \left\{\begin{pmatrix} ijkh \\ ijkh \end{pmatrix}, \begin{pmatrix} ijkh \\ jikh \end{pmatrix}, \begin{pmatrix} ijkh \\ ijhk \end{pmatrix}, \begin{pmatrix} ijkh \\ khij \end{pmatrix}, \begin{pmatrix} ijkh \\ jihk \end{pmatrix}, \begin{pmatrix} ijkh \\ hkji \end{pmatrix}, \begin{pmatrix} ijkh \\ hkij \end{pmatrix}, \begin{pmatrix} ijkh \\ khji \end{pmatrix}\right\}$$

or in cycle notation

$$P = \{(i)(j)(k)(h)\ ,\ (ij)(k)(h)\ ,\ (i)(j)(kh)\ ,\ (ik)(jh)\ ,\ (ij)(kh),\ (ih)(jk)\ ,\ (ihjk)\ ,\ (ikjh)\}$$

Formula (7) yields for this particular case

$$\chi_o(g)=\frac{1}{8}\left(\chi^{(1)}(g)^4+2\chi^{(1)}(g^2)\,\chi^{(1)}(g)^2+3\,\chi^{(1)}(g^2)^2+2\,\chi^{(1)}(g^4)\right)$$

and with the remark following (9)

$$\chi_o(g)=\frac{1}{8}\left((1+\cos\alpha)^4+2(1+2\cos 2\alpha)(1+2\cos\alpha)+3(1+2\cos 2\alpha)^2+2(1+2\cos 4\alpha)\right)$$

since the rotation angle of g^n is simply $n\alpha$.
With the help of common trigonometrical theorems for doubled arguments this becomes

$$\chi_o(g)= 1 - 4\cos^2\alpha + 8\cos^3\alpha + 16\cos^4\alpha \ .$$

Successively subtracting the characters $\chi^{(l)}(g)$, calculated from (9)

EBSCOhost - printed on 2/13/2023 3:45 AM via . All use subject to https://www.ebsco.com/terms-of-use

$$\chi^{(4)}(g) = 1 - 4\cos\alpha - 12\cos^2\alpha + 8\cos^3\alpha + 16\cos^4\alpha$$
$$\chi^{(3)}(g) = -1 - 4\cos\alpha + 4\cos^2\alpha + 8\cos^3\alpha$$
$$\chi^{(2)}(g) = -1 + 2\cos\alpha + 4\cos^2\alpha$$
$$\chi^{(1)}(g) = 1 + 2\cos\alpha$$
$$\chi^{(0)}(g) = 1$$

we find for μ_l in (8)

$$\mu_4 = 1,\ \mu_2 = \mu_0 = 2,\ \mu_3 = \mu_1 = 0.$$

Thus, μ_l of odd l vanish and no C_l^{mn} with odd l occur in the average (5), i.e. the orientation average with the ODF (simple average approximation) for mechanical properties is not affected by the loss of information in pole figures.

Table 1: Does the Loss of Information have Consequences for the Average (5)?

Property	conse-quences	occurring C_l^{mn}	due to symmetry
Spontaneous polarization P_i^s	yes	C_1^{mn}	-
Dielectric constant ε_{ij}	no	C_0^{00}, C_2^{mn}	$\varepsilon_{ij} = \varepsilon_{ji}$
Piezoelectric constant d_{ijk}, e_{ijk}	yes	$C_1^{mn}, C_2^{mn}, C_3^{mn}$	$d_{ijk}=d_{ikj}$ $e_{ijk}=e_{ikj}$
Mechanical compliance S_{ijkh}	no	$C_0^{00}, C_2^{mn}, C_4^{mn}$	$S_{ijkh}=S_{ijhk}=S_{jikh}=S_{khij}$ analog.
stiffness C_{ijkh}	no		

The method presented in sec. 5 was applied to some tensors with results shown in Table 1. Spontaneous polarization and piezoelectricity of PVDF have been considered in ref. (13). In ref. (14) the factors weighing the remaining C_l^{mn} in (5) in case of S_{ijkh} (C_{ijkh}) have been calculated and a more detailed discussion of the mathematical background is given.

EBSCOhost - printed on 2/13/2023 3:45 AM via . All use subject to https://www.ebsco.com/terms-of-use

7. Conclusions

A general method has been developed to decide whether the loss of information (ghost phenomena) on the ODF in experimental pole figures has consequences for the average of the crystalline contribution to physical property in the approximation (3). Polar properties, such as spontaneous polarization or piezoelectric constant were found to be affected by the ghost phenomena, contrary to properties independent of the sense of direction. It should be noticed here, that the ODF-method, highly developed in the field of metal physics, requires long measuring times (one pole figure about one day) and good computer equipment.

Moreover, due to the additional problems for polymers (amorphous scattering, broad and overlapping reflexes, coincidences, low crystal symmetries (cf. sec. 3)) it seems not likely, that the ODF-reproduction will become a routine method in polymer physics. The currently used qualitative or less complete quantitative methods, such as direct analysis of WAXS-patterns and pole figures or determination of orientation factors (15), will keep their inportance. Nevertheless, only the ODF yields complete information (apart from the case of the 10 crystal classes for which the "odd" part cannot be reproduced) about the orientation state of the crystalline phase. Perhaps only the practical experience with ODFs of polymers can show to what extent the ODF-method proves useful in polymer physics. The loss of information does not prevent application in general.

References

1. Bunge, H.J. 1969. Mathematische Methoden der Texturanalyse. Akademie-Verlag, Berlin.

2. Roe, R.-J. 1965. J. Appl. Phys. 36 (6), 2024.

3. Krigbaum, W.R., T. Adachi, J.V. Dawkins. 1968. J. Chem. Phys. 49, 1532

4. Ampe, R., E. Aernoudt, P. Van Houtte, J. Mewis. 1984. In: Proceedings of the 7th International Conference on Textures of Materials. Nordwijkerhout 1984, Zwijndrecht (1984) pp. 465-471

EBSCOhost - printed on 2/13/2023 3:45 AM via . All use subject to https://www.ebsco.com/terms-of-use

5. Mandelkern, L. 1984. The crystalline state. In: Physical Properties of Polymers (chap. 4). A.C.S., Washington, D.C.

6. Matthies, S., K. Helming.1982.Phys.stat.sol. (b) 113, 569.

7. Matthies, S. 1982. Aktuelle Probleme der quantitativen Texturanalyse. Institutspublikation des ZfK Rossendorf (480) ISSN 0138-2950.

8. Boyd, R.H. 1983. J. Polym. Sci., Polym. Phys. Ed. 21, 493.

9. Proceedings of the 6th International Conference on Textures of Materials, Tokyo 1981. Iron and Steel Institute of Japan, Tokyo 1982.

10. Bhagavantam, S. 1966. Crystal Symmetry and Physical Properties, Academic Press, London and New York.

11. Ljubarski, G.J. 1962. Anwendungen der Gruppentheorie in der Physik, VEB Deutscher Verlag der Wissenschaften, Berlin.

12. Nye, J.F. 1960. Physical Properties of Crystals (in Russ.). Izdatelstwo Inostrannoj Literatury, Moscow.

13. Ganster, J., D. Geiss: Polymer (in press)

14. Ganster, J., D. Geiss: Submitted for Phys. stat. sol.

15. Alexander, L.E. 1969. X-ray Diffraction Methods in Polymer Science, John Wiley & Sons, New York.

EBSCOhost - printed on 2/13/2023 3:45 AM via . All use subject to https://www.ebsco.com/terms-of-use

THE VISCOELASTICITY OF TEMPORARY POLYMER NETWORKS

E. Kröner

Institut für Theoretische und Angewandte Physik, Universität Stuttgart und Max-Planck-Institut für Metallforschung, Stuttgart, D 7000 Stuttgart

Abstract

Some physical questions which arose during the preparation of the computer program for our molecular-statistical theory of temporary polymer networks are discussed. In particular we consider (i) the problem of the relaxation time spectrum and its dependence on the chain contour lenghts, (ii) the density of junctions and the average number of junctions per macromolecule (two quantities that have different concentration dependences) and (iii) the distribution of contour lengths (which in the utilized relaxation time approach does not depend on the velocity gradient). The discussions lead us to an improved computer program. First results of this program are reported. These results seem to confirm that the theory yields physically reasonable results.

1. Introduction

In previous works [1-4] a theory was developed which treats the mechanical and optical properties of the (four-functional) so-called "temporary" polymer networks in solution; the term temporary is understood in the sense of former works of Green and Tobolsky, Scott and Stein, Lodge, Yamamoto and others. The junctions of such a network decay and form in certain characterstic time intervals (relaxation times) thereby causing additional network mobility observed macroscopically as

Morphology of Polymers
© 1986 Walter de Gruyter & Co., Berlin · New York - Printed in Germany.

EBSCOhost - printed on 2/13/2023 3:45 AM via . All use subject to https://www.ebsco.com/terms-of-use

viscoelasticity. Both thermodynamics and statistics of the temporary network have been considered, the latter being particularly suited to describe the dynamics of the network.

The theory is formulated in terms of a generalized spring-bead-model in which the junctions are represented by the beads and the polymer chains by the elastic springs. The generalization consists in the assumption that the beads are not "conserved", but decay and form. These phenomena are well described by a master equation for the distribution function $W(\underline{R},Z)$:

$$\frac{\partial W}{\partial t} + \sum_{i=1}^{M} \nabla_i \cdot (\dot{\underline{r}}_i W) = \iint (W' \vec{p} - W \overleftarrow{p})\, d\underline{R}'\, dZ' \qquad (1)$$

Here the integration extends over the whole configuration space and $W' = W(\underline{R}',Z')$. The configuration space is spanned by the set $\{\underline{r}_i\} \equiv \underline{R}$ of bead position vectors and the set $\{z_{ij}\} \equiv Z$, where z_{ij} is the number of elementary units of length l_o (often monomers) that form the chain connecting the junctions i and j. Thus z_{ij} is the contour length of this chain, measured in units of l_o. Furthermore

$$\vec{p}\,dt \equiv p(\underline{R}', Z' \to \underline{R}, Z)\, dt\,, \quad \overleftarrow{p}\,dt \equiv p(\underline{R}, Z \to \underline{R}', Z')\, dt \qquad (2)$$

are transition probability densities (densities with regard to the unprimed and primed $\underline{R}$-variables respectively) for the indicated transitions in the configuration space. Hence the two integrals in eq. (1) give us the rate of formation and decay of configurations $\underline{R}$, Z. This rate includes that of the formation and decay of the junctions.

As usual, eq. (1) has to be complemented by an equation which specifies the physics of the problem. This is a Langevin type of equation here assumed in the form

$$\zeta_i (\dot{\underline{r}}_i - \underline{\underline{\kappa}} \cdot \underline{r}_i) + kT \ln W + \sum_{j=1}^{M} \kappa_{ij}\, \underline{r}_j = 0\,, \qquad (3)$$

where ζ_i is the (effective) friction constant of the ith bead, which for simplicity is taken the same (ζ) for all beads.

EBSCOhost - printed on 2/13/2023 3:45 AM via . All use subject to https://www.ebsco.com/terms-of-use

K_{ij} are the elements of the elasticity matrix defined by the potential energy

$$E_{pot} = \frac{1}{2}\sum_{i,j}^{M} K_{ij}\,\underline{r}_i \cdot \underline{r}_j = \frac{1}{2}\sum_{(ij)}^{2M} k_{ij}\,h_{ij}^2, \quad \underline{h}_{ij} = \underline{r}_j - \underline{r}_i \qquad (4)$$

with k_{ij} as elastic spring constants taken in the known form

$$k_{ij} = \frac{\alpha}{2_{ij}}, \quad \alpha \equiv \frac{3kT\,(1-\cos\psi)}{l l_0 \sigma\,(1+\cos\psi)}, \qquad (5)$$

where l is the bond length, ψ is the bond angle and σ is a factor depending on the structure of the polymer molecule. Eq.(5) implies that the spring constants do not depend on the amount of stretching which is a good approximation as long as the chains are not "almost stretched". Eq.(3) describes the equilibrium of the forces exerted on the bead no. i. In agreement with common usage, inertia forces are neglected. The three terms of eq.(3) represent respectively the friction force, the stochastic force of Brownian motion and the elastic forces transferred by the chains. The forces of hydrodynamic interaction and those of the excluded volume effect can be added if so desired.

Eqs.(1)-(5) together form the completed generalized diffusion equation, from which the distribution function is to be obtained. For this purpose we need to know the transition probabilities which are not given a priori. These have been inferred from the kinetic theory under the simplifying assumptions that (i) each decaying junction is immediately reformed, however, in general, in a new configuration so that the decay and the following reformation is treated as one single elementary process and (ii) that all these processes are uncorrelated. The latter assumption implies that the density of junctions is reasonably low.

Obviously, the decay rate depends strongly on the stress in the network. These stresses represent the elastic forces which tug at the junctions. The calculation of the stresses, however, requires the solution of the diffusion equation. Thus W,

EBSCOhost - printed on 2/13/2023 3:45 AM via . All use subject to https://www.ebsco.com/terms-of-use

$\vec{p}$ and $\overleftarrow{p}$ have to be found simultaneously from the corresponding coupled equations. The particular difficulty consists in the following: The junction processes are rather localized and, therefore, are conveniently treated in the space representation of the theory. The elastic problem, on the other hand, is best treated in a representation in which the elasticity matrix is diagonal, that is the mode representation. These different aspects imply that both eigenvalues and eigenvectors have to be calculated for relatively highdimensional matrices, e.g. 100 x 100. This can only be done numerically.

A computer program has been set up that, however, is rather involved. In developing this program, a few points arose which have to do with the physics of the problem and are worth being discussed (sections 2 - 4). First results gained with the computer program and their comparison with experiments are also reported (section 5). The latter results are not yet final, but they show that the theory is within the realm of the physical reality.

2. Relaxation Time Approach, Transition Probabilities

The integro-differential equation (1) can be approximated by a pure differential equation as follows. First of all note that the right hand side of (1) can also be written as

$$\iint \left[\left(W' - W'_{eq} \right) \vec{p} - \left(W - W_{eq} \right) \overleftarrow{p} \right] d\underline{R}' \, d\vec{z}' , \qquad (6)$$

where W_{eq} is the distribution function in equilibrium (fluid at rest). In fact, the integral in eq. (1) vanishes in equilibrium. The indicated approximation now consists in the omission of the first integral in eq. (6). A qualitative argument is as follows: The system left alone in a nonequilibrium state has a strong tendency to go to equilibrium. Thus processes directed towards equilibrium (second integral in (6)) will be much more frequent than those directed towards non-equilibrium (first integral in (6)).

EBSCOhost - printed on 2/13/2023 3:45 AM via . All use subject to https://www.ebsco.com/terms-of-use

The approximation here applied will be named "relaxation time approach" in analogy to a similar procedures in Boltzmann's kinetic theory. Eq.(1) now reduces to

$$\frac{\partial W}{\partial t} + \sum_{i}^{M} \nabla_{i} \cdot (\dot{\underline{r}}_{i} W) = -(W - W_{eq})/\tau \quad , \tag{7}$$

where

$$\frac{1}{\tilde{\nu}} \equiv \bar{\rho} \equiv \bar{\rho}(\underline{R}, Z) = \iint p(\underline{R}, Z \rightarrow \underline{R}', Z')\, d\underline{R}'\, dZ' \tag{8}$$

and $\tau(\underline{R},Z)$ represents the relaxation time spectrum for the decay of a configuration $\underline{R}$, Z into any other configuration. It turns out that the calculations become much simplified if the space configuration $\underline{R}$ is replaced by its average $\langle \underline{R} \rangle$ in Eq.(8). This should be a reasonable approximation, in particular, if the decays are not too frequent. We shall therefore consider the relaxation time spectrum $\tau(\langle \underline{R} \rangle, Z) = 1/\bar{\rho}(\langle \underline{R} \rangle, Z)$. If as indicated in section 1, we restrict ourselves to a low junction density, so that the coupled decay-formation process at one junction (see Section 1) occurs without correlation with a process at another junction, then we can assume that

$$p(\langle \underline{R} \rangle, Z \rightarrow \underline{R}', Z') = \sum_{i=1}^{M} p_{i}\, \delta_{[i]} \quad , \tag{9}$$

where $\delta_{[i]}$ is the delta function with respect to all chains except those forming the junction i. The occurrence of the delta functions implies that a change in the configuration takes place always in such a way that only statistically independent one-junction processes participate.

Using typical methods of the kinetic theory, the transition probability density per unit time for the single process at junction i has been derived in the form $p(\langle \underline{h}_{i\alpha} \rangle, z_{i\alpha} \rightarrow \underline{h}'_{i\alpha}, z'_{i\alpha})$, where the index α denotes the four junctions adjacent to the ith junction and $\underline{h}$ has the meaning as in eq.(4). The integration implied by eqs.(8,9) yields the result (ref. [2])

$$\bar{\rho}(\langle \underline{R} \rangle, Z) = \sum_{i=1}^{M} B_{i} \exp\left\{ \frac{1}{2kT} \sum_{(i\alpha)}^{4} k_{i\alpha} \langle h_{i\alpha}^{2} \rangle \right\} \tag{10}$$

EBSCOhost - printed on 2/13/2023 3:45 AM via . All use subject to https://www.ebsco.com/terms-of-use

where

$$B_i = \nu^* \left(\frac{kT}{\alpha^*}\right)^3 (z_{ia} + z_{ib})^{\frac{5}{2}} (z_{ic} + z_{id})^{\frac{5}{2}} . \qquad (11)$$

Here α^* is defined by $\alpha^* = \alpha \ell \ell_o$ and has the dimension of an energy (see eq.(5)). a, b, c, d, specify the junctions adjacent to i in such a way that the chains (ia) and (ib) remain coherent in the decay and correspondingly the chains (ic) and (id). ν^*, as B_i has the dimension of a frequency and must be determined from experiment (see below). The exponent in eq.(10) contains the elastic energy at ith junction i.e. the energy stored in the four chains adjacent to this junction. This energy is divided by the thermal energy kT. The form of the exponent implies that the process will occur more easily when the pull at the junction is stronger.

As the mentioned kinetic consideration has shown, the frequency ν^* depends essentially on the activation enthalpies of dissociation and formation of the junctions divided by kT, thus on T, but also on $\overset{\circ}{z}_{ij}$, the contour lenghts in equilibrium. It has been proved in ref. [2] that within the relaxation time approach the distribution of the $\overset{\circ}{z}_{ij}$ equals that of the z_{ij}, so that we could just as well read off from experiment B_i rather than ν^*. In view of later refinements of the theory we shall nevertheless use eq.(11). It is important, however to note that B_i does not depend on the velocity gradients so that B_i can be obtained from results on the fluid at rest.

3. Density of Junctions

A quantity of great importance is the number M of junctions in a network of volume V containing in average $\bar{L}$ elementary polymer units, e.g. monomers, or, equivalently, the average number $\bar{z} = \bar{L}/2M$ of elementary units per chain. The number M is related to the number density n of junctions according to n = M/V where V can be expressed in terms of L and of mass concentration c, i.e. portion of polymer in volume V over V, as

$$c = \bar{L} \mathcal{M}_{mon} / N_A V . \qquad (12)$$

EBSCOhost - printed on 2/13/2023 3:45 AM via . All use subject to https://www.ebsco.com/terms-of-use

Here N_A is Loschmidt's number and M_{mon} the molecular weight of the monomer. In our one-process model, $\bar{z}$ is a conserved quantity. Using extensively results of Flory and coworkers [5-8] we have calculated n in ref. [3] and rewritten the result in terms of $\bar{L}/2M$ in ref. [2], eqs. (42,43). In particular, we have derived a quartic equation for $\bar{L}$, given M. (It would be possible also to prescribe V and calculate M. It is, however, more convenient to prescribe M and then calculate V.) Observing that the theory is good only for $\bar{z} \gg 1$, the quartic can be replaced by a quadratic equation with solution

$$\bar{z} = \frac{M}{M_{mon}} \left(\sqrt{2c/A} - 1 \right), \tag{13}$$

where M is the molecular weight of the polymer and A does not depend on the concentration (see below). Replacing $\bar{z}$ by n we have

$$n = \frac{N_A c}{2M \left(\sqrt{2c/A} - 1 \right)} \tag{14}$$

so that $\bar{z}$ and n increase with concentration c.

This result is perhaps surprising, because the first thought seems to be that the chain length decreases with the concentration. The result is not so surprising, however, if it is observed that with $n = M/V$, $\bar{z} = \bar{L}/2M$ and eq. (12)

$$n\bar{z} = \frac{N_A c}{2 M_{mon}} \tag{15}$$

This equation expresses the fact that $n\bar{z}$, the number of elementary units per unit volume, is proportional to the concentration. The exact equation (15) implies that $\bar{z}$ is independent of the concentration if n increases proportionally to the concentration. If, however, n increases more slowly, then $\bar{z}$ must increase with c. Eq.(15) and all conclusions drawn from it do not depend on the kinetic model. In our case, the model leads, in fact, to an increase in $\bar{z}$ with c. Nevertheless, a more intuitive argument is desirable.

EBSCOhost - printed on 2/13/2023 3:45 AM via . All use subject to https://www.ebsco.com/terms-of-use

The quantity A in eqs. (13,14) is defined as

$$A = A_0 \left[1 + 4 \exp\left\{\frac{-\varepsilon}{kT}\right\} + 3(\lambda^2 - \ln\lambda - 1)\right]^4 \exp\left\{\frac{\mu}{kT}\right\}. \qquad (16)$$

We shall later adapt A to the experiment, so that the energy of a gauche state relative to the trans state, a positive quantity, the chemical potential μ of a junction, a negative quantity, and the front factor λ need not be known (ε and μ are, nevertheless, known). The quantity A_o is constant with respect to c and T and depends essentially on the volume of the solvent molecule (known) and the volume of a junction (unknown). The term $1 + 4 \exp\{-\varepsilon/k\,T\} = 1 - f$ is Flory's "inflexibility" (f the flexibility) of the 4-functional network, see ref. [7]. According to eq.(13) large $\bar{z}$ means also large flexibility, as it should be. Eq.(13) is one of the three thermodynamic equations of state which connect the extensive variables S (entropy), M and L with the intensive variables T, μ and λ , the chemical potential of the elementary unit, later taken as the monomer. The second equation of state was derived in ref.[1] as

$$\bar{L} = 8\bar{M}\, kT/\lambda^*, \qquad \lambda^* \equiv kT \ln \bar{L} - \lambda. \qquad (17)$$

The third equation of state has not yet been derived. It is not needed for the following.

In concluding this section we remark that all results of this section were obtained from the equilibrium theory as described in ref. [1].

4. The Distribution of the Contour Lengths

In our theory the beads and the connecting springs which represent the network chains, form the thermodynamical and statistical system. The solvent, on the other hand, is considered external to the system, namely as a part of the surrounding

EBSCOhost - printed on 2/13/2023 3:45 AM via . All use subject to https://www.ebsco.com/terms-of-use

heat bath. In the equilibrium state, the system finds itself in a fixed volume V with permeable walls. Thus it is treated as an open system, and is therefore a member of a grandcanonical ensemble with grandcanonical density function W in phase space and grandcanonical partition function, say C. This means that both solvent molecules and elementary polymer units can pass through the walls so that the total number L of elementary units in the system fluctuates around some mean value $\bar{L}$. Using the fundamental postulate of equal probabilities, namely that all microstates in V (representing the members of the ensemble) which simultaneously possess the same energy, say H, number of junctions M and elementary units L are equally probable, we can write down immediately the probability density function (later called distribution function) for equilibrium:

$$W = C^{-1} \frac{1}{M!\,L!\,h^{3M}} \exp\left\{-\frac{1}{kT}\left(H - \mu M - \lambda L\right)\right\}. \tag{18}$$

For correctness we have introduced Planck's constant h which determines the cell size in the phase space. h has no influence on our later results, however.

We have shown in ref. [1] that the transformation into normal coordinates $\underline{s}_{i'}$ diagonalizes kinetic and potential energy so that W factorizes into one-mode probability functions. We now assume that M is given from some a priori information, so that $M = \bar{M}$. Integrating the W, written in normal coordinates and momenta, over these coordinates and momenta, we obtain the equilibrium distribution of $z_{i'}$ (the contour lengths transformed from chain to mode) as

$$w_{eq}(z_{i'}) = \frac{a^4}{6} z_{i'}^3 \exp\left\{-a z_{i'}\right\}, \quad a \equiv \lambda^*/2kT. \tag{19}$$

Eq.(19) represents the one-mode probability. The multi-mode (conditional) probability is then given by

$$W_{eq}(\{z_{i'}\}|M) = \left(\frac{a^4}{6}\right)^M \prod_{i'}^{M} z_{i'}^3 \exp\left\{-a z_{i'}\right\}. \tag{20}$$

EBSCOhost - printed on 2/13/2023 3:45 AM via . All use subject to https://www.ebsco.com/terms-of-use

For the computer program sketched in ref. [2] we need, beside (19) or (20), also the probability $w_{eq}(z_{ij})$. In principle, $w_{eq}(z_{ij})$ can be obtained by integration of eq. (18) over all momenta, positions and contour lengths except the one considered. This integration is rather complex; we therefore seek a more direct way. We assume a kind of ergodic hypothesis which asserts that the distribution of states occupied by a single chain in some time interval is the same as the instantaneous distribution of states of the ensemble of chains in the network. Assuming also that states with equal energy and contour length are equally probable, we find, similarly as before, the one-chain probability

$$w_{eq}(z_{ij}) = \frac{b^4}{6} z_{ij}^3 \exp\{-b z_{ij}\} \qquad (21)$$

with b = 4a. The multi-chain probability $W_{eq}(\{z_{ij}\}|M)$, however is not factorized in one-chain probabilities (21). This has the very physical reason, that such a factorization would destroy the fundamental property of our system, namely to form an interconnected network and not an ensemble of independent chains. The arguments given above do not represent a proof for eq. (21). A sort of numerical proof, however, has been achieved as follows. If an elasticity matrix (K_{ij}) is formed with z_{ij}-values that are distributed according to eq. (21), and if this matrix is diagonalized, leading to eigenvalues $\lambda_{i'}$, say, then $\lambda_{i'} = \alpha/z_{i'}$ and the $z_{i'}$ have numerically the right distribution (19).

The program in [2] was developed using eq. (21), however with b/2 instead of b (the mistake arose from the erroneous equation (29) of [1]. This equation should read $L = 2\sum_{i'}^{M} z_{i'}$ instead of $L = \sum_{i}^{M} z_{i'}$.)

This section was intended to clarify and justify the pertaining part of the computer program of ref. [2], which should be consulted for further details.

EBSCOhost - printed on 2/13/2023 3:45 AM via . All use subject to https://www.ebsco.com/terms-of-use

5. First Numerical Results

Since the computer program was successfully run only recently, the present results are rather restricted. We include them, nevertheless, to demonstrate that the theory gives results which are reasonable, thus providing the motivation for further studies along these lines. The program of ref. [2] was slightly changed according to the discussion of the preceding sections. Among many available experimental results we have chosen those of Krozer and Gruber [9] who measured solutions of polystyrol in dekalin. The results selected are those obtained at room temperature (293 K) and concentration of 12.5 %. The molecular parameters used are $M = 2\ 000\ 000$, $M_{mon} = 104$, $l = 2.52$ Å, $l_o = 21$, $\cos\varphi = 1/3$ and $\sigma = 4.84$. ε and μ, though known, were left free by adapting A rather than A_o to the experiment (see eq.(16)). The number M of junctions in V, finally, was chosen as 10. To improve the somewhat poor statistics (with 10 objects) we have taken N = 10 different realizations with 10 junctions each. We plan to increase M and N in later computations.

In [9] the viscoelastic functions for shear flow η and ξ have been measured for velocity gradients q from 0.1 till 100 per second. The results are shown in Fig. 1. The curves in the range below 0.1 s^{-1} and, in particular, the values $\eta(q=0) = \eta_0$ and $\xi(q=0) = \xi_0$ were obtained by extrapolation. The latter values were used to adjust the friction parameter ζ and the frequency factor ν^* in eq.(11). We were able to calculate the equilibrium transition rate $p_{eq}(\langle \underline{R} \rangle, Z)$ for the equilibrium distribution of $\langle \underline{R} \rangle$ and Z. With the help of this result also the nonequilibrium transition rate $p(\underline{R}, Z)$ has been computed as a function of q. Here $\langle \underline{R} \rangle$ was taken as the nonequilibrium average configuration $\langle \underline{R} \rangle$ in space, whereas, in agreement with our former statement, the equilibrium distribution was taken for Z. The curve $\bar{p}(q)$ is shown in Fig. 2.

The adjustment described above leads to the coincidence of the

EBSCOhost - printed on 2/13/2023 3:45 AM via . All use subject to https://www.ebsco.com/terms-of-use

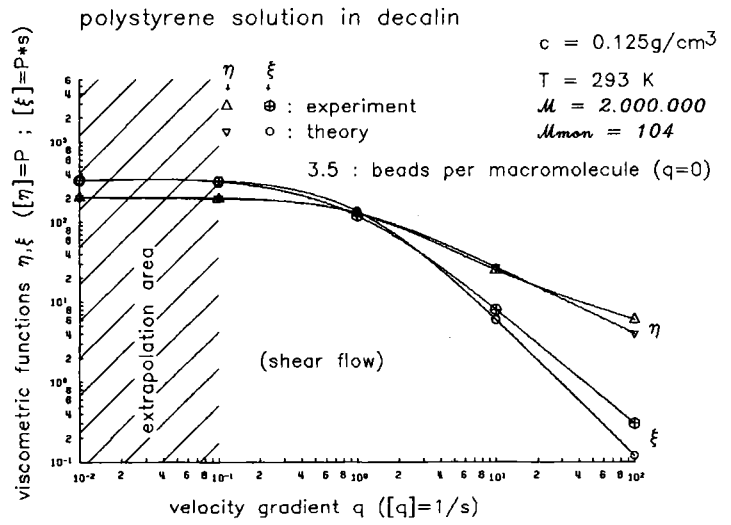

Fig. 1. Measured and calculated viscometric functions (η, ξ) vs. velocity gradient (q) for simple shear flow of a 12.5% solution of polystyrol in dekalin.

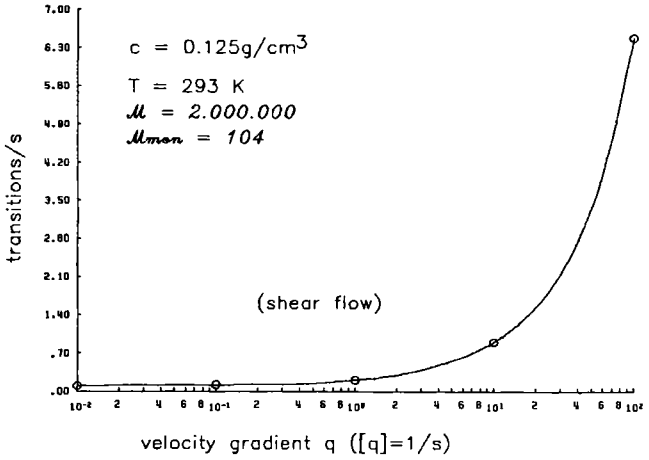

Fig. 2. Mean number of one-junction decay processes per second for solution of Fig. 1.

EBSCOhost - printed on 2/13/2023 3:45 AM via . All use subject to https://www.ebsco.com/terms-of-use

experimental and theoretical curves at very small velocity gradients. As discussed above, also the quantity A has to be adjusted to the experiment. This was done by inspection such as to obtain the best possible agreement between theory and experiment. We are aware that this method is not too satisfactory and hope to improve it later. We are, nevertheless, encouraged by the fact that it is possible to achieve an agreement like that shown in Fig. 1.

The value of z as obtained by the adjustment of A is in rough agreement with experimental estimates (ref. [3]). Whereas there we have calculated results for the values 1 and 1/2 of the front factor λ appearing in eq.(16), the adaption of A here implies that λ is optimally included.

6. Conclusion

In this article we have tried to clarify certain physical questions which arose in the course of the preparation of the computer program. Corresponding to the complexity of the physical situation, the introduction of certain assumptions was unavoidable. As the main shortcomings we consider (i) the omission of the excluded volume effect and (ii) the inaccuracy introduced by the relaxation time approach. This approach implies that the distribution of chain contour lengths does not depend on q, the velocity gradient. Hence, within the frame of our theory, the experimentally and theoretically observed decrease in the viscoelastic functions with increasing q is to be assigned to a higher decay-formation rate rather than to an increase in the number of the junctions.

In future work we hope to predict also the intervals of temperature and concentration in which this theory is valid. The intervals should be those in which the polymer system behaves as a temporary network. At this moment we only know that temperature and concentration should neither be too high nor too low.

EBSCOhost - printed on 2/13/2023 3:45 AM via . All use subject to https://www.ebsco.com/terms-of-use

Acknowledgement

The arguments leading to the distribution of contour lengths (eq.(21)) are taken from the yet unfinished Ph.D. thesis of Dipl. Phys. D. Chassapis, who also set up the computer program. Financial support by the Deutsche Forschungsgemeinschaft is gratefully acknowledged.

References

1. Takserman-Krozer, R., E. Kröner, Rheol. Acta. 23, 1 (1984).
2. Kröner, E., R. Takserman-Krozer: Rheol. Acta 23, 139 (1984).
3. Takserman-Krozer, R., S. Krozer, E. Kröner: Colloid & Polymer Sci. 257, 1033 (1979).
4. Kröner, E., R. Takserman-Krozer: Proc. 4th Int. Conf. Continuum Models of Discrete Systems, Stockholm, O. Brulin, R.K.t. Hsieh (eds.), North-Holland, Amsterdam 1981.
5. Flory, P.J.: J. Chem. Phys. 10, 51 (1942).
6. Flory, P.J.: J. Chem. Phys. 18, 108 (1950).
7. Flory, P.J.: Proc. Roy. Soc. A 234, 60 (1956).
8. Flory, P.J., C.A. Hoeve, A. Ciferri: J. Polymer Sci. 34, 337 (1959).
9. Krozer, S., E. Gruber: Rheol. Acta 18, 86 (1979).

EBSCOhost - printed on 2/13/2023 3:45 AM via . All use subject to https://www.ebsco.com/terms-of-use

ZONE DRAWING OF POLY(VINYL ALCOHOL) GELS

D.T. Grubb and P.D. Garrett
Department of Material Science, Cornell University
Ithaca, New York 14853

Introduction

The drawing of gels, wet or dry, has been shown to be an effective method for producing high modulus fibers from flexible chain crystalline polymers, such as polyethylene (PE) (1-3), polypropylene (4), and poly(vinyl alcohol) (PVAl) (5,6). Several theories exist for the relation of structure to modulus in these fibers which explain how the modulus increases with draw ratio. In all cases the theories assume perfect alignment of the crystals, and when PE is the material drawn, this does not occur until a draw ratio of 10x. Zone drawing uses a small tubular or slotted heater, surrounding a small section of the sample to be drawn. The heater is moved slowly along the specimen while it is extended in a tensile testing machine. The ratio of the cross-head speed to the heater speed is the enforced draw ratio of the specimen.

Zone drawing of polymers has been used to obtain highly drawn and high modulus fibers and films from polypropylene (7), poly (ethylene terephthalate) (8) and nylon 6 (9). A primary advantages of zone drawing is that the materials, prone to degradation or cross-linking at high temperature, are exposed to the high temperature for a short time only. Zone drawing is closer to continuous fiber spinning, and avoids the problem of gripping the ends of samples when they are hot and soft. The disadvantage of zone drawing is that the exact

Morphology of Polymers
© 1986 Walter de Gruyter & Co., Berlin · New York - Printed in Germany.

EBSCOhost - printed on 2/13/2023 3:45 AM via . All use subject to https://www.ebsco.com/terms-of-use

temperature of drawing and the temperature profile of the sample as it moves through the hot zone are difficult to determine. Temperature differences through the thickness of the sample can also be a problem, unless the initial sample is thin or a microwave heater is used.

A recent patent disclosure describes how very high molecular weight PVAl has been formed into gels and has been used in a continuous multi-stage gel drawing process to produce fibers of high modulus and strength at draw ratios of 10-20x (5). A study of gels of lower molecular weight PVAl (~100,000) and their isothermal drawing (6) was limited to draw ratios of ~14, where the degree of orientation of the crystalline phase was still increasing. The modulus of these fibers was 20GPa or less. We report here the results of zone drawing gels of PVAl of the same moderate molecular weight.

Experimental

The gels were prepared from 2% to 9.5% concentration solutions of fully hydrolyzed PVAl in a 2:1 mixture of ethylene glycol and water, as has been previously described (6). The zone heater was simply constructed of aluminum in two parts which closed around the specimen, leaving a 4mmx20mm gap. Two versions were made, where the hot zone, as measured by a thermocouple probe, extended for 5mm and for 10mm along the specimen. There was no cooling system, merely good insulation so that the fiber temperature rapidly fell to room temperature as it passed out of the hot zone. The mechanical properties of the drawn fibers were measured with a rheovibron dynamic mechanical tester.

EBSCOhost - printed on 2/13/2023 3:45 AM via . All use subject to https://www.ebsco.com/terms-of-use

Results

The use of a zone drawing system allowed higher draw ratios to be achieved, compared to isothermal drawing in an oven. from the same starting samples. This is shown in Figure 1, where the maximum draw ratio that could be obtained is plotted against the concentration of the initial solution from which the gel was formed. The maximum draw ratio on isothermal drawing is obtained by measuring the extension of a central portion of the specimen when failure is imminent. In zone drawing the draw ratio is slowly increased during a stable draw, by slowing the motion of the heater, until the sample breaks. On the entanglement network theory of gel drawing (3), draw ratio should vary as $1/\sqrt{C_o}$. It can be seen that there was almost no variation at all when the oven was used, but a fall from 25 to 15 in the zone drawing. This is still far from the predicted variation, but disentanglement during drawing is possible and will increase the draw ratio at all concentrations.

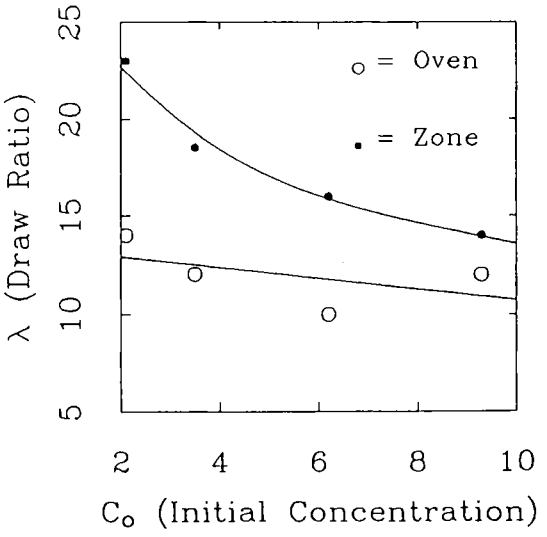

Figure 1. The draw ratios obtained on zone drawing PVAl gels with a 10mm hot zone, compared to isothermal drawing, as a function of concentration of the original solution.

EBSCOhost - printed on 2/13/2023 3:45 AM via . All use subject to https://www.ebsco.com/terms-of-use

Even when there is no chemical degradation, gels may change on holding at high temperature simply by returning to their more highly entangled equilibrium melt state from the disentangled gel state. This is a reason for expecting zone drawing to give higher draw ratios.

On comparing the two zone heaters, there was a significant difference, as shown in Figure 2. The longer zone allowed higher draw ratios, but the shorter had generally lower draw ratios but higher moduli. This does not agree with the simple predictions which say that draw ratio is the most important factor affecting modulus, and they increase together. However it is in agreement with the reported high moduli at comparatively low draw ratios (5).

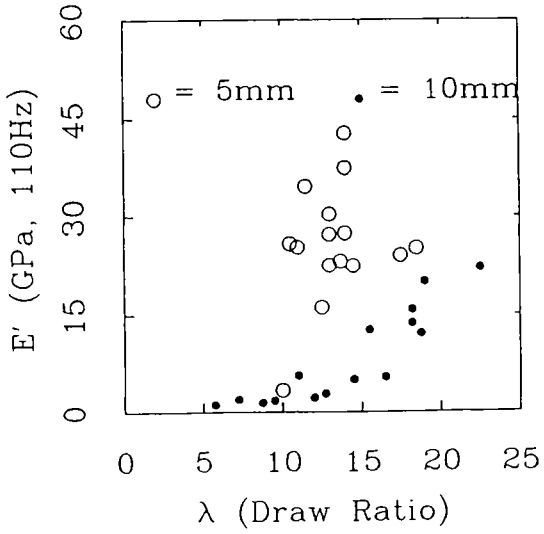

Figure 2. Young's modulus of zone drawn fibers of PVAl as a function of their draw ratio, for short and long zone heaters.

There is a lot of scatter in the data for modulus, which was taken at room temperature and humidity after the drawn samples had been dried, washed in methanol and redried. Some of the scatter is due to the effects of water on the sample, present because of incomplete drying or picked up from the atmosphere.

EBSCOhost - printed on 2/13/2023 3:45 AM via . All use subject to https://www.ebsco.com/terms-of-use

More rigorous drying, using phosphorous pentoxide as a desiccant in the sample chamber of the rheovibron did produce a lower water content, and samples treated in this way are described as "dry". However measurement of the total absorbed water content in the samples is a real difficulty. The water is strongly bound, and if drying conditions are made severe, the polymer will dehydrate to form unsaturation on the main chain and possibly ether cross-links between chains.

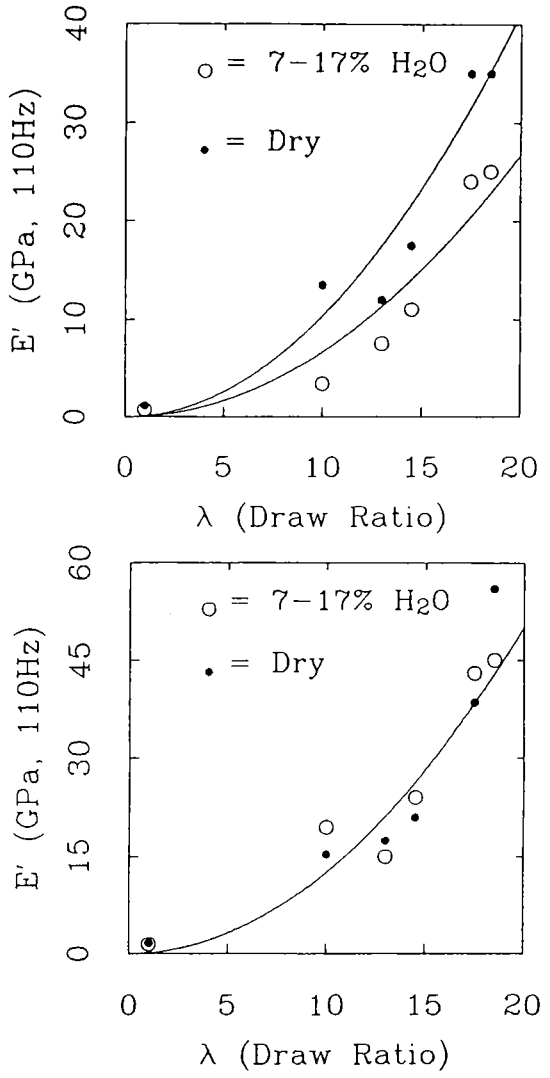

Figure 3 shows the difference in modulus between the "dry" gel drawn fibers of PVAl and fibers allowed to increase in weight from 7-17% by the absorption of atmospheric moisture.

Figure 3a, above, refers to 20°C,

Figure 3b, below, to -100°C data.

EBSCOhost - printed on 2/13/2023 3:45 AM via . All use subject to https://www.ebsco.com/terms-of-use

At room temperature the difference is clear, but not very great. On cooling to -100°C, the difference between "wet" and "dry" samples completely disappears. This is not at all surprising, as the water will plasticize the material and reduce the glass transition of the amorphous material to the region of room temperature. Independant measurement of T_g for the fibers gives a value of 60±5°C for the "dry" material, falling to ~30°C at 10% water content and 5°C at 17%. The single line in Figure 3b is an indication that the difficulties in accurate measurement of modulus caused by the variable water content of the samples can be avoided by making the measurements at low temperature. The modulus measured there will be unrealistically high in terms of practical applications - the maximum modulus in Figure 3b is 60GPa while the maximum in Figure 3a at room temperature is 35GPa. However it is a useful measure for comparative purposes, and low temperature measurement of modulus has been used for polyethylene fibers for much the same reason (10).

Conclusions

Zone drawing is a significantly better method than the isothermal drawing for the extension of dried gels of PVAl. However the modulus and draw ratio obtainable with material of moderate molecular weight is still limited.

Acknowledgement

The financial support of the Office of Naval Research is gratefully acknowledged.

EBSCOhost - printed on 2/13/2023 3:45 AM via . All use subject to https://www.ebsco.com/terms-of-use

References

1. P. Smith, P.J. Lemstra, B. Kalb and A.J. Pennings. 1979 Polym. Bull. 1, 733.
2. B. Kalb and A.J. Pennings. 1980 J. Mater. Sci., 15, 2584.
3. P. Smith, P.J. Lemstra and H. Booij. 1981. J. Polym. Sci., Polym. Phys. Edn. 19, 877 .
4. A. Peguy and R. StJohn Manley. 1984. Polymer Comm. 25, 39.
5. Y.D. Kwon, S.Kavesh and D.C. Prevorsek. 1984. US Patent 4,440,711.
6. Peggy Cebe and D.T. Grubb: J. Mater Sci., (in press).
7. M. Kamezawa, K. Yamada and M. Takayanagi. 1979. J. Appl. Polymer Sci., 24, 1227.
8. T. Kunugi, A. Suzuki and M Hashimoto. 1981 J. Appl. Polymer Sci., 26, 1951.
9. T. Kunugi, T. Ikuta, M. Hashimoto and K. Matsuzaki. 1982 Polymer 23, 1983.
10. A.G.Gibson, G.R. Davies and I.M. Ward. 1978. Polymer 19, 683.

EBSCOhost - printed on 2/13/2023 3:45 AM via . All use subject to https://www.ebsco.com/terms-of-use

EBSCOhost - printed on 2/13/2023 3:45 AM via . All use subject to https://www.ebsco.com/terms-of-use

A MECHANISM OF SUPERMOLECULAR STRUCTURE FORMATION SUGGESTED FOR POLYASSOCIATED COMPLEXES OF GROUP I, III METAL ALKOXIDES

G.F. Bolshakov, Z.T. Dmitrieva
Institute of Petroleum Chemistry, Siberian Division of USSR Academy of Sciences, Tomsk, SU-634055

Introduction

Interaction in solution of macromolecules of various stereoregularity is accompanied with intermolecular association to form stereocomplexes (1,2). Gel formation effect in these cases depends on macromolecule combination according to stereoregularity type and on polymer ratio. The interactions of isotactic and syndiotactic polymethyl methacrylates (it- and st-PMMA) were applied to study a mechanism of supermolecular structure formation (3,4). $M[M'(OR)_4]$ complexes, where M is IA group metal, M' is IIIA group metal and R is alkyl, as well as it- and st-PMMA cause structuring of solutions of low dielectric permittivity (5). The authors studied the mechanism of polyassociation and supermolecular structure formation occurring in solution as well as in crystalline state for $M[B\text{-tert-}OC_4H_9(OR)_3]$ complexes, where M = Li, Na, K; R = C_3H_7-$C_{13}H_{27}$ of normal structure, using methods of rheology, permittivity measurement, mass-spectrometry and small angle X-ray scattering (6,7).

Results

As complexes are formed in solution, they polyassociate to form elastoviscous solutions and gels. The viscosity of structured systems formed is affected by the concentration, complex structure and solvent permittivity. Of great significance is also the effect of metal, the length of alkyl substituent and structural affinity of the solvent for the complex (Fig. 1). The most intensive gel formation occurring due to the polyassociation and sol-

Morphology of Polymers
© 1986 Walter de Gruyter & Co., Berlin · New York - Printed in Germany.

EBSCOhost - printed on 2/13/2023 3:45 AM via . All use subject to https://www.ebsco.com/terms-of-use

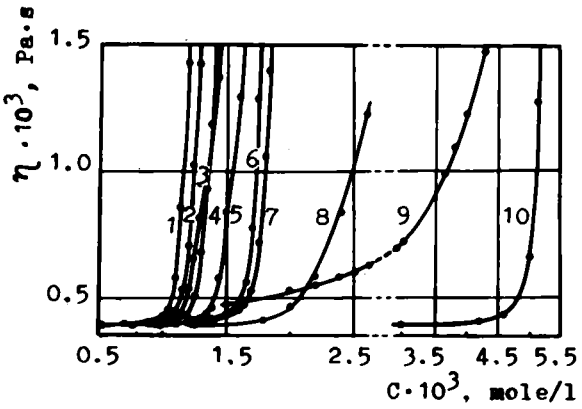

Fig. 1. Critical concentration dependence for gel effect of $Li[B\text{-tert-}OC_4H_9(OR)_3]$ in heptane solution at 298°K, where R: 1 - C_7H_{15}; 2 - C_6H_{13}; 3 - C_5H_{11}; 4 - $C_{10}H_{21}$; 5 - $C_{11}H_{23}$; 6 - C_9H_{19}; 7 - C_8H_{17}; 8 - C_4H_9; 9 - $2\text{-}C_2H_5\text{-}C_6H_{12}$; 10 - $iso\text{-}C_5H_{11}$.

vation of the dissolved complexes is observed in case the length and structure of the solvent molecule correspond to the alkoxide substituent of the complex and solvent permittivity ε is ≤ 5. Structured solutions of complexes have a low activation energy of elastoviscous flow (30-35 kJ/mol) and a high activation heat (150-180 kJ/mol). The entropy of activation of elastoviscous flow is not affected by the shear stress in the region of rates of deformation (5-300 s^{-1}) and by the temperature up to 325°K. Gels flow within a wide region of shear stress, retaining a constant and high viscosity. This is due to the fact that structured solutions of complexes, when subjected to the deformation, exhibit high rates of relaxation 2×10^8-16×10^8 mol/s). With lengthening alkoxide substituent of the complex, a lag in the restitution of the gel structure is observed and the relaxation time of the viscoelastic properties increases due to fluctuation of the three--dimentional structure. The macrokinetics of the structure formation occurring in solutions of $Li[B\text{-tert-}OC_4H_9(OR)_3]$, where R = = $n\text{-}C_4H_9$, $iso\text{-}C_4H_9$, $n\text{-}C_7H_{15}$, $n\text{-}C_8H_{17}$, $n\text{-}C_{10}H_{21}$, was studied using ε - measurement technique (Table 1). ε changes in time depend on a solvent type and on a substituent in the complex (Fig. 2).

EBSCOhost - printed on 2/13/2023 3:45 AM via . All use subject to https://www.ebsco.com/terms-of-use

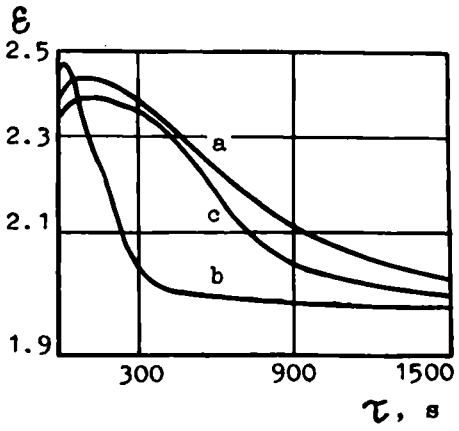

Fig. 2. Kinetics of solvent permittivity variations for solutions of $Li[B\text{-tert-}OC_4H_9(OR)_3]$ in heptane at 293°K, where R:
a - C_4H_9; b - C_7H_{15}; c - $C_{10}H_{21}$.

Broadening of the permittivity diagrams with increasing complex concentration (from 0.008 to 0.025 mol/l) and decreasing temperature (from 323 to 293°K) is an evidence of diffuse kinetic process. The order of structuring reaction is affected by the complex structure, solvent and reaction time. The reaction order increases with the solvent permittivity, while on approaching the condition of structural compatibility between the alkoxide substituent of the complex and the solvent, it decreases to a negative value. The structuring of solutions of complexes is characterized by high reaction rate constants (k_T) and low activation energies, the former increasing, as a rule, and the latter decreasing by the reaction completion. The kinetic parameters of structuring suggest a complex process and are an evidence of a spontaneous association of complexes occurring in space with a concomitant specific solvation thereof by the solvent.
The low permittivity of the media causes a decrease in the energy of complex association. The interaction of metal alkoxides yielding a complex and the association of the complex at the Li...O bond very probably occur spontaneously. The intermolecular association of complexes by alkyl substituents, causing an increase in the viscosity of the medium, is controlling step of the

EBSCOhost - printed on 2/13/2023 3:45 AM via . All use subject to https://www.ebsco.com/terms-of-use

Table 1. Kinetic Parameters for Structuring of Solutions of Complexes Li B-tert-$OC_4H_9(OR)_3$

R	Rotation period	n=1-tg	$\bar{n}$	k_T	E, kJ/mol	n=1-tg	$\bar{n}$	k_T	E, kJ/mol
		Heptane				Isooctane			
n-C_4H_9	1/2	1.5	1.7	16.2	57.33	3.2	2.7	167.0	5.11
	3/4	1.4	1.3	27.0	34.31	2.1	1.6	167.0	5.65
n-C_7H_{15}	1/2		-0.3	28.6	31.68		1.7	25.0	35.86
	3/4		0.3	62.5	14.17		1.2	769.0	11.73
n-$C_{10}H_{21}$	1/2	0.2	0.2	20.4	43.98	3.4	3.0	23.0	36.44
	3/4	0.8	0.7	33.3	26.67	2.3	2.4	23.0	36.71
iso-C_4H_9	1/2		2.4	29.4	25.0				
	3/4		2.3	47.6	15.4				
		Decane				Hexadecane			
n-C_7H_{15}	1/2					1.5	1.3	27.1	33.80
	3/4					1.9	1.9	40.0	23.20
n-$C_{10}H_{21}$	1/2		-0.3	24.4	36.89	-2.0	-2.2	62.5	13.40
	3/4		0.3	40.0	22.55	-1.8	-1.7	71.4	12.00
		Carbon tetrachloride				Tetrachlorethylene			
n-C_8H_{17}	1/2		1.79	37.6	22.36		1.72	18.8	44.62
	3/4		-0.66	140.0	6.00		3.20	75.9	11.41

EBSCOhost - printed on 2/13/2023 3:45 AM via . All use subject to https://www.ebsco.com/terms-of-use

solvent structuring rate. Orientation and solvation of the solvent molecules, affected by the polyassociated complex, seem to be the most responsive step of structuring. Therefore, by the process completion a decrease is observed in the activation energy of structuring, and an increase in the rate constant (Table 1). With increasing solvent permittivity and structural affinity of the complex for the solvent, all the process steps are accelerated and occur almost simultaneously (diagrams are narrowed). When these conditions are not observed, the time interval between the reaction steps increases and the processes overlap (broadening of the diagrams is of wave-like character).

Mass-spectra obtained for $Li[B\text{-tert-}OC_4H_9(OR)_3]$ show an abundance of fragmentary ions $An \pm R'$ (A = complex associate; n = degree of association at Li...O bond of the value 1-4; R' = hydrocarbon fragment of polyassociate elementary chain link); the mass-spectra bear evidence of complex association at the Li...O bond and R. A set of fragmentary ions $An \pm R'$ depends on the length of the alkoxide substituent of the complex. The mass of R' of the fragmentary ion increases with the length of R. The highest degree of complex association, observed in the mass-spectra irrespective of the length of the substituent ($R = C_3H_7\text{-}C_5H_{11}$), is 4. The stability of $An \pm R'$ ions decreases with increasing length of R. The mass-spectra obtained are characterized by a greater stability of $An \pm 3R'$ and $An \pm 2R'$ fragmentary ions with respect to $An \pm R'$. A comparative evaluation of the intensities made for $An \pm R'$ ions leads to a conclusion that in the mass-spectra prevail ions corresponding to trimeric and tetrameric associates of complexes. The fact that the degree of complex association is not affected by the length of the alkyl substituent ($R = C_3H_7\text{-}C_5H_{11}$) may be attributed to the formation of cyclic associates at the Li...O bond. Macrocyclic associates of complexes, bonded by interaction of alkyl substituents, form three-dimensional polyassociates shaped as cylindrical cavities (Fig. 3).

The structured solutions of complexes were studied by small angle X-ray scattering. The scattering curves obtained were smoothed over by an electronic computer, then the intensity of the solvent was subtracted and finally a correction was made for the finite height of collimator slits. Linear dependence $\ln I(\ln \Theta)$ for the angles of scattering from 2' to 30' allowed the maximum radii of

EBSCOhost - printed on 2/13/2023 3:45 AM via . All use subject to https://www.ebsco.com/terms-of-use

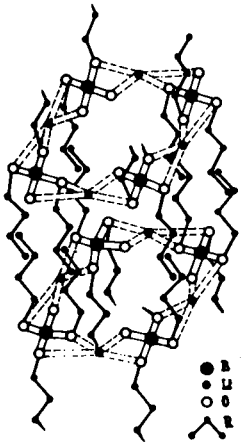

Fig. 3. A model supermolecular structure of polyassociated complexes of lithium tert-butyl--alkyl borates.

inertia to be calculated for regions of inhomogeneous electron density. Analysis of the scattering curves in the range 0.5×10^{-5} to 6×10^{-4} rad^2 yielded the following values of radii of inertia: Rg = 96 and 98 Å for 5% and 10% $Li[B\text{-}tert\text{-}OC_4H_9(OC_7H_{15})_3]$, while the scattering curve obtained for 20% solutions of complexes showed two straight-line segments with an inclination corresponding to radii of inertia 93 and 390 Å. A good agreement of Rg values (93, 96 and 98 Å) observed for varying concentrations of the complex in CCl_4 solution (5, 10 and 20%, respectively) is an evidence of a low degree of dispersion of the scattering particles. If the particles have a spherical shape, these values of radii of inertia correspond to a particle radius of 125 Å. Radii of inertia for solutions of lithium tert-butyltripropyl borate, are 146, 67 and 33 Å, those for lithium tert-butyltri-iso-butyl borate 380 and 86 Å and those for lithium tert-butyltridecyl borate 150, 80 and 42 Å, the radii of spherical scattering particles (187, 86 and 42 Å; 490 and 110 Å; 194, 103 and 54 Å, respectively) corresponding to the radii of inertia. A comparative evaluation of the scattering particle radii derived from the maximums of one-particle scattering function (8) for the structured solutions of complexes (Table 2).

The shape of the scattering particles was derived from the intensity of small angle scattering on the lnI-lnθ coordinates. The exponent of $I(\theta^{-n})$ dependence was derived from the asymptote in-

EBSCOhost - printed on 2/13/2023 3:45 AM via . All use subject to https://www.ebsco.com/terms-of-use

Table 2. Parameters of Small Angle Scattering for Structured Solutions of Complexes

Maximum order	$2\theta^2$, rad^2	S, Å^{-1}	R, Å	
			One-particle scattering	Interparticle scattering
	$Li[B\text{-tert-}OC_4H_9(OC_3H_7)_3]$			
	10% of complex in carbon tetrachloride			
1	$0.65\ 10^{-4}$	$3.28\ 10^{-2}$		76
1	$1.50\ 10^{-4}$	$5.15\ 10^{-2}$	87	
2	$2.50\ 10^{-4}$	$6.40\ 10^{-2}$		90
	$Li[B\text{-tert-}OC_4H_9(OC_7H_{15})_3]$			
	5% of complex in carbon tetrachloride			
1	$1.10\ 10^{-4}$	$4.27\ 10^{-2}$	105	
2	$2.65\ 10^{-4}$	$6.63\ 10^{-2}$	106	
2	$1.55\ 10^{-4}$	$4.97\ 10^{-2}$		114
	10% of complex in carbon tetrachloride			
1	$1.10\ 10^{-4}$	$4.27\ 10^{-2}$	105	
2	$2.80\ 10^{-4}$	$6.82\ 10^{-2}$	103	
2	$1.90\ 10^{-4}$	$5.62\ 10^{-2}$		103
	30% of complex in heptane			
1	$0.80\ 10^{-4}$	$3.64\ 10^{-2}$	125	
2	$1.90\ 10^{-4}$	$5.62\ 10^{-2}$	125	
3	$3.00\ 10^{-4}$	$7.06\ 10^{-2}$	128	
2	$1.30\ 10^{-4}$	$4.65\ 10^{-2}$		125
	$Li[B\text{-tert-}OC_4H_9(OC_{13}H_{27})_3]$			
	5% of complex in carbon tetrachloride			
1	$1.25\ 10^{-4}$	$4.55\ 10^{-2}$	99	
2	$2.00\ 10^{-4}$	$5.76\ 10^{-2}$		100
2	$3.20\ 10^{-4}$	$7.29\ 10^{-2}$	97	
3	$4.50\ 10^{-4}$	$9.02\ 10^{-2}$		100
	30% of complex in heptane			
1	$4.50\ 10^{-5}$	$2.73\ 10^{-2}$		92
2	$2.15\ 10^{-5}$	$5.90\ 10^{-2}$		98

EBSCOhost - printed on 2/13/2023 3:45 AM via . All use subject to https://www.ebsco.com/terms-of-use

clination in the wide angle scattering region. The small angle scattering of dissolved (5-10%) and solid complexes occurs at $2\theta < 1°$ on inhomogeneous tube-shaped particles, while at $2\theta > 1°$ the scattering intensity of solutions of complexes is affected by scattering particles shaped as a cylinder of a radius 90-125 Å. The degree of complex association with the help of alkyl substituents varies from 5 to 10. The complex of $Li[B\text{-}tert\text{-}OC_4H_9\text{-}(OC_7H_{15})_3]$ dissolved in heptane, exemplifying the optimum conditions of structural compatibility, forms the most highly ordered and densely packed supermolecular structure. The scattering experiment data obtained are in good agreement with the mass-spectral analysis results and, on the whole, speak in favour of the formation of complex polyassociates similar in shape to cylindrical cavities of average volume $(1\text{-}1.5) \times 10^4$ Å^3.

References

1. Lignori, A.M., G. Anzuino, V.M. Coiro, M. D'Alagni, P. Santis, M. Savino. 1965. Nature (London). 206, 358.
2. Overbergh N. 1977. Polymer. 18, N 8, 883.
3. Bosscher F., G.T. Brinke, G. Challa. 1982. Macromolecules. 15, 1442.
4. Bosscher F., G.T. Brinke, A. Eshuis, G. Challa. 1982. Macromolecules. 15, 1364.
5. Bolshakov, G.F., Z.T. Dmitrieva, Yu.J. Levus. 1984. The 4th International symposium on homogeneous catalysis. Leningrad, 1, 55.
6. Dmitrieva, Z.T., G.F. Bolshakov, Yu.J. Levus. 1985. Dokl. AN SSSR. 281, N 4, 883.
7. Dmitrieva, Z.T., A.S. Tailashev. Struktura poliassociatov kompleksov alkoksidov metallov I, III grupp. 1984. Tomsk. 58. (Preprint IKhN SO AN SSSR, N 27).
8. Guinier A., G. Fournef. 1955. In: Small Angle Scattering of X-Rays. London-New-York-Paris: Goldon and Breach, p. 199.

EBSCOhost - printed on 2/13/2023 3:45 AM via . All use subject to https://www.ebsco.com/terms-of-use

Other Contributions

EBSCOhost - printed on 2/13/2023 3:45 AM via . All use subject to https://www.ebsco.com/terms-of-use

EBSCOhost - printed on 2/13/2023 3:45 AM via . All use subject to https://www.ebsco.com/terms-of-use

PROGRESS IN POLYMER INVESTIGATIONS BY HIGH VOLTAGE ELECTRON MICROSCOPY

G.H. Michler
Institut für Festkörperphysik und Elektronenmikroskopie
der Akademie der Wissenschaften der DDR, 4020 Halle,
und
Wissenschaftliches Forschungs- und Koordinierungszentrum
im Kombinat VEB Chemische Werke Buna, 4212 Schkopau,
German Dem. Rep.

1. Introduction

Today in polymer research electron microscopy is widely applied, mainly to characterize the morphology. In general, direct investigations of polymers by electron microscopy involve three general problems:

1. Preparing ultra-thin specimens from bulk polymers (as conventional 100 kV transmission electron microscopy (TEM) usually requires) is often difficult.
2. Polymers (as organic substances) are particularly sensitive to electron beam irradiation.
3. The contrast between structural details is very low, since polymers usually consist of the same light elements.

In overcoming these difficulties the use of high voltage electron microscopy (HVEM, accelerating voltage about 1000 kV) has several advantages. Furthermore, its use favours the performance of in situ deformation tests to study directly mechanical microprocesses of deformation.

2. Experimental

To demonstrate the advantage of HVEM for investigating polymeric materials several different polymers were used with ultramicrotomy being the main preparation technique. From the bulk polymeric materials 0.5 up to 5 µm thick sections were produced in

Morphology of Polymers
© 1986 Walter de Gruyter & Co., Berlin · New York - Printed in Germany.

EBSCOhost - printed on 2/13/2023 3:45 AM via . All use subject to https://www.ebsco.com/terms-of-use

an ultramicrotome at room temperature and in a cryo-ultramicrotome, respectively. The samples were investigated in a 1000 kV JEOL HVEM. By using highly sensitive X-ray films the radiation damage of polymers was appreciably reduced (1).

3. Results

3.1. The use of the enlarged penetration depth

The main advantage of HVEM lies in its enlarged penetration depth (2). Because of the low density of polymeric materials, specimens of up to several micrometres thickness can be investigated. Relatively thick specimens are advantageous in several respects.

- Specimen preparation: It is much easier to prepare semi-thin specimens than ultra-thin specimens needed for conventional 100 kV TEM. A very useful preparation technique generally applied is ultramicrotomy. Before cutting ultra-thin sections the polymeric materials usually have to be fixed or hardened, since polymers are relatively weak materials. Semi-thin sections have a noticeably increased mechanical stability and can therefore be cut in an ultramicrotome often without the necessity of fixing or hardening the samples. These sections can have essentially enlarged areas, too. Therefore, structural heterogeneities are better and easier to determine.

- Spatial analysis of structural details: Larger structural details are better visible by using semi-thin specimens (3,4). By way of example, in high-impact polymers the shape and real size of the dispersed rubber particles can be determined more easily - Figure 1: For a commercial sample of a high-impact polystyrene (HIPS), sections of 0.1 to 4.5 µm thickness were investigated in the HVEM. The rubber particles were selectively stained with osmium tetroxide, leading to their dark appearance. The particles with small inclusions of polystyrene in their interior are dispersed in the matrix of polystyrene. Far better than Figure 1 a does Figure 1 c of the thick section show the "blackberry-like" shape and proves the existence of large rubber par-

EBSCOhost - printed on 2/13/2023 3:45 AM via . All use subject to https://www.ebsco.com/terms-of-use

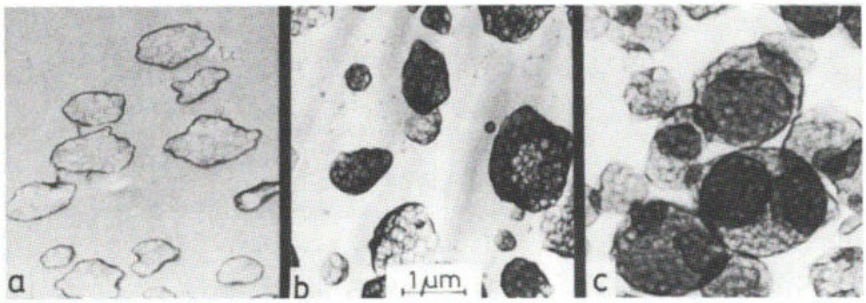

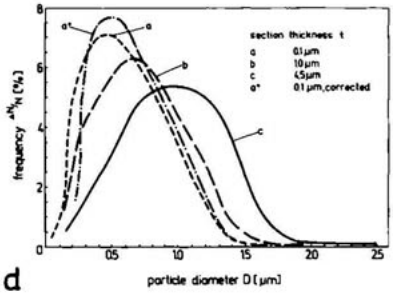

Fig. 1. Visibility of particle structure of HIPS depending on the thickness of the sections (sections stained with OsO_4)
section thickness t:
a) 0.1 µm, b) 1 µm, c) 4.5 µm
d) frequency distribution of particle diameters

ticles. The diagram compares the frequency distributions of the particle diameters on the 0.1 µm ultra-thin sections, on the 1 µm and 4.5 µm thick sections. The largest particles of about 2.5 µm in diameter appear only in the thick sections (4.5 µm thick) with a practically measurable probability.

This technique has a great practical advantage over the frequently used mathematical corrections of the frequency distribution, determined on ultra-thin sections. Mathematical solutions exist for spheres and some other regularly shaped particles (5,6). Practically disadvantageous are these mathematical corrections in as far as that the largest particle must be known which, in general, however, is not given because the ultra-thin sections contain the true diameters of the largest particles with only extremely low probability. Therefore, the mathematical corrections merely shift the maximum of the frequency distribution towards slightly larger diameters, but do not yield any information on the largest particles actually present - see curve a^+ in Figure 1 d, which is the mathematically corrected distribution of curve a. Information on these largest particles is important, since they contain a relatively high phase volume content and usually have a very negative influence on mechanical

EBSCOhost - printed on 2/13/2023 3:45 AM via . All use subject to https://www.ebsco.com/terms-of-use

properties (on strength, elongation and fracture toughness).

- Determination of inorganic filler particles: Composite materials of a polymeric matrix and dispersed inorganic filler particles form an important group of polymers. Hard particles often have diameters of up to some micrometres; thus, they cannot be determined by using ultra-thin specimens. On the other hand, semi-thin sections of composite polymers most clearly show the shape, size, and distribution of inorganic particles - Figure 2.

3.2. Observations in a state of reduced specimen damage

Polymers are particularly sensitive to electron beam. The sensitivity to irradiation increases with decreasing carbon content in the polymeric samples, that means in the sequence PS, PE, PC, PMMA, PVC, PTFE (7). The "critical dose" of damaging the molecular structure is about 0.01 C/cm^2 for PE (8). The irradiation doses of the sample, necessary for exposing usual photographic material at some 1000fold magnification, are nearly the same, i.e., the specimens are damaged solely during exposure. Polymers in a state of strongly damaged molecules are frequently well suited for detecting the supermolecular structure or morphology, because the morphology is often not altered by molecular processes.

There are, however, several problems making the investigation of

Fig. 2. Size and shape of inorganic filler particles of different kind (chalk, talc) in a polymer matrix (polypropylene) (4.5 µm thick section; due to their higher density the particles clearly appear dark).

EBSCOhost - printed on 2/13/2023 3:45 AM via . All use subject to https://www.ebsco.com/terms-of-use

polymeric material in an undamaged state necessary. Using a HVEM reduces the damaging rate to a third, compared with the 100 kV TEM (9). An appreciably reduced damaging rate was achieved by using highly sensitive X-ray films (1). Their high sensitivity arises from double coating with thicker emulsion layers or higher silver halide content. They can therefore be used in the HVEM due to the greater penetration power.

- Determination of irradiation-induced changes: The reduced radiation damage enables the resulting changes in morphology to be investigated over a longer time. Figure 3 shows the same area of a two-phase polymer blend immediately after the beginning of irradiation (on the left) and after stronger irradiation (on the right). The dominant process of radiation damage is mass-loss. Mass-loss is much stronger for the surrounding phase and lower for the particle phase. The blend consists of the two components PVC (polyvinylchloride) and SAN (styrene-acrolonitrile copolymer). Mass-loss is known to be stronger for PVC than for SAN, indicating that the surrounding phase is PVC and the particle is SAN. Therefore, the determination of mass-loss is useful to distinguish between several polymer phases.

Another example of irradiation-induced changes in morphology is demonstrated in Figure 4, showing a cryo-thin section of a segmented polyurethane with a spherulitic structure. At the very beginning of electron beam irradiation the spherulites only show a weak contrast (Fig. 4 a). After electron irradiation the spherulites appear rich in contrast with the radial elements inside the spherulites appearing decidedly sharper (Fig. 4 b). Studying solely the right half of the image, i.e. after irradiation damage, could yield the misinterpretation that the radial elements consist of material of higher density. But the real reason of the fibrils is that amorphous layers between parallely arranged lamellae are contracted due to the influence of the electron beam. Accordingly does the interior of the spherulites show a radial distribution of sticks of parallely arranged amorphous and crystalline elements. This effect of "irradiation-induced contrast enhancement" was recently demonstrated (4).

EBSCOhost - printed on 2/13/2023 3:45 AM via . All use subject to https://www.ebsco.com/terms-of-use

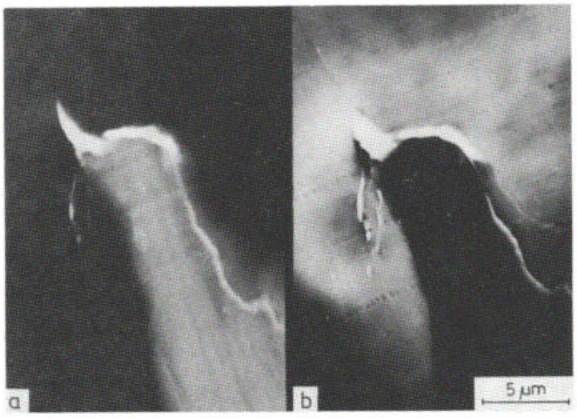

Fig. 3. Different mass-loss of the two polymer phases PVC and SAN by electron irradiation in the HVEM
a) at the beginning,
b) after intense irradiation.

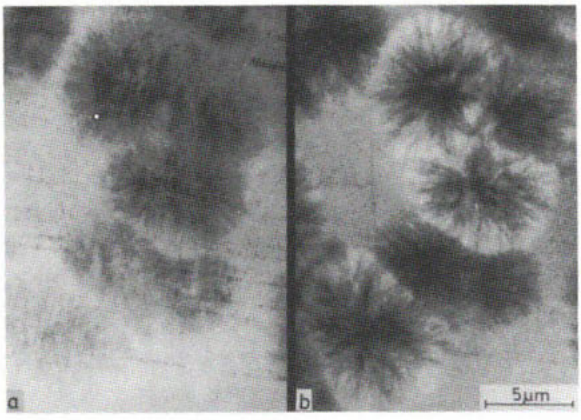

Fig. 4. Development of contrast of the radial elements inside the spherulites in segmented polyurethane
a) at the beginning,
b) after intense irradiation.

- Determination of molecular order: The reduced radiation damage yields a longer life-time of the molecular arrangement and of the crystalline structure of semi-crystalline polymers. Thus, images in bright-field and dark-field contrast and diffraction patterns can be taken from one and the same area of the specimen - Figure 5. The diffraction pattern (Fig. 5c) is nearly the same as for single crystals of PE. This indicates the nearly parallel arrangement of the lamellae and the very well pronounced orientation of the macromolecules inside the lamellae. A comparison of bright-field and dark-field images reveals a better visibility of the crystalline elements and the nearly entire absence of the striations in the dark-field image. These striations are scratches from the cutting in the ultramicrotome. They do not influence the dark-field contrast. They therefore enable a clearer image to be obtained of the interesting structure without these preparation artefacts.

3.3. Deformation experiments

Thick specimens to be used in HVEM have a noticeably increased mechanical stability which facilitates deformation experiments (10). The investigation of deformed specimens is effective in two ways:

EBSCOhost - printed on 2/13/2023 3:45 AM via . All use subject to https://www.ebsco.com/terms-of-use

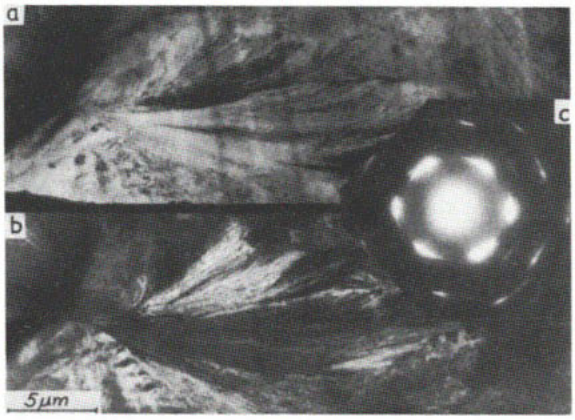

Fig. 5. Sheaf-like structure in branched polyethylene having a molecular weight of M_w = 7600
a) bright-field,
b) dark-field,
c) diffraction pattern.

- The morphology of polymers can be determined using a special effect of "straining-induced contrast enhancement" (4).

- Deformation structures and mechanical microprocesses can be investigated. The technique and results of deformation processes of several polymers have been described elsewhere, e.g. for high-impact polymers in (11) and for polystyrene in (12). Such deformation tests enable "property determining structures" and the strength of adhesion between several phases to be investigated.

An example is demonstrated in Figure 6, snowing a thermoplast/

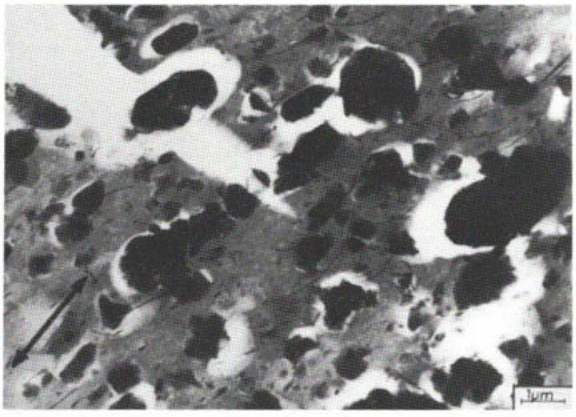

Fig. 6. Deformation and crack propagation in a particle filled polymer composite (deformation direction see arrow).

EBSCOhost - printed on 2/13/2023 3:45 AM via . All use subject to https://www.ebsco.com/terms-of-use

chalk-composite: Under the action of stress the polymer matrix ruptures around the chalk particles and voids appear. This indicates the absence of a remarkable adhesion between particles and polymer matrix. The large voids are starting points of cracks.

References

1. Michler, G.H., Ch. Dietzsch. 1982. Crystal Res. & Technol. 17, 1241-1254.
2. Sharp, J.V., S.G. Burnay. 1970. Proc. 7th Int. Congr. El. Micr., Grenoble, vol. I, p. 49.
3. Ohno, S., K. Yoshida, F. Murata, T. Nagata. 1978. Proc. 9th Int. Congr. El. Micr., Toronto, vol. II, p. 14.
4. Michler, G.H. 1984. Ultramicroscopy 15, 81-100.
5. Lenz, F. 1956. Z. wiss. Mikroskopie 63, 50-56.
6. Voss, K. 1978. Biometrical J. 20, 425-434.
7. Vesely, D., A. Low, M. Bevis. 1976. In: Developments in Electron Microscopy and Analysis (J.A. Venables, ed.). Academic Press, London/New York/San Francisco, pp. 333-336.
8. Grubb, D.T. 1974. J. Mater. Sci. 9, 1715.
9. Richardson, M.J., K. Thomas. 1972. Proc. 5th Europ. Congr. El. Micr., Manchester, p. 562.
10. Bethge, H. 1974. Proc. 8th Int. Congr. El. Micr., Canberra, vol. I., p. 724.
11. Michler, G.H. 1979. Plaste u. Kautschuk 26, 497-501, 680-684; 1984. Proc. 16th Europhysics Conf. Macromolecul. Phys., Brugge, pp. 62-65.
12. Michler, G.H. 1985. Colloid & Polymer Sci. 263, 1-13.

EBSCOhost - printed on 2/13/2023 3:45 AM via . All use subject to https://www.ebsco.com/terms-of-use

THE MORPHOLOGY OF ION EXCHANGE RESINS AND OTHER FUNCTIONAL POLYMERS. COMMENT ON THE SYSTEMATIZATION AND THE TERMINOLOGY

G. Schwachula, K. Häupke

Research Department for Ion Exchangers
VEB Chemical Combine Bitterfeld
DDR 4400 Bitterfeld
German Democratic Republic

In the recent time, the following class of materials is usually summarized under the common top term "functional polymers":

- ion exchange resins,
- adsorbent resins (with ionogen groups),
- adsorbent polymers (without ionogen groups),
- redox resins,
- catalysts - based on organic polymers,
- polymeric reagents,
- polymeric carriers for reagents, catalysts and other agents,
- stationary phases for chromatography - based on organic polymers,
- carriers for solid phase reactions.

Materials complying with this definition show the following common signs: They can interact with components of the surrounding or the penetrating media, in which they do not dissolve, have the character of a bulk material and (at least theoretically) they do not suffer any undesirable chemical alterations during use. They can be brought back to the original state by cyclically recurrent regeneration processes. Using these materials, ionic, side valence or in extreme cases main valence bonds can be produced or solved, catalytic (also biocatalytic) functions can operate, molecular sieve effects and chemical affinities can be utilized and the reaction or transport kinetics peculiar features can be respected. The first precondition for all these functions is the accessibility of active centres or of the areas for transport, stay and reaction; this requires certain dispersity inside the materials. According to our experience, these are not so much problems of the chemical structure which require the systematization and

Morphology of Polymers
© 1986 Walter de Gruyter & Co., Berlin · New York - Printed in Germany.

EBSCOhost - printed on 2/13/2023 3:45 AM via . All use subject to https://www.ebsco.com/terms-of-use

the terminological elucidation. The chemical character of the monomer units can be defined clearly (at least in ideal cases), but significant effects already result in an uneven distribution of different monomer units in the polymeric chain. This is unavoidable, owing to the usually different monomer reactivities, and it leads to weaker and stronger crosslinked regions in the submicroscopical structure of the beads. We have already showed it before.

The functional polymers are usually synthetized by polymerization where the outcomes of the synthesis are practically always macromolecular networks. In the major part of cases, crosslinking is brought about by the copolymerization of a bifunctional monomer (as an important example, styrene should be mentioned) with a polyfunctional monomer (e.g., divinylbenzene).

It should be noted that this, mostly radical initiated copolymerization, is regulary carried out as a suspension polymerization in order that a rather uniform batch of particles is obtained which has a favourable form for technical application.

If any further modifications of the synthesis are neglected - e. g., in the copolymerization of styrene with divinylbenzene - a polymer results which is compact, does not show any manifest areas for transport, stay and reaction, and consequently, it does not meet the definition of functional polymers. This is essentially not altered also through a possibly following introduction of functional groups (e.g., by sulphonation). Below, conditions are given under which these polymers gain the desirable inner dispersity. At first, the second limiting case should be described:

The copolymerization is now carried out in the presence of usually liquid additives which are miscible with monomers but which do not dissolve or homogeneously swell the polymer. Furthermore, they cannot react under the conditions of polymerization, and therefore they are called "inerts". These properties inevitably bring about a separation of phases during the polymerization and cause a markedly heterogeneous character of the polymer formed. Using a formula with a high contribution of crosslinking agent and a quantity of the inert which sufficiently exceeds the lower specific limit for the system, phase separation leads to two coherent colloid dispersed systems consisting of the precipitated

EBSCOhost - printed on 2/13/2023 3:45 AM via . All use subject to https://www.ebsco.com/terms-of-use

polymeric material and of the separated inert. After the latter is removed, in its place, a coherent system of pores remains which penetrates the polymer matrix. A porous material results, characterized by specific surfaces up to 1000 m^2/g. This porosity is essentially retained during modifications by polymer analogous reactions or similar operations.

Consequently, a true porous sorbent or a porous polymeric reagent results in that latter case, the effectiveness of which lies in its colloid structure by preservation a macrostructure (0.01 - 1 mm beads) facilitating the manipulation.

The former structure - which was characterized as essentially inaccessible - can under certain conditions also become quite accessible and therefore functional. This is already demonstrated by mass application of ion exchange resins with unmodified matrices. These polymers possess a limited swelling in affine liquids, according to their degree of crosslinking. If contacted with such a liquid, these polymers take away a certain amount of it and expand the network (volume increase). In this way, the areas for transport, stay and reaction come into existence which are filled with affine liquids and with substances dissolved in them. This state of inner dispersity is hitherto called "swelling porosity" and "microporosity".

The latter term is a subject of our criticism because the areas for transport stay and reaction originated through swelling need not lie on a "micro"-scale at all. At a very low degree of crosslinking, they can be accessible for even larger molecules or ions than for those which can penetrate in the macropores of a porous polymer system. Moreover, we object to the use of the terms "pores" and "porosity" only in connection with polymers of this kind in general. We rather suggest to designate the areas for transport, stay and reaction as "meshes", if their existence depends on the presence of liquids solvating the polymer chains. In this way we would like to differentiate from the term "pores" which can (but are not obliged to) exist even in the absence of such liquids. Owing to this, the formerly mentioned term "swelling porosity" should also be criticized, even if it explicitly describes that the areas for transport, stay and reaction are formed by swelling only. We suggest to replace it with the term "swelling dispersity", if the first limiting state is concerned.

EBSCOhost - printed on 2/13/2023 3:45 AM via . All use subject to https://www.ebsco.com/terms-of-use

Thus, the significance of the formerly described inner dispersity of these systems would be accented.

In connection with the concept of meshes, a quite vivid picture of the areas for transport, stay and reaction appears in such swelling dispersed polymers. This would hold for more or less tight three-dimensional networks - according to the degree of crosslinking - consisting of essentially flexible segments of the polymer chains and in which preferential ways and free areas do not exist. This state indeed could be realized in exceptional cases only. Usually, the width of meshes fluctuates at a mean value statistically as the distribution of the crosslinking points is random.

These "swelling dispersed" functional polymers defined here are also commonly called "gel type" and juxtaposed to the second limiting state "porous" or to the transition states to it. This designation is also worthy of criticism, as these functional polymers do not belong to the gels permanently, but in the swollen state only. Beyond this state, they can be described as glassy polymers.

Contrary to the swelling dispersed functional polymers, we want to consider "pore dispersed" systems or - using a more simple term - "porous polymers".

We define them as:

"Functional polymers which show areas for stay, transport and reaction accessible permanently or after a reasonable pretreatment to gases and which have an inner surface that can be measured by the BET-method, giving values above the measuring error".

Using the term "pore dispersed", we should not forget that the pores penetrate a system of agglomerated microgels which may be considered as inaccessible in limiting cases only. These microgels (globules) have still a fine structure, and therefore they can be essentially accessible:

They are built from a large number of smaller particles (nodules) and their matrix finally consists of a swellable polymer with the corresponding swelling dispersity in accordance with the above description. Certainly, the meshes of the matrix can be so narrow - as it is the second limiting case owing to the typical high crosslinking - that they are often not of use for characteristic applications.

EBSCOhost - printed on 2/13/2023 3:45 AM via . All use subject to https://www.ebsco.com/terms-of-use

This absolutely holds for a typical application of the pore dispersed functional polymers in the absence of swelling solvents, i.e. in gases or in liquid media where the swelling dispersed polymers are practically ineffective. The principal priority of pore dispersed systems is the independence of solvents.
In accordance with the above treatment, the presence of the swelling dispersity of the matrix has always to be considered in the cases of polymers in transition states which are still designated as "pore dispersed" polymers. This is then a reason for the existence of additional spectra of the areas for transport, stay and reaction. The swelling dispersity should be virtually defined as a top term, but this seems not to be practical. The differentiation of both dispersity types - swelling and pore dispersity - has been generally adopted, and so it should not be given up.

Our definition of pore dispersity finds fault with the terms used so far for the description of ion exchange resins as "macroporosity", "true porosity", etc. It has already been indicated before that the "pores" - in accordance with the foregoing definition - can be smaller than meshes, and therefore the term "macroporous" leads to confusion. The designation "true porosity" seems not to be admissible as a general term, too, because it could be mixed with the sub-term "permanent porosity" which seems to be necessary, according to the recent knowledge.
A more detailed work on pore dispersed polymers showed how complicated the description of their structure was. The above mentioned second case of the structure of functional polymers can rather mean a non realizable ideal state. It was observed that the existence of pores - i.e. those measured by gas adsorption at dew point (BET-method), and consequently in the absence of swelling agents - depends on the history of the polymer. This fact already becomes obvious for ion exchange resins which have evidently a pore dispersed character with respect to their turbidity, opacity, or total non-transparency. These can be obtained from glassy polymers, but they apparently lose their "porous character", if dried.
For the elucidation of such quite confused facts, the porosity (the pore dispersity, more corectly) should be seen as a top term, and one should differentiate between latent and permanent

EBSCOhost - printed on 2/13/2023 3:45 AM via . All use subject to https://www.ebsco.com/terms-of-use

porosity. The latter represents the second limiting case which is not absolutely realizable, as already mentioned above. If we wish to comment on these relations, we have to keep in mind that the inhomogenities on a colloidal scale - granting a pore dispersed character of the polymer - result, if the crosslinking copolymerization occurs in the presence of the inerts with a suitable qualitative and quantitative composition of the system and under proper conditions which guarantee phase separation during the copolymerization. In order that the porosity can be quantitatively ascertained, the inerts have to be removed subsequently. This mostly occurs under conditions where the polymer finds oneself in a state above the glass-transition-point for a certain time, owing to swelling or to a temperature increase. In addition, if we realize that the state of separation in colloidal dimensions following from microsyneresis, is rich in energy, and so microsyneresis is less probable, it is evident that the elasticity (the retraction force) of the polymer skeleton tends to suppress this state of separation by the micro-Brownian motion of chain segments. The pores consequently collapse according to the effectiveness of the retraction force of the polymer matrix. As the formation of pores by separation (microsyneresis) takes place on fully relaxed polymer skeletons usually above the glass transition temperature and with no formation of main valence bonds, in accordance with the definition of "porosity", these pores must at least exist as latent after the inerts have been removed. They can be restored through suitable measures after they have partially or fully disappeared in a system comprising a swelling or imbibitional agent. But, for this reason, the retraction force - which acts against the dispersion of the polymer - has to be overcome; hence, another force has to exist, acting in the opposite direction thermodynamically. This force arises as a consequence of the effort to wet the actual and possible inner surfaces of the pores. As such liquids, essentially, all swelling agents for the polymers in question can be used, i.e., all which solvate the polymer chain, and moreover a series of solvents which wet the polymer surface sufficiently, but which cannot penetrate into the matrix. Their efficiency consists in the imbibition into porous polymers, consequently, they can be designated as imbibitional agents.

EBSCOhost - printed on 2/13/2023 3:45 AM via . All use subject to https://www.ebsco.com/terms-of-use

The liquids like this, e.g., in the case of the styrene-divinylbenzene copolymers, liquid aliphatic hydrocarbone, alcohols etc., are operative, so that the actual pores are expanded and/or the latent pores opened, and the polymers are dilated. This has to be differentiated from swelling at which the matrix is also dilated according to the definition. When the swelling or imbibitional agents are removed under such conditions that the retraction forces cannot be operative, then a polymer in the state of maximal porosity remains which is the sum of the permanent and latent porosities. As a minimal porosity, in return, the permanent part can be considered, which is evident under all circumstances. A restriction, however, should be made, because swelling as well as imbibitional agents show different efficiency, and therefore "the maximal porosity" depends on their affinity (wettability) in the respective system. For this reason, it is necessary to know the treatment after which the maximal porosity was measured. This process of the "opening of pores" can be brought about when, e.g. styrene-divinylbenzene copolymers are swollen in a good swelling agent (toluene) at first, and the latter is expelled by a non-swelling imbibitional agent (methanol) later. Provided that drying takes place at a temperature at which the retraction force of the polymer skeleton are still not mobilized (under 81°C), the state of maximal porosity is reached. This is metastable and can be annulated by heating over 81°C or through a contact with swelling agents.

Martinola and collaborators described a similar method of opening the pores for hydrophilic ion exchange resins. They replaced water as the swelling agent by an imbibitional agent, i.e. isopropanol, and the latter repeatedly by hexane, for the sake of the determination of the porosity which usually disappears, partly or totally.

The total porosity of the functional polymers, developed in the presence of the swelling and imbibitional agents, consists of permanent and latent porosity. The former stable part of total porosity exists even in the absence of swelling or imbibitional liquids, but the latter is only evident and measurable when the pores are opened.

With regard to these circumstances, it appears to be not reasonable to use definitions of porosity which include concrete data

EBSCOhost - printed on 2/13/2023 3:45 AM via . All use subject to https://www.ebsco.com/terms-of-use

as the pore diameter, specific and total pore volumes, because these values depend on the pretreatment of materials.
In addition the definition of porosity is limited if the pores (at an extreme increase in the specific surface) become so tight that their detection depends on the molecular size of the measuring gas or if they cannot be measured by this method at all. This is the case at macronet-polymers, described by Davankov and collaborators, which are prepared by subsequent crosslinking chains of soluble linear polymers. It must be admitted that they are pore dispersed according to our definition (though if measured with argon only), but they show a strong dependence of the size of the transports areas on the swelling state, which again is a characteristic feature of swelling dispersity. This property joins macronet polymers to functional polymers prepared by the above mentioned method, aiming at a maximal specific surface. They can also be described as "heterogeneous swelling dispersed". Furthermore, as said before a swelling despersed system is entirely homogeneous only exceptionally. This inhomogeneity can be increased, if the functional polymers are synthetized as described above, using inerts, but the amount of the inert is so low that no porosity according to the definition results. The polymers thus prepared have a swelling dispersed structure which is, however, looser and more heterogeneous than in the case of polymers entirely prepared without additives. They occupy the last space in a continous sequence:

- swelling dispersed, narrow distribution of mesh sizes
- swelling dispersed, wide distribution of mesh sizes
- heterogeneous swelling dispersed
- pore dispersed, without permanent porosity
- pore dispersed, mostly with latent porosity
- pore dispersed, mostly with permanent porosity.

In conclusion, it may be said that a continuous spectrum of properties can be obtained, using all possibilities for manipulating the physical structure of the functional polymers. It is in the interest of the utilization of all these possibilities if an unified language is applied to these relations using explicit definitions of the systems and proper terms.

EBSCOhost - printed on 2/13/2023 3:45 AM via . All use subject to https://www.ebsco.com/terms-of-use

A MODEL OF FREE VOLUME DISTRIBUTION OF AMORPHOUS POLYMERS AT GLASS TRANSITION

V. Bouda
Faculty of Electrical Engineering, Technical University of Prague, 166 27 Praha 6, Czechoslovakia

1. Introduction

The phenomenology of the glass transition of amorphous polymers has been extensively reviewed by a number of authors (1,2,8). The cause of this effect has been treated as a thermodynamic transition of either first or second order, or as a kinetic process. In this paper the glass transition is characterized as a kinetic process retarded due to the reduction in molecular mobility with decreasing temperature.

We started from the Doolittle (3) and WLF (4) concept, i.e. the mobility at any temperature depends primarily on the free volume remaining in the molecular structure. According to the concept, for the great majority of systems the fractional free volume at the glass transition approaches to 0.025. This value is not in accordance with the other free volume concepts (1), which lead to markedly larger numerical values (0.05 - 0.20). Little is known about the effect of internal structure on the transition. The presented model should contribute to better understanding these relations.

2. The Model of Free Volume Distribution

2.1. Free volume at temperature $T > T_m$

Total equilibrium free volume at $T > T_m$: The most convenient measure of the free volume is

$$\Delta V = V - V_c \qquad (1)$$

Morphology of Polymers
© 1986 Walter de Gruyter & Co., Berlin · New York - Printed in Germany.

EBSCOhost - printed on 2/13/2023 3:45 AM via . All use subject to https://www.ebsco.com/terms-of-use

where V is the total observed volume at temperature T, and V_c is the volume occupied by the molecules at temperature T in a closely packed crystalline state.

According to Eyring's theory (5) , unoccupied sites or vacancies in a liquid move at random as they are filled and created anew by molecules jumping from one site to another. Each jump is made by overcoming an energy barrier of height E_v. The fractional free volume at temperature T has the thermodynamic equilibrium value

$$f = \frac{\Delta V}{V_c} = \frac{n}{N} = e^{-\frac{E_v}{kT}} \qquad (2)$$

where N is the number of molecules which would fill the volume of the whole system, and n is the number of vacancies; k is the Boltzmann constant (1.38×10^{-23} $J.K^{-1}$).

For low-molecular-weight substances the energy of formation of vacancy, E_v, can easily be calculated from the heat of evaporation. As polymer cannot be evaporated a reasonably good prediction of E_v cannot be obtained by this method. However, the thermal expansion coefficient of liquids (whether polymeric or not) represents primary creation of additional free volume. The much smaller magnitude of the thermal expansion coefficient of solids arises only from anharmonicity in the dependence of potential energy on interatomic or intermolecular distances. Therefore, the temperature dependence of the free volume ΔV above the glass transition temperature can be approximated by the equation

$$\Delta V = V_c(\alpha_l - \alpha_g)T \qquad (3)$$

where α_l and α_g (K^{-1}) are coefficients of thermal expansion above and below the glass transition temperature respectively.

Free volume distribution at $T > T_m$ (uniform distribution): A two-phase structural model based on experimental evidence has been proposed for amorphous solid state of polymers (6). Two major elements of the model are the grains consisting of ordered spherical domains and the intergrain regions involving molecules that are in more truly random conformation. Also, the glassy

EBSCOhost - printed on 2/13/2023 3:45 AM via . All use subject to https://www.ebsco.com/terms-of-use

solidification can be treated as a kinetic process in a two-phase structure (7). The total volume V of polymer is composed of two parts:

$$V = V_o + V_d \tag{4}$$

where V_o and V_d are the volumes of ordered and disordered regions respectively. We can write that

$$V_o = x_o V \tag{5}$$

$$V_d = x_d V \tag{6}$$

where x_o and x_d are the volume fractions of the ordered and disordered regions respectively. If no other phase is present in the system then $x_o + x_d = 1$.

Also, the sum of the free volumes is composed of two parts:

$$\Delta V = \Delta V_o + \Delta V_d \tag{7}$$

where ΔV_o and ΔV_d are the free volumes in ordered and disordered regions respectively. In the case of uniformly distributed free volume throughout the whole volume of polymer

$$\Delta V_o = x_o \Delta V \tag{8}$$

$$\Delta V_d = x_d \Delta V \tag{9}$$

The decrease in the free volume ΔV, ΔV_o, and ΔV_d above the temperature T_m according to the eqs.(3,8,9) is represented schematically in Fig.1 by heavy lines.

2.2. Free volume redistribution at temperature $T \leq T_m$ (rise of non-uniform distribution at temperature of potential crystallization)

When a liquid is cooled below a temperature of potential crystallization T_m , it may either crystallize or become an undercooled liquid. The later occurs when crystallization is impeded, e.g. by high viscosity and low molecular symmetry. It is usually implied that such a material is incapable of structural

EBSCOhost - printed on 2/13/2023 3:45 AM via . All use subject to https://www.ebsco.com/terms-of-use

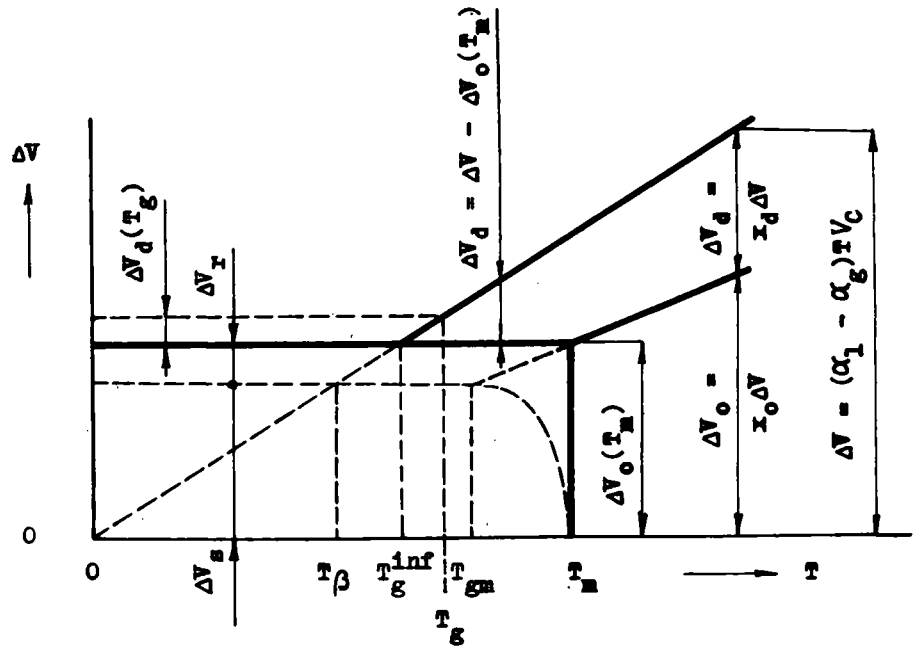

Fig.1. A model of free volume distribution of amorphous polymers

ΔV	free volume $\Delta V = V - V_c$
V	total volume at temperature T
V_c	volume occupied at temp.T in close packed crystalline state
ΔV_o	free volume in ordered regions
ΔV_d	free volume in disordered regions
ΔV_r	residual free volume in ordered regions
ΔV_s	stable part of free volume in ordered regions
$\Delta V_d(T_g)$	free volume in disordered regions "frozen" at temp. T_g
T	absolute temperature
T_m	potential temperature of crystallization
T_{gm}	temperature of transition in rubbery state
T_g	glass transition temperature at real cooling rate
T_g^{inf}	glass transition temperature at infinite slow cooling rate
T_β	temperature of β-relaxation
α_l	coefficient of thermal expansion of polymer liquid
α_g	coefficient of thermal expansion of polymer glass
x_o	volume fraction of ordered regions
x_d	volume fraction of disordered regions

EBSCOhost - printed on 2/13/2023 3:45 AM via . All use subject to https://www.ebsco.com/terms-of-use

organisation of a perfection necessary for normal description of crystallinity. This cannot be so. Atactic polymers must, by the very nature of statistical probability, exhibit local regions of structural regularity which, if not crystallising in the accepted sense, can be locally correlated to form some ordered regions. Also, the fact that melts of semicrystalline molecules, although very viscous, show rapid crystallization when cooled, might be an indication that the conformation of a polymer molecule in such a melt is more irregularly folded than that of completely random coil. It appears that, apart from low-angle X-ray diffraction and light scattering, we do not have suitable tools to investigate structures of this kind. There are some semi-empirical data concerning this structure (5-10). It seems that orientational ordering of the long axis of the molecules exists in ordered domains, i.e. their inner structure is the nematic mesophase. There would exist in this regions the same type of interchain and intrachain interactions that exist in crystallites. Based on density considerations, Robertson (9) suggested that the high densities of amorphous polymers in solid state are caused by molecular chain segments which tend to align more-or-less parallel to one another with nearly constant spacing. With respect to these facts we assume that the density within the ordered regions below the temperature of potential crystallization, T_m, is about the same as that in a real crystal. In terms of free volume in ordered regions we can write $\Delta V_o = 0$.

In contrast to thermodynamic transition of the first order (crystallization of crystalline variety), the amorphous polymers do not undergo any jump in a plot of volume against temperature at temperature T_m (see Fig.1). Therefore, one must admit the process of transformation of the free volume ΔV_o in the different form of free volume. According to ref.(12), the transformation in stable holes occurs at temperature T_m. These holes can represent the "frozen" part of free volume. Ordered region becomes through this process relatively rigid and its thermal contraction is given only by decreasing molecular vibration.

The amount of free volume in disordered regions ΔV_d at temperature $T < T_m$ is governed by the stable part of free volume in ordered

EBSCOhost - printed on 2/13/2023 3:45 AM via . All use subject to https://www.ebsco.com/terms-of-use

regions $\Delta V_o(T_m)$ = const. Under these conditions eq. (7) reduces to

$$\Delta V = \Delta V_o(T_m) + \Delta V_d \tag{10}$$

In this equation the course of ΔV has the same character as in the regions $T > T_m$ (see Fig.1). That is because the amorphous polymers do not undergo even any change in a slope of a plot of volume against temperature at temperature T_m (it is not a thermodynamic transition of the second order). Consequently, during the subsequent cooling down also the free volume in disordered regions diminishes to zero.

2.3. The glass transition

The glass transition can be related to the state when the free volume in disordered regions decreases to zero, i.e. $\Delta V_d = 0$. This can happen at infinite slow cooling rate at temperature T_g^{inf}. From eq.(10) then follows

$$\Delta V(T_g^{inf}) = \Delta V_o(T_m) \tag{11}$$

The glass transition at real cooling rates occurs at temperature T_g. The free volume in disordered regions ΔV_d decreases in this case to definite value of $\Delta V_d(T_g)$. From eq.(10) follows

$$\Delta V(T_g) = \Delta V_o(T_m) + \Delta V_d(T_g) \tag{12}$$

Substitution for $\Delta V_o(T_m)$ in eq.(11) from eq.(8) leads to

$$\Delta V(T_g^{inf}) = x_o \Delta V(T_m) \tag{13}$$

There is no change in a slope of $\Delta V(T)$ at temperature T_m (see paragraph 2.2). Therefore, the approximation from eq.(3) for both $\Delta V(T_g^{inf})$ and $\Delta V(T_m)$ in eq.(13) can be used:

$$T_g^{inf} = x_o T_m \tag{14}$$

EBSCOhost - printed on 2/13/2023 3:45 AM via . All use subject to https://www.ebsco.com/terms-of-use

3. Discussion

The introduced model has been proved in relation with published experimental data (2,6,8, 11-18).

3.1. Free volume distribution at $T > T_m$

The meaning of the unoccupied sites or vacancies in polymers above the melting temperature T_m is rather vague. Eyring (5) suggested that the volume of vacancies in low-molecular liquids has the size of the individual molecule. This view cannot be directly admitted in the case of polymers with complicated macromolecular chains. However, the energy of the vacancy formation, E_v, from eqs.(2) and (3) can be calculated:

$$E_v = -kT \ln(\alpha_l - \alpha_g)T \qquad (15)$$

The calculated value of E_v for temperature $T=T_m$ of some important polymers are shown in Table 1. The average value of E_v of polymers

Table 1. Calculated Values of the Energy of the Vacancy Formation E_v. Data from ref.(2).

	Polymer	T_m,K	$(\alpha_l-\alpha_g)x10^4$	$E_v x10^{20}$,J
1.	Polystyrene	512	4.08	1.11
2.	Poly(methyl methacrylate)	453	3.57	1.14
3.	Poly(vinyl chloride)	540	4.07	1.13
4.	Poly(ethylene terephtalate)	545	5.85	0.86
5.	Polycarbonate of bisphenol A	503	3.24	1.26

indicated (1-4) is 1.06×10^{-20} J and corresponds well to the heat of evaporation per group $-CH_2-$, 1.054×10^{-20} J (refs.11 and 2, p. 132). Also, the value $E_v=1.26 \times 10^{-20}$ J of polycarbonate are in accordance with heat of evaporation per group -O-, 1.58×10^{-20} J. Both groups $-CH_2-$ and -O- represent the smallest group in the main

EBSCOhost - printed on 2/13/2023 3:45 AM via . All use subject to https://www.ebsco.com/terms-of-use

chain of the mentioned polymers. Therefore, one can suppose that the vacancies in polymer melt are in relation to the volume occupied by the smallest groups of the main chain.

3.2. Free volume distribution at $T < T_m$

Relation of ΔV_o to the ductility in glassy state: The process of stable holes generation in ordered regions near below the temp. of potential crystallization T_m was studied previously (12). It has been proved that the kinetics of the process is given by the cummulation of the holes from groups which reach the thermofluctuation energy equal to the energy of vacancy formation E_v. As can be seen in Fig.1, the free volume in ordered regions $\Delta V_o(T_m)$ gradually divides in the "frozen" part of free volume of stabile holes ΔV_s, and in residual free volume ΔV_r. The free volume ΔV_r seems to be in relation to the ductility of material in the glassy state. Fractional free volume $\Delta V_r/V_c$ of polymers in glassy state can be calculated from the theory. Polycarbonate or poly(ethylene terephtalate) with considerably increased ductility relative to vinyl polymers such as polystyrene or poly(methyl methacrylate) have higher calculated value of $\Delta V_r/V_c$. The value of $\Delta V_r/V_c$ = = (0.025 - 0.12) in relation to the cooling rate in the temperature region of T_m follows from the theory as well.

Relation of ΔV_d to the plastic flow: From eq.(10) (and also from Fig.1) can be seen that the thermal expansion of the thermal activated free volume in disordered regions ΔV_d is the only source of the thermal expansion of the total free volume ΔV. In accordance with the concept that the molecular mobility depends primarily on the thermally activated part of free volume, the structural mechanism of the deformation in the rubbery state can be more accurately described. One can say that the free volume in disordered regions allows the relatively rigid ordered domains to move easily as individual units and makes possible the plastic flow. In accordance with the view of Yeh (6), also the plastic flow in the glassy state may be connected with this mechanism.

EBSCOhost - printed on 2/13/2023 3:45 AM via . All use subject to https://www.ebsco.com/terms-of-use

3.3. Free volume distribution in the glassy state ($T < T_g$)

Relation of ΔV_d to the free volume in WLF equation: The amount of the free volume in disordered regions ΔV_d follows from eqs. (12) and (11) or directly from Fig.1:

$$\Delta V_d(T_g) = \Delta V(T_g) - \Delta V(T_g^{inf}) \tag{16}$$

Substituting from eq. (3) we obtain

$$\Delta V_d(T_g) = V_c(\alpha_l - \alpha_g)(T_g - T_g^{inf}) \tag{17}$$

and fractional free volume in disordered regions

$$f_d = \frac{\Delta V_d(T_g)}{V_c} = (\alpha_l - \alpha_g)(T_g - T_g^{inf}) \tag{18}$$

The values of f_d have been calculated for many polymers. Some of the results are listed in Table 2. There are rather great

Table 2. Calculated Values of Fractional Free Volume in Disordered Regions at Glass Transition f_d from eq.(18)(data from ref. 2) in Comparison to the Values of Fractional Free Volume f_g from equation WLF (ref.8, p.277)

Polymer	$(\alpha_l - \alpha_g)\times 10^4$ K^{-1}	T_g^{inf} K	T_g K	f_d model	f_g WLF
Polystyrene	4.08	325	371	0.019	0.033
Poly(methyl methacrylate)	3.57	308	379	0.025	0.013
Poly(ethyl methacrylate)	3.00	270	335	0.020	0.025
Poly(n-butyl methacrylate)	3.00	203	300	0.029	0.026
Poly(methacrylate)	4.00	222	276	0.022	0.024
Polyisobutylene	3.86	101	198	0.037	0.026
Poly(vinyl acetate)	4.09	258	303	0.018	0.028
Average				0.024	0.025

EBSCOhost - printed on 2/13/2023 3:45 AM via . All use subject to https://www.ebsco.com/terms-of-use

differences between the values of calculated fractional free volume f_d and the fractional free volume f_g from WLF equation for individual polymers. This is probably a consequence of the difficulties with the measurement of the coefficients of thermal expansion and rather great variation of their values in literature. The average values of f_d and f_g fit already well. There is also a rule that T_g^{inf} is in average about 50–60 K below the glass transition T_g (13). Tobolsky and Bueche (ref.2, p.68) introduced another rule about the average value of $(\alpha_l - \alpha_g) = 5 \times 10^{-4}\ K^{-1}$. Substituting these average values in eq.(18) one obtains the value of $f_d = (0.025 - 0.03)$. This range fits well to the calculated mean value of the free volume from WLF equation for the majority of systems, 0.025 ± 0.005 (ref.8, p.288).

So, according to the model, the fractional free volume in WLF equation seems to represent the part of the total free volume localized in disordered regions.

Relation of ΔV_r to the other transition temperatures: Certain localities in ordered regions (e.g. the boundary of the ordered regions) probably do not take part in the described processes at temperatures T_m and T_g. The thermodynamic equilibrium amount of the free volume is held in these localities also below the temperatures T_m and T_g^{inf} (see the oblique dashed lines below T_m and T_g^{inf} in Fig.1). The total loss of free volume ΔV_r in some localities resulting from thermal contraction of ordered regions or of the whole volume comes at temperature T_{gm} or T_β, respectively. Both the states can be in relation to the offen investigated transitions in these temperature regions (ref.2, Chap.6).

The difference in the amount of free volume in neighbouring parts of microstructure leads below the temperature T_g to the rise of internal tension (7) which can be in connection with the ductile-brittle transition. Also the generation of crazes in the glassy state may be in relation to this process. Both the effects are shifted to the lower temperatures with larger free volume ΔV_r. This is the case of ductile polymers (e.g. polycarbonate, poly (ethylene terephthalate), amorphous polyamide).

Also, the rather vague process of nonuniform volume contraction induced by cyclic loading on polymers in a glassy state (14) can

EBSCOhost - printed on 2/13/2023 3:45 AM via . All use subject to https://www.ebsco.com/terms-of-use

be explained as a continuation of the decrease of the residual free volume ΔV_r. This process may be the structural reason of the "fatigue" of the polymer during the cyclic loading because of the gradually induced ductile-brittle transition. Similarly, the so-called physical aging in glassy polymers (15) or mechanically enhanced aging of glassy polymers (16) may be in connection with this process.

Relation between the temperatures T_g and T_m: The ratio of glass transition temperature T_g to melting point T_m has nearly the same value for many polymers, $T_g/T_m = 2/3$. This feature was first reported by Boyer (17). No quantitative relation to the polymer structure has been developed up to date. We have investigated the relationship T_g/T_m for the set of 59 polymers (ref.2, p.575-581) and found the ratio to vary with sharp maximum centered around 0.68 ± 0.10 (sample standard deviation). Each polymer in the set is characterized by the minimum and the maximum published experimental value of glass transition temperatures T_{gmin} and T_{gmax}. The average values of temperatures T_{gmin} and T_{gmax} have been used for the calculated ratio 0.68.

The variation of published experimental values of T_g connects with the various rate of cooling or other experimental conditions. In order to calculate the ratio T_g^{inf}/T_m (to check eq.14), the glass transition temperature at infinite slow cooling rate T_g^{inf} has been taken just as T_{gmin}. In this case, the maximum of the ratio T_g^{inf}/T_m is centered around 0.635 ± 0.108. This value fits well to the relative density of 0.63 of the structure of spheres defined as that of dense random packing (18). The relative density of this packing is slightly lower than 0.741 for a perfect f.c.c. close-packed structure. The ratio T_g^{inf}/T_m represents according to the eq.(14) the volume fraction of ordered regions. Therefore, we can suppose that the ordered regions form the structure of dense random packed spheres.

4. Conclusion

The glass transition of amorphous polymers can be investigated as a kinetic process in a two-phase structural model. The rise of

EBSCOhost - printed on 2/13/2023 3:45 AM via . All use subject to https://www.ebsco.com/terms-of-use

non-uniform free volume distribution at the temperature of their potential crystallization is supposed.The validity of the model has been verified in relation with published experimental data. The main practical conclusion seems to be that the properties of amorphous polymers in glassy state are probably formed already by the experimental conditions at the temperature of their potential crystallization.

References

1. Haward, R.N. 1973. The Physics of Glassy Polymers. Applied Science Publishers, London.
2. Krevelen, D.W.van. 1976. Properties of Polymers. Elsevier North Holland.
3. Doolittle, A.K. 1952. J.Appl.Phys. 23, 236.
4. Williams, M.L., R.F. Landel, J.D. Ferry. 1955. J.Am.Chem.Soc. 77, 3701.
5. Eyring, H., M.J. Shon. 1969. Significant Liquid Structures. Wiley, New York.
6. Yeh, G.S.Y. 1972. J.Macromol.Sci. 1972. B6(3), 465.
7. Bouda, V. 1977. IUPAC Symp.MACRO-Dublin, Proceedings IV-20.
8. Ferry, J.D. 1980. Viscoelastic Properties of Polymers. Wiley.
9. Robertson, R.E. 1965. J.Phys.Chem. 69, 1575.
10. Sidorovich, A.V. 1979. J.Macromol.Sci.-Phys. B 16(1), 35.
11. Bondi, A.J. 1968. Physical Properties of Molecular Crystals, Liquids and Glasses, Wiley, New York.
12. Bouda, V. 1982. Polymer Bulletin 7, 639.
13. Adam, G., J.H. Gibbs. 1965. J.Chem.Phys. 43, 139.
14. Bouda, V., V. Zilvar, A.J. Staverman. 1976. J.Polymer Sci.: Polymer Physics Ed. 14, 2313.
15. Struik, L.C.E. 1976. Ann.N.Y.Acad.Sci. 279, 78.
16. Myers, F.A. et al. 1976. Ann.N.Y.Acad.Sci. 279, 94.
17. Boyer, R.F. 1952. 2nd Int.Conf.Phys.Chem. Paris.
18. Bernal, J.D. 1960. Nature 185, 141.

EBSCOhost - printed on 2/13/2023 3:45 AM via . All use subject to https://www.ebsco.com/terms-of-use

Abbreviations

ABS	acrylonitrile-butadiene-styrene terpolymer
BET	Brunauer-Emmett-Teller method
CXA	ethylene-based polymer with vinyl acetate (DuPont Co.)
DRS	diffuse reflectance spectroscopy
DSC	differential scanning calorimetry
DTA	differential thermal analysis
ELS	equal load sharing rule
EPDM	ethylene-propylene-diene (monomer)
EPR	electron paramagnetic resonance (= ESR)
ESR	electron spin resonance (= EPR)
EVA	ethylene-vinyl acetate copolymer
GPC	gel permeation chromatography
HEED	high-energy electron diffraction
IR	infrared spectroscopy
LAM	longitudinal acoustic modes (Raman)
M_w, M_n	molecular weight (weight average, number average)
MWS	Maxwell-Wagner-Sillars effect
NMR	nuclear magnetic resonance
PBPP	poly-bis-(phenoxy)phosphazene
PBFP	poly-bis-(trifluoroethoxy)phosphazene
PCL/SAN	poly-ε-caprolactone/poly(styrene-co-acrylonitrile) blend
PE	polyethylene
PET	polyethylene terephthalate
PMMA	polymethyl methacrylate
PP	polypropylene
PVAC	polyvinyl acetate
PVC	polyvinyl chloride
PVF	polyvinylidene fluoride
RIM	reaction injection moulding
SALS	small-angle light scattering
SANS	small-angle neutron scattering
SAXS	small-angle x-ray scattering
SEM	scanning electron microscopy
TEM	transmission electron microscopy
T_g	glass transition temperature
TSD	thermally stimulated depolarization
TSL	thermally stimulated luminescence
WAXS	wide-angle x-ray scattering
WLF	Williams-Landel-Ferry equation

EBSCOhost - printed on 2/13/2023 3:45 AM via . All use subject to https://www.ebsco.com/terms-of-use

EBSCOhost - printed on 2/13/2023 3:45 AM via . All use subject to https://www.ebsco.com/terms-of-use

Author Index

Abdullaev, Kh.M. 501
Agarwal, A. 87
Alfonso, G.C. 427
Atanassov, A.M. 205,225,235, 249,303

Bakule, R. 197
Baldrian, J. 661
Baltá Calleja, F.J. 27
Bassett, D.C. 47,387
Bechev, Ch. 189,457
Bolshakov, G.F. 739
Bouda, V. 765
Brands, A.M.G. 363
Brenna, A. 271

Chapoy, L.L. 457
Chau, K.W. 87
Chuang, H.-D. 103
Chudáček, I. 689
Cimrová, V. 681
Clark, M. 371
Colet, M.C. 153,171

Daniewska, I. 449
Danz, R. 673
Deutschbein, L. 355
Dmitrieva, Z.T. 739
Dobkowski, Z. 449
Dobreva, B. 303
Dondero, G. 427
Dosière, M. 153,171
Ďurčová, O. 615

Ferdinand, A. 651
Fink, H.-P. 487
Foks, J. 463,549

Ganster, J. 707
Garbarczyk, J. 509
Garrett, P.D. 731
Gedde, U.W. 337
Gehrke, R. 119
Geil, P.H. 87
Geiss, D. 673,707
Głowacki, Z. 463
Groeninckx, G. 421
Grubb, D.T. 731

Han, C.D. 103
Hänsel, H. 699
Häupke, K. 757
Havránek, A. 399
Hepner, M. 631
Hirte, R. 179,527,585

Hnát, V. 527
Hsu, C.C. 87
Hu, H. 411

Jambrich, M. 615
Janik, H. 463,549
Janke, A. 673
Jing, G. 411
Jirouš, M. 555

Kahlert, H. 469
Kašparová, Z. 631
Kausch, H.H. 69
Kechajov, D. 405
Keller, A. 3
Klein-Szymanska, B. 681
Koch, M.H.J. 421
Kocinska, E. 449
Kojima, M. 279,435
Košková, B. 625
Kozłowski, M. 381
Krasteva, M. 477
Krestev, V.P. 303
Kröner, E. 717
Krsová, A. 555
Krustev, V.P. 639
Kudláček, L. 631
Künstler, W. 673
Kurbanaliev, M.K. 501
Kwiatkowska, A. 669

Lednický, F. 541
Leissing, G. 469
Leitner, O. 469
Li, H. 411
Lipp-Symonowicz, B. 601,607
Lotz, B. 259

Magill, J.H. 279,435
Makaruk, L. 515
Maláč, Z. 347
Marcian, V. 573
Mateva, R. 477
Mathot, V.B.F. 363
Melior, J.P. 527
Michalak, G. 591
Michler, G.H. 329,749
Mirzoeva, V.A. 501
Mishinev, J. 189,457
Mitterpachová, M. 615
Mucha, M. 563

Naumann, I. 329
Naumenko, G. 689
Nedbal, J. 197

EBSCOhost - printed on 2/13/2023 3:45 AM via . All use subject to https://www.ebsco.com/terms-of-use

Nedkov, E.T. 303
Nešpůrek, S. 681
Neumann, W. 699

Olley, R.H. 387
Osipiuk, J. 463

Pelzbauer, Z. 521,527
Philipp, B. 487
Pigłowski, J. 381
Pijpers, M.F.J. 363
Plešek, M. 347
Point, J.J. 153,171
Polańska, H. 515
Pospíšil, J. 399
Provazníková, D. 645
Purz, H.J. 487

Raab, M. 527
Reynaers, H. 421
Riekel, C. 421
Roques, R. 297
Russo, S. 427
Rybníkář, F. 309

Satake, H. 279
Schoffeleers, H.M. 363
Schulz, E. 527,585
Schwachula, G. 757
Shankernarayanan, M.J. 279
Shimamura, K. 319
Sirashki, G. 477
Slotfeldt-Ellingsen, D. 271
Springer, J. 651
Stark, W. 673
Stoyanov, A.I. 639
Štrof, P. 197
Sucharda, Z. 555
Sukhareva, L.A. 521
Swiatek, J. 669

Tkaczyk, S. 669
Trotignon, J.P. 297
Turska, E. 141
Turturro, A. 427

Urban, J. 689
Urbanczyk, G.W. 591

Vandermarliere, M. 421
Vaughan, A.S. 387
Verdu, J. 297
Veselý, P. 645
Voß, K.-L. 699

Walter, B. 355
Waszyńska, B. 515
Willing, T. 355
Wittmann, J.C. 259

Xu, X. 411

Zachmann, H.G. 119
Zenke, D. 179,527
Zhou, E. 411

EBSCOhost - printed on 2/13/2023 3:45 AM via . All use subject to https://www.ebsco.com/terms-of-use

ABS-copolymers (acrylonitrile-butadiene-styrene) 546, 547
-, fracture surfaces 546, 547
Acrylic fibres
-, density 640, 642
-, dope concentration 642, 643
-, dyeability 640, 642
-, heat treatment 639-643
-, mol. weight, effect of 640, 643
-,-, coagulation variables 639-641, 643
-, orientation of fibres 640, 642
-, perfection of structure 640-642
-, shrinkage 640-643
-, ultimate tensile properties 643
Activation
-, energy 740
-, entropy of transition 208
-, heat 740
Additives 281
-, interfacial 116
-, strength 521
Adsorbent
-, polymers 575
-, resins 575
Ageing of semicrystalline polymers
-, ageing 297
-, beta-phase content 298
-, crack initiation in fatigue 297
-, crystallinity ratio 298-302
-, DSC data 300
-, diffusivity 299
-, distribution of photostabilizers 297-299
-, distribution of radiochemical oxidation product (PE) 297-299
-, flexural fatigue 300
-, flexural strength 301
-, IR spectrometry 298-300
-, melting point 300, 301
-, photochemical 299
-, photooxidation kinetics 299
-, polypropylene 297
-, radiochemical 299
-, skin-core structure 299
-, skin thickness 301, 302
-, solubility 299
-, spherulite 298, 299
-, surface layer 297
Agents
-, complexing 407
-, interfacial 104
Aggregates 320-322, 324, 326-328, 415
Alkalization of cellulose 487
Aminolysis 633
Amorphous phase/state 75, 121, 124, 125, 133, 211, 235, 239, 249, 355, 359-361, 457, 458, 563, 565
Amorphous polymers 36, 40, 43, 47, 70, 141-143, 146-148, 681-685, 765-776
-, ductility, glassy state 772
-, free volume 768
-, ordered domains 765-776
-, packing density 775
-, vacancies 772
Anionic polymerization
-, polycaprolactam 428, 429
Anisotropy, anisotropic
-, crystal, of 33, 43
-, degree 275
-, electric conductivity 470, 471
-, polyacetylene, of 471, 473
-, properties 271, 274, 707
-, shrinkage 409, 410, 512
Annealing 143, 145, 146, 148, 182, 190, 589, 591-597, 699
Averaged physical properties of texture 707
Avrami equation 190, 191, 193

Bacterial cellulose 493, 494
Beta-phase content 298, 673
Birefringence 66, 70, 280, 458, 461-463, 504, 592, 617, 618, 699
Blends (see also Blends, individual polymers) 103, 118, 167, 193, 260, 347, 348, 350-352, 369
-, different comonomer contents, of 369
-, fast in situ-polymerization, by 430-434
Block copolymerization/copolymers 279, 280, 291-295, 395-401
-, propylene-ethylene 279, 280, 291-295
-, butadiene-styrene 395, 401
Blown extrusion 661
Branching 29, 59, 259, 260, 264, 266-269, 363, 366, 497-499
-, cellulose, of 497-499
-, lamellar 259, 260, 263, 264, 266-269
-, orientation, bimodal 259
-, quadrite formation 259
-, spherulite formation 259
Breakage of chains 71
Bundles of lamellae 392, 393
Butadiene-acrylonitrile rubber 428

Cancer therapy 254
-, gamma radiation 254
-, wave irradiation 254

EBSCOhost - printed on 2/13/2023 3:45 AM via . All use subject to https://www.ebsco.com/terms-of-use

Carbon fibres
-, carbon/epoxy composite 555, 556
-,-, composite damage 555
-,-, crack 560
-,-, failure 560
-,-, flexural loading 556
-,-, fracture surface 555, 556, 558, 559
-,-, interlaminar shear strength 556-560
-,-, optical microscopy 556, 558
-,-, SEM 556, 558, 559
-,-, shear loading 555
-,-, thermooxidative ageing 556, 557
Cell morphology 670
Cell size 671
Cellular microstructure 669, 670
Cellulation 387, 395
Cellulose
-, alkalization of 589
-, bacterial 493, 494
-, branching 497, 499
-, cotton linters 493, 496
-, crystallinity 490, 491, 493
-, crystallite size 492
-, degradation 494, 495, 499
-, disorder parameter 490, 491, 493
-, fringed fibrilar model 497
-, hydrolysis 494, 495
-, lamellae 494
-, microfibrils 487, 492, 493
-, Pearson VII-function 490
-, phase analysis 489
-, reacting structural fraction 499
-, recrystallization 499
-, shish-kebab structure 494, 496
-, sodium cellulose 489
-, spruce wood pulp 493, 496
-, TEM 487, 488, 492
-, water cellulose 489
-, WAXS 487, 489
Cellulose triacetate ageing
-, ageing 501
-,-, oriented and non-oriented films 501, 505
-, birefringence 504
-, destruction degree 504, 505
-, electron microscopy 504, 505
-, heat ageing 501, 505
-, orientation 501, 505
-, oriented films 503, 504
-, stretching degree 501, 502, 505
-, stretching rate 501, 506
-, supermolecular structure 504, 505
-, tensile strength 501, 502
-, thermooxidative degradation 504, 505
-, viscosity 501
Chain 71
-, breakage 71
-, conformation 153
-, contour length 717, 724
-, defects 27, 30
-,-, influence on perfection 27
-,-, lamellar crystals 27
-, extended morphology 439
-,-, of polyphosphazenes 439
-, flexibility 724
-, folding 3
-, length 69, 83
-, loading 71
-, orientation in PP fibres and blends 261
-, rupture 70
-, scission 68-72, 75, 76, 563-569
-, stiffness 69, 75, 79
-, strain 564
-, strength 70, 72
Characteristic length 392
Charge carriers 699
-, amorphous & crystalline PVAC films 681-685
-,-, extrinsic photogeneration 687, 688
-,-, intrinsic photogeneration 684, 686-688
-,-, lamellar structure 686
-,-, Onsager theory 681-685, 687
-,-, primary quantum yields 681, 684, 687
-,-, x-ray diffraction 682
-, photogeneration in poly-N-vinylcarbazole 681
-,-, field dependence 681, 683-685, 687
-,-, influence of crystallinity 681
-,-, photogeneration efficiency 681-687
-,-, quantum efficiency 681-684
Charge transport in thin films
-, charge carriers mobility 689, 699
-, charge carriers transport 689
-, drift mobility 689, 693-696
-, permittivity 690-692
-, photoconductivity 690-695
-, polyvinylcarbazole-N-vinyl-carbazole 689
-, rupture surface 696
-, transite time 690, 691
-, traps concentration 689
Chlorsulfonation of PE 52, 59, 67
Clusters 18
-, energy 602, 605, 605
Comonomer 363, 633
Complexing agents 407
Complex phase transition 421
Composites (see also Composites, individual polymers)
-, carbon/epoxy 555, 556
-, damage 555
-, strength 527, 536
Concentration exponent α 171, 176, 177
Conducting composites, transport, charge 681, 689
Conductivity 699

EBSCOhost - printed on 2/13/2023 3:45 AM via . All use subject to https://www.ebsco.com/terms-of-use

Conformation of macromolecules 69, 76, 87, 88, 93, 143–147, 620
–, amorphous polymers 141–143, 146–148
–, annealing 143, 145, 146, 148
–, conformation 141–143, 145, 149, 153
–, conformational transition 151
–, crystalline areas 147
–, crystalline polymers 142, 143
–, degree of swelling 143, 149
–, entropy of chain segment 235
–, glass transition 145, 147
–, IR analysis 149
–, helix conformation 87, 149
–, microconformation 141–143, 145–149
–, neutron diffraction 143
–, non-crystalline polymers 143, 147
–, NMR investigation 144, 148, 149
–, ordered areas 145, 148
–, polyacrylonitrile 148, 150
–, polybutylene 87, 88, 93
–, polycarbonate 143, 147
–, polyethylene terephthalate 143
–, polystyrene, isotactic 142
–, swelling 143, 149
–, WAXS 146, 150, 151
Contrast enhancement 753
Copolymers 363
–, trioxane-phenylglycidyl ether 477
–,–, crystal growth 481, 484, 485
–,–, crystal lattice 478
–,–, degree of crystallinity 477, 480
–,–, DSC 477–479, 481
–,–, electron diffraction pattern 481
–,–, lamellae 480, 481, 484
–,–, lamellar aggregates 480
–, lactides, L and D 32
–, methyl methacrylate-butadiene-styrene
–, mosaic blocks 478, 479
–, SEM 481, 483
–, supermolecular structure 480
–, TEM 477, 478, 480
Cospherical platelet morphology 435
Cotton linters 493, 496
Crack 49, 51, 408, 460, 550, 587
Craze 408
Critical
–, chain folded nucleus
–,–, primary 218
–,–, secondary 218
–, crystal nucleus 14, 136
–, dissolution time 590, 591, 602–604
Cross fractionation 368–369
–, crystallization/dissolution method 369
Cross hatched morphology 61, 64, 65, 259, 268, 279
Crosslinking
–, crosslinked albumins 307
–, crosslinking density 337, 338
–,–, polyethylene, of 337, 338
–, crosslinking degree effect 430
Cryoultramicrotomy 750
Crystal
–, block 33, 40
–, foams 87
–, growth 4, 10, 11, 14, 16, 17, 120, 481, 484, 485
–, habit 10, 12, 13
–, lattice 47
–, perfection 33
–, region 47
–, regularity 27, 28
–, single 154, 171
–, size 522
–, thickness 29, 42, 57
–, voids 36
Crystalline structures 42, 43, 47, 48, 52, 57, 63, 142, 143, 303, 307, 496, 470, 509, 564, 565
–, polyacetylene 469, 470
–, polycarbonate 452–455
–, polyvinyl acetate films 681, 686
–, region 127, 134, 355, 359, 361
–, spherulitic structure 452, 455
–, state 249
Crystallinity 94, 376, 490, 491, 493, 593, 595, 598, 673, 674, 676, 679, 699, 701
–, cellulose, of 490, 491, 493
–, degree 47, 190, 200, 292, 302, 477–480, 601–605, 700
–, oriented domains 200
–, polypropylene, of 94
–, polyvinyl chloride, of 376
Crystallite size of cellulose 492
Crystallite orientation 271, 273
Crystallization of chain molecules (see also Melt crystallization) 27, 320, 321, 363, 366, 367, 521, 522, 637
–, alkyl branches 35, 36, 39, 42
–, 'amorphous' defects 36, 43
–, anisotropy of crystal 33, 43
–, branching ratio 29
–, chain defect distribution 30
–, chain folded crystallization 3, 5, 14, 17
–, chlorinated PE 32, 37
–, copolymers, L and D lactides 32
–, crystal block dimensions 33, 40
–, crystalline voids 36
–, crystallizable units 29, 30
–, crystallization of rubber 197
–, crystallization temperature 7, 9, 12, 21
–, crystal perfection 33, 43
–, crystal regularity 27, 28
–, crystal thickness 29, 42
–, defect concentration 29, 40–42

EBSCOhost - printed on 2/13/2023 3:45 AM via . All use subject to https://www.ebsco.com/terms-of-use

-, defect inclusion within crystals 28, 32, 35-43
-, defect penetration 37, 39
-, defects in amorphous phase 29
-, defects in crystalline phase 29
-, degree of partioning 28, 29, 32, 37, 39, 40
-, distorsion parameter 30
-, drawn polyethylene 40, 41, 43
-, eccentricity of ellipsoid 35
-, fibre structure 39, 43
-, grain boundaries 35, 43
-, kinetics 255
-, kinetic theories of 36
-, kinks 28, 30-32, 42
-, lamellar thickness 33, 40, 42, 43
-, lateral chain deffects (branches) 27
-, nuclei 262
-, melt crystallized PE 42, 43
-, melting temperature 27
-, monolayer single crystals 28
-, mosaic block structure 35
-, paracrystalline lattice distorsion 30, 33, 42, 43
-, plastic deformation 39
-, polyethylene 27, 29, 31-42, 363
-, polyisoprene (cis 1,4) 197
-, process 119-121, 127
-, relaxation peaks 198
-, rate 199, 207, 225, 230
-, SANS 32
-, SAXS 32
-, supercooling 34, 36, 37
-, temperature 388, 392, 395, 396, 417, 418, 420
-, total exclusion 29
-, TSD method 29
-, TSD spectrum of rubber 197
-, thermal history 199, 201
-, unit cell dimension 27
-, unit cell symmetry 38
-, unit cell volume 34, 41
CXA-resins 104, 107-112

Damage 752
d_{31}-coefficient of PVF 674, 677, 678
Defect
-, amorphous phase 29
-, concentration 29, 39-41
-, crystalline phase 29
-, inclusion within crystals 28-31, 35-43
-, influence on perfection 27
-, lamellar crystals 27
-, penetration 37, 39
Deformation 319, 323, 324, 326-328, 564, 625
Degradation of cellulose 494, 495, 499, 731, 734
Degree of
-, crystallinity 359
-, destruction 504, 505
-, modifier dispergation 385
-, stretching 501, 502, 505
Destruction 504, 505, 589
Dielectric
-, constant
-,-, texture investigation 714
-, permittivity 739
-, properties 699
Differential scanning calorimetry 89, 93-96, 98, 106, 180, 188, 190, 300, 304-306, 340, 363, 364, 421-423, 457, 462, 477-479
-, polyethylene, of 363-365, 367
-, polypropylene, of 340
-, PCL/SAN blend, of 421, 423
Differential thermal analysis (DTA) 189, 340, 399, 401, 409
Diffraction pattern 288, 289, 304, 306, 755
Diffusion equation, generalized 299, 355, 608, 609, 612, 655, 656, 718, 719
Dipole orientation 673, 674, 676, 679
Direct extraction method 365
Disorder parameter of cellulose 490, 491, 493
Dissolution method, crystallization 366, 367
Distorsion parameter 30
Distribution
-, photostabilizers, of 297-299
-, radiochemical oxidation product, of 297, 299
Divinylbenzene 758, 763
Domain structures 373, 374
Drawing 40, 41, 43, 661, 662, 731, 733
Draw(ing) ratio 81, 82, 458, 626, 633, 731, 731, 733, 736
Dyestuff penetration 608, 610
Dynamic viscosity 406, 408

Efficiency, nucleating 268
Elastic matrix 720
Electric conductivity 470
Electric polarization 699
Electron accelerator 645, 646
Electron diffraction 288, 289, 294, 304-306, 322, 481, 754, 755
-, bright-field image 755
-, dark-field image 755
-, diffraction pattern 755
-, polypropylene, of 294
Electron-matter interaction
-, critical dose of damaging 752
-, electron beam irradiation 752
-, mass loss 753, 754
-, reduction of damaging 753
-, specimen damage 752
Electron microscopy (see also SEM, TEM) 322, 324, 437, 443, 634
-, high voltage electron microscopy 749-755
-, scanning electron microscopy (SEM)

EBSCOhost - printed on 2/13/2023 3:45 AM via . All use subject to https://www.ebsco.com/terms-of-use

–, transmission electron microscopy (TEM) 749–755
Electron spin (or paramagnetic) resonance (ESR/EPR) 76–78
Emission
–, heated body, of 249
–, intensity, of 252
–, light, of 250
–, process 227
Entropy 235, 237
–, activation, of 740
–, melting, of 208
–, stress 241
Envelopment 585, 586
Epitaxy 260, 261, 267–269, 587, 590
–, epitaxial binding 587–590
EPR/ESR electron paramagnetic/spin resonance 76–78
Epoxy resins 543–545, 555, 556, 558, 559
Equilibrium melting 235
Ethylene-propylene copolymer 363

Failure 71, 72, 79, 275, 531, 560
Fibre 180, 588, 589, 615–621, 645
–, hard-elastic 573–576, 578, 581
–, lamellar structure 578, 582
–, loading 72
–, microporous 573, 581, 582
–, morphology/texture 39, 43, 441, 573–575, 617
–, supermolecular structure 574, 575, 577–582
–, temperature 732
–, thickness 528
–, ultrahigh strength 527, 531, 539
Fibre orientation
–, laminate microstructure 686
Fibrilar nucleation & growth 273
Fibrillation 280, 284, 286, 288, 661, 667
Fibril lamellar structure 591
Fibrils 440
Fibrous units 392, 470
Filament 607, 609
Fillers 752
Films 285, 287, 437, 441, 450, 503, 504, 527, 529, 530, 533, 586, 587, 589, 560, 652, 654, 655, 661
Flexibility of chain 724
Flexural
–, fatigue 300
–, loading 556
–, strength 301
First melting 180
First normal stress difference 105
Flocculation/crystallization/dissolution method 368, 369
Flow induced crystallization 528, 529
Fold
–, length 4, 7, 9, 13, 14, 21, 22, 24, 25
–, regular folding 157
–, surface free energy 4, 6, 236
Formation of quadrites 259
Formation of spherulites 255
Fractionation 156, 177, 363, 365–369
Fracture
–, amorphous region 75
–, amorphous polystyrene 70
–, bending of skeleton 69
–, birefringence 70
–, breakage of chains 71
–, chain length 69, 83
–, chain rupture 70
–, chain scission 69–72, 75, 76
–, chain stiffness 69, 75, 79
–, chain strength 70, 72
–, critical concentration of cracks 72
–, critical defect concentration 79
–, critical stress transfer length 70
–, conformational transitions 69, 76
–, cooperative coupling of segments 71, 74
–, crystalline superstructure 69
–, distribution of molecular stresses 69
–, draw ratio 81, 82
–, electron spin resonance 76, 78
–, failure 71, 72, 79
–, friction coefficient 68
–, fracture 319, 320, 471, 530, 536, 537
–,–, centres 542, 546
–,–, curves 542
–, fracture surface 49–51, 57, 112, 541–550, 552
–,–, ABS polymers 546, 547
–,–, brittle polymers 542
–,–, epoxy resins 543–545, 555, 556, 558, 559
–,–, heterogeneous polymers 542–544
–,–, morphology 441, 442
–,–, polycarbonate 541
–,–, polymethyl methacrylate 542, 543, 547
–,–, PBFP 441, 442
–, IR absorption 74, 77, 78
–, interfibrilar amorphous fraction 74
–, intermolecular attraction 69
–, kinetics of radical formation 72
–, kink 75, 76
–, loading of chains 71
–, loading of fibres 72
–, matrix 69
–, microcracks 72
–, microfibrils 73, 74, 79, 80
–, microstructure 71
–, molecular chains 69
–, morphological aspects 69, 441, 442
–, NMR 74
–, polyamide fibres 73, 74, 76
–, polydiacetylene 73
–, polyethylene 71, 72

EBSCOhost - printed on 2/13/2023 3:45 AM via . All use subject to https://www.ebsco.com/terms-of-use

-, polypropylene 76, 77
-, radical chain mechanism 72
-, segment deformation 74
-, segment orientation 74
-, shear lag theory 81
-, shear loading 69
-, slip of chain ends 69
-, spherulites 71
-, strain rate 69-71
-, strength 69-82
-, stress 70, 79, 81
-, stress-strain behaviour 73, 77
-, taut tie molecules 72, 74, 75
-, tensile strength 81
-, x-ray 74
Fragmentary ions 743
Free energy of fold surface 236
Free volume distribution 765, 776
Friction coefficient 69
Fringed fibrilar model 497
Functional polymers 757, 760, 764

Gas-phase process 365, 651, 655-658
Gelation of PVC 378
GPC, mol.weight, polydispersity 450, 760
Gel 338-341, 731-734, 739, 760
Glass
-, formation 444
-, transition 107, 145-147, 736, 765-776
Glow curve 399-403
Grain boundary 35, 43
Growth 393-395, 398, 587
-, lamellae, of 240
-, kinetics 155-157
-, rate 149
-, segment, of 209
-, solution grown crystals 155-157
-, spherulitic 411, 413, 416, 418, 419

Hansen solubility parameters 454
Hard-elastic PP fibres 573, 576, 578, 581
-, deformation 575, 577, 578-580
-, drawing 574, 581, 582
-, elastic recovery 574
-, extension 574, 577, 581, 582
-, heat-setting 574
Heat ageing 501, 505
Heat capacity 363, 364, 591, 593, 594
HEE diffraction, high energy electron diffraction 471, 474
Helical conformation 87 ff, 149
Helices 262, 264
Heterogeneity 363, 750
Heterogeneous
-, copolymers 363, 364
-, polymer 381, 542-544
-, polymer blend 103
High energy electron diffraction, HEED 471, 474
High-modulus fibres 731
High-pressure process 365
High-speed melting spinning 574
High-strength fibres 585
Homogeneity 363
Homogeneous copolymers 363, 364, 367
Honeycomb structure 383
Hot channel conception 227
Hydrolysis 494, 495
Hydroperoxide formation 669
Hydrophily parameter 626, 649

Impact
-, properties, epoxy resins 272, 275, 276, 405, 409, 433
-, resistance 382
-, strength 381, 383, 384
Index, refractive 250, 251
Inerts 758, 762
Infrared spectra 18, 19, 69, 77, 78, 149, 298-300, 616, 673
Interactions, molecular 69, 269
Intercalates 165 ff
Interfacial
-, adhesion 116
-, agent 104
Interlamellar regions 576, 582
Interlaminar shear strength 556-560
Intermolecular cohesion 594, 598
Internal stresses 521, 525, 526
Internal structure 525
Intertwinning fibril 440
Ion
-, etching 279-281, 284, 285, 288, 291, 295
-, exchange resins 757, 761, 763
Irradiation, gamma 646
IR spectroscopy, see infrared spectra
Isochronous decoration method 171 ff
Isothermal crystallization 190, 412, 457
-, drawing 732, 733, 746
-, depolarization current 700, 702, 704
-, thickening 4-11, 22

Kinetic length 154
Kinetic theory 723
Kinetics 72, 153, 187, 253, 299
Kinks 28, 30-32, 42, 75, 76

Lamella(e) 10, 13, 23, 48, 49, 51-53, 55-59, 63, 66, 67, 124-126, 136, 154, 205, 240, 274, 321, 322, 324-326, 388-392, 395, 415, 420, 480, 481, 484, 494, 565, 587
Lamellar
-, aggregates 480

EBSCOhost - printed on 2/13/2023 3:45 AM via . All use subject to https://www.ebsco.com/terms-of-use

-, branching 259, 263, 264, 267, 269
-, growth 587
-, structure 3, 320, 321, 325, 387, 418, 522, 577-582, 754
-, thickness 5, 7, 10, 33, 40, 42, 43, 87, 93, 176, 237, 238, 259, 388
Laminate microstructure 686
Langevin equation 718
Latent porosity 767
Layer 290, 608, 610
Light emission 250
Light microscopy, polarized 337, 338, 340-342
Liquid crystal
-, enthalpy and entropy of transition 516
-, polyphosphazenes 442
-, transition temperature 516, 517
Loss modulus 105

Macrogel particles 408
Macromolecular network 758
Macronet polymer 764
Macroporosity 761
Magnetization 356-359
Master equation 718
Mass loss 753, 754
Maximal porosity 763
Mechanical properties, tests, methods 320, 326, 732
-, flexural loading 556
-, shear strength 556-560
-, shear stress 105
-, stiffness 714
-, storage modulus 105
-, strain 69, 73, 77
-, strength 69-82
-, tensile strength 81, 501, 502
-, Young's modulus 268
Melt crystallization (see also Crystallization of chain molecules)
-, amorphous polymers 36, 40, 43, 47, 70, 141-143, 146-148, 681-685
-, annealing 128, 182
-, Avrami equation 190, 191, 193
-, birefringence 66
-, cross-hatched structure 61, 64, 65
-, crystal lattice 47
-, crystalline polymers 47
-, crystalline regions 47
-,-, continuity of 47
-, crystallization half-time 190, 191
-, crystallization isotherm 191, 192
-, crystallization kinetics 189
-, crystallization rate 192
-, crystallization temperature 93, 95
-, crystal thickness 57
-, degree of crystallinity 47, 190
-, DSC 180, 188, 190
-, DTA 189
-, fibres 180
-, first melting 180
-, fixed materials 181, 183, 185, 187
-, fracture surface 49-51, 57
-, interior morphology 49
-, isothermal crystallization 190
-, lamellae 48, 49, 51-53, 55-59, 63, 64, 66, 67
-, melt crystallization 7, 17, 21, 42, 43, 47, 48, 52, 57, 58, 63, 524, 525
-, melting 180-182, 184, 186, 187
-, melting point 87, 193, 522
-, melting temperature 27
-, microstructure 48, 55, 67
-, nucleation 192, 194
-, organization 47, 51
-,-, in melt-crystallized polymer 47
-,-, in solids 51
-, permanganic etching 57, 58
-, polyglycol 192
-, polymer single crystals 48
-, polypropylene 49-53, 56-67, 190, 193
-, polypropylene fibres 87
-, polystyrene 61-63
-, polyvinylidene fluoride 60, 61
-, premelting behaviour 179, 184, 188
-, radiation damage 48, 49
-, recrystallization behaviour 179, 184, 188
-, segregation 59
-, second melting 180, 182, 184
-, shrinking materials 180-187
-, spherulites 49, 58, 59, 63, 64, 67
-, stiffness of fibres 47
-, strength of fibres 47
-, surface grown polyethylene 179
-, textile fibres 51
-, thermogravimetry 189
-, thermomechanical measurement 190
-, TEM 47, 49, 51, 67
-, W-L-F equation 193
-, x-ray scattering 655
Melting
-, behaviour 423
-, entropy 208
-, equilibrium 235
-, peak 106
-, point 87 ff, 300, 301, 522
-, PCL/SAN blend 423
-, polyethylene, of 363
-, polypropylene
-,-, blend 237
-,-, hot drawn 237
-, rate 225
-, temperature 645, 648
Melt properties

EBSCOhost - printed on 2/13/2023 3:45 AM via . All use subject to https://www.ebsco.com/terms-of-use

-, flow 271
-, history 87 ff, 347
Membrane 652
Methylamine 632
Microcracks 72
Microconformation 39-41, 43-47
Microdomains in PVC 373, 374
Microfibrils 487, 493, 587, 661
Microporosity 575, 580-582
Microporous fibres 573, 581, 582
Microstructure 27, 48, 55, 71, 272, 273, 276, 651, 655, 659
Microvoids 573-582
Mobility of charge carriers 689
Model, spring-bead 718
Modifier 381
Modulus 732
-, loss 105
-, storage 105
-, Young's modulus 268
Molar mass 365
Molecular
-, interactions 269, 602-604, 618
-, layers 154, 156
-, order 754
-, weight 156, 177
Morphology A (see also B & C)
-, cross hatched 61, 64, 65, 259, 268, 279
-, filler particles 752
-, fracture surface estimated 541
-, heterogeneities 750
-, lamellar structure 754
-, layered 290
-, molecular order 754
-, morphology 259-261, 269, 319, 337, 347, 405, 430-433, 449, 469, 474, 563, 575, 578, 581, 582, 587, 620, 621, 625-627, 634
-, particle size 751
-, phase adhesion 755, 756
-, phase morphology 751
-, property determining structure 755
-, rubber particles 750
-, shape of particles 751
-, sheaf-like structure 754
-, spatial analysis 750, 751
-, spherulitic structure 754
-, stereology 750, 751
-, terraced 284, 290
Morphology B: (co)polymers, blends, composites (see also A & C)
-, additives 381
-, adhesion 381
-, amorphous region 330, 335
-, branching degree 329, 331, 334
-, chain folded crystallization 3, 5, 14, 17
-, chain folding, specificity 3, 6, 8
-, chain length at interphase 4
-, chlorinated polyethylene 382
-, clusters 18
-, copolymer PE/vinyl acetate (EVA) 382, 384
-, critical nucleus 14
-, crystallization temperature 7, 9, 12, 21
-, crystal growth (rate) 4, 10, 11, 14, 16, 17
-, degree of modifier dispergation 385
-, diffusion coefficient 655, 656
-, effect of
-,-, shear strength 382, 383
-,-, temperature 381
-,-, time 382
-, electron microscopy 12, 329, 330
-, film 652, 654, 655
-, fold length 4, 7, 9, 13, 14, 21, 22, 24, 25
-, fold surface 4, 6
-, gass permeability 651, 655-658
-, heterogeneous polymer system 381, 382
-, honeycomb structure 383
-, impact resistance 382
-, impact strength 381, 383, 384
-, infrared spectroscopy 18, 19
-, isothermal thickening 4, 6, 8, 10, 11, 22
-, lamellae 10, 13, 23, 325-335
-, lamellar crystal 3
-, lamellar thickness 5, 7, 10
-, long period 11
-, low-angle x-ray (= SAXS) 4, 11
-, modifier concentration 381
-, molecular weight, effect of 333, 334
-, melt crystallization 7, 17, 21
-, membrane 652
-, microstructures 651, 655, 659
-, non-selective solvent 652, 655
-, nucleation 16, 17
-, paraffins 20-22, 24, 25
-, permeability coefficients 655, 656
-, permeation through heterogeneous media 652
-,-, model of 652-654
-, phase inversion 381
-, phase separation 651
-, polyacetylene 469-474
-,-, fibrous 470
-,-, films oriented 470
-,-, oriented 472
-,-, voids and fractures 471
-, polyacrylate 382, 384, 385
-, polycaprolactone/polystyrene-co-acrylonitrile blends PCL/SAN 421
-, polycarbonate (Bisphenol A) 449
-, polyethylene 3, 4, 11, 12, 15, 19-22, 24, 329-335, 337
-, polymer blends 381, 383
-, polyvinyl chloride, impact modified 381
-, primary fold length 4

EBSCOhost - printed on 2/13/2023 3:45 AM via . All use subject to https://www.ebsco.com/terms-of-use

-, processing 381, 383
-, quadrupole mass spectrometer 655
-, Raman LAM method 4, 21
-, SANS 15, 18
-, secondary crystal nucleation rate 14, 16
-, selective solvent 652, 655
-, single crystals 14
-, solubility coefficient 655
-, spherulite 13, 329, 330
-, stress hardening/softening 651
-, structure 337, 347, 405, 430-433, 449, 620, 621, 625-627
-, supercooling 7, 9, 15, 22, 24, 25
-, supermolecular structure 329-334
-, synchrotron x-ray source 8, 22, 23
-, TEM 382-385
-, tensile properties 651
-, thermomechanical behaviour 651
-, texture 3
-, ultramicrotomy 329
-, x-ray diffraction 21
Morphology C: indirect methods (see also A & B) 119
-, amorphous region 121, 124, 125, 133
-, critical crystal nucleus 136
-, crystalline region 127, 134
-, crystallization
-,-, process 119-121, 127
-,-, temperature 122-128, 135
-, crystal growth 120
-, crystal lamella 124-126, 136
-, crystal thickness 120, 124, 129, 131, 133, 135, 136
-, degree of crystallinity 121, 123, 129, 131, 132
-, isothermal crystallization 120, 127, 132, 134
-, light scattering 119
-, melting 129, 131, 132, 134, 136
-, neutron scattering (= SANS) 32, 137
-, non crystalline regions 127, 133, 134, 136, 137
-, polarized light microscopy 119
-, polybutadiene, crosslinked 129
-, polyethylene 119, 122, 126, 130
-, polyethylene terephthalate 119, 120, 125, 127, 129, 134, 135
-, polypropylene 127
-, recrystallization 129, 131, 134, 135
-, SALS 119
-, SANS 137
-, SAXS 119, 120, 126, 127, 129
-, spherulites 120-122, 127, 132
-, spinodal decomposition of crystal defects 127
-, synchrotron radiation 119, 125, 127, 129, 132
-, x-ray diffraction 119, 125, 127, 129, 132
-, WAXS 119, 122, 125, 127, 129
Mosaik block 35, 478, 479

Needle-like crystal 443
Net plane normals 674
Neutron scattering, see SANS
Neutron diffraction 143
Nodules
-, polyethylene 342, 343, 345
-,-, size 342, 343, 345
Non-crystalline regions (PP) 127, 133, 134, 136, 137, 141, 145, 577, 578
Normalized thickness 669, 670
Normal stress difference 103
NMR investigation 74, 142, 146, 147, 355, 359
Nucleation 16, 17, 87 ff, 192-194, 236, 347, 348, 352, 457-459, 466, 587
-, enhanced self-nucleation 466
-, mononucleation 154, 156
-, nucleating agents 259, 269
-, nucleating efficiency 268
-, polybutadiene, of 89, 93, 98-101
-, polycarbonate, of 454
-, polynucleation 153, 156-159, 164
-, primary 217-221
-, rate 225
-, secondary 211-217, 225
-, quantum interpretation 211-221
Nucleus 262
-, critical primary chain folded 218
-, criticle secondary chain 218
Nylon 104, 107-112, 208

Oligomer block flexibility 522, 525
Opening of pores 763
Optical microscopy 406, 437, 452, 529, 534, 535, 551-553, 556, 558, 617, 622
Orientation 501-506, 592, 593, 595, 597, 608, 609, 613, 625, 626, 628, 629
-, degree 618
-, distribution function 708
-, modes 674, 675, 678
-, molecular 271, 276
-, oriented, doubly 288, 295
-, PP fibres and blends 261
Oriented 470, 472, 474
-, chalk filled polypropylene
-,-, films (PP) 285, 503, 504
-,-, polyacetylene 472, 474
-,-, spherulites 285
Oxygen diffusion 563
Oxygene uptake 563

Paracrystalline lattice 30, 33, 42, 43
Paraffins 20-22, 24, 25
Particle size 751
Partioning degree 28, 29, 32, 37, 39, 40
Pattern, x-ray diffraction 509, 511, 512
Permanganic etching 57, 58, 387, 389

EBSCOhost - printed on 2/13/2023 3:45 AM via . All use subject to https://www.ebsco.com/terms-of-use

Permeability coefficient 655–658
Permeation 652–654
Phase
–, adhesion 755, 756
–, analysis 489
–, inversion 381
–, morphology 751
–, separation 430, 651
Photogeneration 678, 684–688
Photooxidation kinetics 299
Piezoelectric constant 673, 678, 714
Plantain effect 527, 536, 537
Plasticizer absorption in PVC 378
Plastic deformation 39
Pleated sheet structure 509, 510, 512
Polarized light microscopy 119, 272, 337, 338, 340–342, 463, 465, 466
Pole figure 674, 678, 708
Poling 674, 675, 678
–, time 673, 674
Polyacetylene 469
–, anisotropy 471, 473
–, crystalline 469, 470
–, electric conductivity 470
–, fibrous 470
–, fracture 471
–, HEE diffraction 471, 474
–, morphology 469–474
–, oriented 470, 472, 474
–, SAXS 473, 474
–, SEM 469, 470, 473, 474
–, structure 469
–, voids 471
–, x-ray diffraction 469, 473, 474
Polyacrylates 382, 384, 385
Polyacrylonitrile, conformation 148, 150
Polyamide 6 (poly-e-caprolactam) 104, 107–112, 428, 429
–, anionic synthesis 428, 429
–, impact properties 433
–, morphology 430–433
–, rubber modified 428
Polyamide 11: 57, 260
Polyamide 6 blends
–, polycaprolactam/poly(butadiene-co-acrylonitrile)
–,–, calorimetric data 430
–,–, crosslinking effect 430
–,–, formation 429, 430
–,–, IR data 430
–,–, phase separation 430
–,–, SEM 432, 433
–, polycaprolactam/i-polypropylene 260
Polyamide 6 fibres 73–76
–, electron accelerator 645, 646
–, hydrophily parameter 646, 646, 649
–, irradiation 646
–, melting temperature 645, 648
–, radiation grafting 647
–, SEM 646, 647
–, thermal decomposition 645, 648
Polybutadiene, cis 411
–, aggregates 415
–, crystallization temperature 417, 418, 420
–, effect of MW on morphology 411, 416
–, growth rate of spherulites 411, 413–416, 418, 419
–, IR spectroscopy 411, 412
–, isothermal crystallization 412
–, lamellae 415, 420
–, lamellar structure 418
–, M_w, M_n, by GPC 411–415
–, nucleation 411, 413, 415
–, viscosity 411, 412, 415, 417
–, TEM 412, 413, 417
Poly (butadiene-co/b-styrene)
–, block copolymer 399, 401
–, block dimensions 400
–, DTA 399, 401, 409
–, glow curve 399–403
–, relaxation regions 400, 403
–, statistical copolymer 399, 401
–, thermally stimulated depolarization (TSD) 399
–, thermostimulated luminescence (TSL) 399, 401, 402
–, viscoelastic measurement 399
–, x-ray irradiation 399
Poly (butadiene-co-styrene)/polybutadiene blend
–, complexing agents 407
–, cracks 408
–, crazes 408
–, dynamic viscosity 406–408
–, impact polystyrene 405, 409
–, macrogel particles 408
–, morphologic characteristics 405
–, optical microscopy 406
–, quasi-net inversion 406
–, small elliptical particles 406
–, stabilization of disperse elastomer particles 408
–, TEM 406, 407, 409
Polybutadiene films, cis 669, 670
–, cell morphology 670
–, cell size 671
–, cellular microstructure 669, 670
–, normalized thickness 669, 670
–, surface microstructure 669
–, x-ray irradiation dose 669, 670
Poly-ε-caprolactone/poly-(styrene-co-acrylonitrile) blend, PCL/SAN
–, complex phase transition 421
–, DSC 421–423

EBSCOhost - printed on 2/13/2023 3:45 AM via . All use subject to https://www.ebsco.com/terms-of-use

-, melting behaviour 423
-, synchrotron radiation 421
-, SAXS 421
-, WAXS 421
Polybutylene 87 ff
-, conformation 87, 88, 93
-, crystal forms 87
-, helical conformation 87 ff
-, lamellar thickness 87, 93
-, melting point 87 ff
-, melt history, effect of 87 ff
-, nucleation 93 ff
-, solution history, effect of 93 ff
Polycarbonate (Bisphenol A)
-, amorphous 451
-, annealed 541
-, crystallization induced by organic solvent 449
-, film 451
-, fracture deformation structure 541
-, glass transition 449
-, Hansen solubility parameter 454
-, interference of inner structure 541
-, morphology from fracture surface 541
-, nucleation 454
-, polydispersity degree 450
-, SALS 452, 453
-, spherulites 452-455, 541
-, x-ray diffraction 452, 453
Polychlorotrifluoroethylene 208
Polydiacetylene 83
Polyesters 515
Polyethylene 27, 29, 31-42, 154 ff, 171 ff, 208, 236, 240, 250, 259-261, 263, 267-269, 338-345, 363-365
-, chain defects influence on perfection of crystals 27
-, crosslinked 337, 338
-, crystallization 27
-, drawn 40, 41, 43
-, DSC 340
-, gel 338-341
-, morphology 337
-, nodule size 342, 343, 345
-, SAXS 337, 338, 340, 342
-, sol 338-341
-, supermolecular structure 337
-, wave number 250-252
Polyethylene (linear) 355, 359
-, amorphous region 355, 359, 361
-, crystalline region 355, 359, 361
-, degree of crystallinity 359
-, diffusion model 355
-, lamellar thickness 359
-, magnetization 356-359
-, NMR 355, 359
-, spin diffusion 355
Polyethylene (linear low density, LLDPE) 363
-, blend 369
-, branched chain segments 363, 366
-, comonomer distribution 363
-, copolymer 363
-, cross fractionation 368, 369
-, crystallization 363
-, crystallization/dissolution method 366, 367
-, DSC 363-365, 367
-, direct extraction method 365
-, ethylene-propylene copolymer 363
-, flocculation/crystallization/dissolution method 368, 369
-, heterogeneous copolymers 363, 364
-, high pressure process 365
-, homogeneous copolymers 363, 364, 367
-, melting 363
-, recrystallization 363
-, sequence length distribution 363
Polyethylene composite with glass/silica
-, glass transition 736
-, water, effect of 735
Polyethylene fibres
-, adhesion 586, 588
-, annealing 589
-, chemical behaviour 586
-, cracks 589
-, destruction 589
-, envelopment 585, 586
-, epitaxial binding 587, 590
-, film forming 586
-, films 586, 587, 589, 590
-, high-strength PE fibres 585
-, knotting test 589
-, lamellae 587
-, lamellar growth 587
-, lamellar structure 587
-, microfibrils 587
-, nucleation & growth 587
-, polyethylene fibre 588, 589
-, SEM 586, 588, 589
-, splitting and bending 585, 589, 590
-, supermolecular structure 585
-, surface coating 587-590
-, surface morphology 587
-, tensile strength 585, 586
Polyethylene fibres, 'self-reinforced'
-, adhesion 534, 537-539
-, composite strength 527, 536
-, failure 531
-, fibre thickness 528
-, fibre ultra-high strength 527-531, 539
-, film thickness 528
-, flow induced crystallization 528, 529
-, fracture 530, 536, 537
-, melting 527, 529

EBSCOhost - printed on 2/13/2023 3:45 AM via . All use subject to https://www.ebsco.com/terms-of-use

–, optical microscope 529, 534, 535
–, plantain effect 527, 536, 537
–, polyethylene film 527, 529, 530, 533
–, shrinkage 527, 529–531
–, SEM 529
–, sonic velocity 528, 537
–, stiffness 530
–, strength 530–532
–, stress-strain curve 528, 530, 534, 537, 538
–, tensile strength 527, 536
–, toughness 527, 532, 537
–, Young' modulus 530, 533
Polyethylene spherulites 319–328, 337, 340–342, 345
–, aggregated (banded) spherulites 320–322, 324, 326–328
–, crystallized 320, 321
–, deformation 319, 323, 324, 326–328
–, electron diffraction 322
–, fracture 319, 320
–, lamellae 321, 322, 324–326
–, SEM 324
–, structure 319, 320
–, surface morphology 319
–, surface region 319
–, TEM 322
–, uniaxially drawn fibres 319, 320
Polyethylene adipate 463
Polyethylene oxide 208
Polyethylene succinate 208
Polyethylene terephthalate fibres
–, annealing 591–597
–, birefringence 592, 617, 618
–, cohesion energy, molecular 602, 604, 605
–, critical dissolution time 592, 593, 602–604
–, crystallinity 593, 595, 597, 598
–, crystallinity degree 601, 605, 609
–, DSC 593
–, diffusion 608, 609, 612
–, dyestuff penetration 608–610
–, fibre morphology 617
–, fibres 615, 616, 618, 620, 621
–, fibril lamellar structure 591
–, filament 607, 609
–, heat capacity 591, 593, 594
–, heat treatment 601
–, IR dichroism 602
–, IR spectra 616
–, intermolecular cohesion 594, 598
–, molecular orientation 602–604, 618
–, optical microscopy 617, 622
–, orientation 592, 593, 595, 597, 608, 609, 613
–, polymer layer thickness 608, 610
–, processing 601
–, SEM 618
–, SAXS 617
–, superstructure 615
–, taut tie molecules 592, 595, 598
–, thermal expansivity 591, 596
–, WAXS 602, 603
–, Young's modulus 591
Polyethylene terephthalate fibres, textile
–, conformation changes 620
–, crystallinity degree 625, 627, 628
–, deformation 625
–, drawing ratio 626
–, fibre morphology 617
–, IR spectra 616
–, internal structure 627
–, morphological structure 620, 621, 625–627
–, orientation 625, 626, 628
–, orientation degree 618
–, relaxation modulus 629
–, shift function 625, 627, 628
–, shrinkage resistance 625
–, surface structure 627
–, tensile relaxation 626
–, textil fibres 625
–, viscoelastic properties 625
–, WLF equation 628
Polyethylene terephthalate foils
–, annealing & stretching 699
–, birefringence 699
–, charge carrier mobility 699
–, conductivity 699
–, conformation 143
–, crystallinity 699, 701
–, crystallinity degree 700
–, dielectric properties 699
–, electric polarization 699
–, isothermal depolarization current 700–702, 704
–, storage charge 701, 704
–, structure effect 699
–, thermostimulated depolarization currents 702–704
Polyethylene terephthalate glasses
–, amorphous state 457, 458
–, birefringence 458, 461, 462
–, draw ratio 458
–, DSC 457, 462
–, heating rate 458
–, isothermal melt crystallization 457
–, nucleation 457–459
–, stretch elongation curves 458
–, undrawn fibres 458, 459
–, water shrinkage 458
Polyethylene terephthalate, structure differentiation
–, aminolysis 633 ff
–, comonomer content, effect on 633
–, crystallization during aminolysis 637

EBSCOhost - printed on 2/13/2023 3:45 AM via . All use subject to https://www.ebsco.com/terms-of-use

–, draw ratio, effect on 633
–, electron microscopy 634
–, morphological changes 634
–, spinning velocity, effect on 633
–, weight loss 632
Poly (4-methyl pentene-1) 93
Polyglycine 509, 512
–, anisotropic shrinkage 509, 510, 512
–, crystalline structure
–,–, at low temperature 509
–,–, under extreme conditions 509
–, pleated sheet structure 509, 510, 512
–, x-ray diffraction pattern 509, 511, 512
Polyisoprene, cis 1,4- 197
Polymethyl methacrylate 542, 543, 547
Polyoxyethylene 165 ff
Polyoxymethylene 208
Polyoxypropylene 208
Poly-p-phenylene terephthalamide, 2
Poly-p-phenylene benzbisthiazole, 1
Polyphosphazenes
–, poly-bis(phenoxy)phosphazene, PBPP 435, 437–440
–, poly-bis(trifluoroethoxy)-phosphazene, PBFP 435, 437, 439, 440, 442
–,–, cospherical platelet morphology 435
–,–, electron microscopy 437–443
–,–, fibrilar texture 441
–,–, film 437, 441
–,–, fracture surface morphology 441, 442
–,–, glass formation 444
–,–, liquid crystals 442
–,–, optical microscopy 437
–,–, SEM 437, 441
–,–, T_g 442
–,–, thermotropic transition 435
–,–, twinned crystals 439, 440
Polypropylene 49–53, 56–67, 76, 77, 87, 127, 190, 195
–, crosslinking 307
–, crystalline structure 303, 307
–, DSC 304–306
–, diffraction patterns 288, 289, 304–306
–, fibre structure 573–575
–,–, lamellar 578, 582
–,–, supermolecular 574, 575, 577–582
–, hard-elastic fibres 573–576, 578, 581
–, heat treatment 305
–, high-speed melt spinning 574
–, interlamellar regions 576, 582
–, melting 237, 305
–, microvoids 573, 577–582
–, morphology 575, 578, 581, 582
–, non-crystalline region 577, 578
–, oriented, doubly 288, 295
–, polypropylene (i) 208, 236, 237, 260
–, polypropylene, irradiated 303, 304
–, porosity 575, 579–581
–,–, microporosity 575, 580–582
–,–, microporous fibres 573, 581, 582
–, shear strength 304
–, SAXS 576, 577, 578, 580–582
–, spherulites 279, 280, 283–285
–, tie chains 576, 577, 582
–, WAXS 304, 305, 575, 576
Polypropylene blends
–, blend 189, 193, 194, 347, 348, 350, 351
–, chain orientation 261 ff
–, melt history 347
–, morphology 347
–, nucleation 347, 348, 352
–, PP/polyamide 260 ff
–, PP/polyethylene 259 ff, 347, 348, 350–352
–, PP/polyglycol 189, 193, 194
–, SEM 351
–, spherulites 348, 352, 377
–, surface tension 352
Polypropylene composite with glass fibres, pigments, etc.
–, hard-elastic fibres 573, 576, 578, 581
–,–, elastic recovery 574
Polypropylene: structure and orientation
–, anisotropic mechanical 271, 274
–, anisotropy degree 275
–, chain orientation 261
–, core 273
–, crystallite orientation 271, 273
–, drawing 661, 662
–, failure 275
–, fibrilar nucleation and growth 273
–, fibrillation 661, 667
–, impact properties 272, 275, 276
–, lamellae 274
–, melt flow 271
–, microfibrilar model 661
–, microstructure 272, 273, 276
–, orientation, molecular 271, 273
–, polarization microscopy 272
–, porosity 663
–, proccessing conditions 271
–, propylene-ethylene block
–,–, copolymer 271, 279, 280, 291–295
–, roughness analysis 272
–, SEM 272
–, spherulitic structure 273
–, structure 661
–, tensile properties 272, 275
–, transition zone 273
–, WAXS 272, 274, 276
Polystyrene
–, bundles of lamellae 392, 393
–, cellulation 387, 395

EBSCOhost - printed on 2/13/2023 3:45 AM via . All use subject to https://www.ebsco.com/terms-of-use

–, characteristic length, lamellae 392
–, crystallization temperature 388, 392, 395, 396
–, fibrous units 392
–, growth 393–395, 398
–, lamellae 388–392, 395
–, lamellar organization 387
–, lamellar texture 387
–, lamellar thickness 387
–, permanganic etching 387–389
–, polyethylene 387
–, polypropylene 387, 391
–, polystyrene 208, 388, 393, 395–397
–, TEM 388–393, 396, 397
Polyurethane
–, adhesion strength 521
–, crack 550
–, crystallization kinetics 521, 522
–, crystal size 522
–, fracture surface 549, 550, 552
–,–, below T_g 549
–, internal stresses 521, 525, 526
–, lamellar structure 522
–, melting crystal 524, 525
–, melting point 522
–, mesomorphic state 521, 523
–, oligomer block flexibility 522, 525
–, optical microscopy 551, 553
–, polymerization kinetics 523–525
–, proton magnetic resonance 521
–, SEM 525
–, spherulites 522
–, structure and properties 521
–, supermolecular organization 522, 524–526
–, tensile test 550, 551
Polyvinyl acetate 681, 687
Polyvinyl alcohol gels
–, degradation 731, 734
–, drawing of gel 731, 733
–, draw ratio 731, 733, 734, 736
–, fibre temperature 732
–, gels 731–734, 736
–, high modulus fibres 731
–, isothermal drawing 732, 733, 736
–, mechanical properties 732
–, modulus 734–736
–, tensile testing 731
–, zone drawing 731, 733
Poly-N-vinylcarbazole 681, 689
Polyvinylidene fluoride
–, beta-phase content 673
–, crystallinity 673, 674, 676–679
–, d_3, coefficient 674, 677, 678
–, dipole orientation 673, 674, 676, 679
–,–, distribution of 675, 678
–, drawing 673
–, electric field strength 674–679
–, IR technique 673
–, orientation modes 674, 675
–, piezoelectric measurements 673, 678
–, pole figure 674, 678
–, poling 674, 675, 678
–, poling time 673, 674
–, texture analysis 673
–, transmission technique 674
–, x-ray technique 673, 674
Polyvinyl chloride 754
–, crystallinity 376
–, domains 373, 374
–, extrusion 378
–, gelation 378
–, impact modified 381, 383
–, microdomains (clusters) 373, 374
–, plasticiser absorption 378
–, primary particles 371, 373, 376, 378
–, specific surface area, plasticiser 378
–, steric stabiliser 373
–, suspension, process 371, 373
Pores 759, 761, 762
Porosity 663
–, macroporosity 761
–, maximal 763
–, microporosity 575, 580–582
–, permanent 761
–, swelling porosity 759
Porous
–, microporous fibres 573, 581, 582
–, polymer 760
–, sorbent 759
Premelting 179, 184, 188
Primary
–, fold length 4
–, nucleation 217–221
–, particles 371, 373, 376, 378
Process 281, 291
–, crystallization 119–121, 127
–, emission 227
–, solution 365
Proton magnetic resonance 521

Quadrite 259, 261, 262, 264, 267, 269
Quadrupole mass spectrometer 655
Quantum interpretation 211, 221
–, crystallization rate 225, 229, 231
–, secondary nucleation 225
Quasi-net inversion 406
Quenching 564

Radiation damage 48, 49
Radiation grafting 647
Raman LAM method 4, 21
Rate
–, crystallization 206

EBSCOhost - printed on 2/13/2023 3:45 AM via . All use subject to https://www.ebsco.com/terms-of-use

-, melting 825
Reacting structural fraction, cellulose 499
Reaction injection moulding, RIM 427
Recrystallization 129, 131, 134, 135, 179, 184, 188, 363, 499
Refractive index 850, 851
Regular folding 157
Relaxation
-, modulus 629
-, phenomena 198
-, regions 400, 403
-, time 717, 720, 721
Reptation 214, 217, 225
Resins
-, adsorbent resins 757
-, CXA resin 104, 107-112
-, divinylbenzene 758, 763
-, epoxy resins
-,-, fracture surface 543-545
-, gel type polymer 760
-, inerts 758, 762
-, ion exchange 757, 761, 763
-, macronet polymer 764
-, macromolecular network 764
-, polymer reagent 767
Ring spherulite structure 463
-, birefringence 463, 464, 466
-, enhanced self nucleation 460
-, polarization microscope 463, 465, 466
-, polyethylene adipate, in 463
-, spherulites 463-465
Rheological, viscosity 411, 412, 415, 417
Rolltrusion process 281, 291
Roughness analysis 272
Rubber particles 428, 750

Scanning electron microscopy 292, 324, 337-339, 351, 432, 433, 437, 441, 469, 470, 473, 474, 477, 481, 483, 524, 529, 541, 543-547, 556, 558, 559, 575, 582, 586, 588, 589, 618, 646, 647
Secondary nucleation rate 14, 16, 211-217, 225, 230, 231
Sectors in polymer crystals 158 ff
Seeding temperature 171
Segment
-, amorphous 235
-, deformation 74
-, growing 209
-, orientation 74
-, segregation 59
Selective etching of polyolefins 309
-, amorphous region 309, 310, 313-315, 317
-, defective region 309, 310, 313-315, 317
-, etching efficiency 313
-, etching isotherms 311, 312, 315
-, etching rate 310
-, $KMnO_4$+o-H_3PO_4 309-313
-, $KMnO_4$+H_2SO_4 309-313
-, morphology 317
-, passivation 311, 313, 317
-, polyethylene, linear, branched 309, 313
-, i-polypropylene 309, 310, 313
-, quenched samples 313
-, thickness of removed layer 310, 313-316
Self-seeding method 92, 171
Semicrystalline structure 709
Semithin sections 750, 751
Sequence length distribution 363
Shape
-, particles, of 751
-, sheaf-like structure 754
Shear-lag model 81
Shear
-, loading 69, 555
-, strength 304
-,-, interlaminar 556-560
-, stress 105
-, viscosity 105
Shift function 625, 627, 628
Shish-kebab structure 494-496
Shrinkage 180-187, 509, 510, 512, 527, 529-531, 625
Single crystal 14, 48, 154, 171 ff
Skin-core structure 299
Skin thickness 301, 302
Small-angle light scattering (SALS) 119, 337, 338, 340, 342, 421, 423, 452, 617
Small-angle neutron scattering 15, 18, 32, 137
Small-angle x-ray scattering 4, 11, 32, 93, 99, 119, 120, 126, 338, 340, 342, 421, 473, 474, 541, 575, 576, 578, 580-582, 617
Sodium cellulose 489
Sol 338-341
Sol/gel component 338-341
Solubility 299, 454, 655
Solution history 93
Sonic velocity 528, 537
Spatial analysis 750, 751
Specific surface area 378
Spherulites 13, 49, 58, 59, 63, 64, 67, 71, 120-122, 127, 133, 273, 279, 280, 283-285, 298, 299, 347, 348, 352, 463-465, 522, 563-567, 569
-, birefringence 280
-, films 281
-, growth 401, 413-416, 418, 419
-, morphology 13, 120-.122, 127, 133, 282, 440, 754
-, polybutylene 93 ff
-, polycarbonate 541
-, polyethylene 337, 340-342, 345
-, structure 754
Spin diffusion 355

EBSCOhost - printed on 2/13/2023 3:45 AM via . All use subject to https://www.ebsco.com/terms-of-use

Spinodal decomposition of crystal defects 127
Spinning velocity 633
Splitting and bending 585, 589, 590
Spontaneous polarization 714
Spring bead model 718
Spruce wood pulp 493, 496
Stabilization of disperse elastomer 408
Stereology 750, 751
Steric stabilizers PVC 373
Stiffness 47, 530, 715
Storage charge 701, 704
Storage modulus 105
Strain 73, 77, 528, 530, 534, 537, 538
–, rate 69
Strength 47, 69, 82, 530, 532
Stress 70, 73, 77, 79, 81, 528, 530, 534, 538
–, entropy 241
–, hardening/softening 651
Stretching 458, 501, 506
Structure 273, 319, 329, 469, 661, 754, 755
–, film 661
–, polyacetylene, of 469
–, sheaf-like 754
–, spherulites 278
Structural stability 509
Supercooling 7–9, 15–22, 24, 25, 34, 36, 37
Supermolecular structure/order 69, 337, 421, 480, 504, 505, 522, 524–526, 574, 575, 577–582, 585, 615
Surface 112, 179, 244, 297, 319, 352, 587–590, 669
–, enthalpy 244
–, layer 297
–, microstructure 669
–, morphology 319, 587
–, region 319
–, surface coating 589–590
–, tension 352
Suspension process 371, 373
Swelling
–, behaviour 143, 149
–, dispersity 759, 760
–, porosity 759
Synchrotron radiation 8, 22, 23, 119, 125, 227, 229, 232, 421
Synergism, effect of 114, 115

Taut tie molecules 72, 74, 75, 576, 577, 582, 591, 592, 595, 598
Temporary polymer networks 717, 720, 727
Tensile
–, properties 272, 275, 647
–, relaxation 622
–, strength 81, 501, 502, 527, 536, 585, 586
–, test(ing) 550, 551, 731
Tensor of material constant 710
Terraced morphology 284, 290
Textile fibres 621
Texture
–, analysis 669
–, anisotropic properties 707
–, averaged physical properties 707
–, compliance 714
–, cross-hatched type 279
–, crystalline polymers 3
–, dielectric constant 714
–, orientation distribution function 708
–,–, loss of information 709
–, piezoelectric constant 714
–, pole figure 708
–, semicrystalline structure 709
–, spontaneous polarization 714
–, stiffness 714
–, unit-element model 711
–, x-ray 707
Thermal
–, decomposition 645, 648
–, expansion 591
–, history 199, 201
Thermally stimulated, depolarization (TSD) 197
Thermoanalytical measurements 646, 649
Thermogravimetry 189
Thermomechanical
–, analysis 190
–, behaviour 651
Thermooxidation
–, amorphous phase 563, 565
–, chain scission 563, 569
–, chain strain 564
–, crystalline phase 564, 565
–, deformation 564
–, lamellae 563, 564
–, lamella thickness 565
–, morphology, effect of 563
–, oxygen diffusion 563
–, oxygen uptake 568
–, quenching 564
–, semicrystalline polymers 563
–, SAXS 564
–, spherulites 563, 567, 569
–, thermooxidation process 563, 565, 567, 569
Thermooxidative ageing 504, 505, 556, 557
Thermostimulated depolarization current 702, 704
Thermostimulated luminescence 401, 402
Thermotropic transition 435, 438
Thickness of lamella 12, 176, 203, 237, 238
Toughness 527, 532, 537
Transition
–, activation entropy 208
–, glass transition 107, 145–147, 442, 736, 765, 776
–, probability 720
–, temperatures 107

EBSCOhost - printed on 2/13/2023 3:45 AM via . All use subject to https://www.ebsco.com/terms-of-use

–, zone 273
Transmission electron microscopy, TEM 47, 49, 51, 67, 322, 382–385, 406, 407, 409, 412, 413, 417, 477, 478, 480
Truncation ratio 160, 161, 163
Twinned crystals 439, 440

Ultramicrotomy 749, 750
Ultra thin sections 750
Uniaxially drawn fibres 319, 320
Unit-element model 711

Viscoelastic properties 33
Viscosity 105, 501
Voids 471

Water cellulose 489
Water shrinkage 458
Wavelength 249, 250, 253
Wave number 250–253
Wide-angle x-ray scattering (WAXS) 146, 150, 151, 272, 274, 276, 304, 305, 421, 575, 576, 602, 603
Williams-Landel-Ferry (WLF) equation 193, 206, 628

X-ray 74, 707
X-ray irradiation (dosis) 399, 669, 670

Young's modulus 268, 530, 533, 591

Zone drawing 731, 733

EBSCOhost - printed on 2/13/2023 3:45 AM via . All use subject to https://www.ebsco.com/terms-of-use

Polymer Composites

Proceedings · 28th Microsymposium on Macromolecules
Prague, Czechoslovakia, July 8–11, 1985

Editor B. Sedláček

1986. 17 cm x 24 cm. XII, 627 pages. Numerous illustrations. Hardcover.
DM 290,–; approx. US $131.80 ISBN 3 11 010994 8

Polymer Composites are very modern and effective materials. They considerably extend the palette of unconventional morphological structures (textures) and thus broaden the field of interesting problems to be solved.
The Symposium-Proceedings give useful information about the present state in this important field of research.

Contents (Main Chapters)
Introduction Articles · Preparation-Properties-Use · Mechanical Stability of Composites · Structures and Methods · Abbreviations · Subject Index.

Physical Optics of Dynamik Phenomena and Processes in Macromolecular Systems

Proceedings · 27th Microsymposium on Macromolecules
Prague, Czechoslovakia, July 16–17, 1984

Editor B. Sedláček

1985. 17 cm x 24 cm. XV, 555 pages. Numerous illustrations.
Hardcover. DM 210,–; approx. US $95.50 ISBN 3 11 010234 X

The contributions contained in this book deal with one of the most progressive trends in science, which leads from the "static" average description to the "dynamic" characterization and understanding of "in time or space varying" phenomena and intermolecular or intramolecular processes. Several important theoretical papers and many efficient applications of the methods described present a good survey of the present state of knowledge in this field and a representative cross-section of current topics which are in focus of interest.

Contents (Main Chapters)
Dilute and Semidilute Solutions · Concentrated Systems: Gel and Solids · Intramolecular Phenomena and Process · Intermolecular Phenomena and Processes · Theoretical and Experimental Methods · Contributors · Subject Index.

Prices are subject to change without notice

WALTER DE GRUYTER · BERLIN · NEW YORK

Verlag Walter de Gruyter & Co., Genthiner Str. 13, D-1000 Berlin 30, Tel.: (0 30), 2 60 05-0, Telex 1 84 027
Walter de Gruyter, Inc., 200 Saw Mill River Road, Hawthorne, N.Y. 10532, Tel.: (914) 747-0110, Telex 64 6677

EBSCOhost - printed on 2/13/2023 3:45 AM via . All use subject to https://www.ebsco.com/terms-of-use